IMPACT FACTOR
11.082

#1 NUCLEAR MEDICINE, MOLECULAR IMAGING AND MOLECULAR RADIOTHERAPY JOURNAL

Vol. 63 ■ No. 9 ■ September 2022

JNM

The Journal of Nuclear Medicine

FEATURED ARTICLE

Cardiac Fibroblast Activation in Patients Early After Acute Myocardial Infarction: Integration with MR Tissue Characterization and Subsequent Functional Outcome. Johanna Diekmann et al. See page 1415.

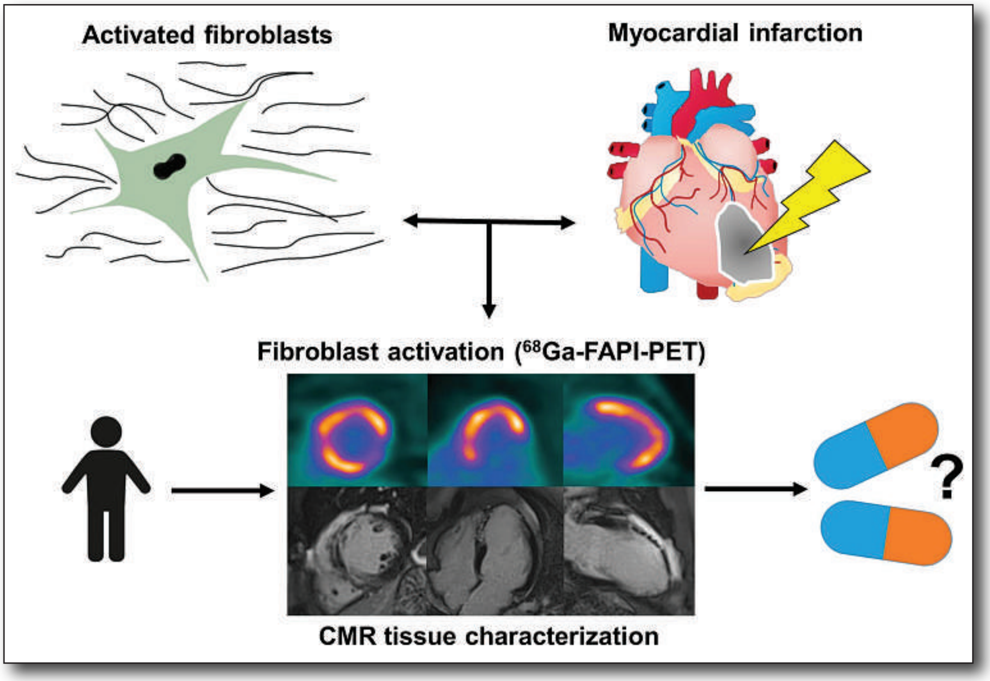

GRPR ligands for therapy: improving ^{177}Lu-labeled gastrin-releasing peptide receptor–targeted ligands for precision prostate and breast cancer treatment. Thomas Günther et al. See page 1364.

SNMMI Value Initiative
SOCIETY OF NUCLEAR MEDICINE & MOLECULAR IMAGING


Bench|mark
Cobalt-57 Flood Source
CAUTION RADIOACTIVE MATERIAL
RADQUAL
Ge-68 Cylinder Phantom
BMCY68-2019 Cylinder
Ge-68 0.000 mCi
Ser #: BMCY68201921057101
Ref. Date: 2/26/2021
CAUTION RADIOACTIVE MATERIAL
FRONT SIDE
BM06E-22
BM06E-33
BM06E-37
Co-57
BM06S-37
BM06S-681
BM06S-33
BM06V-20-37
BM06V-20-57
BM06V-20-33
BM06S-131-M
BM-131-M

SNMMI Therapeutics Conference

November 17-19, 2022 • Washington, DC

Attend the SNMMI Fall Therapeutics Conference

Registration is now available for the **SNMMI Fall Therapeutics Conference, November 17-19, 2022**, at the **Gaylord National Resort and Convention Center**, located on the Potomac River in the Washington, DC metropolitan area. The resort is a short distance from both downtown DC and historic Old Town Alexandria, and is accessible to all three DC area airports. This two-and-a-half-day event will explore the latest innovations and clinical applications in radiopharmaceutical therapy, including:

- Setting up a Theranostics Clinic
- Thyroid Therapies
- Prostate Therapies
- Neuroendocrine Therapies
- Pediatric Therapies
- Radiopharmaceutical Supply Chain
- Dosimetry for Therapies
- Therapy Clinical Trials Primer

Register today: **www.snmmi.org/TC2022**

Early-bird registration deadline: September 29, 2022

PLANNING COMMITTEE

Co-Chairs

Phillip Koo, MD
Banner MD Anderson Cancer Center

Neeta Pandit-Taskar, MD, FSNMMI
Memorial Sloan Kettering Cancer Center

Members

Dmitry D. Beyder, MPA, CNMT
Barnes-Jewish Hospital

Yuni K. Dewaraja, PhD, FSNMMI
University of Michigan

Stephen A. Graves, PhD, DABR
University of Iowa

Thomas A. Hope, MD
University of California San Francisco

Andrei H. Iagaru, MD, FACNM
Stanford University

Daniel Lee, MD
Ochsner Medical Center

Helen R. Nadel, MD, FRCPC, FSNMMI
Lucile Packard Children's Hospital - Stanford

Joseph R. Osborne, MD, PhD, FACNM
New York Presbyterian Hospital (Cornell Campus)

Alan B. Packard, PhD, FSNMMI
Boston Children's Hospital/Harvard Medical School

REACH EVEN GREATER HEIGHTS WITH CARDIAC PET IMAGING

RUBY™ partners with you to help establish and grow your cardiac PET program today – and well into the future. Our RUBY-FILL® (Rubidium Rb 82 Generator) and RUBY Rubidium Elution System™ are supported by our comprehensive line of offerings, including financial modeling, reimbursement consultancy, education, and marketing expertise – as well as 24-hour customer assistance to ensure your growing PET practice runs smoothly and efficiently. **Isn't it time to discover how far you can soar?**

Learn more at: **RUBY-FILL.com**

INDICATION FOR USE:

RUBY-FILL is a closed system used to produce rubidium Rb 82 chloride injection for intravenous use. Rubidium Rb 82 chloride injection is a radioactive diagnostic agent indicated for Positron Emission Tomography (PET) imaging of the myocardium under rest or pharmacologic stress conditions to evaluate regional myocardial perfusion in adult patients with suspected or existing coronary artery disease. (1)

WARNING: HIGH LEVEL RADIATION EXPOSURE WITH USE OF INCORRECT ELUENT AND FAILURE TO FOLLOW QUALITY CONTROL TESTING PROCEDURE

Please see full prescribing information for complete boxed warning

High Level Radiation Exposure with Use of Incorrect Eluent

Using the incorrect eluent can cause high Strontium (Sr 82) and (Sr 85) breakthrough levels (5.1)

- **Use only additive-free 0.9% Sodium Chloride Injection USP to elute the generator (2.5)**
- **Immediately stop the patient infusion and discontinue the use of the affected RUBY-FILL generator if the incorrect solution is used to elute the generator (4)**
- **Evaluate the patient's radiation absorbed dose and monitor for the effects of radiation to critical organs such as bone marrow (2.9)**

Excess Radiation Exposure with Failure to Follow the Quality Control Testing Procedure

Excess radiation exposure occurs when the levels of Sr 82 or Sr 85 in the Rubidium Rb 82 Chloride injection exceed specified limits. (5.2)

- **Strictly adhere to the generator quality control testing procedure (2.6)**
- **Stop using the generator if it reaches any of its Expiration Limit. (2.7)**

The risk information provided here is not comprehensive. Please visit RUBY-FILL.com for full Prescribing Information including BOXED WARNING. You are encouraged to report negative side effects of prescription drugs to the FDA. Visit www.fda.gov/Safety/MedWatch or call 1-800-FDA-1088.

Jubilant DraxImage Inc. dba Jubilant Radiopharma™
16751 Trans-Canada Highway, Kirkland, Quebec, Canada H9H 4J4
Phone: 1.888.633.5343 / 514.630.7080
www.jubilantradiopharma.com
© 2022-US-RUBY-00002

RUBY FILL®
RUBIDIUM Rb82 GENERATOR

JUBILANT
RADIOPHARMA

JNM

Volume 63 • Number 9 • September 2022

SNMMI NEWSLINE

DISCUSSIONS WITH LEADERS

THE STATE OF THE ART

HOT TOPICS

CONTINUING EDUCATION

FOCUS ON MOLECULAR IMAGING

EDITORIAL

THERANOSTICS

Clinical

Basic

ONCOLOGY

Clinical

Translational

Basic

NEUROLOGY

Basic

CARDIOVASCULAR

Clinical

AI/ADVANCED IMAGE ANALYSIS

ENDOCRINOLOGY

Clinical

RADIOBIOLOGY/DOSIMETRY

THE ILLUSTRATED POST

LETTERS TO THE EDITOR

DEPARTMENTS

JNM The Journal of NUCLEAR MEDICINE

The Official Publication of **SNMMI**

MISSION STATEMENT: *The Journal of Nuclear Medicine* advances the knowledge and practice of molecular imaging and therapy and nuclear medicine to improve patient care through publication of original basic science and clinical research.

JNM (ISSN 0161-5505 [print]; ISSN 2159-662X [online]) is published monthly by SNMMI, 1850 Samuel Morse Drive, Reston, VA 20190-5316. Periodicals postage is paid at Herndon, VA, and additional mailing offices. Postmaster, send address changes to *The Journal of Nuclear Medicine,* 1850 Samuel Morse Drive, Reston, VA 20190-5316. The costs of publication of all nonsolicited articles in *JNM* were defrayed in part by the payment of page charges. Therefore, and solely to indicate this fact, these articles are hereby designated “advertisements” in accordance with 18 USC section 1734.

DISCLOSURE OF COMMERCIAL INTEREST: Johannes Czernin, MD, editor-in-chief of *The Journal of Nuclear Medicine,* has indicated that he is a founder of Sofie Biosciences and holds equity in the company and in intellectual property invented by him, patented by the University of California, and licensed to Sofie Biosciences. He is also a founder and board member of Trethera Therapeutics and holds equity in the company and in intellectual property invented by him, patented by the University of California, and licensed to Triangle. He also serves on the medical advisory board of Actinium Pharmaceuticals and on the scientific advisory boards of POINT Biopharma, RayzeBio, and Jubilant Pharma and is a consultant for Amgen. No other potential conflicts of interest were reported. Manuscripts submitted to *JNM* with potential conflicts are handled by a guest editor.

EDITORIAL COMMUNICATIONS should be sent to: Editor-in-Chief, Johannes Czernin, MD, *JNM* Office, SNMMI, 1850 Samuel Morse Drive, Reston, VA 20190-5316. Phone: (703) 326-1185; Fax: (703) 708-9018. To submit a manuscript, go to https://submit-jnm.snmjournals.org.

BUSINESS COMMUNICATIONS concerning permission requests should be sent to the publisher, SNMMI, 1850 Samuel Morse Drive, Reston, VA 20190-5316; (703) 708-9000; home page address: jnm.snmjournals.org. Subscription requests and address changes should be sent to Membership Department, SNMMI at the address above. Notify the Society of change of address and telephone number at least 30 days before date of issue by sending both the old and new addresses. Claims for copies lost in the mail are allowed within 90 days of the date of issue. Claims are not allowed for issues lost as a result of insufficient notice of change of address. For information on advertising, contact Team SNMMI (Kevin Dunn, Rich Devanna, and Charlie Meitner; (201) 767-4170; fax: (201) 767-8065; TeamSNMMI@cunnasso.com). Advertisements are subject to editorial approval and are restricted to products or services pertinent to nuclear medicine. Closing date is the first of the month preceding the date of issue.

INDIVIDUAL SUBSCRIPTION RATES for the 2022 calendar year are $603 within the United States and Canada; $648 elsewhere. Make checks payable to the SNMMI. CPC IPM Sales Agreement No. 1415158. Sales of individual back copies from 1999 through the current issue are available for $60 at http://www.snmmi.org/subscribe (subscriptions@snmmi.org; fax: (703) 667-5134). Individual articles are available for sale online at http://jnm.snmjournals.org.

JNM The Journal of NUCLEAR MEDICINE

EDITOR-IN-CHIEF
Johannes Czernin, MD
University of California at Los Angeles
Los Angeles, California

IMMEDIATE PAST EDITOR
Dominique Delbeke, MD, PhD
Vanderbilt University Medical Center
Nashville, Tennessee

NEWSLINE EDITOR
Harvey A. Ziessman, MD
Takoma Park, Maryland

ASSOCIATE EDITORS, CONTINUING EDUCATION
Hossein Jadvar, MD, PhD, MPH, MBA, FACNM, FSNMMI
University of Southern California
Los Angeles, California
Lale Kostakoglu, MD, MPH
University of Virginia Health System
Charlottesville, Virginia

ASSOCIATE EDITORS
Ramsey Derek Badawi, PhD
UC Davis Medical Center
Sacramento, California
Henryk Barthel, MD, PhD
Leipzig University
Leipzig, Germany
Frank M. Bengel, MD
Hannover Medical School
Hannover, Germany
Lisa Bodei, MD, PhD
Memorial Sloan Kettering Cancer Center
New York, New York
Irene Buvat, PhD
Université Paris Sud
Orsay, France
Jérémie Calais, MD
University of California at Los Angeles
Los Angeles, California
Marcelo F. Di Carli, MD
Brigham and Women's Hospital
Boston, Massachusetts
Alexander E. Drzezga, MD
University Hospital of Cologne
Cologne, Germany
Jan Grimm, MD, PhD
Memorial Sloan Kettering Cancer Center
New York, New York
Ken Herrmann, MD, MBA
Universitätsklinikum Essen
Essen, Germany
Thomas A. Hope, MD
University of California, San Francisco
San Francisco, California
Jason S. Lewis, PhD
Memorial Sloan Kettering Cancer Center
New York, New York
David A. Mankoff, MD, PhD
University of Pennsylvania
Philadelphia, Pennsylvania
Heiko Schöder, MD
Memorial Sloan Kettering Cancer Center
New York, New York
Wolfgang Weber, MD
Technical University of Munich
München, Germany

SERIES EDITOR, FOCUS ON MI
Carolyn J. Anderson, PhD
University of Missouri
Columbia, Missouri

SERIES EDITOR, HOT TOPICS
Heinrich R. Schelbert, MD, PhD
University of California at Los Angeles
Los Angeles, California

CONSULTING EDITORS
Nancy Knight, PhD
University of Maryland School of Medicine
Baltimore, Maryland
Barry A. Siegel, MD
Mallinckrodt Institute of Radiology
St. Louis, Missouri
Arnold M. Strashun, MD
SUNY Downstate Medical Center
Scarsdale, New York
H. William Strauss, MD
Memorial Sloan Kettering Cancer Center
New York, New York

ASSOCIATE EDITORS (INTERNATIONAL)
Gerald Antoch, MD
Dusseldorf, Germany
Richard P. Baum, MD, PhD
Bad Berka, Germany
Ambros J. Beer, MD
Ulm, Germany
François Bénard, MD, FRCPC
Vancouver, Canada
Thomas Beyer, PhD
Vienna, Austria
Andreas K. Buck, MD, PhD
Würzburg, Germany
Ignasi Carrió, MD
Barcelona, Spain
June-Key Chung, MD
Seoul, Korea
Stefano Fanti, MD
Bologna, Italy
Markus Hacker, MD
Wien, Austria
Rodney J. Hicks, MD, FRACP
Melbourne, Australia
Michael S. Hofman, MBBS, FRACP
Melbourne, Australia
Ora Israel, MD
Haifa, Israel
Andreas Kjaer, MD, PhD, DMSc
Copenhagen, Denmark
Adriaan A. Lammertsma, PhD
Amsterdam, The Netherlands
Michael Lassman, PhD
Würzburg, Germany
Helmut R. Mäcke, PhD
Freiburg, Germany
Wim J.G. Oyen, MD, PhD
Milan, Italy
John O. Prior, MD, PhD
Lausanne, Switzerland
Osman Ratib, MD, PhD
Geneva, Switzerland
Mike Sathekge, MBChB, MMed, PhD
Pretoria, South Africa
Markus Schwaiger, MD
München, Germany
Andrew M. Scott, MD
Heidelberg, Australia
Nagara Tamaki, MD, PhD
Kyoto, Japan
Jia-He Tian, PhD
Beijing, China
Mei Tian, MD, PhD
Hangzhou, China

EDITORIAL CONSULTANTS
Martin S. Allen-Auerbach, MD
Los Angeles, California
Magnus Dahlbom, PhD
Los Angeles, California
Andrew Quon, MD
Los Angeles, California
Christiaan Schiepers, MD, PhD
Los Angeles, California
Daniel H. Silverman, MD, PhD
Los Angeles, California
Roger Slavik, PhD
Winterthur, Switzerland

EDITORIAL BOARD
Diane S. Abou, PhD
St. Louis, Missouri
Valentina Ambrosini, MD, PhD
Bologna, Italy
Norbert Avril, MD
Cleveland, Ohio
Shadfar Bahri
Los Angeles, California
Jacques Barbet, PhD
Saint-Herbalin, France
Bradley Jay Beattie, PhD
New York, New York
Matthias Richard Benz, MD
Los Angeles, California
Elie Besserer-Offroy, PhD, FACSc
Los Angeles, California
Pradeep Bhambhvani, MD
Birmingham, Alabama
Angelika Bischof-Delaloye, MD
Lausanne, Switzerland
Christina Bluemel, MD
Würzburg, Germany
Ronald Boellaard, PhD
Groningen, The Netherlands
Nicolaas Bohnen, MD
Ann Arbor, Michigan
Wesley E. Bolch, PhD
Gainesville, Florida
Elias H. Botvinick, MD
San Francisco, California
Winfried Brenner, MD, PhD
Berlin, Germany
Richard C. Brunken, MD
Cleveland, Ohio
Ralph Buchert, PhD
Hamburg, Germany
Alfred Buck, MD
Menzingen, Switzerland
Denis B. Buxton, PhD
Bethesda, Maryland
Weibo Cai, PhD
Madison, Wisconsin
Federico Caobelli, MD
Basel, Switzerland
Giuseppe Carlucci, PhD
Los Angeles, California
Richard E. Carson, PhD
New Haven, Connecticut
Paolo Castellucci, MD
Bologna, Italy
Franscesco Ceci, MD, PhD
Turin, Italy
Juliano J. Cerci
Curitiba, Brazil
Delphine Chen, MD
Seattle, Washington
Xiaoyuan Chen, PhD
Singapore
Simon R. Cherry
Davis, California
Arturo Chiti, MD
Rozzano, Italy
Peter M. Clark, PhD
Los Angeles, California
Christian Cohade, MD
Montreal, Canada
Ekaterina (Kate) Dadachova, PhD
Saskatoon, Canada
Issa J. Dahabreh, MD
Boston, Massachusetts
Heike Elisabeth Daldrup-Link, MD, PhD
Stanford, California
Farrokh Dehdashti, MD
St. Louis, Missouri
Robert C. Delgado-Bolton, MD, PhD
Logroño, Spain
Thorsten Derlin, MD
Hannover, Germany
Elisabeth G.E. de Vries, PhD
Groningen, The Netherlands
David W. Dick, PhD
Iowa City, Iowa
Vasken Dilsizian, MD
Baltimore, Maryland
Sharmila Dorbala, MBBS
Lexington, Massachusetts
Jacob Dubroff, MD, PhD
Philadelphia, Pennsylvania
Janet F. Eary, MD
Bethesda, Maryland
W. Barry Edwards, PhD
Columbia, Missouri
Matthias Eiber, MD
Munich, Germany
David Eidelberg, MD
Manhasset, New York
Georges El Fakhri, PhD
Boston, Massachusetts
Peter J. Ell, MD
London, United Kingdom

EDITORIAL BOARD, continued

Keigo Endo, MD
Nantan, Japan
Einat Even-Sapir, MD, PhD
Tel Aviv, Israel
Frederic H. Fahey, DSc
Boston, Massachusetts
Melpomeni Fani, PhD, MSc
Basel, Switzerland
Wolfgang Peter Fendler, MD
Essen, Germany
James W. Fletcher, MD
Indianapolis, Indiana
Amy M. Fowler, MD, PhD
Madison, Wisconsin
Kirk A. Frey, MD, PhD
Ann Arbor, Michigan
Andrei Gafita
Los Angeles, California
Victor H. Gerbaudo, PhD, MSHCA
Boston, Massachusetts
Frederik L. Giesel, MD, PhD, MBA
Düsseldorf, Germany
Serge Goldman, MD, PhD
Brussels, Belgium
Stanley J. Goldsmith, MD
New York, New York
Martin Gotthardt, MD, PhD
Nijmegen, The Netherlands
Michael Graham, MD, PhD
Iowa City, Iowa
David Groheux, MD, PhD
Paris, France
Uwe A. Haberkorn, MD
Heidelberg, Germany
Mathieu Hatt, PhD, HDR
Brest, France
Wolf-Dieter Heiss, MD
Cologne, Germany
Karl Herholz, MD
Manchester, United Kingdom
Thomas F. Heston, MD
Las Vegas, Nevada
John M. Hoffman, MD
Salt Lake City, Utah
Carl K. Hoh, MD
San Diego, California
Jason P. Holland, DPhil
Zurich, Switzerland
Roland Hustinx, MD, PhD
Liege, Belgium
Andrei H. Iagaru, MD
Stanford, California
Masanori Ichise, MD
Chiba, Japan
Heather A. Jacene, MD
Boston, Massachusetts
Francois Jamar, MD, PhD
Brussels, Belgium
Jae Min Jeong, PhD
Seoul, Korea
John A. Katzenellenbogen, PhD
Urbana, Illinois
Kimberly A. Kelly, PhD
Charlottesville, Virginia
Laura M. Kenny, MD, PhD
London, United Kingdom
Fabian Kiessling, MD
Aachen, Germany
E. Edmund Kim, MD, MS
Orange, California
Francoise Kraeber-Bodéré, MD, PhD
Nantes, France
Clemens Kratochwil, MD
Heidelberg, Germany
Kenneth A. Krohn, PhD
Portland, Oregon
Brenda F. Kurland, PhD
Pittsburgh, Pennsylvania
Constantin Lapa, MD
Augsburg, Germany
Suzanne E. Lapi, PhD
Birmingham, Alabama
Steven M. Larson, MD
New York, New York
Dong Soo Lee, MD, PhD
Seoul, Korea
Jeffrey Leyton, PhD
Sherbrooke, Canada
Hannah M. Linden, MD
Seattle, Washington
Martin A. Lodge, PhD
Baltimore, Maryland
Katharina Lückerath, PhD
Los Angeles, California
Susanne Lütje, MD, PhD
Bonn, Germany
Umar Mahmood, MD, PhD
Boston, Massachusetts
H. Charles Manning, PhD
Nashville, Tennessee
Giuliano Mariani, MD
Pisa, Italy
Chester A. Mathis, PhD
Pittsburgh, Pennsylvania
Alan H. Maurer, MD
Philadelphia, Pennsylvania
Jonathan McConathy, MD, PhD
Birmingham, Alabama
Alexander J.B. McEwan, MD
Edmonton, Canada
Yusuf Menda, MD
Iowa City, Iowa
Philipp T. Meyer, MD, PhD
Freiburg, Germany
Matthias Miederer, MD
Mainz, Germany
Erik Mittra, MD, PhD
Portland, Oregon
Christine E. Mona, PhD
Los Angeles, California
Dae Hyuk Moon, MD
Seoul, Korea
Jennifer Murphy, PhD
Los Angeles, California
Helen Nadel, MD, FRCPC
Stanford, California
Matthias Nahrendorf, MD, PhD
Boston, Massachusetts
Yuji Nakamoto, MD, PhD
Kyoto, Japan
David A. Nathanson, PhD
Los Angeles, California
Sridhar Nimmagadda, PhD
Baltimore, Maryland
Egbert U. Nitzsche, MD
Aarau, Switzerland
Medhat M. Osman, MD, PhD
Saint Louis, Missouri
Christopher J. Palestro, MD
New Hyde Park, New York
Miguel Hernandez Pampaloni, MD, PhD
San Francisco, California
Neeta Pandit-Taskar, MD
New York, New York
Ashwin Singh Parihar, MBBS, MD
Saint Louis, Missouri
Michael E. Phelps, PhD
Los Angeles, California
Gerold Porenta, MD, PhD
Vienna, Austria
Sophie Poty, PhD
Montpellier, France
Edwin (Chuck) Pratt, PhD, MS Eng
New York, New York
Daniel A. Pryma, MD
Philadelphia, Pennsylvania
Valery Radchenko, PhD
Vancouver, Canada
Caius G. Radu, MD
Los Angeles, California
Isabel Rauscher, MD
Munich, Germany
Nick S. Reed, MBBS
Glasgow, United Kingdom
Mark Rijpkema, PhD
Nijmegen, The Netherlands
Steven P. Rowe, MD, PhD
Baltimore, Maryland
Mehran Sadeghi, MD
West Haven, Connecticut
Orazio Schillaci, MD
Rome, Italy
Charles Ross Schmidtlein, PhD
New York, New York
David M. Schuster, MD
Atlanta, Georgia
Travis Shaffer, PhD
Stanford, California
Sai Kiran Sharma, PhD
New York, New York
Anthony F. Shields, MD, PhD
Detroit, Michigan
Barry L. Shulkin, MD, MBA
Memphis, Tennessee
Yu Shyr, PhD
Nashville, Tennessee
Albert J. Sinusas, MD
New Haven, Connecticut
Riemer H.J.A. Slart, MD, PhD
Groningen, The Netherlands
Piotr Slomka, PhD, FACC
Los Angeles, California
Simon John Christoph Soerensen, MD
Stanford, California
Ida Sonni, MD
Los Angeles, California
Michael G. Stabin, PhD
Richland, Washington
Lisa J. States, MD
Philadelphia, Pennsylvania
Sven-Erik Strand, PhD
Lund, Sweden
Rathan M. Subramaniam, MD, PhD, MPH
Dunedin, New Zealand
John Sunderland, PhD
Iowa City, Iowa
Suleman Surti, PhD
Philadelphia, Pennsylvania
Julie Sutcliffe, PhD
Sacramento, California
David Taieb, MD, PhD
Marseille, France
Laura H. Tang, MD, PhD
New York, New York
Ukihide Tateishi, MD, PhD
Tokyo, Japan
James T. Thackeray, PhD
Hannover, Germany
Mathew L. Thakur, PhD
Philadelphia, Pennsylvania
Alexander Thiel, MD
Montreal, Canada
Daniel L.J. Thorek, PhD
St. Louis, Missouri
David W. Townsend, PhD
Singapore
Timothy Turkington, PhD
Durham, North Carolina
Gary A. Ulaner, MD, PhD
Irvine, California
David Ulmert, MD, PhD
Los Angeles, California
Christopher H. van Dyck, MD
New Haven, Connecticut
Douglas Van Nostrand, MD
Washington, District of Columbia
Patrick Veit-Haibach, MD
Toronto, Canada
Nerissa Viola-Villegas, PhD
Detroit, Michigan
John R. Votaw, PhD
Atlanta, Georgia
Richard L. Wahl, MD
St. Louis, Missouri
Anne Marie Wallace, MD
La Jolla, California
Martin A. Walter, MD
Geneva, Switzerland
Rudolf A. Werner, MD
Wuerzburg, Germany
Andreas G. Wibmer, MD
New York, New York
Anna M. Wu, PhD
Duarte, California
Randy Yeh, MD
New York, New York
Hyewon (Helen) Youn, PhD
Seoul, Korea
Pat B. Zanzonico, PhD
New York, New York
Brian M. Zeglis, PhD
New York, New York
Robert Zeiser, MD
Freiburg, Germany
Hong Zhang, MD, PhD
Hangzhou, China
Hongming Zhuang, MD, PhD
Philadelphia, Pennsylvania
Sibylle I. Ziegler, PhD
Munich, Germany

ASSISTANT TO THE EDITOR

Joshua N. Wachtel
Los Angeles, California

THIS MONTH IN
JNM

Discussions with leaders: *JNM* editor-in-chief Johannes Czernin continues a series of interviews with leaders in nuclear and molecular imaging and therapy with a conversation with Ora Israel, highlighting her international achievements in the field. . . . . ***Page 1285***

Best practices in AI evaluation: Jha and members of an SNMMI taskforce propose a 4-class framework to evaluate artificial intelligence algorithms for potential, technical task-specific efficacy, clinical decision making, and postdeployment efficacy.. . . . . ***Page 1288***

SSTR imaging in PPGL: Jha and colleagues look at the relatively limited data comparing [^{68}Ga]Ga-DOTATATE and [^{64}Cu]Cu-DOTATATE in somatostatin receptor imaging, including in patients with pheochromocytoma and paraganglioma. . . . . ***Page 1300***

Pretargeting in RIT: Cheal and colleagues provide an educational overview of the current status of radioimmunotherapy of human tumors and pretargeted radioimmunotherapy success and failure in clinical trials, including recent efforts at optimization with novel pretargeting systems.. . . . . . ***Page 1302***

Antibody engineering in nuclear medicine: Rodriguez and colleagues review advances in applications of antibody engineering in immunoPET, immunoSPECT, and radioimmunotherapy, with a focus on optimizing pharmacokinetics, site-specific bioconjugation, modulating Fc interactions, and creating bispecific constructs. . . . . ***Page 1316***

Radionuclide evaluation of brain death: Zuckier updates previous reporting on a widely covered case of brain death, offering additional clinical history, radionuclide image analysis, and a discussion of associated controversy and questions. . . . . ***Page 1323***

^{212}Pb-DOTAMTATE and NETs: Delpassand and colleagues present preliminary results from a phase 1 first-in-humans dose-escalation trial assessing targeted α-emitter therapy with this novel agent in patients with somatostatin receptor–positive neuroendocrine tumors. . . . . ***Page 1326***

^{18}F-rhPSMA-7.3 PET/CT in PCa staging: Langbein and colleagues detail their experience in primary prostate cancer staging with this lead compound of a new class of radiohybrid prostate-specific membrane antigen ligands. . . ***Page 1334***

PSMA PET and postprostatectomy radiation: Ng and colleagues assess the management impact of ^{18}F-DCFPyL PSMA PET/CT in patients with prostate-specific antigen (PSA) recurrence after radical prostatectomy and report on early biochemical response after radiation treatment. . . . . ***Page 1343***

^{68}Ga-PSMA CLI exposure in prostatectomy: Costa and colleagues document the occupational radiation exposure of surgical and histopathology personnel from Cerenkov luminescence imaging–guided robot-assisted radical prostatectomy in a single-injection ^{68}Ga-PSMA PET/CT CLI protocol. . . . . ***Page 1349***

Biodistribution of ^{68}Ga ligands: Klose and colleagues document organ and tumor biodistributions for various radioligand application routes in healthy mice and models of cancers expressing somatostatin receptors, prostate-specific membrane antigen, and fibroblast-activation protein. . . . . ***Page 1357***

GRPR ligands for radioligand therapy: Günther and colleagues report on basic investigations to stabilize a common ^{177}Lu gastrin-releasing peptide receptor–targeted ligand for applications in therapy of GRPR-expressing malignancies. . . . . ***Page 1364***

uPAR PET in NENs: Carlsen and colleagues report on the utility of a novel urokinase plasminogen activator receptor tracer, ^{68}Ga-NOTA-AE105, for PET assessment of uPAR expression in patients with a range of neuroendocrine neoplasms.. ***Page 1371***

PET prognostic model for HNSCC: Creff and colleagues identify clinical and preoperative PET/CT parameters predicting overall survival and distant metastasis–free survival in head and neck squamous cell carcinoma patients and develop an associated prognostic model. . . . . . . ***Page 1378***

Exploring the immunosuppressive microenvironment: Foray and colleagues use PET/CT and PET/MRI with ^{18}F-FET and ^{18}F-DPA-714 to elucidate the role of glioma-associated microglia and macrophages in glioma initiation, monitor therapy-induced GAMM depletion, and observe GAMM repopulation. . . . . ***Page 1386***

NTR1 imaging in neuroendocrine PCa: Wu and colleagues synthesize the neurotensin receptor subtype 1–targeted tracer ^{68}Ga-DOTA-NT-20.3 and determine its affinity to androgen-dependent and -independent prostate cancer xenografts in mice. . . . . ***Page 1394***

DLL3 PET imaging in NEPC: Korsen and colleagues report on development and preclinical validation of ^{89}Zr-DFO-SC16, a delta-like ligand 3 that targets antibody SC16, for PET imaging of treatment-induced neuroendocrine prostate cancer lesions.. . . . . ***Page 1401***

Short-term induced microglial depletion in stroke: Barca and colleagues investigate the effects of microglial repopulation on inflammation and functional outcomes in an ischemic mouse model using translocator protein PET/CT or PET/MRI, ex vivo characterization, and behavioral tests.. . . . . ***Page 1408***

^{68}Ga-FAPI PET, CMR, and post-AMI outcomes: Diekmann and colleagues correlate fibroblast-activation protein–targeted PET results after acute myocardial infarction with tissue characteristics from cardiac MR imaging and functional outcomes. . . . . ***Page 1415***

PET segmentation in HL: Driessen and colleagues evaluate methods of lesion selection for segmentation in chronic Hodgkin lymphoma to derive metabolic tumor volume on PET and explore the influence of different methods on prognostic value, intensity, and radiomics features. . . . . ***Page 1424***

BAT activity: Erba and colleagues provide perspective on current understanding of brown adipose tissue function and imaging as a preview of an article in this issue of *JNM* on metabolic changes associated with cold activation of such tissue.. . . . . ***Page 1431***

Active BAT-associated metabolic changes: Crandall and colleagues use PET/CT to assess metabolic changes associated with cold activation of brown adipose tissue in healthy adults and compare baseline blood metabolites in participants with varying amounts of active BAT. . . . . ***Page 1433***

MIRDcell V3: Katugampola and members of the SNMMI Committee on Medical Internal Radiation Dose introduce a new version of MIRDcell, a software tool for multicellular dosimetry and bioeffect modeling. . . . . ***Page 1441***

Immuno-PET/MRI of aspergillosis: Schwenck and colleagues offer an illustrated post on an *Aspergillus*-specific, ^{64}Cu-labeled tracer administered in patients with acute myeloid leukemia diagnosed with no invasive pulmonary aspergillosis or with consensus-defined IPA.. . . . . ***Page 1450***

Cardiolite®
Kit for the Preparation of
Technetium Tc99m **Sestamibi** for Injection

Myocardial Perfusion Function and Risk Stratification[1,2]

- **First technetium-labeled myocardial perfusion imaging agent providing physicians prognostic information for patient management decisions related to coronary artery disease[1,3]**
- **Used in over 10 million patients since 1991[3]**

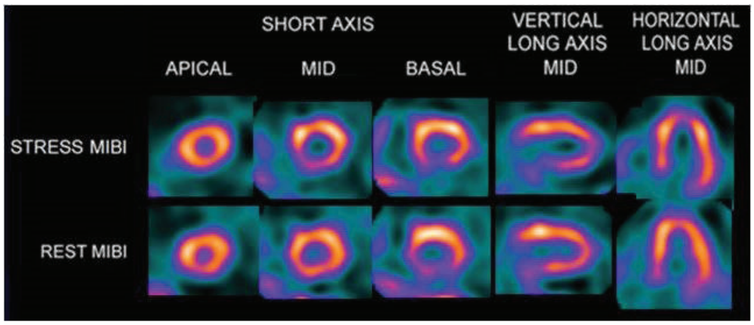

INDICATIONS AND USAGE

Myocardial Imaging: Cardiolite® (Kit for the Preparation of Technetium Tc99m Sestamibi for Injection), is a myocardial perfusion agent that is indicated for detecting coronary artery disease by localizing myocardial ischemia (reversible defects) and infarction (non-reversible defects), in evaluating myocardial function and developing information for use in patient management decisions. Cardiolite® evaluation of myocardial ischemia can be accomplished with rest and cardiovascular stress techniques (e.g. exercise or pharmacologic stress in accordance with the pharmacologic stress agent's labeling).

CONTRAINDICATIONS

None known.

IMPORTANT SAFETY INFORMATION

In studying patients in whom cardiac disease is known or suspected, care should be taken to assure continuous monitoring and treatment in accordance with safe, accepted clinical procedure.

Caution should be exercised and emergency equipment should be available when administering Cardiolite®.

Before administering Cardiolite® patients should be asked about the possibility of allergic reactions to either Cardiolite® or Miraluma®. Miraluma® is an identical compound used in breast imaging.

The contents of the vial are intended only for use in the preparation of Technetium Tc99m Sestamibi and are not to be administered directly to the patient without first undergoing the preparative procedure.

Please see following page(s) for brief Prescribing Information. Full Prescribing Information may be accessed at https://www.lantheus.com/assets/Cardiolite-US-PI-513121-0619mktg.pdf

References:
1. Cardiolite® [package insert]. N. Billerica, MA: Lantheus Medical Imaging.
2. Hachamovitch R, Berman DS, Shaw LJ, et al. Incremental prognostic value of myocardial perfusion single photon emission computed tomography for the prediction of cardiac death: differential stratification for risk of cardiac death and myocardial infarction. *Circulation. 1998;97:535-543.*
3. Data on file. Lantheus Medical Imaging, Inc.

LANTHEUS™

Cardiolite®
Kit for the Preparation of
Technetium Tc99m **Sestamibi** for Injection

FOR DIAGNOSTIC USE

BRIEF SUMMARY

Please see Full Prescribing Information available at https://www.lantheus.com/assets/Cardiolite-US-PI-513121-0619mktg.pdf for complete information.

INDICATION AND USAGE

Myocardial Imaging: CARDIOLITE®, Kit for the Preparation of Technetium Tc99m Sestamibi for Injection, is a myocardial perfusion agent that is indicated for detecting coronary artery disease by localizing myocardial ischemia (reversible defects) and infarction (non-reversible defects), in evaluating myocardial function and developing information for use in patient management decisions. CARDIOLITE® evaluation of myocardial ischemia can be accomplished with rest and cardiovascular stress techniques (e.g., exercise or pharmacologic stress in accordance with the pharmacologic stress agent's labeling).

It is usually not possible to determine the age of a myocardial infarction or to differentiate a recent myocardial infarction from ischemia.

Breast Imaging: MIRALUMA®, Kit for the Preparation of Technetium Tc99m Sestamibi for Injection, is indicated for planar imaging as a second line diagnostic drug after mammography to assist in the evaluation of breast lesions in patients with an abnormal mammogram or a palpable breast mass.

MIRALUMA® is not indicated for breast cancer screening, to confirm the presence or absence of malignancy, and it is not an alternative to biopsy.

CONTRAINDICATIONS

None known

WARNINGS AND PRECAUTIONS

Warnings

In studying patients in whom cardiac disease is known or suspected, care should be taken to assure continuous monitoring and treatment in accordance with safe, accepted clinical procedure. Infrequently, death has occurred 4 to 24 hours after Tc99m Sestamibi use and is usually associated with exercise stress testing.

Pharmacologic induction of cardiovascular stress may be associated with serious adverse events such as myocardial infarction, arrhythmia, hypotension, bronchoconstriction and cerebrovascular events. Caution should be used when pharmacologic stress is selected as an alternative to exercise; it should be used when indicated and in accordance with the pharmacologic stress agent's labeling.

Technetium Tc99m Sestamibi has been rarely associated with acute severe allergic and anaphylactic events of angioedema and generalized urticaria. In some patients the allergic symptoms developed on the second injection during CARDIOLITE® imaging. Patients who receive CARDIOLITE® or MIRALUMA® imaging are receiving the same drug. Caution should be exercised and emergency equipment should be available when administering Technetium Tc99m Sestamibi. Also, before administering either CARDIOLITE® or MIRALUMA®, patients should be asked about the possibility of allergic reactions to either drug.

General Precautions

The contents of the vial are intended only for use in the preparation of Technetium Tc99m Sestamibi and are not to be administered directly to the patient without first undergoing the preparative procedure.

Radioactive drugs must be handled with care and appropriate safety measures should be used to minimize radiation exposure to clinical personnel. Also, care should be taken to minimize radiation exposure to the patients consistent with proper patient management.

Contents of the kit before preparation are not radioactive. However, after the Sodium Pertechnetate Tc99m Injection is added, adequate shielding of the final preparation must be maintained. The components of the kit are sterile and non-pyrogenic. It is essential to follow directions carefully and to adhere to strict aseptic procedures during preparation.

Technetium Tc99m labeling reactions depend on maintaining the stannous ion in the reduced state. Hence, Sodium Pertechnetate Tc99m Injection containing oxidants should not be used.

Technetium Tc99m Sestamibi should not be used more than six hours after preparation.

Radiopharmaceuticals should be used only by physicians who are qualified by training and experience in the safe use and handling of radionuclides and whose experience and training have been approved by the appropriate government agency authorized to license the use of radionuclides.

Stress testing should be performed only under the supervision of a qualified physician and in a laboratory equipped with appropriate resuscitation and support apparatus.

The most frequent exercise stress test endpoints sufficient to stop the test reported during controlled studies (two-thirds were cardiac patients) were:

Fatigue	35%
Dyspnea	17%
Chest Pain	16%
ST-depression	7%
Arrhythmia	1%

ADVERSE REACTIONS

Adverse events were evaluated in 3741 adults who were evaluated in clinical studies. Of these patients, 3068 (77% men, 22% women, and 0.7% of the patient's genders were not recorded) were in cardiac clinical trials and 673 (100% women) in breast imaging trials. Cases of angina, chest pain, and death have occurred. Adverse events reported at a rate of 0.5% or greater after receiving Technetium Tc99m Sestamibi administration are shown in the following table:

Table 2.0
Selected Adverse Events Reported in > 0.5% of Patients Who Received Technetium Tc99m Sestamibi in Either Breast or Cardiac Clinical Studies*

Body System	Breast Studies	Cardiac Studies		
	Women n = 673	Women n = 685	Men n = 2361	Total n = 3046
Body as a Whole	21 (3.1%)	6 (0.9%)	17 (0.7%)	23 (0.8%)
Headache	11 (1.6%)	2 (0.3%)	4 (0.2%)	6 (0.2%)
Cardiovascular	9 (1.3%)	24 (3.5%)	75 (3.2%)	99 (3.3%)
Chest Pain/Angina	0 (0%)	18 (2.6%)	46 (1.9%)	64 (2.1%)
ST segment changes	0 (0%)	11 (1.6%)	29 (1.2%)	40 (1.3%)
Digestive System	8 (1.2%)	4 (0.6%)	9 (0.4%)	13 (0.4%)
Nausea	4 (0.6%)	1 (0.1%)	2 (0.1%)	3 (0.1%)
Special Senses	132 (19.6%)	62 (9.1%)	160 (6.8%)	222 (7.3%)
Taste Perversion	129 (19.2%)	60 (8.8%)	157 (6.6%)	217 (7.1%)
Parosmia	8 (1.2%)	6 (0.9%)	10 (0.4%)	16 (0.5%)

*Excludes the 22 patients whose gender was not recorded.

In the clinical studies for breast imaging, breast pain was reported in 12 (1.7%) of the patients. In 11 of these patients the pain appears to be associated with biopsy/surgical procedures.

The following adverse reactions have been reported in 0.5% of patients: signs and symptoms consistent with seizure occurring shortly after administration of the agent; transient arthritis, angioedema, arrythmia, dizziness, syncope, abdominal pain, vomiting, and severe hypersensitivity characterized by dyspnea, hypotension, bradycardia, asthenia, and vomiting within two hours after a second injection of Technetium Tc99m Sestamibi. A few cases of flushing, edema, injection site inflammation, dry mouth, fever, pruritis, rash, urticaria and fatigue have also been attributed to administration of the agent.

DRUG INTERACTIONS

Specific drug-drug interactions have not been studied.

OVERDOSAGE

The clinical consequences of overdosing with CARDIOLITE® are not known.

PATIENT COUNSELING INFORMATION

CARDIOLITE® and MIRALUMA® are different names for the same drug. Patients should be advised to inform their health care provider if they had an allergic reaction to either drug or if they had an imaging study with either drug.

Lactation: Interruption of breastfeeding after exposure to Technetium Tc99m Sestamibi is not necessary, however, a lactating woman should be advised to consider restricting close contact with her breast fed infant to a maximum of 5 hours in the 24 hour period after Technetium Tc99m Sestamibi administration in order to minimize radiation exposure.

To report SUSPECTED ADVERSE REACTIONS, contact Lantheus Medical Imaging, Inc. at 1-800-362-2668 or FDA at 1-800-FDA-1088 or www.fda.gov/medwatch.

Distributed by:
Lantheus Medical Imaging®
331 Treble Cove Road, N. Billerica, Massachusetts 01862 USA
For Ordering Tel: Toll Free: 800-299-3431
All Other Business: 800-362-2668
(For Massachusetts and International call 978-667-9531)

LANTHEUS™

SNMMI Honors Contributors, Recognizes Scientific Excellence at 2022 Annual Meeting

During its 2022 Annual Meeting, held in Vancouver, Canada, from June 11 to 14, SNMMI recognized contributions to the society and to the field of nuclear medicine, as well as excellence in scientific abstracts and posters. Several award ceremonies were held in plenary and other sessions to recognize service, scientific contributions, and the valuable roles SNMMI members play in advancing the diagnosis and treatment of cancer, heart disease, neurologic, and other conditions.

SNMMI Presidential Distinguished Service Awards

SNMMI Presidential Distinguished Service Awards are given annually to individuals who have made significant impacts within SNMMI during the tenure of each society president. The 9 individuals recognized in 2022 by 2021–2022 President Richard Wahl, MD, have been instrumental in SNMMI outreach efforts, including in virtual education innovations during the pandemic. They were each praised for their "significant contributions to the field of nuclear medicine and molecular imaging." Awardees included: Daniel Lee, MD (Ochsner Medical Center; New Orleans, LA), for extraordinary leadership as cochair of the SNMMI Therapy Strategic Planning Task Force and president of the SNMMI Therapy Center of Excellence; John Sunderland, PhD (University of Iowa Carver College of Medicine; Iowa City), for outstanding efforts on *The Journal of Nuclear Medicine* dosimetry supplement (*J Nucl Med.* 2021;62[suppl 3]); Phillip Koo, MD (Banner MD Anderson Cancer Center; Gilbert, AZ), for extraordinary service as cochair of the SNMMI Theranostics Symposia and chair of the SNMMI Quality Committee; Bonnie Clarke for outstanding service as Senior Director of Research and Discovery and Quality at SNMMI; Arman Rahmim, PhD (University of British Columbia; Vancouver, Canada), and Ronald Boellaard, PhD (VU University Medical Center; Amsterdam, The Netherlands), for their service as cochairs of the SNMMI Artificial Intelligence Task Force; Pat Zanzonico, PhD (Memorial Sloan Kettering Cancer Center; New York, NY), for extraordinary service as cochair of the SNMMI Dosimetry Task Force; and George Sgouros, PhD (Johns Hopkins Medicine; Baltimore, MD), for outstanding service as cochair of the SNMMI Dosimetry Task Force. Harvey Ziessman, MD, received the SNMMI Presidential Distinguished Educator Award, which recognizes SNMMI members who have demonstrated outstanding service and dedication to the field of nuclear medicine through their educational efforts. He was commended for his commitment to global education and training of nuclear medicine professionals, from residents to senior leaders.

International Best Abstract Award Winners

In recognition of the increasing representation of physicists, scientists, and others from the global community at its Annual Meeting, SNMMI created the International Best Abstract Awards, given to the highest scoring accepted abstracts from each country. For 2022, the awardees included:

FIGURE 1. 2021–2022 President Richard Wahl, MD, presented the Presidential Distinguished Service Awards.

Australia: Jackson et al., "Real-world lesion and renal dosimetry for peptide receptor radionuclide therapy (PRRT)"; Austria: Beheshti et al., "Predictive value and accuracy of PET modified response criteria for immunotherapy in patients with advanced melanoma"; Azerbaijan: Novruzov et al., "Head to head comparison of ^{68}Ga-FAPI-46 PET/CT and ^{18}F-FDG PET/CT in breast carcinoma staging: A clinical trial update from Azerbaijan"; Belgium: D'Huyvetter et al., "Preclinical endoradiotherapy using a radiolabeled single-domain antibody targeting fibroblast activation protein"; Brazil: Minozzo et al., "Radionuclides used in nuclear therapeutic medicine: A brief history, properties and main relevant studies of radionuclides with mass number less than 100"; Canada: Lin et al., "Effects of replacing Glu in the PSMA-targeting Lys-urea-Glu pharmacophore of ^{68}Ga-HTK03041 with a close derivative on the uptake of tumor xenograft, kidneys and salivary glands"; China: Song et al., "Non-invasive visualization of liver fibrosis with gallium-68-labeled fibroblast activation protein inhibitor"; Denmark: Carlsen et al., "Prospective phase II trial of prognostication by ^{68}Ga-NODAGA-E[c(RGDyK)]2 PET/CT for integrin alpha v beta 3 imaging in patients with neuroendocrine neoplasms"; Egypt: Nasr et al., "The value of ^{18}F-FDG PET/CT in detection of osteomyelitis in patients with stage IV pressure ulcers"; France: Gauthe et al., "Phase III study of ^{18}F-PSMA-1007 versus ^{18}F-fluorocholine PET to compare the detection rate of prostate cancer lesions in patients with biochemical recurrence after previous definitive treatment for localized prostate cancer"; Herrmann et al., "Multi-cycle dosimetry of ^{177}Lu-PSMA-617 for the treatment of metastatic castration-resistant prostate cancer: results from the VISION trial sub-study"; Koutsikos et al., "The role of lymphoscintigraphy in breast cancer recurrence"; Hong Kong:

FIGURE 2. Nicolas Baudouin, Consul General of France in Vancouver, spoke as part of activities celebrating France as the Highlight Country of the 2022 Annual Meeting.

Ho et al., "Choice of tyrosine kinase inhibitor (TKI) or immune check-point inhibitor guided by dual-tracer (^{11}C-acetate and ^{18}F-FDG) PET/CT improves the progression-free survival in patients with advanced or metastatic HCC"; India: Bal et al., "A phase II clinical study on ^{225}Ac-DOTATATE therapy in advanced stage gastroenteropancreatic neuroendocrine tumor patients"; Iran: Roustaei et al., "In vivo assessment of CXCR4 receptor expression in high-grade glioma using ^{68}Ga-pentixafor PET/CT"; Ireland: Gu et al., "Feasibility of standard and generalized Patlak models for dynamic imaging of multiple organs using the uEXPLORER PET scanner"; Israel: Chicheportiche et al., "Can absorbed doses by organs and tumors after PRRT be predicted from the pre-therapeutic ^{68}Ga-DOTATATE PET/CT study?"; Italy: Bezzi et al., "Imaging parameters and machine learning models to evaluate the prognostic role of ^{18}F-FDG PET in staging endometrial cancer patients"; Japan: Hu et al., "Chemically evolutionary screening of cyclic peptides for PET imaging of PD-L1 protein in tumors"; Jordan: Juweid et al., "Effect of degenerative lumbar changes on trabecular bone score (TBS) in patients assessed for osteoporosis in routine clinical practice"; Kenya: Munemo et al., "Comparison of two methods of semi-quantitative analysis of FDG PET brain scans"; Macao: Chen et al., "Voxel-S-value based treatment planning methods using Tc-99m-MAA SPECT/CT for liver radioembolization"; Mexico: Cardoza-Ochoa et al., "Vaccine-associated hypermetabolic lymphadenopathy on ^{18}F-FDG PET/CT: Experience from a single center in Mexico"; The Netherlands: Eertink et al., "^{18}F-FDG PET radiomics features result in more accurate prediction of outcome for DLBCL patients than currently used IPI score"; Norway: Kyassheim et al., "Quantitative imaging of Pb-212"; Pakistan: Jabeen et al., "Rising frequency of differentiated thyroid cancer in younger population"; Philippines: Pascual et al., "Cost-effectiveness of F-18 FDG PET/CT in lung and colorectal cancer: A systematic review and narrative synthesis"; Poland: Malkowski et al., "^{18}F-FET-PET/MR-guided biopsies of contrast-enhancing gliomas: A prospective study"; Romania: Niculae et al., "Innovative theranostic agents for colon cancers, based on peptide-functionalized iron oxide nanoparticles: Preclinical evaluation"; Serbia: Mihailovic et al., "The diagnostic value of F-18 FDG-PET/CT imaging in detection of recurrent and metastatic breast cancer"; Singapore: Zhang et al., "Long-term efficacy, survival, and toxicity of peptide receptor radionuclide therapy in patients with refractory meningioma"; South Africa: Maserumule et al., "Initial experience of lung metastases response to ^{225}Ac-PSMA-617 therapy in metastatic prostate adenocarcinoma"; South Korea: Ryoo et al., "Distinct subtypes of spatial brain metabolism patterns in Alzheimer's disease identified by deep learning-based FDG PET clusters"; Spain: Riveira et al., "Predictive value of dose metrics from ^{99m}Tc-MAA compared to ^{90}Y SPECT/CT in dosimetry-guided personalized SIRT of hepatocellular carcinoma"; Sri Lanka: Wimalarathne et al., "Impact of time-of-flight (TOF) reconstruction on 40-segmented brain volumes of (±) AD patients with short-lived ^{11}C-Pittsburgh compound-B PET/MR imaging"; Sweden: Lubberink et al., "Evaluation of DOTA as a marker for myocardial blood flow using ^{68}Ga-DOTA and ^{15}O-water PET"; Switzerland: Shiri et al., "Cross-site PET image harmonization by using unsupervised deep generative adversarial network for improving quantitative indices reproducibility"; Taiwan: Guan et al., "A novel ^{177}Lu-labeled dual CA9-targeted probe as a potential theranostic radiopharmaceutical for hypoxic colorectal cancer diagnosis and therapy"; Thailand: Thientunyakit et al., "Multi-modal neuroimaging studies in default mode network areas in predicting a progressive neurocognitive decline in patients with mild cognitive impairment (MCI)"; United Kingdom: Pemberton et al., "Software compatibility analysis for quantitative measures of ^{18}F-flutemetamol amyloid PET burden"; Uruguay: Zirbesegger et al., "Cellular specificity assessment and longitudinal PET study in a transgenic mice model of a ^{18}F-labelled sulforhodamine 101 in astrocytosis processes in Alzheimer's disease"; and Yemen: Alobthani et al., "FDG PET/CT is more likely to detect the primary source of the cancer of unknown primary when presented with cervical lymph nodes metastasis."

In addition, the Education and Research Foundation for Nuclear Medicine and Molecular Imaging/SNMMI this year presented a Best COVID-19 (Physician/Scientist) Award to Khandekwal et al. (Lucknow, India) for "A prospective study to investigate the implementation of semiquantitative inflammatory load in post-COVID-19 lung disease (PCLD) to strategize therapy" and a Best COVID-19 (Technologist) Award to Vyas et al. (Auckland, New Zealand) for "A model for remote installation of radiochemistry synthesiser; Trasis—AllInOne: One step forward to beat Covid-19 pandemic."

Award-Winning Posters

More than 800 posters were on display in the Exhibit Hall at the SNMMI Annual Meeting in Vancouver, with multiple ask-the-author sessions and point-of-display discussions. Winning posters and e-posters were selected from the top 10 candidates in each scientific track, based on visual appearance/quality, content, and original scientific contribution.

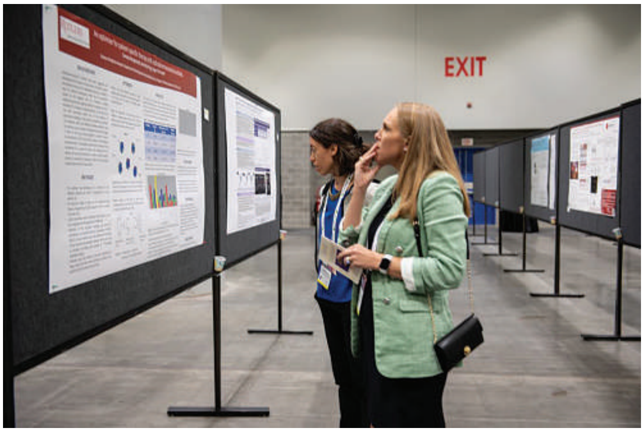

FIGURE 3. More than 800 posters, including e-posters, were available in the Scientific Exhibit Hall at the 2022 SNMMI Annual Meeting.

Posters are available on the website of *The Journal of Nuclear Medicine* at: https://jnm.snmjournals.org/content/snmmi-annual-meeting-abstracts. Poster awardees included:

Cardiovascular Track: First place, Diekmann et al., “Cardiac molecular PET-imaging of fibroblast activation in patients with aortic stenosis undergoing transcatheter aortic valve implantation (TAVI)”; second place, Thorn et al., “Early cardiac gated blood pool imaging with “hotspot” agent provides simultaneous assessment of left ventricular function in an ischemia-reperfusion model”; and third place, Miller et al., “Development and external validation of ischemia risk scores.”

Educational Track: First place, Suthar et al., “^{18}F-FDG PET/CT imaging features of parotid lesions: Case based pictorial review and its multi-modality correlation”; second place, Schroeder et al., “Cue up the video: Visual learning for efficient orientation of trainees to their nuclear medicine rotations”; and third place, Ali et al. “Renal scintigraphy following kidney transplantation: ATN, rejection, and more.”

General Clinical Specialties Track: First place, Bini et al., “Liver and brain levels of 11β-hydroxysteroid dehydrogenase type 1 enzyme in obesity: Preliminary results from PET imaging studies”; Paravastu et al., “Quantitative analysis of ^{18}F-NaF-PET/CT imaging: Evaluation of denosumab treatment in fibrous dysplasia”; and third place, Lawrence et al., “^{99m}Tc-macroaggregated albumin (MAA) stability when used in the SNMMI Procedure Guideline for Adult Solid-Meal Gastric-Emptying Scintigraphy.”

Molecular Targeting Probes, Radioactive and Nonradioactive Track: First place, Mueller et al., “Radiopharmaceutical production of [Pb-203]VMT-α-NET for clinical use”; second place, Yu et al., “Development and preliminary evaluations of novel PET tracers for imaging TARP γ-8 receptors”; and third place, Naka et al., “Development of a novel LAT1-selective PET probe for improved tumor retention.”

Neurosciences Track: First place, Zirbesegger et al., “Cellular specificity assessment and longitudinal PET study in a transgenic mice model of a ^{18}F-labelled sulforhodamine 101 in astrocytosis processes in Alzheimer’s disease”; second place, Takahashi et al., “Small brain nuclei identification using helmet-type positron emission tomography in healthy volunteers”; and third place, Neelamegam et al., “Preclinical evaluation of [^{11}C]MPC-6827, a microtubule PET tracer in synucleinopathy.”

Oncology Basic and Translational Track: First place, Hoffman et al., “In vitro targeted radionuclide therapy studies of a PARP-targeted Meitner-Auger electron emitting radiopharmaceutical”; second place, Watabe et al., “Targeted alpha therapy using astatine (^{211}At)-labeled PSMA5: A preclinical evaluation as a new novel compound”; and third place, Jeanniean et al., “Fibroblast activation protein (FAP) as a target for radioligand therapy in glioblastoma.”

Oncology: Clinical Therapy and Diagnosis Track: First place, Nabavizadeh et al., “^{18}F-fluciclovine PET and multiparametric MRI to distinguish pseudoprogression from tumor progression in post-treatment glioblastoma”; second place, Hotta et al., “Outcome of patients with PSMA-PET/CT screen failure by VISION criteria and treated with ^{177}Lu-PSMA therapy: A multicenter retrospective analysis”; and third place, Hotta et al., “PSMA PET tumor-to-salivary glands ratio (PSG score) to predict response to Lu-177 PSMA radioligand therapy: An international multicenter retrospective study.”

Physics, Instrumentation, and Data Sciences Track: First place, Woolley et al., “Development of a dynamic lung phantom for use in lung ventilation studies”; second place, Cai et al., “An ultrahigh energy resolution SPECT system for quantitative hyperspectral imaging of targeted alpha therapy”; and third place, Pan et al., “Data-driven gated (DDG) CT: An automated respiratory gating method to enable DDG PET/CT.”

Full Steam Ahead for Nuclear Medicine Therapy

Munir Ghesani, MD, SNMMI President

Nuclear medicine therapies have been around for decades but have recently come into their own in a big way. Advances have contributed to treatments for prostate cancer, neuroendocrine tumors, meningiomas, and lymphoma, with more on the horizon. At an SNMMI strategic planning meeting held in April 2022, society leadership identified radiopharmaceutical therapy (RPT) as a one if its top priorities for the next 5 years. Discussions at the meeting centered around ways to expand research, promote the use of therapy, and make it accessible to patients, among other topics.

SNMMI has several therapy-focused efforts in progress and many more planned. Last year the society introduced the Radiopharmaceutical Therapy Centers of Excellence (RPT COEs), in which sites utilizing RPTs could apply to earn designation as a clinical or comprehensive RPTCOE. This designation shows that the site meets strict regulatory, training, qualification, experience, and performance criteria. To date, 34 applications have been received from 22 comprehensive sites, 8 clinical sites, and 4 basic therapy sites. Twenty-two sites have received designation.

The Lu-177 Dosimetry Challenge demonstrated a great interest in personalized RPT dosimetry and a need to train more personnel to perform dosimetry. Thus, the development of a dosimetry certificate program was recently approved by the SNMMI Board of Directors. The certificate program will consist of a web-based curriculum followed by an onsite practicum. It will include separate tracks for physicists, physicians, and technologists. The SNMMI Board of Directors has also approved funding for 2 nuclear oncology fellowships. Applications for certificate programs and fellows will open soon. For technologists, SNMMI is creating an RPT badging program, which will include training materials on the components of therapy delivery. Although the badging program is not a certification or credential, it can be added to CVs to demonstrate proficiency in RPT.

On the education front, SNMMI has created a Nuclear Medicine University with educational content on RPTs and diagnostic procedures designed for residents. In addition, SNMMI is conducting a curriculum review to ensure that all necessary content is available to properly train nuclear medicine physicians to administer therapies.

SNMMI is also ensuring that appropriate use criteria and procedure standards are in place to describe when RPTs should be performed and identify the most important elements of a high-quality procedure. The society is also taking an active role in ensuring that other specialties are educated about RPTs via educational workshops ("road shows") and satellite symposia at related specialty meetings focused on prostate-specific membrane antigen imaging and therapy.

Munir Ghesani, MD

The society will launch a new therapy-specific clinical trials network, the Therapy Clinical Trials Network. The goal of this initiative is to establish a network of investigational sites with the capability of conducting clinical trials of RPTs, similar to ARTnet in Australia and New Zealand. SNMMI Clinical Trials Network database expertise will be utilized to create the new network, and it is anticipated that many of the RPTCOEs will be involved.

As the applications of nuclear medicine therapy continue to grow, ensuring a robust workforce pipeline of both physicians and technologists is always a concern. SNMMI is developing a physician survey to identify physician workforce needs going forward. Understanding that there is currently a shortage of therapy-focused technologists, SNMMI is also working on both short- and long-term solutions to grow the technologist workforce.

SNMMI will host its third annual Therapeutics Conference November 17–19 at the Gaylord National Resort in Washington, DC (www.snmmi.org/TC2022). Following the footprint of previous conferences, the event will explore the latest innovations and clinical applications in RPT. Sessions on radiopharmaceutical delivery, dosimetry, and more will be included in the conference.

At the 2022 Annual Meeting in Vancouver, Canada, SNMMI initiated its Mars Shot fund to radically transform the nature of disease treatment, prevention, diagnosis, and prognosis using visionary nuclear medicine procedures, RPTs, and research projects. By supporting training pathways and fellowships, our hope is to allow nuclear medicine physicians to integrate into patient management teams as key members, rather than as outlying suppliers of imaging and treatment.

Look for more on therapy in future issues of *The Journal of Nuclear Medicine,* and be sure to check out the September issue of the *Journal of Nuclear Medicine Technology,* which focuses on this topic. It is an exciting time for nuclear medicine therapies, and we look forward to what's to come in the future.

www.snmmi.org/2022AwardsGuide

Dana-Farber Cancer Institute | Brigham Cancer Center

CHAIR
DEPARTMENT OF IMAGING
Dana-Farber Cancer Institute

The Dana-Farber Cancer Institute and the Department of Radiology at Brigham and Women's Hospital are seeking an academic leader to serve as the chair of the Department of Imaging at the Dana-Farber Cancer Institute and be a member of the Department of Radiology at Brigham and Women's Hospital. The successful candidate will also hold an appointment at the rank of Professor/Associate Professor of Radiology at Harvard Medical School commensurate with experience.

This individual will be responsible for the research and educational activities of the department as well as clinical activities with the Deputy Chair of the Brigham and Women's Hospital. The Chair will collaborate with other Department Leaders at Mass General Brigham, Harvard Medical School, Boston Children's Hospital, Beth Israel Deaconess Medical Center, and other affiliated institutions. A candidate with a focus on innovative molecular imaging will receive strong consideration.

The candidate should have a demonstrated record as a mentor and as a teacher, national recognition for research accomplishments, and possess exceptional leadership, managerial and collaborative skills. Ideally, this individual would be a proven leader with an international reputation in radiology who can lead a complex and successful department to even higher levels of excellence.

Interested candidates are requested to submit a current Curriculum Vitae and cover letter to the email address below for consideration.

Committee Chair
Bruce E. Johnson, M.D., Professor, Department of Medical Oncology, Dana-Farber Cancer Institute and Department of Medicine, Brigham and Women's Hospital
ImagingCHAIR@dfci.harvard.edu

We are an equal opportunity employer and all qualified applicants will receive consideration for employment without regard to race, color, religion, sex, national origin, disability status, protected veteran status, gender identity, sexual orientation, pregnancy and pregnancy-related conditions or any other characteristic protected by law.

Explore SNMMI's Online Career Center!

Explore the benefits of SNMMI's online career center
by logging in or creating a new account today.

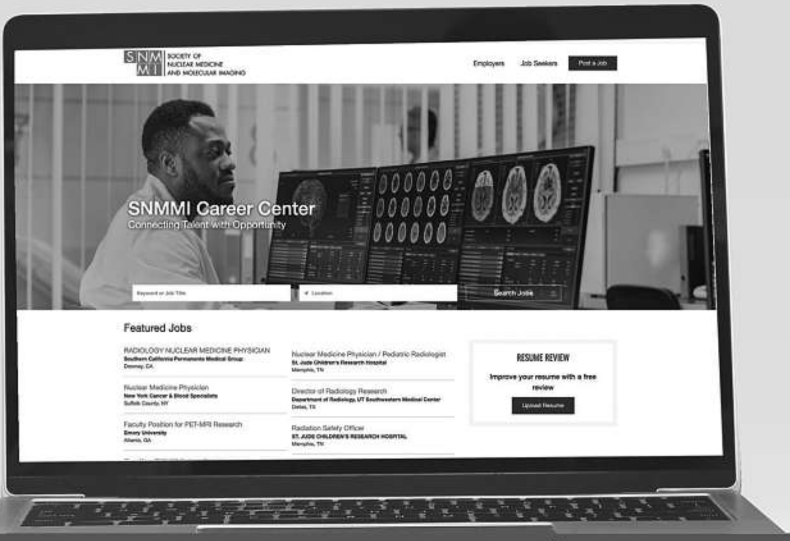

Featured Jobs

RADIOLOGY NUCLEAR MEDICINE PHYSICIAN
Southern California Permanente Medical Group
Downey, CA

Nuclear Medicine Physician / Pediatric Radiologist
St. Jude Children's Research Hospital
Memphis, TN

Nuclear Medicine Physician
New York Cancer & Blood Specialists
Suffolk County, NY

Director of Radiology Research
Department of Radiology, UT Southwestern Medical Center
Dallas, TX

Faculty Position for PET-MRI Research
Emory University
Atlanta, GA

Radiation Safety Officer
ST. JUDE CHILDREN'S RESEARCH HOSPITAL
Memphis, TN

careercenter.snmmi.org

Note: Single sign-on has been enabled for this platform and you can use your member login credentials to access the Career Center. If you are unsure of your password, to go to the SNMMI password reset link to create a new password.

SNMMI Value Initiative
SOCIETY OF NUCLEAR MEDICINE & MOLECULAR IMAGING

CMS Reopens NCD for β-Amyloid PET in Dementia and Neurodegenerative Disease

On June 16, the Centers for Medicare & Medicaid Services (CMS) began a formal reconsideration process for its National Coverage Determination (NCD) for Beta-Amyloid (β-Amyloid) PET in Dementia and Neurodegenerative Disease (CAG-00431R). The current NCD 220.6.20 covers 1 β-amyloid PET scan per patient in CMS-approved studies under coverage with evidence development (CED). CMS opened the NCD analysis based on stakeholder feedback, including public comments received during and after the April 7 finalization of the NCD for Monoclonal Antibodies Directed Against Amyloid for the Treatment of Alzheimer's Disease. The purpose of the NCD reconsideration is to determine whether the current policy of 1 scan per patient per lifetime should be revised.

In a statement released after the April 7 NCD finalization, SNMMI noted that, "unfortunately, the decision included no additional coverage for β-amyloid PET scans; they will continue to be subject to the current policy, which covers them only as required by clinical trial protocol, and, even then, only 1 per patient per lifetime. In stark contrast, the decision explicitly covers other tests for detection of β-amyloid (e.g., cerebral spinal fluid) without limitation, despite the fact that β-amyloid PET is the standard of care—and, in fact, the only test approved by the U.S. Food and Drug Administration—for detecting β-amyloid."

The 30-day public comment period for the formal reconsideration ended on July 15, during which period SNMMI submitted additional comments. The proposed decision by CMS is expected by December 16, with finalization by March 16, 2023.

SNMMI
Centers for Medicare & Medicaid Services

CMS Releases CY 2023 Medicare Physician Fee Schedule Proposed Rule

The Centers for Medicare & Medicaid Services (CMS) released on July 7 its 2023 Medicare Physician Fee Schedule (MPFS) Proposed Rule, along with a 2023 MPFS fact sheet. Unlike the CY2021 and CY2022 MPFSs, which included significant changes for PET (particularly nononcologic PET), the CY 2023 proposed rule included few changes. The removal or retirement of national noncoverage for amyloid PET or retiring national noncoverage for NaF PET were not mentioned in the new rule.

An SNMMI release on July 14 noted that the society had held multiple meetings with CMS and submitted formal comments on the negative impact of national noncoverage determinations for both NaF and amyloid tracers and would continue to advocate for associated changes in coverage.

SNMMI pointed out several items of interest to the nuclear medicine community in the new rule, including proposed changes related to:

Conversion factors: A preliminary summary of the proposed rule proposes a 3.0775 PFS conversion factor in 2023, which is a $1.53 decrease from the 2022 PFS. CMS estimates the overall impact of the MPFS proposed changes to radiology and nuclear medicine to be a 3% decrease and to radiation oncology and radiation therapy centers a 1% decrease, if the rule is finalized.

Clinical labor changes: CMS proposes continuing to move forward with y 2 of the 4-y transition to updated clinical labor input values. CMS proposed updated wages for a few clinical staff types based on information submitted by stakeholders. The agency will continue to consider public comment related to wage updates for clinical staff during the remainder of the 4-y phase-in.

Practice expense (PE) data collection and calculation methodology: CMS is seeking public comment on strategies for updates to PE data collection and methodology. The agency plans to move forward to a standardized and routine approach to valuation of indirect PE and has asked for feedback from stakeholders on what this might entail. The agency plans to propose the new approach to valuation of indirect PE in future rulemaking. A survey on indirect PE may be disseminated in the future. In the current methodology, nuclear medicine is "cross-walked" to radiology for the purposes of indirect PE.

The MPFS proposed rule does not mention the Appropriate Use Criteria Program or Clinical Decision Support implementation. However, CMS published a statement saying that the associated payment penalty phase will not begin on January 1, 2023, even if the Public Health Emergency for COVID-19 ends in 2022. Until further notice, the educational and operations testing period will continue. CMS added that they are unable to forecast when the payment penalty phase will begin.

SNMMI indicated that the society will continue to review the proposed rule and will provide formal comments. A chart comparing important nuclear medicine services in the CY 2022 and CY 2023 MPFSs is available at: http://www.snmmi.org/IssuesAdvocacy/content.aspx?ItemNumber=6502&navItemNumber=24949.

SNMMI
Centers for Medicare & Medicaid Services

COVID-19–Triggered Immune Response and Neurologic Damage

In a study published on July 5 ahead of print in *Brain*, Lee et al. from the National Institute of Neurological Disorders and Stroke (NINDS; Bethesda, MD), the Uniformed Services University of the Health Sciences (Bethesda, MD), the Defense Health Agency (Silver

Spring, MD), the New York University School of Medicine (NY), and the University of Iowa Roy J. and Lucille A. Carver College of Medicine (Iowa City) reported on a post-mortem study characterizing vascular pathology, neuroinflammatory changes, and cellular and humoral immune responses in a group of COVID-19 patients early in the course of the pandemic. "Patients often develop neurological complications with COVID-19, but the underlying pathophysiological process is not well understood," said Avindra Nath, MD, clinical director at NINDS and senior author of the study, in a NINDS press release. "We had previously shown blood vessel damage and inflammation in patients' brains at autopsy, but we didn't understand the cause of the damage."

The study included autopsy results from 9 individuals (7 men, 2 women; age range, 24–73 y) who died suddenly during the first wave of the pandemic and had shown abnormalities on structural brain scans. The study also included comparative autopsy investigation results from an age- and demographic-matched control group. All individuals with COVID had multifocal vascular damage marked by leakage of serum proteins into the brain parenchyma, accompanied by widespread endothelial cell activation. Platelet aggregates and microthrombi were adhered to endothelial cells along the vascular lumina, and immune complexes with activation of the classical complement pathway were found on the endothelial cells and platelets. Microglial nodules were predominant in the hindbrain and were associated with focal neuronal loss and neuronophagia. The authors concluded that antibody-mediated cytotoxicity directed against the endothelial cells was the most likely initiating event that led to vascular leakage, platelet aggregation, neuroinflammation, and neuronal injury. They suggested that therapeutic modalities directed against immune complexes should be considered.

The results of the study may have implications for diagnosing and treating long-term neurologic symptoms after COVID-19. "It is quite possible that this same immune response persists in Long COVID patients, resulting in neuronal injury," said Nath. "There could be a small indolent immune response that is continuing, which means that immune-modulating therapies might help these patients. So these findings have very important therapeutic implications."

National Institute of Neurological Disorders and Stroke

IAEA Partners with GE Healthcare in Global Training

The International Atomic Energy Agency (IAEA) announced on July 14 a partnership with GE Healthcare to train professionals in medical imaging under Rays of Hope, the IAEA's initiative to address global inequity in access to life-saving cancer diagnosis and treatment. It is the first such agreement with a private company under Rays of Hope. Under a 1-y partnership with GE Healthcare, radiologists and nuclear medicine professionals from Africa and Latin America will receive in-person and online training in diagnostic techniques. "A well-trained workforce is a must for a functioning medical sector. Our work together with GE Healthcare will provide these professionals with the necessary skills and knowledge to help save lives," said IAEA Director General Rafael Mariano Grossi during the partnership launch at IAEA headquarters in Vienna. "As part of the IAEA's determined efforts under Rays of Hope to address global imbalances in access to cancer care, we are reaching out to potential partners also in the private sector, which has an indispensable role to play. Our partnership with GE Healthcare is a milestone in this respect and it will be followed by others."

The traditional source of IAEA funding is from its Member States. Earlier this year, 6 countries, including France, Japan, Monaco, the Republic of Korea, Sweden, and the United States, pledged more than €9 million to the program. "I'm very encouraged by the generous support we have received from our Member States and from the private sector. Much more will be needed in the coming months and years to deliver on our pledge to reduce the global gap in access to cancer care, but this is a very promising start," said Grossi.

As a part of the partnership, cutting-edge training will be provided at Zurich University Hospital in Switzerland, the GE Healthcare's partner institution with expertise in PET imaging. The first medical professionals from Kenya will begin their 4-wk training session in September, focusing on PET/CT and PET/MR imaging.

International Atomic Energy Agency

U.S. Life Expectancy, 2000–2019

In an article published on July 16 in *The Lancet* (2022;400[10345]:P25–P38), experts from the Institute for Health Metrics and Evaluation (IHME) at the University of Washington School of Medicine (Seattle), in collaboration with researchers from the National Institutes of Health (NIH), reported that overall life expectancy in the United States increased by 2.3 y in the decade from 2000 to 2019 but that this increase was not consistent among racial and ethnic groups or by geographic area. The study included results at the county level in each state. Most of the gains in life expectancy appear to have been achieved before 2010.

"These varied outcomes in life expectancy raise significant questions. Why is life expectancy worse for some and better for others? The novel details in this study provide us the opportunity to evaluate the impact of social and structural determinants on health outcomes in unprecedented ways. This in turn allows us to better identify responsive and enduring interventions for local communities," said Eliseo J. Pérez-Stable, MD, coauthor and director of the NIH National Institute on Minority Health and Health Disparities.

Among the key findings at the national level, between 2000 and 2019, life expectancy increased most for the Black population (3.9 y), the Asian population (2.9 y), and the Latino population (2.7 y). At the same time, the increase in life expectancy for the white population was more moderate (1.7 y). No improvement in life expectancy was noted for American Indian and Alaskan

Native (AIAN) populations. In 2019, overall life expectancy was 85.7 y for Asian, 82.2 y for Latino, 78.9 y for white, 75.3 y for Black, and 73.1 y for AIAN populations. At the county level, 88% of U.S. counties saw an increase in life expectancy during the 20-y study period; however, most of these gains were from 2000 to 2010. Almost 60% of U.S. counties saw a decrease in life expectancy in the study's second decade. The range of life expectancy varied widely among counties, ranging from <65 y in some to >90 y in others.

In an accompanying press release, NIH emphasized the importance of this study in establishing a baseline for the 2 decades preceding the COVID-19 pandemic and providing context for subsequent changes in mortality and disparities. Provisional estimates for 2020 show substantial declines in life expectancy overall, with declines larger in the Latino and Black populations. "The pandemic exposed stressors and weaknesses in local and national systems that continuously put our most vulnerable populations at risk. These findings offer county, state, and federal leaders a unique look at the pervasiveness of health disparities in their respective communities," said Laura Dwyer-Lindgren, PhD, lead author and assistant professor of health metrics at the IHME.

Detailed county-level results are available from the IHME at www.healthdata.org/data-visualization/us-health-map.

The Lancet
National Institutes of Health

Safe and Equitable Health Care for All: SNMMI Position on the Doctor–Patient Relationship

On July 8, SNMMI leadership released the following statement:

SNMMI believes that physicians must be able to provide safe, effective, and accessible evidence-based health care to patients without the threat of nonmedical outside interference. We condemn any interference with the doctor–patient relationship outside of public health measures and acknowledge that such interference can disproportionately impact historically and economically marginalized and disadvantaged populations. Physicians, legislators, regulators, and patients must work together to ensure safe and equitable health care for all.

Each month the editor of Newsline selects articles on diagnostic, therapeutic, research, and practice issues from a range of international publications. Most selections come from outside the standard canon of nuclear medicine and radiology journals. These briefs are offered as a window on the broad arena of medical and scientific endeavor in which nuclear medicine now plays an essential role. The lines between diagnosis and therapy are increasingly blurred, as radiolabels are used as adjuncts to treatment and/or as active agents in therapeutic regimens, and these shifting lines are reflected in the briefs presented here. We have also added a small section on noteworthy reviews of the literature.

Preclinical Biomarkers of Alzheimer Disease

Long et al. from the Washington University School of Medicine in St. Louis (MO) reported on July 22 ahead of print in *Brain* on a study designed to determine whether amyloid PET imaging and/or cerebrospinal fluid (CSF) biomarkers accurately predict cognitive outcomes in Alzheimer disease (AD) and neuropathologic findings at autopsy. The study included 720 individuals (age range, 42–91 y) who were cognitively normal at baseline, underwent amyloid PET imaging and/or CSF collection within 1 y of initial clinical assessment, and had subsequent clinical follow-ups. Cognitive status was assessed serially over follow-up, and biomarkers were defined by uptake cutoffs for amyloid PET imaging and CSF p-tau181/amyloid-β42 levels. Over the course of the study, 57 participants died, with subsequent post-mortem neuropathologic examination for AD-related changes. Among normal participants with PET or CSF biomarkers defined as positive, 34.4% developed cognitive impairment, compared to only 8.4% with negative biomarkers. Preclinical AD biomarker status, APOE ε4 carrier status, polygenic risk score, and age were identified as significant factors influencing risk of developing cognitive impairment. Among individuals with autopsy results, 90.9% of those who were biomarker-positive and 8.6% of those who were biomarker-negative had AD neuropathologic changes. The combination of the preclinical biomarkers yielded a sensitivity of 87.0%, specificity of 94.1%, and positive- and negative-predictive values of 90.9% and 91.4%, respectively, for subsequent detection of AD neuropathology. As individual predictors, CSF and amyloid PET at baseline were also predictive of AD neuropathologic changes, as well as Thal phase and Braak stage of pathology at autopsy. Of note, participants who were biomarker-negative and went on to develop cognitive impairment were more likely than other participants to exhibit non-AD pathology at autopsy. The authors concluded that “detection of preclinical AD biomarkers is strongly predictive of future cognitive impairment and accurately predicts presence of AD neuropathology at autopsy.”

Brain

^{18}F-Florzolotau PET in Multiple System Atrophy Parkinsonian Subtype

In an article published on July 21 ahead of print in *Movement Disorders*, Lin et al. from Huashan Hospital/Fudan University (Shanghai) and APRINOIA Therapeutics Co., Ltd. (Suzhou; both in China) and representing the Progressive Supranuclear Palsy Neuroimage Initiative reported on a study investigating localization and uptake volume of ^{18}F-florzolotau (previously known as ^{18}F-APN-1607) on PET in patients with the parkinsonian subtype of multiple system atrophy. The study included 31 such patients, 24 with Parkinson disease, and 20 age-matched healthy controls. Uptake in the striatum was visually assessed as positive or negative, and regional binding was evaluated as SUV ratios. In both assessments, patients with the parkinsonian subtype of multiple system atrophy showed elevated tracer uptake in the putamen, globus pallidus, and dentate compared with patients with Parkinson disease. This increased signal was significantly associated with the core clinical symptoms of the parkinsonian subtype of multiple system atrophy. In those patients with the subtype cerebellar ataxia, tracer uptake was elevated in the cerebellar dentate. The authors concluded that “^{18}F-florzolotau tau PET imaging findings may reflect the clinical severity of parkinsonian subtype of multiple system atrophy and can potentially discriminate between this condition and Parkinson disease.”

Movement Disorders

PET/CT of Cranial Arteries in Giant Cell Arteritis

Thibault et al. from Dijon University Hospital, the Centre Georges François Leclerc, and the Université Bourgogne Franche-Comté, INSERM (all in Dijon, France) reported on July 22 ahead of print in *Rheumatology (Oxford)* on a study of the performance of cranial PET/CT in the sometimes challenging diagnosis of giant cell arteritis (GCA). The investigation was part of a clinical trial designed to evaluate the sensitivity and specificity of PET of the cephalic arteries for diagnosis of GCA and compare these with results from echo Doppler and MR imaging of the temporal arterials. A total of 70 adults with suspected GCA were enrolled in the study and underwent baseline cranial artery evaluation with PET/CT before or immediately (within 72 h) after starting glucocorticoid treatment. Cranial PET/CT was considered positive if at least 1 arterial segment showed hypermetabolism similar to or greater than liver uptake. The diagnosis of GCA was retained after ≥6 mo of follow-up when no other diagnosis was considered and the patient had gone into remission after ≥6 consecutive mo of treatment. Cranial PET/CT sensitivity, specificity, and positive- and negative-predictive values were 73.3%, 97.2%, 91.7%, and 89.7%, respectively. Corresponding values for extracranial PET/CT diagnostic performance were 66.7%, 80.6%, 58.8%, and 85.3%. Combining cranial and extracranial PET/CT results improved overall sensitivity (80%) and negative-predictive values (90.3%) but decreased overall specificity (77.8%) and positive-predictive values (60%). The authors concluded that cranial and extracranial PET/CT can be combined with a limited increase in imaging time and show a high accuracy for diagnosis of GCA.

Rheumatology (Oxford)

^{11}C-Flumazenil PET and Neuronal Alterations After Cerebral Infarction

In an article in the July 6 issue of *Stroke*, Yamauchi et al. from Kyoto University and Shiga Medical Centre Research Institute (Moriyama; both in Japan) reported on a study using ^{11}C-flumazenil PET to explore whether secondary thalamic neuronal damage may manifest as a decrease in central benzodiazepine receptors in patients with cerebral infarction and internal carotid artery or middle cerebral artery disease. The retrospective study included data from 140 patients with unilateral cerebral infarction ipsilateral to internal carotid artery or middle cerebral artery disease. All patients underwent ^{11}C-flumazenil PET/CT in the chronic stage, with quantitative measurements of tracer binding potential, cerebral blood flow, and cerebral metabolic oxygen rate. The authors found that in the thalamus ipsilateral to infarcts, these parameter values were significantly lower than those in the contralateral thalamus, with significant correlations between ipsilateral-to-contralateral ratios. Patients with corona radiata infarcts and striatocapsular infarcts had significantly lower ipsilateral-to-contralateral binding ratios in the thalamus than those without. The ipsilateral-to-contralateral ratio of binding in the thalamus was significantly correlated with the ipsilateral-to-contralateral cerebral metabolic rate of oxygen ratio in the frontal cortex and was negatively correlated with lower performance on cognitive tests. The authors concluded that "secondary thalamic neuronal damage may manifest as a decrease in central benzodiazepine receptors in patients with cerebral infarction and internal carotid artery or middle cerebral artery disease, which may be associated with frontal lobe dysfunction."

Stroke

^{68}Ga-FAPI vs ^{18}F-FDG in Newly Diagnosed NSCLC

Wu et al. from the Affiliated Hospital of Southwest Medical University, the Nuclear Medicine and Molecular Imaging Key Laboratory of Sichuan Province, and Academician (Expert) Workstation of Sichuan Province (all in Luzhou, China) reported on July 4 ahead of print in *Frontiers in Oncology* on a study comparing ^{68}Ga–fibroblast-activation protein inhibitor (^{68}Ga-FAPI) and ^{18}F-FDG PET/CT in evaluation of newly diagnosed non–small cell lung cancer (NSCLC). The prospective study included 28 patients (15 women, 13 men; median age, 60.5 y; age range, 35–78 y) with new and histopathologically confirmed NSCLC. All participants underwent both ^{68}Ga-FAPI and ^{18}F-FDG PET/CT imaging, and the performance of the tracers was compared by visual assessment, rates of cancer detection, and semiquantitative parameters for both primary tumors and metastases. The 2 tracers were found to have similar detection performance in primary tumors. ^{68}Ga-FAPI PET/CT was more effective than ^{18}F-FDG PET/CT in evaluation of most metastases, including those in lymph nodes (53 vs 49), pleura (8 vs 7), liver (4 vs 1), and bone (41 vs 35). SUV_{max} and tumor-to-background ratio values for ^{68}Ga-FAPI were significantly superior to those with ^{18}F-FDG in lymph node, pleural, and bone metastases. SUV_{max} assessments for the tracers were comparable in hepatic metastases, but ^{68}Ga-FAPI produced a significantly higher tumor-to-background ratio than ^{18}F-FDG. ^{68}Ga-FAPI PET/CT showed excellent staging accuracy (80% of N and 92.9% of M stage disease). The authors concluded that ^{68}Ga-FAPI PET/CT is excellent for evaluation of newly diagnosed NSCLC and "improves the detection rates of most metastases, facilitating the superior staging of patients with newly diagnosed NSCLC, relative to that achieved by ^{18}F-FDG PET/CT."

Frontiers in Oncology

^{68}Ga-FAPI vs ^{18}F-FDG in Staging/Restaging Gastric Cancer

In an article from some of the same researchers, in the July 1 issue of *Frontiers in Oncology* (2002,12:925100), Zhang et al. from the Affiliated Hospital of Southwest Medical University (Luzhou), Nuclear Medicine and Molecular Imaging Key Laboratory of Sichuan Province (Luzhou), Southwest Medical University (Luzhou), the Fourth People's Hospital of Chengdu, and the Clinical Hospital of Chengdu Brain Science Institute/University of Electronic Science and Technology of China (Chengdu; all in China) reported on a study comparing the diagnostic efficacy of ^{68}Ga–fibroblast-activated protein inhibitor (^{68}Ga-FAPI-04) and that of ^{18}F-FDG PET/CT for primary tumors, lymph nodes, and distant metastatic lesions in gastric cancer and assessing respective results in tumor staging and restaging. The study included 25 patients (mean age, 56 ± 12 y) with pathologically confirmed gastric cancer. Patients underwent imaging with both tracers within a 1-wk period. ^{68}Ga-FAPI-04 showed higher sensitivity than ^{18}F-FDG PET/CT for detecting primary tumors (94.74% vs 68.42%), lymph node metastases (97.40% vs 41.56%), and distant metastases (97.17% vs 43.11%), with significantly higher uptake in tumors (median SUV_{max}, 10.28 vs 3.20), lymph node metastases (9.20 vs 3.15), and distant metastases (8.00 vs 4.20). ^{68}Ga-FAPI-04 PET/CT resulted in new oncologic findings in 14 of the 25 patients and corrected tumor staging or restaging in 7 patients. The authors concluded that these results highlight the potential of ^{68}Ga-FAPI-04 PET/CT tumor staging in increasing the accuracy of gastric cancer diagnosis, "which may facilitate treatment decision making."

Frontiers in Oncology

Early Revascularization, Inducible Ischemia, and Outcomes

Rozanski et al. from Mount Sinai Morningside Hospital and Mount Sinai Heart (New York, NY), the University of Calgary (Alberta, Canada), Cedars-Sinai Medical Center (Los Angeles, CA), and the David Geffen School of Medicine at the University of California, Los Angeles reported in the July 19 issue of the *Journal of the American College of Cardiology* (2022;80[3]202–215) on a study using stress/rest SPECT myocardial perfusion imaging (MPI) to assess the relationships between stress-induced myocardial ischemia, revascularization, and all-cause mortality in patients with normal or low left ventricular ejection fractions (LVEFs). The retrospective study included data from 43,443 patients who underwent stress/rest SPECT MPI from 1998 to 2017, with a median follow-up of 11.4 y. Myocardial ischemia was evaluated for its relationship to early revascularization and mortality. The researchers found that the frequency of myocardial ischemia varied widely depending on LVEF and angina, ranging from 6.7% in patients with LVEF ≥55% and no typical angina to 64.0% in patients with LVEF <45% and typical angina. Of the 39,883 patients with LVEF ≥45%, early revascularization was associated with increased mortality in those without ischemia and lower mortality among patients with severe (≥15%) ischemia. Of the 3,560 patients with LVEF <45%, revascularization was not associated with mortality benefits in those with no or mild ischemia but was associated with decreased mortality in those with moderate (10%–14%) and severe (≥15%) ischemia. The authors summarized their findings that in this very large cohort "early myocardial revascularization was associated with a significant reduction in mortality among both patients with normal LVEF and severe inducible myocardial ischemia and patients with low LVEF and moderate or severe inducible myocardial ischemia."

Journal of the American College of Cardiology

Optimizing Prostate Cancer Lymph Node Staging

In an article published on July 21 ahead of print in *Prostate*, Wang et al. from Xiangya Hospital/Central South University (Changsha City, China) reported on a study developed to explore approaches to improving the utility of ^{68}Ga–prostate-specific membrane antigen (^{68}Ga-PSMA) PET/CT imaging for diagnosing lymph node metastasis in prostate cancer patients through combined evaluation of inflammatory hematologic markers. The retrospective study included pretreatment data on a group of patients, including initial total prostate-specific antigen levels, hematologic findings, biopsy and surgical pathology results, and ^{68}Ga-PSMA PET/CT findings. The researchers identified SUV_{max}, neutrophil/lymphocyte ratio, platelet/lymphocyte ratio, initial prostate-specific antigen levels, and clinical T stage as independent predictors of lymph node metastasis. A nomogram combining optimal cutoff values for these variables was constructed and found to be associated with good predictability. The authors concluded that "SUV_{max}, neutrophil/lymphocyte ratio, platelet/lymphocyte ratio, initial total prostate-specific antigen, and clinical T stage represent valuable independent predictors of lymph node metastasis in prostate cancer patients, offering an opportunity to further optimize lymph node staging."

Prostate

Metabolic Abnormality Patterns in Lewy Body Dementia

Lu et al. from Huashan Hospital/Fudan University (Shanghai), Zhongnan Hospital of Wuhan University, and Shanghai Jiao Tong University Affiliated Sixth People's Hospital (Shanghai; all in China) reported on July 20 ahead of print in *Movement Disorders* on a study designed to identify disease-specific metabolic patterns that can illuminate the question of whether dementia with Lewy bodies (DLB) and Parkinson disease (PD) dementia represent the same disease, distinct entities, or conditions within the same spectrum. Sixty-seven patients with DLB, 50 with PD dementia, and 15 healthy controls were enrolled and assigned to 2 cohorts, 1 for pattern identification and 1 for validation. The study also included 30 patients with PD without dementia for pattern discrimination and differentiation. All participants underwent ^{18}F-FDG PET/CT, with 21 undergoing 2 serial scans. DLB-related and PD dementia–related patterns shared similarities: comparative hypometabolism in the middle temporal gyrus, middle occipital gyrus, lingual gyrus, precuneus, cuneus, angular gyrus, superior and inferior parietal gyri, middle and inferior frontal gyri, cingulate, and caudate, as well as comparative hypermetabolism in the cerebellum, putamen, thalamus, precentral/postcentral gyrus, and paracentral lobule. These metabolic characteristics differed from PD-related patterns. Patients with DLB and PD dementia, however, could not be distinguished from one another successfully by any pattern, but patients with PD could be recognized easily. DLB-related and PD dementia–related pattern expression showed similar efficacies in cross-sectional disease severity assessment and, in the subset of twice-imaged patients, longitudinal progression monitoring. The authors concluded that "consistent abnormalities in metabolic patterns of DLB and PD dementia might underline the potential continuum across the clinical spectrum from PD to DLB."

Movement Disorders

^{18}F-PI-2620 Tau PET Imaging in Alzheimer Disease

In an article published on July 17 ahead of print in *Neuropsychopharmacology Reports*, Bun et al. from Keio University School of Medicine (Tokyo), Eisai Co., Ltd. (Tokyo), and the National Institute of Radiological Sciences/National Institutes for Quantum and Radiological Science and Technology (Chiba; all in Japan) reported on a pilot study of the second-generation tau tracer ^{18}F-PI-2620 in Alzheimer disease (AD). The study included 7 individuals with probable AD and 7 healthy controls. Imaging variables compared between the 2 groups included SUV ratios in regions of interest in the medial temporal region and neocortex. Correlations between these uptake ratios and plasma p-tau181 and cognitive test scores were also assessed. Tracer uptake was significantly increased in AD individuals across all regions of interest. SUV ratios in in these regions were significantly correlated with plasma p-tau181 levels and with cognitive scores. The authors concluded that these results "add to accumulating evidence suggesting that ^{18}F-PI-2620 is a promising tau PET tracer that allows patients with AD to be distinguished from healthy controls." They emphasized the importance of early identification of abnormal tau in the brain for development of new therapeutic interventions and called for larger studies.

Neuropsychopharmacology Reports

^{124}I PET/CT and ^{124}I PET/MR in Resected DTC

Grafe et al. from University Hospital Essen/University Duisburg-Essen and University Hospital Dusseldorf (both in Germany) reported on June 21 in *Cancers (Basel)* (2022;14[13]:3040) on the results of a study of quantitative differences between ^{124}I PET/CT and ^{124}I-PET/MR findings in a group of patients after thyroidectomy for differentiated thyroid carcinoma (DTC). Thirty-five patients (23 female, 12 male; mean age, 52 y; range, 16–85 y) with a total of 43 imaging studies were included. All patients underwent whole-body (skull base to midthigh) PET/CT and a dedicated head–neck (skull base to upper lung) PET/MR examination on the same day, allowing for intraindividual comparisons of the same anatomic areas. CT-based attenuation correction in PET/CT and MR-based attenuation correction in PET/MR with bone atlas were compared. In all, 111 ^{124}I-avid lesions were detected on PET/CT and 132 on PET/MR. The median SUV_{mean} for 98 congruent lesions measured on PET/CT was 12.3. For PET/MR, the median SUV_{mean} was 16.6 with MR-based AC. The authors concluded that although these 2 hybrid imaging approaches in patients with resected DTC provided overall comparable quantitative results in a clinical setting (despite different patient positioning and attenuation correction methods), the number of detected lesions and average SUV_{mean} values for congruent lesions was higher for PET/MR.

Cancers (Basel)

Reviews

Review articles provide an important way to stay up to date on the latest topics and approaches through valuable summaries of pertinent literature. The Newsline editor recommends several general reviews accessioned into the PubMed database in June and July. Parpinel et al. from the Sant'Anna Hospital/University of Turin and the Ospedale degli Infermi (Ponderano; both in Italy) published "Use of positron emission tomography for pregnancy-associated cancer assessment: A review" in the July 1 issue of the *Journal of Clinical Medicine* (2022;11[13]: 3820). In an overview in the July 20 issue of *Expert Review of Molecular Diagnostics*, Faldu and Shah from Nirma University (Ahmedabad, India) provided "Alzheimer's disease: A scoping review of biomarker research and development for effective disease diagnosis." Manafi-Farid et al. from Shariati Hospital/Tehran University of Medical Sciences (Iran), Massachusetts General Hospital and Harvard Medical School (Boston, MA), University Hospital Salzburg/Paracelsus Medical University (Austria), and Iran University of Medical Sciences (Tehran) reported in the June 28 issue of *Frontiers in Medicine (Lausanne)* on "ImmunoPET: Antibody-based PET imaging in solid tumors." An overview of "Immune checkpoint molecules in neuroblastoma: A clinical perspective" was published by Pathania et al. from the University of Nebraska Medical Center (Omaha), the National Institutes of Biomedical Innovation, Health, and Nutrition (Osaka, Japan), Sri Rajiv Gandhi College of Dental Sciences & Hospital (Bengaluru, India), Sree Sai Dental College & Research Institute (Srikakulam, India), and Banaras Hindu University (Varanasi, India) in the July 3 issue of *Seminars in Cancer Biology*. Omorphous et al. from Heartlands Hospital/University Hospitals Birmingham, St. Bartholomew's Hospital (London), Mount Vernon Cancer Centre (London), Lister Hospital (Stevenage), University of Hertfordshire (Northwood), King's College London, Guy's Hospital (London), and Brunel University (London; all in the UK), and Apollo Hospitals Educational and Research Foundation (Chennai, India) surveyed "The increasing indications of FDG-PET/CT in the staging and management of invasive bladder cancer" on July 5 ahead of print in *Urologic Oncology.*

A Life in Nuclear Medicine in Israel

A Conversation Between Ora Israel and Johannes Czernin

Ora Israel[1] and Johannes Czernin[2]

[1]Rappaport School of Medicine, the Technion, Haifa, Israel; and [2]David Geffen School of Medicine at UCLA, Los Angeles, California

Johannes Czernin, MD, editor in chief of *The Journal of Nuclear Medicine*, talked with Ora Israel, MD, Emeritus Professor of Imaging at the Rappaport School of Medicine, the Technion (Haifa, Israel). In 2018, she retired from clinical duties and from her 18 y as Director of Nuclear Medicine at the Rambam Health Care Campus. She also served as Deputy Director for Research at Rambam for 4 y. For more than 4 decades, her main scientific interests included multimodality tumor imaging, in vivo radionuclide quantitation, and imaging of infection and inflammation. She has been involved in the development of hybrid imaging, including SPECT/CT and PET/CT (since its beginnings in the late 1990s), and, in recent decades, in developing guidelines for clinical implementation of these technologies. She is the author of 3 textbooks on hybrid imaging, more than 200 scientific articles, and more than 30 book chapters.

Dr. Israel has led the training of physicians and scientists in Israel and throughout the international nuclear medicine community. She was a long-time visiting professor in the Harvard Joint Program in Nuclear Medicine, on the faculty of the Johns Hopkins Nuclear Medicine course in Baltimore, MD, served as faculty in the PET/CT course of the Royal Society of Medicine (London, UK), and was a participant in educational programs organized by the International Atomic Energy Agency. She serves as an associate editor of *The Journal of Nuclear Medicine* (*JNM*) and the *European Journal of Nuclear Medicine and Molecular Imaging*. She is a consultant for molecular imaging for GE Healthcare. Dr. Israel is a fellow of SNMMI and an honorary member of the European Association of Nuclear Medicine. She also received the Life Achievement Award from the SNMMI General Imaging Council and the Barry Siegel Lectureship award from the SNMMI Correlative Imaging Council. She is a founding member of the Israeli Academy of Medicine.

Dr. Czernin: *Thank you, Ora, for taking the time to speak with me. Can you provide our readers with a little bit of background on your life and career?*

Dr. Israel: I was born, raised, and educated in Romania, in a German-speaking family. My grandmother came from Austria. I completed my medical studies at the Institute for Medicine and Pharmacy in Bucharest. After I married my husband of 50 y, Stefan, and graduated, we immigrated to Israel. We have two accomplished children and four beautiful grandchildren. Having completed medical school and internship, I had to choose a residency. My first choices had been either intensive care or nephrology. But when we came to Israel I was offered a position in nuclear medicine—and immediately said no! When they asked why, I said "Because I'm afraid of radiation." But then they told me that they had just recruited a very promising new chief of nuclear medicine at Rambam, Dov Front, and that it could be a lot of fun. So, I changed my mind. Until today, most people who come out of medical school don't really know what nuclear medicine is all about.

Ora Israel, MD

Dr. Czernin: *How many years of training did you have in Israel?*

Dr. Israel: It was 4-and-a-half years of training, as it is now. But some of the components have changed over the years. At present, residency consists of 2 y in nuclear medicine, 6 mo of PET/CT, 1 y in diagnostic radiology, 6 mo of clinical rotations, and also 6 mo of basic research, which I consider to be very important.

Dr. Czernin: *Is nuclear medicine an independent department in Israel or is it part of radiology?*

Dr. Israel: It is independent. There was a letter to the editor in *JNM* in 1993, signed by Dov Front and me, with the title "Nuclear medicine in Israel: independent, alive and well" (*J Nucl Med.* 1993;34[10]:1826). I am happy to say it still is like that!

Dr. Czernin: *Looking at your bibliography, your SPECT/CT work is an important contribution to nuclear medicine.*

Dr. Israel: We also had the privilege to work with the first PET/CT that was manufactured in Haifa and published quite a few important studies on the subject. With that being said, I always considered SPECT/CT as an important modality.

Dr. Czernin: In 2020, *you published with Van den Wyngaert and other authors a very nice review article in* JNM *(2020;61[9]:1284–1291), in which you listed accomplishments of but also barriers and challenges to SPECT/CT in clinical practice. You mentioned subpar CT resolution. How do you see development of the CT component in SPECT/CT? What do you foresee as the standard of care in SPECT/CT from a technology point of view?*

Dr. Israel: First, the clinical indications for SPECT/CT are often not in oncology, and studies are often done in younger patients. Therefore, radiation exposure is a concern. There are very few clinical indications for which we have to do a whole-body SPECT/CT. Most often we need to do a limited field-of-view study. We also have to inject as little tracer activity as possible. We have to look at SPECT/CT technology from both sides: SPECT has seen major advances in detector technology, such as the advent of cadmium–zinc–telluride detectors. We can inject lower doses while obtaining high image quality. With respect to the CT part, it depends on the clinical indication. Do we need a diagnostic CT, or do we need to increase the specificity of our SPECT images? We have to be

---

Received Jul. 22, 2022; revision accepted Jul. 22, 2022.

DOI: 10.2967/jnumed.122.264711

able—and we are able with the new technology— to juggle and to find the best way to use this modality.

Dr. Czernin: *If you say that you want to increase the specificity, then often a low dose is good enough. But optimized device design has to be versatile to meet any clinical scenario. What would a device like this look like?*

Dr. Israel: Actually, I think that there are 2 devices that look like this that are available today. Both come from Israel. But first, we, the physicians, need to switch mentally from planar to tomographic imaging using single-photon emitting agents. And here we have 2 challenges. One is in our mind: to forget planar imaging of bone, lung, or kidneys. The other major impediment is the lack of development of new tracers. I know of very few developments and trials for new SPECT tracers, and this is a major problem.

Dr. Czernin: *If the industry doesn't buy in and if tracers are handled just like drugs for regulatory purposes but not reimbursed at a reasonable level, then a huge section of the market drops out, because there's no money in it. There's not enough money in diagnostics. The same used to be true for PET tracers if they were not linked to a therapeutic, like in theranostics.*

Dr. Israel: I see a chance to overcome these challenges when we talk about treatment, about the need for dosimetry. I do believe that SPECT/CT can play a very important role here.

Dr. Czernin: *But you need to commercialize imaging probes, and the return on investment for diagnostics is much worse than for therapeutics. Business translation is a really important aspect, because if you cannot monetize it, it will not happen in large sections of the world.*

Dr. Israel: I understand that. But it really saddens me. It shouldn't be like this; it should not be like this at all!

Dr. Czernin: *This would be an interesting political and economic discussion. You mentioned new tracers. Can you give examples of what specifically you would want to see?*

Dr. Israel: I thought about ^{99}Tc-labeled somatostatin receptor– or prostate-specific membrane antigen (PSMA)–targeted tracers. These studies are absolutely beautiful, mainly when used with SPECT/CT. The problem is that there are very few, if any, well-designed big studies. We are shooting ourselves in the foot if there are no good studies.

Dr. Czernin: *You mentioned dosimetry as a key potential application for SPECT/CT, and I completely agree, because it's irrational to administer the same activity to each patient. I believe that we often "underdose" patients. In the United Stated we need to get solid reimbursement for doing dosimetry, as this is very labor intensive. Can you do sequential early, 24-, 48-, 72-h dosimetry scans in Israel? And what does it mean for workflow?*

Dr. Israel: Workflow can be one of the problems. If you rearrange your workflow to add SPECT/CT to standalone SPECT or planar, imaging, everybody gets mad at you. But if you plan your schedule well, you can do it. For the moment we cannot and should not do these studies in a nonresearch environment. It would not be ethical to do it, because we have not proven yet that dosimetry calculations based on SPECT/CT lead to improved outcomes. So we are not there yet, but I do believe that this is the main direction to take.

Dr. Czernin: *There is a major SNMMI initiative called the Dosimetry Challenge. This aims at simplifying data acquisition without compromising data robustness. When you look at radiation oncology, they have dosimetrists who do nothing but dosimetry-based radiation planning. We believe that the annual number of theranostic cycles in the United States will be very high. To manage the volume we will need well-trained nuclear medicine dosimetrists in addition to nursing and well-trained physicians to accommodate these high patient volumes.*

Dr. Israel: I agree, but there is also a lot of work being done by industry; there is new software, and this will make the work of physicists and dosimetrists much easier.

Dr. Czernin: *Do you do dosimetry for your PSMA-targeted therapies?*

Dr. Israel: Not clinically. As I said before, the studies documenting beneficial dosimetry impact on outcomes need to be well-designed. The new therapies are what will keep us alive and well in the future. But we have to do it right, based on a lot of research.

Dr. Czernin: *I agree that this is the future, because we are the only discipline that can achieve whole-body precision medicine.*

Dr. Israel: Exactly. You can first identify patients who are likely to respond to therapy and then optimize the administered activity to achieve further improvements in outcome.

Dr. Czernin: *How do you best promote the concept that we do precision oncology, and what are the best examples for you?*

Dr. Israel: We have to have the best partnerships with oncologists, both clinical and radiation oncologists. We need to understand their unmet needs and what we can provide them.

Dr. Czernin: *That's exactly true. I call it the integrated independence of nuclear medicine.*

Dr. Israel: I have always advocated for independent nuclear medicine. You can teach radiologists to read PET/CT studies and which radiotracer to use. But FDG is not just another contrast agent. I have witnessed in more than 40 y of my career that only people who are 100% dedicated to nuclear medicine can move this field forward. Nothing that has ever moved nuclear medicine forward has come from somebody who was not 100% dedicated to the field There is no other way unless you are completely dedicated to this specialty, which I think is beautiful. I love it. I've loved it for my whole career.

Dr. Czernin: *Different topic: Do you produce therapeutic compounds onsite? How is this done in Israel? Do you produce onsite or compound?*

Dr. Israel: We have 3 centralized radiopharmacies that supply demand for the whole country.

Dr. Czernin: *Are they private or government run?*

Dr. Israel: Two are private, and 1 is government run. Some centers, are also very active in research with respect to new radiotracers and new ways of production.

Dr. Czernin: *We're coming to the final portions of this discussion. I am always interested in different health care systems. Can you provide us with brief insights into the Israeli system? Is it a mixed, private, or government-funded health care environment?*

Dr. Israel: Health care in Israel is socialized. We have mandatory health care insurance.

> ˋ[Y]ou have to love what you do.˝

Dr. Czernin: *It's a European-style system?*

Dr. Israel: There are 4 health care funds, and we are all members of one of them. And everything is very well documented and monitored.

Dr. Czernin: *Is there additional private insurance that one can buy on top of the government-managed system?*

Dr. Israel: Yes. This can help in choosing a surgeon and perhaps getting into a private care facility. This could also help a patient go overseas for surgery or for some forms of treatment that cannot be done yet in Israel. But the basic health care system is very good. Life expectancy is high, and infant mortality rates are very low.

Dr. Czernin: *Is there societal agreement that health care is a right for everyone—that health care is a human right?*

Dr. Israel: There is no such thing as an ideal place. But, yes, everybody has the right and access to, in my opinion, high-level health care.

Dr. Czernin: *What about the future of nuclear medicine?*

Ora Israel: There was a dry spell 10–15 y ago when we really had problems here recruiting talented young people. But over the last few years most of the centers have had waiting lists for acceptance into nuclear medicine residency. And there is also a new trend: double-certified imaging physicians. They spend 7–7.5 y in training through both diagnostic radiology and nuclear medicine (some periods of training overlap, thus the shorter total number of months or years). No cutting corners! The right way to go!

Dr. Czernin: *Do you think that is why more people are interested in joining the field?*

Dr. Israel: I think that hybrid imaging, PET/CT and SPECT/CT, had an impact, as well as theranostics.

Dr. Czernin: *What about therapeutics?*

Dr. Israel: There are new opportunities in therapeutics. The next generation of nuclear medicine physicians will finally be able to treat patients in addition to precisely diagnosing their disease! Therapeutics will make a change. If I were still in charge of a department today, I would see as my main job for the next 2 or 3 y to find the right person to take charge of therapies. Everybody has to know and do everything, but someone should be in charge of establishing a strong therapy unit. This is also important in order to have a key point person to interact and communicate with the clinicians and patients.

Dr. Czernin: *We have reached the end of this discussion. Can you provide a word of wisdom or advice for the young people joining the field?*

Dr. Israel: First, you have to love what you do. You have to always try and do whatever your task is at the highest level. And although not everybody can, I think that doing research just brightens your mind. It gives you a different perspective on life and a lot of excitement. The moment you get the galley proofs of a paper accepted by *JNM* is something you will always cherish.

Dr. Czernin: *I like the* JNM *angle! Ora, your insights are going to be very much appreciated by our readers and, of course, by me. Thank you so much for taking the time.*

Nuclear Medicine and Artificial Intelligence: Best Practices for Evaluation (the RELAINCE Guidelines)

Abhinav K. Jha[1], Tyler J. Bradshaw[2], Irène Buvat[3], Mathieu Hatt[4], Prabhat KC[5], Chi Liu[6], Nancy F. Obuchowski[7], Babak Saboury[8], Piotr J. Slomka[9], John J. Sunderland[10], Richard L. Wahl[11], Zitong Yu[12], Sven Zuehlsdorff[13], Arman Rahmim[14], and Ronald Boellaard[15]

[1]Department of Biomedical Engineering and Mallinckrodt Institute of Radiology, Washington University in St. Louis, Missouri; [2]Department of Radiology, University of Wisconsin-Madison, Madison, Wisconsin; [3]LITO, Institut Curie, Université PSL, U1288 Inserm, Orsay, France; [4]LaTiM, INSERM, UMR 1101, Univ Brest, Brest, France; [5]Center for Devices and Radiological Health, Food and Drug Administration, Silver Spring, Maryland; [6]Department of Radiology and Biomedical Imaging, Yale University, Connecticut; [7]Quantitative Health Sciences, Cleveland Clinic, Cleveland, Ohio; [8]Department of Radiology and Imaging Sciences, Clinical Center, National Institutes of Health, Maryland; [9]Department of Imaging, Medicine, and Cardiology, Cedars-Sinai Medical Center, California; [10]Departments of Radiology and Physics, University of Iowa, Iowa; [11]Mallinckrodt Institute of Radiology, Washington University in St. Louis, Missouri; [12]Department of Biomedical Engineering, Washington University in St. Louis, St. Louis, Missouri; [13]Siemens Medical Solutions USA, Inc., Hoffman Estates, Illinois; [14]Departments of Radiology and Physics, University of British Columbia, Canada; and [15]Department of Radiology & Nuclear Medicine, Cancer Centre Amsterdam, Amsterdam University Medical Centers, Netherlands

An important need exists for strategies to perform rigorous objective clinical-task-based evaluation of artificial intelligence (AI) algorithms for nuclear medicine. To address this need, we propose a 4-class framework to evaluate AI algorithms for promise, technical task-specific efficacy, clinical decision making, and postdeployment efficacy. We provide best practices to evaluate AI algorithms for each of these classes. Each class of evaluation yields a claim that provides a descriptive performance of the AI algorithm. Key best practices are tabulated as the RELAINCE (Recommendations for EvaLuation of AI for NuClear medicinE) guidelines. The report was prepared by the Society of Nuclear Medicine and Molecular Imaging AI Task Force Evaluation team, which consisted of nuclear-medicine physicians, physicists, computational imaging scientists, and representatives from industry and regulatory agencies.

Key Words: artificial intelligence; evaluation; best practices; clinical task; PET; SPECT; technical efficacy; clinical decision making; postdeployment; generalizability

J Nucl Med 2022; 63:1288–1299
DOI: 10.2967/jnumed.121.263239

I. INTRODUCTION

Artificial intelligence (AI)–based algorithms are showing tremendous promise across multiple aspects of nuclear medicine, including image acquisition, reconstruction, postprocessing, segmentation, diagnostics, and prognostics. Translating this promise to clinical reality requires rigorous evaluations of these algorithms. Insufficient evaluation of AI algorithms may have multiple adverse consequences, including reducing credibility of research findings, misdirection of future research, and, most importantly, yielding tools that are useless or even harmful to patients (*1*). The goal of this report is to provide best practices to evaluate AI algorithms developed for different parts of the imaging pipeline ranging from image acquisition to postprocessing to clinical decision making in the context of nuclear medicine. We provide these practices in the context of evaluating AI algorithms that use artificial neural network–based architectures, including deep learning. However, many principles are broadly applicable to other machine-learning and physics-based algorithms. In the rest of the report, AI algorithms refer to those that use artificial neural networks.

Evaluation has a well-established and essential role in the translation of any imaging technology but is even more critical for AI algorithms due to their working principles. AI algorithms are typically not programmed with user-defined rules, but instead learn rules via analysis of training data. These rules are often not explicit and thus not easily interpretable, leading to unpredictability in output. This leads to multiple unique challenges. First, AI algorithms may yield inaccurate results that may adversely impact performance on clinical tasks. For example, AI-based reconstruction may introduce spurious lesions (*2*), AI-based denoising may remove lesions (*3*), and AI-based lesion segmentation may incorrectly identify healthy tissue as malignancies (*4*). Evaluations are thus crucial to assess the algorithm's clinical utility. A second challenge is that of generalizability. AI algorithms are often complicated models with many tunable parameters. These algorithms may perform well on training data, but may not generalize to new data, such as from a different institution (*5*), population groups (*6,7*), or scanners (*8*). Possible reasons for this include that the algorithm uses data features that correlate with the target outcome only within training data, or that the training data does not sufficiently represent the patient population. Evaluations are needed to assess the generalizability of these algorithms. A third challenge is data drift during clinical deployment. When using AI systems clinically, over time, the input-data distribution may drift from that of the training data due to changes in patient demographics, hardware, acquisition and analysis protocols (*9*). Evaluation in postdeployment settings can help identify this data drift. Rigorous evaluation of AI algorithms is also necessary because AI is being explored to support decisions in high-risk applications, such as guiding treatment.

Received Sep. 17, 2021; revision accepted May 11, 2022.

For correspondence or reprints, contact Abhinav K. Jha (a.jha@wustl.edu).

In summary, there is an important need for carefully defined strategies to evaluate AI algorithms, and such strategies should be able to address the unique challenges associated with AI techniques. To address this need, the Society of Nuclear Medicine and Molecular Imaging put together an Evaluation team within the AI Task Force. The team consisted of computational imaging scientists, nuclear medicine physicians, nuclear medicine physicists, biostatisticians, and representatives from industry and regulatory agencies. The team was tasked with defining best practices for evaluating AI algorithms for nuclear medicine imaging. This report has been prepared by this team.

In medical imaging, images are acquired for specific clinical tasks. Thus, AI algorithms developed for the various parts of the imaging pipeline, including acquisition, reconstruction, postprocessing, and segmentation, should be evaluated on the basis on how well they assist in the clinical tasks. As described later, these tasks can be broadly classified into 3 categories: classification, quantification, or a combination of both (*10,11*). An oncologic PET image may be acquired for the task of tumor-stage classification or for quantification of tracer uptake in tumor. However, current AI-algorithm evaluation strategies are often task agnostic. For example, AI algorithms for reconstruction and postprocessing are often evaluated by measuring image fidelity to a reference standard using figures of merit (FoMs) such as root mean square error. Similarly, AI-based segmentation algorithms are evaluated using FoMs such as Dice scores. However, studies, including recent ones, show that these evaluation strategies may not correlate with clinical-task performance and task-based evaluations may be needed (*2,3,11–15*). One study observed that evaluation of a reconstruction algorithm for whole-body FDG PET using fidelity-based FoMs indicated excellent performance, but on the lesion-detection task, the algorithm was yielding both false-negatives and -positives due to blurring and pseudo-low uptake patterns, respectively (*2*). Similarly, an AI-based denoising method for cardiac SPECT studied using realistic simulations seemed to yield excellent performance as evaluated using fidelity-based FoMs. However, on the task of detecting perfusion defects, no performance improvement was observed compared with noisy images (*3*). Such findings show that task-agnostic approaches to evaluate AI algorithms have crucial limitations in quantifying performance on clinical tasks. Thus, evaluation strategies that specifically measure performance on clinical tasks are needed.

Evaluation studies should also quantitatively describe the generalizability of the AI algorithm to different population groups and to different portions of the imaging pipeline, including scanners, acquisition, and analysis protocols. Finally, evaluations should yield quantitative measures of performance to enable clear comparison with standard of care and other methods and provide guidance for clinical utility. To incorporate these needs, we recommend that an AI-algorithm evaluation strategy should always produce a claim consisting of the following components (Fig. 1):

- A clear definition of the task
- Patient population(s) for whom the task is defined
- Definition of the imaging process (acquisition, reconstruction, and analysis protocols)
- Process to extract task-specific information
- FoM to quantify task performance, including process to define reference standard

We describe each component in the next section. We next propose an evaluation framework that categorizes the evaluation strategies into 4 classes: proof of concept, technical, clinical and postdeployment evaluation. This framework will serve as a guide to conduct the evaluation study that provides evidence to support the intended claim. We also provide best practices for conducting evaluations for each class. Key best practices are summarized as the RELAINCE (Recommendations for EvaLuation of AI for NuClear medicinE) guidelines.

In this report, the terms “training,” “validation,” and “testing” will denote the building of a model on a specific dataset, the tuning/optimization of the model parameters, and the evaluation of the optimized model, respectively. The focus of this report is purely on testing/evaluation of an already developed AI algorithm. Best practices for development of AI algorithms are described in a companion paper (*16*).

NOTEWORTHY

- AI algorithms should be evaluated on clinical tasks.
- AI algorithm evaluations should yield a claim that provides a clear and descriptive characterization of the performance of the AI algorithm on a clinical task. The claim should include a definition of the clinical task, patient population for whom the task is defined, definition of the imaging process, procedure to extract task-specific information, and figure of merit to quantify task performance.
- We propose a 4-class framework that evaluates AI algorithms for nuclear-medicine imaging on clinical tasks and yields a claim. The 4 classes in the framework include promise, technical, clinical, and postdeployment evaluation of AI algorithms.
- We provide best practices for determining study type, data collection, defining reference standard, and choosing figures of merit for each class of evaluation.
- Key recommendations are summarized as the RELAINCE (Recommendations for EvaLuation of AI for NuClear medicinE) guidelines.

II. COMPONENTS OF THE CLAIM

The claim provides a clear and descriptive characterization of the performance of an AI algorithm based on how well it assists in the clinical task. The components of a claim are shown in Figure 1 and described below.

II.1. Definition of the Clinical Task

In this paper, the term “task” refers to the clinical goal for which the image was acquired. Broadly, in nuclear medicine, tasks can be grouped into 3 categories: classification (including lesion detection), quantification, or joint classification and quantification. A classification task is defined as one where the patient image is used to classify the patient into one of several categories. For example, identifying if cancer is present or absent or the cancer stage from an oncologic PET image. Similarly, predicting whether a patient would/would not respond to therapy would be a classification task. A quantification task is defined as one where some numeric or statistical feature is estimated from the patient image. Examples include quantifying SUV, metabolic tumor volume (MTV), intralesion heterogeneity, or kinetic parameters from oncologic PET images.

II.2. Patient Population for Whom the Task Is Defined

The performance of an imaging algorithm can be affected by the physical and statistical properties of the imaged patient

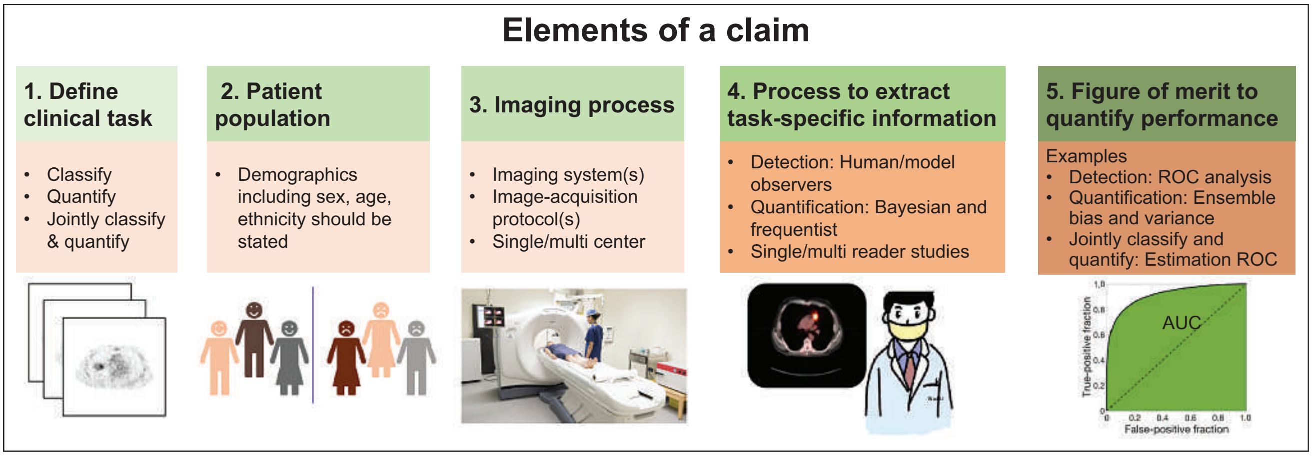

FIGURE 1. The components of a claim. (Scanner image: iStock photo.)

population. Results for one population may not necessarily translate to others (*5,7*). Thus, the patient population should be defined in the claim. This includes aspects such as sex, ethnicity, age group, geographic location, disease stage, social determinants of health, and other disease and application-relevant biologic variables.

II.3. Definition of Imaging Process

The imaging system, acquisition protocol, and reconstruction and analysis parameters may affect task performance. For example, an AI algorithm evaluated for a high-resolution PET system may rely on high-frequency features captured by this system and thus not apply to low-resolution systems (*8*). Depending on the algorithm, specific acquisition protocol parameters may need to be specified or the requirement to comply with a certain accreditation standard, such as SNMMI-Clinical Trial Network, RSNA QIBA profile, and the EARL standards, may need to be stated. For example, an AI-based denoising algorithm for ordered-subsets-expectation-maximization (OSEM)–based reconstructed images may not apply to images reconstructed using filtered backprojection or even for a different number of OSEM iterations since noise properties change with iteration numbers. Thus, depending on the application, the claim should specify the imaging protocol. Further, if the algorithm was evaluated across multiple scanners, or with multiple protocols, that should be specified.

II.4. Process to Extract Task-Specific Information

Task-based evaluation of an imaging algorithm requires a strategy to extract task-specific information from the images. For classification tasks, a typical strategy is to have human observer(s) read the images, detect lesions, and classify the patient or each detected lesion into a certain class (e.g., malignant or benign). Here, observer competency (multiple trained radiologists/one trained radiologist/resident/untrained reader) will impact task performance. The choice of the strategy may impact confidence of the validity of the algorithm. This is also true for quantification and joint classification/quantification tasks. Thus, this strategy should be specified in the claim.

II.5. Figure of Merit (FoM) to Quantify Task Performance

FoMs quantitatively describe the algorithm's performance on the clinical task, enabling comparison of different methods, comparison to standard of care, and defining quantitative metrics of success. FoMs should be accompanied by confidence intervals (CIs), which quantify uncertainty in performance. To obtain the FoM, a reference standard is needed. The process to define the reference standard should be stated.

The Claim Describes the Generalizability of an AI Algorithm: Generalizability is defined as an algorithm's ability to properly work with new, previously unseen data, such as that from a different institution, scanner, acquired with a different image-acquisition protocol, or processed by a different reader. By providing all the components of a claim, an evaluation study will describe the algorithm's generalizability to unseen data, since the claim will specify the characteristics of the population used for evaluation, state whether the evaluation was single or multicenter, define the image acquisition and analysis protocols used, as well as the competency of the observer performing the evaluation study. Figure 2 presents a schematic showing how different kinds of generalizability could be established. Some key points from this figure are:

- Providing evidence for generalizability requires external validation. This is defined as validation where some portion of the testing study, such as the data (patient population demographics) or the process to acquire the data, is different from that in the development cohort. Depending on the level of external validation, the claim can be appropriately defined.
- For a study that claims to be generalizable across populations, scanners, and readers, the external cohort would be from different patient demographics, with different scanners, and analyzed by different readers than the development cohort, respectively.
- Multicenter studies provide higher confidence about generalizability compared with single-center studies since they typically include some level of external validation (patients from different geographical locations/different scanners/different readers).

III. METHODS FOR EVALUATION

The evaluation framework for AI algorithms is provided in Figure 3. The 4 classes of this framework are differentiated based on their objectives, as briefly described below, with details provided in the ensuing subsections. An example for an AI low-dose PET reconstruction algorithm is provided. Figure 3 contains another example for an AI-based automated segmentation algorithm. A detailed example of using this framework to evaluate a hypothetical AI-based transmission-less attenuation compensation method for SPECT

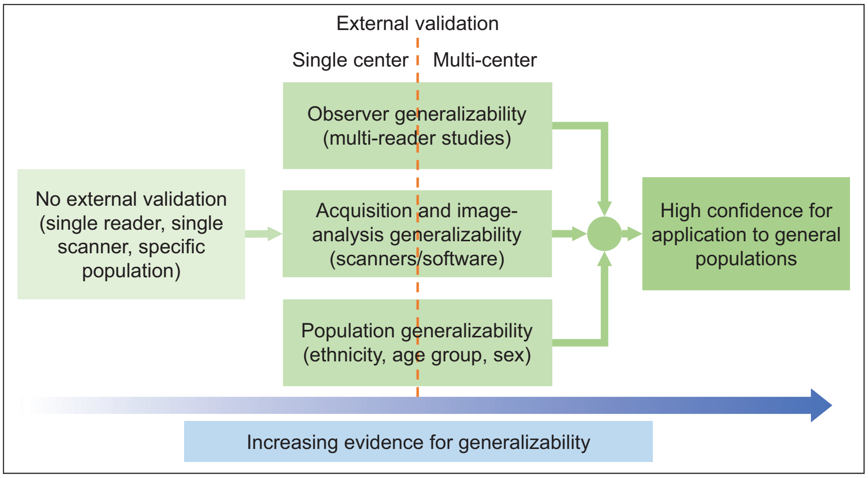

FIGURE 2. Increasing levels of rigor of evaluation, and how they in turn provide increased confidence in the generalizability.

(Supplemental Fig. 1; supplemental materials are available at http://jnm.snmjournals.org) (*17*) is provided in Supplemental section A.

- Class 1: Proof-of-concept (POC) evaluation: Shows the novelty and promise of an algorithm proposed using task-agnostic FoMs. Provides promise for further clinical task-specific evaluation.
  Example: Evaluating the AI PET reconstruction algorithm using root mean square error.
- Class 2: Technical task-specific evaluation: Quantifies technical performance of an algorithm on a clinical task using measures such as accuracy, repeatability, and reproducibility.
  Example: Evaluating accuracy on the task of lesion detection with the AI low-dose PET reconstructed images.
- Class 3: Clinical evaluation: Quantifies the algorithm's efficacy to assist in making clinical decisions. AI algorithms that claim improvements in making diagnostic, predictive, prognostic, or therapeutic decisions require clinical evaluation.
  Example: Evaluating the AI reconstruction algorithm on the task of clinically diagnosing patients referred with the suspicion of recurrence of cancer.
- Class 4: Postdeployment evaluation: Monitors algorithm performance in dynamic real-world settings after clinical deployment. This may also assess off-label use, such as the algorithm's utility in populations and diseases beyond the original claim or with improved imaging cameras and reconstructions that were not used during training. Additionally, this evaluation assesses clinical utility and value over time.
  Example: Evaluating whether the AI PET reconstruction algorithm remains effective over time after clinical deployment.

In the subsections below, for each class of evaluation, we provide the key objectives, the best practices for study design (including determining study type, data collection, defining a reference standard, and choosing FoMs (Fig. 4)), and finally, a generic structure for the claim.

III.1. Proof-of-Concept (POC) Evaluation

III.1.1. Objective: The objective of POC evaluation is to quantitatively demonstrate the technologic innovations of newly developed AI algorithms using task-agnostic FoMs and provide evidence that motivates clinical task-specific evaluation. Clinical or task-specific technical claims should not be put forth based on POC evaluation.

Rationale for Task-Agnostic Objective: A newly developed AI algorithm may be suitable for multiple clinical tasks. For example, a segmentation algorithm may be applicable to radiation therapy planning, estimating volumetric or radiomic features, or monitoring therapy response. Evaluating the algorithm on all these tasks would

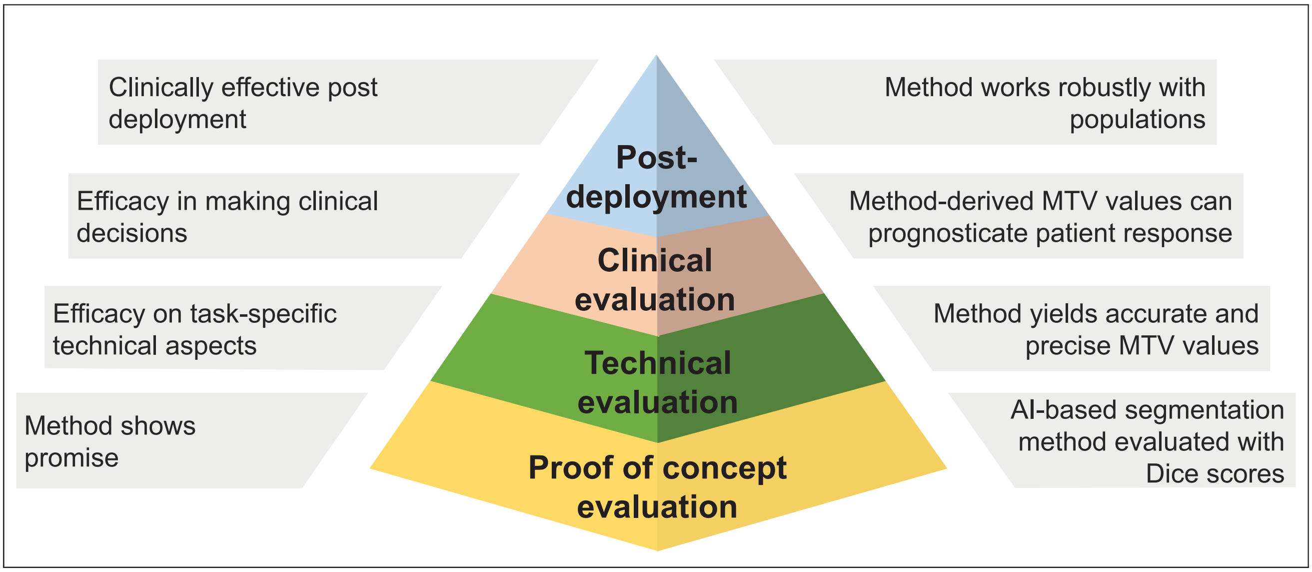

FIGURE 3. Framework for evaluation of AI-based algorithms. The left of the pyramid provides a brief description of the phase, and the right provides an example of evaluating an AI-based segmentation algorithm on the task of evaluating MTV using this framework.

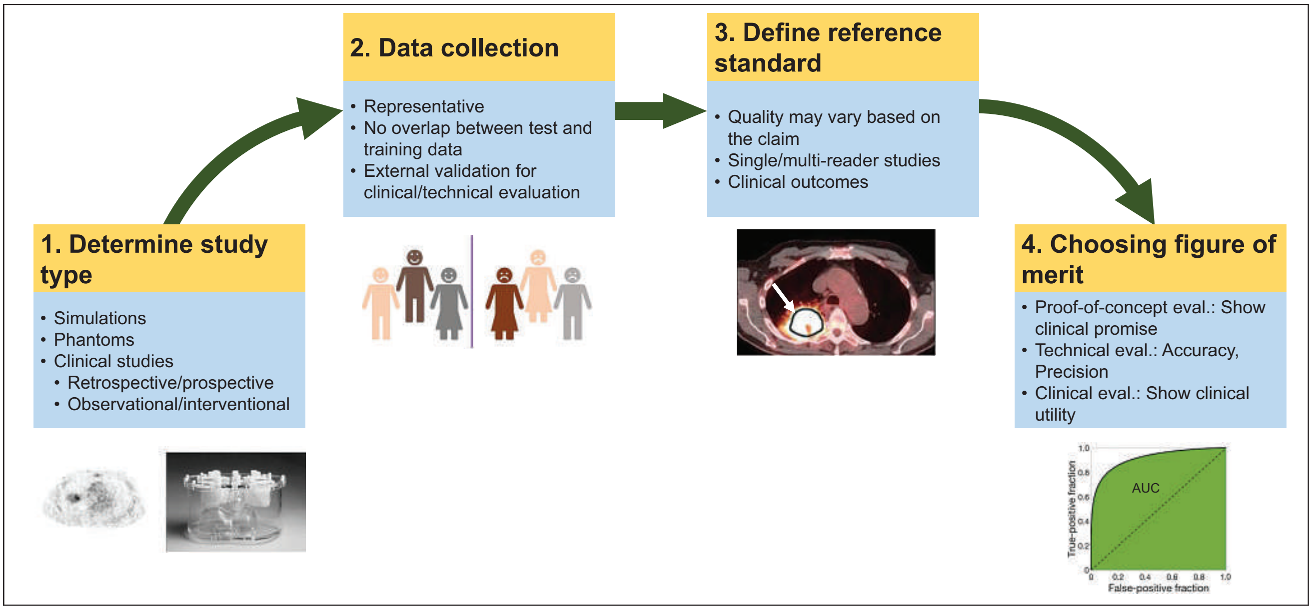

FIGURE 4. Elements of study design for each class of evaluation.

require multiple studies. Further, necessary resources (such as a large, representative dataset) may not be available to conduct these studies. Thus, a task-agnostic objective facilitates timely dissemination and widens the scope of newly developed AI methods.

III.1.2. Study Design: The following are recommended best practices to conduct POC evaluation of an AI algorithm. Best practices to develop the algorithm are covered in the companion paper (*16*).

Data Collection: In POC evaluation, the study can use realistic simulations, physical phantoms, or retrospective clinical or research data, usually collected for a different purpose, for example, routine diagnosis. The data used for evaluation may come from the development cohort, that is, the same overall cohort that the training and validation cohorts were drawn from. However, there must be no overlap between these data. Public databases, such as those available at The Cancer Imaging Archive (*18*) and from medical image analysis challenges, such as at https://grand-challenge.org, can also be used.

Defining Reference Standard: For POC evaluations conducted with simulation and physical phantoms, the ground truth is known. For clinical data, curation by readers may be used, but that may not be of the highest quality. For example, curations by a single reader may be sufficient.

Testing Procedure: The testing procedure should be designed to demonstrate promising technologic innovation. The algorithm should thus be compared against reference and/or standard-of-care methods and preferably other state-of-the-art algorithms.

Figures of Merit: While the evaluation is task-agnostic, the FoMs should be carefully chosen to show promise for progression to clinical task evaluation. For example, evaluating a new denoising algorithm that overly smooths the image at the cost of resolution using the FoM of contrast-to-noise ratio may be misleading. In those cases, a FoM such as structural similarity index may be more relevant. We recommend evaluation of the algorithms using multiple FoMs. A list of some FoMs is provided in Supplemental Table 1.

III.1.3. Output Claim of the POC Study: The claim should state the following:

- The application (e.g., segmentation, reconstruction) for which the method is proposed.
- The patient population.
- The imaging and image analysis protocol(s).
- Process to define reference standard.
- Performance as quantified with a task-agnostic evaluation metric.

We reemphasize that the POC study claim should not be interpreted as an indication of the algorithm's expected performance in a clinical setting or on any clinical task.

Example Claim: Consider the evaluation of a new segmentation algorithm. The claim could read as follows:

> "An AI-based PET tumor-segmentation algorithm evaluated on 50 patients with locally advanced breast cancer acquired on a single scanner with single-reader evaluation yielded mean Dice scores of 0.78 (95% CI 0.71-0.85)."

III.2 Technical Task-Specific Evaluation

III.2.1. Objective: The objective of technical task-specific evaluation is to evaluate the technical performance of an AI algorithm on specific clinically relevant tasks such as those of detection and quantification using FoMs that quantify aspects such as accuracy (discrimination accuracy for detection task and measurement bias for quantification task) and precision (reproducibility and repeatability). The objective is not to assess the utility of the method in clinical decision making, because clinical decision making is a combination of factors beyond technical aspects, such as prior clinical history, patient biology, other patient characteristics (age/sex/ethnicity), and results of other clinical tests. Thus, this evaluation does not consider clinical outcomes.

For example, evaluating the accuracy of an AI-based segmentation method to measure MTV would be a technical efficacy study. This study would not assess whether more accurate MTV measurement led to any change in clinical outcome.

III.2.2. Study Design: Given the goal of evaluating technical performance, the evaluation should be performed in controlled settings. Practices for designing such studies are outlined below. A framework and summary of tools to conduct these studies in the context of PET is provided in Jha et al. (*10*).

TABLE 1

Technical Evaluation: Comparison of Different Study Types, Associated Trade-Offs, and Criteria That Can Be Evaluated with the Study Type

		Simulation studies	Physical phantoms	Clinical studies
Advantage	Known ground truth	Y	Y	Rarely
	Scanner-based		Y	Y
	Model patient biology	Yes, but limited		Y
	Model population variability	Y		Y
Criterion that can be evaluated	Accuracy	Y	Y	
	Repeatability/reproducibility/noise sensitivity with multiple replicates	Y	Y	
	Repeatability/reproducibility/noise sensitivity with test–retest replicates		Y	Yes and recommended
	Biologic repeatability/reproducibility/noise sensitivity			Y
Other factors to consider	Costs	Low	Medium	High
	Time	Low	Medium	High
	Confidence about clinical realism	Low	Medium	High

Study Type: A technical evaluation study can be conducted through the following mechanisms:

1. Realistic simulations are studies conducted with anthropomorphic digital phantoms simulating patient populations, where measurements corresponding to these phantoms are generated using accurately simulated scanners. This includes virtual clinical trials, which can be used to obtain population-based inferences (*19–21*).
2. Anthropomorphic physical phantom studies are conducted on the scanners with devices that mimic the human anatomy and physiology.
3. Clinical-data-based studies where clinical data are used to evaluate the technical performance of an AI algorithm, for example, repeatability of an AI algorithm measuring MTV in test-retest PET scans.

The tradeoffs with these 3 study types are listed in Table 1. Each study type can be single or multiscanner/center, depending on the claim:

- Single-center/single-scanner studies are typically performed with a specific system, image acquisition, and reconstruction protocol. In these studies, the algorithm performance can be evaluated for variability in patients, including different demographics, habitus, or disease characteristics, while keeping the technical aspects of the imaging procedures constant. These studies can measure the sensitivity of the algorithm to patient characteristics. They can also study the repeatability of the AI algorithm. Reproducibility may be explored by varying factors such as reconstruction settings.
- Multicenter/multiscanner studies are mainly suitable to explore the sensitivity of the AI algorithm to acquisition variabilities, including variability in imaging procedures, systems, reconstruction methods and settings, and patient demographics if using clinical data. Typically, multicenter studies are performed to improve patient accrual in trials and therefore the same inclusion and exclusion criteria are applied to all centers. Further, multicenter studies can help assess the need for harmonization of imaging procedures and system performances.

Data Collection:

- Realistic simulation studies: To conduct realistic simulations, multiple digital anthropomorphic phantoms are available (*22*). In virtual clinical trial–based studies, the distribution of simulated image data should be similar to that observed in clinical populations. For this purpose, parameters derived directly from clinical data can be used during simulations (*4*). Expert reader-based studies can be used to validate realism of simulations (*23*).
  Next, to simulate the imaging systems, tools such as GATE (*24*), SIMIND (*25*), SimSET (*26*), PeneloPET (*27*), and others (*10*) can be used. Different system configurations, including those replicating multicenter settings, can be simulated. If the methods use reconstruction, then clinically used reconstruction protocols should be simulated. Simulation studies should not use data used for algorithm training/validation.
- Anthropomorphic physical phantom studies: For clinical relevance, the tracer uptake and acquisition parameters when imaging these phantoms should mimic that in clinical settings. To claim generalizable performance across different scanner protocols, different clinical acquisition and reconstruction protocols should be used. A phantom used during training should not be used during evaluation irrespective of changes in acquisition conditions between training and test phases.
- Clinical data: Technical evaluation studies will typically be retrospective. Use of external datasets, such as those from an institution or scanner not used for method training/validation, is

recommended. Public databases may also be used. Selection criteria should be defined.

Process to Extract Task-Specific Information:

- Classification task: Performance of AI-based reconstruction or postreconstruction algorithms should ideally be evaluated using psychophysic studies by expert readers. Methods such as 2 alternative forced-choice tests and ratings-scale approaches could be used. When human-observer studies are infeasible, validated numeric anthropomorphic observers, such as the channelized Hotelling observer with anthropomorphic channels, could be used (*11,28,29*). This may be a better choice than using untrained human observers, who may yield misleading measures of task performance. AI algorithms for optimizing instrumentation/acquisition can be evaluated directly on projection data. This provides the benefit that the evaluation would be agnostic to the choice of the reconstruction and analysis method (*30,31*). In this case, observers that are optimal in some sense, such as the ideal observer (which yields the maximum possible area under the receiver-operating-characteristics [ROC] curve [AUC] of all observers) should be used (*28*). The ideal observer can be challenging to compute in clinical settings, and to address this different strategies are being developed (*32,33*). An example of evaluating a hypothetical AI method for improving timing resolution in a time-of-flight PET system is presented in Jha et al. (*10*).
- Quantification task: The task should be performed using optimal quantification procedures to ensure that the algorithm evaluation is not biased due to a poor quantification process. Often, performing quantification requires an intermediate manual step. For example, the task of regional uptake quantification from reconstructed images may require manual delineation of regions of interest. Expert readers should perform these steps. Nuclear medicine images are noisy and corrupted by image-degrading processes. Thus, the process of quantification should account for the physics and statistical properties of the measured data. For example, if evaluating a segmentation algorithm on the task of quantifying a certain feature from the image, the process of estimating that feature should account for the image-degrading processes and noise (*10*). Maximum-likelihood estimation methods could be an excellent choice since they are often unbiased and if an efficient estimator exists, they are efficient (*11*). If using prior information on the parameters to be estimated, maximum-a-posteriori (*34*) and posterior-mean (*35*) estimators could be used. In several cases, measuring quantitative features directly from projection data may yield optimal quantification (*36,37*) and can be considered.
- Joint classification/quantification task: These tasks should again be performed optimally. If manual inputs are needed for the classification or quantification component of the task, these should be provided by expert readers. Numeric observers such as channelized scanning linear observers (*38*) and those based on deep learning (*39*) can also be used.

Defining a Reference Standard: For simulation studies, the ground-truth is known. Experimental errors may arise when obtaining ground truth from physical-phantom studies, and preferably, these should be modeled during the statistical analysis. For clinical studies, ground truth is commonly unavailable. A common workaround is to define a reference standard. The quality of curation to define this standard should be high. When the reference standard is expert defined, multireader studies are preferred where the readers have not participated in the training of the algorithm, and where each reader independently interprets images, blinded to the results of the AI algorithm and the other readers (*40*). In other cases, the reference standard may be the current clinical practice. Finally, another approach is to use no-gold-standard evaluation techniques, which have shown ability to evaluate algorithm performance on quantification tasks without ground truth (*41–43*).

Figures of Merit: A list of FoMs for different tasks is provided in Supplemental Table 2. Example FoMs include AUC to quantify accuracy on classification tasks, bias, variance, and ensemble mean square error to quantify accuracy, precision, and overall reliability on quantification tasks, and area under the estimation ROC curve for joint detection/classification tasks. Overall, we recommend the use of objective task-based measures to quantify performance, and not measures that are subjective and do not correspond to the clinical task. For a multicenter study, variability of these FoMs across centers, systems, or observers should be reported.

III.2.3. Output Claim from Evaluation Study: The claim will consist of the following components:

- The clinical task (detection/quantification/combination of both) for which the algorithm is evaluated.
- The study type (simulation/physical phantom/clinical).
- If applicable, the imaging and image analysis protocol.
- If clinical data, process to define ground truth.
- Performance, as quantified with task-specific FoMs.

Example Claim: Consider the same automated segmentation algorithm as mentioned in the proof-of-concept section being evaluated to estimate MTV. The claim could be:

> "An AI-based fully automated PET tumor-segmentation algorithm yielded MTV values with a normalized bias of X% (95% confidence intervals) as evaluated using physical-phantom studies with an anthropomorphic thoracic phantom conducted on a single scanner in a single center."

III.3 Clinical Evaluation

III.3.1. Objective: Evaluate the impact of the AI algorithm on making clinical decisions, including diagnostic, prognostic, predictive, and therapeutic decisions for primary endpoints such as improved accuracy or precision in measuring clinical outcome. While technical evaluation is geared toward quantifying the performance of a technique in controlled settings, clinical evaluation investigates clinical utility in a practical setting. This evaluation will assess the added value that the AI algorithm brings to clinical decision making.

III.3.2. Study Design:

Study Type: The following study types can be used:

- Retrospective study: A retrospective study uses existing data sources. In a blinded retrospective study, readers analyzing the study data are blinded to the relevant clinical outcome. Retrospective studies are the most common mechanism to evaluate AI algorithms. Advantages of these studies include low costs and quicker execution. These studies can provide considerations for designing prospective studies. With rare diseases, these may be the only viable mechanism for evaluation. However, these studies cannot conclusively demonstrate causality between the algorithm output and the clinical outcome. Also, these studies may be affected by different biases such as patient-selection bias.
- Prospective observational study: In this study, the consequential outcomes of interest occur after study commencement, but the

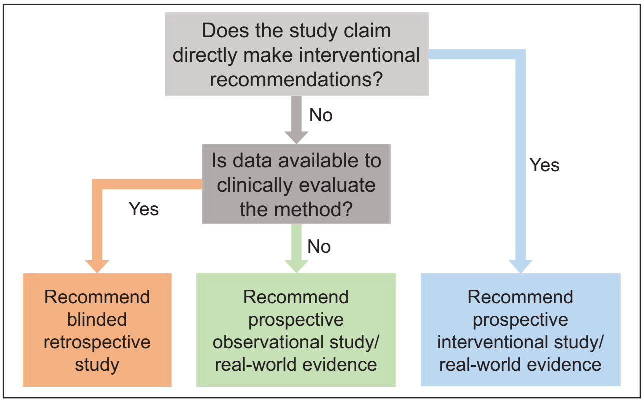

FIGURE 5. Flowchart to determine the clinical evaluation strategy.

decision to assign participants to an intervention is not influenced by the algorithm (*44*). These studies are often secondary objectives of a clinical trial.
- Prospective interventional study: In a prospective interventional study of an AI algorithm, the decision to assign the participant to an intervention depends on the AI algorithm output. These studies can provide stronger evidence for causation of the AI algorithm output to clinical outcome. The most common and strongest prospective interventional study design are randomized control trials, although other designs such as nonrandomized trials and quasiexperiments are possible (*45*). Randomized control trials are considered the gold standard of clinical evaluation but are typically logistically challenging, expensive, and time consuming, and should not be considered as the only means to ascertain and establish effective algorithms.
- Real-world postdeployment evaluation studies: These studies use real-world data from AI algorithms that have received regulatory clearance (*43*). Such studies have the potential to provide information on a wider patient population compared with a prospective interventional study. Moreover, the real-world data can be leveraged not only to improve performance of the initially cleared AI device but also to evaluate new clinical applications that require the same data or data similar to the initially cleared AI module, thus saving time and cost. The study design should be carefully crafted with a study protocol and analysis plan defined before retrieving/analyzing the real-world data (*46,47*), with special attention paid to negate bias (*48*).

Choosing the study type is a multifactorial decision (Fig. 5). To decide on the appropriate study type, we make a distinction between AI algorithms that make *direct* interventional recommendations (prescriptive AI) and those that do not (descriptive AI):

- A purely descriptive AI algorithm does not make direct interventional recommendations but may alter clinical decision making. The algorithms can be further categorized into those that describe the present (e.g., for diagnosis, staging, therapy response assessment) versus those that predict the future (e.g., prognosis of therapy outcome, disease progression, overall survival). There are close links between these 2 categories, and the line between them will likely be increasingly blurred in the era of AI: for example, more-refined AI-derived cancer staging that is trained with outcome data and therefore becomes highly predictive of outcome. A well-designed blinded retrospective study is sufficient to evaluate a purely descriptive AI system. However, if clinical data for a retrospective study do not exist, a prospective observational or real-world study is required.
- A prescriptive AI algorithm makes direct interventional recommendation(s). It may have no autonomy (i.e., only making a recommendation to a physician) or full autonomy (no supervision), or grades in between. For a prescriptive AI algorithm that is not autonomous, a prospective interventional study is recommended. A well-designed real-world study may be used as a substitute. However, for a fully autonomous prescriptive AI system of the future (e.g., fully automated therapy delivery), such a study may be required. Future studies and recommendations are needed for autonomous prescriptive AI systems, as the field is not mature enough. Thus, we limit the scope of this section to only those systems that have expert physician supervision.

Data Collection: An AI algorithm yielding strong performance using data from one institution may perform poorly on data from other institutions (*5*). Thus, we recommend that for clinical evaluation, test data should be collected from different, and preferably multiple, institutions. Results from external institutions can be compared with internal hold-out samples (data from the same institution not used for training) to evaluate generalizability. To avoid variation due to site selection used for the external validation, or random bias in internal sample selection, a leave-one-site repeated hold-out (e.g., 10-fold cross-validation) strategy can be used with a dataset that is completely independent from the training and validation dataset.

To demonstrate applicability over a certain target population, the collected data should be representative of that population in terms of demographics. When the goal is studying performance on a specific population subset (e.g., patients with large body mass indices) or checking sensitivity of the method to certain factors (e.g., patients with metallic implants), the other criteria for patient selection should be unbiased. This ensures that the evaluation specifically studies the effect of that factor.

In studies that are retrospective or based on real-world data, once a database has been set up corresponding to a target population using existing datasets, patients should be randomly selected from this database to avoid selection bias.

Sample-size considerations: The study must have a predefined statistical analysis plan (*49*). The sample size is task dependent. For example, if the claim of improved AUC with the AI method versus a non-AI approach or standard clinical analysis is studied, then the sample size will be dictated by the detection of the expected change between the 2 AUCs. Inputs required for power analysis to compute sample size may be obtained from POC and technical evaluation studies or separate pilot studies.

Defining a Reference Standard: For clinical evaluation, the reference standard should be carefully defined. This requires in-depth clinical and imaging knowledge of the data. Thus, medical experts should be involved in defining task-specific standards. Some reference standards are listed below:

- Clinical outcomes: Eventually the goal of imaging is to improve clinical outcomes. Outcomes such as overall survival, progression-free survival, major clinical events, and hospitalization could thus serve as gold standards, especially for demonstrating clinical utility in predictive and prognostic tasks. A decrease in the use of resources because of the AI tool with comparable outcomes could also be a relevant and improved outcome (e.g., fewer nonessential call back tests with AI).
- External standard: For disease diagnosis tasks, when available, an external standard such as invasive findings, for example, biopsy-pathology or invasive coronary angiography, or some

other definitive diagnosis (derived from other means than the images used) could be considered.

- Trained-reader-defined clinical diagnosis: For diagnostic tasks, expert reader(s) can be used to assess the presence/absence of the disease. Similar best practices as outlined for evaluating technical efficacy should be followed to design these studies. However, note that, unlike technical evaluation, here the goal is disease diagnosis. Thus, the readers should also be provided other factors that are used to make a clinical decision, such as the patient age, sex, ethnicity, other clinical factors that may impact disease diagnosis, and results from other clinical tests. Note that if the reference standard is defined using a standard-of-care clinical protocol, it may not be possible to claim improvement over this protocol. In such a case, agreement-based studies can be performed and concordance with these protocol results could be claimed within certain confidence limits. For example, to evaluate the ability of an AI-based transmission-less attenuation compensation algorithm for SPECT/PET, we may evaluate agreement of the estimates yielded by this algorithm with that obtained when a CT is used for attenuation compensation (*50*).

Figure of Merit: We recommend quantifying performance on strong, impactful, and objectively measurable endpoints such as improved accuracy or precision in measuring clinical outcome. The FoMs are summarized in Supplemental Table 2. To evaluate performance on diagnosis tasks, the FoMs of sensitivity, specificity, ROC curves, and AUC can be used. Since the goal is demonstrating the performance of the algorithm in clinical decision making, sensitivity and specificity may be clinically more relevant than AUC. To demonstrate clinical utility in predictive and prognostic decision making, in addition to AUC, FoMs that quantify performance in predicting future events such as Kaplan–Meier estimators, prediction risk score, and median time of future events can be used.

III.3.3. Output Claim from Clinical Evaluation Study: The claim will state the following:

- The clinical task for which the algorithm is evaluated.
- The patient population over which the algorithm was evaluated.
- The specific imaging and image-analysis protocol(s) or standards followed.
- Brief description of study design: Blinded/nonblinded, randomized/nonrandomized, retrospective/prospective/postdeployment, observational/interventional, number of readers.
- Process to define reference standard and FoM to quantify performance in clinical decision making.

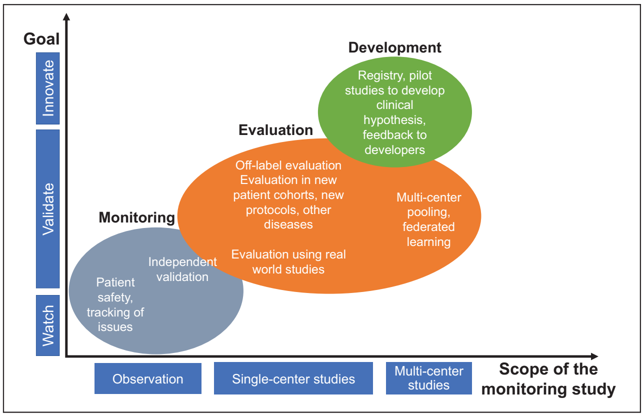

FIGURE 6. Chart showing the different objectives of postdeployment monitoring, grouped as a function of the scope and goal of the study.

Example Claims:

i. Retrospective study: The average AUC of 3 experienced readers on the task of detecting obstructive coronary artery disease from myocardial perfusion PET scans improved from X to Y, representing an estimated difference of Δ (95% CI for Δ), when using an AI-based diagnosis tool compared with not using this tool, as evaluated using a blinded retrospective study.
ii. Prospective observational study: Early change in MTV measured from FDG PET using an AI-based segmentation algorithm yielded an increase in AUC from X to Y, representing an estimated difference of Δ (95% CI for Δ) in predicting pathologic complete response in patients with stage II/III breast cancer, as evaluated using a nonrandomized prospective observational study.
iii. Prospective interventional study: Changes in PET-derived quantitative features estimated with the help of an AI algorithm during the interim stage of therapy were used to guide treatment decisions in patients with stage III non–small cell lung cancer. This led to an X% increase (95% CI) in responders than when the AI algorithm was not used to guide treatment decisions, as evaluated using a randomized prospective interventional study.

III.4. Postdeployment Evaluation

III.4.1. Objective: Postdeployment evaluation has multiple objectives. A key objective is monitoring algorithm performance after clinical deployment including evaluating clinical utility and value over time. Other objectives include off-label evaluation and collecting feedback for proactive development (Fig. 6).

III.4.2. Evaluation Strategies:

Monitoring: Quality and patient safety are critical factors in postdeployment monitoring of an AI algorithm. It is imperative to monitor devices and follow reporting guidelines (such as adverse events), recalls, and corrective actions. Fortunately, applicable laws and regulations require efficient processes in place. Often, logging is used to identify root causes for equipment failure. However, the concept of logging can be expanded: advanced logging mechanisms could be used to better understand use of an AI algorithm. A simple use case is logging the frequency of using an AI algorithm in clinical workflow. Measuring manual intervention for a workflow step that was designed for automation could provide a first impression of the performance in a clinical environment. However, more complex use cases may include the aggregation of data on AI algorithm performance and its impact on patient and disease management. For wider monitoring, feedback should be sought from customers, including focus groups, customer complaint and inquiry tracking, and ongoing technical performance benchmarking (*51*). This approach may provide additional evidence on algorithm performance and could assist in finding areas of improvements, clinical needs not well served or even deriving a hypothesis for further development. Advanced data logging and sharing must be compliant with applicable patient privacy and data protection laws and regulations.

Routinely conducted image-quality phantom studies also provide a mechanism for postdeployment evaluation by serving as sanity checks to ensure that the AI algorithm was not affected by a maintenance operation such as a software update. These studies could include assessing contrast or SUV recovery, absence of nonuniformities or artifacts, cold-spot recovery, and other specialized tests depending on the AI algorithm. Also, tests can be conducted to

TABLE 2
RELAINCE Guidelines

Class of evaluation	Recommendation
Proof of concept evaluation	Ensure no overlap between development and testing cohort. Check that ground-truth quality is reasonable. Provide comparison with conventional and state-of-the-art methods. Choose figures of merit that motivate further clinical evaluation.
Technical task-specific evaluation	Choose clinically relevant tasks: Detection/quantification/combination of both. Determine the right study type: Simulation/phantom/clinical. Ensure that simulation studies are realistic and account for population variability. Testing cohort should be external. Reference standard should be high quality and correspond to the task. Use a reliable strategy to extract task-specific information. Choose figures of merit that quantify task performance.
Clinical evaluation	Determine study type: Retrospective, prospective observational, prospective interventional, or postdeployment real-world studies. Testing cohort must be external. Collected data should represent the target population as stated in the claim. Reference standard should be high quality and be representative of those used for clinical decision making. Figure of merit should reflect performance on clinical decision making.
Postdeployment evaluation	Monitor devices and follow reporting guidelines. Consider phantom studies as sanity checks to assess routine performance. Periodically monitor data drift. For off-label evaluation, follow recommendations as in clinical/technical evaluation depending on objective.

ensure that there is a minimal or harmonized image quality as required by the AI tool for the configurations as stated in the claim.

AI systems likely will operate on data generated in nonstationary environments with shifting patient populations and clinical and operational practices changing over time (*9*). Postdeployment studies can help identify these dataset shifts and assess if recalibration or retraining of the AI method may be necessary to maintain performance (*52,53*). Monitoring the distribution of various patient population descriptors, including demographics and disease prevalence, can provide cues for detecting dataset shifts. In the case of changes in these descriptors, the output of the AI algorithm can be verified by physicians for randomly selected test cases. A possible solution to data shift is continuous learning of the AI method (*54*). In Supplemental Section B, we discuss strategies (*55–57*) to evaluate continuous-learning-based methods.

Off-Label Evaluation: Typically, an AI algorithm is trained and tested using a well-defined cohort of patients, in terms of patient demographics, applicable guidelines, practice preferences, reader expertise, imaging instrumentation, and acquisition and analysis protocols. However, the design of the algorithm may suggest acceptable performance in cohorts outside the intended scope of the algorithm. Here, a series of cases is appropriate to collect preliminary data that may suggest a more thorough trial. An example is a study where an AI algorithm that was trained on patients with lymphoma and lung cancer (*58*) showed reliable performance in patients with breast cancer (*59*).

Collecting Feedback for Proactive Development: Medical products typically have a long lifetime. This motivates proactive development and maintenance to ensure that a product represents state of the art throughout its lifetime. This may be imperative for AI, where technologic innovations are expected to evolve at a fast pace in the coming years. A deployed AI algorithm offers the opportunity to pool data from several users. Specifically, registry approaches enable cost-efficient pooling of uniform data, multicenter observational studies, and POC studies that can be used to develop a new clinical hypothesis or evaluate specific outcomes for particular diseases.

Figures of Merit: We provide the FoMs for the studies where quantitative metrics of success are defined.

- Monitoring study with clinical data: Frequency of clinical usage of the AI algorithm, number of times the AI-based method changed clinical decisions or affected patient management.
- Monitoring study with routine physical phantom studies: Since these are mostly sanity checks, FoMs similar to those used when evaluating POC studies may be considered. In case task-based evaluation is required, FoMs as provided in Supplemental Table 1 may be used.
- Off-label evaluation: FoMs similar to those used when performing technical and clinical evaluation may be considered.

IV. DISCUSSION

The key recommendations from this article are summarized in Table 2. These are referred to as the RELAINCE (Recommendations for EvaLuation of AI for NuClear medicinE) guidelines, with the goal of improving the reliance of AI for clinical applications. Unlike other guidelines for the use of AI in radiology (*60–62*), these guidelines are exclusively focused on best practices for AI algorithm evaluation.

This report advocates that an evaluation study should be geared toward putting forth a claim. The objective of the claim can be guided by factors such as the degree of impact on patient management, level of autonomy, and the risk that the method poses to patients. Risk categories have been proposed for medical software by the International Medical Device Regulators Forum and subsequently adopted by the Food and Drug Administration (*63*). The proposed risk categories range from 1 (low risk) to 4 (highest risk) depending on the vulnerability of the patient and the degree of control that the software has in patient management. The pathway that a developing technology will take to reach clinical adoption will ultimately depend on which risk category it belongs to, and investigators should assess risk early during algorithm development and plan accordingly (*64*).

In this report, we have proposed a 4-class framework for evaluation. For clinical adoption, an algorithm may not need to pass through all classes. The POC evaluation is optional as the objective of this class is to only demonstrate promise for further evaluation. Further, not all these classes may be fully relevant to all algorithms. For example, an AI segmentation algorithm may require technical but not necessarily clinical evaluation for clinical adoption. The types of studies required for an algorithm will depend on the claim. For example, an AI algorithm that claims to make improvement in making clinical decisions will require clinical evaluation. For clinical acceptability of an AI algorithm, evaluating performance on clinical tasks is most important. POC, technical, and clinical evaluation could all be reported in the same multipart study.

The evaluation studies should preferably be multidisciplinary and include computational imaging scientists, physicians, physicists, and statisticians right from the study conception stage. Physicians should be closely involved because they are the end users of these algorithms. Previous publications have outlined the important role of physicians in evaluation of AI algorithms (*65*), including for task-based evaluation of AI algorithms for nuclear medicine (*10*).

The proposed best practices are generally applicable to evaluating a wide class of AI algorithms, including supervised, unsupervised, and semisupervised approaches. For example, we recommend that for even semisupervised and unsupervised learning algorithms, the algorithm should be evaluated on previously unseen data. Additionally, these best practices are broadly applicable to other machine learning as well as physics-based algorithms for nuclear medicine imaging. Further, whereas these guidelines are being proposed in the context of nuclear medicine imaging, they are also broadly applicable to other medical imaging modalities.

In addition to the above practices, we also recommend that in each class of evaluation, evaluation studies should attempt to assess the interpretability of the algorithm. In fact, rigorous evaluations may provide a mechanism to make the algorithm more interpretable. For example, a technical efficacy study may observe suboptimal performance of an AI-based denoising algorithm on the tumor-detection task. Then, the evaluation study could investigate the performance of the algorithm for different tumor properties (size/tumor-to-background ratio) on the detection task (*66*). This will provide insights on the working principles of the algorithm, thus improving the interpretability of the algorithm.

In summary, AI-based algorithms present an exciting toolset for advancing nuclear medicine. We envision that following these best practices for evaluation will assess suitability and provide confidence for clinical translation of these algorithms, and provide trust for clinical application, ultimately leading to improvements in the quality of health care.

DISCLOSURE

Sven Zuehlsdorff is a full-time employee of Siemens Medical Solutions USA, Inc. Nancy Obuchowski is a contracted statistician for QIBA. Tyler Bradshaw receives research support from GE Healthcare. Ronald Boellaard is (unpaid) scientific advisor for the EARL PET/CT accreditation program. Piotr Slomka has a research grant from Siemens Medical Solutions, is a consultant for IBA, and receives royalties from Cedars-Sinai for nuclear cardiology software. No other potential conflict of interest relevant to this article was reported.

ACKNOWLEDGMENTS

The Task Force members thank Kyle J. Myers, PhD, for helpful discussions and Bonnie Clarke for all her help throughout this project.

REFERENCES

1. Topol EJ. High-performance medicine: the convergence of human and artificial intelligence. *Nat Med.* 2019;25:44–56.
2. Yang J, Sohn JH, Behr SC, Gullberg GT, Seo Y. CT-less direct correction of attenuation and scatter in the image space using deep learning for whole-body FDG PET: potential benefits and pitfalls. *Radiol Artif Intell.* 2020;3:e200137.
3. Yu Z, Rahman MA, Schindler T, et al. AI-based methods for nuclear-medicine imaging: need for objective task-specific evaluation [abstract]. *J Nucl Med.* 2020;61(suppl 1):575.
4. Leung KH, Marashdeh W, Wray R, et al. A physics-guided modular deep-learning based automated framework for tumor segmentation in PET. *Phys Med Biol.* 2020;65:245032.
5. Zech JR, Badgeley MA, Liu M, Costa AB, Titano JJ, Oermann EK. Variable generalization performance of a deep learning model to detect pneumonia in chest radiographs: a cross-sectional study. *PLoS Med.* 2018;15:e1002683.
6. Gianfrancesco MA, Tamang S, Yazdany J, Schmajuk G. Potential biases in machine learning algorithms using electronic health record data. *JAMA Intern Med.* 2018;178:1544–1547.
7. Noor P. Can we trust AI not to further embed racial bias and prejudice? *BMJ.* 2020;368:m363.
8. Reuzé S, Orlhac F, Chargari C, et al. Prediction of cervical cancer recurrence using textural features extracted from ^{18}F-FDG PET images acquired with different scanners. *Oncotarget.* 2017;8:43169–43179.
9. Finlayson SG, Subbaswamy A, Singh K, et al. The clinician and dataset shift in artificial intelligence. *N Engl J Med.* 2021;385:283–286.
10. Jha AK, Myers KJ, Obuchowski NA, et al. Objective task-based evaluation of artificial intelligence-based medical imaging methods: framework, strategies and role of the physician. *PET Clin.* 2021;16:493–511.
11. Barrett HH, Myers KJ. *Foundations of Image Science.* First vol. Wiley; 2004.
12. Liu Z, Mhlanga J, Siegel S, Jha A. Need for objective task-based evaluation of segmentation methods in oncological PET: a study with ACRIN 6668/RTOG 0235 multi-center clinical trial data [abstract]. *J Nucl Med.* 2022;63(suppl 2):2413.
13. KC P., Zeng R, Farhangi MM, Myers KJ. Deep neural networks-based denoising models for CT imaging and their efficacy. *Proc SPIE Med Imag.* 2021;11595:105–117.
14. Myers KJ, Barrett HH, Borgstrom MC, Patton DD, Seeley GW. Effect of noise correlation on detectability of disk signals in medical imaging. *J Opt Soc Am A.* 1985;2:1752–1759.
15. Harris JL. Resolving power and decision theory*†. *J Opt Soc Am.* 1964;54:606–611.
16. Bradshaw TJ, Boellaard R, Dutta J, et al. Nuclear medicine and artificial intelligence: best practices for algorithm development. *J Nucl Med.* 2021;63:500–510.
17. Garcia EV. SPECT attenuation correction: an essential tool to realize nuclear cardiology's manifest destiny. *J Nucl Cardiol.* 2007;14:16–24.

18. Clark K, Vendt B, Smith K, et al. The Cancer Imaging Archive (TCIA): maintaining and operating a public information repository. *J Digit Imaging.* 2013;26: 1045–1057.
19. Abadi E, Segars W, Tsui BM, et al. Virtual clinical trials in medical imaging: a review. *J Med Imaging (Bellingham).* 2020;7:042805.
20. Yu Z, Rahman MA, Laforest R, Norris SA, Jha AK. A physics and learning-based transmission-less attenuation compensation method for SPECT. *Proc SPIE Med Imag.* 2021;11595:1159512.
21. Badano A, Graff CG, Badal A, et al. Evaluation of digital breast tomosynthesis as replacement of full-field digital mammography using an in silico imaging trial. *JAMA Netw Open.* 2018;1:e185474.
22. Kainz W, Neufeld E, Bolch WE, et al. Advances in computational human phantoms and their applications in biomedical engineering: a topical review. *IEEE Trans Radiat Plasma Med Sci.* 2019;3:1–23.
23. Liu Z, Laforest R, Moon H, et al. Observer study-based evaluation of a stochastic and physics-based method to generate oncological PET images. *Proc SPIE Med Imag.* 2021;11599:1159905.
24. Jan S, Santin G, Strul D, et al. GATE: a simulation toolkit for PET and SPECT. *Phys Med Biol.* 2004;49:4543–4561.
25. Ljungberg M, Strand S, King M. The SIMIND Monte Carlo program. In: Ljungberg M, Strand S-E, King MA, eds. *Monte Carlo Calculation in Nuclear Medicine: Applications in Diagnostic Imaging.* CRC Press: 1998:145–163.
26. Lewellen T, Harrison R, Vannoy S. The SimSET program. In: Ljungberg M, Strand S-E, King MA, eds. *Monte Carlo Calculations in Nuclear Medicine: Applications in Diagnostic Imaging.* Vol. 87. CRC Press: 2012.
27. España S, Herraiz JL, Vicente E, Vaquero JJ, Desco M, Udias JM. PeneloPET, a Monte Carlo PET simulation tool based on PENELOPE: features and validation. *Phys Med Biol.* 2009;54:1723–1742.
28. Barrett HH, Yao J, Rolland JP, Myers KJ. Model observers for assessment of image quality. *Proc Natl Acad Sci USA.* 1993;90:9758–9765.
29. Abbey CK, Barrett HH. Human- and model-observer performance in ramp-spectrum noise: effects of regularization and object variability. *J Opt Soc Am A Opt Image Sci Vis.* 2001;18:473–488.
30. Gross K, Kupinski M, Peterson T, Clarkson E. *Optimizing a Multiple-Pinhole SPECT System Using the Ideal Observer.* Vol. 5034. SPIE; 2003.
31. Rong X, Ghaly M, Frey EC. Optimization of energy window for ^{90}Y bremsstrahlung SPECT imaging for detection tasks using the ideal observer with model-mismatch. *Med Phys.* 2013;40:062502.
32. Clarkson E, Shen F. Fisher information and surrogate figures of merit for the task-based assessment of image quality. *J Opt Soc Am A Opt Image Sci Vis.* 2010;27: 2313–2326.
33. Li X, Jha AK, Ghaly M, Link JM, Frey E. Use of sub-ensembles and multi-template observers to evaluate detection task performance for data that are not multivariate normal. *IEEE Trans Med Imaging.* 2017;36:917–929.
34. Whitaker MK, Clarkson E, Barrett HH. Estimating random signal parameters from noisy images with nuisance parameters: linear and scanning-linear methods. *Opt Express.* 2008;16:8150–8173.
35. Liu Z, Mhlanga JC, Laforest R, Derenoncourt P-R, Siegel BA, Jha AK. A Bayesian approach to tissue-fraction estimation for oncological PET segmentation. *Phys Med Biol.* 2021;66:10.1088/1361-6560/ac01f4.
36. Carson RE. A maximum likelihood method for region-of-interest evaluation in emission tomography. *J Comput Assist Tomogr.* 1986;10:654–663.
37. Li Z, Benabdallah N, Abou D, et al. A projection-domain low-count quantitative SPECT method for alpha-particle emitting radiopharmaceutical therapy. arxiv, Cornell University, website. https://arxiv.org/abs/2107.00740. Revised May 11, 2022. Accessed August 3, 2022.
38. Tseng H-W, Fan J, Kupinski MA. Combination of detection and estimation tasks using channelized scanning linear observer for CT imaging systems. *Proc SPIE Med Imag.* 2015;9416:94160H.
39. Li K, Zhou W, Li H, Anastasio MA. A Hybrid approach for approximating the ideal observer for joint signal detection and estimation tasks by use of supervised learning and markov-chain monte carlo methods. *IEEE Trans Med Imaging.* 2022;41:1114–1124.
40. Miller DP, O'shaughnessy KF, Wood SA, Castellino RA. Gold standards and expert panels: a pulmonary nodule case study with challenges and solutions. *Proc SPIE Med Imag.* 2004;5372:173–184.
41. Hoppin JW, Kupinski MA, Kastis GA, Clarkson E, Barrett HH. Objective comparison of quantitative imaging modalities without the use of a gold standard. *IEEE Trans Med Imaging.* 2002;21:441–449.
42. Jha AK, Caffo B, Frey EC. A no-gold-standard technique for objective assessment of quantitative nuclear-medicine imaging methods. *Phys Med Biol.* 2016; 61:2780–2800.
43. Jha AK, Mena E, Caffo B, et al. Practical no-gold-standard evaluation framework for quantitative imaging methods: application to lesion segmentation in positron emission tomography. *J Med Imaging (Bellingham).* 2017;4:011011.
44. Berger ML, Dreyer N, Anderson F, Towse A, Sedrakyan A, Normand S-L. Prospective observational studies to assess comparative effectiveness: The ISPOR good research practices task force report. *Value Health.* 2012;15:217–230.
45. Thiese MS. Observational and interventional study design types; an overview. *Biochem Med (Zagreb).* 2014;24:199–210.
46. Sherman RE, Anderson SA, Dal Pan GJ, et al. Real-world evidence: what is it and what can it tell us? *N Engl J Med.* 2016;375:2293–2297.
47. US Food Drug Administration. *Use of Real-World Evidence to Support Regulatory Decision-Making for Medical Devices.* 2017. FDA website. https://www.fda.gov/regulatory-information/search-fda-guidance-documents/use-real-world-evidence-support-regulatory-decision-making-medical-devices. Accessed August 19, 2022.
48. Tarricone R, Boscolo PR, Armeni P. What type of clinical evidence is needed to assess medical devices? *Eur Respir Rev.* 2016;25:259.
49. Hemingway H, Riley RD, Altman DG. Ten steps towards improving prognosis research. *BMJ.* 2009;339:b4184.
50. Shi L, Onofrey JA, Liu H, Liu YH, Liu C. Deep learning-based attenuation map generation for myocardial perfusion SPECT. *Eur J Nucl Med Mol Imaging.* 2020; 47:2383–2395.
51. Larson DB, Harvey H, Rubin DL, Irani N, Tse JR, Langlotz CP. Regulatory frameworks for development and evaluation of artificial intelligence-based diagnostic imaging algorithms: Summary and recommendations. *J Am Coll Radiol.* 2021;18:413–424.
52. Davis SE, Greevy RA Jr, Fonnesbeck C, Lasko TA, Walsh CG, Matheny ME. A nonparametric updating method to correct clinical prediction model drift. *J Am Med Inform Assoc.* 2019;26:1448–1457.
53. Feng J. Learning to safely approve updates to machine learning algorithms. *Proc Conf on Health, Inference, and Learning.* 2021:164–173.
54. Baweja C, Glocker B, Kamnitsas K. Towards continual learning in medical imaging. arxiv, Cornell University, website. https://arxiv.org/abs/1811.02496. Submitted November 26, 2018. Accessed August 3, 2022.
55. Díaz-Rodríguez N, Lomonaco V, Filliat D, Maltoni D. Don't forget, there is more than forgetting: new metrics for continual learning. arxiv, Cornell University, website. https://arxiv.org/abs/1810.13166. Submitted October 31, 2018. Accessed August 3, 2022.
56. Goodfellow IJ, Mirza M, Xiao D, Courville A, Bengio Y. An empirical investigation of catastrophic forgetting in gradient-based neural networks. arxiv, Cornell University, website. https://arxiv.org/abs/1312.6211v3. Revised March 4, 2015. Accessed August 3, 2022.
57. Chaudhry A, Dokania PK, Ajanthan T, Torr PH. Riemannian walk for incremental learning: Understanding forgetting and intransigence. *ECCV.* 2018:532–547.
58. Sibille L, Seifert R, Avramovic N, et al. ^{18}F-FDG PET/CT uptake classification in lymphoma and lung cancer by using deep convolutional neural networks. *Radiology.* 2020;294:445–452.
59. Weber M, Kersting D, Umutlu L, et al. Just another "Clever Hans"? Neural networks and FDG PET-CT to predict the outcome of patients with breast cancer. *Eur J Nucl Med Mol Imaging.* 2021;48:3141–3150.
60. Dikici E, Bigelow M, Prevedello LM, White RD, Erdal BS. Integrating AI into radiology workflow: levels of research, production, and feedback maturity. *J Med Imaging (Bellingham).* 2020;7:016502.
61. Mongan J, Moy L, Kahn CE. Checklist for artificial intelligence in medical imaging (CLAIM): a guide for authors and reviewers. *Radiol Artif Intell.* 2020;2:e200029.
62. Omoumi P, Ducarouge A, Tournier A, et al. To buy or not to buy—evaluating commercial AI solutions in radiology (the ECLAIR guidelines). *Eur Radiol.* 2021; 31:3786–3796.
63. *Software as a Medical Device (SaMD): Clinical Evaluation.* Center for Devices and Radiological Health, United States Food and Drug Administration; 2017. FDA website. https://www.fda.gov/regulatory-information/search-fda-guidance-documents/software-medical-device-samd-clinical-evaluation. Accessed August 19, 2022.
64. *Factors to Consider When Making Benefit-Risk Determinations in Medical Device Premarket Approval and de Novo Classifications: Guidance for Industry and Food and Drug Administration Staff.* Center for Devices and Radiological Health, USA Food and Drug Administration; 2012. FDA website. https://www.fda.gov/regulatory-information/search-fda-guidance-documents/factors-consider-when-making-benefit-risk-determinations-medical-device-premarket-approval-and-de. Accessed August 19, 2022.
65. Rubin DL. Artificial intelligence in imaging: The radiologist's role. *J Am Coll Radiol.* 2019;16:1309–1317.
66. Yu Z, Rahman MA, Jha AK. Investigating the limited performance of a deep-learning-based SPECT denoising approach: an observer study-based characterization. *Proc SPIE Med Imag.* 2022. 12035:120350D.

Choice Is Good at Times: The Emergence of [^{64}Cu]Cu-DOTATATE–Based Somatostatin Receptor Imaging in the Era of [^{68}Ga]Ga-DOTATATE

Abhishek Jha[1], Mayank Patel[1], Jorge A. Carrasquillo[1], Clara C. Chen[1], Corina Millo[1], Roberto Maass-Moreno[1], Alexander Ling[1], Frank I. Lin[1], Ronald M. Lechan[2], Thomas A. Hope[3], David Taïeb[4], Ali Cahid Civelek[5], and Karel Pacak[1]

[1]*National Institutes of Health, Bethesda, Maryland;* [2]*Tufts University School of Medicine, Boston, Massachusetts;* [3]*University of California, San Francisco, California;* [4]*La Timone University Hospital, CERIMED, Aix-Marseille University, Marseille, France; and* [5]*Johns Hopkins Medicine, Baltimore, Maryland*

Somatostatin receptor (SSTR) imaging has brought about impactful changes in clinical management of neuroendocrine tumors (NETs), including pheochromocytoma and paraganglioma (PPGL) (*1,2*). It allows tumor detection and disease characterization and is mandatory for selecting patients who are likely to benefit from peptide receptor radionuclide therapy (commonly referred to as theranostics). In 2016, [^{68}Ga]Ga-DOTATATE (Netspot; Advanced Accelerator Applications) received Food and Drug Administration approval. Recently in 2020, the Food and Drug Administration approved the radiopharmaceutical [^{64}Cu]Cu-DOTATATE (Detectnet; Curium) as an SSTR imaging option.

[^{68}Ga]Ga-SSTR PET/CT has been increasingly evaluated in PPGLs of various genetic backgrounds (*3,4*). A recent metaanalysis showed the pooled PPGL detection rate of [^{68}Ga]Ga-SSTR PET/CT in patients with unknown genetic status to be 93%, which was significantly higher than that of [^{18}F]-fluorodihydroxyphenylalanine ([^{18}F]-FDOPA) PET/CT (80%), [^{18}F]-FDG PET/CT (74%), and [$^{123/131}$I]-metaiodobenzylguanidine scintigraphy [(38%), $P < 0.001$ for all] (*5*). These studies reflect the clinical utility of [^{68}Ga]Ga-SSTR in PPGL imaging. However, [^{18}F]-FDOPA is the preferred radiopharmaceutical of choice in cluster 1B (pseudohypoxia-related: *VHL/HIF2A/PHD1/2*) or cluster 2 (kinase signaling–related: *RET/NF1/TMEM127/MAX*) mutated PPGLs (*3,4*).

Recently, DOTATATE was radiolabeled with Copper-64, which should be inspected from a clinical perspective. In a prospective head-to-head comparison between [^{64}Cu]Cu-DOTATATE and [^{68}Ga]Ga-DOTATOC PET/CT in 59 NET patients, Johnbeck et al. reported a slightly higher detection rate for the former (99.1% vs. 95.6%), with 701 concordant lesions on both scans (*6*). Of 40 additional true-positive lesions detected on either scan, significantly more true-positive lesions were detected by [^{64}Cu]Cu-DOTATATE ($n = 33$) than by [^{68}Ga]Ga-DOTATOC (82.5% vs. 17.5%, $P < 0.0001$). Although the authors attributed the better detection rate to the shorter positron range of Copper-64 (*6*), one must consider that the study used different peptides (DOTATATE vs. DOTATOC) linked to Copper-64 versus Gallium-68, respectively. In a prospective phase III clinical trial from the United States on 42 NET patients and 21 healthy volunteers, Delpassand et al. determined that PET/CT images of diagnostic quality can be acquired with a dose of 148 MBq of [^{64}Cu]Cu-DOTATATE, achieving a sensitivity of 100.0% with 96.8% specificity by masked readers (*7*). In another study, on 112 NET patients, when [^{64}Cu]Cu-DOTATATE was compared with [^{111}In]In-diethylenetriamine pentaacetate-octreotide the former detected more lesions (1,213 vs. 603) and more organ involvement (in 36% of patients) (*8*). These 2 studies led to approval of [^{64}Cu]Cu-DOTATATE by the Food and Drug Administration in September 2020 for the localization of NETs (*8*).

Tumor detectability also depends on the radionuclide's physical properties, which can have a significant impact on diagnostic performance (*6*). Gallium-68 has a lower positron energy than Copper-64 (0.65 vs. 1.90 MeV), resulting in a lower positron range (0.56 vs. 3.5 mm) that provides superior spatial resolution, improved imaging quality, and enhanced detection of small lesions (*7*). Since Copper-64 suffers from a lower positron yield than Gallium-68 (17% vs. 88%), Copper-64 would theoretically require a higher injected activity to achieve the same positron count as Gallium-68 (*6*). However, PET/CT images of diagnostic quality were acquired with a dose of 148 MBq of [^{64}Cu]Cu-DOTATATE (*7*). Nevertheless, the radiation exposure associated with 200 MBq of [^{68}Ga]Ga-DOTATATE (4.3 mSv) is lower than that associated with 148 MBq of [^{64}Cu]Cu-DOTATATE (4.7 mSv), per the package inserts. Furthermore, the long half-life of Copper-64 (12.7 h) has potential advantages over Gallium-68 (1.1 h). This longer half-life allows a scanning window of at least 1–3 h after injection, potentiating a better tumor-to-background ratio and offering logistic benefits in coordinating radiochemical production and patient arrival (*6*). Additionally, serial multiple-time-point imaging is possible with a longer half-life, enabling dosimetric calculations. Lastly, this longer half-life along with centralized production of Copper-64 allows for easier distribution of Copper-64 to remote geographic areas. The physical properties, including other characteristics of both [^{68}Ga]Ga-DOTATATE and [^{64}Cu]Cu-DOTATATE, are summarized in Supplemental Table 1 (supplemental materials are available at http://jnm.snmjournals.org).

Received Mar. 27, 2022; revision accepted May 16, 2022.

For correspondence or reprints, contact Karel Pacak (karel@mail.nih.gov).

DOI: 10.2967/jnumed.122.264183

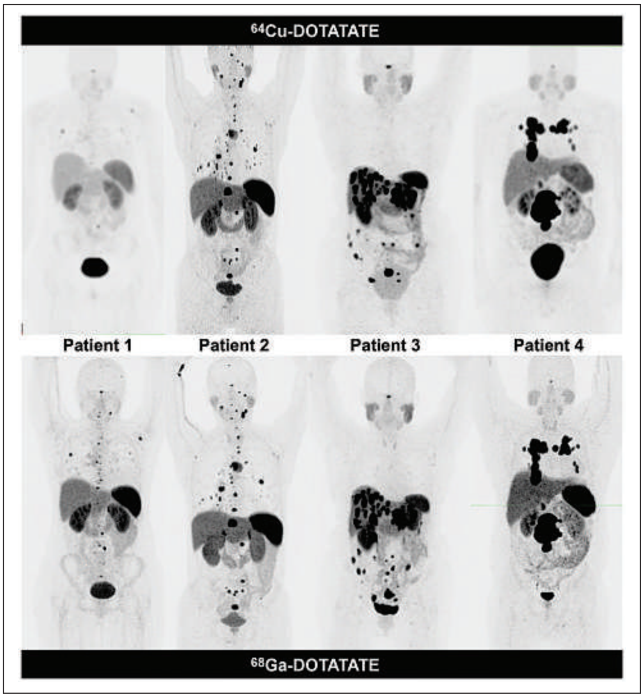

FIGURE 1. SSTR imaging with [^{64}Cu]Cu-DOTATATE and [^{68}Ga]Ga-DOTATATE in PPGL. Figure shows maximum-intensity projection images in 4 patients who underwent imaging with both [^{64}Cu]Cu-DOTATATE (top panel) and [^{68}Ga]Ga-DOTATATE (bottom panel). Leveling of all maximum-intensity projection images is at same SUV$_{max}$, ranging from 0 to 14.

Five patients (4 new, 1 follow-up) who had undergone [^{64}Cu]Cu-DOTATATE at outside institutions presented to us and underwent [^{68}Ga]Ga-DOTATATE scans prospectively at the National Institutes of Health. The institutional review board of the *Eunice Kennedy Shriver* National Institute of Child Health and Human Development (clinical trial number NCT00004847) approved this study, and all subjects gave written informed consent. Four of these 5 patients (2 women, 2 men; mean age, 52.3 ± 21.0 y; range, 32–75 y; 1 *SDHB*, 1 *SDHD*, and 2 sporadic) did not receive any new antitumor intervention between the 2 scans. The median interval between the [^{64}Cu]Cu-DOTATATE scan (mean activity, 148 ± 11.1 MBq; mean uptake time, 71.8 ± 10.9 min) and the [^{68}Ga]Ga-DOTATATE scan (mean activity, 199.8 ± 7.4 MBq; mean uptake time, 60.3 ± 1.3 min) was 2 mo (range, 1–4 mo). Details on the PET/CT imaging techniques, scanner, and protocol are summarized in Supplemental Tables 2 and 3. All 4 patients were positive on both scans (Fig. 1). In patient 1, who was undergoing cold somatostatin analog therapy with lanreotide, [^{68}Ga]Ga-DOTATATE seemed to detect more lesions than [^{64}Cu]Cu-DOTATATE, and one might conclude that there had been progression of disease despite therapy. However, this observation could also be attributable to a difference in spatial resolution between scanners, differences in image acquisition and reconstruction methods, or a combination of these factors. Therefore, it is also important to optimize [^{64}Cu]Cu-DOTATATE image acquisition and reconstruction methods, using protocols optimized for the physical properties of Copper-64.

Intraindividual head-to-head comparison between [^{64}Cu]Cu-DOTATATE and [^{68}Ga]Ga-DOTATATE is lacking in PPGLs. It is too early to answer the question of whether Copper-64 or Gallium-68 should be used for PPGL imaging, especially in the widespread landscape of functional imaging options available ([^{18}F]-FDOPA, [^{18}F]-FDG, and [^{123}I]-metaiodobenzylguanidine) (*4,9*). Until we gather more evidence, both [^{68}Ga]Ga-DOTATATE and [^{64}Cu]Cu-DOTATATE should be considered interchangeable; however, we do suggest remaining consistent with the SSTR imaging choice for follow-up imaging. This is vital in those patients who are in a watch-and-wait scheme (stable for a considerable time because of their slow progression), and the incorrect determination could lead to an unwarranted change in management. Seamless availability and distribution of SSTR imaging to the users is necessary to adequately meet an increasing and broader geographic demand.

In conclusion, despite the theoretic advantages of each radiopharmaceutical over the other, currently available comparison data are not conclusive about the superiority of one over the other. Therefore, until definitive data emerge, both [^{68}Ga]Ga-DOTATATE and [^{64}Cu]Cu-DOTATATE can be used interchangeably, if one remains consistent with the SSTR imaging choice for follow-up imaging. The future looks bright for SSTR theranostics with the advent of novel promising radionuclides that will substantially expand their use in NETs, including PPGLs.

DISCLOSURE

This work was supported by the Intramural Research Program of the National Institutes of Health and the *Eunice Kennedy Shriver* National Institute of Child Health and Human Development. Thomas Hope is a consultant for Curium Pharma. No other potential conflict of interest relevant to this article was reported.

REFERENCES

1. Barrio M, Czernin J, Fanti S, et al. The impact of somatostatin receptor-directed PET/CT on the management of patients with neuroendocrine tumor: a systematic review and meta-analysis. *J Nucl Med.* 2017;58:756–761.
2. Kong G, Schenberg T, Yates CJ, et al. The role of ^{68}Ga-DOTA-octreotate PET/CT in follow-up of SDH-associated pheochromocytoma and paraganglioma. *J Clin Endocrinol Metab.* 2019;104:5091–5099.
3. Taïeb D, Hicks RJ, Hindié E, et al. European Association of Nuclear Medicine practice guideline/Society of Nuclear Medicine and Molecular Imaging procedure standard 2019 for radionuclide imaging of phaeochromocytoma and paraganglioma. *Eur J Nucl Med Mol Imaging.* 2019;46:2112–2137.
4. Taïeb D, Jha A, Treglia G, Pacak K. Molecular imaging and radionuclide therapy of pheochromocytoma and paraganglioma in the era of genomic characterization of disease subgroups. *Endocr Relat Cancer.* 2019;26:R627–R652.
5. Han S, Suh CH, Woo S, Kim YJ, Lee JJ. Performance of ^{68}Ga-DOTA-conjugated somatostatin receptor-targeting peptide PET in detection of pheochromocytoma and paraganglioma: a systematic review and metaanalysis. *J Nucl Med.* 2019;60:369–376.
6. Johnbeck CB, Knigge U, Loft A, et al. Head-to-head comparison of ^{64}Cu-DOTATATE and ^{68}Ga-DOTATOC PET/CT: a prospective study of 59 patients with neuroendocrine tumors. *J Nucl Med.* 2017;58:451–457.
7. Delpassand ES, Ranganathan D, Wagh N, et al. Cu-DOTATATE PET/CT for imaging patients with known or suspected somatostatin receptor-positive neuroendocrine tumors: results of the first U.S. prospective, reader-masked clinical trial. *J Nucl Med.* 2020;61:890–896.
8. Pfeifer A, Knigge U, Binderup T, et al. ^{64}Cu-DOTATATE PET for neuroendocrine tumors: a prospective head-to-head comparison with ^{111}In-DTPA-octreotide in 112 patients. *J Nucl Med.* 2015;56:847–854.
9. Carrasquillo JA, Chen CC, Jha A, et al. Imaging of pheochromocytoma and paraganglioma. *J Nucl Med.* 2021;62:1033–1042.

Somatostatin Receptor Imaging in PPGL • Jha et al. 1301

Pretargeting: A Path Forward for Radioimmunotherapy

Sarah M. Cheal*[1], Sebastian K. Chung*[2], Brett A. Vaughn*[1], Nai-Kong V. Cheung[3], and Steven M. Larson[1,4]

[1]*Molecular Pharmacology Program, Memorial Sloan Kettering Cancer Center, New York, New York;* [2]*Department of Surgery, Memorial Sloan Kettering Cancer Center, New York, New York;* [3]*Department of Pediatrics, Memorial Sloan Kettering Cancer Center, New York, New York; and* [4]*Department of Radiology, Memorial Sloan Kettering Cancer Center, New York, New York*

Learning Objectives: On successful completion of this activity, participants should be able to describe (1) the current status of radioimmunotherapy of human tumors with radioimmunoconjugates; (2) the concept of pretargeted radioimmunotherapy and successes/failures in clinical trials; (3) recent efforts to optimize pretargeted radioimmunotherapy, including the development of novel pretargeting systems; and (4) the future outlook for pretargeted radioimmunotherapy, including clinical trials on the horizon.

Financial Disclosure: Drs. Cheal, Cheung, and Larson are listed as coinventors on multiple patents related to this work owned by MSKCC, some of which are licensed to Y-mAbs Therapeutics, Inc. Dr. Cheal receives royalties from Y-mAbs Therapeutics Inc. Dr. Cheung receives investment interest in Y-mAbs Therapeutics, Inc., and Abpro Labs; is a consultant/advisor to Eureka Therapeutics; receives royalties from Biotec Pharmacon/Lallemand; and receives sponsored research support from Y-mAbs Therapeutics, Inc. Dr. Larson receives commercial research grants from Y-mAbs Therapeutics Inc., Genentech, Inc., Wilex AG, Telix Pharmaceuticals Limited, and Regeneron Pharmaceuticals, Inc.; holds ownership interest/equity in Voreyda Theranostics Inc. and Elucida Oncology Inc.; holds stock in ImaginAb, Inc., and Y-mAbs Therapeutics, Inc.; is the inventor and owner of issued patents both currently unlicensed and licensed by MSKCC to Samus Therapeutics, Inc., Y-mAbs Therapeutics Inc., and Elucida Oncology, Inc.; and serves as a consultant to Cynvec LLC, Eli Lilly & Co., Prescient Therapeutics Limited, Advanced Innovative Partners, LLC, Gerson Lehrman Group, Progenics Pharmaceuticals, Inc., Bristol Myers Squib, and Janssen Pharmaceuticals, Inc. The authors of this article have indicated no other relevant relationships that could be perceived as a real or apparent conflict of interest.

CME Credit: SNMMI is accredited by the Accreditation Council for Continuing Medical Education (ACCME) to sponsor continuing education for physicians. SNMMI designates each *JNM* continuing education article for a maximum of 2.0 AMA PRA Category 1 Credits. Physicians should claim only credit commensurate with the extent of their participation in the activity. For CE credit, SAM, and other credit types, participants can access this activity through the SNMMI website (http://www.snmmilearningcenter.org) through September 2025.

Pretargeted radioimmunodiagnosis and radioimmunotherapy aim to efficiently combine antitumor antibodies and medicinal radioisotopes for high-contrast imaging and high–therapeutic-index (TI) tumor targeting, respectively. As opposed to conventional radioimmunoconjugates, pretargeted approaches separate the tumor-targeting step from the payload step, thereby amplifying tumor uptake while reducing normal-tissue exposure. Alongside contrast and TI, critical parameters include antibody immunogenicity and specificity, availability of radioisotopes, and ease of use in the clinic. Each of the steps can be optimized separately; as modular systems, they can find broad applications irrespective of tumor target, tumor type, or radioisotopes. Although this versatility presents enormous opportunity, pretargeting is complex and presents unique challenges for clinical translation and optimal use in patients. The purpose of this article is to provide a brief historical perspective on the origins and development of pretargeting strategies in nuclear medicine, emphasizing 2 protein delivery systems that have been extensively evaluated (i.e., biotin–streptavidin and hapten-bispecific monoclonal antibodies), as well as radiohaptens and radioisotopes. We also highlight recent innovations, including pretargeting with bioorthogonal chemistry and novel protein vectors (such as self-assembling and disassembling proteins and Affibody molecules). We caution the reader that this is by no means a comprehensive review of the past 3 decades of pretargeted radioimmunodiagnosis and pretargeted radioimmunotherapy. But we do aim to highlight major developmental milestones and to identify benchmarks for success with regard to TI and toxicity in preclinical models and clinically. We believe this approach will lead to the identification of key obstacles to clinical success, revive interest in the utility of radiotheranostics applications, and guide development of the next generation of pretargeted theranostics.

Key Words: general oncology; radionuclide therapy; radiopharmaceuticals; multistep; pretargeted radioimmunotherapy; radioimmunotherapy

J Nucl Med 2022; 63:1302–1315
DOI: 10.2967/jnumed.121.262186

Monoclonal antibodies (mAbs) are attractive vehicles for delivering cytotoxic payloads to tumors using cell-surface targets as ZIP codes. However, the complexity of the tumor microenvironment and the pharmacokinetics of mAbs in vivo have created major hurdles in radioimmunodiagnosis and radioimmunotherapy (*1*). Radioimmunoconjugates have been approved by the U.S. Food and Drug Administration for clinical oncology use (4 imaging agents, beginning with OncoScint [Cytogen Corp.] for imaging of tumor-associated glycoprotein 72 [TAG-72] in 1992 and Zevalin [Acrotech Biopharma] and Bexxar [GlaxoSmithKline] for therapy targeting CD20 in the early 2000s). However, clinical use (and hence, commercial success) has been hampered by unanticipated physician preferences (*2*) and numerous challenges universal to radiopharmaceutical therapies (*3*).

Despite the success in treating radiosensitive hematologic malignancies, radioimmunotherapy in the treatment of solid tumors has been clinically unsuccessful (*1*). Nevertheless, a recent revision of the radiobiologic paradigms of targeted α-therapy has revealed a highly complex response cascade comprising direct, bystander, and systemic effects (*4*), proving remarkably effective against β-refractive and bulky disease (*5*). Coupled with an enhanced development and application of theranostics in nuclear medicine, this response cascade has fueled development of a new generation of mAb theranostics against solid-tumor antigens, particularly with α-emitting

---

Received Mar. 28, 2022; revision accepted Jun. 7, 2022.

For correspondence or reprints, contact Sarah M. Cheal (cheals@mskcc.org).

*Contributed equally to this work.

isotopes (e.g., City of Hope's anti–carcinoembryonic antigen [CEA] ^{225}Ac-DOTA-5MA NCT05204147; Bayer's suite of ^{227}Th-IgG drugs targeting mesothelin, prostate-specific membrane antigen, or human epidermal growth factor receptor 2 [HER2] antigens NCT03507452, NCT03724747, and NCT04147819; Janssen's ^{225}Ac-DOTA-h11B6 targeting human kallikrein 2 NCT04644770; and Fusion's ^{225}Ac-FPI-1434 targeting insulinlike growth factor type 1 receptor). More details can be found in several excellent reviews (*6–9*).

The field waits with great interest to see the outcome of these radioimmunotherapy clinical trials of directly labeled mAbs. Nonetheless, based on prior experience with other radioimmunotherapeutics, there is concern that hematopoietic toxicity will prove to be dose-limiting, a common hurdle for molecularly targeted radiopharmaceuticals (*3,10*). Fundamentally, the necessary therapeutic indices (TIs, or tumor–to–normal-tissue absorbed dose ratios) for meaningful radioimmunotherapy of solid-tumor masses were not achieved, partly because of inadequate mAb uptake (subtherapeutic radiation dose for solid tumors), dose-limiting toxicities (DLTs) because of poor TIs (causing myelotoxicity and renal toxicity), and antidrug antibodies (ADAs) (*1*). The radiopharmacology of radioimmunoconjugates has so far permitted mostly suboptimal TIs, especially for critical radiosensitive tissues such as bone marrow and kidney. Current and future advances in protein engineering and radioligand chemistry are necessary to overcome these barriers.

Pretargeted radioimmunodiagnosis (PRID) and pretargeted radioimmunotherapy (PRIT) separate the tumor targeting and the radiocarrier (e.g., a radiohapten) delivery steps, vastly improving the contrast and TIs while creating modular systems with individual optimization ease (Fig. 1). The tumor-targeting bispecific protein can be engineered to improve tumor uptake and TI; a chase molecule or clearing agent (CA) can be designed to sequester unbound proteins from blood to liver for metabolism. After an optimal pretargeting interval of hours or days, an intravenous payload with high affinity for the second specificity in the protein seeks out the bispecific protein targeted to the tumor or clears from the body in minutes to hours.

Current PRID and PRIT approaches harness advances in protein engineering and bioorthogonal chemistry to overcome the limitations of previous PRID and PRIT systems. However, PRID and PRIT present additional complexity in terms of drug manufacture (developing at least 2 products, and perhaps a CA) and dosing protocol optimization (both dose and pretargeting interval). Here, we provide a historical perspective of PRID and PRIT and explore potential ways by which PRID and PRIT can be further optimized to deliver a high radiation dose to tumor while improving TIs substantially for critical radiosensitive tissues.

HISTORICAL PERSPECTIVE

Concept of PRID and PRIT

Building on initial investigations of in vivo tumor targeting with radiolabeled polyclonal antibodies (*11,12*) and fueled by the discovery of mAbs by Köhler and Milstein (*13*), radioimmunodiagnosis using mAbs surged in the late 1970s, and radioimmunotherapy soon followed (*14,15*). However, despite the antigen specificity of mAbs, most did not translate into high-contrast tumor imaging (*15*). The critical hurdle—that is, disappointingly low overall tumor uptake and high normal-tissue background with radiolabeled IgG mAbs—was realized early on, requiring ^{99m}Tc blood-pool agents for computer subtraction from ^{131}I-mAb images (*16*).

In the mid 1980s, Goodwin et al. pioneered one of the first examples of pretargeting of radioisotopes by engineering metal chelate–specific mAbs (*17*). This example was predicated on the physicochemical properties of metal chelate complexes (often low-molecular-weight and hydrophilic combined with net negative charge and high kinetic stability under physiologic conditions) possessing extremely favorable in vivo pharmacokinetics and biodistribution. The antichelate mAb CHA255 passively entered tumors and, after a pretargeting interval of 24 h, was chased with a metal chelate hapten, indium (III)-4-[*N*′-(2-hydroxyethyl)thioureido]-L-benzyl-ethylenediaminetetraacetic acid (*18*). The concept of chelate chase—that is, using pharmacologic doses of an empty nonradioactive chelate hapten to force rapid renal excretion—significantly enhanced contrast, thereby reducing normal-organ radiation exposure by as much as 95% (*18,19*). Soon after, Stickney et al. conducted the first clinical trial of PRID in patients with CEA-expressing colorectal cancer (CRC) using a bispecific antibody (BsAb) anti-CEA/anti–metal chelate hapten system (*20*). Besides establishing the feasibility of the approach in this study of 14 patients, 20 of 21 known lesions were detected, for an overall sensitivity of 95%; 8 of 9 new lesions were confirmed; and high contrast was observed at as early as 4 h (Fig. 2A) (*20*).

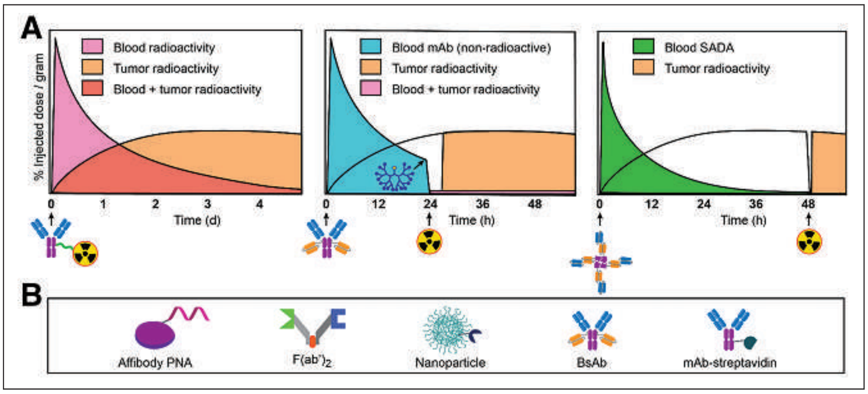

FIGURE 1. Comparison of conventional radioimmunotherapy and PRID/PRIT and compatible vector survey. (A) Injection of radioimmunoconjugate (left) leads to low TIs, especially in hematopoietic and highly perfused tissues. With 3-step BsAb pretargeting (middle), BsAb is administered, followed 1 d later by CA to quickly reduce circulating BsAb. During final step, administered radiocarrier (e.g., radiohapten) is captured by intratumoral BsAb or rapidly cleared. A 2-step approach (right) is feasible with SADA BsAb innovation. (Adapted from (*153*)). (B) Select bispecific antitumor/antiradiocarrier vectors.

A Surge in PRID—Especially Driven by Biotin–Streptavidin Approaches—and the Potential of PRIT

Although PRID with BsAb showed considerable promise, issues related to TIs as a consequence of insufficient affinity or avidity for the hapten (e.g., low-nanomolar range) prompted the development of alternatives. Streptavidin (53 kDa protein from the bacterium *Streptomyces avidinii*) and avidin (66 kDa protein found in egg whites) are both tetrameric proteins, with each individual subunit able to bind a single molecule of biotin (244 Da) with similar affinities (femtomolar). With these significantly higher affinities, the biotin–streptavidin system was an attractive candidate for pretargeting.

One of the first pretargeting applications of the biotin–streptavidin system was devised by Hnatowich et al. in 1987, consisting of an

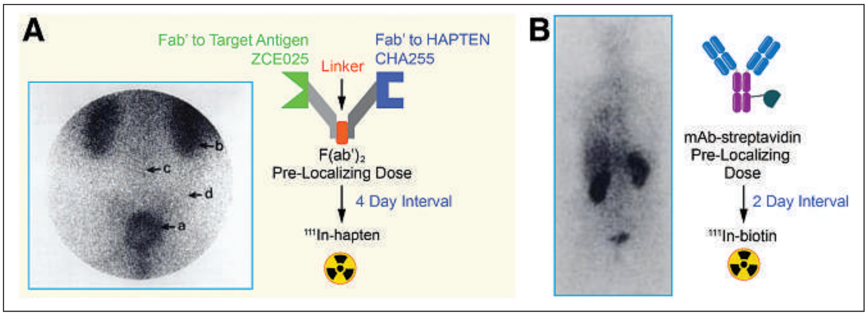

FIGURE 2. Initial PRID studies of tumors in patients. (A) BsAb pretargeting system. Planar posterior pelvic scan (coronal view) of patient with recurrent CRC invading right sacral area was obtained 3 d after injection of ^{111}In-hapten. a = tumor; b = kidneys; c = spine; d = iliac crest. (Reprinted with permission of (*20*).) (B) Biotin–streptavidin pretargeting system. Anterior chest and upper abdomen image (coronal view) of patient with recurrent squamous cell carcinoma of right lung was obtained 2 h after injection of ^{111}In-biotin. a = tumor; b = kidneys; c = bladder. (Reprinted from (*26*).)

antitumor mAb–streptavidin conjugate, a chase molecule, and radiolabeled biotin (*21*). Afterward (1987–1988), multiple research groups explored various biotin–streptavidin reagents, establishing the immunoreactivity and in vivo fate of biotinylated or mAb–streptavidin pharmacokinetics, clearance of radiolabeled forms of biotin and streptavidin, and safety in animals (*22,23*). Notably, Pimm et al. documented that radioiodinated avidin and streptavidin were cleared from the circulation via the kidneys, but with prolonged renal retention (*22*). In addition to issues of immunogenicity, this renal retention of streptavidin (and hence low TI for the kidney) became problematic and dose-limiting, prompting efforts at alleviation via chemical modification (e.g., with succinic anhydride or 1,2-cyclohexanedione) or engineering of recombinant streptavidin (*24,25*). In 1990, Kalofonos et al. reported the clinical feasibility of biotin–streptavidin PRID (*26*). In 10 patients with squamous cell carcinoma of the lung, the investigators infused antihuman milk fat globule antigen 1 mAb–streptavidin for tumor targeting, followed 2–3 d later with ^{111}In-biotin (*26*). Positive imaging was observed in 8 of 10 lung tumors (Fig. 2B) (*26*).

In 1991, Paganelli et al. conducted their first biotin–streptavidin PRID clinical study on 19 patients with a confirmed histologic diagnosis of tumors using an optimized 3-step regimen consisting of biotinylated anti-CEA mAb, an avidin chase, and ^{111}In-biotin (*27*). Tumors and metastases were detected in 18 of 19 patients (the remaining patient was a true-negative) less than 3 h after administration of ^{111}In-biotin by γ-scintigraphy, with no evidence of toxicity and with favorable contrast (*27*).

Although PRID showed promise, its development was soon blunted by the advent of oncologic ^{18}F-FDG PET/CT (*28*). Also, for diagnosis, sufficient image contrast and a single-day imaging procedure was achievable with rapidly clearing antibody-based probes. Unlike radioimmunodiagnosis, for which high tumor–to–normal-tissue contrast is necessary at only 1 specific time point, radioimmunotherapy requires high contrast at all time points in order to achieve high TIs. PRIT soon became the major platform to further the science and its clinical translation. The primary consideration for PRID is its theranostic potential: directing the surgical procedure to sites of the body with a high likelihood of finding antigen-bearing tumor, and performing dosimetry using quantifiable radioisotopes, a critical predictor of tumor response to PRIT. Tables 1 and 2 summarize the clinical and preclinical PRIT studies, respectively, with an emphasis on dosimetry and TIs described here.

Published in 1997, pilot clinical PRIT studies by Paganelli et al., using ^{111}In/^{90}Y-biotin targeting against various tumor types with anti-CEA, anti-TAG-72, and antitenascin mAbs (*29*), demonstrated that favorable TIs could be achieved. Mean absorbed doses (as cGy/37 MBq) to tumor, marrow, kidney, and liver were 15.2 ± 8.7, 1.1 ± 0.6 (TI, 13.8), 4.5 ± 2.1 (TI, 3.4), and 1.5 ± 1.0 (TI, 10.1), respectively. Eleven patients with various tumors (breast, brain, colon) were administered ^{90}Y-biotin doses ranging from 1.85 to 5.55 GBq; the treatment was well tolerated, and no acute toxicity was observed. However, ADA to streptavidin was observed in all patients.

Over the next decade, Paganelli et al. studied multiple biotin–streptavidin PRIT dosing protocols and injection routes (reviewed by Papi et al. (*30*)). Remarkably, from 1994 to 2005, over 500 glioblastoma patients were treated with biotin–streptavidin PRIT. For example, during a phase I/II study (*31*), they treated 48 patients (possessing histologically confirmed grade III and IV gliomas) using 5-step intravenous antitenascin PRIT with ^{111}In/^{90}Y-biotin (^{90}Y-biotin dose range, 2.22–2.96 GBq/m^2). The DLT was hematologic, and the maximum tolerated dose (MTD) was 2.96 GBq/m^2. They reported tumor, brain, kidney, liver, and marrow mean absorbed doses (as cGy/37 MBq) of 15.20 ± 8.70, 0.6 ± 0.3 (TI, 25.3), 2.7 ± 1.6 (TI, 5.63), 1.5 ± 1.0 (TI, 10.1), and 0.8 ± 0.5 (TI, 19.0), respectively. ADA to streptavidin was observed in all patients.

These early clinical PRIT studies inspired many groups to explore biotin–streptavidin PRIT in the mid to late 1990s (*32,33*). Much effort was devoted to improving BsAb design and alternative second specificities (besides biotin or metal chelator haptens), including complementary oligomeric pretargeting systems (*34–36*). Using morpholino complementary oligomers, Liu et al. and Hnatowich et al. have shown success for in vivo applications (reviewed by Liu (*37*)), although they have not been investigated clinically.

NeoRx Corporation exploited mAb–streptavidin fusion proteins to pretarget tumors before administration of radiobiotin. During the early to mid 1990s, they developed a mAb–streptavidin chemical conjugate (mAb NR-LU-10 specific for epithelial cell adhesion molecule) to target multiple solid-tumor types (*38*). In 2000, they showed how a single treatment with pretargeted ^{90}Y-biotin was curative in nude mice bearing human tumor xenografts (CRC, lung, and breast) without significant toxicity (*39*). Although TIs were not reported, an approximately 20-fold improvement in the tumor-to-blood area under the curve (AUC) ratio (calculated from 0 to 120 h after injection) for PRIT versus conventional radioimmunotherapy was demonstrated (tumor-to-blood AUC ratio: 28.3 and 1.22, respectively). At doses of up to 29.6 MBq (MTD not reached) of pretargeted ^{90}Y-biotin per mouse, 28 of 30 cures were achieved with transient myelosuppression and no apparent sequelae. Moreover, kidney uptake and retention were relatively low, at approximately 2% of the injected dose per gram from 2 to 120 h after injection. During a phase I dose escalation study (*40*), the MTD was determined to be 4.07 GBq/m^2, the DLT at 5.18 GBq/m^2 was gastrointestinal toxicity, and the recommended phase 2 dose was 4.44 GBq/m^2. These findings were considered highly remarkable because DLT was not hematologic and ^{90}Y doses approximately 5 times higher than radioimmunotherapy could be administered without marrow DLT or use of stem cell support (*41*). Imaging and dosimetry studies (*42*) revealed tumor, small-intestine, large-intestine, kidney, liver, and marrow mean absorbed doses

TABLE 1
Select Clinical PRIT and Targeted Radiotherapy Studies with Emphasis on Dosimetry

Year	Vehicle	TRT type	No. of steps	Antigen targets	Tumor types	No. of patients	RIT/PRIT radiocarrier	Administered activity	cGy/37 MBq to tumor	TI			Reference
										Marrow	Kidney	Liver	
1997	IgG–biotin	PRIT	5*	CEA, TAG-72, tenascin	Advanced metastatic (breast, brain, colon)	11	^{90}Y-biotin	1.85–5.55 GBq	15.2 ± 8.7	13.8	3.4	10.1	*(29)*
1997	IgG	RIT	1	TAG-72	Metastatic gastrointestinal tract carcinomas	12	^{90}Y-IgG	0.640–1.421 GBq	34.5 ± 24.6 (7.0–80.9)	15.2 (3.6–42.1)	ND	0.9 (0.3–1.5)	*(45)*
1998	mAb–streptavidin	PRIT	3	Epcam	Various†	40	^{90}Y-biotin	2.035–10.693 GBq (0.925–5.18 GBq/m^2)	16.4 ± 13.2	48.2	1.43	5.47	*(40,42)*
1999	IgG–biotin	PRIT	5*	Tenascin	High-grade glioma	48	^{90}Y-biotin	2.22–2.96 GBq/m^2	15.20 ± 8.70	19.0	5.63	10.1	*(31)*
1999	F(ab)′ × F(ab)′	PRIT	2	CEA	MTC	26	^{131}I-diDTPA(indium)-hapten	0.888–2.22 GBq/m^2 (1.41–4.14 GBq)	44.33 ± 53.39 (2.91–184)	29.62 ± 35.32	8.36 ± 10.02	10.86 ± 13.55	*(71)*
2000	mAb–streptavidin	PRIT	3	CD20	Non-Hodgkin lymphoma	7	^{90}Y-biotin	1.11 or 1.85 GBq/m^2	29 ± 23	181	5.8	18	*(41)*
2004	(scFv)$_4$–streptavidin	PRIT	3	CD20	Non-Hodgkin lymphoma	15	^{90}Y-biotin	0.555 GBq/m^2	26 ± 4 (2–69)	104	3.4	22	*(57)*
2005	(scFv)$_4$–streptavidin	PRIT	3	TAG-72	Metastatic CRC	9	^{90}Y-biotin	0.37 GBq/m^2	28.9 (4.18–121.6)	117.4 (25.8–399.1)	4.12	8.0 (1.9–17.6)	*(46)*
2014	DNL	PRIT	2	CEA	Metastatic CRC	20	^{177}Lu-IMP288	2.5–7.4 GBq	ND‡	^{177}Lu: 4.68 (0.68–10.91); simulated ^{90}Y: 5.41 (0.99–13.72)	ND	ND	*(110)*

---

*IgG-biotin/avidin chase/streptavidin/biotinylated albumin CA/^{90}Y-biotin.

†Refractory epithelial (including ovary, colon, prostate, breast).

‡Not reported as cGy/37 MBq, but based on absorbed doses to tumor determined using Monte Carlo-based 3D-RD dosimetry package (0.46–4.52 Gy) and corresponding administered activities (5.6 and 2.5 GBq for 0.46 and 4.52 Gy, respectively), range of 0.30–6.69 cGy/37 MBq was calculated.

TRT = targeted radiotherapy; RIT = radioimmunotherapy; ND = not determined.

All treatments were administered intravenously.

TABLE 2
Select Preclinical PRIT and Targeted Radiotherapy Studies with Emphasis on Dosimetry

Vehicle	TRT type	RIT/PRIT radiocarrier	cGy/MBq to tumor	cGy/37 MBq to tumor	TI Blood	TI Kidney	TI Liver	Reference
IgG	RIT	^{131}I-3F8 (^{131}I-naxitamab)	237.4 ± 40.4	8,784 ± 1,495	3	13	19	(*51*)
F(ab′)$_2$	RIT	^{131}I-F6 F(ab′)$_2$	184	6,800	5	10	17	(*157*)
Peptide	PRRT	^{177}Lu-DOTATATE (Lutathera*)	34 ± 0.4	1,258 ± 14.8	ND	3	46	(*158*)
IgG–streptavidin	PRIT	^{177}Lu-biotin or ^{90}Y-biotin	^{177}Lu: 62	^{177}Lu: 2,294	^{177}Lu: 9	^{177}Lu: 2	^{177}Lu: 9	(*103*)
			^{90}Y: 134	^{90}Y: 4,958	^{90}Y: 12	^{90}Y: 4	^{90}Y: 8	
scFv–streptavidin	PRIT	^{90}Y-biotin	153.1 ± 8.3	5,665 ± 307	170	3	21	(*51*)
Antitumor F(ab′)$_2$ × anti-HSG Fab	PRIT	^{177}Lu-IMP241 or ^{90}Y-IMP241	^{177}Lu: 151	^{177}Lu: 5,587	^{177}Lu: 45	^{177}Lu: 9	^{177}Lu: 35	(*84*)
			^{90}Y: 388	^{90}Y: 14,356	^{90}Y: 35	^{90}Y: 8	^{90}Y: 26	
DNL	PRIT	^{177}Lu-IMP325 or ^{90}Y-IMP325	^{177}Lu: 72.8	^{177}Lu: 2,695	^{177}Lu: 169	^{177}Lu: 7	ND	(*91*)
			^{90}Y: 135	^{90}Y: 5,011	^{90}Y: 158	^{90}Y: 7		
IEDDA click	PRIT	^{177}Lu-Tz	556	20,572	11	21	26	(*140*)
DOTA-PRIT	PRIT	^{177}Lu-DOTA	85	3,145	142	23	40	(*120*)
Affibody-PNA	PRIT	^{177}Lu-HP2	108	3,996	269	5	81	(*132*)
SADA-PRIT	PRIT	^{177}Lu-DOTA	320	11,840	109	25	32	(*127*)

---

*Advanced Accelerator Applications.

TRT = targeted radiotherapy; RIT = radioimmunotherapy; ND = not determined; IEDDA = inverse electron-demand Diels–Alder.

All therapies were given intravenously to immunocompromised mice bearing subcutaneous human cancer xenografts.

(as cGy/37 MBq) of 16.4 ± 13.2, 49.2 ± 25.3 (TI, 0.33), 34.8 ± 17.9 (TI, 0.47), 11.5 ± 5.6 (TI, 1.43), 3.0 ± 1.8 (TI, 5.47), and 0.34 ± 0.08 (TI, 48.2), respectively. High doses of ^{90}Y-biotin in the gastrointestinal tract resulted from cross-reactivity of the mAb NR-LU-10 with the bowel epithelium. Moreover, tumor response was seen in the 2 patients with the highest estimated dose to tumor (4,000–6,000 cGy); grade IV diarrhea was observed in patients estimated to have received 6,850–14,000 cGy to the large-intestine wall; and delayed renal toxicity was observed in patients estimated to have received 2,170 or 3,072 cGy. In the same year, Knox et al. reported disappointing results from a phase II clinical study on 25 patients with metastatic CRC after a single dose of mAb–streptavidin pretargeted ^{90}Y-biotin, 4.07 GBq/m^2 (mean administered dose, 3.941 ± 0.381 GBq/m^2) (*43*). The overall response rate was modest (8%), and both hematologic and nonhematologic toxicities were observed (severe diarrhea in 30% of patients and delayed renal toxicity in 2 patients).

NeoRx moved on to an alternative pan-carcinoma mAb/antigen system, in which a mAb–streptavidin chemical conjugate (mAb CC49 specific for TAG-72) was used to deliver radiobiotin (*44*). Anti-TAG-72 radioimmunotherapy was studied clinically in the mid 1990s; for example, ^{111}In/^{90}Y-CC49 was evaluated in 12 patients with metastatic gastrointestinal tract carcinomas (*45*). Preclinical pretargeting studies on nude mice bearing human tumor xenografts were promising, as the tumor-to-blood AUC ratios were 179, 170, and 371 for ^{149}Pm-, ^{166}Ho-, and ^{177}Lu-biotin, respectively (no TIs were reported), and kidney uptake was minimal, at approximately 1%–2% of the injected dose per gram from 1 to 168 h after injection (*44*). In 2005, a phase I 3-step PRIT trial was performed using a CC49-(single-chain variable fragment [scFv])$_4$–streptavidin fusion (*46*). A total of 9 advanced-CRC patients received CC49-(scFv)$_4$–streptavidin, CA, and ^{111}In/^{90}Y-biotin (^{90}Y-biotin dose of 0.37 GBq/m^2). Imaging and dosimetry studies revealed a patient-specific mean ^{90}Y radiation dose (as cGy/37 MBq) of 7.02 (range, 3.36–11.2) to kidneys, 3.75 (range, 0.63–6.89) to liver, 0.22 (range, 0.12–0.34) to marrow, and 28.9 (range, 4.18–121.6) to tumors, corresponding to TIs of 4.12, 7.71, and 131 for kidney, liver, and marrow, respectively (*46*). MTD, DLT, and recommended phase 2 dose were not defined; however, the low TI for kidney was projected to be dose-limiting. Förster et al. demonstrated that succinylation of the CC49-(scFv)$_4$–streptavidin construct could reduce kidney uptake (*47*), but this was never tested clinically.

Additional solid-tumor mAb/antigen systems studied by NeoRx for PRIT included Lewis Y antigen (with ^{213}Bi-biotin (*48*) or ^{90}Y-biotin (*49*)) and mesothelin (with ^{177}Lu-biotin or ^{90}Y-biotin (*50*)). Also, using a novel antidisialoganglioside (GD2)-(scFv)$_4$–streptavidin fusion protein, highly efficient GD2 targeting was demonstrated with ^{111}In-biotin in nude mice bearing human tumor xenografts (*51*). Tumor-absorbed radiation doses (as cGy/37 MBq) were 8,784 ± 1,495 and 5,665 ± 307 for conventional radioimmunotherapy and PRIT with ^{90}Y-biotin, respectively (*51*). For radioimmunotherapy, TIs of 3, 13, and 19 were determined for blood, kidney, and liver, respectively. In comparison, for PRIT with ^{90}Y-biotin, TI was improved for blood (TI, 170) but diminished for kidney (TI, 3) and similar for liver (TI, 21). Although highly promising in terms of reducing myelotoxicity, the poor TI for kidney limited its translational potential.

NeoRx also developed reagents for PRIT of hematologic cancers. In the mid 1990s, remarkably, anti-CD20 radioimmunotherapy was shown to be curative in patients with relapsed B-cell lymphomas; however, highly aggressive myeloablative treatments with bone marrow rescue were needed (*52*). In 2002, the results from the anti-

CD20 radioimmunotherapy phase 3 study of ^{90}Y-ibritumomab were reported, showing that treatment was well tolerated and superior to rituximab in terms of overall response rate and complete response rate (*53*). NeoRx collaborated with Press et al. at the Fred Hutchinson Cancer Research Center and the University of Washington to develop anti-CD20 biotin–streptavidin PRIT to improve the safety profile of anti-CD20 radioimmunotherapy (*54*). They prepared an anti-CD20–streptavidin chemical conjugate for PRIT with ^{90}Y-biotin and performed preclinical studies on nude mice bearing human Ramos xenografts, making direct comparisons with radioimmunotherapy (*54*). Although no TIs were reported, tumor-to-blood ratios at 24 h were markedly improved with PRIT (3 and 0.4 for PRIT and radioimmunotherapy, respectively). Notably, superior tumor uptake was also shown with PRIT, establishing the potential advantage of PRIT particularly for noninternalizing antibodies. A lethal dose of 14.8 MBq was reported for radioimmunotherapy, with all treated animals dying of marrow suppression and infection on day 10. In contrast, 9 of 9 mice receiving pretargeted ^{90}Y-biotin (29.6 MBq) achieved CRs by day 12, leading to 8 of 9 cures (no recurrences during observation period of >140 d) and minimal toxicity.

These highly promising preclinical PRIT studies led to a phase I/II study on non-Hodgkin lymphoma patients (*41*). Seven patients with relapsed or refractory non-Hodgkin lymphoma received ^{111}In/^{90}Y-biotin (^{90}Y-biotin dose of 1.11 or 1.85 GBq/m^2). Tumor, kidney, liver, and marrow mean absorbed doses (as cGy/37 MBq) were 29 ± 23, 5.0 ± 1.7 (TI, 5.8), 1.6 ± 0.5 (TI, 18), and 0.16 ± 0.1 (TI, 181), respectively; also, the estimate of tumor–to–whole-body dose ratio (38:1) achieved with PRIT was higher than has been achieved using conventional radioimmunotherapy. Furthermore, doses of ^{90}Y 3 times the MTD of radioimmunotherapy could be given without significant myelosuppression. As a result, 6 of 7 achieved objective tumor regression, including 3 complete response and 1 partial response (*41*). Only grade I/II nonhematologic toxicity was observed, and grade III hematologic toxicity was transient in 5 of 7 patients. Six of 10 patients developed measurable ADA. MTD was not defined but was noted to be "likely more than 1.85 GBq/m^2" on the basis of dose-limiting hematologic toxicity, and kidneys showed the highest uptake (5.0 ± 1.7 cGy/37 MBq vs. 1.3 cGy/37 MBq for unbound radiobiotin (*55*)).

To generate well-defined and homogeneous fusion proteins and greatly simplify manufacturing, the group developed a second-generation, genetically engineered anti-CD20–streptavidin fusion protein (as a (scFv)$_4$–streptavidin fusion, B9E9FP (*56*)), documented a tumor-to-blood AUC ratio of more than 60 in nude mice bearing Ramos xenografts, and performed a phase I pilot trial in B-cell non-Hodgkin lymphoma (*57*). Fifteen non-Hodgkin lymphoma patients received B9E9FP, CA, and ^{111}In/^{90}Y-biotin (^{90}Y-biotin dose, 0.555 GBq/m^2). Mean absorbed doses to tumor, kidney, liver, and marrow (as cGy/37 MBq) were 26 ± 4, 7.7 ± 1.7 (TI, 3.4), 1.2 ± 0.2 (TI, 22), and 0.25 ± 0.04 (TI, 104), respectively. MTD, DLT, and recommended phase 2 dose were not defined. ADA was substantial 3 patients, and 5 patients had transient low antibody responses.

Additional hematologic tumor mAb/antigen systems studied by NeoRx for PRIT included CD25 (with ^{90}Y-biotin or ^{213}Bi-biotin (*58*)) and CD45 (with ^{90}Y-biotin (*59*)). In a notable study, Pantelias et al. (*60*) evaluated multiantigen PRID with mAb–streptavidin (anti-CD20, anti-human leukocyte antigen DR, anti-CD22) and ^{111}In-biotin. Interestingly, the most favorable tumor–to–normal-organ ratios of absorbed radioactivity were obtained using single conjugates optimized for target tumor antigen expression rather than the combination therapy (*60*). Of these additional PRIT systems, CD45 has been evaluated clinically.

Second-Generation BsAb PRIT with Multivalent Haptens

Alongside biotin–streptavidin PRIT development in the late 1980s, groups were also looking to optimize contrast by improving hapten selectivity for intratumoral BsAb over circulating BsAb. In 1989, Le Doussal et al. (Immunotech) evaluated PRID with bivalent hapten tracers to image CEA-expressing CRC (*61*). Coined "affinity enhancement," they showed greater affinity to cell-bound than to unbound BsAb via cooperative cross-linking of intratumoral BsAb, resulting in additional tumor-absorbed dose (*61*). Also, a chase or CA was not required for high contrast, greatly simplifying the pretargeting regimen. Around the same time, Goodwin et al. reported a bivalent Janus hapten for pretargeting with their antichelate mAbs (*62*).

Between 1993 and 1998, Immunotech performed clinical PRID studies with an anti-CEA mAb/metal chelate–specific mAb BsAb. The metal chelate-specific mAb was against indium-diethylenetriaminepentaacetic acid (indium-DTPA). With a bivalent ^{111}In-diDPTA-tyrosyl-lysine hapten for PRID, they demonstrated that high-contrast images could be obtained in patients with CRC (*63*), medullary thyroid cancer (MTC) (*64,65*), and small-cell lung cancer (*66*). Although the images were impressive, the use of murine BsAb led to ADA in most patients (e.g., ~60% (*63*)). Furthermore, for PRIT with ^{131}I, instead of developing a new metal chelate–specific mAb, they used stable indium-DTPA as an affinity handle to generate ^{131}I-labeled diDTPA(In)-tyrosyl-lysine radiohapten (^{131}I-diDTPA(indium)-hapten) and analogs for chelation of ^{99m}Tc and ^{188}Re (*67–69*). In nude mice bearing human MTC xenografts, pretargeting of 92.5 MBq of ^{131}I-diDTPA(indium)-hapten was demonstrated to be more efficient (leading to significantly longer growth delays) and less toxic than radioimmunotherapy (*70*). Soon after, this approach was evaluated in patients.

Initially, 2 phase I/II clinical trials assessing PRIT with ^{131}I-diDTPA(indium)-hapten were performed on patients with either MTC (*71*) or small-cell lung cancer (*72*). The BsAb was a F(ab)′ × F(ab)′ chemical conjugate. Twenty-six MTC patients received 1–3 treatments at ^{131}I-diDTPA(indium)-hapten doses ranging from 0.888 to 2.22 GBq/m^2 (*71*). Tumor, kidney, liver, and marrow mean absorbed doses (as cGy/37 MBq) were 44.33 ± 53.39, 5.61 ± 2.02 (TI, 8.36 ± 10.02), 5.19 ± 2.23 (TI, 10.86 ± 13.55), and 1.60 ± 0.82 (TI, 29.62 ± 35.32), respectively (*71*). Myelosuppression was the crucial factor for DLT, and MTD (and recommended phase 2 dose) was 1.78 GBq/m^2 (*71*). Among the 17 evaluable patients, 5 minor tumor responses were observed in patients with mainly a small tumor burden (*71*). ADA was observed in 9 of 17 (53%) patients (*71*). During the second clinical trial, 14 patients with small-cell lung cancer were treated with ^{131}I-diDTPA(indium)-hapten ranging from 1.48 to 6.66 GBq (*72*). Tumor, kidney, liver, and marrow absorbed doses (as cGy/37 MBq) were 1.8–32.2, 3.9–5.0, 1.6–5.0, and 0.4–1.7, respectively. MTD without hematologic rescue was 5.55 GBq (*72*). Of the 12 patients, 2 partial response and 1 stabilization of more than 24 mo was observed (*72*). Although no recommended phase 2 dose was specified, dose escalation was reported to be continuing to reach 11.1 GBq (*72*). Among 5 evaluable patients for ADA, 1 patient showed significant ADA after 2 mo, which persisted at 12 mo (*72*).

A subsequent clinical trial was performed to optimize reagent dosing and timing of administration with humanized BsAb in 35 patients with CEA-expressing tumors (*73*). BsAb doses ranged from 10 to 100 mg/m^2, ^{131}I-diDTPA(indium)-hapten doses ranged from 1.9 to 5.5 GBq, and a pretargeting interval of 5 or 7 d was studied (*73*). With optimized PRIT (e.g., with 40 mg/m^2 of BsAb and a 5-d pretargeting interval), ^{131}I-diDTPA(indium)-hapten doses of up to 5.5 GBq were well tolerated in the absence of bone marrow involvement (*73*).

In a follow-up trial on 22 patients with CEA-expressing tumors, the humanized BsAb dose (40–75 mg/m^2) and ^{131}I-diDTPA(indium)-hapten dose (1.8–2.9 GBq/m^2; 1.9–5.5 GBq) were varied to evaluate antitumor efficacy and toxicity (*74*). Myelosuppression was BsAb dose–dependent, with 75 mg/m^2 leading to high hematologic toxicity, and nonhematologic toxicity was hepatic (transient grade I or II) (*74*). With a BsAb dose of 75 mg/m^2, higher whole-body and liver mean radiation doses were observed (0.38 and 1.9 Gy for whole body and liver, respectively) than for 40 mg/m^2 (0.33 and 1.4 Gy for whole body and liver, respectively), and mean tumor doses did not differ significantly with BsAb dose (75 mg/m^2, 10.7 Gy [range, 1.7–53.5 Gy]; 40 mg/m^2, 18.5 Gy [range, 2.4–49.3 Gy]) (*74*). Modest therapeutic efficacy was reported, with no CRs or PRs (*74*). The MTD was determined to be 3 GBq of ^{131}I-diDTPA(indium)-hapten in MTC patients and was not defined in non-MTC patients (escalated beyond 5.5 GBq) (*74*). Human antimouse antibody elevation was observed in 1 patient (8%), and human antihuman antibody was observed in 4 patients (33%) (*74*).

In 2006, Chatal et al. reviewed their clinical experience and compared the survival of advanced-MTC patients who underwent PRIT (^{131}I-diDTPA(indium)-hapten doses ranging from 1.9 to 5.5 GBq) with that of contemporaneous untreated patients for whom data were collected by the French Endocrine Tumor Group (*75*). Notably, they showed a survival benefit for those treated with PRIT, underscoring its clinical promise (*75*).

Besides CEA-expressing tumors, a PRID approach to imaging renal cell carcinoma was developed with bivalent haptens. Use of an anti–renal cell carcinoma/anti–indium-DTPA hapten BsAb and a refined tetrapeptide bivalent hapten, ^{111}In-diDTPA-Phe-Lys-Tyr-Lys (^{111}In-diDTPA-FKYK), showed highly efficient tumor targeting (*76,77*). During comparative studies with monovalent ^{111}In-DTPA and ^{111}In-diDTPA-FKYK, they achieved dramatic improvements in tumor uptake with the bivalent hapten (in nude mice bearing human renal cell carcinoma xenografts: ~78% vs. ~2% of the injected dose per gram at 4 h after injection for the bivalent and monovalent haptens, respectively) without sacrificing promising tumor-to-blood ratios (*76*). The ^{111}In-diDTPA-FKYK was also prepared with D-amino acids to make it more resistant to in vivo peptidases and improve the residualization of ^{125}I during PRIT (*78*). Efficient targeting of CEA was also demonstrated via this approach (with ^{111}In, ^{99m}Tc, nonresidualizing ^{125}I, or residualizing ^{125}I) (*79*); however, antichelate mAbs were falling out of favor compared with alternative antihapten mAbs.

Third-Generation BsAb PRIT with Anti–Histidine-Succinyl-Glycine (HSG) mAb and BsAb Prepared via Dock-and-Lock (DNL)

The anti–^{111}In-DTPA hapten approach was limited by mAb specificity and could not be used to target ^{90}Y or ^{177}Lu (*80*). Although additional antichelate mAbs were prepared (e.g., anti–copper-triethylenetetramine and anti–yttrium-1,4,7,10-tetraazacyclododecane-1,4,7,10-tetraacetic acid (yttrium-DOTA) (*81*)), alternative antihapten mAbs were evaluated for PRIT, including anti-2,4-dinitrophenyl (*61*) and anti-HSG pseudopeptide (*82*). Also, around this time, novel BsAb formats with divalent tumor-antigen binding (e.g., anti-CEA IgG or anti-CEA F(ab′)$_2$ chemically conjugated to anti–indium-DTPA Fab′) were studied (*83*). Notably, pretargeting with anti-CEA IgG × anti–indium-DTPA Fab′ led to the most favorable tumor uptake and retention in the tumor, but use of a CA was necessary to achieve acceptable tumor-to-blood ratios (*83*). Therefore, a F(ab′)$_2$–Fab′ BsAb (~80 kDa) was considered optimum in terms of balancing tumor uptake and clearance without the need for a CA step (*83*).

In 2003, Sharkey et al. significantly advanced the HSG system for PRIT by developing a novel BsAb (e.g., anti-CEA F(ab′)$_2$ or anticolon-specific antigen-p F(ab′)$_2$ chemically conjugated to anti-HSG Fab) and a suite of HSG peptides suitable for targeting a variety of clinically relevant radionuclides (IMP241 for ^{90}Y, ^{111}In, and ^{177}Lu, and IMP245 for ^{99m}Tc and ^{188}Re) (*84*). Dosimetry projections for pretargeting anticolon-specific antigen-p with ^{90}Y- or ^{177}Lu-IMP241 in nude mice bearing human xenografts were 5,587–14,356 cGy/37 MBq for tumor, with corresponding TIs of 35–45, 8–9, and 26–35 for blood, kidney, and liver, respectively (*84*). In 2005, they clearly demonstrated the advantage of this pretargeting approach over a clinically used ^{99m}Tc-labeled CEA-specific F(ab′) for CRC imaging in mice bearing human xenografts (*85*). In 2006, an alternative peptide scaffold to IMP241 with less kidney retention was developed. IMP288 and PRID with ^{124}I was reported (*86*).

As was done for mAb–streptavidin fusions for biotin–streptavidin pretargeting, recombinant antitumor/antihapten BsAbs were replacing chemical conjugates. In 2003, Rossi et al. described a trivalent BsAb (hBS14: bivalent CEA and monovalent HSG); however, the engineering approach using transgenic myeloma cells led to low expression yield (*87*). Soon after, they described the DNL approach to assemble a multivalent tri-Fab antitumor/anti-HSG hapten BsAb with a molecular weight of approximately 157 kDa by exploiting regulatory protein kinase A dimerization and docking domains, and the anchoring domain of an interactive A-kinase anchoring protein, to form a stably tethered complex (Fig. 3A) (*88,89*). Interestingly, the blood clearance of the DNL BsAb was much faster than that of IgG (~150 kDa) since the BsAb lacks the CH$_2$ domain to enable neonatal Fc receptor recycling. DNL BsAbs have been generated against a variety of tumor antigens, including CEA (TF2), CD20 (TF4), and trophoblast cell surface antigen 2 (TF12); detailed reviews have been published (*28,90*). Dosimetry results for IMP325 (i.e., IMP288 saturated with nonradioactive indium) pretargeted to CEA-expressing LS-174T human CRC subcutaneous tumors were quite favorable; for example, for pretargeting of ^{177}Lu-IMP325, the authors reported TIs of 169 and 7 for blood and kidney, respectively, with an estimated tumor-absorbed dose of 2,695 cGy/37 MBq (*91*).

In one notable DNL PRIT preclinical study, they prepared anti-PAM4-antigen BsAb TF10 for targeting of ^{90}Y-IMP288 (*92*). They demonstrated in nude mice bearing established Capan-1 human pancreatic cancer xenografts that PRIT could be safely combined with gemcitabine and CRs could be achieved (*92*). Furthermore, they showed that doses of up to 33.3 MBq of pretargeted ^{90}Y-IMP288 were well tolerated over 9 mo with no evidence of chronic nephrotoxicity (MTD not reached), a marked improvement from initial ^{90}Y-IMP288 PRIT studies (*93*).

Initial clinical experience with the DNL BsAb platform included a phase 0 clinical study of ^{131}I-TF2 in 2 patients with suspected CRCs to characterize the clearance kinetics of the BsAb, and a first-in-patients PRID study with ^{111}In-IMP288 in a metastatic CRC patient (*94*). Although optimization of the TF2 dose was necessary, highly promising dosimetry projections of PRIT with ^{90}Y-IMP288 were reported (kidney, 1.4 cGy/37 MBq; marrow, 0.1 cGy/37 MBq) (*94*). Soon afterward, PRIT clinical trials with ^{111}In/^{177}Lu-IMP288 commenced.

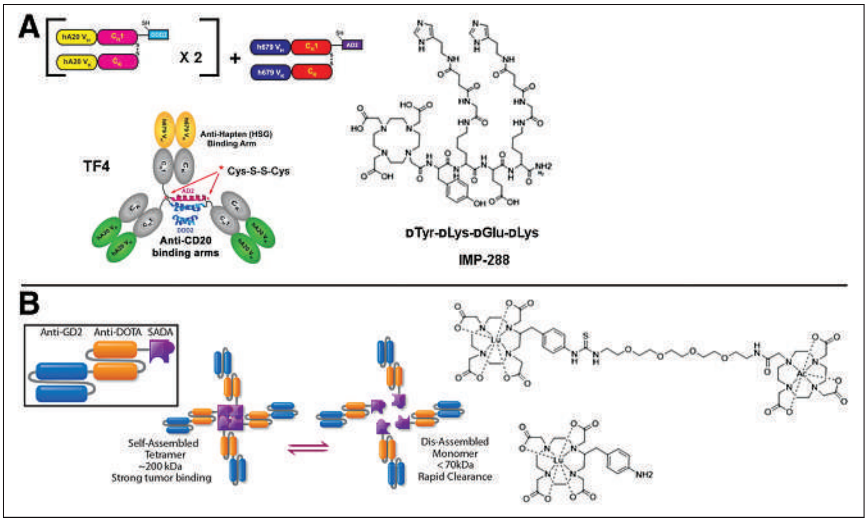

FIGURE 3. BsAb pretargeting with DNL BsAb or with SADA BsAb platform. (A) Structure of tri-Fab TF4 made by DNL method and associated HSG hapten, IMP-288. DNL BsAb has single binding site for hapten and 2 binding sites for tumor antigen. (Reprinted with permission of (*154*).) (B) Structure of anti-GD2/anti-DOTA SADA BsAb and ^{225}Ac-DOTA-hapten (reprinted from (*123*)) and ^{177}Lu-aminobenzyl-DOTA (reprinted with permission of (*127*)). SADA BsAb has 4 binding sites for both DOTA hapten and tumor antigen. hA20 = humanized anti-CD20 IgG hA20 (veltuzumab); VH = heavy chain variable domain; VK = light chain variable domain; CH1 = heavy-chain constant domain 1; CK = light-chain constant domain; DDD2 = dimerization and docking domain with SEQ ID NO: 2; AD2 = anchoring domain with SEQ ID NO: 4.

SELECTED PRETARGETING ADVANCES OF THE PAST DECADE

PRIT with Biotin–Streptavidin System

In 2013, Mawad et al. reported clinical PRIT with ^{111}In/^{90}Y-biotin in high-risk acute myeloid leukemia/myelodysplastic syndrome patients undergoing allogenic hematopoietic cell transplantation (*95*). Five patients received a 0.7 mg/kg dose of anti-CD45 mAb–streptavidin followed 48 h later by a 1.3 mg/m^2 dose of ^{90}Y-biotin (median, 2.775 GBq; range, 2.294–4.144 GBq) based on ^{111}In-biotin pretreatment dosimetry (*95*). No participants were withdrawn from the study because of toxicities; 2 grade 3 gastrointestinal adverse events (enterocolitis, typhlitis) were identified as unexpected and considered possibly related to PRIT, with the only grade 4 event being expected hematopoietic cell transplantation–related cytopenia (*95*). A single patient was in complete remission a year after protocol treatment, and the other 4 patients died of progressive disease, with a median time to relapse of 28 d (range, 12–155 d) (*95*).

More recently, in 2015, a trial was initiated with anti-CD20 B9E9 with ^{111}In/^{90}Y-biotin in patients with high-risk B-cell malignancies to evaluate the safety of combining PRIT with carmustine, etoposide, cytarabine, and melphalan chemotherapy and autologous stem cell transplantation (NCT02483000).

Paganelli et al. performed a locoregional PRIT clinical trial on 11 breast cancer patients (*96*). Avidin was injected around the tumor, followed by intravenous administration of 111 MBq of ^{90}Y-biotin. Remarkably, ADA to avidin has been shown to not limit therapy (*97*). De Santis et al. described AvidinOX (Alfasigma S.p.A.), an avidin variant designed to prolong the tissue half-life (2 wk compared with 2 h for native avidin) and to demonstrate cellular and interstitial protein tropism for enhanced PRIT (*98*). In addition to showing therapeutic promise in preclinical studies (*98–101*), AvidinOX PRIT has been studied in clinical investigations (NCT02053324 and NCT03188328, both of which were terminated because of low recruitment).

Preclinically, PRIT development continued (e.g., with ^{211}At-biotin-succinylated poly-L-lysine (*102*), and comparative efficacy of ^{177}Lu and ^{90}Y for anti-CD20 PRIT of B-cell lymphomas (*103*)). However, a head-to-head study comparing the efficacy and toxicity of anti-CD20 biotin–streptavidin PRIT and a novel BsAb PRIT platform with an ultra-high-affinity anti-yttrium-DOTA scFv antibody (C825) revealed preferred use of BsAb PRIT in future clinical trials (*104,105*).

BsAb Pretargeting

The DNL system has been extensively studied both preclinically (primarily in the development of additional haptens) and clinically, with multiple trials featuring DNL anti-CEA TF2 and radiolabeled IMP288. Two notable hapten developments included a novel radiolabeled/near-infrared multimodal DNL hapten, RDC018, for image-guided surgery of various carcinomas (*106*) and ^{213}Bi-IMP288 for α-PRIT (*107*).

In 2013, a landmark phase I PRIT study was reported with ^{111}In/^{177}Lu-IMP288 in 20 patients with CEA-expressing CRC (*108*). The ^{177}Lu-IMP288 dose was designed to deliver no more than 1.25 Gy to marrow or 15 Gy to kidneys (3.7–7.4 GBq) based on pretreatment dosimetry with ^{111}In-IMP288. Absorbed doses were less than 1.85 cGy/37 MBq for kidney, and mean marrow dose ranged from 0.0296 to 0.222 cGy/37 MBq based on the dosing cohort (*109*). Tumor doses were 0.46–4.52 Gy, and red marrow doses ranged from 0.12 to 0.97 Gy (mean TI, 4.68) (*110*). Furthermore, they projected an approximately 25% higher marrow TI for treatment with ^{90}Y-IMP288 instead of ^{177}Lu-IMP288 (mean TI simulated for ^{90}Y-IMP288, 5.41). DLT was hematologic, and no recommended phase 2 dose was indicated. Since TF2 is humanized and lacked Fc, ADAs were unexpected but observed in about 50% of the patients on repeated injection. However, a reduced infusion rate and preadministration of prophylactics were effective at reducing associated adverse events. A PRIT trial with ^{90}Y-IMP288 in metastatic CRC patients is ongoing (NCT02300922).

Soon after the phase I PRIT study in CRC patients, a phase I PRIT study with ^{111}In/^{177}Lu-IMP288 on 9 patients with CEA-expressing small-cell lung cancer was reported in 2015 (*111*), and first-in-humans PRID with TF2/^{68}Ga-IMP288 in MTC patients was reported in 2016 (*112*). In the last 2 y, additional clinical studies with TF2/^{68}Ga-IMP288 were performed on CRC (*113*) and HER2-negative/CEA-positive metastatic breast cancer patients (*114*). In 2021, Bodet-Milin et al. reported clinical data using TF2/^{68}Ga-IMP288 in MTC patients, demonstrating improved sensitivity for metastatic lesion detection over ^{18}F-L-dihydroxyphenylalanine PET/CT (*115*). Select examples of recent clinical PRID studies with TF2/IMP288 are shown in Figure 4.

Alongside the DNL BsAb pretargeting system, 2 additional BsAb pretargeting approaches using ultra-high-affinity (picomolar to femtomolar) antichelate mAbs have made significant progress in the last decade. Orcutt et al. affinity-matured the anti-DOTA chelate mAb 2D12.5 (*62*) and reformatted it as an scFv called C825 (*116*). C825 was shown to bind DOTA complexes of lutetium, yttrium, and gadolinium with similar affinity (low-picomolar range) (*116*).

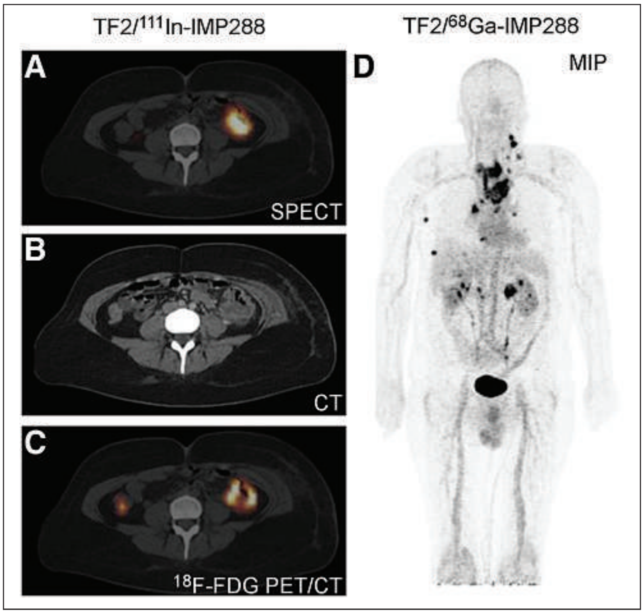

FIGURE 4. Select examples of recent clinical BsAb PRID with DNL TF2 and radiolabeled IMP288 (TF2/IMP288). (A) Scintigraphic images (axial views) of CRC patient imaged with TF2/^{111}In-IMP288, with highly specific targeting of primary colon tumor, confirmed by CT and ^{18}F-FDG PET/CT (B and C, respectively). (Reprinted from (*108*).) (D) PET image (coronal view) of MTC patient imaged with TF2/^{68}Ga-IMP288, with maximum-intensity-projection (MIP) image showing several pathologic lesions. (Reprinted from (*115*).)

Also, Orcutt reported a highly modular tetravalent IgG-scFv BsAb format (*117*) and carefully screened candidate DOTA-radiohaptens to determine which had the most favorable in vivo properties for PRIT, reporting estimated human liver, kidney, and red marrow doses for ^{90}Y-labeled haptens of 0.130–0.192, 0.703–0.999, and 0.029–0.048 cGy/37 MBq respectively (*118*). Also, in combination with a dextran-hapten CA, highly efficient anti-CEA mAb/C825 pretargeting with ^{177}Lu- or ^{111}In-haptens in nude mice bearing LS174T human CRC xenografts was demonstrated (*119*). These studies led to the antichelate BsAb platform called DOTA-based PRIT, or DOTA-PRIT. Between 2014 and 2018, Cheal et al. demonstrated DOTA-PRIT with ^{177}Lu-DOTA-hapten targeting a wide variety of solid tumors (antigen targets: GD2 (*120*), glycoprotein A33 (*121*), HER2 (*122*)). More recently, that team developed a ^{225}Ac-DOTA-hapten for α-PRIT (*123*). When DOTA-PRIT was used to pretarget ^{177}Lu-DOTA-hapten in nude mice bearing human xenografts, TIs of 28–142 for blood, 7–23 for kidney, and 12–47 for liver were achieved, with estimated tumor-absorbed doses ranging from 1,476 to 8,473 cGy/37 MBq (*120,122,124*). Notably, the lowest TIs (blood, 28; kidney, 7; and liver, 12) and estimated tumor dose (1,476 cGy/37 MBq) were observed for the anti-HER2 DOTA-PRIT system, which is known to internalize (*122*). Green et al. also used C825 BsAb for pretargeting ^{90}Y-DOTA-hapten to a variety of hematologic cancer targets (e.g., CD20 (*104*), CD45 (*125*), and CD38 (*126*)), reporting TIs of 6.75–21.4 for blood, 15.9–24.9 for kidney, and 5.52–7.24 for liver, with estimated tumor-absorbed dose ranging from 3,981 to 7,781 cGy/37 MBq.

Santich et al. reported a novel BsAb platform designed as a fusion of a self-assembling-and-disassembling (SADA) domain to a tandem single-chain BsAb for highly efficient 2-step radiohapten pretargeting (Fig. 3B) (*127*). With anti-GD2 SADA-PRIT plus ^{177}Lu-DOTA-hapten in nude mice bearing human cancer xenografts, an exceptional balance of high tumor targeting and high TIs was achieved: TIs were 100 for blood, 25 for kidney, and 32 for liver, with estimated tumor-absorbed dose of 11,840 cGy/37 MBq. Also, safe and tumoricidal anti-GD2 SADA-PRIT plus ^{177}Lu-DOTA-hapten or ^{225}Ac-DOTA-hapten was established (*127*). Initial clinical trials of anti-GD2 SADA-PRIT plus ^{177}Lu-DOTA-hapten are planned for this year on patients with recurrent or refractory metastatic GD2-expressing solid tumors, including small-cell lung cancer, sarcoma, and malignant melanoma (NCT05130255).

In 2018–2019, the team of Hoffmann-La Roche, Inc., and Orano Med LLC described a novel BsAb antitumor/antichelate hapten pretargeting system (antigen targets: CD20, HER2, and CEA) based on an anti-1,4,7,10-tetrakis(carbamoylmethyl)-1,4,7,10-tetraazacyclododecane (DOTAM) antibody with femtomolar affinity for lead-DOTAM complexes (*128*). Specifically, for the anti-CEA/DOTAM BsAb PRIT-0213, they reported dissociation constants of 0.84 pM and 5.7 pM for lead-DOTAM and bismuth-DOTAM, respectively (*128*). In nude mice bearing human cancer xenografts, they reported dosimetry for 3-step pretargeting (i.e., with CA) of 0.74 MBq of ^{212}Pb-DOTAM. On the basis of relative biologic effectiveness equal to 5, they estimated an absorbed dose of 99.55 Gy to BxPC3 tumor and TIs of 28, 14, and 91 for blood, kidney, and liver, respectively (*128*). Also, they highlighted preclinical anti-CEA PRIT therapy results, detailing strong tumor growth inhibition and significantly prolonged survival with 3 cycles of 1.11 MBq (*129*).

Harnessing Affibody (Affibody AB) Molecules as PRIT Vectors

Although IgG-based mAbs and BsAb have traditionally been used as PRIT vectors, their prolonged circulation can make timing of complete clearance difficult, leading to unintended bystander toxicity. Advances in protein engineering have given rise to alternative protein constructs such as minibodies (80 kDa), diabodies (50 kDa), and engineered scaffold proteins (4–20 kDa) (*6*). These smaller constructs have proven to be especially favorable as radionuclide imaging vectors (*6*). Affibody molecules are a highly promising class of engineered scaffold proteins that can be optimized to have high affinity and slow internalization kinetics. The anti-HER2 Affibody radiolabeled with ^{111}In (^{111}In-ABY-025) has been investigated clinically for imaging of disseminated HER2-expressing breast cancer (*130*). However, as vectors for radioimmunotherapy, Affibody molecules have been shown to be suboptimal for residualizing radiometal labels, leading to significant renal uptake (*131*).

Between 2016 and 2021, numerous studies describing Affibody PRID and PRIT were reported (*132,133*). Figure 5 illustrates and contrasts the pretargeting systems: first is an approach using synthetic DNA-analog peptide nucleic acids (PNAs) originally described by Hnatowich et al. in 1997 for PRID with ^{99m}Tc (*35*), and further work applying a bioorthogonal approach using click chemistry (described in the following section). A PNA strand is covalently conjugated to a targeting vector, in this case, an Affibody, and the radionuclide payload is delivered on a complementary PNA strand, injected after an optimized pretargeting interval of 16 h (*132*). The hybridization of complementary PNAs as a pretargeting technique supplies several advantages, including high affinity (picomolar dissociation constant), low immunogenicity, and resistance to in vivo degradation (*132*). For the Affibody-PNA approach, they reported for PRIT with ^{177}Lu-PNA (^{177}Lu-HP2) in nude mice bearing human cancer xenografts an estimated absorbed dose of 3,996 cGy/37 MBq to tumor and TIs of 269, 5, and 81 for blood, kidney, and liver, respectively (*132*). These results were

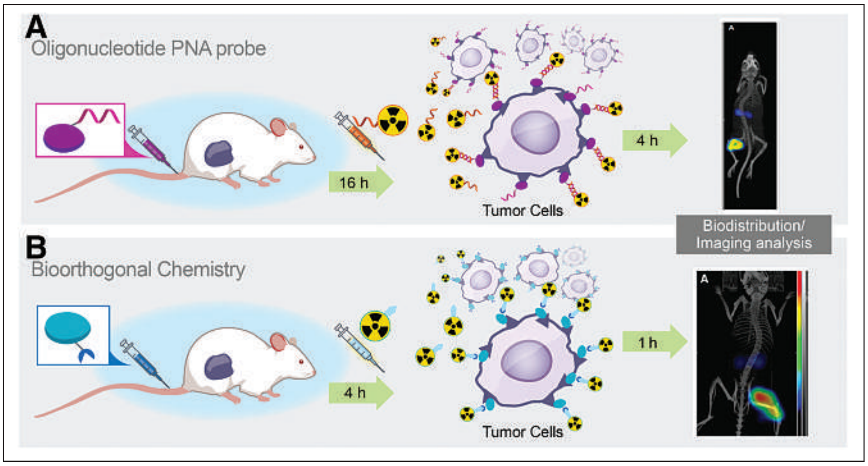

FIGURE 5. Affibody pretargeting with PNAs (A) or bioorthogonal inverse electron-demand Diels–Alder click chemistry (B). (Portions reprinted from (*133,155*).)

achieved using a 2-step approach, that is, without using CA. PRIT treatment efficacy was established using a fractionated PRIT approach (total administered ^{177}Lu-HP2, 96 MBq/mouse) in nude mice bearing subcutaneous SKOV-3 xenografts. Median survival was significantly prolonged in PRIT-treated mice in comparison to controls, and treatment was well tolerated, with no nephrotoxicity (*132*). Interestingly, they reported less efficient Affibody-PRIT using the bioorthogonal chemistry approach; although mouse dosimetry was not reported, the tumor-to-kidney AUC ratio was only 1.4 (*133*). However, this was a marked improvement from conventional Affibody-radioimmunotherapy, which results in a tumor-to-kidney AUC ratio of less than 1 and shows the promise of PRIT to substantially reduce radiometal accumulation in the kidneys with engineered scaffold proteins (*132*).

Bioorthogonal Pretargeting

Meares' elegant affinity capture pretargeting strategy, consisting of an antibody/ligand pair with complementary reactive groups that become covalently linked when they are near the antibody/ligand complex, was applied to antichelate mAb-based reporter gene imaging for noninvasive tracking of chimeric antigen receptor T cells by Krebs et al. (*134*). In contrast to affinity capture, with the very rapid kinetics of the bioorthogonal inverse electron-demand Diels–Alder click reaction ($k_2 > 10^3$ M^{-1}s^{-1}), probe attachment can occur by direct reaction with a chemically modified antibody (*135,136*). In 2010, initial in vivo PRID studies with the inverse electron-demand Diels–Alder reaction were reported (*137*). Soon after, many groups took an interest. Early development efforts included novel tetrazine-based radioprecursors for numerous radioisotopes, second-generation radiolabeled tetrazine molecules with improved pharmacokinetic and biodistribution properties, and incorporation of a chase step or CA (reviewed recently by Rondon and Degoul (*138*)).

Significant progress has also been made for PRIT using transcyclooctene-modified mAbs and radiolabeled tetrazine for inverse electron-demand Diels–Alder. In 2017, PRIT was demonstrated using ^{212}Pb-tetrazine in mice bearing TAG-72–expressing human CRC xenografts (*139*). Between 2017 and 2018, PRIT using ^{177}Lu-tetrazine (*140,141*) and ^{225}Ac-tetrazine (*142*), respectively, was demonstrated in multiple human tumor xenografts (CRC and pancreatic). For PRIT with ^{177}Lu-tetrazine in nude mice bearing human xenografts, TIs of blood (10.4–17.7), kidney (12.0–19.9), and liver (19.0–40.1) were achieved, with estimated tumor-absorbed doses ranging from 9,472 to 30,821 cGy/37 MBq (*140,143*). Moreover, PRIT with the highly promising ^{64}Cu/^{67}Cu pair was recently reported (*144*), with the authors nicely demonstrating efficient sequential radiolabeled tetrazine administration and safe and effective theranostic treatment. For PRIT with ^{67}Cu-tetrazine, the authors reported TIs of 6.5–9.7 for blood, 7.2–9.1 for kidney, and 4.0–4.2 for liver, with estimated tumor-absorbed doses ranging from 2,116 to 2,331 cGy/37 MBq depending on the pretargeting interval (*144*).

Recent efforts at bioorthogonal pretargeting development have focused on a combination of new chemistries (e.g., adamantane/cucurbituril (*145*)), new vectors (e.g., with nanoparticles (*146*); also, more details are provided in a recent review (*147*)), and continued optimization of radiolabeled tetrazine (*148*). Clinical bioorthogonal pretargeting chemotherapy trials are ongoing (NCT04106492), and bioorthogonal PRID trials are planned for the near future (*149*).

A ROAD MAP FOR DEVELOPMENT: RADIOBIOLOGIC GOALS OF PRIT

Our goal for PRIT should be to cure the tumor while safeguarding against excessive toxicity to normal tissues. To achieve this, we need better methods for dosimetry of internal radioemitters. We suggest that *Primer 2020,* the Medical Internal Radiation Dosimetry Committee publication soon to be released by the Society of Nuclear Medicine and Molecular Imaging, has provided us with the computational basis for tumor and normal-tissue dosimetry measurement to meet the goal of safe and efficacious targeted radiotherapy of advanced human tumors. Supplemental Figure 1 and the other supplemental information provide a more detailed rationale (supplemental materials are available at http://jnm.snmjournals.org).

As a starting point for radiation doses needed for curing while avoiding catastrophic damage to normal tissue, we propose the following. In a prior publication, we suggested quantitative radiobiologic targets to be met to achieve a high probability of cure for solid human tumors (*1*). The reasoning is that a sufficient radiation dose (cGy) must be absorbed by all cells in the tumor while minimizing the dose absorbed by normal tissues (i.e., the maximizing of TI). A series of reasonable benchmarks for effective treatment can be provided on the basis of laboratory and clinical experience, even though the response to radioimmunotherapy varies depending on several factors, including tumor size, target density, tumor structure (e.g., liquid or solid, tumor microenvironment), the type of radiation administered, the heterogeneity of targeting at the microscopic level, and the ability to repair radiation damage.

A curative watershed for PRIT of solid tumors is the set of benchmarks that achieves a cumulative total of 8,000–10,000 cGy of absorbed radiation dose to individual tumor lesions while at the same time minimizing the dose to radiosensitive tissues, such as bone marrow (<150 cGy; TI, 40–100), small intestine (<250 cGy; TI, 40–60), and kidney (<1,500 cGy; TI, 6–10) (*1*). Two critical parameters to control for are tumor size and target density, because these directly influence tumor dose and TIs. We have called this collective of PRIT achievable properties the sweet spot. As shown in Tables 1 and 2, various forms of PRIT have the chance to achieve the sweet-spot high tumor radiation dose and high TIs. Real-life examples from living systems support these ideas. These include the effectiveness of ^{131}I-NaI, a medium-energy β-emitter in certain thyroid cancers (*150*), and the cures achieved without histopathologic evidence of radiotoxicity in animal tumor models of human xenografts.

CONCLUSIONS AND OUTLOOK

PRIT is a form of targeted radiotherapy with internally administered radioemitters (radionuclide endotherapy, or unsealed radionuclides). As we have used the term here, an *antitumor vector* (e.g., Affibody, mAb, or nanoparticle) is the basis for tumor targeting and is modified to achieve desired properties of radionuclide capture during the targeting procedure. PRIT is a groundbreaking achievement because its components can be delivered in a time sequence that maximizes radiation to tumor while minimizing radiation to normal tissues. In this review, we have illustrated the current status of PRIT, with an emphasis on radiohapten capture (e.g., reversible binding using antihapten BsAb or biotin–streptavidin binding), bioorthogonal techniques (irreversible binding), and Affibody-PNA pretargeting that have shown high TIs in animal tumor models of human xenografts. In all 3 approaches, modified antitumor proteins provide the targeting specificity to tumor. As shown in Figure 1, other antitumor vectors and radionuclide forms for complementary radioligand capture, are proliferating.

During PRIT, the targeting vector and the radiohapten/carrier radiopharmacology are key parameters for high TI. Building on advances in protein engineering and mAb humanization, previous obstacles such as insufficient mAb/hapten affinity and immunogenicity can be overcome. Furthermore, we can more precisely balance the attributes of affinity, molecular size, and physicochemical properties of antibody-based carriers to improve tumor localization and penetration while limiting retention in normal tissues via rapid renal clearance. Also, with innovation in BsAb design, sufficient contrast and TI can be achieved without the aid of chase or CA, which would greatly simplify dosing to 2 steps and reagents.

Another exciting new frontier is high–linear-energy-transfer radiation, in which fewer quantitative guideposts for PRIT exist. There is an unmet need to define the dosimetry more completely, with α-emitters such as ^{225}Ac showing great promise (*151*). Work to estimate relative biologic effectiveness during PRIT with α-emitting radioisotopes is beginning (*152*).

In summary, pretargeting in nuclear medicine has achieved many milestones (Supplemental Table 1), including early-phase clinical testing (Supplemental Table 2). Pioneering clinical PRIT studies have demonstrated safety and that meaningful tumor doses can be achieved in select patients, but dosing is typically limited by insufficient TI, ADA, and the complexity of the approach. Still, clinical investigation of PRIT and radiotheranostics demonstrates increasing value for patient selection and treatment planning, permitting optimized reagent dosing during PRIT (Table 1). It is likely that individualized dosimetry will predict an optimized dose that will reduce the risk of underdosing tumors (leading to treatment failure) and overdosing normal tissues (leading to radiation toxicity).

REFERENCES

1. Larson SM, Carrasquillo JA, Cheung NK, Press OW. Radioimmunotherapy of human tumours. *Nat Rev Cancer.* 2015;15:347–360.
2. Wahl R. The success and failure of radioimmunotherapy for lymphoma [abstract]. *Endocrine Abstracts.* 2016;47:OC39.
3. Divgi C, Carrasquillo JA, Meredith R, et al. Overcoming barriers to radiopharmaceutical therapy (RPT): an overview from the NRG-NCI working group on dosimetry of radiopharmaceutical therapy. *Int J Radiat Oncol Biol Phys.* 2021;109:905–912.
4. Pouget JP, Constanzo J. Revisiting the radiobiology of targeted alpha therapy. *Front Med (Lausanne).* 2021;8:692436.
5. Kratochwil C, Bruchertseifer F, Giesel FL, et al. ^{225}Ac-PSMA-617 for PSMA-targeted alpha-radiation therapy of metastatic castration-resistant prostate cancer. *J Nucl Med.* 2016;57:1941–1944.
6. Tsai WK, Wu AM. Aligning physics and physiology: engineering antibodies for radionuclide delivery. *J Labelled Comp Radiopharm.* 2018;61:693–714.
7. Parakh S, Lee ST, Gan HK, Scott AM. Radiolabeled antibodies for cancer imaging and therapy. *Cancers (Basel).* 2022;14:1454.
8. Chomet M, van Dongen G, Vugts DJ. State of the art in radiolabeling of antibodies with common and uncommon radiometals for preclinical and clinical immuno-PET. *Bioconjug Chem.* 2021;32:1315–1330.
9. Moek KL, Giesen D, Kok IC, et al. Theranostics using antibodies and antibody-related therapeutics. *J Nucl Med.* 2017;58(suppl 2):83S–90S.
10. Sgouros G, Bodei L, McDevitt MR, Nedrow JR. Radiopharmaceutical therapy in cancer: clinical advances and challenges. *Nat Rev Drug Discov.* 2020;19:589–608.
11. Pressman D, Day ED, Blau M. The use of paired labeling in the determination of tumor-localizing antibodies. *Cancer Res.* 1957;17:845–850.
12. Bale WF, Spar IL, Goodland RL. Experimental radiation therapy of tumors with I-131-carrying antibodies to fibrin. *Cancer Res.* 1960;20:1488–1494.
13. Köhler G, Milstein C. Continuous cultures of fused cells secreting antibody of predefined specificity. *Nature.* 1975;256:495–497.
14. Goldenberg DM. Imaging and therapy of cancer with radiolabeled monoclonal antibodies. *Prog Clin Biol Res.* 1989;288:413–427.
15. Larson SM, Carrasquillo JA, Reynolds JC. Radioimmunodetection and radioimmunotherapy. *Cancer Invest.* 1984;2:363–381.
16. Kim EE, Deland FH, Casper S, Corgan RL, Primus FJ, Goldenberg DM. Radioimmunodetection of colorectal cancer. *Cancer.* 1980;45:1243–1247.
17. Reardan DT, Meares CF, Goodwin DA, et al. Antibodies against metal chelates. *Nature.* 1985;316:265–268.
18. Goodwin DA, Meares CF, McTigue M, David GS. Monoclonal antibody hapten radiopharmaceutical delivery. *Nucl Med Commun.* 1986;7:569–580.
19. Goodwin DA, Meares CF, McCall MJ, McTigue M, Chaovapong W. Pre-targeted immunoscintigraphy of murine tumors with indium-111-labeled bifunctional haptens. *J Nucl Med.* 1988;29:226–234.
20. Stickney DR, Anderson LD, Slater JB, et al. Bifunctional antibody: a binary radiopharmaceutical delivery system for imaging colorectal carcinoma. *Cancer Res.* 1991;51:6650–6655.
21. Hnatowich DJ, Virzi F, Rusckowski M. Investigations of avidin and biotin for imaging applications. *J Nucl Med.* 1987;28:1294–1302.
22. Pimm MV, Fells HF, Perkins AC, Baldwin RW. Iodine-131 and indium-111 labelled avidin and streptavidin for pre-targetted immunoscintigraphy with biotinylated anti-tumour monoclonal antibody. *Nucl Med Commun.* 1988;9:931–941.
23. Paganelli G, Riva P, Deleide G, et al. In vivo labelling of biotinylated monoclonal antibodies by radioactive avidin: a strategy to increase tumor radiolocalization. *Int J Cancer Suppl.* 1988;2:121–125.
24. Wilbur DS, Hamlin DK, Meyer DL, et al. Streptavidin in antibody pretargeting. 3. Comparison of biotin binding and tissue localization of 1,2-cyclohexanedione and succinic anhydride modified recombinant streptavidin. *Bioconjug Chem.* 2002;13:611–620.
25. Wilbur DS, Stayton PS, To R, et al. Streptavidin in antibody pretargeting: comparison of a recombinant streptavidin with two streptavidin mutant proteins and two commercially available streptavidin proteins. *Bioconjug Chem.* 1998;9:100–107.
26. Kalofonos HP, Rusckowski M, Siebecker DA, et al. Imaging of tumor in patients with indium-111-labeled biotin and streptavidin-conjugated antibodies: preliminary communication. *J Nucl Med.* 1990;31:1791–1796.
27. Paganelli G, Magnani P, Zito F, et al. Three-step monoclonal antibody tumor targeting in carcinoembryonic antigen-positive patients. *Cancer Res.* 1991;51:5960–5966.
28. Kraeber-Bodéré F, Rousseau C, Bodet-Milin C, et al. A pretargeting system for tumor PET imaging and radioimmunotherapy. *Front Pharmacol.* 2015;6:54.
29. Paganelli G, Chinol M, Grana C, et al. Therapy trials in cancer patients using an improved 3-step pretargeting approach. In: Bergmann H, Kroiss A, Sinzinger H, eds. *Radioactive Isotopes in Clinical Medicine and Research*: Springer; 1997: 513–517.
30. Papi S, Grana CG, Bartolomei M, et al. Pretargeted radioimmunotherapy in cancer: an overview. In: Hayat MA, ed. *Methods of Cancer Diagnosis, Therapy, and Prognosis: General Overviews, Head and Neck Cancer and Thyroid Cancer.* Springer; 2010:80–98.
31. Paganelli G, Grana C, Chinol M, et al. Antibody-guided three-step therapy for high grade glioma with yttrium-90 biotin. *Eur J Nucl Med.* 1999;26:348–357.

32. Goodwin DA, Meares CF, Osen M. Biological properties of biotin-chelate conjugates for pretargeted diagnosis and therapy with the avidin/biotin system. *J Nucl Med.* 1998;39:1813–1818.
33. Sharkey RM, Karacay H, Griffiths GL, et al. Development of a streptavidin-anti-carcinoembryonic antigen antibody, radiolabeled biotin pretargeting method for radioimmunotherapy of colorectal cancer: studies in a human colon cancer xenograft model. *Bioconjug Chem.* 1997;8:595–604.
34. Kuijpers WH, Bos ES, Kaspersen FM, Veeneman GH, van Boeckel CA. Specific recognition of antibody-oligonucleotide conjugates by radiolabeled antisense nucleotides: a novel approach for two-step radioimmunotherapy of cancer. *Bioconjug Chem.* 1993;4:94–102.
35. Rusckowski M, Qu T, Chang F, Hnatowich DJ. Pretargeting using peptide nucleic acid. *Cancer.* 1997;80:2699–2705.
36. Bos ES, Kuijpers WH, Meesters-Winters M, et al. In vitro evaluation of DNA-DNA hybridization as a two-step approach in radioimmunotherapy of cancer. *Cancer Res.* 1994;54:3479–3486.
37. Liu G. Use of morpholino oligomers for pretargeting. In: Moulton HM, Moulton JD, eds. *Morpholino Oligomers: Methods and Protocols.* Springer; 2017:161–179.
38. Axworthy D, Beaumier P, Bottino B, et al. Preclinical optimization of pretargeted radioimmunotherapy components: high efficiency, curative ^{90}Y delivery to mouse tumor xenografts. *Tumor Targeting.* 1996;2:156.
39. Axworthy DB, Reno JM, Hylarides MD, et al. Cure of human carcinoma xenografts by a single dose of pretargeted yttrium-90 with negligible toxicity. *Proc Natl Acad Sci USA.* 2000;97:1802–1807.
40. Murtha A, Weiden P, Knox S, et al. Phase I dose escalation trial of pretargeted radioimmunotherapy (PRIT) with ^{90}yttrium. *Proc Am Soc Clin Oncol* [abstract]. 1998;17:438.
41. Weiden PL, Breitz HB, Press O, et al. Pretargeted radioimmunotherapy (PRIT) for treatment of non-Hodgkin's lymphoma (NHL): initial phase I/II study results. *Cancer Biother Radiopharm.* 2000;15:15–29.
42. Breitz HB, Fisher DR, Goris ML, et al. Radiation absorbed dose estimation for ^{90}Y-DOTA-biotin with pretargeted NR-LU-10/streptavidin. *Cancer Biother Radiopharm.* 1999;14:381–395.
43. Knox SJ, Goris ML, Tempero M, et al. Phase II trial of yttrium-90-DOTA-biotin pretargeted by NR-LU-10 antibody/streptavidin in patients with metastatic colon cancer. *Clin Cancer Res.* 2000;6:406–414.
44. Lewis MR, Zhang J, Jia F, et al. Biological comparison of ^{149}Pm-, ^{166}Ho-, and ^{177}Lu-DOTA-biotin pretargeted by CC49 scFv-streptavidin fusion protein in xenograft-bearing nude mice. *Nucl Med Biol.* 2004;31:213–223.
45. Leichner PK, Akabani G, Colcher D, et al. Patient-specific dosimetry of indium-111- and yttrium-90-labeled monoclonal antibody CC49. *J Nucl Med.* 1997;38:512–516.
46. Shen S, Forero A, LoBuglio AF, et al. Patient-specific dosimetry of pretargeted radioimmunotherapy using CC49 fusion protein in patients with gastrointestinal malignancies. *J Nucl Med.* 2005;46:642–651.
47. Förster GJ, Santos EB, Smith-Jones PM, Zanzonico P, Larson SM. Pretargeted radioimmunotherapy with a single-chain antibody/streptavidin construct and radiolabeled DOTA-biotin: strategies for reduction of the renal dose. *J Nucl Med.* 2006;47:140–149.
48. Yao Z, Zhang M, Garmestani K, et al. Pretargeted alpha emitting radioimmunotherapy using ^{213}Bi 1,4,7,10-tetraazacyclododecane-*N,N′,N′′,N′′′*-tetraacetic acid-biotin. *Clin Cancer Res.* 2004;10:3137–3146.
49. Yao Z, Zhang M, Axworthy DB, et al. Radioimmunotherapy of A431 xenografted mice with pretargeted B3 antibody-streptavidin and ^{90}Y-labeled 1,4,7,10-tetraazacyclododecane-*N,N′,N′′,N′′′*-tetraacetic acid (DOTA)-biotin. *Cancer Res.* 2002; 62:5755–5760.
50. Sato N, Hassan R, Axworthy DB, et al. Pretargeted radioimmunotherapy of mesothelin-expressing cancer using a tetravalent single-chain Fv-streptavidin fusion protein. *J Nucl Med.* 2005;46:1201–1209.
51. Cheung NK, Modak S, Lin Y, et al. Single-chain Fv-streptavidin substantially improved therapeutic index in multistep targeting directed at disialoganglioside GD2. *J Nucl Med.* 2004;45:867–877.
52. Press OW, Appelbaum F, Martin P, et al. Phase II trial of ^{131}I-B1 (anti-CD20) antibody therapy with autologous stem cell transplantation for relapsed B cell lymphomas. *Lancet.* 1995;346:336–340.
53. Witzig TE, Gordon LI, Cabanillas F, et al. Randomized controlled trial of yttrium-90-labeled ibritumomab tiuxetan radioimmunotherapy versus rituximab immunotherapy for patients with relapsed or refractory low-grade, follicular, or transformed B-cell non-Hodgkin's lymphoma. *J Clin Oncol.* 2002;20:2453–2463.
54. Press OW, Corcoran M, Subbiah K, et al. A comparative evaluation of conventional and pretargeted radioimmunotherapy of CD20-expressing lymphoma xenografts. *Blood.* 2001;98:2535–2543.
55. Breitz HB, Weiden PL, Beaumier PL, et al. Clinical optimization of pretargeted radioimmunotherapy with antibody-streptavidin conjugate and ^{90}Y-DOTA-biotin. *J Nucl Med.* 2000;41:131–140.
56. Schultz J, Lin Y, Sanderson J, et al. A tetravalent single-chain antibody-streptavidin fusion protein for pretargeted lymphoma therapy. *Cancer Res.* 2000;60:6663–6669.
57. Forero A, Weiden PL, Vose JM, et al. Phase 1 trial of a novel anti-CD20 fusion protein in pretargeted radioimmunotherapy for B-cell non-Hodgkin lymphoma. *Blood.* 2004;104:227–236.
58. Zhang M, Zhang Z, Garmestani K, et al. Pretarget radiotherapy with an anti-CD25 antibody-streptavidin fusion protein was effective in therapy of leukemia/lymphoma xenografts. *Proc Natl Acad Sci USA.* 2003;100:1891–1895.
59. Pagel JM, Hedin N, Subbiah K, et al. Comparison of anti-CD20 and anti-CD45 antibodies for conventional and pretargeted radioimmunotherapy of B-cell lymphomas. *Blood.* 2003;101:2340–2348.
60. Pantelias A, Pagel JM, Hedin N, et al. Comparative biodistributions of pretargeted radioimmunoconjugates targeting CD20, CD22, and DR molecules on human B-cell lymphomas. *Blood.* 2007;109:4980–4987.
61. Le Doussal JM, Martin M, Gautherot E, Delaage M, Barbet J. In vitro and in vivo targeting of radiolabeled monovalent and divalent haptens with dual specificity monoclonal antibody conjugates: enhanced divalent hapten affinity for cell-bound antibody conjugate. *J Nucl Med.* 1989;30:1358–1366.
62. Goodwin DA, Meares CF, Watanabe N, et al. Pharmacokinetics of pretargeted monoclonal antibody 2D12.5 and ^{88}Y-Janus-2-(p-nitrobenzyl)-1,4,7,10-tetraazacyclododecanetetraacetic acid (DOTA) in BALB/c mice with KHJJ mouse adenocarcinoma: a model for ^{90}Y radioimmunotherapy. *Cancer Res.* 1994;54:5937–5946.
63. Le Doussal JM, Chetanneau A, Gruaz-Guyon A, et al. Bispecific monoclonal antibody-mediated targeting of an indium-111-labeled DTPA dimer to primary colorectal tumors: pharmacokinetics, biodistribution, scintigraphy and immune response. *J Nucl Med.* 1993;34:1662–1671.
64. Peltier P, Curtet C, Chatal JF, et al. Radioimmunodetection of medullary thyroid cancer using a bispecific anti-CEA/anti-indium-DTPA antibody and an indium-111-labeled DTPA dimer. *J Nucl Med.* 1993;34:1267–1273.
65. Barbet J, Peltier P, Bardet S, et al. Radioimmunodetection of medullary thyroid carcinoma using indium-111 bivalent hapten and anti-CEA × anti-DTPA-indium bispecific antibody. *J Nucl Med.* 1998;39:1172–1178.
66. Vuillez JP, Moro D, Brichon PY, et al. Two-step immunoscintigraphy for non-small-cell lung cancer staging using a bispecific anti-CEA/anti-indium-DTPA antibody and an indium-111-labeled DTPA dimer. *J Nucl Med.* 1997;38:507–511.
67. Bardiès M, Bardet S, Faivre-Chauvet A, et al. Bispecific antibody and iodine-131-labeled bivalent hapten dosimetry in patients with medullary thyroid or small-cell lung cancer. *J Nucl Med.* 1996;37:1853–1859.
68. Barbet J, Kraeber-Bodere F, Vuillez JP, Gautherot E, Rouvier E, Chatal JF. Pretargeting with the affinity enhancement system for radioimmunotherapy. *Cancer Biother Radiopharm.* 1999;14:153–166.
69. Karacay H, McBride W, Griffiths G, et al. Experimental pretargeting studies of cancer with a humanized anti-CEA× murine anti-[In-DTPA] bispecific antibody construct and a ^{99m}Tc-/^{188}Re-labeled peptide. *Bioconjug Chem.* 2000;11:842–854.
70. Kraeber-Bodéré F, Faivre-Chauvet A, Saï-Maurel C, et al. Bispecific antibody and bivalent hapten radioimmunotherapy in CEA-producing medullary thyroid cancer xenograft. *J Nucl Med.* 1999;40:198–204.
71. Kraeber-Bodéré F, Bardet S, Hoefnagel CA, et al. Radioimmunotherapy in medullary thyroid cancer using bispecific antibody and iodine 131-labeled bivalent hapten: preliminary results of a phase I/II clinical trial. *Clin Cancer Res.* 1999; 5(suppl):3190s–3198s.
72. Vuillez J-P, Kraeber-Bodéré F, Moro D, et al. Radioimmunotherapy of small cell lung carcinoma with the two-step method using a bispecific anti-carcinoembryonic antigen/anti-diethylenetriaminepentaacetic acid (DTPA) antibody and iodine-131 Di-DTPA hapten: results of a phase I/II trial. *Clin Cancer Res.* 1999;5(suppl):3259s–3267s.
73. Kraeber-Bodéré F, Faivre-Chauvet A, Ferrer L, et al. Pharmacokinetics and dosimetry studies for optimization of anti-carcinoembryonic antigen × anti-hapten bispecific antibody-mediated pretargeting of iodine-131-labeled hapten in a phase I radioimmunotherapy trial. *Clin Cancer Res.* 2003;9:3973S–3981S.
74. Kraeber-Bodéré F, Rousseau C, Bodet-Milin C, et al. Targeting, toxicity, and efficacy of 2-step, pretargeted radioimmunotherapy using a chimeric bispecific antibody and ^{131}I-labeled bivalent hapten in a phase I optimization clinical trial. *J Nucl Med.* 2006;47:247–255.
75. Chatal J-F, Campion L, Kraeber-Bodéré F, et al. Survival improvement in patients with medullary thyroid carcinoma who undergo pretargeted anti-carcinoembryonic-antigen radioimmunotherapy: a collaborative study with the French Endocrine Tumor Group. *J Clin Oncol.* 2006;24:1705–1711.
76. Boerman OC, Kranenborg MH, Oosterwijk E, et al. Pretargeting of renal cell carcinoma: improved tumor targeting with a bivalent chelate. *Cancer Res.* 1999;59: 4400–4405.
77. van Schaijk FG, Oosterwijk E, Molkenboer-Kuenen JD, et al. Pretargeting with bispecific anti-renal cell carcinoma x anti-DTPA(In) antibody in 3 RCC models. *J Nucl Med.* 2005;46:495–501.

78. van Schaijk FG, Broekema M, Oosterwijk E, et al. Residualizing iodine markedly improved tumor targeting using bispecific antibody-based pretargeting. *J Nucl Med.* 2005;46:1016–1022.
79. van Schaijk FG, Oosterwijk E, Soede AC, et al. Pretargeting of carcinoembryonic antigen–expressing tumors with a biologically produced bispecific anticarcinoembryonic antigen × anti-indium–labeled diethylenetriaminepentaacetic acid antibody. *Clin Cancer Res.* 2005;11:7130s–7136s.
80. Sharkey RM, Goldenberg DM. Advances in radioimmunotherapy in the age of molecular engineering and pretargeting. *Cancer Invest.* 2006;24:82–97.
81. Feng X, Pak R, Kroger L, et al. New anti-Cu-TETA and anti-Y-DOTA monoclonal antibodies for potential use in the pre-targeted delivery of radiopharmaceuticals to tumor. *Hybridoma.* 1998;17:125–132.
82. Janevik-Ivanovska E, Gautherot E, Hillairet de Boisferon M, et al. Bivalent hapten-bearing peptides designed for iodine-131 pretargeted radioimmunotherapy. *Bioconjug Chem.* 1997;8:526–533.
83. Karacay H, Sharkey R, McBride W, et al. Pretargeting for cancer radioimmunotherapy with bispecific antibodies: role of the bispecific antibody's valency for the tumor target antigen. *Bioconjug Chem.* 2002;13:1054–1070.
84. Sharkey RM, McBride WJ, Karacay H, et al. A universal pretargeting system for cancer detection and therapy using bispecific antibody. *Cancer Res.* 2003;63:354–363.
85. Sharkey RM, Cardillo TM, Rossi EA, et al. Signal amplification in molecular imaging by pretargeting a multivalent, bispecific antibody. *Nat Med.* 2005;11:1250–1255.
86. McBride WJ, Zanzonico P, Sharkey RM, et al. Bispecific antibody pretargeting PET (immunoPET) with an ^{124}I-labeled hapten-peptide. *J Nucl Med.* 2006;47:1678–1688.
87. Rossi EA, Sharkey RM, McBride W, et al. Development of new multivalent-bispecific agents for pretargeting tumor localization and therapy. *Clin Cancer Res.* 2003;9:3886S–3896S.
88. Chang C-H, Rossi EA, Goldenberg DM. The dock and lock method: a novel platform technology for building multivalent, multifunctional structures of defined composition with retained bioactivity. *Clin Cancer Res.* 2007;13:5586s–5591s.
89. Goldenberg DM, Rossi EA, Sharkey RM, McBride WJ, Chang CH. Multifunctional antibodies by the dock-and-lock method for improved cancer imaging and therapy by pretargeting. *J Nucl Med.* 2008;49:158–163.
90. Goldenberg DM, Chang CH, Rossi EA, McBride JW, Sharkey RM. Pretargeted molecular imaging and radioimmunotherapy. *Theranostics.* 2012;2:523–540.
91. Frampas E, Maurel C, Saëc R-L, et al. Pretargeted radioimmunotherapy of colorectal cancer metastases: models and pharmacokinetics predict influence of the physical and radiochemical properties of the radionuclide. *Eur J Nucl Med Mol Imaging.* 2011;38:2153–2164.
92. Karacay H, Sharkey RM, Gold DV, et al. Pretargeted radioimmunotherapy of pancreatic cancer xenografts: TF10–^{90}Y-IMP-288 alone and combined with gemcitabine. *J Nucl Med.* 2009;50:2008–2016.
93. Karacay H, Brard P-Y, Sharkey RM, et al. Therapeutic advantage of pretargeted radioimmunotherapy using a recombinant bispecific antibody in a human colon cancer xenograft. *Clin Cancer Res.* 2005;11:7879–7885.
94. Sharkey RM, Rossi EA, McBride WJ, Chang C-H, Goldenberg DM. Recombinant bispecific monoclonal antibodies prepared by the dock-and-lock strategy for pretargeted radioimmunotherapy. *Semin Nucl Med.* 2010;40:190–203.
95. Mawad R, Gooley T, Rajendran JG, et al. Pretargeted radioimmunotherapy using an anti-CD45 antibody-streptavidin conjugate and radiolabeled DOTA-biotin in patients with high-risk acute leukemia or myelodysplastic syndrome undergoing allogeneic hematopoietic cell transplantation [abstract]. *Biol Blood Marrow Transplant.* 2013;19(suppl):S123–S124.
96. Paganelli G, Ferrari M, Ravasi L, et al. Intraoperative avidination for radionuclide therapy: a prospective new development to accelerate radiotherapy in breast cancer. *Clin Cancer Res.* 2007;13:5646s–5651s.
97. Petronzelli F, Pelliccia A, Anastasi AM, et al. Therapeutic use of avidin is not hampered by antiavidin antibodies in humans. *Cancer Biother Radiopharm.* 2010;25:563–570.
98. De Santis R, Leoni B, Rosi A, et al. AvidinOX for highly efficient tissue-pretargeted radionuclide therapy. *Cancer Biother Radiopharm.* 2010;25:143–148.
99. Albertoni C, Leoni B, Rosi A, et al. Radionuclide therapy of unresectable tumors with AvidinOX and ^{90}Y-biotinDOTA: tongue cancer paradigm. *Cancer Biother Radiopharm.* 2015;30:291–298.
100. De Santis R, Leoni B, Rosi A, et al. AvidinOX for highly efficient tissue-pretargeted radionuclide therapy. *Cancer Biother Radiopharm.* 2010;25:143–148.
101. Vesci L, Carollo V, Rosi A, De Santis R. Therapeutic efficacy of intra-tumor AvidinOX and low systemic dose biotinylated cetuximab, with and without cisplatin, in an orthotopic model of head and neck cancer. *Oncol Lett.* 2019;17:3529–3536.
102. Frost SH, Bäck T, Chouin N, et al. Comparison of ^{211}At-PRIT and ^{211}At-RIT of ovarian microtumors in a nude mouse model. *Cancer Biother Radiopharm.* 2013;28:108–114.
103. Frost SH, Frayo SL, Miller BW, et al. Comparative efficacy of ^{177}Lu and ^{90}Y for anti-CD20 pretargeted radioimmunotherapy in murine lymphoma xenograft models. *PLoS One.* 2015;10:e0120561.
104. Green DJ, Frayo SL, Lin Y, et al. Comparative analysis of bispecific antibody and streptavidin-targeted radioimmunotherapy for B-cell cancers. *Cancer Res.* 2016;76:6669–6679.
105. Green DJ, Press OW. Whither radioimmunotherapy: to be or not to be? *Cancer Res.* 2017;77:2191–2196.
106. Lütje S, Rijpkema M, Goldenberg DM, et al. Pretargeted dual-modality immuno-SPECT and near-infrared fluorescence imaging for image-guided surgery of prostate cancer. *Cancer Res.* 2014;74:6216–6223.
107. Heskamp S, Hernandez R, Molkenboer-Kuenen JDM, et al. α- versus β-emitting radionuclides for pretargeted radioimmunotherapy of carcinoembryonic antigen-expressing human colon cancer xenografts. *J Nucl Med.* 2017;58:926–933.
108. Schoffelen R, Boerman OC, Goldenberg DM, et al. Development of an imaging-guided CEA-pretargeted radionuclide treatment of advanced colorectal cancer: first clinical results. *Br J Cancer.* 2013;109:934–942.
109. Schoffelen R, Woliner-van der Weg W, Visser EP, et al. Predictive patient-specific dosimetry and individualized dosing of pretargeted radioimmunotherapy in patients with advanced colorectal cancer. *Eur J Nucl Med Mol Imaging.* 2014;41:1593–1602.
110. Woliner-van der Weg W, Schoffelen R, Hobbs RF, et al. Tumor and red bone marrow dosimetry: comparison of methods for prospective treatment planning in pretargeted radioimmunotherapy. *EJNMMI Phys.* 2015;2:5.
111. Bodet-Milin C, Ferrer L, Rauscher A, et al. Pharmacokinetics and dosimetry studies for optimization of pretargeted radioimmunotherapy in CEA-expressing advanced lung cancer patients. *Front Med (Lausanne).* 2015;2:84.
112. Bodet-Milin C, Faivre-Chauvet A, Carlier T, et al. Immuno-PET using anticarcinoembryonic antigen bispecific antibody and ^{68}Ga-labeled peptide in metastatic medullary thyroid carcinoma: clinical optimization of the pretargeting parameters in a first-in-human trial. *J Nucl Med.* 2016;57:1505–1511.
113. Touchefeu Y, Bailly C, Frampas E, et al. Promising clinical performance of pretargeted immuno-PET with anti-CEA bispecific antibody and gallium-68-labelled IMP-288 peptide for imaging colorectal cancer metastases: a pilot study. *Eur J Nucl Med Mol Imaging.* 2021;48:874–882.
114. Rousseau C, Goldenberg DM, Colombie M, et al. initial clinical results of a novel immuno-PET theranostic probe in human epidermal growth factor receptor 2-negative breast cancer. *J Nucl Med.* 2020;61:1205–1211.
115. Bodet-Milin C, Faivre-Chauvet A, Carlier T, et al. Anti-CEA pretargeted immuno-PET shows higher sensitivity than DOPA PET/CT in detecting relapsing metastatic medullary thyroid carcinoma: post hoc analysis of the iPET-MTC study. *J Nucl Med.* 2021;62:1221–1227.
116. Orcutt KD, Slusarczyk AL, Cieslewicz M, et al. Engineering an antibody with picomolar affinity to DOTA chelates of multiple radionuclides for pretargeted radioimmunotherapy and imaging. *Nucl Med Biol.* 2011;38:223–233.
117. Orcutt KD, Ackerman ME, Cieslewicz M, et al. A modular IgG-scFv bispecific antibody topology. *Protein Eng Des Sel.* 2010;23:221–228.
118. Orcutt KD, Nasr KA, Whitehead DG, Frangioni JV, Wittrup KD. Biodistribution and clearance of small molecule hapten chelates for pretargeted radioimmunotherapy. *Mol Imaging Biol.* 2011;13:215–221.
119. Orcutt KD, Rhoden JJ, Ruiz-Yi B, Frangioni JV, Wittrup KD. Effect of small-molecule-binding affinity on tumor uptake in vivo: a systematic study using a pretargeted bispecific antibody. *Mol Cancer Ther.* 2012;11:1365–1372.
120. Cheal SM, Xu H, Guo HF, Zanzonico PB, Larson SM, Cheung NK. Preclinical evaluation of multistep targeting of diasialoganglioside GD2 using an IgG-scFv bispecific antibody with high affinity for GD2 and DOTA metal complex. *Mol Cancer Ther.* 2014;13:1803–1812.
121. Cheal SM, Xu H, Guo HF, et al. Theranostic pretargeted radioimmunotherapy of colorectal cancer xenografts in mice using picomolar affinity ^{86}Y- or ^{177}Lu-DOTA-Bn binding scFv C825/GPA33 IgG bispecific immunoconjugates. *Eur J Nucl Med Mol Imaging.* 2016;43:925–937.
122. Cheal SM, Xu H, Guo HF, et al. Theranostic pretargeted radioimmunotherapy of internalizing solid tumor antigens in human tumor xenografts in mice: curative treatment of HER2-positive breast carcinoma. *Theranostics.* 2018;8:5106–5125.
123. Cheal SM, McDevitt MR, Santich BH, et al. Alpha radioimmunotherapy using ^{225}Ac-proteus-DOTA for solid tumors: safety at curative doses. *Theranostics.* 2020;10:11359–11375.
124. Cheal SM, Patel M, Yang G, et al. An *N*-acetylgalactosamino dendron-clearing agent for high-therapeutic-index DOTA-hapten pretargeted radioimmunotherapy. *Bioconjug Chem.* 2020;31:501–506.
125. Orozco JJ, Kenoyer AL, Lin Y, et al. Therapy of myeloid leukemia using novel bispecific fusion proteins targeting CD45 and ^{90}Y-DOTA. *Mol Cancer Ther.* 2020;19:2575–2584.

126. Green DJ, O'Steen S, Lin Y, et al. CD38-bispecific antibody pretargeted radioimmunotherapy for multiple myeloma and other B-cell malignancies. *Blood.* 2018; 131:611–620.
127. Santich BH, Cheal SM, Ahmed M, et al. A self-assembling and disassembling (SADA) bispecific antibody (BsAb) platform for curative two-step pretargeted radioimmunotherapy. *Clin Cancer Res.* 2021;27:532–541.
128. Torgue J, Jurek P, Rojas-Quijano F, et al., inventors; Hoffmann-La Roche Inc., Orano Med SAS, assignees. Antibodies for chelated radionuclides and clearing agents. World Intellectual Property Organization patent WO2019202399A8. December 12, 2019.
129. Frost S, Pichard A, Haas A, et al. Preclinical evaluation of CEA-PRIT, a novel pretargeted alpha therapy regimen for treatment of CEA-positive tumours with Pb-212 [abstract]. *Eur J Nucl Med Mol Imaging.* 2019;46(suppl):S56–S57.
130. Sörensen J, Sandberg D, Sandstrom M, et al. First-in-human molecular imaging of HER2 expression in breast cancer metastases using the ^{111}In-ABY-025 affibody molecule. *J Nucl Med.* 2014;55:730–735.
131. Tolmachev V, Orlova A, Pehrson R, et al. Radionuclide therapy of HER2-positive microxenografts using a ^{177}Lu-labeled HER2-specific Affibody molecule. *Cancer Res.* 2007;67:2773–2782.
132. Westerlund K, Altai M, Mitran B, et al. Radionuclide therapy of HER2-expressing human xenografts using affibody-based peptide nucleic acid-mediated pretargeting: in vivo proof of principle. *J Nucl Med.* 2018;59:1092–1098.
133. Altai M, Perols A, Tsourma M, et al. Feasibility of affibody-based bioorthogonal chemistry-mediated radionuclide pretargeting. *J Nucl Med.* 2016;57:431–436.
134. Krebs S, Ahad A, Carter LM, et al. Antibody with infinite affinity for in vivo tracking of genetically engineered lymphocytes. *J Nucl Med.* 2018;59:1894–1900.
135. Day JJ, Marquez BV, Beck HE, Aweda TA, Gawande PD, Meares CF. Chemically modified antibodies as diagnostic imaging agents. *Curr Opin Chem Biol.* 2010;14:803–809.
136. Scinto SL, Bilodeau DA, Hincapie R, et al. Bioorthogonal chemistry. *Nat Rev Methods Primers.* 2021;1:30.
137. Rossin R, Verkerk PR, van den Bosch SM, et al. In vivo chemistry for pretargeted tumor imaging in live mice. *Angew Chem Int Ed Engl.* 2010;49:3375–3378.
138. Rondon A, Degoul F. Antibody pretargeting based on bioorthogonal click chemistry for cancer imaging and targeted radionuclide therapy. *Bioconjug Chem.* 2020; 31:159–173.
139. Shah MA, Zhang X, Rossin R, et al. Metal-free cycloaddition chemistry driven pretargeted radioimmunotherapy using alpha-particle radiation. *Bioconjug Chem.* 2017;28:3007–3015.
140. Houghton JL, Membreno R, Abdel-Atti D, et al. Establishment of the in vivo efficacy of pretargeted radioimmunotherapy utilizing inverse electron demand Diels-Alder click chemistry. *Mol Cancer Ther.* 2017;16:124–133.
141. Membreno R, Cook BE, Fung K, Lewis JS, Zeglis BM. Click-mediated pretargeted radioimmunotherapy of colorectal carcinoma. *Mol Pharm.* 2018;15: 1729–1734.
142. Poty S, Carter LM, Mandleywala K, et al. Leveraging bioorthogonal click chemistry to improve ^{225}Ac-radioimmunotherapy of pancreatic ductal adenocarcinoma. *Clin Cancer Res.* 2019;25:868–880.
143. Membreno R, Keinänen OM, Cook BE, et al. Toward the optimization of click-mediated pretargeted radioimmunotherapy. *Mol Pharm.* 2019;16:2259–2263.
144. Keinänen O, Fung K, Brennan JM, et al. Harnessing ^{64}Cu/^{67}Cu for a theranostic approach to pretargeted radioimmunotherapy. *Proc Natl Acad Sci USA.* 2020; 117:28316–28327.
145. Strebl MG, Yang J, Isaacs L, Hooker JM. Adamantane/cucurbituril: a potential pretargeted imaging strategy in immuno-PET. *Mol Imaging.* 2018;17:1536012118799838.
146. Au KM, Tripathy A, Lin CP, et al. Bespoke pretargeted nanoradioimmunotherapy for the treatment of non-Hodgkin lymphoma. *ACS Nano.* 2018;12:1544–1563.
147. Huang Z, Hu Y, Yang Y, Huang W, Wang Y, Ye D. Recent advances in pretargeted imaging of tumors in vivo. *Analysis Sensing.* April 21, 2022 [Epub ahead of print].
148. Stéen EJL, Jørgensen JT, Denk C, et al. Lipophilicity and click reactivity determine the performance of bioorthogonal tetrazine tools in pretargeted in vivo chemistry. *ACS Pharmacol Transl Sci.* 2021;4:824–833.
149. Jallinoja VIJ, Houghton JL. Current landscape in clinical pretargeted radioimmunoimaging and therapy. *J Nucl Med.* 2021;62:1200–1206.
150. Maxon HR, Thomas SR, Samaratunga RC. Dosimetric considerations in the radioiodine treatment of macrometastases and micrometastases from differentiated thyroid cancer. *Thyroid.* 1997;7:183–187.
151. Kratochwil C, Haberkorn U, Giesel FL. ^{225}Ac-PSMA-617 for therapy of prostate cancer. *Semin Nucl Med.* 2020;50:133–140.
152. Poty S, Mandleywala K, O'Neill E, Knight JC, Cornelissen B, Lewis JS. ^{89}Zr-PET imaging of DNA double-strand breaks for the early monitoring of response following α- and β-particle radioimmunotherapy in a mouse model of pancreatic ductal adenocarcinoma. *Theranostics.* 2020;10:5802–5814.
153. Robillard MS, Rossin R. In-vivo chemistry for pretargeted tumor imaging and therapy in mice. *Medicamundi.* 2010;54:55–62.
154. Sharkey RM, Karacay H, Litwin S, et al. Improved therapeutic results by pretargeted radioimmunotherapy of non-Hodgkin's lymphoma with a new recombinant, trivalent, anti-CD20, bispecific antibody. *Cancer Res.* 2008;68:5282–5290.
155. Tano H, Oroujeni M, Vorobyeva A, et al. Comparative evaluation of novel ^{177}Lu-labeled PNA probes for affibody-mediated PNA-based pretargeting. *Cancers (Basel).* 2021;13:500.
156. Altai M, Strand J, Rosik D, et al. Influence of nuclides and chelators on imaging using affibody molecules: comparative evaluation of recombinant affibody molecules site-specifically labeled with ^{68}Ga and ^{111}In via maleimido derivatives of DOTA and NODAGA. *Bioconjug Chem.* 2013;24:1102–1109.
157. Hosono M, Hosono MN, Kraeber-Bodéré F, Devys A. Biodistribution and dosimetric study in medullary thyroid cancer xenograft using bispecific antibody and iodine-125-labeled bivalent hapten. *J Nucl Med.* 1998;39:1608–1613.
158. Feijtel D, Doeswijk GN, Verkaik NS, et al. Inter and intra-tumor somatostatin receptor 2 heterogeneity influences peptide receptor radionuclide therapy response. *Theranostics.* 2021;11:491–505.

FOCUS ON MOLECULAR IMAGING

Antibody Engineering for Nuclear Imaging and Radioimmunotherapy

Cindy Rodriguez[1–3], Samantha Delaney[1,3,4], Samantha M. Sarrett[1,3,4], Outi M. Keinänen[1,3,5], and Brian M. Zeglis[1–4,6]

[1]Department of Chemistry, Hunter College, City University of New York, New York, New York; [2]Ph.D. Program in Chemistry, Graduate Center of City University of New York, New York, New York; [3]Department of Radiology, Memorial Sloan Kettering Cancer Center, New York, New York; [4]Ph.D. Program in Biochemistry, Graduate Center of City University of New York, New York, New York; [5]Department of Chemistry, University of Helsinki, Helsinki, Finland; and [6]Department of Radiology, Weill Cornell Medical College, New York, New York

Radiolabeled antibodies have become indispensable tools in nuclear medicine. However, the natural roles of antibodies within the immune system mean that they have several intrinsic limitations as a platform for radiopharmaceuticals. In recent years, the field has increasingly turned to antibody engineering to circumvent these issues while retaining the manifold benefits of the immunoglobulin framework. In this "Focus on Molecular Imaging" review, we cover recent advances in the application of antibody engineering to immunoPET, immunoSPECT, and radioimmunotherapy. Specifically, we address how antibody engineering has been used to improve radioimmunoconjugates on four fronts: optimizing pharmacokinetics, facilitating site-specific bioconjugation, modulating Fc interactions, and creating bispecific constructs.

Key Words: PET; radioimmunotherapy; antibody; antibody fragment; antibody engineering; Fc receptor

J Nucl Med 2022; 63:1316–1322
DOI: 10.2967/jnumed.122.263861

Since the pioneering work of Pressman and Korngold over half a century ago, the field of nuclear medicine has been captivated by the promise of monoclonal antibodies (mAbs) as tools for the delivery of radionuclides to tumors (*1,2*). Decades of advancements in this area have culminated in an array of promising clinical results in radioimmunotherapy with ^{131}I-, ^{225}Ac-, and ^{177}Lu-labeled radioimmunoconjugates as well as immunoPET with an ever-expanding array of ^{89}Zr-labeled mAbs (Fig. 1). Yet even a cursory look at the immunoPET, immunoSPECT, and radioimmunotherapy literature reveals a common thread: the development of effective radioimmunoconjugates often requires addressing the intrinsic limitations of antibodies themselves (*3*). Nature, after all, did not design immunoglobulins as simple vehicles for the delivery of cargoes to target cells. Rather, antibodies evolved as multifunctional components of complex immune systems. Turning to nature for a radiopharmaceutical vector is thus a double-edged sword. On the one hand, radiolabeled antibodies offer exquisite specificity and affinity for cancer antigens, tremendous *in vivo* stability, and high levels of tumoral accretion. On the other hand, they are difficult to synthesize in a well-defined and homogeneous manner, can have problematically long biological residence times, and can produce elevated uptake in healthy tissues.

The innate advantages of antibodies as radiopharmaceutical vectors have fueled a great deal of research dedicated to circumventing their limitations and optimizing their performance as diagnostics, theranostics, and therapeutics. This work has generally followed three different veins. In one approach—*in vivo* pretargeting—the antibody is decoupled from the radioactivity, the former is injected days before the latter, and the two components combine at the target site via a highly selective ligation (*4*). This strategy alleviates the dosimetric challenges associated with traditional radioimmunoconjugates but inevitably introduces significant scientific and logistical complexity. Others have sought to create radiopharmaceuticals based on antibody mimetics, synthetic biomolecules such as Affibody molecules and designed ankyrin repeat proteins that are inspired by the structure and function of immunoglobulins (*5,6*). These constructs frequently offer improved pharmacokinetic profiles compared to radiolabeled antibodies but lose other benefits associated with IgG-based scaffolds, including bivalency, high tumoral uptake, and *in vivo* stability.

In this installment of the "Focus on Molecular Imaging" series, we will discuss the third approach: antibody engineering. In the broadest sense, antibody engineering is predicated on using molecular biology to make modifications—large or small—to the immunoglobulin framework to improve the performance of antibodies or immunoconjugates. The best-known medical application of antibody engineering is easily the humanization of antibodies, and the wide array of methods used for antibody engineering have been skillfully reviewed elsewhere (*7,8*). In the specific context of nuclear medicine, antibody engineering offers an opportunity to optimize the performance of radioimmunoconjugates without the inherent complexity of pretargeting or the attendant sacrifices of antibody mimetics. These efforts generally seek to achieve one of four objectives: shortening the pharmacokinetic profile of full-length antibodies, facilitating site-specific bioconjugation, modulating Fc interactions, or creating constructs capable of binding multiple targets.

OPTIMIZING PHARMACOKINETICS

The neonatal Fc receptor (FcRn)–mediated recycling and size of full-length IgG gives traditional radioimmunoconjugates elongated, multiday serum half-lives. This pharmacokinetic behavior often manifests in high uptake in tumor lesions. However, it can also produce elevated activity concentrations in the blood and other healthy tissues, a phenomenon that can lower image contrast

---

Received Apr. 15, 2022; revision accepted Jul. 7, 2022.

For correspondence or reprints, contact Brian M. Zeglis (bz102@hunter.cuny.edu).

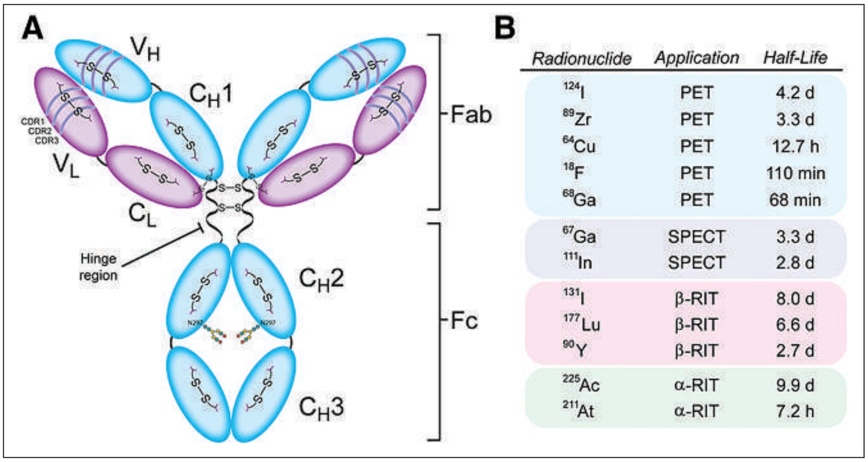

Radionuclide	Application	Half-Life
^{124}I	PET	4.2 d
^{89}Zr	PET	3.3 d
^{64}Cu	PET	12.7 h
^{18}F	PET	110 min
^{68}Ga	PET	68 min
^{67}Ga	SPECT	3.3 d
^{111}In	SPECT	2.8 d
^{131}I	β-RIT	8.0 d
^{177}Lu	β-RIT	6.6 d
^{90}Y	β-RIT	2.7 d
^{225}Ac	α-RIT	9.9 d
^{211}At	α-RIT	7.2 h

FIGURE 1. Anatomy of IgG_1 antibody (A) and radionuclides discussed in this review (B). RIT = radioimmunotherapy.

and reduce therapeutic indices (*3*). Antibody fragments offer an alternative platform with more rapid pharmacokinetic profiles, as they retain the binding properties of full-length mAbs but come in a smaller package. A variety of fragments have been harnessed for nuclear imaging and therapy, including F(ab′)$_2$ fragments (∼110 kDa), (scFv)$_2$-Fc fragments (∼100 kDa), minibodies (∼75 kDa), diabodies (∼60 kDa), F(ab) fragments (∼50 kDa), single-chain variable fragments (scFv, ∼27 kDa), and single-domain antibodies (sdAb, ∼15 kDa; also known as VHH and Nanobodies [Ablynx]) (Fig. 2A). The more rapid pharmacokinetic profiles of antibody fragments provide an opportunity to replace the long-lived radionuclides typically used with full-length IgG (i.e., ^{89}Zr, ^{131}I, ^{225}Ac, and ^{177}Lu) with isotopes bearing shorter physical half-lives (e.g., ^{64}Cu, ^{18}F, ^{68}Ga, and ^{211}At), a switch that only enhances the dosimetric and logistical benefits of fragments. The improved pharmacokinetic profiles of fragments often come with a price, however. Fragment-based radioimmunoconjugates generally produce lower uptake in tumor tissue than their full-length analogs, and some fragments accumulate at very high levels in the kidneys during renal elimination.

Several promising preclinical imaging and therapy studies featuring antibody fragments have emerged in the last half-decade. In 2018, for example, Seo *et al.* reported the use of a ^{64}Cu-labeled anti-CD8 cys-diabody—dubbed 169cDb—to image CD8-positive T-cell density in FVB, BALB/c, and C57BL/6 mice (*9*). The tracer proved capable of delineating and quantifying CD8-positive T-cell populations in lymphoid organs, suggesting that a similar approach to imaging could be used in the clinic to quantify T-cell density and monitor

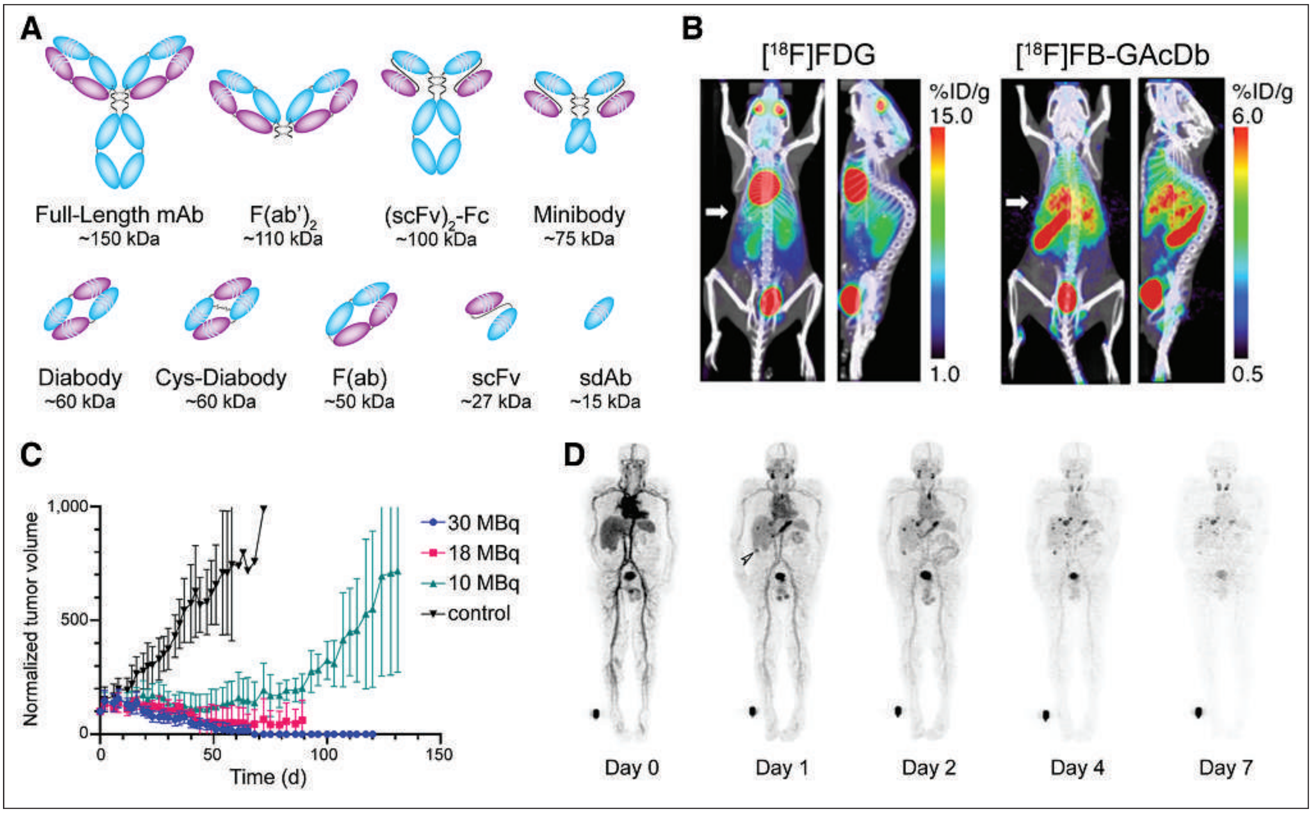

FIGURE 2. (A) Commonly used antibody fragments. (B) Uptake of cys-diabody—[^{18}F]FB-GAcDb—in liver metastases in a transgenic murine model of B-cell lymphoma. (Reprinted with permission of (*10*).) (C) Normalized tumor volumes observed after the treatment of mice bearing HER2-positive breast cancer xenografts with iso-[^{131}I]SGMIB-VHH_1028. (Reprinted from (*12*).) (D) Whole-body PET images of a patient injected with TAG-72–targeted pegylated diabody, [^{124}I]I-PEG-AVP0458. (Reprinted from (*17*).) %ID/g = percent injected dose per gram.

the response of patients to immunotherapy. A year later, a team at UCLA described the development of a CD20-targeting cys-diabody for the same-day immunoPET of B-cell lymphoma. The authors used transgenic mice that expressed human CD20 on mature B cells to demonstrate the ability of an ^{18}F-labeled diabody, [^{18}F]FB-GAcDb, to detect both endogenous compartments expressing human CD20 and B-cell lymphoma liver metastases (Fig. 2B) (*10*). Shifting to radioimmunotherapy, Pruszynski *et al.* evaluated the biodistribution of a ^{225}Ac-labeled human epidermal growth factor receptor 2 (HER2)–targeting sdAb in murine models of HER2-positive ovarian cancer and HER2-negative triple-negative breast cancer. The radioimmunoconjugate produced 15-fold higher uptake in HER2-positive than in HER2-negative tumors at 48 h after injection, as well as producing promising HER2-positive tumor–to–healthy-tissue activity concentration ratios at the same time point ($>$100 for blood; $>$40 for muscle; $>$8 for bone), suggesting that sdAbs may be suitable vectors for targeted radionuclide therapy with α-emitting isotopes (*11*). In a separate study, Feng *et al.* used a HER2-targted sdAb bearing a residualizing ^{131}I-labeled prosthetic group for radioimmunotherapy in murine models of HER2-positive breast and ovarian cancer. In mice bearing BT474 xenografts, the radioimmunoconjugate—iso-[^{131}I]SGMIB-VHH_1028—yielded a tumor-to-kidney therapeutic index of more than 8.5 and produced nearly complete tumor growth inhibition after doses of 18 and 30 MBq (Fig. 2C) (*12*). The same team recently reported preliminary data demonstrating the efficacy of HER2-targeted radioimmunotherapy with a sdAb bearing a similar residualizing prosthetic group labeled with the α-emitting radiohalogen ^{211}At (*13*).

Even more exciting than these preclinical results are a handful of recent clinical trials. In 2016, Pandit-Taskar *et al.* reported the first-in-human application of [^{89}Zr]Zr-IAB2M—a ^{89}Zr-labeled minibody engineered from the prostate-specific membrane antigen (PSMA)–targeting mAb J591—for the imaging of patients with metastatic prostate cancer (*14*). This initial study verified that the radioimmunoconjugate was safe, exhibited a favorable pharmacokinetic profile, and provided good lesion visualization 48 h after injection. Subsequent trials have explored the utility of [^{89}Zr]Zr-IAB2M in PSMA-positive localized prostate cancer and have revealed that the radioimmunoconjugate exhibits performance comparable to that of [^{68}Ga]Ga-PSMA-11 (*15*). Yet another minibody-based probe—the CD8-targeting [^{89}Zr]Zr-IAB22M2C—was recently translated to the clinic for the imaging of CD8-positive T-cells. A first-in-human study in 2020 demonstrated that [^{89}Zr]Zr-IAB22M2C was safe, well tolerated, and successfully targeted CD8-positive T-cell–rich regions such as the lymph nodes and the spleen (*16*). Finally, in 2020, Scott *et al.* reported on the use of a ^{124}I-labeled diabody that had been pegylated to reduce first-pass renal clearance and thus increase circulation time ([^{124}I]I-PEG-AVP0458) for PET in patients with ovarian cancer, metastatic prostate cancer, or primary prostate cancer (*17*). Whole-body PET scans acquired as early as 1 d after injection clearly demonstrate the promise of the radiotracer as a tool for delineating TAG-72–expressing cancers (Fig. 2D).

SITE-SPECIFIC BIOCONJUGATION

An abiding paradox in the study and use of radioimmunoconjugates is that these tools that are supposed to enable precision medicine are themselves synthesized in a surprisingly imprecise way. The overwhelming majority of radioimmunoconjugates are created via the stochastic ligation of amine-reactive prosthetic groups—most often chelators but occasionally radiohalogenated moieties—to lysines within the mAb. This approach, though facile, produces heterogeneous constructs and can interfere with the ability of the mAb to bind its antigen. A wide range of site-specific and site-selective approaches to bioconjugation have been developed to circumvent these issues, and the data consistently show that site-specifically modified radioimmunoconjugates exhibit better *in vivo* performance than randomly synthesized analogs (*18*). Precision is especially critical in the synthesis of fragment-based radioimmunoconjugates, as their smaller size increases the odds that cargoes will inadvertently be attached within their antigen-binding domains. The most frequently used approach to site-specific bioconjugation relies on ligations between thiol-reactive probes (e.g., maleimides) and cysteines generated via the reduction of the antibody's interchain disulfide linkages. This strategy is an improvement over traditional methods, but the maleimide–thiol reaction is reversible under physiologic conditions, and the formation of 4–8 free cysteine residues in full-length IgG (depending on the reduction conditions) means that some heterogeneity remains inevitable. Not surprisingly, the field has increasingly turned to antibody engineering for more robust and reliable approaches to site-specific bioconjugation.

The incorporation of amino acids—either natural or unnatural—at unique sites within the antibody for bioconjugation has proven a promising strategy, particularly in the context of fragment-based probes. For example, Chigoho *et al.* used an hPD-L1–targeting sdAb with a C-terminal cysteine residue and a maleimide-bearing variant of NOTA to create [^{68}Ga]Ga-NOTA-mal-hPD-L1, a radiotracer that displayed promising *in vivo* performance (*19*). Sharma *et al.* followed a slightly different approach to create a [^{89}Zr]Zr-desferrioxamine (DFO)-labeled probe for the visualization of delta-like ligand 3 expression. In this case, the authors did not incorporate new cysteines into the mAb. Rather, the heavy-chain cysteines within the upper hinge region that would normally form disulfide linkages were mutated to serine residues, leaving a pair of free cysteines on the light chains that the team specifically modified with phenyloxadiazolyl methylsulfone–bearing chelators (Fig. 3A) (*20*). Genetic code expansion to incorporate unnatural amino acids with orthogonally reactive moieties offers a more sophisticated variation on this theme with unrivaled site specificity. In 2020, Ahn *et al.* leveraged this technology to create a variant of trastuzumab containing a quartet of *p*-azido-methyl-phenylalanine residues in the Fc region. The authors used the strain-promoted azide-alkyne cycloaddition reaction to couple dibenzocyclooctyne-bearing variants of DFO and DO3A to the mAb and subsequently labeled the site-specifically modified immunoconjugates with ^{89}Zr and ^{111}In, respectively (Fig. 3B) (*21*).

Antibody engineering has also been used to build peptide recognition sites into immunoglobulins for chemoenzymatic modifications. In 2021, for example, Rudd *et al.* used the transpeptidase sortase A to catalyze the attachment of glycine-bearing chelators to an epidermal growth factor receptor–targeting Fab bearing a C-terminal LPETG recognition sequence, ultimately creating both ^{64}Cu- and ^{89}Zr-labeled radioimmunoconjugates that displayed excellent *in vivo* performance in a murine model of epidermal growth factor receptor–positive epidermoid carcinoma (Figs. 3C and 3D) (*22*). Bridoux *et al.* used a similar approach to append a variant of NOTA with a GGGYK tag to an hPD-L1–targeting sdAb bearing a C-terminal LPETG recognition element. Critically, the authors demonstrated that the site-specifically modified radioimmunoconjugate—[^{68}Ga]Ga-NOTA-(hPD-L1)—outperformed a randomly labeled analog *in vivo* (*23*). The Fc region of full-length IgG has also attracted interest for engineering-driven bioconjugation. To wit, Jeger *et al.* developed a variant of the L1CAM-targeted mAb chCE7 with a N297Q mutation that

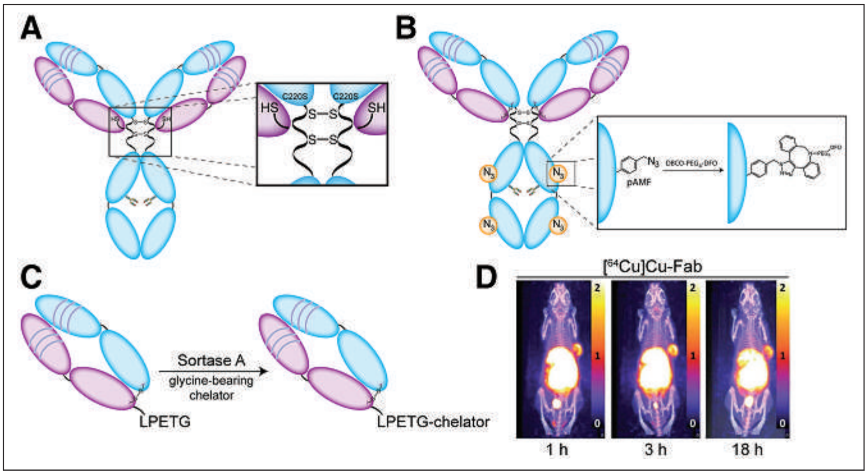

FIGURE 3. (A–C) Schematics illustrating the creation of free cysteine residues via a pair of C220S mutations (A), the site-specific modification of unnatural pAMF via strain-promoted azide-alkyne cycloaddition reaction (B), and the sortase-mediated bioconjugation of glycine-bearing chelator to Fab fragment bearing C-terminal LPETG tag (C). (D) Serial PET images of mice bearing A431 xenografts obtained after the administration of an EGFR-targeting Fab that has been site-specifically labeled with ^{64}Cu. (Reprinted with permission of (*22*).)

eliminated glycosylation and allowed for the transglutaminase-mediated attachment of DFO at the Q297 and Q295 sites of each heavy chain (*24*). The resulting radioimmunoconjugate—[^{67}Ga]Ga-DFO$_4$-chCE7agl—displayed markedly better *in vivo* behavior than an analogous randomly conjugated variant.

MODULATING FC INTERACTIONS

The interactions between the Fc domains of immunoglobulins and Fc receptors are instrumental in determining the *in vivo* behavior of mAbs. Although FcRn is responsible for the recycling of immunoglobulins, a variety of Fcγ receptors—including receptors I, II, IIIA, and IIIB—mediate the interplay between antibodies, immunocomplexes, and the immune system. In light of this, it is not surprising that the field has turned to the engineering of the Fc region as a route to improved radioimmunoconjugates.

Several laboratories have sought to improve the behavior of mAb-based radioimmunoconjugates by attenuating or enhancing Fc receptor binding. Nazarova *et al.* explored immunoSPECT imaging using a HER2-targeting ^{111}In-labeled mAb bearing a pair of histidine mutations—H310A and H435Q—that abrogated FcRn binding (*25*). The double mutant displayed a more rapid pharmacokinetic profile and greater tumor-to-blood activity concentration ratios than its wild-type parent but at the cost of reduced tumoral uptake and lower tumor-to-spleen and tumor-to-liver contrast (Fig. 4A). Burvenich *et al.* made similar observations with ^{111}In- and ^{177}Lu-labeled anti-Lewis-Y mAbs with two mutations (I253A and H310A) that reduce FcRn binding (*26*). The critical role of the heavy-chain glycans in modulating the Fcγ receptor engagement of mAb has led others to pursue glycoengineered radioimmunoconjugates. In 2019, Vivier *et al.* demonstrated that the enzymatic deglycosylation of [^{89}Zr]Zr-DFO-trastuzumab attenuates FcγRI binding and reduces uptake in healthy tissues in tumor-bearing NSG and huNSG mice compared with a fully glycosylated analog (*27*). More recently, Sharma *et al.* demonstrated the power of this approach using two glycoengineered variants of the L1CAM-targeting radioimmunoconjugate [^{89}Zr]Zr-DFO-HuE71 (Fig. 4B) (*28*). An afucosylated variant with enhanced FcγRIIIA binding exhibited reduced tumoral uptake and enhanced accretion in the liver and lymphoid tissues compared with the parent radioimmunoconjugate. In contrast, an aglycosylated variant with abrogated Fcγ receptor binding yielded dramatically reduced accretion in the bone and lymph nodes compared to parent [^{89}Zr]Zr-DFO-HuE71. Finally, Bensch *et al.* recently reported a clinical trial focused on immunoPET with [^{89}Zr]Zr-lumretuzumab, a HER3-targeting mAb glycoengineered to exhibit enhanced FcγRIIIA engagement and thus antibody-dependent cellular cytotoxicity (*29*).

The differing Fc interactions of the four subclasses of IgG—IgG$_1$, IgG$_2$, IgG$_3$, and IgG$_4$—have also been leveraged to create better radioimmunoconjugates (Fig. 4C). In 2020, Bicak *et al.* created an IgG$_3$-based radioimmunoconjugate of the hexokinase 2–targeting mAb hu11B6 for the ^{225}Ac-radioimmunotherapy of prostate cancer (*30*). The investigators hypothesized that the enhanced complement activation and Fcγ receptor engagement of the IgG$_3$ scaffold would lead to “immunotherapeutically enhanced” radioimmunotherapy, but in practice neither [^{225}Ac]Ac-hu11B6-IgG$_3$ nor an analog bearing a R435H mutation to rescue FcRn binding produced improved therapeutic efficacy over [^{225}Ac]Ac-hu11B6-IgG$_1$. In the study from Sharma *et al.* mentioned above, the authors also explored ^{89}Zr-immunoPET with two L1CAM-targeting IgG$_4$-based radioimmunoconjugates, as this subclass has attracted attention in the immunotherapeutics community because it elicits reduced effector functions relative to other subclasses (Fig. 4D) (*28*). Although a radioimmunoconjugate based on the wild-type IgG$_4$ framework produced high levels of nonspecific uptake in the kidneys, this behavior was eliminated in a variant with S228P mutations in the hinge region that facilitated the formation of IgG$_1$-like interchain disulfides and thus mitigated *in vivo* Fab arm exchange. Finally, Man *et al.* moved beyond the IgG isotype, using immunoSPECT to study the *in vivo* behavior of an IgE-based anti-CSPG4 antibody designed to elicit a more potent immune response (*31*). In the absence of FcRn-mediated recycling, the [^{111}In]In-IgE was cleared from the blood of tumor-bearing mice much more rapidly than its [^{111}In]In-IgG counterpart. Furthermore, the [^{111}In]In-IgE produced low activity concentrations in tumor tissue alongside high accretion in the liver, but its very low uptake in the blood yielded tumor-to-blood activity concentration ratios comparable to the analogous IgG.

Radioimmunoconjugates based on fusion proteins that combine antigen-binding fragments and Fc domains lie at the intersection of two threads of our discussion. These single-chain constructs offer many characteristics of full-length mAbs—that is, large size, multivalency, and control over FcRn engagement—in a package that is easier to produce given that there is no need for the coexpression of both heavy and light chains. In 2014, Rochefort *et al.* developed an effective CA19-9–targeting ^{124}I-labeled (scFv)$_2$-Fc that included an H310A mutation that abrogated FcRn binding (*32*). More recently, Delage *et al.* described a ^{177}Lu-labeled anti-TEM-1 (scFv)$_2$-Fc that produced moderate uptake in TEM-1–positive xenografts, but the authors made no mention of Fc engagement or mutations (*33*).

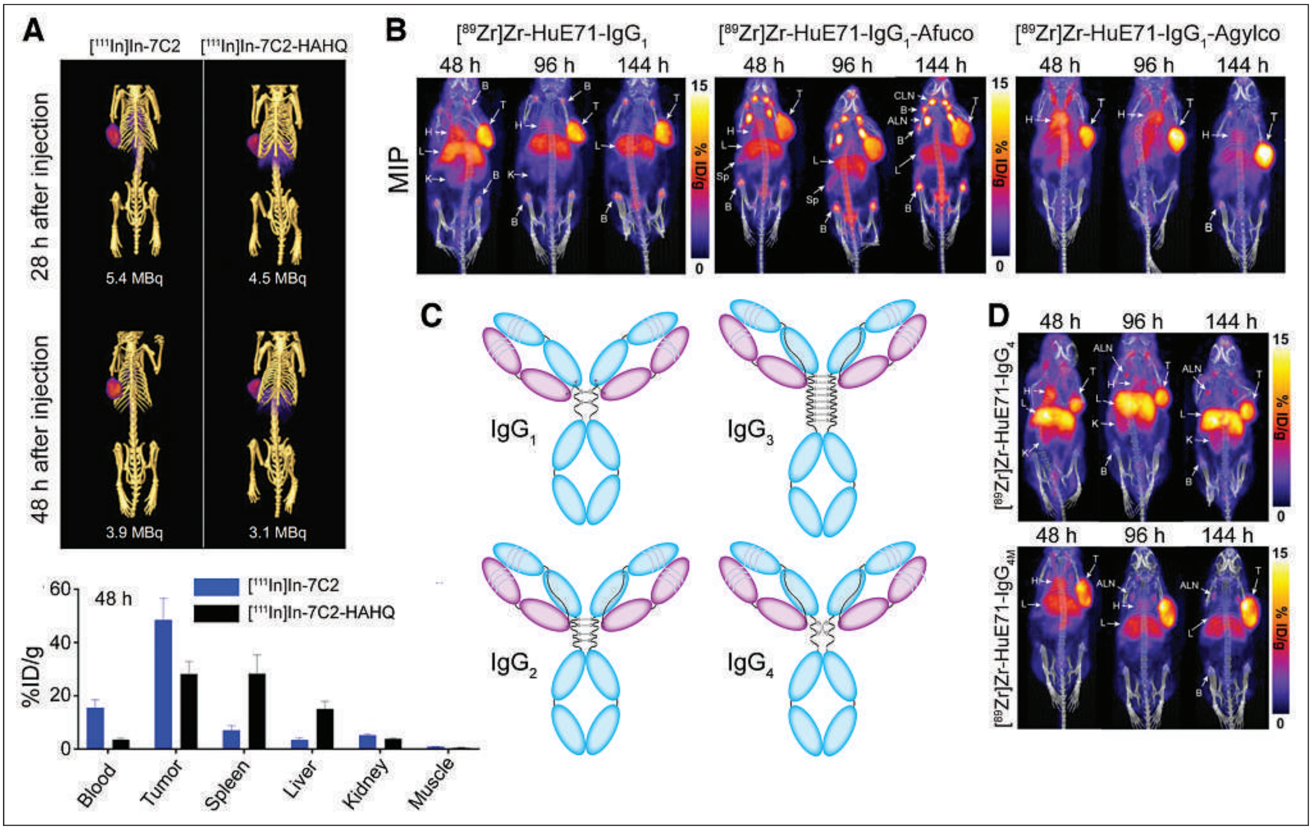

FIGURE 4. (A) SPECT images (top) and biodistribution data (bottom) collected 28 and 48 h after the administration of a HER2-targeting radioimmunoconjugate ([^{111}In]In-7C2) or a mutant with abrogated FcRn binding ([^{111}In]In-7C2-HAHQ) to mice bearing KPL-4 xenografts. (Reprinted with permission of (*25*).) (B) Serial PET images obtained using wild-type, afucosylated, and aglycosylated [^{89}Zr]Zr-IgG$_1$ in mice bearing L1CAM-expressing SKOV3 xenografts. (Reprinted with permission of (*28*).) (C) Four subclasses of IgG. (D) Serial PET images obtained using wild-type IgG$_4$-based [^{89}Zr]Zr-mAb ([^{89}Zr]Zr-HuE71-IgG$_4$) and an analog mutated to have IgG$_1$-like interchain disulfide linkages ([^{89}Zr]Zr-HuE71-IgG$_{4M}$). (Reprinted from (*28*).)

BINDING MULTIPLE TARGETS

Antibody engineering has also been harnessed to create radioimmunoconjugates based on bispecific antibodies (BsAbs), immunoglobulins designed to target more than one antigen. BsAbs offer several advantages over their monospecific cousins, as the ability to bind a second antigen can be harnessed to elicit synergistic antitumor effects, circumvent drug resistance, recruit immune cells, or block protumor signaling pathways. Generally speaking, full-length BsAbs consist of a heavy-chain/light-chain pair from one mAb and a second from another mAb (Fig. 5A). However, a wide variety of bi- and trispecific constructs have been developed using fragment-based frameworks.

BsAbs, like mAbs, have increasingly been used as companion imaging agents for therapeutic counterparts. Along these lines, a clinical trial focused on immunoPET with a ^{89}Zr-labeled T-cell–engaging BsAb capable of binding CD3 and carcinoembryonic antigen in patients with gastrointestinal adenocarcinoma (*34*). The CD3/carcinoembryonic antigen–targeting BsAb accumulated in both lymphoid organs and tumor lesions, thus providing data on the heterogeneity of antigen expression that could aid in the selection of patients likely to respond to therapy and in planning personalized drug dosing schedules. In 2019, Crawford *et al.* evaluated the *in vivo* behavior of another T-cell–engaging BsAb that targets CD3 and mucin 16 in a murine model of ovarian cancer and found the highest activity concentrations in the tumor tissue and lymphoid organs (*35*). A blocking study elegantly illustrated the role of the probe's dual specificity in this behavior: blocking with a CD3-specific mAb selectively reduced uptake in the lymphoid tissues, whereas blocking with a mucin 16–specific mAb did the same for the tumor (Fig. 5B).

The field has also turned to BsAbs to create radioimmunoconjugates capable of crossing the blood–brain barrier. The size and polarity of mAbs generally precludes their transport across the blood–brain barrier, thus curtailing the use of radiolabeled antibodies for neuroimaging and therapy. However, the incorporation of a transferrin-binding Fab fragment in a BsAb has been shown to facilitate the transferrin receptor–mediated transcytosis of the bispecific construct across the blood–brain barrier. In 2017, Syvänen *et al.* used this technique to create a ^{124}I-labeled tribody for the visualization of amyloid-β protofibrils—protein aggregates implicated in Alzheimer disease—in the brain (*36*).

A third application of BsAbs in nuclear medicine lies in pretargeted imaging and therapy (*4,37*). In this context, the BsAb is designed to bind both a cancer antigen and an exogeneous radiolabeled hapten. The unlabeled BsAb is administered first and allowed to accumulate at the tumor and clear from the blood. Once the BsAb has reached this optimal biodistribution, the radiolabeled hapten is administered, and the high affinity and selectivity of the BsAb for the hapten facilitates the *in vivo* ligation between the two components. This strategy enables the use of short-lived radionuclides that are not normally compatible with mAb-based vectors and reduces radiation dose rates to healthy tissues. Two

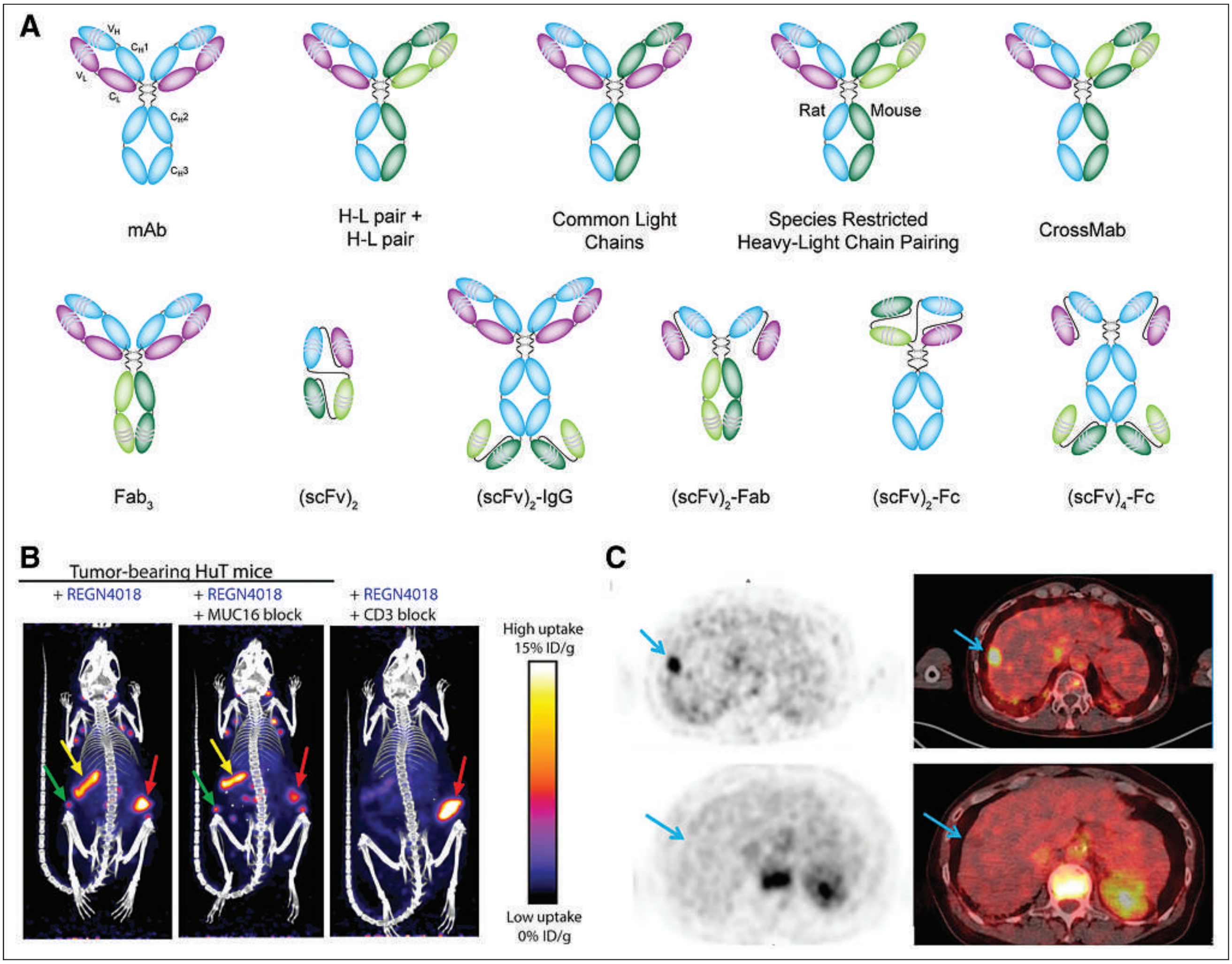

FIGURE 5. (A) Examples of BsAb. (B) ImmunoPET images obtained from mice bearing HuT tumors 6 d after the administration of bispecific [^{89}Zr]Zr-REGN4018 (left), [^{89}Zr]Zr-REGN4018 plus unlabeled mucin 16-binding mAb (middle), and [^{89}Zr]Zr-REGN4018 plus unlabeled CD3-binding mAb (right). Spleen is indicated by yellow arrow; lymph nodes by green arrow; and tumor by red arrow. (Reprinted with permission of (*35*).) (C) Pretargeted immunoPET with TF2 and [^{68}Ga]Ga-IMP288 in a patient with HER2-negative breast cancer produces high uptake in liver lesion (arrow, top) which was not seen by [^{18}F]FDG PET (bottom). (Reprinted from (*39*).)

recent clinical studies have explored the use of pretargeted PET with a carcinoembryonic antigen–targeted BsAb (TF2) and a ^{68}Ga-labeled peptidic hapten ([^{68}Ga]Ga-IMP288) in patients with breast cancer and colon cancer and have found that this approach not only was safe but also provided better sensitivity and specificity than [^{18}F]FDG (Fig. 5C) (*38,39*). Importantly, a second approach to *in vivo* pretargeting predicated on BsAbs capable of binding tumor biomarkers as well as DOTA-based haptens has also shown promise for both imaging and radioimmunotherapy in murine models of disease (*40*).

CONCLUSION

The next few years will undoubtedly be critical for work at the intersection of nuclear medicine and antibody engineering. It is undeniably easy to get excited about the preclinical data produced by many of these innovations, including sdAb-based radioimmunotherapeutics, new approaches to site-specific bioconjugation, and novel strategies for pretargeted imaging and therapy. Yet the key step for many of these technologies will be the move from the laboratory to the clinic. This is, admittedly, easier said than done, but their impact on patient care will ultimately hinge on clinical outcomes, so generating clinical data as soon as possible is imperative. There is more to do in the laboratory, too. For example, the preliminary work on the interplay between radioimmunoconjugates and Fc receptors is intriguing, but it behooves the field to explore these relationships in murine models that better recapitulate the human immune system. Finally, we hope to see even more bridges built between the nuclear medicine community and those studying immunotherapy and antibody–drug conjugates, as the cross-pollination of ideas between these fields can only lead to improved technologies for the clinic.

DISCLOSURE

Support was received from the NIH (R01CA240963, U01CA221046, R01CA204167, R21EB030275, and R01CA244327 to Brian Zeglis) and the Academy of Finland (331659 to Outi Keinänen). No potential conflict of interest relevant to this article was reported.

REFERENCES

1. Pressman D. Radiolabeled antibodies. *Ann N Y Acad Sci.* 1957;69:644–650.
2. Miller DG, Korngold L. Monoclonal immunoglobulins in cancer. *Med Clin North Am.* 1966;50:667–674.
3. Vivier D, Sharma SK, Zeglis BM. Understanding the in vivo fate of radioimmunoconjugates for nuclear imaging. *J Labelled Compd Radiopharm.* 2018;61:672–692.
4. Altai M, Membreno R, Cook B, Tolmachev V, Zeglis BM. Pretargeted imaging and therapy. *J Nucl Med.* 2017;58:1553–1559.
5. Tolmachev V, Orlova A. Affibody molecules as targeting vectors for PET imaging. *Cancers (Basel).* 2020;12:651.
6. Rasool M, Malik A, Hussain M, et al. DARPins bioengineering and its theranostic approaches: emerging trends in protein engineering. *Curr Pharm Des.* 2017;23:1610–1615.
7. Ministro J, Manuel AM, Goncalves J. Therapeutic antibody engineering and selection strategies. *Adv Biochem Eng Biotechnol.* 2020;171:55–86.
8. Waldmann H. Human monoclonal antibodies: the benefits of humanization. *Methods Mol Biol.* 2019;1904:1–10.
9. Seo JW, Tavare R, Mahakian LM, et al. CD8(+) T-cell density imaging with ^{64}Cu-labeled cys-diabody informs immunotherapy protocols. *Clin Cancer Res.* 2018;24:4976–4987.
10. Zettlitz KA, Tavare R, Tsai WK, et al. ^{18}F-labeled anti-human CD20 cys-diabody for same-day immunoPET in a model of aggressive B cell lymphoma in human CD20 transgenic mice. *Eur J Nucl Med Mol Imaging.* 2019;46:489–500.
11. Pruszynski M, D'Huyvetter M, Bruchertseifer F, Morgenstern A, Lahoutte T. Evaluation of an anti-HER2 nanobody labeled with ^{225}Ac for targeted alpha-particle therapy of cancer. *Mol Pharm.* 2018;15:1457–1466.
12. Feng Y, Meshaw R, McDougald D, et al. Evaluation of an ^{131}I-labeled HER2-specific single domain antibody fragment for the radiopharmaceutical therapy of HER2-expressing cancers. *Sci Rep.* 2022;12:3020.
13. Feng Y, Jannetti SA, Meshaw R, Vaidyanathan G, Zalutsky MR. Therapeutic efficacy of single-dose iso-[^{211}At]SAGMB-anti-HER2 sdAb in mice with subcutaneous HER2-expressing breast carcinoma xenografts [abstract]. *J Nucl Med.* 2021; 62(suppl 1):1484.
14. Pandit-Taskar N, O'Donoghue JA, Ruan S, et al. First-in-human imaging with ^{89}Zr-Df-IAB2M anti-PSMA minibody in patients with metastatic prostate cancer: pharmacokinetics, biodistribution, dosimetry, and lesion uptake. *J Nucl Med.* 2016; 57:1858–1864.
15. Vlachostergios PJ, Niaz MJ, Thomas C, et al. Pilot study of the diagnostic utility of ^{89}Zr-df-IAB2M and ^{68}Ga-PSMA-11 PET imaging and multiparametric MRI in localized prostate cancer. *Prostate.* 2022;82:483–492.
16. Pandit-Taskar N, Postow MA, Hellmann MD, et al. First-in-humans imaging with ^{89}Zr-Df-IAB22M2C anti-CD8 minibody in patients with solid malignancies: preliminary pharmacokinetics, biodistribution, and lesion targeting. *J Nucl Med.* 2020; 61:512–519.
17. Scott AM, Akhurst T, Lee FT, et al. First clinical study of a pegylated diabody ^{124}I-labeled PEG-AVP0458 in patients with tumor-associated glycoprotein 72 positive cancers. *Theranostics.* 2020;10:11404–11415.
18. Adumeau P, Sharma SK, Brent C, Zeglis BM. Site-specifically labeled immunoconjugates for molecular imaging—part 2: peptide tags and unnatural amino acids. *Mol Imaging Biol.* 2016;18:153–165.
19. Chigoho DM, Lecocq Q, Awad RM, et al. Site-specific radiolabeling of a human PD-L1 nanobody via maleimide-cysteine chemistry. *Pharmaceuticals (Basel).* 2021;14:550.
20. Sharma SK, Pourat J, Abdel-Atti D, et al. Noninvasive interrogation of DLL3 expression in metastatic small cell lung cancer. *Cancer Res.* 2017;77:3931–3941.
21. Ahn SH, Vaughn BA, Solis WA, Lupher ML Jr, Hallam TJ, Boros E. Site-specific ^{89}Zr- and ^{111}In-radiolabeling and in vivo evaluation of glycan-free antibodies by azide-alkyne cycloaddition with a non-natural amino acid. *Bioconjug Chem.* 2020; 31:1177–1187.
22. Rudd SE, Van Zuylekom JK, Raicevic A, et al. Enzyme mediated incorporation of zirconium-89 or copper-64 into a fragment antibody for same day imaging of epidermal growth factor receptor. *Chem Sci.* 2021;12:9004–9016.
23. Bridoux J, Broos K, Lecocq Q, et al. Anti-human PD-L1 nanobody for immuno-PET imaging: validation of a conjugation strategy for clinical translation. *Biomolecules.* 2020;10:1388.
24. Jeger S, Zimmermann K, Blanc A, et al. Site-specific and stoichiometric modification of antibodies by bacterial transglutaminase. *Angew Chem Int Ed Engl.* 2010; 49:9995–9997.
25. Nazarova L, Rafidi H, Mandikian D, et al. Effect of modulating FcRn binding on direct and pretargeted tumor uptake of full-length antibodies. *Mol Cancer Ther.* 2020;19:1052–1058.
26. Burvenich IJ, Lee FT, O'Keefe GJ, et al. Engineering anti-Lewis-Y hu3S193 antibodies with improved therapeutic ratio for radioimmunotherapy of epithelial cancers. *EJNMMI Res.* 2016;6:26.
27. Vivier D, Sharma SK, Adumeau P, Rodriguez C, Fung K, Zeglis BM. The impact of FcγRI binding on immuno-PET. *J Nucl Med.* 2019;60:1174–1182.
28. Sharma SK, Suzuki M, Xu H, et al. Influence of Fc modifications and IgG subclass on biodistribution of humanized antibodies targeting L1CAM. *J Nucl Med.* 2022; 63:629–636.
29. Bensch F, Lamberts LE, Smeenk MM, et al. ^{89}Zr-lumretuzumab PET imaging before and during HER3 antibody lumretuzumab treatment in patients with solid tumors. *Clin Cancer Res.* 2017;23:6128–6137.
30. Bicak M, Lückerath K, Kalidindi T, et al. Genetic signature of prostate cancer mouse models resistant to optimized hK2 targeted α-particle therapy. *Proc Natl Acad Sci USA.* 2020;117:15172–15181.
31. Man F, Koers A, Karagiannis P, et al. In vivo trafficking of a tumor-targeting IgE antibody: molecular imaging demonstrates rapid hepatobiliary clearance compared to IgG counterpart. *OncoImmunology.* 2021;10:1966970.
32. Rochefort MM, Girgis MD, Knowles SM, et al. A mutated anti-CA19-9 scFv-Fc for positron emission tomography of human pancreatic cancer xenografts. *Mol Imaging Biol.* 2014;16:721–729.
33. Delage JA, Faivre-Chauvet A, Fierle JK, et al. ^{177}Lu radiolabeling and preclinical theranostic study of 1C1m-Fc: an anti-TEM-1 scFv-Fc fusion protein in soft tissue sarcoma. *EJNMMI Res.* 2020;10:98.
34. Moek KL, Waaijer SJH, Kok IC, et al. ^{89}Zr-labeled bispecific T-cell engager AMG 211 PET shows AMG 211 accumulation in CD3-rich tissues and clear, heterogeneous tumor uptake. *Clin Cancer Res.* 2019;25:3517–3527.
35. Crawford A, Haber L, Kelly MP, et al. A mucin 16 bispecific T cell-engaging antibody for the treatment of ovarian cancer. *Sci Transl Med.* 2019;11:eaau7534.
36. Syvänen S, Fang XT, Hultqvist G, Meier SR, Lannfelt L, Sehlin D. A bispecific tribody PET radioligand for visualization of amyloid-beta protofibrils: a new concept for neuroimaging. *Neuroimage.* 2017;148:55–63.
37. Jallinoja VIJ, Houghton JL. Current landscape in clinical pretargeted radioimmunoimaging and therapy. *J Nucl Med.* 2021;62:1200–1206.
38. Touchefeu Y, Bailly C, Frampas E, et al. Promising clinical performance of pretargeted immuno-PET with anti-CEA bispecific antibody and gallium-68-labelled IMP-288 peptide for imaging colorectal cancer metastases: a pilot study. *Eur J Nucl Med Mol Imaging.* 2021;48:874–882.
39. Rousseau C, Goldenberg DM, Colombié M, et al. Initial clinical results of a novel immuno-PET theranostic probe in human epidermal growth factor receptor 2-negative breast cancer. *J Nucl Med.* 2020;61:1205–1211.
40. Chandler CS, Bell MM, Chung SK, et al. Intraperitoneal pretargeted radioimmunotherapy for colorectal peritoneal carcinomatosis. *Mol Cancer Ther.* 2022;21: 125–137.

Radionuclide Evaluation of Brain Death in the Post-McMath Era: Epilogue and Enigmata

Lionel S. Zuckier

Division of Nuclear Medicine, Department of Radiology, Montefiore Medical Center and the Albert Einstein College of Medicine, Bronx, New York

On occasion, a patient's medical odyssey emerges from obscurity into the public domain. Jahi McMath was an unfortunate 13-y-old girl who suffered a cardiac arrest after surgery and was subsequently declared dead by neurologic criteria (hereafter referred to as brain death [BD]). Her family successfully petitioned the courts to prevent interruption of supportive care. She was maintained on a ventilator for 4.5 y until experiencing cardiopulmonary arrest in June 2018.

Because the profound and protracted legal arguments surrounding Jahi's medical course resulted in extensive media coverage, many clinical details were disclosed in the public domain, which served as a nidus for editorials and reviews in the medical literature. An article on radionuclide evaluation of BD appeared in this journal in 2016, reviewing the initial course of Jahi McMath's illness and discussing the role of scintigraphy in the determination of BD (*1*). Jahi's entire medical records were released, including images from a radionuclide BD examination (*2*). This editorial updates the prior report by providing additional clinical history, radionuclide images and their analysis, and a discussion of controversy and questions engendered by this tragic case. Clinical information presented here is in the public domain, either in previously published literature or with permission granted by Jahi's mother.

CHRONOLOGY

In 2013, Jahi McMath presented with symptoms of obstructive sleep apnea and underwent surgery to resect offending tonsillar tissues (chronology in Supplemental Table 1; supplemental materials are available at http://jnm.snmjournals.org). In the postoperative period, she bled into her airway, suffered a cardiac arrest, was resuscitated, and then was placed on a ventilator. On postoperative day 3, hospital physicians determined that she met the clinical criteria for BD (*3*); however, the family insisted that supportive therapy be maintained. Electroencephalogram studies at that time were isoelectric. On day 14, a ^{99m}Tc-bicisate study was performed, which supported the diagnosis of BD, and a court-appointed pediatric neurologist meticulously repeated the clinical determination of BD, independently confirming the diagnosis. By legal means, the family compelled the hospital to maintain life support until Jahi was released to her mother on day 27. She was then moved to New Jersey, where an exemption to BD can be invoked to accommodate personal religious beliefs, initially to a medical facility and subsequently to a private apartment. She remained on a ventilator until experiencing cardiovascular collapse 4.5 y after the initial BD pronouncement.

SCINTIGRAPHIC IMAGING AND FINDINGS

According to guidelines, ancillary studies are not required to establish the diagnosis of BD unless certain elements of the physical examination cannot be properly performed. Ancillary studies may still have a role to play for social reasons, such as allowing family members to better comprehend the diagnosis (*3*), which most aptly fits the current circumstance. Brain scintigraphy with lipophilic compounds may also play a separate role in prognosticating potential recovery in patients with catastrophic brain injury, even when not directly related to BD determination, and may be helpful to family and caregivers in decision making.

On day 14 of Jahi's course, a perfusion study of the brain was performed after injection of 1.0 GBq of ^{99m}Tc-bicisate (Neurolite; Lantheus). Twenty scintigraphic imaging files were provided on an eFilm Lite disk (version 4.1.0; Merge Healthcare); these were provided without any editorial stipulations. Representative images are displayed in Figures 1–3; additional images are presented in the supplemental materials. Tomographic information was provided as secondary-capture images, not amenable to scrolling or to triangulation between planes, and lacking the original dynamic range of counts (though the windowing appears grossly adequate). These limitations should not be regarded as consequential because, according to guidelines, tomographic imaging is an optional component of BD studies. The examination was otherwise technically adequate, with performance closely conforming to published guidelines (*4,5*). No intracranial blood flow or parenchymal perfusion was visualized on dynamic, static, or tomographic phases of the examination.

CONTROVERY REGARDING THE MEDICAL COURSE

Although inconsistency in BD determination has been documented in the literature and potentially could lead to a false-positive diagnosis, it is unlikely that both of Jahi's clinical examinations were invalid, because of the enhanced expertise focused on her high-profile case. Her perfusion study was fully compliant with relevant guidelines, and no intracranial blood flow or parenchymal brain uptake was apparent.

Received Feb. 3, 2022; revision accepted May 11, 2022.

For correspondence or reprints, contact Lionel S. Zuckier (LZuckier@montefiore.org).

DOI: 10.2967/jnumed.122.263972

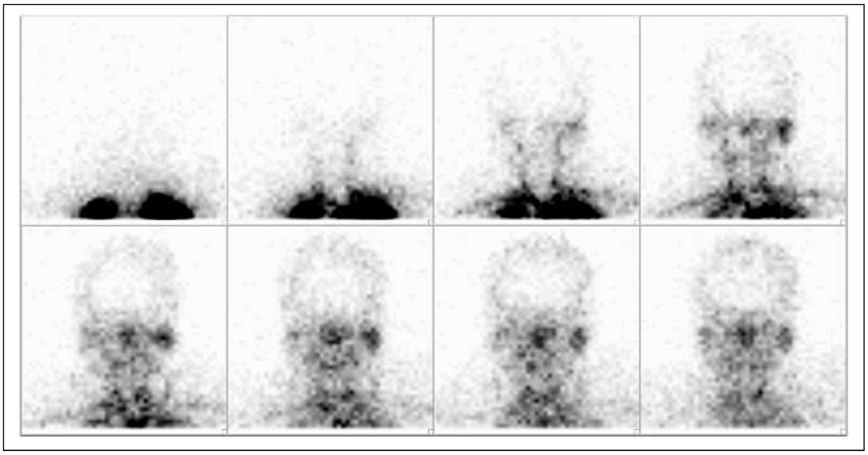

FIGURE 1. ^{99m}Tc-bicisate, 1.0 GBq, was injected via femoral central line with scalp tourniquet in place. Representative dynamic tomographic images were selected from series of 95 rapid sequential images acquired in anterior projection at 1- or 2-s intervals (timing details not specified in images or report). Activity is clearly seen within common carotid arteries; however, no intracranial flow is visualized.

Physicians who perform radionuclide BD studies should be aware of wide-ranging discussions in the clinical literature regarding Jahi McMath's case (*2,6*). Initial conceptualization of BD frequently included rationalization that lack of central control and coordination precluded continued integration of the organism. Although this dogma was largely abandoned, it is still distinctly unusual for a BD patient to maintain homeostasis over a span of several years, regulate body temperature, develop signs of puberty, and experience several menstrual cycles, as Jahi did. Jahi's course was also exceptional in that most patients for whom BD is declared will immediately proceed to organ donation or be removed from the ventilator, leaving no opportunity for subsequent observation; under these circumstances, the frequency of delayed return of function cannot be estimated. Despite this paradigm, occasional case reports have surfaced in which neurologic function is noted to return after pronouncement of BD (*7*), similar to our narrative. Several medical personnel, including a prominent pediatric neurologist, came to believe that Jahi could intermittently respond in a purposeful manner to verbal commands (such as "move your arm") (*2*). Additionally, the MRI examination performed 10 mo after the initial cardiac arrest unexpectedly demonstrated large regions of grossly intact brain, including cortex, basal ganglia, thalamus, upper brain stem, and cerebellum, which could serve as a structural basis for intermittent consciousness (*8*). Return of minimal responsiveness, if present, would directly challenge the presumption that BD is definitive and permanent.

DISCUSSION

Along with broader concerns raised by Jahi McMath's case, it is also opportune to consider several questions pertaining to nuclear medicine. Thresholds of minimal detectable perfusion have never been determined for scintigraphic studies using either lipophobic or lipophilic radiopharmaceuticals, though these parameters are basic to their interpretation. For lipophobic radiopharmaceuticals, marginal perfusion would certainly be difficult to appreciate on noisy 1- or 2-s dynamic images. For lipophilic compounds, the brain stem and small cortical regions adjacent to the calvarium represent areas where identification of minimal perfusion would be challenging, even with tomography. Coupled with uncertainty regarding the amount of blood flow required to maintain the structural integrity and function of neurologic tissue, it is difficult to assert that lack of visualization of blood flow on a scintigraphic study would predict complete necrosis of the brain or even guarantee absence of function. This concern seemed realized in Jahi's case, with perfusion not being visible on the ^{99m}Tc-bicisate study yet large regions of cerebral cortex remaining intact, and according to some experts, a minimally conscious state emerged. Previous analysis of PET perfusion data in adults has suggested that the minimal regional cerebral blood flow necessary for preservation of tissue integrity is at least 15 mL of blood per 100 g of tissue per minute whereas that required for normal neurologic function is at least 19 mL of blood per 100 g of tissue per minute (*9*). Could this amount of perfusion have been present but not visible on the ^{99m}Tc-bicisate study? Conversely, was perfusion absent during scintigraphy, possibly because of a transient hypotensive episode, but subsequently returned? Our fundamental lack of knowledge regarding the behavior of the ^{99m}Tc-bicisate examination prevents us from arriving at definitive answers.

A related issue concerns estimating the specificity of scintigraphy for determination of BD. Characterization of specificity requires evaluation of the examination in a population of subjects similar to that possessing the condition in question but lacking the particular condition itself. The ancillary examination must therefore be studied in a cohort of patients with catastrophic brain injury but without complete loss of function. Such an evaluation has not occurred for many of the modalities, because this group of patients is simply not sent for ancillary study; if the clinical examination reveals any residual neurologic function, the blood flow study is deferred. This fundamental limitation has compromised validation studies in the nuclear medicine literature, which has included only a handful of appropriately non–brain-dead subjects. In one study using lipophobic methods,

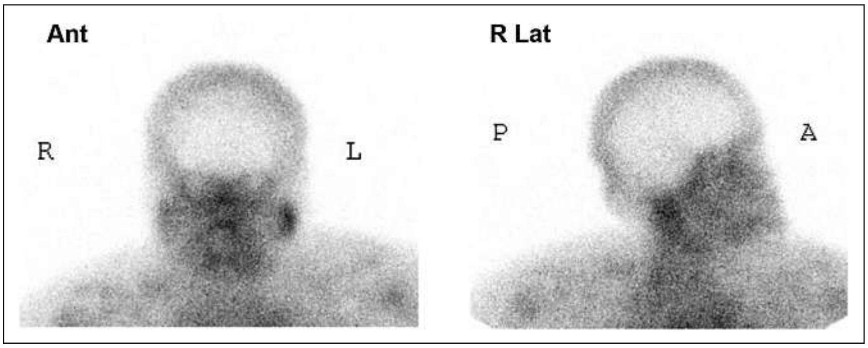

FIGURE 2. Anterior and right lateral views of ^{99m}Tc-bicisate tomographic images obtained several minutes after injection demonstrate activity in extracranial tissues of face and skull. No activity is localized in cerebrum or cerebellum. Ant and A = anterior; Lat = lateral; P = posterior.

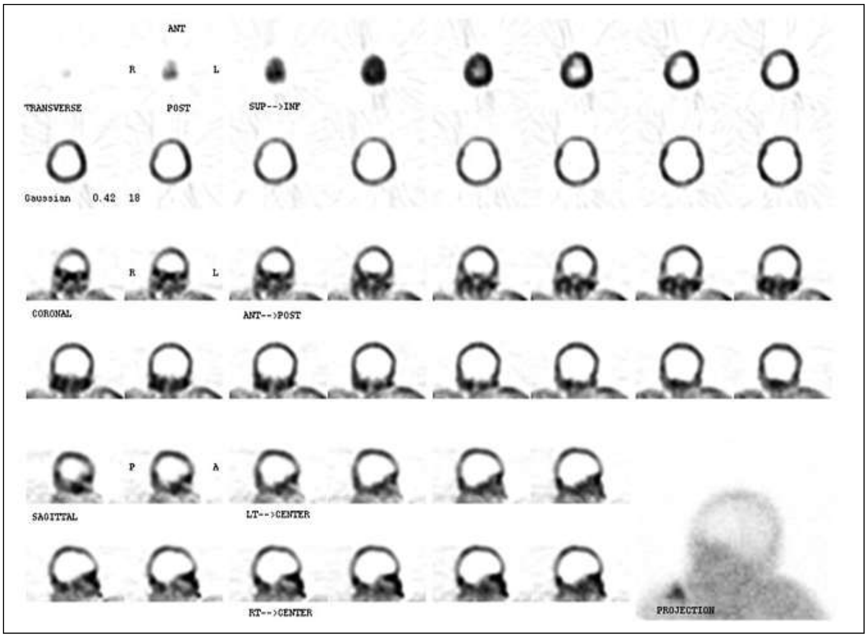

FIGURE 3. Representative ^{99m}Tc-bicisate tomographic images displayed in transaxial, coronal, and sagittal planes. No activity is visualized within calvarium. Additional images appear in supplemental materials. ANT = anterior; INF = inferior; LT = left; POST = posterior; RT = right; SUP = superior.

10 appropriate non-BD patients were enrolled, but specificity for determining BD was a paltry 50% (*10*). Presumably, lipophilic radiopharmaceuticals would possess higher specificity, but this has not been rigorously demonstrated.

CONCLUSION

Jahi McMath's tragic narrative highlights several unanswered questions relevant to the diagnosis of BD. For several decades, radionuclide techniques have served an important ancillary role in complementing incomplete clinical BD examinations though they remain incompletely characterized. Radionuclide BD examinations are invaluable when they demonstrate unexpected intracranial blood flow, preventing erroneous determination of BD; inferences when blood flow is not visualized remain more enigmatic. The threshold of blood flow required for visualization remains unknown. The accepted role of an ancillary test is to supplement but never replace the physical BD examination, as is congruent with an imperfect specificity of these ancillary tests. For this reason, Society of Nuclear Medicine and Molecular Imaging guidelines appropriately recommend that the impression of a positive study conclude "shows no evidence of brain perfusion" rather than "demonstrates BD" (*4*). The subjective formulation "shows no evidence" is also particularly appropriate in that it avoids the fundamentally unsubstantiated claim that "no blood flow is present." A more thorough and robust understanding of these tests, combined with an effort to standardize their implementation, could serve to bolster their role in the determination of BD, especially in difficult or controversial circumstances.

DISCLOSURE

No potential conflict of interest relevant to this article was reported.

ACKNOWLEDGMENTS

Appreciation is extended to Dr. D. Alan Shewmon, who provided clinical materials for review; to Jahi's mother, Nailah Winkfield, for authorizing publication of her daughter's medical data; and to colleagues who have provided insightful review and comments.

REFERENCES

1. Zuckier LS. Radionuclide evaluation of brain death in the post-McMath era. *J Nucl Med.* 2016;57:1560–1568.
2. Shewmon DA, Salamon N. The extraordinary case of Jahi McMath. *Perspect Biol Med.* 2021;64:457–478.
3. Nakagawa TA, Ashwal S, Mathur M, et al. Clinical report: guidelines for the determination of brain death in infants and children—an update of the 1987 task force recommendations. *Pediatrics.* 2011;128:e720–e740.
4. Donohoe KJ, Agrawal G, Frey KA, et al. SNM practice guideline for brain death scintigraphy 2.0. *J Nucl Med Technol.* 2012;40:198–203.
5. ACR–ACNM–SNMMI–SPR practice parameter for the performance of single-photon emission brain perfusion imaging (including SPECT and SPECT/CT). ACR website. https://www.acr.org/-/media/ACR/Files/Practice-Parameters/BrainPerf-SPECT.pdf. Revised 2021. Accessed June 2, 2022.
6. Lewis A. Reconciling the case of Jahi McMath. *Neurocrit Care.* 2018;29:20–22.
7. Nair-Collins M, Joffe AR. Frequent preservation of neurologic function in brain death and brainstem death entails false-positive misdiagnosis and cerebral perfusion. *AJOB Neurosci.* September 29, 2021 [Epub ahead of print].
8. Shewmon DA, Salamon N. The MRI of Jahi McMath and its implications for the global ischemic penumbra hypothesis. *J Child Neurol.* 2022;37:35–42.
9. Powers WJ, Grubb RL Jr, Darriet D, Raichle ME. Cerebral blood flow and cerebral metabolic rate of oxygen requirements for cerebral function and viability in humans. *J Cereb Blood Flow Metab.* 1985;5:600–608.
10. Flowers WM Jr, Patel BR. Radionuclide angiography as a confirmatory test for brain death: a review of 229 studies in 219 patients. *South Med J.* 1997;90:1091–1096.

Targeted α-Emitter Therapy with ^{212}Pb-DOTAMTATE for the Treatment of Metastatic SSTR-Expressing Neuroendocrine Tumors: First-in-Humans Dose-Escalation Clinical Trial

Ebrahim S. Delpassand[1,2], Izabela Tworowska[2], Rouzbeh Esfandiari[1], Julien Torgue[3], Jason Hurt[3], Afshin Shafie[1], and Rodolfo Núñez[1]

[1]Excel Diagnostics and Nuclear Oncology Center, Houston, Texas; [2]RadioMedix, Inc., Houston, Texas; and [3]Orano Med, Plano, Texas

Peptide receptor radiotherapy with somatostatin analogs has been successfully used for years as a treatment for somatostatin-overexpressing tumors. Treatment of neuroendocrine tumors (NETs) with the β-particle emitter ^{177}Lu-DOTATATE is currently considered the standard of care for subjects with gastroenteropancreatic NETs. Despite the success of ^{177}Lu-DOTATATE, there remains significant room for improvement in terms of both safety and efficacy. Targeted α-emitter therapy with isotopes such as ^{212}Pb has the potential to improve both. Here, we present the preliminary results of the phase 1 first-in-humans dose-escalation trial evaluating ^{212}Pb-DOTAMTATE (a bifunctional metal chelator [DOTAM] and the SSTR-targeting peptide [TATE]) in patients with somatostatin receptor–positive NETs. **Methods:** Twenty subjects with histologically confirmed NETs, prior positive somatostatin analog scans, and no prior history of ^{177}Lu/^{90}Y/^{111}In peptide receptor radiotherapy, with different primary sites of the disease, were enrolled. Treatment began with single ascending doses of ^{212}Pb-DOTAMTATE, with subsequent cohorts receiving an incremental 30% dose increase, which was continued until a tumor response or a dose-limiting toxicity was observed. This was followed by a multiple ascending dose regimen. The recommended phase 2 dose regimen consisted of 4 cycles of 2.50 MBq/kg (67.6 μCi/kg) of ^{212}Pb-DOTAMTATE administered at 8-wk intervals, intravenously. **Results:** Ten subjects received the highest dose, 2.50 MBq/kg/cycle (67.6 μCi/kg/cycle). Treatment was well tolerated, with the most common treatment-emergent adverse events being nausea, fatigue, and alopecia. No serious treatment-emergent adverse events were related to the study drug, and no subjects required treatment delay or a dose reduction. An objective radiologic response of 80% was observed for the first 10 subjects treated at the recommended phase 2 dose. **Conclusion:** Targeted α-therapy with ^{212}Pb-DOTAMTATE has been shown to be well tolerated. Preliminary efficacy results are highly promising. If these results are confirmed in a larger, multicenter clinical trial, ^{212}Pb-DOTAMTATE would provide a substantial benefit over currently Food and Drug Administration–approved therapies for patients with metastatic or inoperable SSTR-expressing NETs regardless of the grade and location of the primary tumor.

Key Words: TAT; PRRT; ^{212}Pb-DOTAMTATE; NET; NEN, phase 1

J Nucl Med 2022; 63:1326–1333
DOI: 10.2967/jnumed.121.263230

Neuroendocrine tumors (NETs) are a heterogeneous group of rare neoplasms that originate from neuroendocrine cells. These neoplasms occur mostly in the gastrointestinal tract and pancreas but can also occur in other tissues, including thymus and lung, as well as uncommon sites such as ovaries, heart, and prostate. Regardless of their primary site, NETs share histologic, immunohistochemical, and ultrastructural features. NETs retain multipotent differentiation capacities, including the ability to produce and secrete a variety of metabolically active substances such as amines, peptides, and prostaglandins (*1*).

Most NETs strongly express somatostatin receptors (SSTRs), predominantly of the somatostatin 2 subtype (*2*), providing the basis of antisecretory and antiproliferative therapy with somatostatin analogs (short- and long-acting octreotide and long-acting lanreotide). These drugs are highly effective in controlling symptoms associated with carcinoid syndrome and have been shown to improve progression-free survival (PFS) in the metastatic setting in gastroenteropancreatic NETs (*3*). Although PFS can be prolonged, a high percentage of patients will progress and require additional therapy. Current guidelines recommend that patients with locoregional advanced disease or distant metastases for NETS of the gastrointestinal tract be treated with systemic therapy such as everolimus, sunitinib, or peptide receptor radionuclide therapy (PRRT) with the β-emitter ^{177}Lu-DOTATATE (*4*). This is currently the only PRRT approved by the U.S. Food and Drug Administration for patients with SSTR-expressing gastroenteropancreatic NETs (*5*). The NETTER-1 study demonstrated a clinically meaningful and statistically significant increase in PFS and objective radiologic response (ORR) in subjects with advanced gastroenteropancreatic NETs treated with ^{177}Lu-DOTATATE and long-acting octreotide (30 mg) compared with those treated with high-dose long-acting octreotide. At the data-cutoff date for the primary analysis, the estimated PFS at month 20 was 65.2% in the ^{177}Lu-DOTATATE group and 10.8% in the control group (*6*). Although the NETTER-1 trial demonstrated a tremendous benefit in PFS and overall survival, the ORR was only 13% in the ^{177}Lu-DOTATATE group versus 3% in the octreotide group, with only 1 complete response (CR) and 14 (12%) partial responses (PR) in the ^{177}Lu-DOTATATE group (*7*). It stands to reason that a radiopharmaceutical that provides a superior ORR will likely also improve PFS and overall survival.

^{212}Pb-DOTAMTATE is the first ^{212}Pb-labeled octreotate analog to treat SSTR-expressing NETs and targets SSTR-expressing malignancies regardless of their primary organ of origin and their

---

Received Sep. 15, 2021; revision accepted Jan. 4, 2022.

For correspondence or reprints, contact Rodolfo Núñez (rnunez@exceldiagnostics.com).

proliferative index. The drug consists of 3 linked components: the ^{212}Pb isotope, a bifunctional metal chelator (DOTAM), and the SSTR-targeting peptide (TATE).

The physical half-life of ^{212}Pb is 10.6 h, and it is an in vivo generator of α-emitting particles. ^{212}Pb itself is not an α-emitter, but its decay scheme includes 2 α-particles (1 per branch) with potent cytotoxicity to cell nuclei (*8,9*).

Compared with currently used β-emitters such as ^{177}Lu-DOTATATE (*10,11*), ^{212}Pb-DOTAMTATE provides a significantly higher linear energy transfer delivered in a shorter pathlength. In theory, a higher linear energy transfer should induce more double-stranded DNA damage to the tumor cells, ultimately resulting in irreparable tumor cell injury, apoptosis, and cell death. Additionally, because of the shorter pathlength, there are fewer side effects for subjects receiving targeted α-therapy (TAT) (*12*). Accordingly, to address an unmet need of TAT in the field of PRRT for NET, we are undertaking a phase 1 study with the main objective of determining the safety and dose-limiting toxicity of ascending doses of ^{212}Pb-DOTAMTATE used for TAT in subjects with SSTR-expressing NETs. A secondary objective was to determine the pharmacokinetic properties as well as the preliminary effectiveness of ascending doses of ^{212}Pb-DOTAMTATE.

MATERIALS AND METHODS

Study Design

This open-label, nonrandomized, dose-escalation and dose-expansion phase 1 trial (NCT03466216) was conducted at a single center in the United States (Excel Diagnostics Nuclear Oncology Center, Houston, Texas). This prospective study was performed in accordance with the Helsinki Declaration and followed the International Conference on Harmonization good-clinical-practice guidelines. The study was approved by the Biomedical Research Alliance of New York Institutional Review Board; all subjects gave written informed consent before enrollment. The study was conducted in full compliance with the U.S. Health Insurance Portability and Accountability Act. Eligible patients included men and women at least 18 y old with an Eastern Cooperative Oncology Group performance status of 0–2. They had to have a life expectancy of at least 12 wk and a histologically confirmed diagnosis of NET, either unresectable or metastatic progressive disease, with at least 1 site of measurable disease per RECIST 1.1. All patients were required to have SSTR imaging within 4 wk of the first dose. Patients who had been treated with prior whole-body radiotherapy or PRRT using ^{177}Lu/^{90}Y/^{111}In-DOTATATE/DOTATOC or TAT were excluded. Therapeutic use of any somatostatin analog, including long-acting octreotide acetate (within 28 d) and octreotide acetate (within 1 d), before administration of the study drug was exclusionary.

The study was designed as a single-ascending-dose (SAD)/multiple-ascending-dose (MAD) trial using a 3 + 3 dose-escalation scheme with an 8-wk dose-limiting toxicity period. Dose escalation proceeded as per Table 1. The initial dose to be examined was 1.13 MBq/kg (30.7 μCi/kg), and subsequent cohorts received an incremental 30% dose increase until a tumor response or a dose-limiting toxicity was observed. The maximum total dose per subject in the SAD cohort was 296 MBq (8 mCi). The maximum total dose per subject in the MAD cohort was 888 MBq (24 mCi). All these limits were assigned by human dosimetry calculations performed on subjects having received the ^{203}Pb-AlphaMedix (RadioMedix, Inc.) surrogate under investigational new drug 130,960. The activity of each cycle was not to exceed 203.5 MBq ± 10%. (5.5 mCi ± 10%), regardless of the subject's weight, and the cumulative dose was not to exceed 888 MBq (24 mCi). The data safety monitoring board was responsible for determining both dose escalation in the SAD cohorts and dose at which expansion into the MAD cohorts would occur. The board recommended transitioning to the MAD cohort if there was clinical efficacy and lack of any dose-limiting toxicities.

TABLE 1
Dose Escalation per Cycle in SAD and MAD Cohorts

Cohort	Dose per cycle (MBq/kg ± 10%)
1	1.13 (30.7)
2	1.48 (40.0)
3	1.92 (52.0)
4	2.50 (67.6)

Data in parentheses are microcuries.

Nonhematologic dose-limiting toxicities were defined as all grade 3 toxicities (except alkaline phosphatase) not responsive within 72 h of supportive care and any grade 4 toxicities. Hematologic dose-limiting toxicities were defined as any toxicity that did not recover to grade 2 or less within 8 wk after administration of the study drug. A dose-modifying toxicity was defined as any grade 3 or 4 hematologic toxicity (except lymphopenia) that did not resolve within 8 wk from the prior administration or a grade 2 or higher serum creatinine level that did not resolve within 8 wk from the prior administration.

The MAD treatment regimen began at the 1.92 MBq/kg (52.0 μCi/kg) dose level and was escalated to the fourth cohort (MAD4) at a dose of 2.50 MBq/kg (67.6 μCi/kg/cycle). The cohort was then expanded to include 7 more patients for a total of 10. Thirty minutes before each dose, an amino acid solution of lysine and arginine was administered at 250 mL/h over 4 h for kidney protection against the effects of radiation. Before each injection cycle, the subjects had a physical exam, filled out the quality-of-life questionnaire of the European Organization for the Research and Treatment of Cancer, and had routine blood testing (including complete blood count, comprehensive metabolic panel with estimated glomerular filtration rate [eGFR], and tumor markers), an electrocardiogram, and medical imaging. Baseline and follow-up imaging included contrast-enhanced MRI or CT for RECIST 1.1 evaluation. ^{99m}Tc-diethylenetriaminepentaacetic acid renal scanning and ^{68}Ga-DOTATATE PET/CT were also performed. ^{18}F-FDG PET/CT and bone scanning were performed on selected patients at the principal investigator's discretion. ^{18}F-FDG PET/CT was repeated if positive at the baseline evaluation.

For all subjects, safety follow-up visits were scheduled at 2, 5, 8, and 12 mo after the single injection in the SAD cohorts and after the fourth injection in the MAD cohorts. The 12-mo safety follow-up visit was also the end-of-study visit. From months 13 to 36, a structured, semiannual telephone follow-up call was made to collect information on late toxicity, any hospitalizations, recent imaging results, and new treatment. Efficacy assessments per RECIST 1.1 were performed after each cycle, as was functional imaging. Objective radiographic response (ORR) was assessed according to RECIST 1.1. Following our own preestablished criteria, the PET/CT imaging response was defined as CR when all SSTR-positive lesions were resolved or as PR when there was a reduction of more than 50% of the visually estimated tumor burden. Visual estimation of the overall tumor burden for each patient by ^{68}Ga-DOTATATE PET/CT was subjective and done by an experienced (>25 y) board-certified nuclear medicine physician estimating the reduction in tumor burden, considering that the baseline ^{68}Ga-DOTATATE PET/CT scan reflected 100% of the tumor burden. Duration of response was defined as the time that measurement criteria were first met for CR/PR by RECIST 1.1 until the date that recurrent

TABLE 2

Patient Characteristics, Including Relevant Clinical Trial Data

Patient*	Age (y)	Sex	Type of NET	Grade	Ki-67	Stage	Time gap (y)	No. of cycles	Total dose (MBq)	RECIST 1.1 response[†]	^{68}Ga PET response[‡]	Duration of response (mo)[§]
SAD1-01	75	M	Small bowel	2	4	IV	6.4	1	81 (2.2)	Stable disease	NA	NP
SAD1-02	76	F	Pancreatic	2	NA	IV	8.8	1	85 (2.3)	Stable disease	NA	NP
SAD1-03	77	M	Pancreatic	3	27	IV	4.5	1	85 (2.3)	Stable disease	NA	NP
SAD2-01	56	M	Rectal	2	NA	IV	5.2	1	122 (3.3)	Stable disease	NA	NP
SAD2-02	27	F	Small bowel	1	NA	IV	4.7	1	100 (2.7)	Stable disease	NA	NP
SAD2-03	72	F	Small bowel	1	2	IV	6.1	1	115 (3.2)	Stable disease	NA	NP
MAD3-01	61	F	Small bowel	2	6	IV	10.7	3	574 (15.5)	Stable disease	NSC	0
MAD3-02	62	F	Pancreatic	2	3	IV	7.2	2[‖]	329 (8.9)	Stable disease	NSC	0
MAD3-03	68	F	Small bowel	NA	NA	IV	10.7	3	266 (7.2)	Stable disease	NSC	0
MAD3-04	51	M	Pancreatic	NA	NA	IV	5.6	3	455 (12.3)	Stable disease	−40%	0
MAD4-01	62	M	Small bowel	3	22	IV	2.2	4	814 (22.0)	PR	−95%	22
MAD4-02	45	M	Bronchial carcinoid	1	>20	IV	6.2	4	796 (21.5)	PR	−100%	22
MAD4-03	71	F	Bronchial carcinoid	2	15	III	4.8	4	707 (19.8)	CR	−100%	20
MAD4-04	39	F	Rectal	3	30	IV	5.1	4	807 (21.8)	Stable disease	−40%	0
MAD4-05	62	M	Pancreatic	1	2	IV	7.3	4	873 (23.6)	PR	−80%	8
MAD4-06	49	F	Pancreatic	2	19	IV	2.9	4	681 (18.4)	PR	−100%	14
MAD4-07	45	M	Rectal	2	12	IV	5.7	4	858 (23.2)	PR	−95%	5
MAD4-08	60	M	Small bowel	2	5	IV	0.3	4	692 (18.7)	Stable disease	−15%	0
MAD4-09	80	M	Bronchial carcinoid	2	10	IV	1.1	4	836 (22.6)	PR	−60%	1
MAD4–10	59	F	Bronchial carcinoid	2	5	IV	1.8	4	847 (22.9)	PR	−30%	5

---

*MAD3 cohort started as SAD3 cohort, with single injection of 1.92 MBq/kg (52.0 μCi/kg). When quality-of-life improvements were reported after first cycle, approval was obtained from disease safety monitoring board and these subjects were transitioned to MAD cohort, with 2 additional cycles at same dose administered at 8-wk intervals.

[†] For SAD cohort, response was established 2 mo after injection, before other therapies began.

[‡] Percentage decrease in overall tumor burden on ^{68}Ga-DOTATATE PET/CT was visually estimated.

[§] As of June 2021.

[‖] Subject dropped out of study after second cycle.

NA = not available; NP = not applicable; NSC = no significant change.

As per 2017 WHO classification: G1 = <3, G2 = 3–20, and G3 = >20 Ki-67 index. Data in parentheses are microcuries. Time gap is difference in years between original histopathologic diagnosis and first treatment cycle with ^{212}Pb-DOTAMTATE.

or progressive disease was objectively documented (*13*) or last clinical contact (June 2021). Time to response was defined as the time between the first administration of study drug and the time when RECIST measurement criteria were first met for CR/PR.

The primary endpoint was assessment of the safety and dose-limiting toxicities of ascending doses of ^{212}Pb-DOTAMTATE used for TAT of subjects with SSTR-expressing NETs. Secondary endpoints included pharmacokinetics, dosimetry, and determination of preliminary effectiveness of ^{212}Pb-DOTAMTATE. Adverse events were coded using the National Cancer Institute Common Terminology Criteria for Adverse Events, version 4.03. eGFR was calculated using the Chronic Kidney Disease Epidemiology Collaboration equation. Pharmacokinetics were evaluated through the collection of several blood samples at multiple time points and urine collection before and after the intravenous administration of ^{212}Pb-DOTAMTATE.

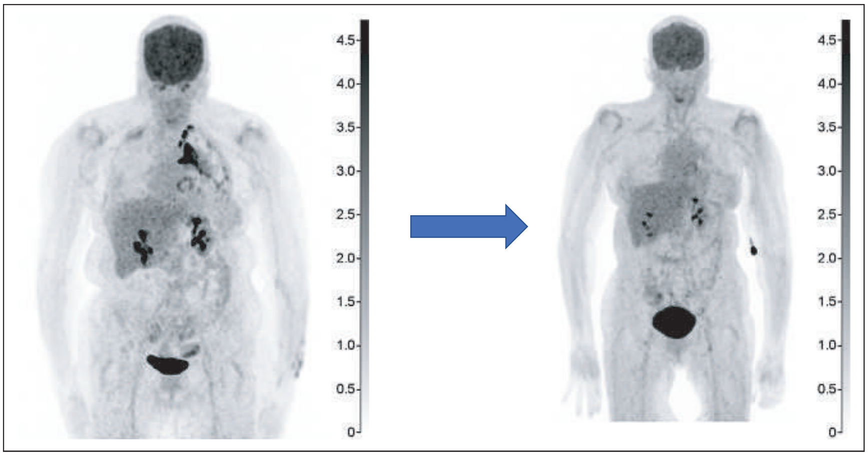

FIGURE 1. Volume-rendered images of ^{18}F-FDG PET/CT scans from subject MAD4-03 before (left) and after (right) treatment with 4 cycles of ^{212}Pb-DOTAMTATE.

Dosimetry data were obtained for 6 subjects in the MAD4 cohort and will be reported in a separate article.

The Student *t* test was used to compare the means and derive *P* values using JMP Clinical, version 8.0 (SAS Institute Inc.).

RESULTS

Twenty PRRT-naïve subjects (10 male, 10 female) have been treated to date (median age, 62 y; range, 27–80 y), with 10 of 10 subjects (100%) receiving 4 cycles of ^{212}Pb-DOTAMTATE at the highest dose level, 2.50 MBq/kg/cycle (67.6 μCi/kg/cycle) (Table 2). The mean cumulative dose administered over 4 cycles based on a dose of 2.50 MBq/kg (67.6 μCi/kg) was 791 MBq (21.4 mCi), with a range of 681–873 MBq (18.4–23.6 mCi). All patients had received or declined all Food and Drug Administration–approved medications for their disease, except for PRRT, including somatostatin analogs, and progressed before enrollment. The time between the histopathologic diagnosis and the first cycle of treatment with ^{212}Pb-DOTAMTATE varied considerably from patient to patient, ranging from 0.3 to 10.7 y, with a mean of 5.36 y.

Radiographic Results

No ORR by RECIST 1.1 was seen in cohorts SAD1 or SAD2 or in the first MAD cohort (MAD3). In the MAD4 cohort, the ORR by RECIST was 80% (1 CR, 7 PR, 2 stable disease). One subject (10%) in the MAD4 cohort (MAD4-06) demonstrated an objective response 8 wk after the first injection, 6 of 7 subjects [86%]) demonstrated an objective response after the third cycle of therapy, and 1 subject (MAD4-07) achieved a PR after completion of all 4 cycles. The only CR by RECIST was in subject MAD4-03, after the 10-mo visit (Fig. 1). Four patients (40%) had at least a 50% decrease in the sum of the diameters of the target lesions. The largest percentage decrease in the sum of the diameters that was not a CR was seen in subject MAD4-02, with an 85% decrease (Figs. 2 and 3). The median decrease in the sum of the diameters for all patients was 41%.

Response by ^{68}Ga-DOTATATE PET/CT in the MAD4 cohort demonstrated 3 CR (patients MAD4-02, -03, and -06), 4 PR, and 3 stable disease (Fig. 4). The mean decrease in the sum of the diameters per RECIST in those patients who demonstrated a CR by ^{68}Ga-DOTATATE PET/CT was 84% (range, 70%–100%). Although patient MAD4-04 did not meet the definition of PR per RECIST,

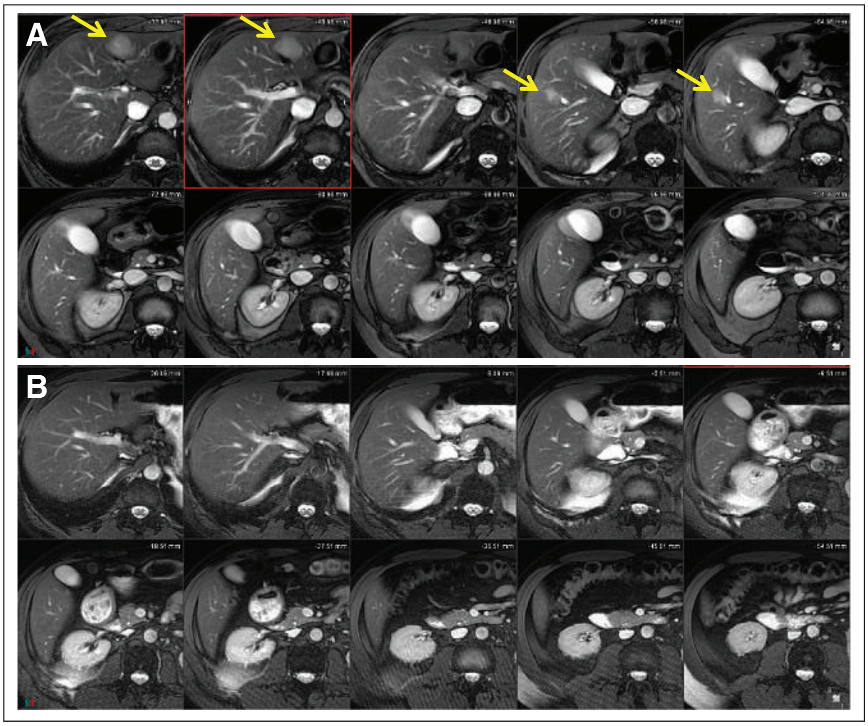

FIGURE 2. MRI of liver before (A) and after (B) treatment with 4 cycles of ^{212}Pb-DOTAMTATE in subject MAD4-02. Arrows point to liver metastases. Near-complete resolution of liver metastases is seen in B.

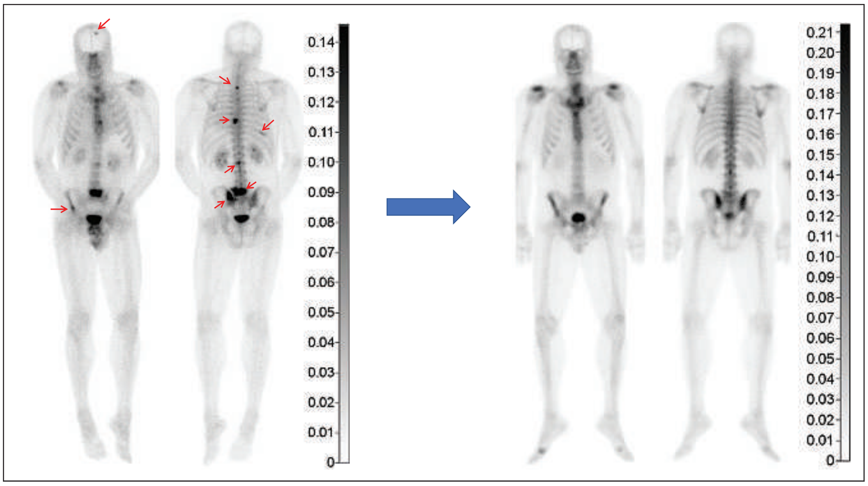

FIGURE 3. Bone scans of subject MAD4-02 before (left) and after (right) treatment with 4 cycles of ^{212}Pb-DOTAMTATE. Most lesions on initial baseline bone scan (arrows) are completely healed on bone scan after treatment.

with only a 26% decrease in the sum of the diameters of the target lesions, ^{68}Ga-DOTATATE PET/CT demonstrated obvious improvement in tumor burden.

No progression of disease was noted for 9 of 10 subjects (90%) who completed treatment. One subject experienced disease progression approximately 10 mo after completing all 4 cycles of treatment (16 mo after treatment initiation). Interestingly, the new lesions were not seen on ^{68}Ga-DOTATATE PET/CT but were seen on ^{18}F-FDG PET/CT, suggestive of an undifferentiated NET or a non–SSTR-expressing malignancy.

At the time of the last data collection, all MAD4 patients were alive, with the median length of follow-up being 17.4 mo (range, 9–26 mo). The median duration of response was 14 mo (range, 5–22 mo), and the median time to response was 5.2 mo (range, 1.7–10.3 mo).

Safety

No dose-limiting toxicities were noted during dose escalation or expansion, and no subject required a delay in treatment or a reduction or cancellation of dose. In total, 170 adverse events were reported. Eighty-two (46%) were reported in the SAD cohort and 97 (54%) in the MAD cohort. Of the adverse events, 49 (29%) were grade 2, 7 (5%) were grade 3, and none (0%) were grade 4. Thirty-two treatment-emergent adverse events (TEAEs) were considered related to the study drug, with the most common being alopecia (25%) and nausea (31%).

Fifteen serious TEAEs, including 2 deaths, were reported (Table 3). Most serious TEAEs were reported in the SAD cohorts (9/15) and were reported by 4 patients. Six serious TEAEs were reported in the MAD cohort by only 2 patients. The preferred terms for the reported serious TEAEs, by patient, were disease progression for SAD1-01; pain, malignancy-associated pain, dehydration, low eGFR (grade 3), and disease progression for SAD2-02; acute renal failure and renal failure for MAD3-01; worsening achalasia for MAD4-01; and fatigue, acute cerebrovascular accident, hypoglycemia, dyspnea, and chronic kidney disease for MAD4-03. None of the reported serious TEAEs were considered related to the study drug.

Vital Signs

There were no clinically significant changes in systolic blood pressure, diastolic blood pressure, heart rate, or QT interval from baseline compared with the last cycle of treatment for all subjects.

Hematologic, Hepatic, and Renal Parameters

In the MAD4 cohort after 6 mo of treatment, there was no statistically significant difference from screening in platelets (median,

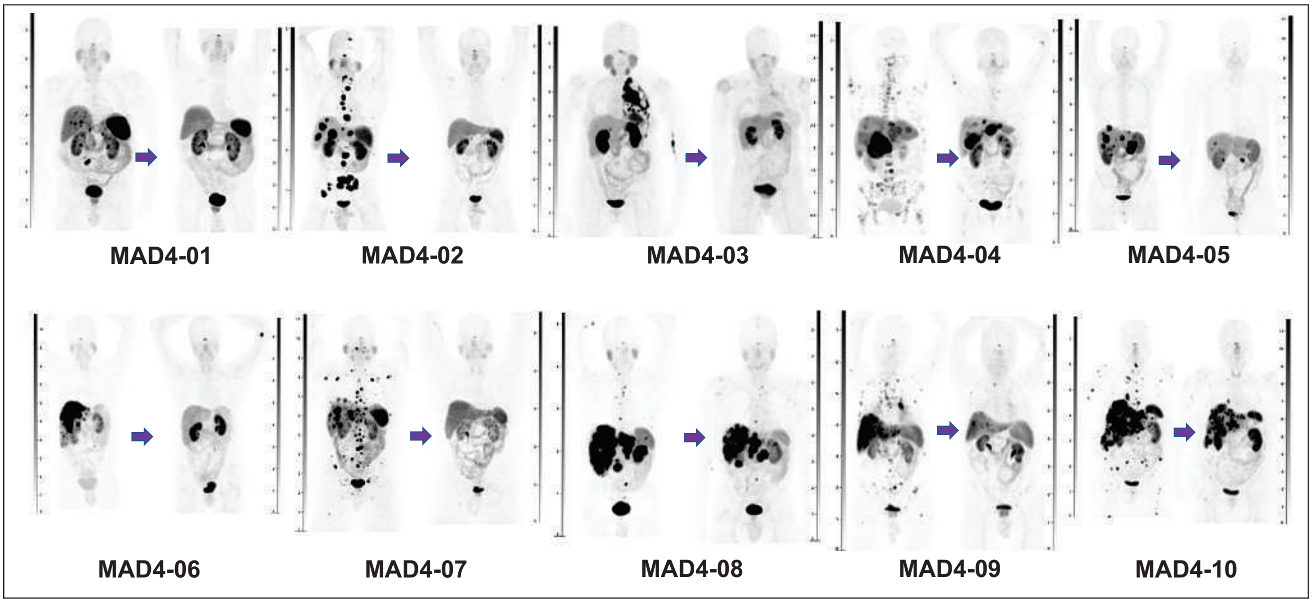

FIGURE 4. Volume-rendered images of ^{68}Ga-DOTATATE PET/CT scans from first 10 subjects enrolled in cohort 4 (MAD4) before treatment (left side of each panel) and after treatment (right side of each panel) with 4 cycles of ^{212}Pb-DOTAMTATE at dose of 2.50 MBq/kg (67.6 μCi/kg) for each cycle.

TABLE 3
All Serious Adverse Events

Subject	Event preferred term	Causality	Grade	Outcome
SAD1-01	Disease progression	Not related	5	Fatal
SAD2-02	Pain	Not related	2	Recovered
SAD2-02	Cancer pain	Not related	2	Recovered
SAD2-02	Dehydration	Not related	2	Recovered
SAD2-02	Disease progression	Not related	5	Fatal
SAD2-02	Low glomerular filtration rate	Not related	3	Recovered
MAD3-01	Acute kidney injury	Unlikely	2	Recovered
MAD3-01	Renal failure	Unlikely	3	Not recovered
MAD3-04	Abdominal pain	Unlikely	3	Recovering
MAD4-01	Worsening achalasia	Not related	3	Recovered
MAD4-03	Dyspnea	Unlikely	3	Recovered
MAD4-03	Fatigue	Unlikely	2	Resolved
MAD4-03	Hypoglycemia	Unlikely	2	Resolved
MAD4-03	Cerebrovascular accident	Unlikely	2	Resolved
MAD4-03	Chronic kidney disease	Unlikely	2	Not recovered

264 × 10^9/L; range, 124–417 × 10^9/L; $P = 0.304$), hemoglobin (median, 13.4 g/dL; range, 10.3–16.3 g/dL; $P = 0.1475$), absolute neutrophil count (median, 3.52 × 10^9/L; range, 2.08–5.1 × 10^9/L; $P = 0.1833$), or white blood cells (median, 5.7 × 10^9/L; range, 3.27–9 × 10^9/L; $P = 0.0868$).

Regarding the mean lymphocyte count, there was no significant change when comparing baseline screening with cycle 1. There was a statistically significant change when comparing cycle 2 with screening ($P = 0.0043$), cycle 3 with screening ($P = 0.0003$), and cycle 4 with screening ($P = 0.0014$); however, at 6 mo after treatment, there were no statistically significant differences from screening (median, 1.09 × 10^9/L; range, 0.3–2.42 10^9/L; $P = 0.0508$).

There were no statistically significant changes in alanine transaminase at 6 mo after treatment ($P = 0.091984$). There were statistically significant changes in aspartate aminotransferase ($P = 0.0454$) when comparing screening with the 6-mo time point.

The mean and median baseline eGFRs of all enrolled patients were 86.4 mL/min/1.72 m^2 and 92.7 mL/min/1.72 m^2, respectively. The mean eGFR for the MAD4 cohort at screening was 90.4 mL/min/1.72 m^2, and at the end of cycle 4 it was 86.64 mL/min/1.72 m^2. This was not a statistically significant difference ($P = 0.06499$). At 3 mo after completion of cycle 4, the mean eGFR was 78.34 mL/min/1.72 m^2, which was not significantly different from baseline ($P = 0.8650$). At the 6-mo follow-up, the mean eGFR was 73.38 mL/min/1.72 m^2, which was significantly different from screening ($P < 0.001$) but had no clinical significance.

DISCUSSION

The current study on adults with progressive metastatic or inoperable SSTR-expressing NETs suggests that treatment with ^{212}Pb-DOTAMTATE provides a clear clinical benefit regardless of the location of the primary site or grade of the tumor. This is a paradigm change from conventional ideas that PRRT needs to be done only on G1 or G2 gastroenteropancreatic NETs. We are treating these patients on the basis of their molecular biology and receptor affinity. Of the 10 subjects who received all 4 cycles, 8 (80%) demonstrated an objective, long-lasting radiologic response by RECIST 1.1, which is highly encouraging. In the pivotal multinational, randomized, double-blind, placebo-controlled phase 3 trial of sunitinib in patients with advanced, well-differentiated pancreatic NETs, sunitinib demonstrated an ORR of 9.3%, compared with 0% in the placebo group (*14*). In the more recent NETTER-1 study, which enrolled only patients with midgut NETs, the initial ORR was 18% in the ^{177}Lu-DOTATATE group compared with only 3% in the octreotide group (*7*). These data were later updated to a 13% ORR in the ^{177}Lu-DOTATATE group and 4% in the control group (*6*). Despite the relatively low ORR, substantial improvements were made in both PFS and overall survival. In the current study, although the number of patients was small, at the time of this data evaluation (median follow-up, 17.4 mo) the duration of response (14 mo) was extremely encouraging. Follow-up continues to determine the true duration of response. The phase II study is planned.

In terms of safety, ^{212}Pb-DOTAMTATE appears to be well tolerated, with mild and manageable side effects. We did not find clinically significant hematologic or hepatic toxicity, although the number of patients treated at the highest dose was small and further follow-up is necessary. We did find a statistically significant change from baseline in aspartate aminotransferase, likely explained by 1 subject whose aspartate aminotransferase level was approximately 1.5 times the upper limit of normal and likely of no clinical concern.

We did not observe any statistically significant changes in most hematologic parameters; however, we did observe an expected, statistically significant decrease in the absolute lymphocyte count during treatment that trended toward normal after completion of therapy. Although there was a decrease in the lymphocyte count, the absolute neutrophil count remained normal throughout the treatment period. No other hematologic parameters had a statistically significant change in values at the 6-mo follow-up compared with baseline.

Kidney reabsorption of radiolabeled peptides can lead to dose-limiting nephrotoxicity after PRRT. The time frame for kidney damage is unknown; however, data from external-beam radiotherapy indicate that chronic kidney failure may occur in up to 5% of patients within 5 y of a dose higher than 23 Gy (*15,16*). This concept has not been proven to be accurate for radioligand therapy but, at the moment, is the only available principle for regulatory agencies. Nevertheless, some centers strictly following the recommended kidney tolerance thresholds and not exceeding 4 × 7.4 GBq ^{177}Lu-DOTATATE reported either no grade 3 or 4 subacute nephrotoxicity (in 323 patients) (*17*) or only 1.5% grade 3 or 4 nephrotoxicity (in 807 patients) (*18*). Results from a recently published retrospective review on a 5-y follow-up of NET patients treated with ^{225}Ac-DOTATOC show there was an average eGFR loss of 8.4 mL/min per year, which was more pronounced in patients treated with higher doses (*19*). In the present study, 3 patients experienced serious TEAEs related to the kidney. Two patients in the SAD cohort had transient decreases in renal function due to dehydration; these were determined to be unrelated to the investigational drug. Patient MAD4-03, who obtained a CR from treatment, experienced acute kidney injury and resultant persistent chronic kidney disease. This 75-y-old patient had several confounding factors, including a longstanding history of obesity, hypertension, and poorly controlled type 2 diabetes mellitus and experienced a cerebrovascular accident before the kidney insult. Baseline serum creatinine and eGFR were 0.84 mg/dL and 92.5 mL/min/1.72 m^2, respectively. Both values remained relatively stable throughout treatment and began to change approximately 2 wk after the last treatment with ^{212}Pb-DOTAMTATE. The serum creatinine continued to rise to a high of 1.97 mg/dL, and the eGFR decreased to 28.5 mL/min/1.72 m^2, consistent with stage 3 chronic kidney disease. Renal function data collection continues for all MAD4 cohort patients, and long-term follow-up should shed light on what impact, if any, ^{212}Pb-DOTAMTATE has on the kidneys. The most common nonhematologic, nonrenal, or nonhepatic adverse event reported was nausea, followed by transient alopecia. Alopecia was moderate, and hair growth resumed quickly after treatment had been completed.

It is difficult to perform appropriate comparisons with the few published clinical trials of TAT in NET patients, since the radiopharmaceuticals used, and subject selection, among other factors, differ from ours. Nonetheless, data published by Kratochwil et al. in 2014 showed preliminary good results using ^{213}Bi-DOTATOC TAT (*20*). Prolonged responses were reported for the 7 patients in the study. Recently, data from Ballal et al. using ^{225}Ac-DOTATATE TAT in advanced, progressive, or PRRT-refractory gastroenteropancreatic NET patients reported a PR in 15 of 24 (62.5%) evaluable patients (by conventional imaging) and stable disease in 9 of 24 (37.5%) (*21*). In contrast to our study, all patients in the study of Ballal et al. had already been treated with ^{177}Lu-DOTATATE, and more than half (56%) had progressive disease. Nevertheless, the results show that ^{225}Ac-DOTATATE TAT is a promising treatment option, even in patients previously treated with ^{177}Lu-DOTATATE PRRT.

To the best of our knowledge, our study is the first in humans to evaluate the safety and response of ^{212}Pb-DOTAMTATE in NET. Although the number of patients is small, the results are promising (Fig. 4).

Strengths of this study include robust imaging data and inclusion of subjects with progressive metastatic NETs regardless of location of primary tumor and Ki-67 grade. Limitations of this study include a small number of patients recruited from only 1 clinical site, lack of central imaging, and limited follow-up.

CONCLUSION

^{212}Pb-DOTAMTATE is safe. Preliminary efficacy results are highly promising. If these results are confirmed in a larger, randomized, multicenter clinical trial, ^{212}Pb-DOTAMTATE would provide a substantial benefit over currently Food and Drug Administration–approved therapies for patients with metastatic or inoperable SSTR-expressing NETs regardless of the grade and location of the primary tumor.

DISCLOSURE

This research was sponsored by RadioMedix, Inc. and was funded in part with federal funds from the National Cancer Institute, National Institutes of Health, Department of Health and Human Services, under SBIR NCI phase II contract HHSN261201800048C. Ebrahim Delpassand and Izabela Tworowska are employees and equity holders of RadioMedix. Julien Torgue and Jason Hurt are employees at Orano Med. No other potential conflict of interest relevant to this article was reported.

ACKNOWLEDGMENTS

We gratefully acknowledge all participating patients and the support provided by the nuclear medicine and laboratory staff of Excel Diagnostics and Nuclear Oncology Center, RadioMedix, and Orano Med.

KEY POINTS

QUESTION: Is ^{212}Pb-DOTAMTATE TAT a feasible and effective treatment modality for NET patients?

PERTINENT FINDINGS: The preliminary results in this first-in-humans study of ^{212}Pb-DOTAMTATE TAT show that it is a well-tolerated treatment with an overall response rate of 80% in the first 10 subjects treated with the effective dose.

IMPLICATIONS FOR PATIENT CARE: TAT with ^{212}Pb-DOTAMTATE in NET patients has shown great potential, exceeding the standard-of-care treatments currently available, and thus, a phase 2 study will start soon.

REFERENCES

1. Oronsky B, Ma PC, Morgensztern D, Carter CA. Nothing but NET: a review of neuroendocrine tumors and carcinomas. *Neoplasia.* 2017;19:991–1002.
2. Fani M, Nicolas GP, Wild D. Somatostatin receptor antagonists for imaging and therapy. *J Nucl Med.* 2017;58(suppl 2):61S–66S.
3. Stueven AK, Kayser A, Wetz C, et al. Somatostatin analogues in the treatment of neuroendocrine tumors: past, present and future. *Int J Mol Sci.* 2019;20:3049.
4. Shah MH, Goldner WS, Halfdanarson TR, et al. NCCN guidelines insights: neuroendocrine and adrenal tumors, version 2.2018. *J Natl Compr Canc Netw.* 2018;16:693–702.

5. Das S, Al-Toubah T, El-Haddad G, Strosberg J. ^{177}Lu-DOTATATE for the treatment of gastroenteropancreatic neuroendocrine tumors. *Expert Rev Gastroenterol Hepatol.* 2019;13:1023–1031.
6. Mittra ES. Neuroendocrine tumor therapy: ^{177}Lu-DOTATATE. *AJR.* 2018;211: 278–285.
7. Strosberg J, El-Haddad G, Wolin E, et al. Phase 3 trial of ^{177}Lu-Dotatate for midgut neuroendocrine tumors. *N Engl J Med.* 2017;376:125–135.
8. Li M, Sagastume EA, Lee D, et al. $^{203/212}$Pb theranostic radiopharmaceuticals for image-guided radionuclide therapy for cancer. *Curr Med Chem.* 2020;27: 7003–7031.
9. Nelson BJB, Andersson JD, Wuest F. Targeted alpha therapy: progress in radionuclide production, radiochemistry, and applications. *Pharmaceutics.* 2020;13:49.
10. Kwekkeboom DJ, de Herder WW, Kam BL, et al. Treatment with the radiolabeled somatostatin analog [^{177}Lu-DOTA^0,Tyr^3]octreotate: toxicity, efficacy, and survival. *J Clin Oncol.* 2008;26:2124–2130.
11. Khan S, Krenning EP, van Essen M, Kam BL, Teunissen JJ, Kwekkeboom DJ. Quality of life in 265 patients with gastroenteropancreatic or bronchial neuroendocrine tumors treated with [^{177}Lu-DOTA^0,Tyr^3]octreotate. *J Nucl Med.* 2011;52: 1361–1368.
12. Makvandi M, Dupis E, Engle JW, et al. Alpha-emitters and targeted alpha therapy in oncology: from basic science to clinical investigations. *Target Oncol.* 2018;13: 189–203.
13. Huang B, Tian L, Talukder E, Rothenberg M, Kim DH, Wei LJ. Evaluating treatment effect based on duration of response for a comparative oncology study. *JAMA Oncol.* 2018;4:874–876.
14. Raymond E, Dahan L, Raoul JL, et al. Sunitinib malate for the treatment of pancreatic neuroendocrine tumors. *N Engl J Med.* 2011;364:501–513.
15. Bergsma H, Konijnenberg MW, van der Zwan WA, et al. Nephrotoxicity after PRRT with ^{177}Lu-DOTA-octreotate. *Eur J Nucl Med Mol Imaging.* 2016;43: 1802–1811.
16. Marks LB, Yorke ED, Jackson A, et al. Use of normal tissue complication probability models in the clinic. *Int J Radiat Oncol Biol Phys.* 2010;76(suppl) S10–S19.
17. Bergsma H, Konijnenberg MW, van der Zwan WA, et al. Nephrotoxicity after PRRT with ^{177}Lu-DOTA-octreotate. *Eur J Nucl Med Mol Imaging.* 2016;43:1802–1811.
18. Bodei L, Kidd M, Paganelli G, et al. Long-term tolerability of PRRT in 807 patients with neuroendocrine tumours: the value and limitations of clinical factors. *Eur J Nucl Med Mol Imaging.* 2015;42:5–19.
19. Kratochwil C, Apostolidis L, Rathke H, et al. Dosing ^{225}Ac-DOTATOC in patients with somatostatin-receptor-positive solid tumors: 5-year follow-up of hematological and renal toxicity. *Eur J Nucl Med Mol Imaging.* 2021;49:54–63.
20. Kratochwil C, Giesel FL, Bruchertseifer F, et al. ^{213}Bi-DOTATOC receptor-targeted alpha-radionuclide therapy induces remission in neuroendocrine tumours refractory to beta radiation: a first-in-human experience. *Eur J Nucl Med Mol Imaging.* 2014;41:2106–2119.
21. Ballal S, Yadav MP, Bal C, Sahoo RK, Tripathi M. Broadening horizons with ^{225}Ac-DOTATATE targeted alpha therapy for gastroenteropancreatic neuroendocrine tumour patients stable or refractory to ^{177}Lu-DOTATATE PRRT: first clinical experience on the efficacy and safety. *Eur J Nucl Med Mol Imaging.* 2020;47: 934–946.

Utility of ^{18}F-rhPSMA-7.3 PET for Imaging of Primary Prostate Cancer and Preoperative Efficacy in N-Staging of Unfavorable Intermediate- to Very High-Risk Patients Validated by Histopathology

Thomas Langbein[1], Hui Wang[1,2], Isabel Rauscher[1], Markus Kroenke[1], Karina Knorr[1], Alexander Wurzer[3], Kristina Schwamborn[4], Tobias Maurer[5], Thomas Horn[6], Bernhard Haller[7], Hans-Jürgen Wester[3], and Matthias Eiber[1]

[1]Department of Nuclear Medicine, Klinikum Rechts der Isar, School of Medicine, Technical University of Munich, Munich, Germany; [2]Department of Nuclear Medicine, West China Hospital, Sichuan University, Chengdu, China; [3]Chair of Radiopharmacy, Technical University of Munich, Munich, Germany; [4]Institute of Pathology, Klinikum Rechts der Isar, School of Medicine, Technical University of Munich, Munich, Germany; [5]Martini-Klinik and Department of Urology, University Hospital Hamburg–Eppendorf, Hamburg, Germany; [6]Department of Urology, Klinikum Rechts der Isar, School of Medicine, Technical University of Munich, Munich, Germany; and [7]Institute of Medical Informatics, Statistics and Epidemiology, School of Medicine, Technical University of Munich, Munich, Germany

^{18}F-rhPSMA-7.3, the lead compound of a new class of radiohybrid prostate-specific membrane antigen (rhPSMA) ligand, is currently in phase III trials for prostate cancer (PCa) imaging. Here, we describe our experience in primary PCa staging. **Methods:** We retrospectively identified 279 patients with primary PCa who underwent ^{18}F-rhPSMA-7.3 PET/CT (staging cohort). A subset of patients (83/279) subsequently underwent prostatectomy with lymph node (LN) dissection without prior treatment (efficacy cohort). The distribution of tumor lesions was determined for the staging cohort and stratified by National Comprehensive Cancer Network risk score. Involvement of pelvic LNs was assessed retrospectively by 3 masked independent central readers, and a majority rule was used for analysis. Standard surgical fields were rated on a 5-point scale independently for PET and for morphologic imaging. Results were compared with histopathologic findings on a patient, right-vs.-left, and template basis. **Results:** For the staging cohort, ^{18}F-rhPSMA-7.3 PET was positive in 275 of 279 (98.6%), 106 of 279 (38.0%), 46 of 279 (16.5%), 65 of 279 (23.3%), and 5 of 279 (1.8%) patients for local, pelvic nodal, extrapelvic nodal, metastatic bone, and visceral metastatic disease, respectively. In the efficacy cohort, LN metastases were present in 24 of 83 patients (29%) and were located in 48 of 420 (11%) resected templates and in 33 of 166 (19.9%) hemipelvic templates in histopathology. The majority vote results showed that patient-level sensitivity, specificity, and accuracy for pelvic nodal metastases were 66.7% (95% CI, 44.7%–83.6%), 96.6% (95% CI, 87.3%–99.4%), and 88.0% (95% CI, 78.5%–93.8%), respectively, for ^{18}F-rhPSMA-7.3 PET and 37.5% (95% CI, 19.6%–59.2%), 91.5% (95% CI, 80.6%–96.8%), and 75.9% (95% CI, 65.0%–84.3%), respectively, for morphologic imaging. ^{18}F-rhPSMA-7.3 showed higher interobserver agreement than morphologic imaging (patient-level Fleiss $\kappa = 0.54$ [95% CI, 0.47–0.62] vs. 0.24 [95% CI, 0.17–0.31]). A mean SUV ratio of 6.6 (95% CI, 5.2–8.1) documented a high image contrast between local tumors and adjacent low urinary tracer retention. **Conclusion:** ^{18}F-rhPSMA-7.3 PET offers diagnostic performance superior to morphologic imaging for primary N-staging of newly diagnosed PCa, shows lower interreader variation, and offers good distinction between primary-tumor activity and bladder background activity. With increasing National Comprehensive Cancer Network risk group, an increasing frequency of extraprostatic tumor lesions was observed.

Key Words: ^{18}F-rhPSMA-7.3; PET; primary prostate cancer; lymph node metastases; histopathology; interobserver agreement

J Nucl Med 2022; 63:1334–1342
DOI: 10.2967/jnumed.121.263440

In recent years, prostate-specific membrane antigen (PSMA) PET with tracers such as ^{68}Ga-PSMA-11 has become increasingly used for diagnostic imaging in patients with prostate cancer (PCa) (*1*). The proPSMA trial established that ^{68}Ga-PSMA-11 PET, compared with conventional imaging, is a superior imaging modality for patients with primary high-risk PCa but histopathologic validation of the ^{68}Ga-PSMA-11 PET findings is lacking in most lesions (*2*). Most recently, a bicentric phase III trial reported the diagnostic accuracy of ^{68}Ga-PSMA-11 for pelvic N-staging (*3*). In addition to multiple mainly retrospective series, these studies were pivotal for the recent integration of PSMA-ligand PET into various guidelines and for the Food and Drug Administration approval of ^{68}Ga-PSMA-11 (*4–6*).

However, ^{68}Ga-PSMA-11 is not without disadvantages. Substantial accumulation in the urinary bladder through rapid urinary excretion can hinder detection of pelvic lesions (*7,8*). Conversely, because of the longer half-life of ^{18}F-labeled PSMA ligands, along with their potential for larger-batch production and their lower positron range resulting in higher image spatial resolution, they offer several logistical benefits and potential for better performance than their ^{68}Ga-labeled counterparts (*9*). ^{18}F-DCFPyL was recently approved by the Food and Drug Administration for biochemical recurrence, but it also exhibits high tracer retention in the urinary system (*10,11*).

Radiohybrid PSMA (rhPSMA) ligands are a new class of diagnostic and therapeutic PSMA ligands that can be efficiently labeled

---

Received Oct. 26, 2021; revision accepted Dec. 28, 2021.

For correspondence or reprints, contact Thomas Langbein (thomas.langbein@tum.de).

with ^{18}F and with radiometals (*12*). Promising preliminary imaging data (*13,14*) have been reported for ^{18}F-rhPSMA-7, which comprises 4 diastereoisomers. One of these, ^{18}F-rhPSMA-7.3, was selected as the lead rhPSMA compound for clinical development based on preclinical data (*15*). To date, the safety and biodistribution of ^{18}F-rhPSMA-7.3 have been established in healthy volunteers and PCa patients. ^{18}F-rhPSMA-7.3 has been shown to have low average urinary excretion, and diagnostic efficacy has been demonstrated in patients with biochemical recurrence of PCa (*16–18*). ^{18}F-rhPSMA-7.3 is currently under evaluation in 2 phase III studies, for primary and biochemical recurrence of PCa (NCT04186845 and NCT04186819).

The present retrospective analysis provides the first data, to our knowledge, on use of ^{18}F-rhPSMA-7.3 PET for primary staging in patients with newly diagnosed PCa. Specifically, we aimed to describe the distribution of tumor lesions stratified by National Comprehensive Cancer Network (NCCN) risk groups (*4*) and to evaluate interobserver variability and diagnostic performance for preoperative N-staging in patients with unfavorable intermediate- to very high-risk disease.

MATERIALS AND METHODS

Study Design and Patient Populations

We retrospectively extracted data from all patients included in our institution's database who underwent ^{18}F-rhPSMA-7.3 PET/CT for primary staging of PCa between November 2018 and April 2020 (staging cohort; $n = 279$). To analyze the interobserver variability and diagnostic efficacy of ^{18}F-rhPSMA-7.3 PET for N-staging validated by histopathology, we selected all patients who underwent subsequent radical prostatectomy and extended pelvic lymph node (LN) dissection (efficacy cohort; $n = 83$). Table 1 presents patient characteristics for both groups. Figure 1 details the cohorts and outlines the clinical, imaging, and histopathologic data that were collected.

The retrospective analysis was approved by the Ethics Committee of the Technical University Munich (permit 99/19), and the requirement to obtain informed consent was waived. The administration of ^{18}F-rhPSMA-7.3 complied with the German Medicinal Products Act, AMG §13 2b, and the responsible regulatory body (Government of Oberbayern).

^{18}F-rhPSMA-7.3 Synthesis, Administration, and Image Acquisition

^{18}F-rhPSMA-7.3 was synthesized as recently reported (*12*) and administered as an intravenous bolus (median, 335 MBq; range, 301–372 MBq) a median of 72 min (range, 65–80 min) before the scan. Patients underwent ^{18}F-rhPSMA-7.3 PET/CT on a Biograph mCT Flow scanner (Siemens Medical Solutions) as recently described (*13,14*). All patients received a diagnostic CT scan after intravenous contrast injection (Iomeron 300 [Bracco], weight-adapted, 1.5 mL/kg) and oral intake of diluted contrast medium (300 mg ioxitalamate [Telebrix; Guerbet]). Furosemide (20 mg intravenously) was administered to all patients at the time of ^{18}F-rhPSMA-7.3 injection, and patients were asked to void urine before the scan. PET scans were acquired in 3-dimensional mode with an acquisition time of 2 min per bed position in flow technique (1.1 mm/s). Emission data were corrected for randoms, dead time, scatter, and attenuation and were reconstructed iteratively by an ordered-subsets expectation maximization algorithm (4 iterations, 8 subsets) followed by a postreconstruction smoothing gaussian filter (5 mm in full width at half maximum).

Image Analysis

In the staging cohort, the distribution of tumor lesions was described using the molecular imaging TNM system from the Prostate Cancer Molecular Imaging Standardized Evaluation system (*19*). The results for this cohort were taken from the clinical reads. To determine the efficacy for pelvic N-staging, dedicated rereads of the ^{18}F-rhPSMA-7.3 PET/CT datasets from the efficacy cohort were performed by 3 board-certified nuclear medicine physicians (3, 6, and 9 y of experience in PSMA-ligand PET). The readers did not know the histopathology results. In a first step, the anatomic data using the diagnostic contrast-enhanced CT dataset were analyzed by the readers. Next, after at least 4 wk, a second read of the corresponding ^{18}F-rhPSMA-7.3 scan was performed using anatomic images only to correlate an area of suggestive uptake to the corresponding LN template. Findings for both reads were reported on a template level using a 5-point Likert scale (1, tumor manifestation; 2, probably tumor manifestation, 3, equivocal, 4, probably benign, 5, benign).

To determine the contrast between local primary-tumor uptake and bladder retention of ^{18}F-rhPSMA-7.3, SUV_{mean} for ^{18}F-rhPSMA-7.3 was determined within standardized isocontour volumes of interest with 40% of the SUV_{max}, drawn over the bladder and the primary-tumor lesion.

Histopathology

Extended pelvic lymphadenectomy was performed as previously described (*20,21*) to collect right/left common iliac vessel, right/left internal iliac vessel, right/left external iliac vessel, and right/left obturator fossa standard LN templates. Further templates (e.g., presacral/pararectal) were resected if the ^{18}F-rhPSMA-7.3 PET had shown positive LNs outside these regions. The uropathologists did not know the imaging data.

Statistical Analysis

For quantitative measurements, mean values and SDs are presented. ^{18}F-rhPSMA-7.3 PET and morphologic imaging results were compared with histopathologic results from resected LNs on a patient, right-vs.-left, and template basis. Overall diagnostic accuracy was assessed using receiver-operating-characteristic (ROC) analyses. Areas under the ROC curves, with 95% CIs, were compared for both ^{18}F-rhPSMA-7.3 PET and morphologic imaging. For the patient-based analysis, the method by DeLong et al. (*22*) for 2 correlated ROC curves was used, and that by Obuchowski (*23*) was used for right-vs.-left–based and template-based analyses to account for the multiple assessments within a patient.

A dichotomization of the 5-point Likert scale ratings was performed for analysis of the sensitivity, specificity, and accuracy of the ^{18}F-rhPSMA-7.3 PET and morphologic imaging. To reflect a real-world approach, equivocal findings were counted as positive. To estimate cumulative diagnostic results from all 3 readers, a majority vote was used. The results from all 3 readers dichotomized into negative and positive assessments were compared, and in cases of any disagreement, the final assessment was based on the majority decision (i.e., a 2:1 decision).

For the patient-level analyses, exact CIs were estimated for these measures. For the right-vs.-left–based and template-based analyses, logistic generalized estimating equation models were fitted to the data to account for the correlation of multiple observations within the same patient (*24,25*). For the generalized estimating equation model, an independent correlation structure was assumed. To investigate a correlation between NCCN risk groups and frequency of extraprostatic lesions, a χ^2 test was used. A significance level of 5% was used throughout. All statistical analyses were performed using the statistical software R (*26*), with pROC (*27*) and geepack (*28*).

Interobserver agreement was evaluated using Fleiss multiple-rater κ (*29*) on a patient, right-vs.-left, and template basis, with 95% CIs reported. Interpretation of κ was based on a reproducibility classification provided by Landis and Koch (*30*). Significant differences between

TABLE 1
Characteristics of Staging and Efficacy Cohorts

Characteristic	Staging cohort	Efficacy cohort
Patients	279 (100%)	83 (29.7%)
Age (y)		
Median	70	66
Interquartile range	63–76	62–74
Prostate-specific antigen (ng/mL)*[†]		
Median	13.0	11
Interquartile range	7.2–26.9	7.0–17.8
ISUP grading[§]		
1		0 (0%)
2	46 (16.5%)	15 (18.1%)
3	61 (21.9%)	25 (30.1%)
4	65 (23.3%)	23 (27.7%)
5	85 (30.5%)	19 (22.9%)
Neoadjuvant treatment before PET/CT	16 (5.7%)	0 (0%)
NCCN risk group		
Very low	1 (0.4%)	0 (0.0%)
Low	7 (2.5%)	0 (0.0%)
Favorable intermediate	18 (6.5%)	0 (0.0%)
Unfavorable intermediate	74 (26.5%)	36 (43.4%)
High	107 (38.4%)	32 (38.6%)
Very high	72 (25.8%)	15 (18.1%)
Time between PET/CT and surgery (d)		
Median		29
Interquartile range		15–46
Pathologic T-stage		
≤pT2c		28 (33.7%)
pT3a		18 (21.7%)
≥pT3b		37 (44.6%)
Pathologic N-stage		
pN0		59 (71.1%)
pN1		24 (28.9%)
Size of largest LN metastasis per patient (mm)		
Median		8
Range		1.5–55

ISUP = International Society of Urological Pathology.
*At time of imaging.
[†] Unavailable for 2 patients of staging cohort.
[§] Unavailable for 9 patients in staging cohort and for 1 patient in efficacy cohort.
Qualitative data are number and percentage.

methods were considered present when the 95% CI were not overlapping.

RESULTS

Distribution of Tumor Lesions on ^{18}F-rhPSMA-7.3 PET

For the staging cohort based on clinical reads, ^{18}F-rhPSMA-7.3 PET was positive for local disease in 275 of 279 patients (98.6%), for pelvic LN metastases in 106 of 279 (38.0%), for extrapelvic LN metastases in 46 of 279 (16.5%), for bone metastases in 65 of 279 (23.3%), and for visceral metastases in 5 of 279 (1.8%). On a patient level, 156 patients had only disease limited to the prostate (N0M0), and 42 patients had locoregional LN metastases but no distant metastases (N1M0). In 15 patients, extrapelvic LN metastases but no other distant metastases were present (NxM1a), and 15 patients presented with local tumor and only bone metastases (N0M1b). The distribution of extrapelvic lesions stratified by

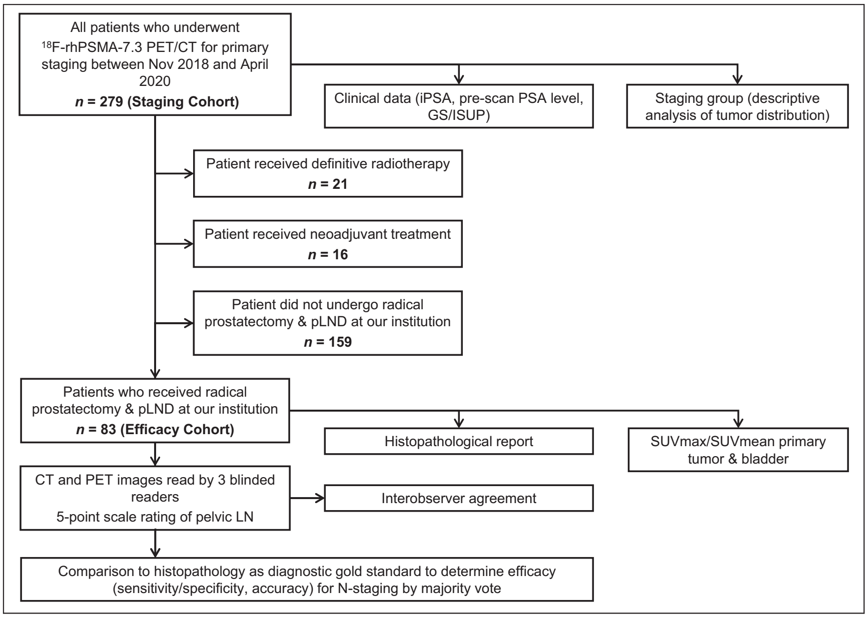

FIGURE 1. Flowchart of patient selection and data analysis. GS = Gleason score; iPSA = initial prostate-specific antigen; ISUP = International Society of Urological Pathology; pLND = pelvic LN dissection; PSA = prostate-specific antigen.

NCCN risk group is presented in Figure 2. The patient-based pattern of lesion distribution is presented in Supplemental Table 1. A moderate but highly significant correlation between risk groups and the frequency of extraprostatic lesions was found, with an increasing prevalence in higher-risk groups (Pearson χ^2 test for miN1: $\chi^2_5 = 65.6$, $P < 0.001$, $\varphi = 0.485$; for miM1: $\chi^2_5 = 31.4$, $P < 0.001$, $\varphi = 0.335$).

On the basis of clinical reads in the efficacy cohort, ^{18}F-rhPSMA-7.3 PET was positive in 82 of 83 (98.8%) and 20 of 83 (24.1%) subjects for local and pelvic nodal disease (N1M0), respectively. One and 6 patients underwent primary surgery, with distant metastases being either only extrapelvic nodal (M1a) or only metastatic bone disease (M1b), respectively. Postoperative histopathology showed LN metastases in 24 of 83 patients; the median size of the largest LN metastasis per patient was 8 mm (range, 1.5–55 mm).

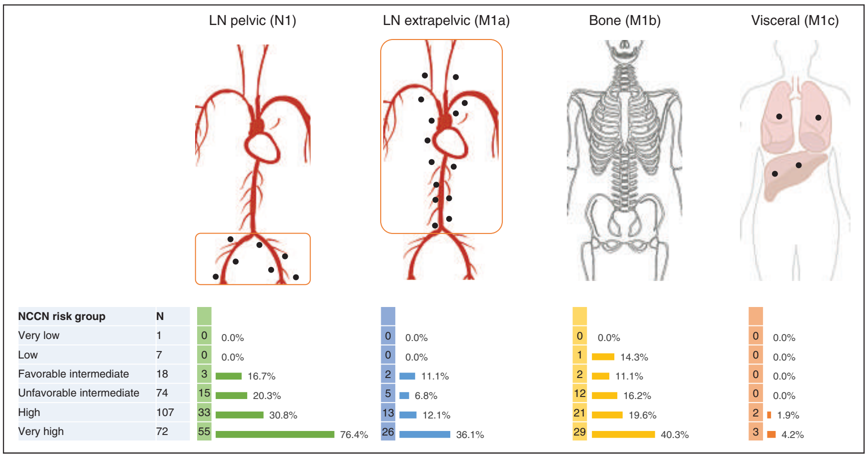

FIGURE 2. Distribution of extraprostatic tumor lesions in staging cohort (*n* = 279)

Diagnostic Accuracy of ^{18}F-rhPSMA-7.3 PET and Morphologic Imaging for Pelvic LN Metastases

In the efficacy cohort, LN metastases were present in 48 of 420 (11%) resected templates, in 33 of 166 (20%) hemipelvic templates, and in 24 of 83 patients (29%). In total, 1,763 nodes were removed, with a median of 20 (interquartile range, 15–27) per patient. A patient example is presented in Figure 3.

On patient-level–based majority reads, ^{18}F-rhPSMA-7.3 PET was read to be positive in 18 of 83 patients, resulting in 16 true-positive and 2 false-positive cases. It was read to be negative in 65 patients, including 8 false-negative and 57 true-negative cases. The result was a patient-level sensitivity, specificity, and accuracy for pelvic nodal metastases of 66.7% (95% CI, 44.7%–83.6%), 96.6% (95% CI, 87.3%–99.4%), and 88.0% (95% CI, 78.5%–93.8%), respectively. Morphologic imaging was read to be positive in 14 of 83 patients, resulting in 9 true-positive and 5 false-positive cases. It was read to be negative in 69 patients, including 15 false-negative and 54 true-negative cases. The corresponding patient-level sensitivity, specificity, and accuracy were 37.5% (95% CI, 19.6%–59.2%), 91.5% (95% CI, 80.6%–96.8%), and 75.9% (95% CI, 65.0%–84.3%), respectively.

On hemipelvic-based majority reads, ^{18}F-rhPSMA-7.3 PET was read to be positive in 25 of 166 assessments, resulting in 23 true-positive and 2 false-positive assessments. It was read to be negative in 141 assessments, including 10 false-negative and 131 true-negative assessments. The result was a sensitivity, specificity, and accuracy for pelvic nodal metastases of 69.7% (95% CI, 50.0%–84.1%), 98.5% (95% CI, 94.3%–99.6%), and 92.8% (95% CI, 87.4%–96.0%), respectively. Morphologic imaging was read to be positive in 15 of 166 assessments, resulting in 9 true-positive and 6 false-positive assessments. It was read to be negative in 151 assessments, including 24 false-negative and 127 true-negative assessments. The corresponding sensitivity, specificity, and accuracy were 27.3% (95% CI, 16.5%–41.6%), 95.5% (95% CI, 89.3%–98.2%), and 81.9% (95% CI, 74.9%–87.3%), respectively.

On template-based majority reads, ^{18}F-rhPSMA-7.3 PET had a sensitivity, specificity, and accuracy for pelvic nodal metastases of 70.8% (95% CI, 55.6%–82.5%), 98.3% (95% CI, 96.6%–99.2%), and 95.5% (95% CI, 93.1%–97.1%), respectively. Morphologic imaging showed a template-level sensitivity, specificity, and accuracy of 12.5% (95% CI, 6.0%–24.3%), 98.3% (95% CI, 96.6%–99.2%), and 89.5% (95% CI, 83.9%–93.4%), respectively. Detailed results for individual readers are provided in Table 2.

The ROC analysis showed a higher diagnostic performance for ^{18}F-rhPSMA-7.3 than for morphologic imaging for all 3 readers on both a patient basis and a hemipelvic

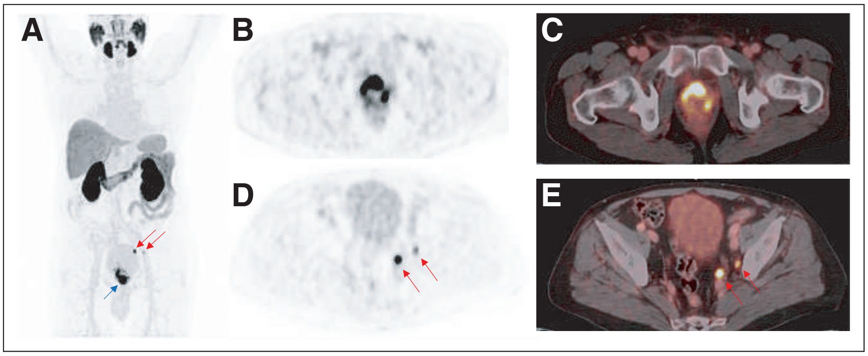

FIGURE 3. A 72-y-old patient with high-risk PCa (iPSA, 44 ng/mL) who underwent ^{18}F-rhPSMA-7.3 PET/CT illustrating primary tumor (blue arrow) and pelvic LN metastases (red arrows) histologically confirmed by radical prostatectomy (pT3b pN1 [2/34]; Gleason score, 3 + 4 = 7b): maximum-intensity projection (A); PET (B and D); fused PET/CT (C and E).

basis. On the patient-level analysis, the differences in the areas under the ROC curves were statistically significant for readers 1 and 2 on a patient basis and for all readers on a hemipelvic and template basis (Table 3).

Interobserver Agreement for Pelvic N-Staging

Interobserver agreement was significantly higher for ^{18}F-rhPSMA-7.3 PET than for morphologic imaging for assessment on a patient basis, on a hemipelvic basis, and per LN template. The patient-level interobserver agreement was moderate (Fleiss $\kappa = 0.54$; 95% CI, 0.47–0.62) for ^{18}F-rhPSMA-7.3 PET versus fair (Fleiss $\kappa = 0.24$; 95% CI, 0.17–0.31) for morphologic imaging. Similarly, interobserver agreement was moderate for left-sided nodes (Fleiss $\kappa = 0.58$; 95% CI, 0.50–0.66) and right-sided nodes (Fleiss $\kappa = 0.57$; 95% CI, 0.49–0.65) in ^{18}F-rhPSMA-7.3 PET but was only fair for left-sided nodes (left: Fleiss $\kappa = 0.20$ [95% CI, 0.12–0.27]; right: Fleiss $\kappa = 0.24$ [95% CI, 0.17–0.32]) in morphologic imaging. Supplemental Figure 1 displays the interobserver agreements and data for template-based assessments.

Uptake in Primary Tumor and Tracer Retention in Urinary Tract

^{18}F-rhPSMA-7.3 uptake in the prostate was present in 82 of 83 patients who underwent surgery, with a mean SUV_{mean} of 13.0 (range, 2.0–54.4). Retention in the urinary bladder at the time of imaging was rather low, with a mean SUV_{mean} of 2.5 (range, 0.9–18.5). Consequently, tumor-to-bladder contrast was high, with a mean ratio of 6.6 (range, 0.8–40.1) for SUV_{mean}. Data are presented in Table 4 and Supplemental Figure 2.

DISCUSSION

Here, we present a retrospective analysis on the use of ^{18}F-rhPSMA-7.3 PET/CT for primary staging of newly diagnosed PCa. The distribution of pelvic LN metastases and extrapelvic tumor lesions in this cohort was clearly associated with NCCN risk groups. In a subset of patients, we determined a high diagnostic performance of ^{18}F-rhPSMA-7.3 PET for N-staging of patients with unfavorable intermediate- to very high-risk PCa, validated by histopathology. Interobserver agreement of ^{18}F-rhPSMA-7.3 PET for N-staging among 3 independent readers showed sufficient consistency.

Currently, the standard of care for N-staging PCa relies on cross-sectional imaging and bone scintigraphy mainly in high-risk PCa (*4*). The reliable detection of LN metastases is especially challenging given the presence of LN metastases in morphologically nonenlarged LNs (*31*). Therefore, detection efficacy is low and based mainly on size, with known limitations, especially for LNs under 8 mm (*32,33*).

The clinical introduction of PSMA-targeting PET tracers offers a high potential to increase detection of LN metastases, and several studies have shown promising results with ^{68}Ga-labeled compounds (*34,35*). A prospective, multicenter study compared the accuracy of ^{68}Ga-PSMA-11 PET/CT and conventional imaging with CT and bone scanning for primary staging of pelvic LN metastases and distant metastases (*2*). The accuracy of ^{68}Ga-PSMA-11 PET/CT was superior to that of conventional imaging (92% vs. 65%), and only 15% of patients had a change of clinical management after conventional imaging, compared with 28% after ^{68}Ga-PSMA-11 PET/CT. However, the study lacked histopathologic validation of LN involvement in a substantial number of patients (only 83/302 patients underwent pelvic LN sampling). Maurer et al. conducted an early retrospective study of ^{68}Ga-PSMA-11 PET for LN staging in 130 patients with intermediate- to high-risk PCa and reported a 65.9% and 68.3% sensitivity, and a 98.9% and 99.1% specificity, on patient- and template-based analyses, respectively (*36*).

Similar specificity but lower sensitivity was reported by Klingenberg et al. in a larger retrospective investigation of newly diagnosed patients with high-risk PCa (*37*). For ^{68}Ga-PSMA-11, they reported a sensitivity, specificity, and accuracy of 30.6%, 96.5%, and 83.1%, respectively. For ^{68}Ga-PSMA-I&T in 40 patients with intermediate- or high-risk disease, Cytawa et al. found a per-region sensitivity, specificity, and accuracy of 35.0%, 98.4%, and 93.0%, respectively, for nodal metastasis detection (*38*).

Data for the recently approved ^{18}F-DCFPyL from the OSPREY trial, which investigated the detection performance for pelvic LN metastases in men with high-risk PCa, showed a specificity ranging from 96% to 99% across 3 readers, whereas sensitivity ranged from 31% to 42% (*11*). Similar to data reported for all other PSMA ligands, the specificity of ^{18}F-rhPSMA-7.3 for pelvic LN metastases is high.

The sensitivity of ^{18}F-rhPSMA-7.3 in this study (e.g., 66.7% on a patient level) appears substantially higher than that indicated by the above-mentioned data for ^{68}Ga-PSMA or ^{18}F-DCFPyL. A possible reason might be the nodal lesion size. In the efficacy cohort of our study, the median size of the largest LN metastasis per patient was 8 mm. Hope et al. demonstrated a higher sensitivity of ^{68}Ga-PSMA-11 PET in larger pelvic LN metastasis ($>$10 mm) (*3*). Comparable findings were shown by the OSPREY trial, where the sensitivity of ^{18}F-DCFPyL was clearly dependent on lesion size. Exclusion of lesions smaller than 5 mm resulted in a sensitivity of 60.0% (*11*). Potential other factors might also include scanner technique and reader experience.

Our retrospective analysis of the novel PSMA ligand ^{18}F-rhPSMA-7.3 confirms superiority of PSMA-targeted molecular imaging over conventional imaging for N-staging in patients with intermediate- to very high-risk primary PCa. ^{18}F-rhPSMA-7.3 achieved an overall accuracy of 88.0%, 92.8%, and 95.5% for the patient-level, hemipelvic-level, and template analyses, respectively, compared with 75.9%, 81.9%, and 89.5%, respectively, for conventional imaging.

TABLE 2
Histologically Verified Diagnostic Accuracy of ^{18}F-rhPSMA-7.3 PET and Morphologic Imaging for Preoperative N-Staging

		^{18}F-rhPSMA-7.3 PET/CT			Morphologic imaging		
Base	Reader	Sensitivity	Specificity	Accuracy	Sensitivity	Specificity	Accuracy
Patient	1	66.7% (44.7%–84.4%)	94.9% (85.9%–98.9%)	86.7% (77.5%–93.2%)	29.2% (12.6%–51.1%)	94.9% (85.9%–98.9%)	75.9% (65.3%–84.6%)
	2	70.8% (48.9%–87.4%)	96.6% (88.3%–99.6%)	89.2% (80.4%–94.9%)	41.7% (22.1%–63.4%)	89.8% (79.2%–96.2%)	75.9% (65.3%–84.6%)
	3	66.7% (44.7%–84.4%)	94.9% (85.9%–98.9%)	86.7% (77.5%–93.2%)	58.3% (36.6%–77.9%)	84.7% (73.0%–92.8%)	77.1% (66.6%–85.6%)
	Majority vote	66.7% (44.7%–83.6%)	96.6% (87.3%–99.4%)	88.0% (78.5%–93.8%)	37.5% (19.6%–59.2%)	91.5% (80.6%–96.8%)	75.9% (65.0%–84.3%)
Right vs. left	1	69.7% (50.0%–84.1%)	97.7% (93.3%–99.3%)	92.2% (86.7%–95.5%)	21.1% (11.1%–36.6%)	97.7% (93.3%–99.3%)	82.5% (75.3%–88.0%)
	2	69.7% (50.0%–84.1%)	97.0% (90.5%–99.1%)	91.6% (85.1%–95.4%)	30.3% (19.4%–43.9%)	94.0% (86.8%–97.4%)	81.3% (74.3%–86.7%)
	3	69.7% (50.0%–84.1%)	97.0% (90.6%–99.1%)	91.6% (85.6%–95.2%)	42.4% (28.4%–57.8%)	90.2% (83.5%–94.4%)	80.7% (73.8%–86.2%)
	Majority vote	69.7% (50.0%–84.1%)	98.5% (94.3%–99.6%)	92.8% (87.4%–96.0%)	27.3% (16.5%–41.6%)	95.5% (89.3%–98.2%)	81.9% (74.9%–87.3%)
Template	1	62.5% (48.5%–74.7%)	97.6% (95.5%–98.8%)	94.0% (91.0%–96.1%)	10.4% (4.5%–22.2%)	99.0% (97.5%–99.6%)	90.0% (84.2%–93.8%)
	2	64.6% (50.3%–76.6%)	97.6% (95.2%–98.8%)	94.2% (91.2%–96.2%)	18.7% (11.9%–28.4%)	97.9% (95.5%–99.0%)	89.7% (84.7%–93.3%)
	3	70.8% (55.6%–82.5%)	97.6% (95.0%–98.9%)	94.9% (92.1%–96.7%)	18.7% (8.8%–35.7%)	96.9% (94.9%–98.1%)	88.9% (83.2%–92.8%)
	Majority vote	70.8% (55.6%–82.5%)	98.3% (96.6%–99.2%)	95.5% (93.1%–97.1%)	12.5% (6.0%–24.3%)	98.3% (96.6%–99.2%)	89.5% (83.9%–93.4%)

Data in parentheses are 95% CI.

TABLE 3
DeLong Test for Correlated ROC

Basis	Reader	AUC: ^{18}F-rhPSMA-7.3 PET/CT	AUC: Morphologic imaging	*P*
Patient	1	0.821 (0.716–0.926)	0.724 (0.606–0.843)	0.09774
	2	0.850 (0.738–0.963)	0.672 (0.526–0.817)	0.01226
	3	0.829 (0.720–0.939)	0.779 (0.662–0.896)	0.2785
Right vs. left	1	0.841 (0.745–0.938)	0.699 (0.597–0.800)	0.01195
	2	0.853 (0.762–0.944)	0.657 (0.557–0.757)	0.00041
	3	0.817 (0.708–0.925)	0.699 (0.602–0.795)	0.02655
Template	1	0.796 (0.726–0.865)	0.645 (0.579–0.712)	$6.879e^{-05}$
	2	0.822 (0.759–0.885)	0.652 (0.568–0.736)	0.00045
	3	0.847 (0.772–0.922)	0.630 (0.551–0.710)	$1.062e^{-07}$

AUC = area under ROC curve.
Data in parentheses are 95% CI.

As expected in clinical routine, we observed a clear tendency toward more frequent pelvic and extrapelvic tumor lesions with increasing NCCN group. Comparable findings have been described for the correlation of increasing prostate-specific antigen (PSA) values and the occurrence of bone metastases on bone scintigraphy for PCa staging (*39*). For example, the prevalence of bone metastases was only 2.3% at a PSA of less than 10 ng/mL, 6% at a PSA of more than 10 but less than 19.9 ng/mL, and 74.9% at a PSA of more than 100 ng/mL. For PSMA-ligand PET, the mentioned association should be considered crucial, especially in the context of primary N-staging, as nodal involvement in particular can be detected much earlier now, with a high potential to impact clinical management.

^{18}F-rhPSMA-7.3 is a single diastereoisomer of ^{18}F-rhPSMA-7, for which diagnostic accuracy has been well reported. Kroenke et al. reported the patient-level sensitivity, specificity, and accuracy of ^{18}F-rhPSMA-7 PET to be 72.2%, 92.5%, and 86.2%, respectively (*14*), which are comparable to the data in the present study. This finding supports earlier data that indicate ^{18}F-rhPSMA-7 and ^{18}F-rhPSMA-7.3 to have similar diagnostic performance for restaging patients with biochemical recurrence after radical prostatectomy (*13,18*).

A particular strength of our retrospective analysis was the evaluation of imaging data by 3 independent readers, allowing us to conduct an interobserver comparison to determine the reproducibility of interpretation of ^{18}F-rhPSMA-7.3 PET compared with morphologic imaging. The data show that the variability between ^{18}F-rhPSMA-7.3 PET readings is lower than for CT and thus suggests a more consistent, reader-independent diagnostic performance. Similar high interobserver agreement has been reported for ^{68}Ga-PSMA-11 (*40*).

A well-documented limitation of PSMA-targeting radiotracers such as ^{68}Ga-PSMA-11 and ^{18}F-DCFPyL is high retention in the urinary system and especially high accumulation in the bladder (*7,8*). For rhPSMA ligands, low retention in the urinary bladder has been reported (*41*). Our analyses for ^{18}F-rhPSMA-7.3 also revealed low urinary retention and high uptake of tumor lesions, resulting in a favorable tumor-to-bladder ratio (mean, 6.6). This could potentially increase the detection of local tumor deposits, especially in the prostate base.

Our analysis has several limitations. First, it was conducted retrospectively on a limited number of patients. This approach could—especially for the efficacy cohort—lead to a selection bias given that the cohort of patients who underwent surgery was dependent on clinical parameters, imaging results, and the patient's general health and preference. Second, the template-based analysis was limited in that the mapping between a certain LN territory in images and the surgical field is prone to errors. Third, histopathologic assessment of distant metastases was not available for most patients. ^{18}F-labeled PSMA ligands such as ^{18}F-rhPSMA-7 and ^{18}F-PSMA-1007 have been reported to exhibit a higher number of non–PCa-related uptake than ^{68}Ga-PSMA-11 (*42–45*). However, adequate reader training, interpretation in consensus with cross-sectional imaging, and the clinical context allow differentiation between

TABLE 4
^{18}F-rhPSMA-7.3 SUV_{max} and SUV_{mean} for Primary Tumors and Urinary Bladder

	Primary tumor (*n* = 82)		Urinary bladder (*n* = 82)		Primary tumor/urinary bladder (*n* = 82)	
Parameter	SUV_{max}	SUV_{mean}	SUV_{max}	SUV_{mean}	SUV_{max} ratio	SUV_{mean} ratio
Mean	22.4	13.0	4.3	2.5	6.6	6.6
95% CI	18.3–26.4	10.5–15.65	3.5–5.1	2.0–3.0	5.2–8.0	5.2–8.1
Range	3.6–86.9	2.0–54.4	1.6–31.4	0.9–18.5	0.8–34.2	0.8–40.1

benign uptake and disease. Fourth, our patient cohort was not exclusively patients with unfavorable intermediate- to high-risk disease. Given the local preference and, rarely, strong patient request, a few patients in lower NCCN groups underwent ^{18}F-rhPSMA-7.3 for N-staging—typical of a real-world setting.

CONCLUSION

The present study provided real-world clinical evidence that ^{18}F-rhPSMA-7.3 has moderate-to-high sensitivity and specificity for the detection of LN metastases in patients with intermediate- to very high-risk PCa. The data further showed that ^{18}F-rhPSMA-7.3 is a more reliable tool than morphologic imaging, with lower variability in image interpretation. A distinct association of nodal and extrapelvic tumor involvement with NCCN risk groups was found. ^{18}F-rhPSMA-7.3 compares well with other PSMA ligands and shows potential for good differentiation between primary-tumor uptake and background bladder retention.

DISCLOSURE

A patent application has been filed for rhPSMA (Hans-Jürgen Wester, Alexander Wurzer, and Matthias Eiber). Hans-Jürgen Wester and Matthias Eiber received funding from Blue Earth Diagnostics Ltd., Oxford, U.K. (licensee for rhPSMA), as part of an academic collaboration. Hans-Jürgen Wester is a founder, shareholder, and advisory board member of Scintomics GmbH, Fuerstenfeldbruck, Germany. Matthias Eiber reports prior consulting activities for Blue Earth Diagnostics Ltd., Novartis, Telix, Progenics, Bayer, Point Biopharma, and Janssen. No other potential conflict of interest relevant to this article was reported.

ACKNOWLEDGMENTS

Editorial support was provided by Dr. Catriona Turnbull (Blue Earth Diagnostics Ltd.). We thank Hannah Wörther for her contribution to the data collection.

KEY POINTS

QUESTION: What is the diagnostic efficacy of ^{18}F-rhPSMA-7.3 for N-staging of patients with intermediate- to very high-risk PCa in the primary setting?

PERTINENT FINDINGS: Compared with morphologic imaging, ^{18}F-rhPSMA-7.3 PET provides superior N-staging of high-risk primary PCa. The efficacy of ^{18}F-rhPSMA-7.3 compares well with published data for other PSMA ligands and offers a good tumor-to-bladder uptake ratio.

IMPLICATIONS FOR PATIENT CARE: ^{18}F-rhPSMA-7.3 PET can significantly improve primary N-staging versus conventional imaging.

REFERENCES

1. Lawhn-Heath C, Salavati A, Behr SC, et al. Prostate-specific membrane antigen PET in prostate cancer. *Radiology.* 2021;299:248–260.
2. Hofman MS, Lawrentschuk N, Francis RJ, et al. Prostate-specific membrane antigen PET-CT in patients with high-risk prostate cancer before curative-intent surgery or radiotherapy (proPSMA): a prospective, randomised, multicentre study. *Lancet.* 2020;395:1208–1216.
3. Hope TA, Eiber M, Armstrong WR, et al. Diagnostic accuracy of ^{68}Ga-PSMA-11 PET for pelvic nodal metastasis detection prior to radical prostatectomy and pelvic lymph node dissection: a multicenter prospective phase 3 imaging trial. *JAMA Oncol.* 2021;7:1635–1642.
4. NCCN clinical practice guidelines in oncology (NCCN Guidelines®): prostate cancer. NCCN website. https://www.nccn.org/professionals/physician_gls/pdf/prostate.pdf. Published May 10, 2021. Accessed June 14, 2022.
5. S3-leitlinie prostatakarzinom. Leitlinienprogramm Onkologie website. https://www.leitlinienprogramm-onkologie.de/fileadmin/user_upload/Downloads/Leitlinien/Prostatakarzinom/Version_6/LL_Prostatakarzinom_Langversion_6.1.pdf. Published July 2021. Accessed June 14, 2022.
6. FDA approves first PSMA-targeted PET imaging drug for men with prostate cancer. FDA website. https://www.fda.gov/news-events/press-announcements/fda-approves-first-psma-targeted-pet-imaging-drug-men-prostate-cancer. Published December 1, 2020. Accessed June 14, 2022.
7. Fendler WP, Eiber M, Beheshti M, et al. ^{68}Ga-PSMA PET/CT: joint EANM and SNMMI procedure guideline for prostate cancer imaging—version 1.0. *Eur J Nucl Med Mol Imaging.* 2017;44:1014–1024.
8. Heußer T, Mann P, Rank CM, et al. Investigation of the halo-artifact in ^{68}Ga-PSMA-11-PET/MRI. *PLoS One.* 2017;12:e0183329.
9. Werner RA, Derlin T, Lapa C, et al. ^{18}F-labeled, PSMA-targeted radiotracers: leveraging the advantages of radiofluorination for prostate cancer molecular imaging. *Theranostics.* 2020;10:1–16.
10. FDA approves second PSMA-targeted PET imaging drug for men with prostate cancer. FDA website. https://www.fda.gov/drugs/drug-safety-and-availability/fda-approves-second-psma-targeted-pet-imaging-drug-men-prostate-cancer. Updated May 27, 2021. Accessed June 14, 2022.
11. Pienta KJ, Gorin MA, Rowe SP, et al. A phase 2/3 prospective multicenter study of the diagnostic accuracy of prostate specific membrane antigen PET/CT with ^{18}F-DCFPyL in prostate cancer patients (OSPREY). *J Urol.* 2021;206:52–61.
12. Wurzer A, Di Carlo D, Schmidt A, et al. Radiohybrid ligands: a novel tracer concept exemplified by 18F- or 68Ga-labeled rhPSMA inhibitors. *J Nucl Med.* 2020;61:735–742.
13. Eiber M, Kroenke M, Wurzer A, et al. 18F-rhPSMA-7 PET for the detection of biochemical recurrence of prostate cancer after radical prostatectomy. *J Nucl Med.* 2020;61:696–701.
14. Kroenke M, Wurzer A, Schwamborn K, et al. Histologically-confirmed diagnostic efficacy of ^{18}F-rhPSMA-7 positron emission tomography for N-staging of patients with primary high risk prostate cancer. *J Nucl Med.* 2019;61:710–715.
15. Wurzer A, Parzinger M, Konrad M, et al. Preclinical comparison of four [^{18}F, natGa]rhPSMA-7 isomers: influence of the stereoconfiguration on pharmacokinetics. *EJNMMI Res.* 2020;10:149.
16. Tolvanen T, Kalliokoski KK, Malaspina S, et al. Safety, biodistribution and radiation dosimetry of ^{18}F-rhPSMA-7.3 in healthy adult volunteers. *J Nucl Med.* 2021;62:679–684.
17. Malaspina S, Oikonen V, Kuisma A, et al. Kinetic analysis and optimisation of ^{18}F-rhPSMA-7.3 PET imaging of prostate cancer. *Eur J Nucl Med Mol Imaging.* 2021;48:3723–3731.
18. Rauscher I, Karimzadeh A, Schiller K, et al. Detection efficacy of ^{18}F-rhPSMA-7.3 PET/CT and impact on patient management in patients with biochemical recurrence of prostate cancer after radical prostatectomy and prior to potential salvage treatment. *J Nucl Med.* 2021;62:1719–1726.
19. Eiber M, Herrmann K, Calais J, et al. Prostate cancer molecular imaging standardized evaluation (PROMISE): proposed miTNM classification for the interpretation of PSMA-ligand PET/CT. *J Nucl Med.* 2018;59:469–478.
20. Heck MM, Retz M, Bandur M, et al. Topography of lymph node metastases in prostate cancer patients undergoing radical prostatectomy and extended lymphadenectomy: results of a combined molecular and histopathologic mapping study. *Eur Urol.* 2014;66:222–229.
21. Maurer T, Souvatzoglou M, Kubler H, et al. Diagnostic efficacy of [^{11}C]choline positron emission tomography/computed tomography compared with conventional computed tomography in lymph node staging of patients with bladder cancer prior to radical cystectomy. *Eur Urol.* 2012;61:1031–1038.
22. DeLong ER, DeLong DM, Clarke-Pearson DL. Comparing the areas under two or more correlated receiver operating characteristic curves: a nonparametric approach. *Biometrics.* 1988;44:837–845.
23. Obuchowski NA. Nonparametric analysis of clustered ROC curve data. *Biometrics.* 1997;53:567–578.
24. Smith PJ, Hadgu A. Sensitivity and specificity for correlated observations. *Stat Med.* 1992;11:1503–1509.
25. Zeger SL, Liang KY. Longitudinal data analysis for discrete and continuous outcomes. *Biometrics.* 1986;42:121–130.
26. The R project for statistical computing. R Project website https://www.R-project.org/. Accessed June 14, 2022.

27. Robin X, Turck N, Hainard A, et al. pROC: an open-source package for R and S+ to analyze and compare ROC curves. *BMC Bioinformatics.* 2011;12:77.
28. Højsgaard S, Halekoh U, Yan J. The R package geepack for generalized estimating equations. *J Stat Softw.* 2005;15:1–11.
29. Hale CA, Fleiss JL. Interval estimation under two study designs for kappa with binary classifications. *Biometrics.* 1993;49:523–534.
30. Landis JR, Koch GG. The measurement of observer agreement for categorical data. *Biometrics.* 1977;33:159–174.
31. Heesakkers RA, Hovels AM, Jager GJ, et al. MRI with a lymph-node-specific contrast agent as an alternative to CT scan and lymph-node dissection in patients with prostate cancer: a prospective multicohort study. *Lancet Oncol.* 2008;9:850–856.
32. Hövels AM, Heesakkers RA, Adang EM, et al. The diagnostic accuracy of CT and MRI in the staging of pelvic lymph nodes in patients with prostate cancer: a meta-analysis. *Clin Radiol.* 2008;63:387–395.
33. Prostate cancer. EAU website. http://uroweb.org/guideline/prostate-cancer/. Accessed June 14, 2022.
34. von Eyben FE, Picchio M, von Eyben R, Rhee H, Bauman G. ^{68}Ga-labeled prostate-specific membrane antigen ligand positron emission tomography/computed tomography for prostate cancer: a systematic review and meta-analysis. *Eur Urol Focus.* 2018;4:686–693.
35. Petersen LJ, Zacho HD. PSMA PET for primary lymph node staging of intermediate and high-risk prostate cancer: an expedited systematic review. *Cancer Imaging.* 2020;20:10.
36. Maurer T, Gschwend JE, Rauscher I, et al. Diagnostic efficacy of ^{68}gallium-PSMA positron emission tomography compared to conventional imaging for lymph node staging of 130 consecutive patients with intermediate to high risk prostate cancer. *J Urol.* 2016;195:1436–1443.
37. Klingenberg S, Jochumsen MR, Ulhoi BP, et al. ^{68}Ga-PSMA PET/CT for primary lymph node and distant metastasis NM staging of high-risk prostate cancer. *J Nucl Med.* 2021;62:214–220.
38. Cytawa W, Seitz AK, Kircher S, et al. ^{68}Ga-PSMA I&T PET/CT for primary staging of prostate cancer. *Eur J Nucl Med Mol Imaging.* 2020;47:168–177.
39. Abuzallouf S, Dayes I, Lukka H. Baseline staging of newly diagnosed prostate cancer: a summary of the literature. *J Urol.* 2004;171:2122–2127.
40. Fendler WP, Calais J, Allen-Auerbach M, et al. ^{68}Ga-PSMA-11 PET/CT interobserver agreement for prostate cancer assessments: an international multicenter prospective study. *J Nucl Med.* 2017;58:1617–1623.
41. Oh SW, Wurzer A, Teoh EJ, et al. Quantitative and qualitative analyses of biodistribution and PET image quality of a novel radiohybrid PSMA, ^{18}F-rhPSMA-7, in patients with prostate cancer. *J Nucl Med.* 2020;61:702–709.
42. Grünig H, Maurer A, Thali Y, et al. Focal unspecific bone uptake on [^{18}F]-PSMA-1007 PET: a multicenter retrospective evaluation of the distribution, frequency, and quantitative parameters of a potential pitfall in prostate cancer imaging. *Eur J Nucl Med Mol Imaging.* 2021;48:4483–4494.
43. Arnfield EG, Thomas PA, Roberts MJ, et al. Clinical insignificance of [^{18}F]PSMA-1007 avid non-specific bone lesions: a retrospective evaluation. *Eur J Nucl Med Mol Imaging.* 2021;48:4495–4507.
44. Kroenke M, Mirzoyan L, Horn T, et al. Matched-pair comparison of ^{68}Ga-PSMA-11 and ^{18}F-rhPSMA-7 PET/CT in patients with primary and biochemical recurrence of prostate cancer: frequency of non-tumor-related uptake and tumor positivity. *J Nucl Med.* 2021;62:1082–1088.
45. Rauscher I, Krönke M, König M, et al. Matched-pair comparison of ^{68}Ga-PSMA-11 PET/CT and ^{18}F-PSMA-1007 PET/CT: frequency of pitfalls and detection efficacy in biochemical recurrence after radical prostatectomy. *J Nucl Med.* 2020;61:51–57.

Changes in Management After ^{18}F-DCFPyL PSMA PET in Patients Undergoing Postprostatectomy Radiotherapy, with Early Biochemical Response Outcomes

Michael Ng[1], Mario Guerrieri[2], Lih Ming Wong[3,4], Kim Taubman[5], Tom Sutherland[6,7], Angela Benson[8], Graeme Byrne[9], Sam Koschel[8], Kelvin Yap[6], Michelle Starmans[8], Grace Ong[10], Craig Macleod[11], Marcus Foo[12], and Michael Chao[13]

[1]GenesisCare St. Vincent's Hospital, Melbourne, Victoria, Australia; [2]GenesisCare, Footscray, Victoria, Australia; [3]Department of Surgery, University of Melbourne, Melbourne, Victoria, Australia; [4]Department of Surgery, St. Vincent's Hospital, Melbourne, Victoria, Australia; [5]Department of Nuclear Medicine, St. Vincent's Hospital, Melbourne, Victoria, Australia; [6]Department of Medical Imaging, St. Vincent's Hospital, Melbourne, Victoria, Australia; [7]Faculty of Medicine, University of Melbourne, Melbourne, Victoria, Australia; [8]GenesisCare CancerCare Research, Melbourne, Victoria, Australia; [9]La Trobe University Statistics Consultancy Platform, Melbourne, Victoria, Australia; [10]GenesisCare, Shepparton, Victoria, Australia; [11]GenesisCare, Albury, New South Wales, Australia; [12]GenesisCare, Berwick, Victoria, Australia; and [13]GenesisCare, Ringwood, Victoria, Australia

Prostate-specific membrane antigen (PSMA) tracers have increased sensitivity in the detection of prostate cancer, compared with conventional imaging. We assessed the management impact of ^{18}F-DCFPyL PSMA PET/CT in patients with prostate-specific antigen (PSA) recurrence after radical prostatectomy (RP) and report early biochemical response in patients who underwent radiation treatment. **Methods:** One hundred patients were enrolled into a prospective study, with a prior RP for prostate cancer, a PSA of 0.2–2.0 ng/mL, and no prior treatment. All patients underwent diagnostic CT and PSMA PET/CT, and management intent was completed at 3 time points (original, post-CT, and post-PSMA) and compared. Patients who underwent radiotherapy with 6-mo PSA response data are presented. **Results:** Ninety-eight patients are reported, with a median PSA of 0.32 ng/mL (95% CI, 0.28–0.36), pT3a/b disease in 71.4%, and an International Society of Urological Pathology grade group of at least 3 in 59.2%. PSMA PET/CT detected disease in 46.9% of patients, compared with 15.5% using diagnostic CT (PSMA PET, 29.2% local recurrence and 29.6% pelvic nodal disease). A major change in management intent was higher after PSMA than after CT (12.5% vs. 3.2%, $P = 0.010$), as was a moderate change in intent (31.3% vs. 13.7%, $P = 0.001$). The most common change was an increase in the recommendation for elective pelvic radiation (from 15.6% to 33.3%), nodal boost (from 0% to 22.9%), and use of concurrent androgen deprivation therapy (ADT) (from 22.9% to 41.7%) from original to post-PSMA intent because of detection of nodal disease. Eighty-six patients underwent ^{18}F-DCFPyL–guided radiotherapy. Fifty-five of 86 patients either did not receive ADT or recovered after ADT, with an 18-mo PSA response from 0.32 to 0.02 ng/mL; 94.5% of patients had a PSA of no more than 0.20 ng/mL, and 74.5% had a PSA of no more than 0.03 ng/mL. **Conclusion:** ^{18}F-DCFPyL PET/CT has a significant impact on management intent in patients being considered for salvage radiotherapy after RP with PSA recurrence. Increased detection of disease, particularly in the pelvic lymph nodes, resulted in increased pelvic irradiation and concurrent ADT use. Early results in patients who are staged with ^{18}F-DCFPyL PET/CT show a favorable PSA response.

Key Words: ^{18}F-DCFPyL; management change; prostate cancer; prostatectomy; PET; PSMA

J Nucl Med 2022; 63:1343–1348
DOI: 10.2967/jnumed.121.263521

Prostate-specific antigen (PSA) recurrence after radical prostatectomy (RP) for prostate cancer occurs in up to 20%–50% (*1,2*) and is defined by a PSA level of more than 0.2 ng/mL. Salvage radiotherapy, most commonly to the prostate bed, results in 5-y biochemical control of 56% (*3*). Failure after salvage radiotherapy is most likely due to disease outside the prostate bed, which can include the pelvic lymph nodes, paraaortic lymph nodes, and distant metastases.

PET using prostate-specific membrane antigen (PSMA) tracers have increased detection of disease compared with more conventional imaging with CT and bone scintigraphy. PSMA is a type II cell-surface glycoprotein overexpressed in more than 90% of prostate cancer epithelial cells (*4*). Various PSMA tracers are available, including ^{68}Ga-PSMA-11, which has the most evidence for superior sensitivity in detecting disease. Newer PSMA tracers include ^{18}F-labeled agents such as ^{18}F-DCFPyL and have the advantages of increased manufacturing capacity, improved spatial resolution, and higher tumor-to-background ratio (*5*). PSMA PET/CT is now recommended in international guidelines as a staging method for biochemical failure when PSA is more than 0.2 ng/mL (*6*).

We aimed to evaluate the role of ^{18}F-DCFPyL PET/CT in patients being considered for salvage radiotherapy, primarily assessing the change in management, and also reporting the early 6-mo biochemical response rate in patients who then undergo radiation therapy.

MATERIALS AND METHODS

We performed a prospective nonrandomized trial at 9 GenesisCare sites within Victoria, Australia. Between August 2018 and July 2020, we recruited 100 patients who had evidence of a rising PSA level of between 0.2 and 2.0 ng/mL after RP and were referred to a radiation oncologist for consideration of salvage radiotherapy. Exclusion criteria

---

Received Nov. 16, 2021; revision accepted Jan. 12, 2022.

For correspondence or reprints, contact Michael Ng (michael.ng@genesiscare.com).

included previous pelvic radiotherapy and previous androgen deprivation therapy (ADT). The protocol was approved by the St. Vincent's Hospital Melbourne Human Research Ethics Committee and was registered with the Australian New Zealand Clinical Trials Registry (ACTRN12618001530213). All patients gave written informed consent.

All patients underwent diagnostic CT of the chest, abdomen, and pelvis and PSMA PET/CT on the same day at the Department of Nuclear Medicine of St. Vincent's Hospital. Scans were performed on a Discovery 710 PET/CT device (GE Healthcare) combining a 64-slice multidetector CT scanner with a dedicated, full-ring PET scanner. For the diagnostic CT of the chest, abdomen, and pelvis, 100 mL of intravenous contrast medium were administered, and patients were scanned from the apex of the lungs to the lesser trochanters 70 s afterward. An additional 10-min delayed pelvic CT scan was also obtained to assist in distinguishing between the ureters and lymph nodes. For the PSMA PET/CT scan, 250 MBq of good-manufacturing-practice–quality ^{18}F-DCFPyL manufactured by Cyclotek Australia was injected, followed by an uptake time of 120 min.

Imaging Acquisition and Interpretation

CT images of the chest, abdomen, and pelvis were interpreted by an experienced genitourinary radiologist, and PSMA PET/CT images were interpreted by 2 experienced nuclear medicine physicians. The reporting physicians did not have access to the images or reports of the other modality, except for the delayed pelvic CT scan to allow the nuclear medicine physician to localize the ureters and anastomosis on the PET images.

Both scans were reported using a standardized template that encompassed local, nodal, and distant disease, with each section being designated as positive, equivocal, or negative. Positive or equivocal disease was defined as focal uptake on PSMA PET/CT that was not physiologic and was higher than the surrounding background. Local recurrence was subclassified into prostate bed (including the anastomosis) or seminal vesicle bed (the bilateral rectovesical lateral areas on CT where soft-tissue densities are seen and where the seminal vesicles are usually located, with or without surgical clips). Lymph node involvement on CT of the chest, abdomen, and pelvis was defined on the basis of size and morphology and designated as positive, equivocal, or negative.

Changes in Management

After patient registration and before imaging, the radiation oncologist was required to outline the treatment plan on a questionnaire (Supplemental Table 1; supplemental materials are available at http://jnm.snmjournals.org), specifying whether radiotherapy or the proposed alternative management would be offered. If radiotherapy were to be offered, target-site dose and fractions needed to be specified, as well as whether pelvic nodal boost, stereotactic radiotherapy, and addition of ADT would be used. This treatment plan was referred to as the original intent, and after its completion, patients underwent diagnostic CT of the chest, abdomen, and pelvis and PSMA PET/CT. The diagnostic CT results were released first, and the clinician was required to complete a second questionnaire (post-CT intent). Then, the results of the PSMA PET/CT scan were released and the clinician completed a final questionnaire (post-PSMA intent). Change in management was graded on the basis of the impact on management and was defined as major, minor, or no change, as demonstrated in Table 1. This grading system was based on a publication by van Leeuwen et al. and further modified (*7*).

Radiotherapy and Disease Outcome

For this analysis, we assessed early biochemical response at 6 mo after the last day of radiotherapy and performed a subgroup analysis for patients who did not receive concurrent ADT. The radiotherapy protocol did not mandate the target volumes and dose prescription. However, clinical target volume guidelines for the prostate bed (*8*) and elective pelvic nodal irradiation (*9*) were provided; the recommendation was a dose of 70.2 Gy to the prostate bed, elective nodal irradiation of 56 Gy, and a nodal boost of 68 Gy in 39 fractions. Stereotactic radiotherapy to nodes or bone was recommended in 3–5 fractions with a dose range of 30–40 Gy. Concurrent ADT, if prescribed, was recommended using a luteinizing hormone–releasing agonist for 6 mo.

TABLE 1
Impact of Changes in Management Intent

Impact	Definition
None	No change in management intent or plan
Moderate	Change in treatment delivery of RT but no change in intent, including change in RT volume, change in RT dose, change in volume and dose (e.g., addition of elective pelvic nodal RT and dose escalation to involved PSMA-positive pelvic node [nodal boost]), and addition of ADT to salvage RT
Major	Significant change in treatment intent, including detection of significant metastatic disease resulting in change in palliative intent, recommendation of no salvage RT, or change in palliative-intent RT; detection of oligometastatic disease resulting in change in intent to treat oligometastases, such as with stereotactic RT

RT = radiotherapy.

Statistical Methods

The McNemar exact test was used to compare changes in management between original intent and post-CT intent versus original intent and post-PSMA intent. The Kendall τ-b correlation was used to assess associations of change in intent with positive versus negative scan results (both CT and PSMA PET/CT), International Society of Urological Pathology (ISUP) grade, and pretreatment PSA. Statistical summaries were performed for patients undergoing radiotherapy with 6-mo PSA response data available. Particularly, for patients who did not receive ADT, we used *t* tests, ANOVA with multiple comparisons, and regression to compare differences and percentage changes between PSA at the 6-mo follow-up and prescan PSA across levels of several factors (PET scan positivity, pTN staging, ISUP grade, margin status, biochemical recurrence vs. persistence).

RESULTS

Between August 2018 and July 2020, 100 participants were enrolled across 9 sites by 6 radiation oncologists. Two patients were excluded on review because their prescan PSA level was outside the eligibility criteria (PSA $\geq$ 2.0), leaving 98 patients suitable for final analysis (Supplemental Fig. 1). A further 2 patients were excluded because of incomplete management intent forms, leaving 96 patients eligible for this analysis. Baseline characteristics (Supplemental Table 2) included a median age of 68.0 y, a median prescan PSA of 0.32 ng/mL (95% CI, 0.28–0.36 ng/mL); 58.9% had an ISUP grade group of at least 3 at RP. Biochemical recurrence occurred in 60.2% of patients, versus biochemical persistence in 39.8%. Pelvic nodal sampling or dissection was performed in only 32.7% of patients, with a median nodal count of 5.0 (95% CI, 4.1–7.9); 5.1% overall had pN1 disease. Histopathologic

TABLE 2

Change in Management Intent from Original to Post-CT Versus Post-PSMA

Parameter	Major change	Moderate change	No change	Total
Original to post-CT intent	3 (3.2%)	13 (13.7%)	79 (83.2%)	95 (100.0%)
Original to post-PSMA intent	12 (12.5%)	30 (31.3%)	54 (56.3%)	96 (100.0%)

characteristics from RP revealed extraprostatic extension in 68.4%, seminal vesicle invasion in 24.5%, and a positive surgical margin in 37%.

Patterns of Disease Detection on PSMA PET/CT and Diagnostic CT of the Chest, Abdomen, and Pelvis

Overall, 46.9% ($n = 46$) of our cohort had positive PSMA PET/CT results, and a further 5.1% ($n = 5$) had equivocal results. The location of PSMA-avid disease is shown in Supplemental Table 3. Local disease recurrence was identified in 28 patients (29.2%), nodal disease in 29 patients (29.6%), and distant bony metastases in 7 patients (7.1%). One patient was unable to undergo the CT of the chest, abdomen, and pelvis, resulting in 97 available for analysis. Local recurrence was diagnosed in 9 patients (5 positive, 4 equivocal), nodal disease in 11 patients (9 positive, 2 equivocal), and an equivocal distant bone metastasis in 1 patient.

Changes in Management

Changes in treatment from original intent to postscan intent (post-CT and post-PSMA) are shown in Table 2. Overall, 43.8% (42/96) of patients demonstrated a change in management (major or moderate) after PSMA, versus 16.7% (16/95) after diagnostic CT of the chest, abdomen, and pelvis. There was a 12.5% versus 3.2% major change for post-PSMA versus post-CT, the difference being significant ($P = 0.010$). There were more patients with moderate changes after PSMA than after CT, 31.3% versus 13.7% ($P = 0.001$). Either a positive or an equivocal finding on CT or PSMA was strongly associated with a major or moderate treatment intent change ($P < 0.001$). Particularly for positive or equivocal PSMA findings, there were major or moderate changes in 42 of 50 patients (84%), compared with no changes in 46 patients with negative findings. Both higher PSA ($P = 0.009$) and higher ISUP grade ($P < 0.001$) were associated with higher likelihood of major or moderate changes in management after PSMA (Supplemental Fig. 2). Positive nodal disease findings on PSMA (nodal only or in combination) always resulted in a change in management (moderate or major) (Supplemental Table 4).

Changes in Management: Original Versus Post-CT Versus Post-PSMA. Changes in management after CT and PSMA are shown in Figure 1 and Supplemental Table 5. The original treatment intent was curative for most patients (94/96), with a minimal change after CT (92/95) and PSMA (92/95). The number of patients for whom radiotherapy was recommended was similar originally ($n = 88$), after CT ($n = 87$), and after PSMA ($n = 88$). Of these, prostate bed radiotherapy was recommended for almost all (original, $n = 88$; post-CT, $n = 87$; post-PSMA, $n = 88$). The largest effect from both CT and PSMA PET was an increased recommendation for elective pelvic radiotherapy, nodal boost, or concurrent ADT. Elective nodal irradiation increased to 20% (19/95) after CT and 33.3% (32/96) after PSMA, compared with 15 of 96 (15.6%) originally. Nodal boost was offered in more patients after PSMA, at 22.9% (22/96), versus 7.4% (7/95) after CT. Concurrent ADT use increased from 22.9% (22/96) originally to 24.2% (23/95) after CT and 41.7% (40/96) after PSMA. No stereotactic radiotherapy was recommended at original intent, with only small numbers of patients receiving a recommendation for stereotactic nodal irradiation (post-CT, $n = 1$; post-PSMA, $n = 1$) or stereotactic irradiation to bony metastases (post-CT, $n = 1$; post-PSMA, $n = 4$). There was only 1 patient with a change in dose (not fractions), with dose escalation of prostate bed PSMA-avid local recurrence (from 70.2 to 75.6 Gy).

Individual Changes in Management from Original Intent to Post-PSMA Intent. Figure 2 depicts the change in management flow for each patient between original intent and the post-PSMA scan. For most patients (61/96), prostate bed radiotherapy alone and after PSMA was originally recommended; 41 remained with the same recommendation (no change). In 19 patients, a change in radiotherapy treatment volume was recommended (moderate change); in 1 patient, a change to no radiotherapy was recommended (major change); and in 1 patient, additional stereotactic radiotherapy was recommended (major change). In the remaining 27 of 96 patients, the original intent was a recommendation for prostate bed radiotherapy, with ADT in 22 patients and elective pelvic radiotherapy in 15 patients. After PSMA, there were some changes in these 27 patients, with no consistent dominant change.

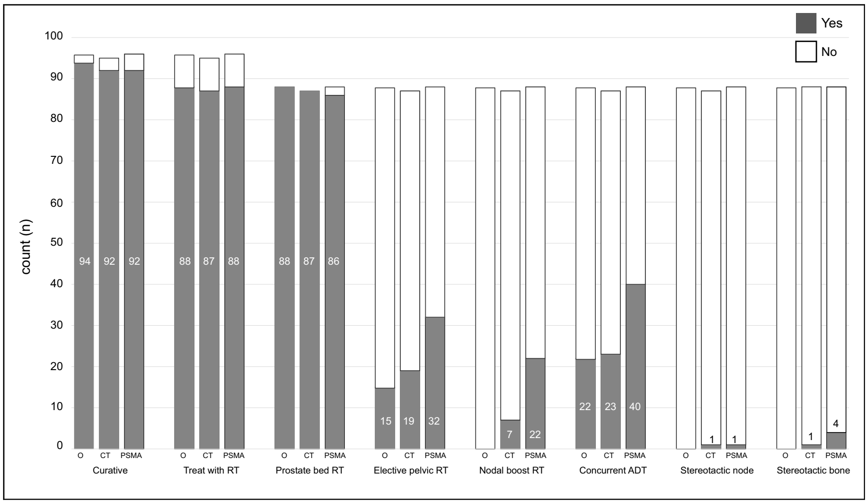

FIGURE 1. Overall management intent at original (O) vs. post-CT (CT) vs. post-PSMA (PSMA). RT = radiotherapy.

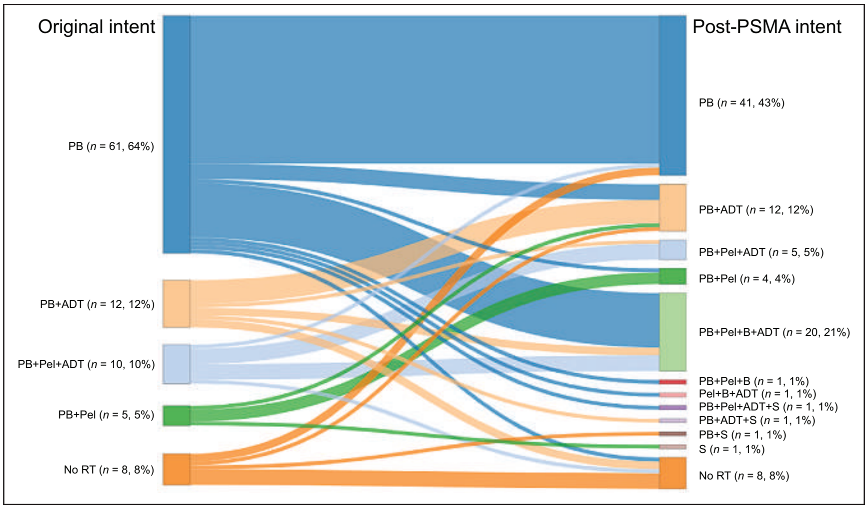

FIGURE 2. Sankey diagram demonstrating specific change in management per patient from original intent to post-PSMA scan, particularly for radiation target volumes. B = boost to node; PB = prostate bed; Pel = elective pelvic radiation; RT = radiotherapy; S = stereotactic radiotherapy.

Twelve patients had a major change in management after PSMA. Four of 8 changed from active surveillance originally to radiotherapy after PSMA. Four of 88 (4.5%) changed from radiotherapy originally to no radiotherapy after PSMA (ADT alone, *n* = 1; ADT plus chemotherapy, *n* = 2; surveillance, *n* = 1). Four of 88 patients received a recommendation that stereotactic radiotherapy be added to nodal or bone metastases.

Biochemical Response in Patients Undergoing Salvage Radiotherapy

In total, 86 patients received radiotherapy. Most received prostate bed radiotherapy only (50/86), and ADT was prescribed in 33 patients (6-mo duration) (Table 3). The median pretreatment PSA was 0.32 ng/mL (range, 0.20–1.84 ng/mL), and 59 patients had 18-mo posttreatment PSA response data with a median PSA of 0.02 ng/mL (range, 0.01–0.29 ng/mL).

Of the 59 patients with 18-mo follow-up data, 55 either had not received concurrent ADT or had ADT recovery. At the 18-mo follow-up, 52 of 54 (92.5%) had a PSA of no more than 0.20 ng/mL and 41 of 54 (74.5%) had an undetectable PSA (≤0.03), with no difference between a positive and negative PSMA scan.

DISCUSSION

Our prospective study showed that just under 50% of patients for whom salvage radiotherapy is planned because of PSA recurrence after RP have a change in management when undergoing ^{18}F-DCFPyL PET/CT. The change in management was more than double that with diagnostic CT. There have been various studies demonstrating significant changes in management using ^{68}Ga-PSMA-11 (10–12) and ^{18}F-DCFPyL (*13–15*) in PET imaging for prostate cancer. Many of these studies were limited in that they enrolled heterogenous groups of patients, such as patients for whom PET was used for staging or for PSA failure; patients for whom prior treatment included surgery, radiotherapy, and ADT; and patients with a high prescan PSA. We postulate that the slightly lower management changes in our study are due to lower detection rates and a homogeneous post-RP cohort without prior treatment, with a lower pretreatment PSA (mean, 0.32 ng/mL), and with lower proportion of higher-grade disease (ISUP ≥ 4 was <20%).

We previously reported patterns of disease detection and the safety of ^{18}F-DCFPyL PET/CT in our cohort (*16*) and provided a nomogram to predict a positive scan result. The improved detection of pelvic nodal disease was responsible for the moderate management change (31.3%) in our study, doubling the recommendation for pelvic nodal irradiation, nodal boost, and concurrent ADT with prostate bed radiotherapy. Many studies have shown that PSMA scans have improved the detection of disease after RP outside the prostate bed (*10,11,17–19*) which is not encompassed by standard salvage prostate bed radiotherapy volumes.

Major changes were small and occurred in only 12.5% (12/96) of patients after ^{18}F-DCFPyL PET/CT. These were patients for whom radiotherapy was not recommended because of detection of metastatic disease, patients for whom surveillance was changed to treatment, and patients for whom stereotactic radiotherapy was added (node or bone). Improved detection of distant metastasis in the PSA recurrence setting can avoid radiotherapy toxicity and costs by omitting futile prostate bed radiotherapy, and the use

TABLE 3

Radiotherapy Treatment Volumes and Dose and Fractionations Delivered

Parameter	All patients (*n* = 86)	No ADT (*n* = 53)
PB alone	50	41
PB + elective pelvic RT	13	4
PB + elective pelvic RT + nodal boost	18	5
Stereotactic RT ± pelvis RT	5	3
PB		
Median dose (Gy)	70.2 (68.0–75.6)	
Median fraction	39 (34–42)	
Elective pelvic		
Median dose (Gy)	56.0 (54.0–56.0)	
Median fraction	39 (34–39)	
Nodal boost		
Median dose (Gy)	68.0 (64.0–70.2)	
Median fraction	39 (39–39)	
Stereotactic nodal		
Median dose (Gy)	30.0 (30.0–30.0)	
Median fraction	3 (3–5)	
Stereotactic bone		
Median dose (Gy)	27.0 (25.0–30.0)	
Median fraction	5 (3–5)	

PB = prostate bed; RT = radiotherapy.
Data in parentheses are range.

of targeted radiotherapy to oligometastatic disease can improve progression-free survival (*20*) or delay the use of ADT (*21*). It important to recognize that there was no change in management in 56.3% of patients using ^{18}F-DCFPyL PET/CT—a choice that was driven by a negative scan. The rate of positive versus negative scans in our study is similar to that of other studies in the post-RP PSA recurrence setting using ^{68}Ga-PSMA-11 (22–24) and ^{18}F-DCFPyL (*15,25–29*). The high negative scan rate raises questions regarding the additional role of elective nodal radiotherapy to prostate bed radiation, with trials supporting improved biochemical control (*30,31*).

With the impact on management change by ^{18}F-DCFPyL staging, we have shown an early favorable PSA response in patients who then underwent radiotherapy. Of patients who had 18-mo response data available, who did not receive ADT, or who had ADT recovery, 92.5% had a PSA of less than 0.20 ng/mL and 74.5% had an undetectable PSA, with no difference in patients with a positive or negative scan. Previous studies have shown that using ^{68}Ga-PSMA-11–guided salvage radiotherapy has favorable disease outcomes with similar follow-up (*32,33*). These studies, including ours, have shown that a negative PSMA scan is not associated with inferior response or outcomes, and we recommend salvage radiotherapy in patients with a negative PSMA scan. A recent randomized trial by Jani et al. showed that ^{18}F-fluciclovine PET/CT–staged patients undergoing salvage radiotherapy have improved 3-y event survival compared with patients who were conventionally staged (*34*), and we await the results of a similar trial using ^{18}F-DCFPyL (*35*).

Strengths of our study include the prospective design, with controlled high-compliance stepwise assessment of management intent change. Our eligibility criteria reflect a common scenario facing patients and clinicians with a rising PSA after RP: having had no prior therapy, with a PSA entry criterion of 0.2–2.0 ng/mL. Our study is relevant given that recent guidelines and trials support early referral for radiotherapy when PSA is more than 0.1–0.2 ng/mL (*36–38*). The limitations of our study include the lack of histopathologic or radiologic confirmation of disease, the fact that management change could vary at different institutions, and the limited follow-up. We will follow up patients until 3 y after radiotherapy to validate ^{18}F-DCFPyL–staged radiotherapy. Another limitation is that our analysis of ^{18}F-DCFPyL PET/CT scans did not use newer guidelines (PROMISE, PSMA-RADS, E-PSMA), which were not available at the time of protocol development; we will incorporate these in future trials.

CONCLUSION

^{18}F-DCFPyL PET/CT has a significant impact on patients being considered for salvage radiotherapy. With improved detection of local recurrence and nodal disease, ^{18}F-DCFPyL PET/CT improves confidence when irradiating the prostate bed and results in increased use of pelvic nodal irradiation. We recommend that PSMA PET/CT be considered for all patients for whom salvage radiotherapy is being considered after RP and for whom PSA is more than 0.2 ng/mL. Early results for ^{18}F-DCFPyL–staged patients receiving radiotherapy show a favorable PSA response rate, but longer-term follow-up is needed.

DISCLOSURE

The sponsor, GenesisCare, along with Cyclotek (Aust.) Pty. Ltd., provided financial support and access to their good-manufacturing-practice–approved product, ^{18}F-DCFPyL-PSMA radiopharmaceutical. Cyclotek provided support through a project grant from the Department of Industry, Science, Energy, and Resources Cooperative Research Centre Program. No other potential conflict of interest relevant to this article was reported.

KEY POINTS

QUESTION: How does improved detection of disease by ^{18}F-DCFPyL PSMA PET change management in prostate cancer patients being considered for salvage radiotherapy because of PSA recurrence after prostatectomy?

PERTINENT FINDINGS: ^{18}F-DCFPyL PSMA PET detected disease in 46.9% of patients, resulting in a major change in management in 12.5% and a moderate change in 31.3%; the greatest change was the increase in pelvic nodal irradiation.

IMPLICATIONS FOR PATIENT CARE: Increased detection of disease by PSMA PET allows better selection of patients for salvage radiotherapy, as well as selection of appropriate radiation fields for a favorable treatment response in patients who received PSMA-guided radiotherapy.

REFERENCES

1. Han M, Partin AW, Zahurak M, Piantadosi S, Epstein JI, Walsh PC. Biochemical (prostate specific antigen) recurrence probability following radical prostatectomy for clinically localized prostate cancer. *J Urol.* 2003;169:517–523.
2. Wiegel T, Bottke D, Steiner U, et al. Phase III postoperative adjuvant radiotherapy after radical prostatectomy compared with radical prostatectomy alone in pT3 prostate cancer with postoperative undetectable prostate-specific antigen: ARO 96-02/AUO AP 09/95. *J Clin Oncol.* 2009;27:2924–2930.
3. Tendulkar RD, Agrawal S, Gao T, et al. Contemporary update of a multi-institutional predictive nomogram for salvage radiotherapy after radical prostatectomy. *J Clin Oncol.* 2016;34:3648–3654.
4. Ananias HJ, van den Heuvel MC, Helfrich W, de Jong IJ. Expression of the gastrin-releasing peptide receptor, the prostate stem cell antigen and the prostate-specific membrane antigen in lymph node and bone metastases of prostate cancer. *Prostate.* 2009;69:1101–1108.
5. Rowe SP, Gorin MA, Pomper MG. Imaging of prostate-specific membrane antigen using [^{18}F]DCFPyL. *PET Clin.* 2017;12:289–296.
6. Cornford P, van den Bergh RCN, Briers E, et al. EAU-EANM-ESTRO-ESUR-SIOG guidelines on prostate cancer. Part II-2020 update: treatment of relapsing and metastatic prostate cancer. *Eur Urol.* 2021;79:263–282.
7. van Leeuwen PJ, Stricker P, Hruby G, et al. ^{68}Ga-PSMA has a high detection rate of prostate cancer recurrence outside the prostatic fossa in patients being considered for salvage radiation treatment. *BJU Int.* 2016;117:732–739.
8. Sidhom MA, Kneebone AB, Lehman M, et al. Post-prostatectomy radiation therapy: consensus guidelines of the Australian and New Zealand Radiation Oncology Genito-Urinary Group. *Radiother Oncol.* 2008;88:10–19.
9. Michalski JM, Lawton C, El Naqa I, et al. Development of RTOG consensus guidelines for the definition of the clinical target volume for postoperative conformal radiation therapy for prostate cancer. *Int J Radiat Oncol Biol Phys.* 2010;76:361–368.
10. Müller J, Ferraro DA, Muehlematter UJ, et al. Clinical impact of ^{68}Ga-PSMA-11 PET on patient management and outcome, including all patients referred for an increase in PSA level during the first year after its clinical introduction. *Eur J Nucl Med Mol Imaging.* 2019;46:889–900.
11. Roach PJ, Francis R, Emmett L, et al. The impact of ^{68}Ga-PSMA PET/CT on management intent in prostate cancer: results of an Australian prospective multicenter study. *J Nucl Med.* 2018;59:82–88.
12. Afaq A, Alahmed S, Chen SH, et al. Impact of ^{68}Ga-prostate-specific membrane antigen PET/CT on prostate cancer management. *J Nucl Med.* 2018;59:89–92.
13. Metser U, Zukotynski K, Liu W, et al. Preliminary results of a prospective, multicenter trial assessing the impact of ^{18}F-DCFPyL-PET/CT on the management of patients with recurrent prostate cancer. *J Nucl Med.* 2020;61(suppl 1):40.
14. Morris MJ, Rowe SP, Gorin MA, et al. Diagnostic performance of ^{18}F-DCFPyL-PET/CT in men with biochemically recurrent prostate cancer: results from the CONDOR phase III, multicenter study. *Clin Cancer Res.* 2021;27:3674–3682.

15. Rousseau E, Wilson D, Lacroix-Poisson F, et al. A prospective study on ^{18}F-DCFPyL PSMA PET/CT imaging in biochemical recurrence of prostate cancer. *J Nucl Med.* 2019;60:1587–1593.
16. Koschel S, Taubman K, Sutherland T, et al. Patterns of disease detection using [^{18}F]DCFPyL PET/CT imaging in patients with detectable PSA post prostatectomy being considered for salvage radiotherapy: a prospective trial. *Eur J Nucl Med Mol Imaging.* 2021;48:3712–3722.
17. Boreta L, Gadzinski AJ, Wu SY, et al. Location of recurrence by gallium-68 PSMA-11 PET scan in prostate cancer patients eligible for salvage radiotherapy. *Urology.* 2019;129:165–171.
18. Kranzbühler B, Müller J, Becker AS, et al. Detection rate and localization of prostate cancer recurrence using 68Ga-PSMA-11 PET/MRI in patients with low PSA values $\leq$ 0.5 ng/mL. *J Nucl Med.* 2020;61:194–201.
19. Farolfi A, Ceci F, Castellucci P, et al. ^{68}Ga-PSMA-11 PET/CT in prostate cancer patients with biochemical recurrence after radical prostatectomy and PSA $<$0.5 ng/ml: efficacy and impact on treatment strategy. *Eur J Nucl Med Mol Imaging.* 2019; 46:11–19.
20. Phillips R, Shi WY, Deek M, et al. Outcomes of observation vs stereotactic ablative radiation for oligometastatic prostate cancer: the ORIOLE phase 2 randomized clinical trial. *JAMA Oncol.* 2020;6:650–659.
21. Ost P, Reynders D, Decaestecker K, et al. Surveillance or metastasis-directed therapy for oligometastatic prostate cancer recurrence: a prospective, randomized, multicenter phase II trial. *J Clin Oncol.* 2018;36:446–453.
22. Calais J, Czernin J, Cao M, et al. ^{68}Ga-PSMA-11 PET/CT mapping of prostate cancer biochemical recurrence after radical prostatectomy in 270 patients with a PSA level of less than 1.0 ng/ml: impact on salvage radiotherapy planning. *J Nucl Med.* 2018;59:230–237.
23. Emmett L, van Leeuwen PJ, Nandurkar R, et al. Treatment outcomes from ^{68}Ga-PSMA PET/CT-informed salvage radiation treatment in men with rising PSA after radical prostatectomy: prognostic value of a negative PSMA PET. *J Nucl Med.* 2017;58:1972–1976.
24. Perera M, Papa N, Roberts M, et al. Gallium-68 prostate-specific membrane antigen positron emission tomography in advanced prostate cancer: updated diagnostic utility, sensitivity, specificity, and distribution of prostate-specific membrane antigen-avid lesions—a systematic review and meta-analysis. *Eur Urol.* 2020;77:403–417.
25. Lindenberg L, Mena E, Turkbey B, et al. Evaluating biochemically recurrent prostate cancer: histologic validation of ^{18}F-DCFPYL PET/CT with comparison to multiparametric MRI. *Radiology.* 2020;296:564–572.
26. Mena E, Lindenberg ML, Turkbey IB, et al. ^{18}F-DCFPyL PET/CT imaging in patients with biochemically recurrent prostate cancer after primary local therapy. *J Nucl Med.* 2020;61:881–889.
27. Rowe SP, Campbell SP, Mana-Ay M, et al. Prospective evaluation of PSMA-targeted ^{18}F-DCFPyL PET/CT in men with biochemical failure after radical prostatectomy for prostate cancer. *J Nucl Med.* 2020;61:58–61.
28. Wondergem M, Jansen BHE, van der Zant FM, et al. Early lesion detection with ^{18}F-DCFPyL PET/CT in 248 patients with biochemically recurrent prostate cancer. *Eur J Nucl Med Mol Imaging.* 2019;46:1911–1918.
29. Perry E, Talwar A, Taubman K, et al. [^{18}F]DCFPyL PET/CT in detection and localization of recurrent prostate cancer following prostatectomy including low PSA $<$ 0.5 ng/mL. *Eur J Nucl Med Mol Imaging.* 2021;48:2038–2046.
30. Pollack A, Karrison TG, Balogh AG Jr, et al. Short term androgen deprivation therapy without or with pelvic lymph node treatment added to prostate bed only salvage radiotherapy: the NRG Oncology/RTOG 0534 SPPORT Trial. *Int J Radiat Oncol Biol Phys.* 2018;102:1605.
31. Murthy V, Maitre P, Kannan S, et al. Prostate-only versus whole-pelvic radiation therapy in high-risk and very high-risk prostate cancer (POP-RT): outcomes from phase III randomized controlled trial. *J Clin Oncol.* 2021;39:1234–1242.
32. Emmett L, Tang R, Nandurkar R, et al. 3-year freedom from progression after ^{68}Ga-PSMA PET/CT-triaged management in men with biochemical recurrence after radical prostatectomy: results of a prospective multicenter trial. *J Nucl Med.* 2020;61:866–872.
33. Schmidt-Hegemann NS, Stief C, Kim TH, et al. Outcome after PSMA PET/CT based salvage radiotherapy in patients with biochemical recurrence after radical prostatectomy: a bi-institutional retrospective analysis. *J Nucl Med.* 2019;60: 227–233.
34. Jani AB, Schreibmann E, Goyal S, et al. ^{18}F-fluciclovine-PET/CT imaging versus conventional imaging alone to guide postprostatectomy salvage radiotherapy for prostate cancer (EMPIRE-1): a single centre, open-label, phase 2/3 randomised controlled trial. *Lancet.* 2021;397:1895–1904.
35. Calais J, Zhu S, Hirmas N, et al. Phase 3 multicenter randomized trial of PSMA PET/CT prior to definitive radiation therapy for unfavorable intermediate-risk or high-risk prostate cancer [PSMA dRT]: study protocol. *BMC Cancer.* 2021; 21:512.
36. Kneebone A, Fraser-Browne C, Duchesne GM, et al. Adjuvant radiotherapy versus early salvage radiotherapy following radical prostatectomy (TROG 08.03/ANZUP RAVES): a randomised, controlled, phase 3, non-inferiority trial. *Lancet Oncol.* 2020;21:1331–1340.
37. Parker CC, Clarke NW, Cook AD, et al. Timing of radiotherapy after radical prostatectomy (RADICALS-RT): a randomised, controlled phase 3 trial. *Lancet.* 2020; 396:1413–1421.
38. Pisansky TM, Thompson IM, Valicenti RK, D'Amico AV, Selvarajah S. Adjuvant and salvage radiation therapy after prostatectomy: ASTRO/AUA guideline amendment, executive summary 2018. *Pract Radiat Oncol.* 2019;9:208–213.

Radiation Protection and Occupational Exposure on ^{68}Ga-PSMA-11–Based Cerenkov Luminescence Imaging Procedures in Robot-Assisted Prostatectomy

Pedro Fragoso Costa[1,2], Wolfgang P. Fendler[1,2], Ken Herrmann[1,2], Patrick Sandach[1,2], Hong Grafe[1,2], Maarten R. Grootendorst[3], Lukas Püllen[2,4], Claudia Kesch[2,4], Ulrich Krafft[2,4], Jan P. Radtke[2,4], Stephan Tschirdewahn[2,4], Boris A. Hadaschik[2,4], and Christopher Darr[2,4]

[1]Department of Nuclear Medicine, University Hospital Essen, Essen, Germany; [2]German Cancer Consortium (DKTK)-University Hospital Essen, Essen, Germany; [3]Clinical Department, Lightpoint Medical Ltd., Chesham, United Kingdom; and [4]Department of Urology and Urological Oncology, University Hospital Essen, Essen, Germany

Cerenkov luminescence imaging (CLI) was successfully implemented in the intraoperative context as a form of radioguided cancer surgery, showing promise in the detection of surgical margins during robot-assisted radical prostatectomy. The present study was designed to provide a quantitative description of the occupational radiation exposure of surgery and histopathology personnel from CLI-guided robot-assisted radical prostatectomy after the injection of ^{68}Ga-PSMA-11 in a single-injection PET/CT CLI protocol. **Methods:** Ten patients with preoperative ^{68}Ga-PSMA-11 administration and intraoperative CLI were included. Patient dose rate was measured before PET/CT ($n = 10$) and after PET/CT ($n = 5$) at a 1-m distance for 4 patient regions (head [A], right side [B], left side [C], and feet [D]). Electronic personal dosimetry (EPD) was used for intraoperative occupational exposure ($n = 10$). Measurements included the first surgical assistant and scrub nurse at the operating table and the CLI imager/surgeon at the robotic console and encompassed the whole duration of surgery and CLI image acquisition. An estimation of the exposure of histopathology personnel was performed by measuring prostate specimens ($n = 8$) with a germanium detector. **Results:** The measured dose rate value before PET/CT was 5.3 ± 0.9 (average ± SD) μSv/h. This value corresponds to a patient-specific dose rate constant for positions B and C of 0.047 μSv/h·MBq. The average dose rate value after PET/CT was 1.04 ± 1.00 μSv/h. The patient-specific dose rate constant values corresponding to regions A to D were 0.011, 0.026, 0.024, and 0.003 μSv/h·MBq, respectively. EPD readings revealed average personal equivalent doses of 9.0 ± 7.1, 3.3 ± 3.9, and 0.7 ± 0.7 μSv for the first surgical assistant, scrub nurse, and CLI imager/surgeon, respectively. The median germanium detector–measured activity of the prostate specimen was 2.96 kBq (interquartile range, 2.23–7.65 kBq). **Conclusion:** Single-injection ^{68}Ga-PSMA-11 PET/CT CLI procedures are associated with a reasonable occupational exposure level, if kept under 110 procedures per year. Excised prostate specimen radionuclide content was below the exemption level for ^{68}Ga. Dose rate–based calculations provide a robust estimation for EPD measurements.

Key Words: Cerenkov luminescence imaging; radioguided surgery; prostate cancer; margin assessment; radical prostatectomy

J Nucl Med 2022; 63:1349–1356
DOI: 10.2967/jnumed.121.263175

In men with local prostate cancer (PC), surgery or radiotherapy is the treatment modality of choice. Radical prostatectomy (RP) with complete removal of the prostate and the PC aims to cure the patient; however, collateral damage, such as impotence and incontinence, may occur. These problems greatly impair the quality of life, so that in the context of RP, the anatomic structures for continence and potency should be spared as much as possible (*1*). In this regard, positive resection margins (PSM) may occur in nerve-sparing RP or in locally advanced PC. The presence of PSM is associated with an increased risk of biochemical recurrence (*2*). In addition, the risk of metastasis is increased with PSM of greater than 2 mm or multiple PSM. Preoperative MRI and prostate sampling with systematic and fusion-guided biopsy cores help to guide neurovascular bundle preservation planning without increasing the risk and number of PSM (*3–5*). Intraoperative frozen-section analysis can help the surgeon to preserve these structures (*1,6*). However, besides resource consumption, there is also some conflicting evidence, as studies have demonstrated high false-negative rates of intraoperative frozen-section analysis—potentially resulting in unjustified nerve-sparing surgery (*6,7*).

For PC, PET/CT molecular imaging with radiopharmaceuticals targeting prostate-specific membrane antigen (PSMA) has been established in recent years. PSMA PET/CT is used for highly specific oncologic diagnostic imaging, especially in the setting of biochemical recurrence (*8–12*). Interestingly, PET imaging agents also emit optical photons via a phenomenon called Cerenkov luminescence. This property enables optical imaging, called Cerenkov luminescence imaging (CLI), using the novel LightPath system (Lightpoint Medical Ltd.) (*13*). Cerenkov photons are emitted by a charged particle (e.g., positron or electron) when traveling through a dielectric medium at a faster speed than the velocity of light in that medium (*13,14*). Although Cerenkov luminescence has a broad wavelength spectrum, it predominantly comprises ultraviolet light and blue light. These short wavelengths are highly attenuated in biologic tissue. Therefore, CLI is limited to the detection of signals emitted in superficial tissue layers. In contrast to PET, CLI is unable to detect photons emitted by more deeply located tissues or

---

Received Sep. 6, 2021; revision accepted Nov. 30, 2021.

For correspondence or reprints, contact Pedro Fragoso Costa (pedro.fragoso-costa@uni-duisburg-essen.de) and Christopher Darr (christopher.darr@uk-essen.de).

tumors (*15,16*). Intraoperative imaging with CLI is promising because it allows evaluation of the entire surface of the prostate, whereas intraoperative frozen-section analysis includes only a limited number of prostatic slices and thus is susceptible to sampling errors. Initial feasibility studies for intraoperative use in PC show promising results. So far, these have been based on small patient cohorts and selected patients, mainly with intermediate- to high-risk PC. One difference between the studies is the number of injections. In Olde Heuvel et al. (*17*), preoperative PET/CT was performed 4 wk before surgery with intraoperative tracer injection, whereas Darr et al. (*18*) examined immediate preoperative PET/CT without intraoperative tracer injection.

CLI could significantly improve the oncologic outcome of this patient group in the future; however, the safety of the medical staff must also be guaranteed and ensured. Radiation exposure has been thoroughly evaluated for sentinel lymph node procedures with ^{99m}Tc-labeled compounds and has shown consistent values of exposure from 1 to 10 μSv (*19–22*) per procedure. However, PET tracers carry an inherent risk of additional radiation exposure because of the higher energy and number of annihilation γ-photons in comparison to the γ-photons from ^{99m}Tc (*23*). Olde Heuvel et al. presented first data with a maximum radiation exposure of 0.016 mSv per procedure as the radiation exposure of medical personnel from 5 patients undergoing CLI-guided RP after intraoperative ^{68}Ga-PSMA-11 administration (*17*).

To calculate a possible scenario for radiation exposure in a new situation, such as radioguided surgery using positron emitters, medical physicists must rely on evidence-based publications. However, these are mostly available for different situations, such as clinical technologist exposure from patients undergoing PET/CT imaging or metrological data—which is either theoretically determined or measured in very controlled situations not corresponding to a realistic clinical operation (*24,25*). *Exposure limits must be observed and, if necessary, the operation theater must be reclassified as a temporary radiation-controlled area.*

The objective of this study was to provide a quantitative description of the total additional occupational exposure that would occur for surgery personnel and pathologists from patients undergoing preoperative ^{68}Ga-PSMA PET/CT and subsequent radioguided RP.

MATERIALS AND METHODS

Surgery and Intraoperative CLI

Ten patients with preoperative ^{68}Ga-PSMA-11 administration and intraoperative CLI were included in the present radiation exposure study (5 of whom were included for post-PET/CT γ-field dose rate investigations). The work flow of our "1-stop-shop" protocol is shown in Figure 1. Patients received 141.9 ± 57.86 (average ± SD) MBq of ^{68}Ga-PSMA-11 for PET/CT, in accordance with guideline recommendations (*26*). After ^{68}Ga-PSMA PET/CT, radioguided RP was performed. A urinary catheter was inserted in the operating room to drain the urine. The excised prostate specimen was immediately retrieved from the abdomen, wiped to clear blood and fluids, positioned in a specimen tray, and then imaged with the LightPath system. After the imaging was done, the prostate gland was assessed for radioactivity quantification with a germanium detector.

Patient Dose Rate

An initial evaluation of the detector response consisted of 3 measurements of a point source of 60 MBq using a proportional counter–based dose rate meter (FH 40 G-L; Thermo Fisher Scientific); all measurements included background subtraction.

Subsequently, we evaluated the impact of patient orientation toward the radiation detector, compared with a point source, and later provided a rough estimation of the fraction of tracer elimination until prostatectomy. For this step, we obtained measurements from 10 patients

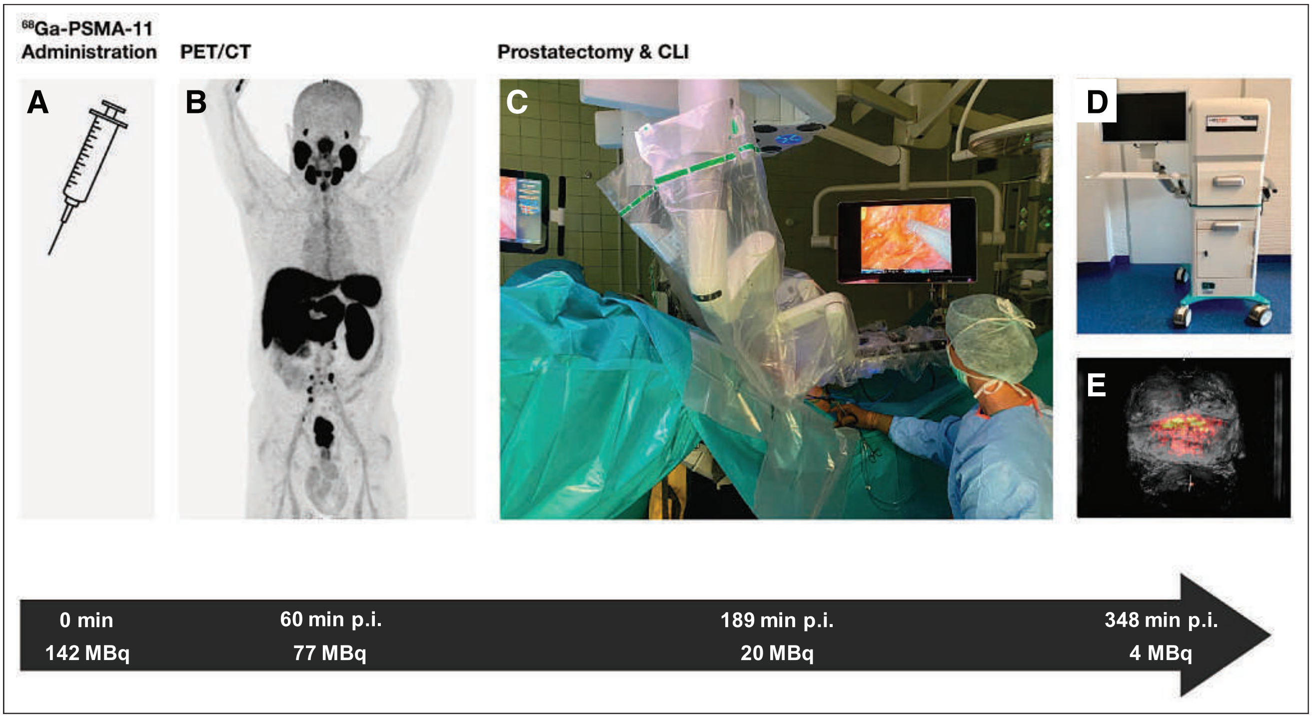

FIGURE 1. One-stop-shop protocol, including tracer administration (A), PET/CT imaging (B), and CLI during prostatectomy (C–E), permitted by remainder of ^{68}Ga-PSMA-11 uptake in prostate. Temporal sequence (black arrow) shows median time points after injection (p.i.) and decay-corrected whole-body activity expected for each step of protocol.

injected with ^{68}Ga-PSMA-11 (10.4 ± 4.6 min after injection), in the standing position facing the right and left sides of the waist, with the condition that the patients did not eliminate any tracer via urine excretion (pre-PET/CT). At 100.2 ± 27.5 min after ^{68}Ga-PSMA-11 PET/CT scanning, measurements were obtained from 5 patients in the supine position (post-PET/CT). In total, 4 predefined positions were measured (coded as head [A], right side of the waist [B], left side of the waist [C], and feet [D]) at a distance of 1 m. These predefined positions corresponded to the locations around the patient where staff members (e.g., scrub nurse, surgical assistant) were likely to be in stationary positions during surgery including CLI. In total, 20 individual measurements were obtained.

The measured dose rates were plotted as a function of the injected tracer activity decay corrected to the time of the measurement, and a linear fit (least squares method) was applied, constraining the fit to pass at the origin (i.e., the condition in which there is no tracer; the dose rate output will be equal to that measured as the background signal). We postulated that the slope of the fit would provide an estimate of the patient-specific dose rate constant at the defined positions.

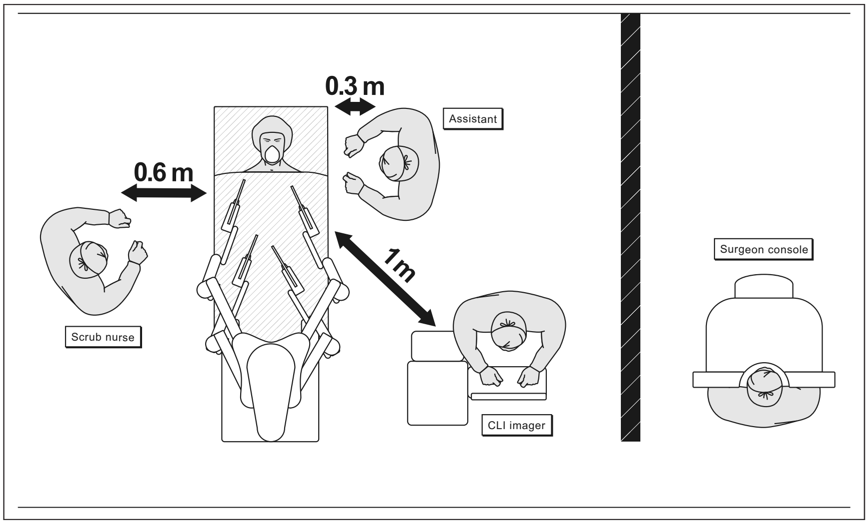

FIGURE 2. Setup in operating theater and respective distances used for calculated personal equivalent doses based on patient-specific dose rate constants.

Electronic Personal Dosimetry (EPD)

The exposure of the medical personnel was assessed in 10 procedures using EPD. RAD-60 (Mirion Technologies) dosimeters were positioned at waist level. Measurements included the first surgical assistant and scrub nurse at the operating table and the CLI imager/surgeon at the robotic console and encompassed the whole duration of surgery.

EPD Versus Dose Rate Predictions

On the basis of the different patient-specific dose rate constants at the defined positions, the exposure during the procedure was calculated as:

$$\dot{H}^*(10) = \frac{\Gamma_{H^*} \cdot A}{r^2} \cdot RF, \qquad \text{Eq. 1}$$

where $\dot{H}^*(10)$ is the ambient dose equivalent rate at a 10-mm depth, and Γ_{H^*} is the dose rate constant. A is the radionuclide activity, and r is the distance from the source to the detector. Because ^{68}Ga is a short-lived radionuclide (half-life value of 67.71 min), the activity present in a given sample will decrease as a function of the time of measurement, thus causing a decrease in the dose rate. Taking this phenomenon into account, we introduced a correction factor that was obtained by integrating the dose rate over the measured time (t); this factor was referred to as a reduction factor (*25*):

$$RF = 1.433 \cdot \frac{T_{1/2}}{t} \cdot \left(1 - \exp\left[\frac{0.693 \cdot t}{T_{1/2}}\right]\right). \qquad \text{Eq. 2}$$

Because operating room personnel are mostly stationary in robot-assisted surgery, it is reasonable to assume that the point source exposure modeling will provide a reasonable estimation. If we measure the typical distance from the source to the exposed first assistant, scrub nurse, and CLI imager (Fig. 2), we find that r is equal to 0.3, 0.6, and 1 m, respectively (the CLI imager is also a conservative surrogate for the anesthetist and the primary surgeon at the console). To accommodate any uncertainty related to the exact position of each health care professional, 2 additional points at ±10 cm of the reference position were considered. The health care professional positions were then superimposed on Figure 3, such that the first surgical assistant and the CLI imager/surgeon were attributed the dose rate value corresponding to position C, whereas the scrub nurse was attributed that corresponding to position B.

Prostate Gland Specimens

To access the tracer activity present in the prostate gland, as an indicator for the pathologist's skin exposure, 8 prostate specimens were measured with a Hyper-Pure germanium detector (HPGe) (Canberra) after prostate excision and CLI. To ensure adequate pathologic processing afterward, the specimens had already been placed in formalin. The radiation measurement was performed using a 20-min protocol,

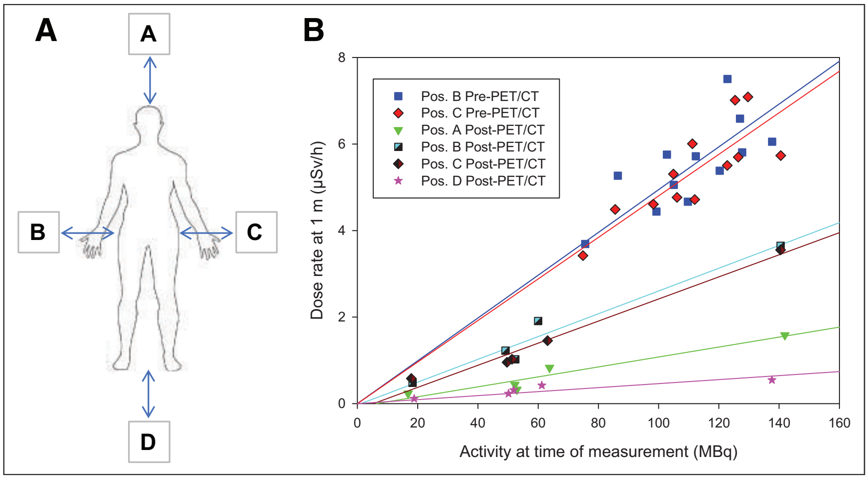

FIGURE 3. Dose rate measurements at predefined positions (Pos.) (A) and respective linear regression lines (B). Positions are as follows: A = at head; B = right side; C = left side; D = at feet. Post-PET/CT = dose rate readings immediately before entering operating room; Pre-PET/CT = measurements immediately after tracer injection.

TABLE 1

Summary of Dose Rate Measurements, Activity at Time of Measurement, and Respective Patient-Specific Dose Rate Constants (Dose Rate/Activity)

Position	Activity, MBq		Dose Rate/Activity, μSv · h^{-1} · MBq^{-1}		
	Average	SD	Average	SD	r^2
Point source (1 m)	69.96	2.3	0.145	0.002	
Patient before PET (1 m)	112.2	17.7			
B			0.047	0.004	0.70
C			0.047	0.005	0.66
Patient after PET (1 m)	64.5	41.7			
A			0.011	0.003	0.92
B			0.026	0.004	0.96
C			0.024	0.005	0.97
D			0.003	0.004	0.84

followed by an automatic sequence for the identification of the 511-keV energy peak and further quantification based on energy and efficiency calibration curves.

The detected activity for HPGe provided an estimate of the exposure of the pathologists who performed frozen-section procedures. As a threshold, we used nuclide-specific exemption limits (^{68}Ga < 100 kBq) (*27*).

Because not all centers may have access to HPGe detectors, we present an alternative method for accessing the amount of radiotracer present in the excised specimen on the basis of ^{68}Ga-PSMA-11 imaging. The method consists of defining a region delimited by the prostate anatomic boundaries on the basis of CT imaging. The same volume is then overlaid on the PET reconstructed images to provide an estimate of the total amount of tracer.

RESULTS

Patient Dose Rate

Initial measurements around the patient showed a decreased dose rate constant compared with a point source. The measured dose rate values averaged 5.3 ± 0.9 μSv/h. If a linear relationship between the dose rate and tracer activity (decay corrected to the time of measurement) is assumed, then the patient-specific dose rate constant for each measured position can be extracted, showing both position B ($n = 10$) and position C ($n = 10$): 0.047 μSv/h·MBq versus 0.145 ± 0.002 μSv/h·MBq for the point source (Table 1).

The dose rate measurements immediately before surgery (post-PET/CT) averaged 1.04 ± 1.00 μSv/h (minimum: 0.115 μSv/h; maximum, 3.65 μSv/h). The lowest dose rates were detected at the head and the feet of the patients. The patient-specific dose rate constant values obtained from a linear modulation were 0.011, 0.026, 0.024, and 0.003 μSv/h·MBq, corresponding to the head (A), right waist (B), left waist (C), and feet (D), respectively.

Patient Demographics and Oncologic Data

Patient characteristics are displayed in Table 2. In total, 10 patients with histologically confirmed PC were included; of those, 50% had locally advanced disease and 50% had high-risk PC. The median time from tracer injection until CLI was 328.5 min (interquartile range [IQR], 298.75–371.75 min). This study received formal ethics committee approval (19–8749-BO), and all subjects provided written informed consent.

EPD

For the 10 procedures considered, the average EPD monitoring duration was 242 ± 14 min, starting 189 ± 38 min after ^{68}Ga-PSMA-11 administration. EPD readings revealed average personal equivalent doses [Hp(10)] of 9.0 ± 7.1, 3.3 ± 3.9, and 0.7 ± 0.7 μSv for first surgical assistant, scrub nurse, and CLI imager/surgeon at the robotic console, respectively.

EPD Versus Dose Rate Predictions

Regarding the calculated Hp(10) based on patient-specific dose rate constants, we observed average Hp(10) of 11.7 ± 10.0, 2.7 ± 1.7, and 0.8 ± 0.5 μSv for the first surgical assistant, scrub nurse, and CLI imager/surgeon, respectively. These values correspond to success rates (the condition in which the read EPD falls within the ±10-cm uncertainty–calculated exposure) of 90%, 40%, and 20% for the first surgical assistant, scrub nurse, and CLI imager/surgeon, respectively. The procedure-specific values for exposure are shown in Figure 4.

Prostate Gland Specimens

Prostate gland specimens were excised and analyzed by CLI at medians of 348 min (IQR, 282–437 min) after ^{68}Ga-PSMA-11 administration and 276 min (IQR, 194–369 min) after PET/CT imaging. The measurements with the HPGe were obtained 71 min (IQR, 42–143 min) after prostate excision. All activity values were decay corrected to the time of prostate excision.

HPGe measurements revealed activities between 0.9 and 38.6 kBq for ^{68}Ga. The median HPGe measured activity was 2.96 kBq (IQR, 2.23–7.65 kBq), whereas the median total activity encompassed in the prostate region PET reconstructed images accounted for 3.83 kBq (IQR, 2.83–8.50 kBq).

The deviation between HPGe values and PET activity values was characterized by a systematic overestimation (median of 18.9%) of PET activity values compared with HPGe values, as depicted in Figure 5. There were no statistical differences between HPGe and PET datasets with regard to prostate activity levels ($P = 0.090$).

DISCUSSION

In the present study, we were able to provide a systematic evaluation of the patient as a radioactive source in each of the different procedural steps encountered in PET/CT imaging and subsequent CLI for the evaluation of surgical margins during robot-assisted

TABLE 2
Demographic and Oncologic Data for 10 Patients

Characteristic	Value
Patient and imaging*	
Age, in y	63 (56.5–69)
BMI, in kg/m^2	30.37 (24.25–34.68)
Injected activity, in MBq	122 (99.25–185)
Activity derived from HPGe, in kBq/mL, corrected to time of excision	2.96 (2.24–7.65)
Activity derived from PET/CT in prostate, in kBq/mL, corrected to time of excision	3.83 (2.83–8.50)
Duration from tracer injection to CLI, in min	328.5 (298.75–371.75)
Duration from skin incision to CLI, in min	130.2 (125.4–145.2)
Surgical and oncologic†	
Organ-confined PC	5 (50)
Locally advanced PC	5 (50)
Initial PSA, in ng/mL*	12.5 (8.3–15.25)
Risk stratification according to D'Amico (*34*)	
Intermediate-risk PC	5 (50)
High-risk PC	5 (50)
ISUP-GGG	
2	4 (40)
3	4 (40)
4	0
5	2 (20)
Prostate specimen weight, in g*	43.5 (41.25–55)

---

*Reported as medians, with interquartile ranges in parentheses.

†Reported as numbers of patients, with percentages in parentheses, unless otherwise indicated.

BMI = body mass index; PSA = prostate-specific antigen; ISUP-GGG = International Society of Urological Pathology Gleason grading group.

prostatectomy for a single administration protocol (i.e., 1-stop-shop protocol) (Fig. 1). For this purpose, methods for prospective and department planning radiation protection calculations for this entirely new application of ^{68}Ga-PSMA-11 were used and included a point source exposure calculation and a reduction factor expected for long exposures to short-lived radionuclides.

In the first step of the present study, a measurement was elected to illustrate how the point source exhibits a similar dose rate per unit of activity at a 1-m distance. The resulting dose rate at 1 m normalized for activity showed a good concordance with the DIN (Deutsches Institut für Normung [German Institute for Standardisation Registered Association]) tabulated value of 0.1581 (0.145 measured) μSv · h^{-1} · MBq^{-1} for ^{68}Ga. The observed discrepancy was mainly due to a decreased detector responsivity to 511 keV, compared with the calibration γ-lines of ^{137}Cs (661.6 keV). However, for patients, partially because of self-attenuation (*28*), a discrepancy between tabulated values and those based on dose rate meter measurements was observed (Table 1). The positioning of the dose rate meter at a distance of 1 m from the radiation source, with a height greater than this distance, will result in a lower dose rate than that of a point source (*29*). Dose rate measurements performed after the PET/CT scan showed a decreased dose rate constant because much of the tracer had been excreted at this point, leading to a decrease in dose rate constants of approximately 50% compared with the values immediately after tracer injection (i.e., pre-PET/CT).

Despite being a simple and limited method, the point source approximation using patient-specific dose rate constants provided a plausible approximation for the occupational exposure measured by dosimeters, especially for the position of the assistant surgeon because a relaxation of ±10 cm in the stationary condition could predict 90% of the measured doses. The greatest impairment of the dose estimation was due to very low exposure levels, illustrated by the CLI imager/surgeon position, for which most values of exposure were found to be between 0 and 1 μSv; these data suggested that the limiting factor was the lack of accuracy of EPD for measurements below the measuring range (1 μSv–9.99 Sv). The remainder of outliers could be explained by a higher proximity to the source or orientation of the dosimeter toward the radiation field outside the efficient angular range of EPD.

With respect to the measured Hp(10), it is evident from Equation 2 that the professional who operated nearest to the patient would have the highest exposure. Considering the general public exposure limit of 1 mSv as a threshold, that professional with the highest exposure (the first surgical assistant) (Fig. 4A) would be able to perform CLI after ^{68}Ga-PSMA-11 PET/CT for 110 radioguided RP procedures per year.

The presented "1-stop-shop" single administration for both PET/CT and CLI has been validated in a feasibility study (*18*) and serves as an example of the ALARA (as low as reasonably achievable) principle for radiation exposure optimization applied to radioguided

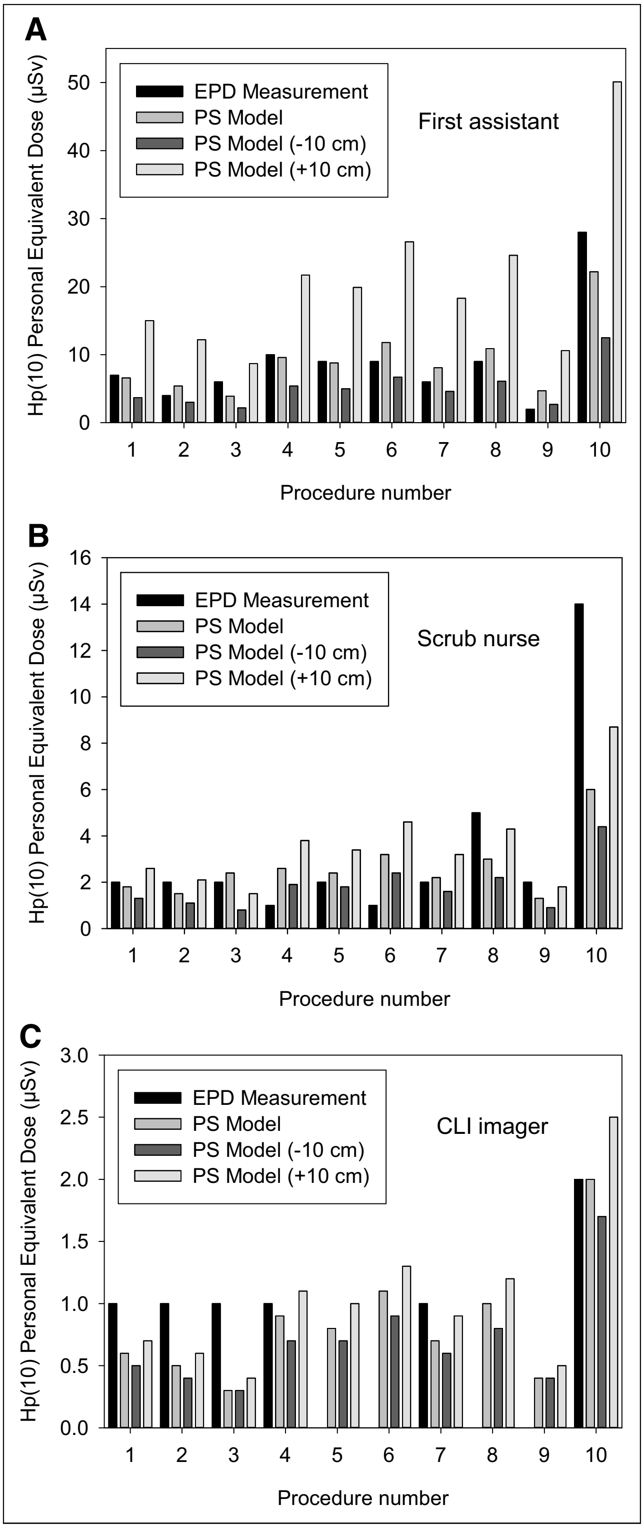

FIGURE 4. EPD measurements (black bars) alongside computed values based on point source (PS) model (medium gray bars) at measured distance *r*. Variations of minus −10 cm (dark gray bars) and +10 cm (light gray bars) from distance r using PS assumption are shown.

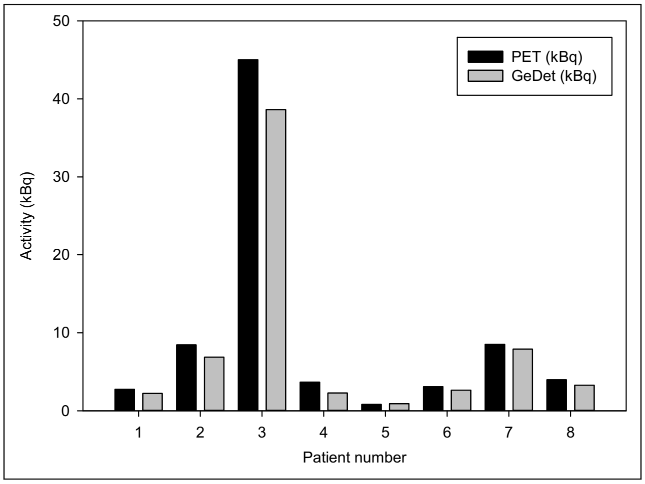

FIGURE 5. Activity quantification of excised prostate specimens decay corrected to time of excision. Black bars represent PET-based quantification (median, 3.83 kBq; IQR, 2.83–8.50 kBq). Gray bars represent HPGe measurement (GeDet) (median, 2.96 kBq; IQR, 2.23–7.65 kBq).

surgery—not only for the medical exposure of the patient by relinquishing a dedicated tracer injection of about 100 MBq, resulting in a patient effective dose of 2 mSv, but also by effectively decreasing the occupational exposure of the medical personnel. In a ^{68}Ga-PSMA-11 CLI primary prostate cancer study (*18*), with perioperative radiotracer administration of 100 MBq, an Hp(10) of 16 µSv was recorded for the most exposed medical professional. The data presented were for the sterile scrub nurse and were comparable to our collected data. However, no other exposure data were collected from other staff roles. According to our findings, the exposure values for the scrub nurse were quite variable, with an average Hp(10) of 3.3 ± 3.9 µSv, whereas the exposure values for the assistant were very precise and therefore more informative.

Other intraoperative CLI applications include the use of 2-^{18}F-FDG for the identification of surgical margins in breast-conserving surgery. From published studies, there is evidence that the preoperative administration of about 300 MBq of 2-^{18}F-FDG would deliver maximal personal equivalent doses of 34.0–61.8 µSv (*15,30*). Interestingly, when the ^{18}F decay characteristics and the assumption of the administration of 300 MBq were substituted in our model, then we obtained exposure levels of 51.3, 15.3, and 4.6 µSv per procedure for the first surgical assistant, scrub nurse, and surgeon, respectively.

CLI has been important in preclinical evaluations of disease models using several β-emitters, mostly because of the small dimensions of the image samples (mostly from mice), which are favorable for CLI, and the cost-efficiency compared with preclinical PET/CT scanners. With translation in the intraoperative environment, it is conceivable that new radionuclides (such as the longer-lived ^{89}Zr or ^{64}Cu) will become relevant in CLI-radioguided surgery; for these radionuclides, our exposure model could provide some insight in terms of predicting occupational exposures (*31*).

Our approach for the pathologist's exposure was a conservative surrogate for a direct measurement of exposure with a ring dosimeter; we directly measured the activity contained in the prostate gland using the HPGe. On the basis of our data, there was no significant radiation exposure to pathology staff. Additionally, we provided an independent measurement based on PET data obtained before CLI. Our results indicated a systematic overestimation of the activity levels found by PET in comparison with the HPGe. The systematic result suggests that this method of tracer amount estimation may be limited by the presence of activity in surrounding tissues, namely, the bladder, that would overestimate the radioactivity content in the prostate specimen. However, with the exception of

1 specimen, the PET estimate could predict the HPGe value below 10% error. Various standardized exposure situations are given in the literature. Delacroix et al. described hand contact on a glass beaker filled with 50 mL of ^{68}Ga solution (*27*). With this method, a dose of approximately 4 μSv would be expected from a 1-h contact. This specification is consistent with our results, considering the 50-mSv radiation exposure limit to the skin for members of the public (*32*).

The present study has several limitations. First, our study was related to the low radiation field that provides poor statistics for counting devices. This limitation also translates to difficulty for the point source model in predicting such low exposures. Second, the fact that we used point source geometry is also a limitation, as in real life the patient is not a point source. Further studies using anthropomorphic mathematic phantoms as the source of external exposure could address this limitation (*33*). Finally, we did not provide measured evidence of skin exposure by means of a ring dosimeter and therefore could not directly correlate the activity levels in the specimen with the finger exposure of the histopathology staff.

CONCLUSION

The single-injection PET/CT CLI-guided RP protocol can be performed in about 110 procedures per year before the limit for public radiation exposure is reached. All prostate specimen radionuclide content was below the exemption level for ^{68}Ga at the time of excision. Overall, the occupational risk of the 1-stop-shop protocol appears to be quite low, meaning that it is not necessary to reclassify the operation theater as a temporary radiation-controlled area. Furthermore, no radiation safety measures are required for specimen handling in the pathology department. Further validation for other radionuclides with the potential for CLI-radioguided surgery or other types of radioguided surgery, such as ^{18}F-PSMA-1007, should be addressed in future studies.

DISCLOSURE

Boris A. Hadaschik has had advisory roles for ABX, Astellas, AstraZeneca, Bayer, Bristol Myers Squibb, Janssen R&D, Lightpoint Medical Ltd., and Pfizer; has received research funding from Astellas, Bristol Myers Squibb, German Research Foundation, Janssen R&D, and Pfizer; and has received compensation for travel from Astellas, AstraZeneca, and Janssen R&D. Wolfgang P. Fendler reports fees from BTG (consultant), Calyx (consultant), RadioMedix (PET reader), Bayer (speakers bureau), and Parexel (image reader) outside the submitted work. Ken Herrmann reports personal fees from Bayer, personal fees from Sofie Biosciences, personal fees from SIRTEX, nonfinancial support from ABX, personal fees from Adacap, personal fees from Curium, personal fees from Endocyte, grants and personal fees from BTG, personal fees from IPSEN, personal fees from Siemens Healthineers, personal fees from GE Healthcare, personal fees from Amgen, personal fees from Novartis, personal fees from ymabs, personal fees from Aktis Oncology, personal fees from Theragnostics, and personal fees from Pharma15 outside the submitted work. Ken Herrmann is an associate editor of *JNM.* Maarten R. Grootendorst is an employee of Lightpoint Medical Ltd. No other potential conflict of interest relevant to this article was reported.

ACKNOWLEDGMENTS

We thank the technologists of the nuclear medicine teams and the nurses of the urology surgery teams for their ongoing logistic support.

KEY POINTS

QUESTION: What is the radiation exposure risk for CLI-radioguided surgery after ^{68}Ga-PSMA-11 administration for surgery personnel?

PERTINENT FINDINGS: The protocol can be performed at about 110 procedures per year before the limit for public radiation exposure is reached.

IMPLICATIONS FOR PATIENT CARE: Implementation of CLI-radioguided surgery procedures does not involve additional radioprotection hurdles.

REFERENCES

1. *EAU Guidelines*. Edn. presented at the EAU Annual Congress Amsterdam 2022. EAU Guidelines Office. European Association of Urology website. https://uroweb.org/guidelines. Accessed August 9, 2022.
2. Martini A, Gandaglia G, Fossati N, et al. Defining clinically meaningful positive surgical margins in patients undergoing radical prostatectomy for localised prostate cancer. *Eur Urol Oncol.* 2021;4:42–48.
3. Gandaglia G, Ploussard G, Valerio M, et al. The key combined value of multiparametric magnetic resonance imaging, and magnetic resonance imaging–targeted and concomitant systematic biopsies for the prediction of adverse pathological features in prostate cancer patients undergoing radical prostatectomy. *Eur Urol.* 2020;77:733–741.
4. Radtke JP, Hadaschik BA, Wolf MB, et al. The impact of magnetic resonance imaging on prediction of extraprostatic extension and prostatectomy outcome in patients with low-, intermediate- and high-risk prostate cancer: try to find a standard. *J Endourol.* 2015;29:1396–1405.
5. Petralia G, Musi G, Padhani AR, et al. Robot-assisted radical prostatectomy: multiparametric MR imaging–directed intraoperative frozen-section analysis to reduce the rate of positive surgical margins. *Radiology.* 2015;274:434–444.
6. Schlomm T, Tennstedt P, Huxhold C, et al. Neurovascular structure-adjacent frozen-section examination (NeuroSAFE) increases nerve-sparing frequency and reduces positive surgical margins in open and robot-assisted laparoscopic radical prostatectomy: experience after 11,069 consecutive patients. *Eur Urol.* 2012;62:333–340.
7. Gillitzer R, Thüroff C, Fandel T, et al. Intraoperative peripheral frozen sections do not significantly affect prognosis after nerve-sparing radical prostatectomy for prostate cancer. *BJU Int.* 2011;107:755–759.
8. Perera M, Papa N, Roberts M, et al. Gallium-68 prostate-specific membrane antigen positron emission tomography in advanced prostate cancer: updated diagnostic utility, sensitivity, specificity, and distribution of prostate-specific membrane antigen-avid lesions—a systematic review and meta-analysis. *Eur Urol.* 2020;77:403–417.
9. Yaxley JW, Raveenthiran S, Nouhaud FX, et al. Risk of metastatic disease on ^{68}gallium-prostate-specific membrane antigen positron emission tomography/computed tomography scan for primary staging of 1253 men at the diagnosis of prostate cancer. *BJU Int.* 2019;124:401–407.
10. Koschel S, Murphy DG, Hofman MS, Wong L-M. The role of prostate-specific membrane antigen PET/computed tomography in primary staging of prostate cancer. *Curr Opin Urol.* 2019;29:569–577.
11. Kalapara AA, Nzenza T, Pan HYC, et al. Detection and localisation of primary prostate cancer using ^{68}gallium prostate-specific membrane antigen positron emission tomography/computed tomography compared with multiparametric magnetic resonance imaging and radical prostatectomy specimen pathology. *BJU Int.* 2020;126:83–90.
12. Morris MJ, Carroll PR, Saperstein L, et al. Impact of PSMA-targeted imaging with ^{18}F-DCFPyL-PET/CT on clinical management of patients (pts) with biochemically recurrent (BCR) prostate cancer (PCa): results from a phase III, prospective, multicenter study (CONDOR). *Am J Clin Oncol.* 2020;38(suppl):5501.
13. Das S, Thorek DL, Grimm J. Cerenkov imaging. *Adv Cancer Res.* 2014;124:213–234.
14. Grootendorst MR, Cariati M, Kothari A, Tuch DS, Purushotham A. Cerenkov luminescence imaging (CLI) for image-guided cancer surgery. *Clin Transl Imaging.* 2016;4:353–366.
15. Grootendorst MR, Cariati M, Pinder SE, et al. Intraoperative assessment of tumor resection margins in breast-conserving surgery using ^{18}F-FDG Cerenkov luminescence imaging: a first-in-human feasibility study. *J Nucl Med.* 2017;58:891–898.

16. Chin PT, Welling MM, Meskers SC, Olmos RAV, Tanke H, van Leeuwen FW. Optical imaging as an expansion of nuclear medicine: Cerenkov-based luminescence vs fluorescence-based luminescence. *Eur J Nucl Med Mol Imaging.* 2013;40:1283–1291.
17. Olde Heuvel J, van der Poel HG, Bekers EM, et al. ^{68}Ga-PSMA Cerenkov luminescence imaging in primary prostate cancer: first-in-man series. *Eur J Nucl Med Mol Imaging.* 2020;47:2624–2632.
18. Darr C, Harke NN, Radtke JP, et al. Intraoperative ^{68}Ga-PSMA Cerenkov luminescence imaging for surgical margins in radical prostatectomy: a feasibility study. *J Nucl Med.* 2020;61:1500–1506.
19. Bekiş R, Celik P, Uysal B, et al. Exposure of surgical staff to radiation during surgical probe applications in breast cancer. *J Breast Cancer.* 2009;12:27–31.
20. Klausen TL, Chakera A, Friis E, Rank F, Hesse B, Holm S. Radiation doses to staff involved in sentinel node operations for breast cancer. *Clin Physiol Funct Imaging.* 2005;25:196–202.
21. Waddington WA, Keshtgar M, Taylor I, Lakhani S, Short M, Eli P. Radiation safety of the sentinel lymph node technique in breast cancer. *Eur J Nucl Med.* 2000;27:377–391.
22. Brenner W, Ostertag H, Peppert E, et al. Radiation exposure to the personnel in the operating room and in the pathology due to SLN detection with Tc-99m-nanocolloid in breast cancer patients. *Nuklearmedizin.* 2000;39:142–145.
23. Heckathorne E, Dimock C, Dahlbom M. Radiation dose to surgical staff from positron-emitter-based localization and radiosurgery of tumors. *Health Phys.* 2008;95:220–226.
24. Costa PF, Reinhardt M, Poppe B. Occupational exposure from F-18-FDG PET/CT: implementation to routine clinical practice. *Radiat Prot Dosimetry.* 2018;179:291–298.
25. Madsen MT, Anderson JA, Halama JR, et al. AAPM task group 108: PET and PET/CT shielding requirements. *Med Phys.* 2006;33:4–15.
26. Fendler WP, Eiber M, Beheshti M, et al. ^{68}Ga-PSMA PET/CT: joint EANM and SNMMI procedure guideline for prostate cancer imaging: version 1.0. *Eur J Nucl Med Mol Imaging.* 2017;44:1014–1024.
27. Delacroix D, Guerre JP, Leblanc P, Hickman C. Radionuclide and radiation protection data handbook 2nd edition (2002). *Radiat Prot Dosimetry.* 2002;98:9–168.
28. Zeff BW, Yester MV. Patient self-attenuation and technologist dose in positron emission tomography. *Med Phys.* 2005;32:861–865.
29. Yi Y, Stabin M, McKaskle M, Shone M, Johnson A. Comparison of measured and calculated dose rates near nuclear medicine patients. *Health Phys.* 2013;105:187–191.
30. Jurrius PA, Grootendorst MR, Krotewicz M, et al. Intraoperative [^{18}F]FDG flexible autoradiography for tumour margin assessment in breast-conserving surgery: a first-in-human multicentre feasibility study. *EJNMMI Res.* 2021;11:28.
31. Collamati F, van Oosterom MN, Hadaschik BA, et al. Beta radioguided surgery: towards routine implementation? *Q J Nucl Med Mol Imaging.* 2021;65:229–243.
32. The 2007 Recommendations of the International Commission on Radiological Protection. ICRP publication 103. *Ann ICRP.* 2007;37:1–332.
33. Xu XG. An exponential growth of computational phantom research in radiation protection, imaging, and radiotherapy: a review of the fifty-year history. *Phys Med Biol.* 2014;59:R233–R302.
34. D'Amico AV, Whittington R, Malkowicz SB, et al. Biochemical outcome after radical prostatectomy, external beam radiation therapy, or interstitial radiation therapy for clinically localized prostate cancer. *JAMA* 1998;280:969–974.

Administration Routes for SSTR-/PSMA- and FAP-Directed Theranostic Radioligands in Mice

Jasmin M. Klose[1], Jasmin Wosniack[1], Janette Iking[1], Magdalena Staniszewska[1], Fadi Zarrad[1], Marija Trajkovic-Arsic[2,3], Ken Herrmann[1], Pedro Fragoso Costa[1], Katharina Lueckerath[1,4], and Wolfgang P. Fendler[1]

[1]Department of Nuclear Medicine, University Hospital Essen, University of Duisburg–Essen, Essen, Germany; [2]Division of Solid Tumor Translational Oncology, German Cancer Consortium, West German Cancer Center, University Hospital Essen, Essen, Germany; [3]German Cancer Consortium and German Cancer Research Center, Heidelberg, Germany; and [4]Ahmanson Translational Theranostics Division, Department of Molecular and Medical Pharmacology, David Geffen School of Medicine, UCLA, Los Angeles, California

The NETTER-1, VISION, and TheraP trials proved the efficacy of repeat intravenous application of small radioligands. Application by subcutaneous, intraperitoneal, or oral routes is an important alternative and may yield comparable or favorable organ and tumor radioligand uptake. Here, we assessed organ and tumor biodistribution for various radioligand application routes in healthy mice and models of cancer expressing somatostatin receptor (SSTR), prostate-specific membrane antigen (PSMA), and fibroblast activation protein (FAP). **Methods:** Healthy and tumor-bearing male C57BL/6 or NOD SCID γ-mice, respectively, were administered a mean of 6.0 ± 0.5 MBq of ^{68}Ga-DOTATOC (RM1-SSTR allograft), 5.3 ± 0.3 MBq of ^{68}Ga-PSMA11 (RM1-PSMA allograft), or 4.8 ± 0.2 MBq of ^{68}Ga-FAPI46 (HT1080-FAP xenograft) by intravenous, intraperitoneal, subcutaneous, or oral routes. In vivo PET images and ex vivo biodistribution in tumor, organs, and the injection site were assessed up to 5 h after injection. Healthy mice were monitored for up to 7 d after the last scan for signs of stress or adverse reactions. **Results:** After intravenous, intraperitoneal, and subcutaneous radioligand administration, average residual activity at the injection site was less than 17 percentage injected activity per gram (%IA/g) at 1 h after injection, less than 10 %IA/g at 2 h after injection, and no more than 4 %IA/g at 4 h after injection for all radioligands. After oral administration, at least 50 %IA/g remained within the intestines until 4 h after injection. Biodistribution in organs of healthy mice was nearly equivalent after intravenous, intraperitoneal, and subcutaneous application at 1 h after injection and all subsequent time points ($\leq$1 %IA/g for liver, blood, and bone marrow; 11.2 ± 1.4 %IA/g for kidneys). In models for SSTR-, PSMA- and FAP-expressing cancer, tumor uptake was increased or equivalent for intraperitoneal/subcutaneous versus intravenous injection at 5 h after injection (ex vivo): SSTR, 7.2 ± 1.0 %IA/g (P = 0.0197)/6.5 ± 1.3 %IA/g (P = 0.0827) versus 2.9 ± 0.3 %IA/g, respectively; PSMA, 3.4 ± 0.8 %IA/g (P = 0.9954)/3.9 ± 0.8 %IA/g (P = 0.8343) versus 3.3 ± 0.7% IA/g, respectively; FAP, 1.1 ± 0.1 %IA/g (P = 0.9805)/1.1 ± 0.1 %IA/g (P = 0.7446) versus 1.0 ± 0.2 %IA/g, respectively. **Conclusion:** In healthy mice, biodistribution of small theranostic ligands after intraperitoneal/subcutaneous application is nearly equivalent to that after intravenous injection. Subcutaneous administration resulted in the highest absolute SSTR tumor and tumor-to-organ uptake as compared with the intravenous route, warranting further clinical assessment.

Key Words: radioligand; biodistribution; small-animal PET; theranostic; intravenous; subcutaneous

J Nucl Med 2022; 63:1357–1363
DOI: 10.2967/jnumed.121.263453

NETTER-1 (*1*), and the more recent clinical trials TheraP (*2*) and VISION (*3*), established somatostatin receptor (SSTR)– and prostate-specific membrane antigen (PSMA)–directed small-ligand radiotheranostics as efficacious cancer therapy with favorable safety profiles. Recently, fibroblast activation protein (FAP)–targeting small ligands have emerged for PET and therapy of cancers (*4*). Intravenous application is the standard route for radioligands. However, oral, intraperitoneal, and subcutaneous administrations are faster and require a lower level of training than does intravenous administration, both in the preclinical and in the clinical settings. The volume of preclinical and clinical radioligand applications is growing rapidly, and thus, there is an urgent unmet need to assess alternative application routes to address the increasing demand. In addition, the field of FAP-directed therapies is dynamic and evolving, highlighting the emerging need for optimization of administration routes for these novel radioligands for ongoing preclinical and clinical assessment. With this intent, assessment of biodistribution and administration routes for ^{68}Ga-FAPI46 (FAP inhibitor [FAPI]) was requested by the German Federal Institute for Drugs and Medical Devices for recent approval of a prospective clinical trial on ^{68}Ga-FAPI46 PET/CT for various types of cancer (NCT04571086).

We hypothesized that intraperitoneal/subcutaneous application would yield organ and tumor biodistribution nearly equivalent to that of the routine intravenous injection. We further hypothesized that organ and tumor uptake would be significantly lower after oral application of radioligands. Here, we compare tumor and organ biodistribution after intravenous, intraperitoneal, subcutaneous, and oral application of small radioligands in healthy mice and mouse models of SSTR-, PSMA-, and FAP-expressing cancer.

MATERIALS AND METHODS

Cell Culture

RM1 cells, virally stably transduced with SFG-Egfp/Luc (RM1-PGLS) or pMSCV-IRES-YFP II-hSSTR (RM1-SSTR) to express high levels of cell surface human PSMA or SSTR2 (*5*), were obtained from

---

Received Oct. 29, 2021; revision accepted Dec. 28, 2021.

For correspondence or reprints, contact Wolfgang P. Fendler (wolfgang.fendler@uk-essen.de).

Johannes Czernin (UCLA). HT1080-FAP cells were a gift from Uwe Haberkorn (University Hospital of Heidelberg). HT1080 cells were stably transfected with the plasmid pcDNAI/neo-FAP (expressing the untagged full-length complementary DNA of human FAP) followed by neomycin selection (*6*). RM1-PSMA and RM1-SSTR were maintained in RPMI 1640 medium (GIBCO) and HT1080-FAP in Dulbecco modified Eagle medium (GIBCO), both with 10% fetal bovine serum (Thermo Fisher Scientific) and with 0.5% penicillin/streptomycin (GIBCO), at 37°C with 5% CO_2. Cells were thawed for 2 wk or passaged 3 times before inoculation. Cells were routinely assessed for *Mycoplasma* contamination using the VenorGeM OneStep kit (Minerva Biolabs).

Radiosynthesis

^{68}Ga-DOTATOC, ^{68}Ga-PSMA11, and ^{68}Ga-FAPI46 were obtained from the radiopharmacy of our clinic. Clinical-grade radiolabeling of precursors (DOTATOC, PSMA11, FAPI46) was performed using the Modular-Lab eazy for DOTATOC and PSMA or Scintomics GRP 3V for FAPI using commercially available reagent kits. The final solution had less than 5 μg/mL for ^{68}Ga-DOTATOC, less than 3 μg/mL for ^{68}Ga-PSMA, and approximately 50 μg/mL for ^{68}Ga-FAPI, with a 100-μL injected volume per mouse. Radiochemical purity was determined with radio–high-performance liquid chromatography (FAPI: Chromolith Performance RP18e column from Merck [100 × 3 mm], gradient of 0%–20% MeCN + 0.1% trifluoroacetic acid in 5 min, run time of 15 min; PSMA: 5%–40% MeCN + 0.1% trifluoroacetic acid in 10 min, run time of 15 min; DOTATOC: 24% MeCN + 0.1% trifluoroacetic acid for 8 min, then 24%–60% in 1 min, run time of 15 min; and instant thin-layer chromatography–silica gel [ammonium acetate, 77 g/L, and methanol R, 50:50 v/v]). The radiochemical purity exceeded 98% for all radioligands.

Mice and Tumor Models

Male C57BL/6 and NOD SCID Gamma mice were purchased from Charles River Laboratories (6–8 wk old) and housed under specific pathogen-free conditions with food and water available ad libitum. The health status of the mice was monitored by assessing a summarized score twice a week (healthy animals) or daily (tumor-bearing animals). The study was approved by the North Rhine–Westphalia State Agency for Nature, Environment, and Consumer Protection, Germany (permit AZ.81-02.04.2018.A090).

For subcutaneous tumors, 0.1×10^6 RM1-SSTR or RM1-PSMA (C57BL/6) cells or 1.0×10^6 HT1080-FAP (NOD SCID Gamma) cells in Matrigel (Corning)/phosphate-buffered saline (50:50 ratio) were injected into the shoulder region of the mice. Tumor volume (V) was calculated by measuring the length (L) and width (W) of tumors by caliper and using the formula $V = \frac{1}{2}(L \times W^2)$ (*7*). PET scans were acquired 7–10 d after tumor inoculation, as described previously (*5,8*). Mean (+SEM) tumor volumes were 0.39 ± 0.09 cm^3 (interquartile range, 0.07–0.66 cm^3) for RM1-SSTR tumors, 0.05 ± 0.01 cm^3 (interquartile range, 0.02–0.08 cm^3) for RM1-PSMA tumors, and 0.22 ± 0.03 cm^3 (interquartile range, 0.06–0.25 cm^3) for HT1080-FAP tumors.

Radioligand Application and Small-Animal PET/CT

Healthy or tumor-bearing anesthetized mice (1.5%–2% isoflurane) received a mean of 6.0 ± 0.5 MBq of ^{68}Ga-DOTATOC, 5.3 ± 0.3 MBq of ^{68}Ga-PSMA11, or 4.8 ± 0.2 MBq of ^{68}Ga-FAPI46 intravenously (tail vein), intraperitoneally, subcutaneously, or orally (oral HT1080-FAP tumor-bearing mice only) (differences between injected activities were not statistically significant). Each healthy mouse received intravenous, intraperitoneal, subcutaneous, and oral administration, with a 1-wk

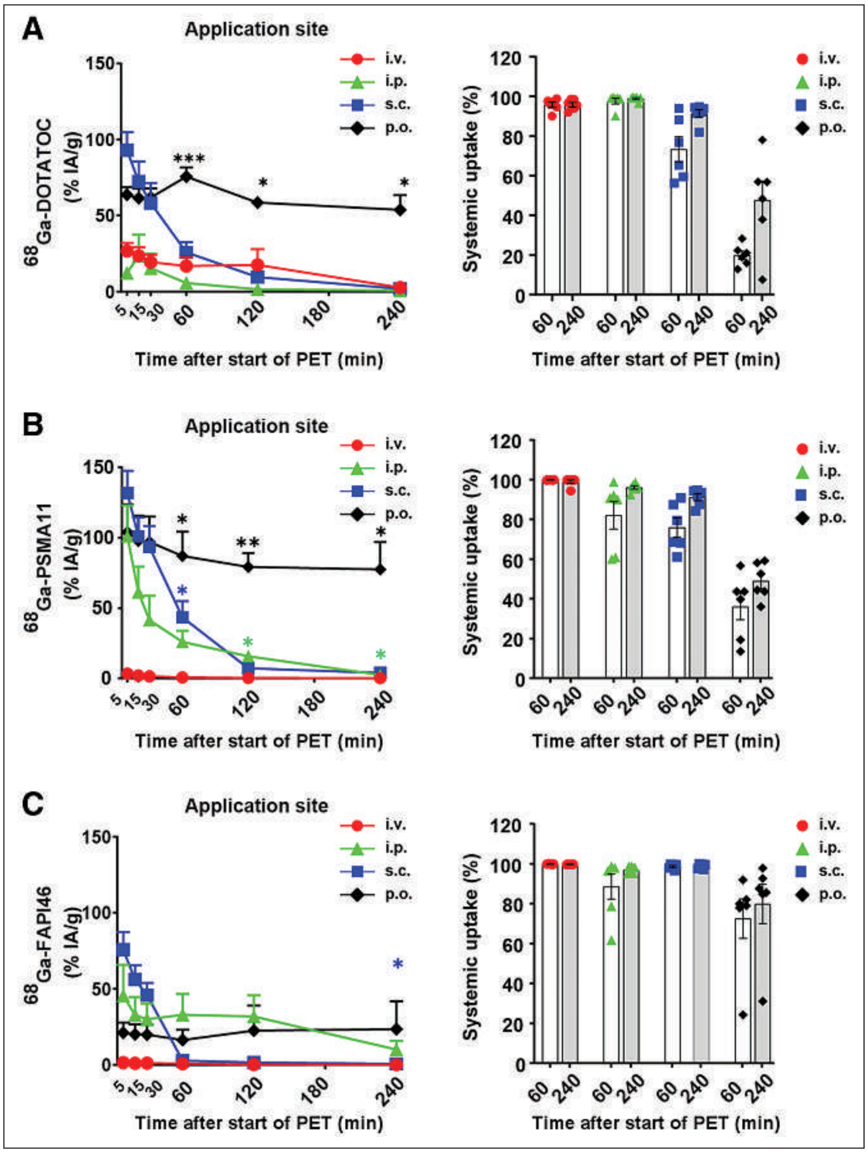

FIGURE 1. Activity at application site and systemic availability over time in healthy mice. Retention of ^{68}Ga-DOTATOC (A), ^{68}Ga-PSMA11 (B), and ^{68}Ga-FAPI46 (C) is shown in healthy mice (6/group) at application site. (Left) Time–activity curves illustrate radioligand dynamics at application site for intravenous, intraperitoneal, subcutaneous, and oral application. (Right) Relative systemic uptake of whole-body VOI excluding application site VOI is displayed as percentage total-body uptake. Each dot represents a mouse. Data are mean + SEM. i.p. = intraperitoneal; i.v. = intravenous; p.o. = oral; s.c. = subcutaneous. *$P < 0.05$ compared with intravenous application. **$P < 0.01$ compared with intravenous application. ***$P < 0.001$ compared with intravenous application.

interval between PET/CT scans (Supplemental Fig. 1A; supplemental materials are available at http://jnm.snmjournals.org). Each tumor-bearing mouse was scanned twice, at 1 and 4 h after injection, after either intravenous, intraperitoneal, or subcutaneous application and was sacrificed at about 5 h after injection for ex vivo analysis (Supplemental Fig. 1B). Imaging was performed with a β-CUBE (PET) and X-CUBE (CT) (Molecubes) in temperature-controlled beds with monitoring of breathing frequency. PET/CT was performed (PET, 15 min; CT, 5 min) in list mode with frames for 5, 10, and 15 min (dynamic scans; maximum delay between injection and scan start, 5 min) and static scans at 1, 2, and 4 h after injection for healthy mice and 1 and 4 h after injection for tumor groups.

Image Reconstruction and Processing

Images were reconstructed using an iterative image space reconstruction algorithm (30 iterations) with attenuation correction of the corresponding CT image. PET data were reconstructed into a 192 × 192 transverse matrix, producing a 400-μm isometric voxel size. PET images were evaluated with PMOD software (PMOD Technologies LLC). Decay-corrected mean percentage injected activity per gram (%IA/g) of the tumor and organs of interest was derived from DICOM images. Volumes of interest (VOIs) were defined as spheres with a diameter of 5 mm (lung, liver, spleen, intestines, heart, brain, kidneys) and 2.5 mm (bone marrow, thigh muscle, blood pool, injection site, tumor) in tissues of interest. %IA/g was calculated from the average pixel values reported in Bq/mL within these VOIs corrected for radioactive decay and mouse body weight.

Ex Vivo Analysis

Approximately 5 h after injection, the animals were killed and organs of interest were extracted, dabbed dry, weighed, and measured for radioactivity in an automated γ-counter (Perkin-Elmer γ-Counter 2480 Wizard^2). Organ and tumor uptake was calculated from radioactive counts, decay-corrected, and expressed as %IA/g.

Data and Statistical Analysis

Data are presented as mean ± SEM unless indicated otherwise. All statistical analyses were performed using GraphPad Prism (version 9.1.0; GraphPad Software). Tumor-to-organ uptake ratios were calculated for blood, kidney, liver, and bone marrow (femur) using %IA/g at 1 h and 4 h in in vivo VOIs and at 5 h for ex vivo γ-counter measurements (%IA/g tumor/%IA/g organ). Statistical significance was assessed using the Brown–Forsythe and Welch ANOVA test with the Dunnett T3 multiple-comparisons test or the Tukey multiple-comparisons test. *P* values below 0.05 were considered statistically significant.

RESULTS

Local and Systemic Activity

To assess the biodistribution of radioligands applied via different routes, we measured the activity retained at the injection site versus the overall systemic activity distribution excluding the application site. Activity at the injection site decreased over time after intravenous, intraperitoneal, and subcutaneous administration in healthy mice (Fig. 1; Supplemental Fig. 1). For all radioligands, mean residual activity at the injection site 4 h after injection was 1.0 ± 0.3 %IA/g for intravenous, 4.4 ± 2.1 %IA/g for intraperitoneal, and 2.1 ± 0.5 %IA/g for subcutaneous; this correlated inversely with increased systemic availability of radioligands. Oral administration resulted in significant and prolonged retention of radioligands in the stomach and proximal small bowel as well as a low systemic distribution (Figs. 1A–1C). After oral administration, average systemic uptake was highest for ^{68}Ga-FAPI46 (Fig. 1C). Therefore, oral application was further explored in HT1080-FAP tumor-bearing mice.

Near-Equivalent Organ Biodistribution of Radioligands After Intraperitoneal, Subcutaneous, and Intravenous Application in Healthy Mice

In healthy mice, intraperitoneal, subcutaneous, and intravenous injection of radioligands resulted in near-equivalent organ biodistribution in vivo (Figs. 2–4; Supplemental Figs. 2 and 3). Radioligand retention in blood and kidney is listed in Supplemental Table 1. Blood retention in healthy mice was significantly higher after intraperitoneal/subcutaneous than after intravenous application of ^{68}Ga-PSMA11 (intraperitoneal: $P = 0.0226$ at 1 h, 0.0463 at 2 h, and 0.0394 at 4 h; subcutaneous: $P = 0.0880$ at 1 h, 0.0021 at 2 h, and 0.065 at 4 h). For ^{68}Ga-DOTATOC and ^{68}Ga-FAPI46, blood and kidney distribution after intraperitoneal/subcutaneous application were comparable to those after intravenous injection (Figs. 2–4). In further organs, including liver, bone marrow, lung, heart, spleen, intestines, brain, and muscle, the intraperitoneal, subcutaneous, and intravenous application routes exhibited comparable physiologic biodistribution (Supplemental Fig. 2). Moreover, in healthy mice, no short-term or longer-term adverse effects of radioligand application and PET/CT procedures were noted during the study duration (5 wk).

Increased or Comparable Tumor Uptake After Intraperitoneal/Subcutaneous Versus Intravenous Injection of Radioligands

To evaluate the impact of the application route on tumor uptake of ^{68}Ga-DOTATOC, ^{68}Ga-PSMA11, or ^{68}Ga-FAPI46, we assessed in vivo and ex vivo tumor and organ uptake in SSTR-, PSMA- and

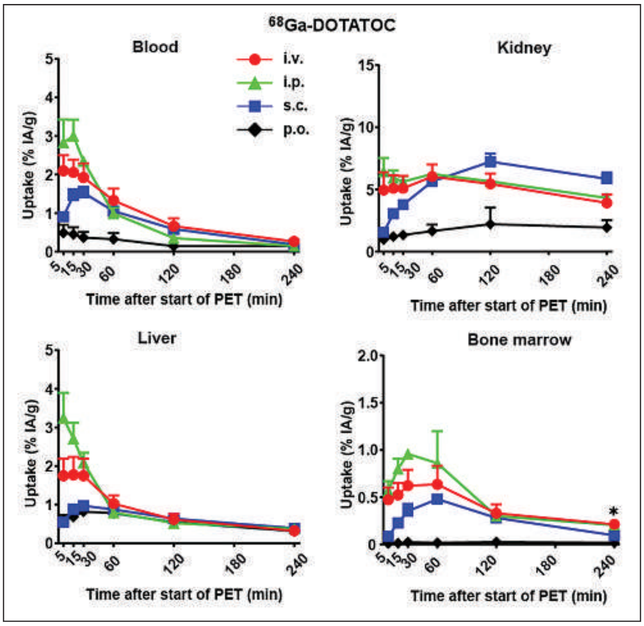

FIGURE 2. In healthy mice, organ biodistribution at ≥1 h after intraperitoneal/subcutaneous radioligand application is nearly equivalent to that after intravenous injection. Healthy mice (6/group) underwent PET after intravenous, intraperitoneal, subcutaneous, and oral radioligand application at minutes 0–30 after start of PET and after 1, 2, and 4 h and were subsequently killed. Time–activity curves illustrate in vivo PET biodistribution of ^{68}Ga-DOTATOC dynamics in VOIs at indicated times for intravenous, intraperitoneal, subcutaneous, and oral application. Data are mean + SEM. i.p. = intraperitoneal; i.v. = intravenous; p.o. = oral; s.c. = subcutaneous. *$P < 0.05$ compared with intravenous injection.

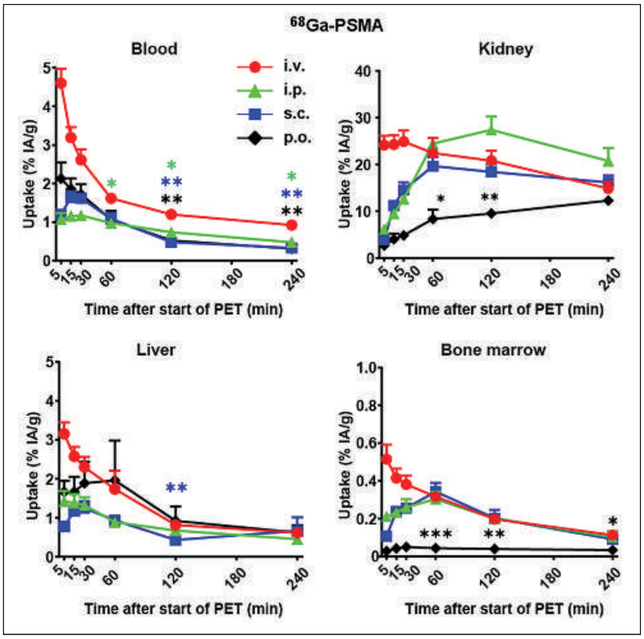

FIGURE 3. In healthy mice, organ biodistribution at ≥1 h after intraperitoneal/subcutaneous radioligand application is nearly equivalent to that after intravenous injection. Healthy mice (6/group) underwent PET after intravenous, intraperitoneal, subcutaneous, and oral radioligand application at minutes 0–30 after start of PET and after 1, 2, and 4 h and were subsequently killed. Time–activity curves illustrate in vivo PET biodistribution of ^{68}Ga-PSMA dynamics in VOIs at indicated times for intravenous, intraperitoneal, subcutaneous, and oral application. Data are mean + SEM. i.p. = intraperitoneal; i.v. = intravenous; p.o. = oral; s.c. = subcutaneous. $^{*}P < 0.05$ compared with intravenous injection. $^{**}P < 0.01$ compared with intravenous injection. $^{***}P < 0.001$ compared with intravenous injection.

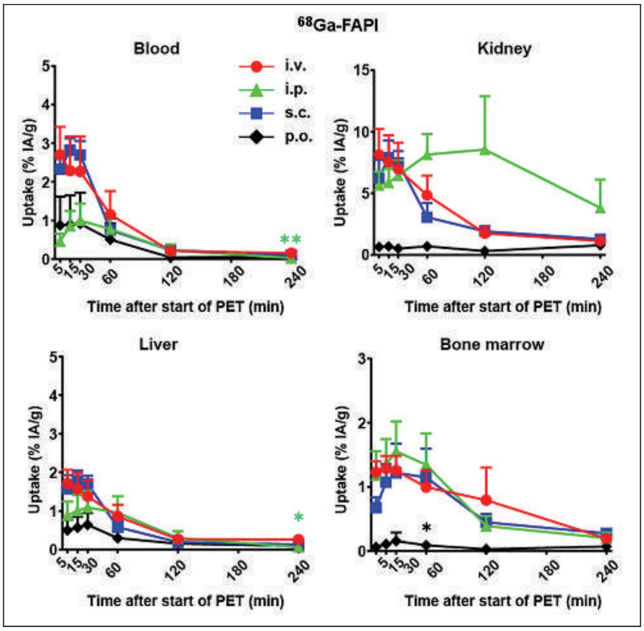

FIGURE 4. In healthy mice, organ biodistribution at ≥1 h after subcutaneous radioligand application is nearly equivalent to that after intravenous injection. Healthy mice (6/group) underwent PET scans after intravenous, intraperitoneal, subcutaneous, and oral radioligand application at minutes 0–30 after start of PET and after 1, 2, and 4 h and were subsequently killed. Time–activity curves illustrate in vivo PET biodistribution of ^{68}Ga-FAPI dynamics in VOIs at indicated times for intravenous, intraperitoneal, subcutaneous, and oral application. Data are mean + SEM. i.p. = intraperitoneal; i.v. = intravenous; p.o. = oral; s.c. = subcutaneous. $^{*}P < 0.05$ compared with intravenous injection. $^{**}P < 0.01$ compared with intravenous injection.

FAP-expressing tumor models (Table 1; Figs. 5–7; Supplemental Figs. 4 and 5).

In mice bearing SSTR tumors, intraperitoneal/subcutaneous application resulted in significantly higher mean tumor uptake than did intravenous application: $P = 0.0124$ and 0.0377, respectively, at 1 h; $P = 0.0301$ and 0.0411, respectively, at 4 h; and $P = 0.0197$ and 0.0827, respectively, at 5 h [ex vivo]) (Table 1; Supplemental Fig. 4). Tumor uptake of ^{68}Ga-PSMA11 or ^{68}Ga-FAPI46 after intraperitoneal/subcutaneous injection in mice bearing PSMA- or FAP-expressing tumors was comparable to the uptake observed after intravenous injection (Table 1).

Oral administration in mice bearing FAP-expressing tumors did not result in notable tumor uptake (Table 1; Supplemental Fig. 4). Oral application of ^{68}Ga-FAPI46 in tumor-bearing mice yielded biodistribution characteristics comparable to those seen in healthy mice (Supplemental Fig. 4), with high gastrointestinal retention of the radioligand and low systemic distribution.

Tumor-to-organ uptake ratios of organs relevant to dosimetry (*9,10*) for intraperitoneal/subcutaneous versus intravenous application are depicted in Figures 5–7. Intraperitoneal/subcutaneous application resulted in increased or equivalent tumor-to-liver ratios at 5 h after injection when compared with intravenous (mean ratio 5 h after injection): ^{68}Ga-DOTATOC: 27.4 ± 2.2-fold ($P = 0.0138$)/25.3 ± 5.6-fold ($P = 0.2756$) versus 13.9 ± 2.9-fold, respectively; ^{68}Ga-PSMA11: 28.2 ± 7.4-fold ($P = 0.4504$)/39.4 ± 5.7-fold ($P = 0.0259$) versus 16.9 ± 2.8-fold, respectively; and ^{68}Ga-FAPI46: 6.1 ± 1.6-fold ($P = 0.4198$)/12.0 ± 1.1-fold ($P = 0.0005$) versus 3.7 ± 0.4-fold, respectively (Figs. 5–7). Tumor-to-marrow ratios were higher for intraperitoneal than for intravenous application in mice bearing SSTR-expressing tumors: 50.7 ± 4.3 versus 25.7 ± 4.9, respectively ($P = 0.0096$) (Fig. 5). Subcutaneous application resulted in higher tumor-to-blood ratios than did intravenous application in mice bearing PSMA-expressing tumors: 24.5 ± 4.2-fold versus 6.0 ± 0.9-fold, respectively ($P = 0.0186$). For other tumor-to-organ uptake ratios, no significant difference was observed (Fig. 6). Oral application of ^{68}Ga-FAPI46 resulted in negligible uptake in organs and tumors (Table 1; Supplemental Fig. 4).

DISCUSSION

The current delivery method for radioligands for nuclear imaging or therapy is intravenous injection. However, comparing different application routes is important for the translation of novel FAP ligands and optimization of current clinical protocols for PSMA or SSTR ligands.

The current study aimed at comparing the biodistribution of SSTR-, PSMA-, and FAP-directed small radioligands administered intraperitoneally, subcutaneously, or orally with the standard intravenous application. Alternative application routes may alter systemic distribution and tumor uptake (*11–13*), such as by slowing absorption because of a reduced rate of molecular transport via the lymphatics and blood flow to the organs of interest or tumor (*14*).

Administration of small radioligands intravenously, intraperitoneally, and subcutaneously was feasible and well tolerated as assessed by a scoring system including the behavior and overall physical appearance of mice. Small-radioligand systemic availability and biodistribution were comparable for intraperitoneal/subcutaneous versus intravenous application (Fig. 1–4). In addition,

TABLE 1
Intraperitoneal/Subcutaneous Application Led to Increased or Equivalent Tumor Uptake Compared with Intravenous Injection

Radioligand	IV	IP	SC	PO	*P*		
					IV vs. IP	IV vs. SC	IV vs. PO
RM1-SSTR (^{68}Ga-DOTATOC)							
In vivo, 1 h	5.3 ± 0.6	9.9 ± 1.0	10.8 ± 1.6	NA	0.0124*	0.0377*	NA
In vivo, 4 h	4.4 ± 0.7	8.6 ± 1.1	11.1 ± 2.0	NA	0.0301*	0.0411*	NA
Ex vivo, 5 h	2.9 ± 0.3	7.2 ± 1.1	6.5 ± 1.3	NA	0.0197*	0.0827	NA
RM1-PSMA (^{68}Ga-PSMA11)							
In vivo, 1 h	2.9 ± 0.2	3.0 ± 0.6	2.6 ± 0.4	NA	0.9837	0.8297	NA
In vivo, 4 h	2.6 ± 0.2	2.6 ± 0.7	2.9 ± 0.5	NA	0.9996	0.8289	NA
Ex vivo, 5 h	3.3 ± 0.7	3.4 ± 0.8	3.9 ± 0.8	NA	0.9954	0.8343	NA
HT1080-FAP (^{68}Ga-FAPI46)							
In vivo, 1 h	1.2 ± 0.2	2.0 ± 0.4	2.2 ± 1.1	0.1 ± 0.03	0.3024	0.6732	0.0032†
In vivo, 4 h	1.0 ± 0.2	1.5 ± 0.3	1.1 ± 0.6	0.1 ± 0.04	0.4559	0.9911	0.0087†
Ex vivo, 5 h	1.0 ± 0.2	1.1 ± 0.1	1.4 ± 0.4	0.02 ± 0.01	0.9805	0.7446	0.0058†

---

*$P < 0.05$.

†$P < 0.01$.

IV = intravenous; IP = intraperitoneal; SC = subcutaneous; PO = oral; NA = not applicable.

Data are mean %IA/g ± SEM of 6 mice per group.

intraperitoneal/subcutaneous administration in mice resulted in significantly higher ^{68}Ga-DOTATOC tumor uptake (Table 1), tumor-to-liver ratio, and tumor-to-marrow ratio in SSTR-expressing tumors than was the case with intravenous injection (Fig. 5).

These findings have implications for preclinical and clinical radioligand administration, since they could offer advantages for both fields. In mice, intravenous injection requires highly trained personnel and is more error-prone (e.g., paravenous injection) and time-consuming. Intraperitoneal/subcutaneous administration may serve as simple alternative application routes for imaging at later time points after injection or therapy, allowing a higher throughput in mouse studies, with lower dropout rates and high reproducibility. In mice, intraperitoneal administration did not compromise radioligand tumor accumulation despite a high initial absorbed dose in the intestines (*15*). However, because of slower systemic bioavailability after intraperitoneal/subcutaneous injection, intravenous application is recommended for early dynamic imaging.

In clinical routine, use of alternatives to intravenous application may improve outpatient care and benefit potential new therapy schemes, allowing repeat radioligand application at short intervals.

In patients, intraperitoneal application is limited by a higher likelihood of infection or abdominal organ damage. However, subcutaneous application is already well established as a standard route for injectable medications in outpatients and has an emerging role in delivery of biotherapeutics and monoclonal antibodies (*16,17*). Indeed, in patients with accidental paravenous infusion of ^{177}Lu-DOTATOC, absorption from the paravenous injection site occurs with a half-life of less than 4 h (Supplemental Fig. 6); this is in line with a short drainage observed after subcutaneous injection in mice. We therefore expect that subcutaneous application in patients would be feasible.

Still, an increased radiation dose to organs such as kidneys, bone marrow, blood, lungs, or liver may limit benefit from intraperitoneal/

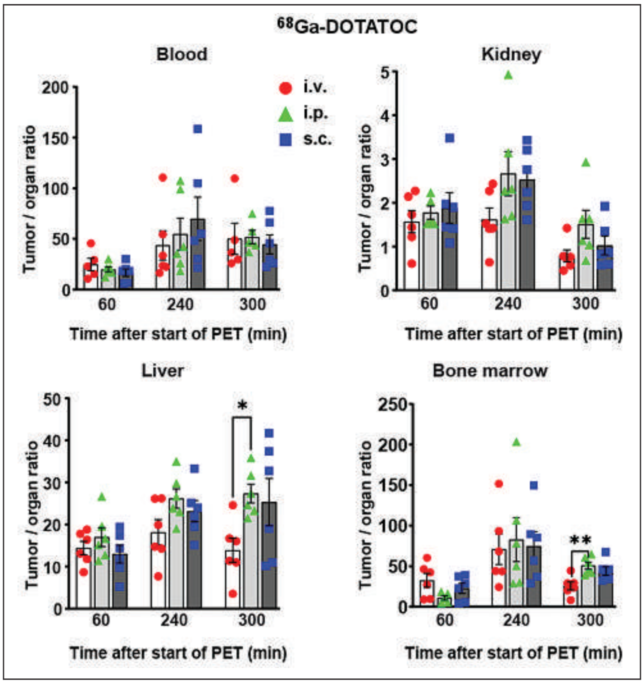

FIGURE 5. Intraperitoneal/subcutaneous radioligand application increases tumor-to-liver uptake compared with intravenous injection. Mice with subcutaneous RM1-SSTR tumors (6/group) received intravenous, intraperitoneal, and subcutaneous administration of ^{68}Ga-DOTATOC; underwent PET after 1 and 4 h; and then were killed (5 h), followed by assessment of radioactivity in organs and tumors by γ-counter. Plots show tumor-to-organ ratios after intravenous, intraperitoneal, and subcutaneous administration of ^{68}Ga-DOTATOC. Each dot represents a mouse. Data are mean ± SEM. i.p. = intraperitoneal; i.v. = intravenous; s.c. = subcutaneous. *$P < 0.05$ compared with intravenous injection. **$P < 0.01$ compared with intravenous injection.

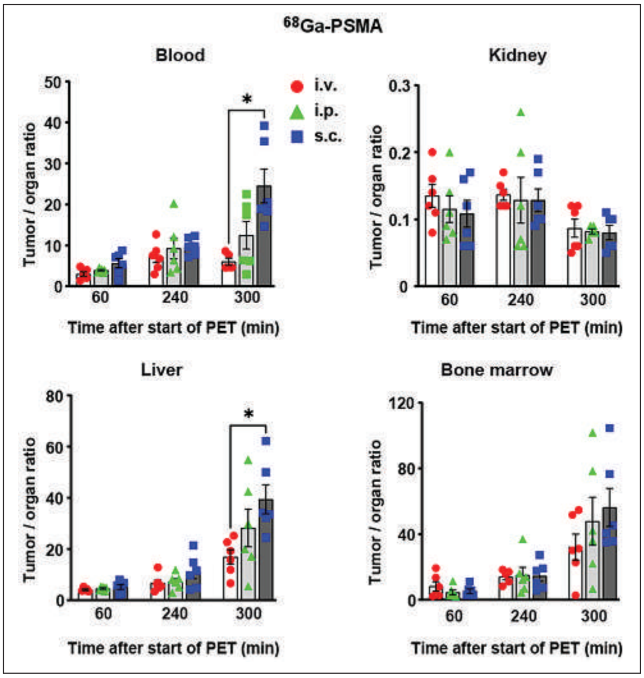

FIGURE 6. Intraperitoneal/subcutaneous radioligand application increases tumor-to-liver uptake compared with intravenous injection. Mice with subcutaneous RM1-PSMA tumors (6/group) received intravenous, intraperitoneal, and subcutaneous administration of ^{68}Ga-PSMA; underwent PET after 1 and 4 h; and then were killed (5 h), followed by assessment of radioactivity in organs and tumors by γ-counter. Plots show tumor-to-organ ratios after intravenous, intraperitoneal, and subcutaneous administration of ^{68}Ga-PSMA. Each dot represents a mouse. Data are mean ± SEM. i.p. = intraperitoneal; i.v. = intravenous; s.c. = subcutaneous. $^{*}P < 0.05$ compared with intravenous injection.

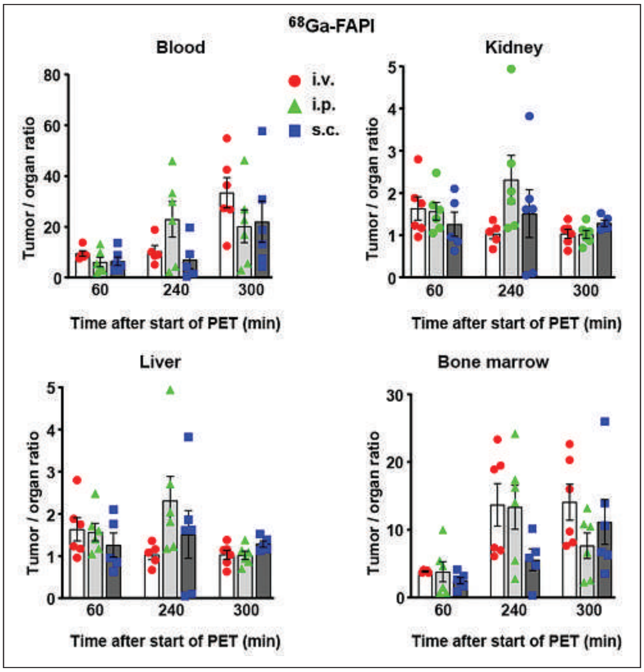

FIGURE 7. Intraperitoneal/subcutaneous radioligand application increases tumor-to-liver uptake compared with intravenous injection. Mice with subcutaneous HT-1080 tumors (6/group) received intravenous, intraperitoneal, and subcutaneous administration of ^{68}Ga-FAPI; underwent PET after 1 and 4 h; and then were killed (5 h), followed by assessment of radioactivity in organs and tumors by γ-counter. Plots show tumor-to-organ ratios after intravenous, intraperitoneal, and subcutaneous administration of ^{68}Ga-FAPI. Each dot represents a mouse. i.p. = intraperitoneal; i.v. = intravenous; s.c. = subcutaneous. Data are mean ± SEM.

subcutaneous injection. However, if radioligand therapy regimens were changed to a weekly or biweekly schedule using subcutaneous application, activities for each administration could probably be reduced in favor of these more frequent treatments. Weekly or biweekly intraperitoneal/subcutaneous application could be realized by outpatient care, reducing the patient's time in the hospital, personnel capacities, and, thus, costs.

In this study, uptake in nontarget tissues did not exceed critical values or radiation dose as suggested from measured uptake in %IA/g (Figs. 2–4). Therefore, we assume that a detrimental radiation burden to organs at risk (mainly kidneys) after intraperitoneal/subcutaneous application when compared with the standard intravenous route is unlikely. Notably, preclinical and clinical studies for DOTA-TOC- and PSMA-targeting radiotherapies demonstrated that after intravenous administration, absorbed doses in organs at risk are not likely to cause relevant radiotoxicity (*9,10,18,19*). However, to precisely estimate the additional absorbed dose to the adjacent tissue (by the intraperitoneal/subcutaneous route) after radioligand therapy, further studies with ^{177}Lu-labeled ligands and quantitative preclinical SPECT imaging should be performed. Yet, if we assume a half-life of 2.3 h for the change in local activity over time at the injection site, as recently published by Tylski et al. (*20*), we would not expect to detect a change in dosimetry between 1 ^{177}Lu administration and, for example, 2–3 administrations spaced by 48 h.

To date, the entire theranostics routine is based on rather conservative application schemes with few possibilities of patient-specific modification. Our observation that subcutaneous application showed similar tumor uptake to intravenous application may open new opportunities for alternative application schemes in the clinical routine—for example, weekly or biweekly applications, which are less feasible if using repeat intravenous injections. Also, subcutaneous application is faster and easier than intravenous and could thus be realized in outpatient care by medical laboratory assistants in a time-efficient manner for both patient and clinic personnel. Furthermore, it would be interesting to investigate the influence of intravenous application rate (applied dose per time) on tumor uptake. This investigation could be realized in a clinical study or observational trial on patients with poor vein status.

This study had some limitations. It assessed ^{68}Ga-ligands for PET imaging and did not examine therapeutic ^{177}Lu-labeled ligands. Furthermore, in-bed injection with concurrent dynamic PET acquisition was not performed, and because of the short ^{68}Ga half-life, time points beyond 5 h after injection were not feasible.

CONCLUSION

In mice, PET imaging after intravenous, intraperitoneal, or subcutaneous injection of SSTR-. PSMA-, or FAP-directed small radioligands is feasible. Intraperitoneal/subcutaneous administration of SSTR-ligands resulted in increased absolute tumor and relative tumor-to-organ uptake compared with intravenous administration, a finding that may translate into improved tumor irradiation in the setting of radioligand therapies and warrants further translational assessment.

DISCLOSURE

This study was funded in part by the Doktor Robert Pfleger-Stiftung, Hallstadt, Germany. Wolfgang Fendler was a consultant for Janssen and Calyx, and he received fees from Bayer and Parexel outside the submitted work. Ken Herrmann reports personal fees from Bayer, Sofie Biosciences, SIRTEX, Adacap, Curium, Endocyte, BTG, IPSEN, Siemens Healthineers, GE Healthcare, Amgen, Novartis, ymabs, Aktis Oncology, Theragnostics, and Pharma15; other fees from Sofie Biosciences; nonfinancial support from ABX; and grants from BTG, outside the submitted work. Katharina Lueckerath reports paid consulting activities for Sofie Biosciences/iTheranostics and funding from AMGEN outside the submitted work. No other potential conflict of interest relevant to this article was reported.

ACKNOWLEDGMENTS

We thank Prof. Dr. Med Uwe Haberkorn for providing HT1080-hFAP cells, and we thank the nuclear medicine team at University Hospital Essen for their support.

KEY POINTS

QUESTION: Are there alternatives to intravenous injection of SSTR-, PSMA-, or FAP-directed radioligands?

PERTINENT FINDINGS: In healthy mice, intraperitoneal/subcutaneous application of small radiotheranostic ligands resulted in near-equivalent systemic availability and organ biodistribution at early (1 h) and late (4 h) time points after injection when compared with intravenous injection. Intraperitoneal/subcutaneous administration significantly increased absolute tumor and relative tumor-to-organ uptake in SSTR tumors (^{68}Ga-DOTATOC) compared with the intravenous route.

IMPLICATIONS FOR PATIENT CARE: Intraperitoneal/subcutaneous application is feasible in animal models of small-radioligand imaging or therapy. Tumor uptake and tolerability of subcutaneous application warrants assessment in clinical studies.

REFERENCES

1. Strosberg J, Wolin E, Chasen B, et al. NETTER-1 phase III in patients with midgut neuroendocrine tumors treated with ^{177}Lu-Dotatate: efficacy and safety results [abstract]. *J Nucl Med.* 2016;57(suppl 2):629.
2. Hofman MS, Emmett L, Sandhu S, et al. [^{177}Lu]Lu-PSMA-617 versus cabazitaxel in patients with metastatic castration-resistant prostate cancer (TheraP): a randomised, open-label, phase 2 trial. *Lancet.* 2021;397:797–804.
3. Sartor O, de Bono J, Chi KN, et al. Lutetium-177-PSMA-617 for metastatic castration-resistant prostate cancer. *N Engl J Med.* 2021;385:1091–1103.
4. Hathi DK, Jones EF. ^{68}Ga FAPI PET/CT: tracer uptake in 28 different kinds of cancer. *Radiol Imaging Cancer.* 2019;1:e194003.
5. Fendler WP, Stuparu AD, Evans-Axelsson S, et al. Establishing ^{177}Lu-PSMA-617 radioligand therapy in a syngeneic model of murine prostate cancer. *J Nucl Med.* 2017;58:1786–1792.
6. Loktev A, Lindner T, Burger EM, et al. Development of fibroblast activation protein-targeted radiotracers with improved tumor retention. *J Nucl Med.* 2019;60: 1421–1429.
7. Jensen MM, Jorgensen JT, Binderup T, Kjaer A. Tumor volume in subcutaneous mouse xenografts measured by microCT is more accurate and reproducible than determined by ^{18}F-FDG-microPET or external caliper. *BMC Med Imaging.* 2008; 8:16.
8. Lückerath K, Stuparu AD, Wei L, et al. Detection threshold and reproducibility of ^{68}Ga-PSMA11 PET/CT in a mouse model of prostate cancer. *J Nucl Med.* 2018; 59:1392–1397.
9. Sandström M, Garske-Roman U, Granberg D, et al. Individualized dosimetry of kidney and bone marrow in patients undergoing ^{177}Lu-DOTA-octreotate treatment. *J Nucl Med.* 2013;54:33–41.
10. Delker A, Fendler WP, Kratochwil C, et al. Dosimetry for ^{177}Lu-DKFZ-PSMA-617: a new radiopharmaceutical for the treatment of metastatic prostate cancer. *Eur J Nucl Med Mol Imaging.* 2016;43:42–51.
11. Strigari L, Konijnenberg M, Chiesa C, et al. The evidence base for the use of internal dosimetry in the clinical practice of molecular radiotherapy. *Eur J Nucl Med Mol Imaging.* 2014;41:1976–1988.
12. Gafita A, Rauscher I, Retz M, et al. Early experience of rechallenge ^{177}Lu-PSMA radioligand therapy after an initial good response in patients with advanced prostate cancer. *J Nucl Med.* 2019;60:644–648.
13. Current K, Meyer C, Magyar CE, et al. Investigating PSMA-targeted radioligand therapy efficacy as a function of cellular PSMA levels and intratumoral PSMA heterogeneity. *Clin Cancer Res.* 2020;26:2946–2955.
14. Sánchez-Félix M, Burke M, Chen HH, Patterson C, Mittal S. Predicting bioavailability of monoclonal antibodies after subcutaneous administration: open innovation challenge. *Adv Drug Deliv Rev.* 2020;167:66–77.
15. Dou S, Smith M, Wang Y, Rusckowski M, Liu G. Intraperitoneal injection is not always a suitable alternative to intravenous injection for radiotherapy. *Cancer Biother Radiopharm.* 2013;28:335–342.
16. Bittner B, Richter W, Schmidt J. Subcutaneous administration of biotherapeutics: an overview of current challenges and opportunities. *BioDrugs.* 2018;32:425–440.
17. Viola M, Sequeira J, Seica R, et al. Subcutaneous delivery of monoclonal antibodies: how do we get there? *J Control Release.* 2018;286:301–314.
18. Wehrmann C, Senftleben S, Zachert C, Muller D, Baum RP. Results of individual patient dosimetry in peptide receptor radionuclide therapy with ^{177}Lu DOTA-TATE and ^{177}Lu DOTA-NOC. *Cancer Biother Radiopharm.* 2007;22:406–416.
19. Kabasakal L, AbuQbeitah M, Aygun A, et al. Pre-therapeutic dosimetry of normal organs and tissues of ^{177}Lu-PSMA-617 prostate-specific membrane antigen (PSMA) inhibitor in patients with castration-resistant prostate cancer. *Eur J Nucl Med Mol Imaging.* 2015;42:1976–1983.
20. Tylski P, Pina-Jomir G, Bournaud-Salinas C, Jalade P. Tissue dose estimation after extravasation of ^{177}Lu-DOTATATE. *EJNMMI Phys.* 2021;8:33.

Substitution of L-Tryptophan by α-Methyl-L-Tryptophan in ^{177}Lu-RM2 Results in ^{177}Lu-AMTG, a High-Affinity Gastrin-Releasing Peptide Receptor Ligand with Improved In Vivo Stability

Thomas Günther, Sandra Deiser, Veronika Felber, Roswitha Beck, and Hans-Jürgen Wester

Chair of Pharmaceutical Radiochemistry, Technical University of Munich, Garching, Germany

Theranostic applications targeting the gastrin-releasing peptide receptor (GRPR) have shown promising results. When compared with other peptide ligands for radioligand therapy, the most often used GRPR ligand, DOTA-Pip^5-D-Phe^6-Gln^7-Trp^8-Ala^9-Val^{10}-Gly^{11}-His^{12}-Sta^{13}-Leu^{14}-NH$_2$ (RM2), may be clinically impacted by limited metabolic stability. With the aim of improving the metabolic stability of RM2, we investigated whether the metabolically unstable Gln^7-Trp^8 bond within the pharmacophore of RM2 can be stabilized via substitution of L-Trp^8 by α-methyl-L-tryptophan (α-Me-L-Trp) and whether the corresponding DOTAGA analog might also be advantageous. A comparative preclinical evaluation of ^{177}Lu-α-Me-L-Trp^8-RM2 (^{177}Lu-AMTG) and its DOTAGA counterpart (^{177}Lu-AMTG2) was performed using ^{177}Lu-RM2 and ^{177}Lu-NeoBOMB1 as reference compounds. **Methods:** Peptides were synthesized by solid-phase peptide synthesis and labeled with ^{177}Lu. Lipophilicity was determined at pH 7.4 ($\log D_{7.4}$). Receptor-mediated internalization was investigated on PC-3 cells (37°C, 60 min), whereas GRPR affinity (half-maximal inhibitory concentration) was determined on both PC-3 and T-47D cells. Stability toward peptidases was examined in vitro (human plasma, 37°C, 72 ± 2 h) and in vivo (murine plasma, 30 min after injection). Biodistribution studies were performed at 24 h after injection, and small-animal SPECT/CT was performed on PC-3 tumor–bearing mice at 1, 4, 8, 24, and 28 h after injection. **Results:** Solid-phase peptide synthesis yielded 9%–15% purified labeling precursors. ^{177}Lu labeling proceeded quantitatively. Compared with ^{177}Lu-RM2, ^{177}Lu-AMTG showed slightly improved GRPR affinity, a similar low internalization rate, slightly increased lipophilicity, and considerably improved stability in vitro and in vivo. In vivo, ^{177}Lu-AMTG exhibited the highest tumor retention (11.45 ± 0.43 percentage injected dose/g) and tumor-to-blood ratio (2,702 ± 321) at 24 h after injection, as well as a favorable biodistribution profile. As demonstrated by small-animal SPECT/CT imaging, ^{177}Lu-AMTG also revealed a less rapid clearance from tumor tissue. Compared with ^{177}Lu-AMTG, ^{177}Lu-AMTG2 did not show any further benefits. **Conclusion:** The results of this study, particularly the superior metabolic stability of ^{177}Lu-AMTG, strongly recommend a clinical evaluation of this novel GRPR-targeted ligand to investigate its potential for radioligand therapy of GRPR-expressing malignancies.

Key Words: AMTG; GRPR; RM2; prostate cancer; increased metabolic stability; NeoBOMB1

J Nucl Med 2022; 63:1364–1370
DOI: 10.2967/jnumed.121.263323

Radioligand therapy has emerged as a powerful alternative to conventional treatment options in oncology. This emergence can be attributed mainly to the success of DOTATOC- and DOTATATE-based theranostics in the case of neuroendocrine tumors and to prostate-specific membrane antigen (PSMA)–targeted inhibitors in the case of prostate cancer (*1,2*). In view of the overexpression of the gastrin-releasing peptide receptor (GRPR, bombesin-2 receptor) at a high density and frequency already in early stages of prostate cancer (∼5,000 disintegrations/min [dpm]/mg of tissue, with >2,000 dpm/mg being considered clinically relevant) and breast cancer (∼10,000 dpm/mg), GRPR has been identified as a promising target for both cancer types (*3,4*).

In a recent study, 50 patients with biochemically recurrent prostate cancer were examined with either ^{68}Ga-PSMA11 or ^{18}F-DCFPyL PET/CT and additionally with ^{68}Ga-RM2 PET/MRI (where RM2 is DOTA-Pip^5-D-Phe^6-Gln^7-Trp^8-Ala^9-Val^{10}-Gly^{11}-His^{12}-Sta^{13}-Leu^{14}-NH$_2$). Thirty-six lesions were visible only with ^{68}Ga-PSMA11/^{18}F-DCFPyL PET/CT, and 7 only with ^{68}Ga-RM2 PET/MRI, which again suggests a complementary role for GRPR- and PSMA-targeted theranostics (*5*). Moreover, estrogen receptor–rich breast cancer (estrogen receptor being expressed in over 80% of all breast cancers), in particular, shows high GRPR expression, which is retained in 95% of nodal metastases (*6,7*). Not surprisingly, successful high-contrast PET imaging of breast cancer using ^{68}Ga-NOTA-RM26 or ^{68}Ga-RM2 has already been described (*8,9*).

The 2 most promising GRPR-targeted radiopharmaceuticals, ^{68}Ga-RM2 and ^{68}Ga-NeoBOMB1, have already shown favorable initial results and are being assessed in phase 1 and 2 clinical studies (*10–13*). A first-in-humans study on ^{177}Lu-RM2 in PSMA-negative/GRPR-positive prostate cancer revealed encouraging dosimetry data (*14*). Nevertheless, limited metabolic stability of some bombesin derivatives, such as RM2, is well known and caused mainly by the neutral endopeptidase (Enzyme Commission no. 3.4.24.11), which reportedly cleaves linear peptides at the *N* terminus side of hydrophobic amino acids (*15*). Incubation of ^{177}Lu-labeled DOTA-4-aminobenzoyl-Gln^7-Trp^8-Ala^9-Val^{10}-Gly^{11}-His^{12}-Leu^{13}-Met^{14}-NH$_2$ (AMBA) in murine and human plasma in vitro revealed several

---

Received Oct. 4, 2021; revision accepted Dec. 28, 2021.

For correspondence or reprints, contact Thomas Günther (thomas.guenther@tum.de).

cleavage sites, especially at the *C* terminus and the Gln^7-Trp^8 site (*16*). Similar observations were made in 5 healthy patients, as the administered ^{68}Ga-RM2 showed only 19% intact tracer in blood at 65 min after injection (*17*). Considering this rather small fraction of intact compound early after injection, a metabolically stabilized RM2 analog could result in improved tumor uptake, tumor retention, and thus tumor dose. In recent years, many groups developed bombesin analogs that were modified at the *C* or *N* termini, but not within the pharmacophoric sequence (Gln^7-Trp^8-Ala^9-Val^{10}-Gly^{11}-His^{12}) (*18–22*).

As we hypothesized that the use of statine (i.e., Sta^{13}) at the *C* terminus of RM2 and its derivatives would result in sufficient metabolic stabilization at this part of the molecule, we concluded that further improvements might be possible by stabilizing the Gln^7-Trp^8 sequence. For this purpose, we substituted α-methyl-L-tryptophan (α-Me-L-Trp) for L-Trp^8 in ^{177}Lu-RM2 and its DOTAGA analog (Fig. 1) and evaluated these novel compounds alongside the potent reference ligands ^{177}Lu-RM2 and ^{177}Lu-NeoBOMB1. The comparative preclinical evaluation comprises affinity studies (half-maximal inhibitory concentration, or IC_{50}) on PC-3 and T-47D cells, quantification of receptor-mediated internalization on PC-3 cells, determination of lipophilicity at pH 7.4 (log$D_{7.4}$), investigations of stability against peptidases in vitro in human plasma and in vivo in plasma and urine of mice, and biodistribution studies on PC-3 tumor–bearing mice.

MATERIALS AND METHODS

Chemical Synthesis and Labeling Procedures

RM2 derivatives were prepared via standard Fmoc-based solid-phase peptide synthesis using *H*-Rink amide ChemMatrix resin (35- to 100-mesh particle size, 0.4–0.6 mmol/g loading; Merck KGaA). NeoBOMB1 was synthesized according to a reported procedure (*20*) and purified by reversed-phase high-performance liquid chromatography (RP-HPLC).

Both ^{nat}Lu and ^{177}Lu labeling was according to a modified procedure (*23*). The radiolabeled reference, 3-^{125}I-D-Tyr^6-MJ9 (Supplemental Figs. 1 and 2; supplemental materials are available at http://jnm.snmjournals.org), was prepared according to a reported procedure (*24*). A detailed description of the synthesis, labeling, and characterization of RM2 and its analogs is provided in Supplemental Figures 3–12.

In Vitro Experiments

A detailed description of all cell-based experiments is provided in the supplemental materials.

Affinity Determinations (IC_{50}) and Internalization Studies. Competitive binding studies were performed on both PC-3 and T-47D cells (1.5×10^5 cells in 1 mL/well) via incubation at room temperature for 2 h using 3-^{125}I-D-Tyr^6-MJ9 (0.2 nM/well) as a radiolabeled reference ($n = 3$). Internalization studies of the ^{177}Lu-labeled conjugates (1.0 nM/well) were performed on PC-3 cells (1.5×10^5 cells in 1 mL/well) at 37°C for 1 h ($n = 6$). Data were corrected for nonspecific binding (competition by 10^{-3} M ^{nat}Lu-RM2).

*Determination of Lipophilicity (*n*-Octanol–Phosphate-Buffered Saline Distribution Coefficient, log$D_{7.4}$).* Approximately 1 MBq of the ^{177}Lu-labeled compound was dissolved in 1 mL of phosphate-buffered saline (pH 7.4) and *n*-octanol (v/v = 1/1). After stirring for 3 min at room temperature in a vortex mixer and subsequent centrifugation at 9,000 rpm for 5 min (Biofuge 15; Heraeus Sepatech GmbH), 200-μL aliquots of both layers were measured separately in a γ-counter. The experiment was repeated at least 5 times.

In Vitro Stability Studies. Metabolic stability in vitro was determined through a procedure published by Linder et al. that was slightly modified (*16*). Immediately after labeling, 200 μL of human plasma were added and the mixture was incubated at 37°C for 72 ± 2 h. Proteins were precipitated by treatment with ice-cold EtOH (150 μL) and ice-cold MeCN (450 μL), followed by centrifugation (13,000 rpm, 20 min). The supernatants were decanted and further centrifuged (13,000 rpm, 10 min) using a Costar Spin-X (Corning) centrifuge tube filter (0.45 μm). The filtrated plasma samples were analyzed using radio–RP-HPLC.

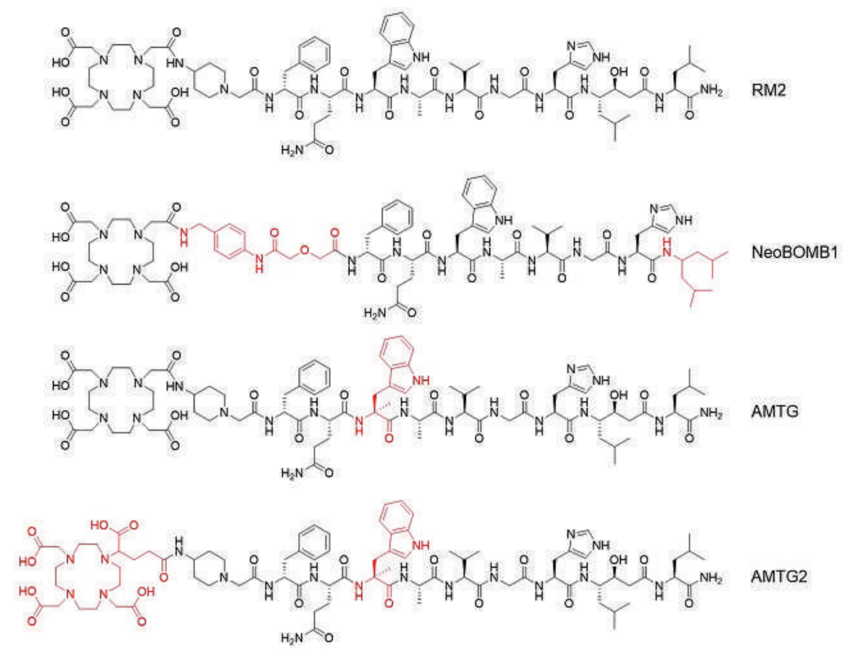

FIGURE 1. Chemical structure of RM2 and its α-Me-L-Trp (α-Me-L-Trp^8) modified derivatives AMTG and AMTG2, as well as reference ligand NeoBOMB1. Structural differences from RM2 are highlighted in red.

In Vivo Experiments

All animal experiments were conducted in accordance with general animal welfare regulations in Germany (German animal protection act, as amended on 18.05.2018, article 141 G v. 29.3.2017 I 626, approval ROB-55.2-2532.Vet_02-18-109) and the institutional guidelines for the care and use of animals.

In Vivo Stability Studies. Approximately 30–40 MBq (1 nmol, 150 μL) of the ^{177}Lu-labeled compounds were injected into the tail vein of anesthetized CB17-SCID mice ($n = 3$). After euthanasia at 30 min after injection, blood and urine samples were collected. Blood proteins were precipitated by treatment with ice-cold MeCN (v/v = 1/1), followed by centrifugation (13,000 rpm, 20 min). The supernatants were decanted and further centrifuged (13,000 rpm, 10 min) using a Costar Spin-X centrifuge tube filter (0.45 μm). The filtrated plasma samples and the urine samples were analyzed using radio–RP-HPLC.

Biodistribution and Small-Animal SPECT/CT Imaging Studies. A detailed description of tumor inoculation is provided in the supplemental materials. Approximately 2–5 MBq (100 pmol, 150 μL) of the ^{177}Lu-labeled GRPR ligands were injected into the tail vein of anesthetized (2% isoflurane) PC-3 tumor–bearing mice (biodistribution, $n = 4$; imaging, $n = 1$).

For biodistribution studies, organs were removed, weighed, and measured in a γ-counter (Perkin Elmer) after euthanasia at 24 h after injection.

Imaging studies were performed on a MILabs VECTor^4 small-animal SPECT/PET/optical imaging/CT device (MILabs). Data were reconstructed using the MILabs Rec software (version 10.02) and a pixel-based algorithm (similarity-regulated ordered-subsets expectation maximization), followed by data analysis using PMOD software (version 4.0; PMOD Technologies LLC). Static images were recorded at t = 1, 4, 8, 24, and 28 h after injection with an acquisition time of t + (45–60 min) using a high-energy general-purpose rat and mouse collimator and a stepwise multiplanar bed movement.

For all competition studies, 3.62 mg/kg (40 nmol) of ^{nat}Lu-RM2 (10^{-3} M in phosphate-buffered saline) were coadministered.

RESULTS

Synthesis and Radiolabeling

Uncomplexed ligands were synthesized via standard Fmoc-based solid-phase peptide synthesis, yielding 9%–15% of each labeling precursor after purification by RP-HPLC (chemical purity > 98%, determined by RP-HPLC at $\lambda = 220$ nm). Complexation of all ligands with a 2.5-fold excess of $^{nat}LuCl_3$ resulted in quantitative yields. The remaining free Lu^{3+} did not affect the cell-based assay in a brief competition study (Supplemental Fig. 13); thus, purification before affinity studies was dispensed with. ^{125}I-iodination of D-Tyr^6-MJ9 by means of the Iodo-Gen (Pierce Biotechnology, Inc.) method resulted in 3-^{125}I-D-Tyr^6-MJ9 with radiochemical yields of 33%–48% and radiochemical purities of more than 98% after RP-HPLC purification. ^{177}Lu labeling of all compounds was performed manually, each resulting in quantitative radiochemical yields, radiochemical purities of more than 98%, and molar activities of 40 ± 10 GBq/µmol. All ^{177}Lu-labeled ligands were used without further purification.

In Vitro Characterization

In vitro data on the examined bombesin-based ligands are summarized in Figure 2 and Supplemental Table 1. The cold counterpart of 3-^{125}I-D-Tyr^6-MJ9 showed an IC_{50} of 1.3 ± 0.4 nM on PC-3 cells. The ^{nat}Lu-labeled compounds exhibited IC_{50} values in a range of 3.0–4.7 on PC-3 cells and 1.0–4.6 nM on T-47D cells. ^{177}Lu-α-Me-L-Trp^8-RM2 (^{177}Lu-AMTG) and ^{177}Lu-RM2 were internalized by PC-3 cells within 1 h in similar amounts (3.03% ± 0.18% vs. 2.92% ± 0.20%). ^{177}Lu-DOTAGA-α-Me-L-Trp^8-RM2 (^{177}Lu-AMTG2) (5.88% ± 0.33%) and ^{177}Lu-NeoBOMB1 (13.91% ± 0.64%) were taken up in higher amounts. Whereas the distribution coefficients ($\log D_{7.4}$) were quite similar for ^{177}Lu-RM2 and its analogs (−2.3 to −2.5), ^{177}Lu-NeoBOMB1 was considerably more lipophilic (−0.57 ± 0.03). The highest amounts of intact compound in vitro in human plasma were found for ^{177}Lu-AMTG (77.7% ± 8.7%). Whereas ^{177}Lu-AMTG2 and ^{177}Lu-NeoBOMB1 exhibited only a slightly reduced stability in vitro (66.2% ± 5.1% vs. 61.9% ± 2.1%), only 38.7% ± 9.3% intact ^{177}Lu-RM2 was found after incubation in human plasma at 37°C for 72 ± 2 h (Fig. 2; Supplemental Fig. 14).

In Vivo Characterization

In vivo stability in murine plasma at 30 min after injection was highest for ^{177}Lu-AMTG (92.9% ± 0.7% intact tracer). Again, slightly decreased metabolic stability was observed for ^{177}Lu-NeoBOMB1 (75.9% ± 0.6%) and ^{177}Lu-AMTG2 (77.6% ± 3.1%), whereas ^{177}Lu-RM2 was quite unstable (11.4% ± 3.7%). In addition to these findings, ^{177}Lu-AMTG and ^{177}Lu-AMTG2 were excreted into the urine at 30 min after injection, predominantly as intact tracers (68.2% ± 3.1% and 61.6% ± 1.6%, respectively) (Fig. 2; Supplemental Figs. 15 and 16). Interestingly, after injection of ^{177}Lu-RM2 and ^{177}Lu-NeoBOMB1, radioactivity appeared in the urine almost quantitatively in the form of their metabolites (0.5% ± 0.1% vs. 3.9% ± 1.3% intact tracer).

Biodistribution studies on PC-3 tumor–bearing mice were performed at 24 h after injection (Table 1). ^{177}Lu-RM2 and its derivatives showed low activity levels in most organs at 24 h after injection, indicating a rapid clearance from nontumor tissue, as is especially important for blood and GRPR-positive organs such as pancreas and intestine. ^{177}Lu-NeoBOMB1 showed increased activity levels in several nontumor organs at 24 h after injection, particularly in lung, liver, spleen, pancreas, intestine, and adrenals. Bone uptake was slightly enhanced for ^{177}Lu-RM2, a finding that was attributed to incomplete labeling (radiochemical yield, ~95%; chromatogram not shown) and thus free $^{177}LuCl_3$. Tumor retention was comparable for all compounds except ^{177}Lu-AMTG, which exhibited distinctly increased values at 24 h after injection (7.2–8.5 vs.

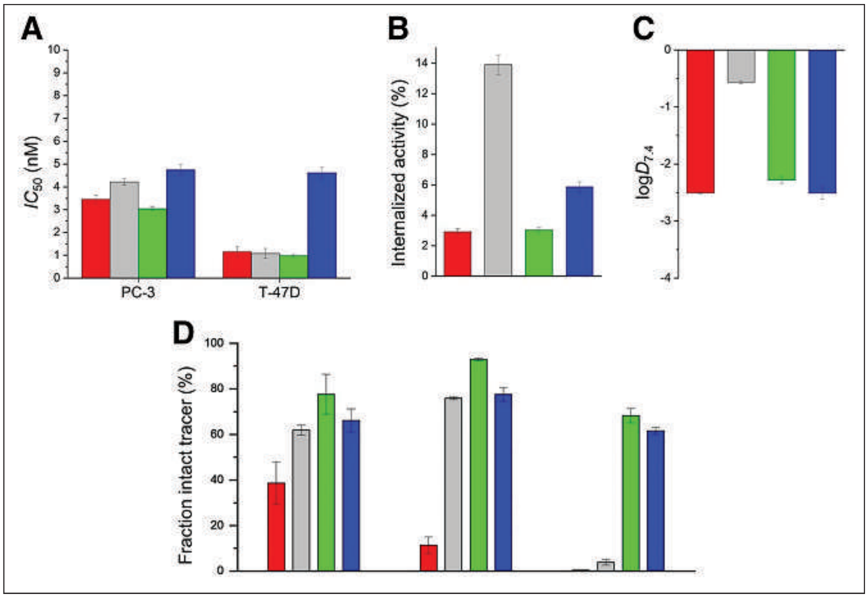

FIGURE 2. Preclinical data of $^{nat/177}$Lu-RM2 (red), $^{nat/177}$Lu-NeoBOMB1 (gray), $^{nat/177}$Lu-AMTG (green), and $^{nat/177}$Lu-AMTG2 (blue). (A) Affinity data on PC-3 and T-47D cells (1.5×10^5 cells/mL/well) using 3-^{125}I-D-Tyr^6-MJ9 (0.2 nM/well) as radiolabeled reference (2 h, room temperature, Hanks' balanced salt solution plus 1% bovine serum albumin [*v/v*]). (B) GRPR-mediated internalization (0.25 pmol/well) on PC-3 cells as percentage of applied activity (incubation at 37°C for 1 h, Dulbecco modified Eagle medium/F-12 plus 5% bovine serum albumin [*v/v*], 1.5×10^5 cells/mL/well). Data were corrected for nonspecific binding (10^{-3} M ^{nat}Lu-RM2). (C) Lipophilicity at pH 7.4 ($\log D_{7.4}$). (D) Metabolic stability in vitro in human plasma (left) (37°C, 72 ± 2 h; $n = 4$), and metabolic stability in vivo in murine plasma (middle) and murine urine (right) at 30 min after injection ($n = 3$). Data are expressed as mean ± SD. Metabolic stability of ^{177}Lu-RM2 derivatives was determined in vitro and in vivo.

TABLE 1

Biodistribution of ^{177}Lu-RM2, ^{177}Lu-NeoBOMB1, ^{177}Lu-AMTG, and ^{177}Lu-AMTG2 in Selected Organs at 24 Hours After Injection in PC-3 Tumor–Bearing CB17-SCID Mice (100 pmol Each)

Organ	^{177}Lu-RM2	^{177}Lu-NeoBOMB1	^{177}Lu-AMTG	^{177}Lu-AMTG competition study	^{177}Lu-AMTG2	^{177}Lu-AMTG2 competition study
Blood	0.012 ± 0.001	0.057 ± 0.027	0.004 ± 0.001	0.003 ± 0.000	0.011 ± 0.000	0.002 ± 0.001
Heart	0.06 ± 0.00	0.10 ± 0.03	0.02 ± 0.00	0.02 ± 0.01	0.03 ± 0.02	0.02 ± 0.01
Lung	0.10 ± 0.02	0.43 ± 0.00	0.04 ± 0.01	0.27 ± 0.15	0.05 ± 0.01	1.18 ± 1.49
Liver	0.45 ± 0.03	1.60 ± 0.62	0.14 ± 0.03	1.40 ± 0.86	0.32 ± 0.14	0.74 ± 0.44
Spleen	0.20 ± 0.02	1.94 ± 0.97	0.10 ± 0.02	2.97 ± 2.01	0.15 ± 0.07	1.06 ± 1.08
Pancreas	0.43 ± 0.06	8.48 ± 0.92	0.56 ± 0.30	0.05 ± 0.03	0.95 ± 0.14	0.07 ± 0.01
Stomach	0.19 ± 0.06	1.29 ± 0.12	0.10 ± 0.04	0.04 ± 0.02	0.12 ± 0.03	0.04 ± 0.01
Intestine	0.22 ± 0.04	0.85 ± 0.05	0.20 ± 0.10	0.27 ± 0.21	0.30 ± 0.04	0.34 ± 0.35
Kidney	1.79 ± 0.05	1.90 ± 0.72	1.16 ± 0.20	1.17 ± 0.26	1.87 ± 0.27	1.63 ± 0.44
Adrenal	0.80 ± 0.16	3.44 ± 0.25	0.46 ± 0.22	0.09 ± 0.07	0.26 ± 0.14	0.03 ± 0.02
Muscle	0.011 ± 0.011	0.010 ± 0.005	0.005 ± 0.003	0.003 ± 0.002	0.003 ± 0.003	0.003 ± 0.002
Bone	1.31 ± 0.56	0.20 ± 0.06	0.05 ± 0.02	0.05 ± 0.03	0.22 ± 0.05	0.02 ± 0.01
Tumor	8.45 ± 0.19	7.23 ± 0.91	11.45 ± 0.43	0.33 ± 0.20	7.97 ± 1.34	0.36 ± 0.25

Data are mean %ID/g ± SD ($n = 4$). Competition studies (mean ± SD, $n = 3$) were performed by coinjection of ^{nat}Lu-RM2 (3.62 mg/kg).

11.5 percentage injected dose per gram; %ID/g). Not surprisingly, ^{177}Lu-AMTG showed the highest tumor-to-background ratios at 24 h after injection. The tumor-to-blood ratio of ^{177}Lu-AMTG (2,702 ± 321) was almost 4 times higher than that of ^{177}Lu-RM2 and ^{177}Lu-AMTG2 and approximately 15 times higher than that of ^{177}Lu-NeoBOMB1 (Supplemental Table 2).

Small-animal SPECT/CT studies with ^{177}Lu-RM2 and ^{177}Lu-AMTG at 1, 4, 8, 24, and 28 h after injection in PC-3 tumor–bearing mice revealed low background activity for both tracers at 4 h and beyond and, for ^{177}Lu-AMTG, considerably higher activity in both tumor and pancreas (Fig. 3). For both tracers, specificity of tumor uptake was confirmed via competition experiments with an excess of ^{nat}Lu-RM2 (Table 1; Supplemental Fig. 17).

DISCUSSION

With regard to radioligand therapy, the 2 most promising GRPR ligands, ^{68}Ga-RM2 and ^{68}Ga-NeoBOMB1, present some disadvantages: ^{68}Ga-RM2 suffers from rapid metabolic degradation (*17*), which is why tumor accumulation and tumor dose for ^{177}Lu-RM2 are likely limited as well—especially important in the context of radioligand therapy. In contrast, ^{177}Lu-NeoBOMB1, which exhibits a higher metabolic stability in vivo, shows enhanced activity retention in tumor tissue but also in blood (*19*). This characteristic results in unfavorable dosimetry and higher doses to the red bone marrow (*25*). With the aim of retaining the excellent pharmacokinetics of RM2, we substituted the unnatural amino acid α-Me-L-Trp for the metabolically less stable Gln^7-Trp^8 sequence of ^{177}Lu-RM2 and its DOTAGA analog and compared these new ligands with ^{177}Lu-RM2 and ^{177}Lu-NeoBOMB1 as references.

Synthesis was easily accessible via solid-phase peptide synthesis, and complexation with ^{nat}Lu or ^{177}Lu proceeded quantitatively.

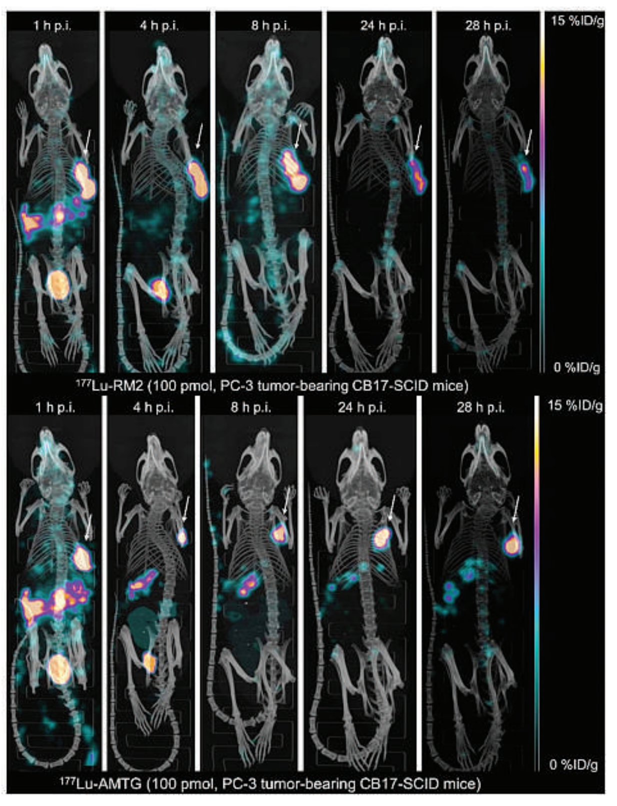

FIGURE 3. Maximum-intensity projection of PC-3 tumor–bearing CB17-SCID mice injected with ^{177}Lu-RM2 and ^{177}Lu-AMTG (100 pmol each). Images were acquired at 1, 4, 8, 24, and 28 h after injection into PC-3 tumors (arrows). p.i. = after injection.

All 4 compounds contain a similar pharmacophore typical of bombesin analogs, resulting in high affinities that were in the range of IC_{50} values reported for ^{nat}In-RM2 (9.3 nM), several ^{nat}Ga-RM26 derivatives (2.3–10.0 nM), ^{nat}Ga-NeoBOMB1 (2.5 nM), and SB3 (3.5 nM) (*18,19,21,26*). Apart from ^{nat}Lu-AMTG2, higher cellular uptake of 3-^{125}I-D-Tyr^{6}-MJ9, as well as slightly higher IC_{50} values on PC-3 cells than on T-47D cells, was observed (Supplemental Figs. 18 and 19). These findings were attributed to an increased number of receptors on PC-3 cells.

We could show that α-Me-L-Trp–for–L-Trp^{8} and DOTAGA-for-DOTA substitution had only minimal impact on GRPR affinity, lipophilicity (log$D_{7.4}$), and receptor-mediated internalization, demonstrating that these modifications might allow the in vivo kinetics of ^{177}Lu-RM2 to be kept almost unaffected. In contrast, higher internalization levels and lipophilicity already indicate the in vivo limitations of ^{177}Lu-NeoBOMB1.

Besides retaining the favorable in vitro data of ^{177}Lu-RM2, the primary aim of this study was to chemically stabilize the Gln-Trp bond to potentially improve its longtime behavior in vivo. Comparative stability studies in vitro and in vivo, as well as the resulting biodistribution profiles, substantiated our working hypothesis of addressing the major metabolic instability at the Gln-Trp site in RM2 and other bombesinlike compounds. Both ^{177}Lu-AMTG and ^{177}Lu-AMTG2 exhibited equal or even increased amounts of intact compound in human plasma in vitro and in murine plasma and urine in vivo, in comparison with the 2 references. For ^{68}Ga-RM2 and ^{177}Lu-NeoBOMB1, the fraction of intact tracer in murine blood was reported to be 55% (15 min after injection) (*27*) and 90% (30 min after injection) (*19*), respectively, which are lower than the value we determined for ^{177}Lu-AMTG (30 min after injection).

Unlike Linder et al. in a stability study on ^{177}Lu-AMBA (*16*), we observed fewer metabolites for each ligand after incubation in human plasma (Supplemental Fig. 14), as can be explained by the *C* terminus modifications present in each of the 4 compounds tested in this study. Popp et al. observed 1 major and 2 minor metabolites for ^{68}Ga-RM2 in murine plasma at 15 min after injection (*27*), whereas we detected only 1 major and 1 minor metabolite for ^{177}Lu-RM2 at 30 min after injection. This difference could be due either to our analysis method or to the effect reported by Linder et al. that the minor metabolites can be further metabolized to yield the major metabolite, the longer the circulation in vivo takes place.

Not surprisingly, increased metabolic stability observed in human and murine plasma for ^{177}Lu-AMTG resulted in a 35% higher activity level in PC-3 tumor for ^{177}Lu-AMTG than for ^{177}Lu-RM2 at 24 h after injection (Fig. 4). Both ^{177}Lu-AMTG and ^{177}Lu-AMTG2 exhibited excellent clearance kinetics and thus low activity levels in nontumor organs, with the highest values obtained for the kidneys (1.2–1.9 %ID/g). Both compounds were cleared mostly intact (Supplemental Fig. 16), a finding that could favor ^{177}Lu-AMTG and ^{177}Lu-AMTG2 over ^{177}Lu-RM2 and ^{177}Lu-NeoBOMB1, as charged metabolites tend to be taken up by and retained in the kidneys. Most importantly, the activity concentration in the blood and in the GRPR-positive pancreas was low for all ^{177}Lu-RM2 analogs at 24 h after injection (<0.01 and <1 %ID/g, respectively), which we considered another prerequisite for successful translation into humans.

In contrast, ^{177}Lu-NeoBOMB1 displayed enhanced activity in most nontumor organs and thus the lowest tumor-to-background ratios in most organs, especially in blood, liver, spleen, pancreas, and adrenals, a finding that was also observed by other groups (*19,25*). The biodistribution profiles confirmed our concerns about increased lipophilicity and internalization rates. It might be speculated that retention in the GRPR-positive pancreas could be caused by a partial agonistic behavior observed in our internalization study, since GRPR agonists such as PESIN or AMBA that exhibit internalization rates of more than 25% at 1 h in vitro typically show a slow clearance from the pancreas over time (*28,29*).

Although reduced internalization might have other causes, the high structural similarity of ^{177}Lu-AMTG/^{177}Lu-AMTG2 to the known GRPR antagonist ^{177}Lu-RM2 and the comparably low

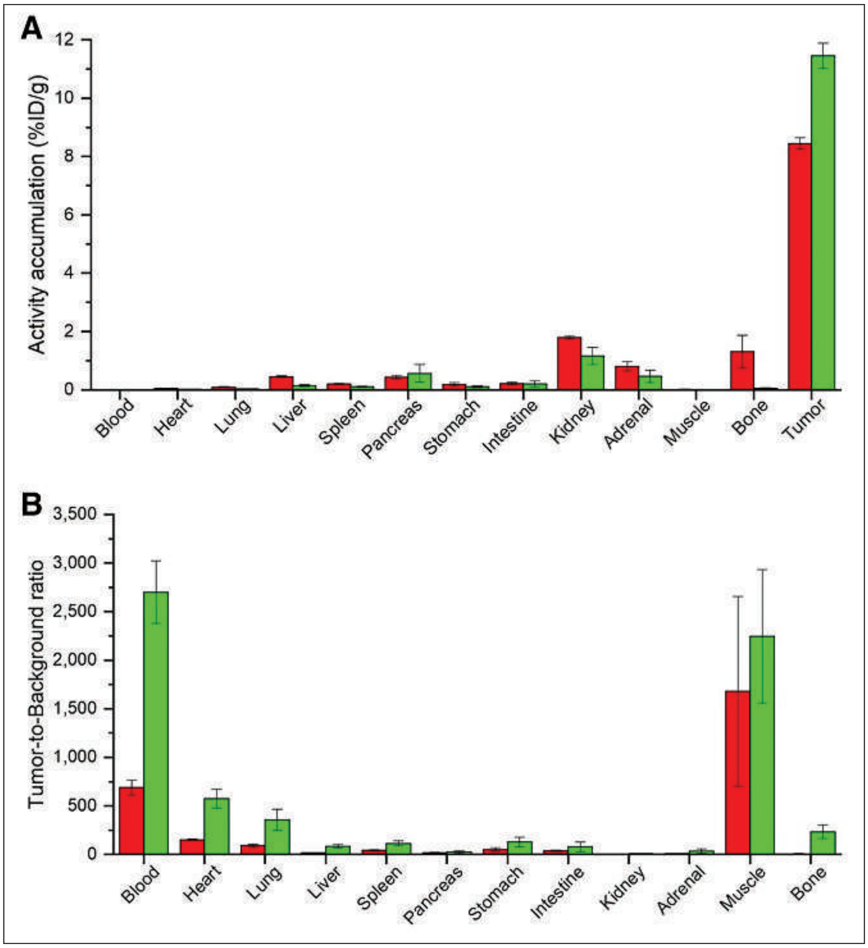

FIGURE 4. (A) Biodistribution of ^{177}Lu-RM2 (red) and ^{177}Lu-AMTG (green) in selected organs at 24 h after injection in PC-3 tumor–bearing CB17-SCID mice (100 pmol each). Data are %ID/g, mean ± SD (n = 4). (B) Tumor-to-background ratios for selected organs for ^{177}Lu-RM2 (red) and ^{177}Lu-AMTG (green) at 24 h after injection in PC-3 tumor–bearing CB17-SCID mice. Data are mean ± SD (n = 4).

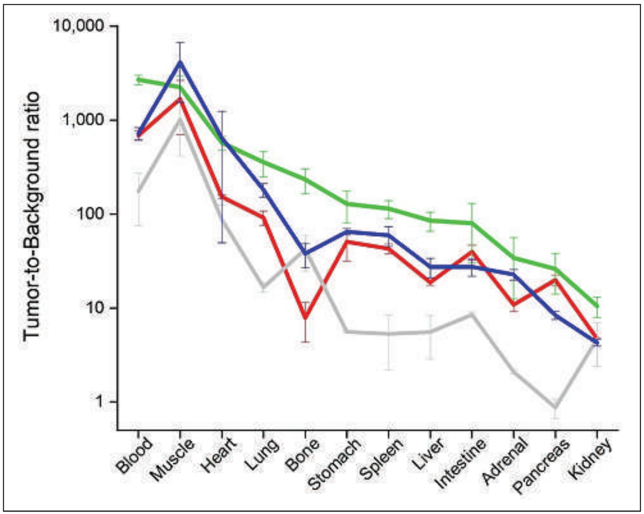

FIGURE 5. Graphic comparison of tumor-to-background ratios for selected organs for ^{177}Lu-RM2 (red), ^{177}Lu-NeoBOMB1 (gray), ^{177}Lu-AMTG (green), and ^{177}Lu-AMTG (blue). Biodistribution studies were performed at 24 h after injection in PC-3 tumor–bearing CB17-SCID mice. Data are mean ± SD ($n = 4$).

internalization pattern observed in our studies are strong indicators of antagonistic behavior by these new compounds. This assumption is further corroborated by rapid pancreatic clearance within 24 h after injection and the resulting favorable biodistribution profiles. Evidence was also provided by small-animal SPECT/CT scans with ^{177}Lu-RM2 and ^{177}Lu-AMTG over time, both of which showed high tumor retention and fast clearance from nontumor organs, even the GRPR-positive pancreas. It is noteworthy that clearance from pancreas and tumor was less rapid for ^{177}Lu-AMTG, confirming our hypothesis on increased metabolic stability in vivo generated by a simple modification at the Trp^{8} site. Thus, it is not surprising that tumor-to-background ratios for ^{177}Lu-AMTG were highest in all organs, except for the tumor-to-muscle ratio (Fig. 5).

Regarding dose-limiting organs in the context of radioligand therapy, the excellent tumor-to-kidney and tumor-to-blood ratios make ^{177}Lu-AMTG a highly attractive alternative to ^{177}Lu-RM2 (*30*). In fact, ^{177}Lu-AMTG seems to synergistically combine the advantages of ^{177}Lu-RM2 and ^{177}Lu-NeoBOMB1 regarding pharmacokinetics and stability while simultaneous offering the best GRPR affinity, both on PC-3 cells and on T-47D cells. Thus, a clinical assessment (e.g., clinical phase I study) with ^{177}Lu-AMTG seems warranted.

In summary, we were able to successfully introduce an α-Me-L-Trp–for–L-Trp^{8} substitution within the pharmacophore of ^{177}Lu-RM2 that not only resulted in a new tracer (^{177}Lu-AMTG) with comparable affinity, internalization, and lipophilicity but also resulted in considerably improved metabolic stability. Hence, improved tumor uptake and pharmacokinetics superior to those of the parent peptide, ^{177}Lu-RM2, or the second reference compound, ^{177}Lu-NeoBOMB1, were observed for ^{177}Lu-AMTG. A noteworthy finding is that improved metabolic stability was achieved without coadministration of peptidase inhibitors (*21*), such as phosphoramidon; this finding could facilitate clinical translation. It seems legitimate to conclude that other bombesin derivatives published in recent years, which have been modified at the *N* or *C* terminus but not at the unstable dipeptide sequence Gln^{7}-Trp^{8} (*20–22*), would also benefit from an α-Me-L-Trp–for–L-Trp^{8} substitution. Nevertheless, studies on prostate and breast cancer patients have to be performed to show whether these promising preclinical results are reflected on a clinical level.

CONCLUSION

We could demonstrate that the new ^{177}Lu-RM2 derivative ^{177}Lu-AMTG offers better overall preclinical performance than ^{177}Lu-RM2 or ^{177}Lu-NeoBOMB1. On the basis of these results, a clinical translation of ^{177}Lu-AMTG is highly recommended to assess a potential improved therapeutic value for radioligand therapy of GRPR-expressing malignancies, such as prostate and breast cancer. In addition, we expect that substitution of L-amino acids by their corresponding α-alkyl-L-amino acid analogs could also be a valuable approach to stabilize the pharmacophore of other peptidic ligands that suffer from insufficient stability in vivo.

DISCLOSURE

A patent application has been filed on modified GRPR-targeted ligands, including AMTG, with Thomas Günther and Hans-Jürgen Wester as inventors. Parts of this study were funded by the SFB 824 (DFG Sonderforschungsbereich 824, project Z [Hans-Jürgen Wester]) from the Deutsche Forschungsgemeinschaft, Bonn, Germany. Hans-Jürgen Wester is founder and shareholder of Scintomics GmbH, Munich, Germany. No other potential conflict of interest relevant to this article was reported.

ACKNOWLEDGMENTS

We thank Sandra te Heesen for her help with the evaluation of our compounds on T-47D cells, and we thank Daniel Di Carlo and Leon Stopper for their help with the graphics.

KEY POINTS

QUESTION: Is it possible to overcome the major limitation of ^{177}Lu-RM2, its metabolic instability, with regard to future GRPR-targeted radioligand therapy by means of a tiny modification without negatively influencing overall pharmacokinetics?

PERTINENT FINDINGS: Substitution of L-Trp^{8} by α-Me-L-Trp^{8} in the pharmacophoric sequence of ^{177}Lu-RM2 retains the favorable tracer pharmacokinetics while enhancing metabolic stability, making ^{177}Lu-AMTG a highly promising novel GRPR-targeted radiopharmaceutical for radioligand therapy.

IMPLICATIONS FOR PATIENT CARE: Although the clinical value of ^{177}Lu-AMTG has to be determined in clinical studies, this study could open new possibilities for complementary treatment of prostate and breast cancer.

REFERENCES

1. Maqsood MH, Tameez Ud Din A, Khan AH. Neuroendocrine tumor therapy with lutetium-177: a literature review. *Cureus.* 2019;11:e3986.
2. Rahbar K, Afshar-Oromieh A, Jadvar H, Ahmadzadehfar H. PSMA theranostics: current status and future directions. *Mol Imaging.* 2018;17:1536012118776068.
3. Reubi JC, Wenger S, Schmuckli-Maurer J, Schaer JC, Gugger M. Bombesin receptor subtypes in human cancers: detection with the universal radioligand ^{125}I-[D-TYR^{6}, beta-ALA^{11}, PHE^{13}, NLE^{14}] bombesin(6-14). *Clin Cancer Res.* 2002;8:1139–1146.
4. Reubi C, Gugger M, Waser B. Co-expressed peptide receptors in breast cancer as a molecular basis for in vivo multireceptor tumour targeting. *Eur J Nucl Med Mol Imaging.* 2002;29:855–862.

5. Baratto L, Song H, Duan H, et al. PSMA- and GRPR-targeted PET: results from 50 patients with biochemically recurrent prostate cancer. *J Nucl Med.* 2021;62: 1545–1549.
6. Dalm SU, Sieuwerts AM, Look MP, et al. Clinical relevance of targeting the gastrin-releasing peptide receptor, somatostatin receptor 2, or chemokine C-X-C motif receptor 4 in breast cancer for imaging and therapy. *J Nucl Med.* 2015;56:1487–1493.
7. Morgat C, MacGrogan G, Brouste V, et al. Expression of gastrin-releasing peptide receptor in breast cancer and its association with pathologic, biologic, and clinical parameters: a study of 1,432 primary tumors. *J Nucl Med.* 2017;58:1401–1407.
8. Zang J, Mao F, Wang H, et al. ^{68}Ga-NOTA-RM26 PET/CT in the evaluation of breast cancer: a pilot prospective study. *Clin Nucl Med.* 2018;43:663–669.
9. Stoykow C, Erbes T, Maecke HR, et al. Gastrin-releasing peptide receptor imaging in breast cancer using the receptor antagonist ^{68}Ga-RM2 and PET. *Theranostics.* 2016;6:1641–1650.
10. 68-Ga-RM2 PET/MRI in imaging patients with estrogen receptor-positive breast cancer. https://ClinicalTrials.gov/show/NCT03831711. ClinicalTrials.gov website. Published February 6, 2019. Updated December 13, 2021. Accessed June 9, 2022.
11. ^{68}Ga-RM2 PET/CT in detecting regional nodal and distant metastases in patients with intermediate or high-risk prostate cancer. ClinicalTrials.gov website. https://ClinicalTrials.gov/show/NCT03113617. Published April 13, 2017. Updated December 7, 2020. Accessed June 9, 2022.
12. ^{68}Ga-RM2 PET/MRI in biochemically recurrent prostate cancer. ClinicalTrials.gov website. https://ClinicalTrials.gov/show/NCT02624518. Published December 8, 2015. Updated May 3, 2022. Accessed June 9, 2022.
13. ^{177}Lu-NeoB in patients with advanced solid tumors and with ^{68}Ga-NeoB lesion uptake. ClinicalTrials.gov website. https://ClinicalTrials.gov/show/NCT03872778. Published March 13, 2019. Updated February 3, 2022. Accessed June 9, 2022.
14. Kurth J, Krause BJ, Schwarzenböck SM, Bergner C, Hakenberg OW, Heuschkel M. First-in-human dosimetry of gastrin-releasing peptide receptor antagonist [^{177}Lu]Lu-RM2: a radiopharmaceutical for the treatment of metastatic castration-resistant prostate cancer. *Eur J Nucl Med Mol Imaging.* 2020;47:123–135.
15. Shipp MA, Tarr GE, Chen CY, et al. CD10/neutral endopeptidase 24.11 hydrolyzes bombesin-like peptides and regulates the growth of small cell carcinomas of the lung. *Proc Natl Acad Sci USA.* 1991;88:10662–10666.
16. Linder KE, Metcalfe E, Arunachalam T, et al. In vitro and in vivo metabolism of Lu-AMBA, a GRP-receptor binding compound, and the synthesis and characterization of its metabolites. *Bioconjug Chem.* 2009;20:1171–1178.
17. Roivainen A, Kahkonen E, Luoto P, et al. Plasma pharmacokinetics, whole-body distribution, metabolism, and radiation dosimetry of ^{68}Ga bombesin antagonist BAY 86-7548 in healthy men. *J Nucl Med.* 2013;54:867–872.
18. Mansi R, Wang X, Forrer F, et al. Development of a potent DOTA-conjugated bombesin antagonist for targeting GRPr-positive tumours. *Eur J Nucl Med Mol Imaging.* 2011;38:97–107.
19. Kaloudi A, Lymperis E, Giarika A, et al. NeoBOMB1, a GRPR-antagonist for breast cancer theragnostics: first results of a preclinical study with [^{67}Ga]NeoBOMB1 in T-47D cells and tumor-bearing mice. *Molecules.* 2017;22:1950.
20. Lau J, Rousseau E, Zhang Z, et al. Positron emission tomography imaging of the gastrin-releasing peptide receptor with a novel bombesin analogue. *ACS Omega.* 2019;4:1470–1478.
21. Bakker IL, van Tiel ST, Haeck J, et al. In vivo stabilized SB3, an attractive GRPR antagonist, for pre- and intra-operative imaging for prostate cancer. *Mol Imaging Biol.* 2018;20:973–983.
22. Mitran B, Thisgaard H, Rosenstrom U, et al. High contrast PET imaging of GRPR expression in prostate cancer using cobalt-labeled bombesin antagonist RM26. *Contrast Media Mol Imaging.* 2017;2017:6873684.
23. Weineisen M, Simecek J, Schottelius M, Schwaiger M, Wester HJ. Synthesis and preclinical evaluation of DOTAGA-conjugated PSMA ligands for functional imaging and endoradiotherapy of prostate cancer. *EJNMMI Res.* 2014;4:63.
24. Nakagawa T, Hocart SJ, Schumann M, et al. Identification of key amino acids in the gastrin-releasing peptide receptor (GRPR) responsible for high affinity binding of gastrin-releasing peptide (GRP). *Biochem Pharmacol.* 2005;69:579–593.
25. Dalm SU, Bakker IL, de Blois E, et al. ^{68}Ga/^{177}Lu-NeoBOMB1, a novel radiolabeled GRPR antagonist for theranostic use in oncology. *J Nucl Med.* 2017;58: 293–299.
26. Varasteh Z, Mitran B, Rosenstrom U, et al. The effect of macrocyclic chelators on the targeting properties of the ^{68}Ga-labeled gastrin releasing peptide receptor antagonist PEG2-RM26. *Nucl Med Biol.* 2015;42:446–454.
27. Popp I, Del Pozzo L, Waser B, et al. Approaches to improve metabolic stability of a statine-based GRP receptor antagonist. *Nucl Med Biol.* 2017;45:22–29.
28. Mansi R, Wang X, Forrer F, et al. Evaluation of a 1,4,7,10-tetraazacyclododecane-1,4,7,10-tetraacetic acid-conjugated bombesin-based radioantagonist for the labeling with single-photon emission computed tomography, positron emission tomography, and therapeutic radionuclides. *Clin Cancer Res.* 2009;15:5240–5249.
29. Zhang H, Schuhmacher J, Waser B, et al. DOTA-PESIN, a DOTA-conjugated bombesin derivative designed for the imaging and targeted radionuclide treatment of bombesin receptor-positive tumours. *Eur J Nucl Med Mol Imaging.* 2007;34: 1198–1208.
30. Coleman CN, Blakely WF, Fike JR, et al. Molecular and cellular biology of moderate-dose (1-10 Gy) radiation and potential mechanisms of radiation protection: report of a workshop at Bethesda, Maryland, December 17-18, 2001. *Radiat Res.* 2003;159:812–834.

Prospective Phase II Trial of Prognostication by ^{68}Ga-NOTA-AE105 uPAR PET in Patients with Neuroendocrine Neoplasms: Implications for uPAR-Targeted Therapy

Esben Andreas Carlsen[1,2], Mathias Loft[1,2], Annika Loft[1,2], Anne Kiil Berthelsen[1,2], Seppo W. Langer[2–4],
Ulrich Knigge[2,5], and Andreas Kjaer[1,2]

[1]Department of Clinical Physiology and Nuclear Medicine & Cluster for Molecular Imaging, Copenhagen University Hospital – Rigshospitalet & Department of Biomedical Sciences, University of Copenhagen, Copenhagen, Denmark; [2]ENETS Neuroendocrine Tumor Center of Excellence, Copenhagen University Hospital–Rigshospitalet, Copenhagen, Denmark; [3]Department of Oncology, Copenhagen University Hospital – Rigshospitalet, Copenhagen, Denmark; [4]Department of Clinical Medicine, University of Copenhagen, Copenhagen, Denmark; and [5]Departments of Clinical Endocrinology and Surgical Gastroenterology, Copenhagen University Hospital–Rigshospitalet, Copenhagen, Denmark

The clinical course for patients with neuroendocrine neoplasms (NENs) ranges from indolent to highly aggressive. Noninvasive tools to improve prognostication and guide decisions on treatment are warranted. Expression of urokinase plasminogen activator receptor (uPAR) is present in many cancer types and associated with a poor outcome. Therefore, using an in-house–developed uPAR PET tracer [^{68}Ga]Ga-NOTA-Asp-Cha-Phe-D-Ser-D-Arg-Tyr-Leu-Trp-Ser-OH (^{68}Ga-NOTA-AE105), we aimed to assess uPAR expression in NENs. We hypothesized that uPAR expression was detectable in a significant proportion of patients and associated with a poorer outcome. In addition, as uPAR-targeted radionuclide therapy has previously proven effective in preclinical models, the study would also indicate the potential for uPAR-targeted radionuclide therapy in NEN patients. **Methods:** In a prospective clinical phase II trial, we included 116 patients with NENs of all grades, of whom 96 subsequently had uPAR PET/CT performed with evaluable lesions. PET/CT was performed 20 min after injection of approximately 200 MBq of ^{68}Ga-NOTA-AE105. uPAR target-to-liver ratio was used to define lesions as uPAR-positive when lesion SUV$_{\text{max}}$–to–liver SUV$_{\text{mean}}$ ratio was at least 2. Patients were followed for at least 1 y to assess progression-free and overall survival. **Results:** Most patients had small intestinal NENs ($n = 61$) and metastatic disease ($n = 86$). uPAR-positive lesions were seen in 68% ($n = 65$) of all patients and in 75% ($n = 18$) of patients with high-grade (grade 3) NENs. During follow-up (median, 28 mo), 59 patients (62%) experienced progressive disease and 28 patients (30%) died. High uPAR expression, defined as a uPAR target-to-liver ratio above median, had a hazard ratio of 1.87 (95% CI, 1.11–3.17) and 2.64 (95% CI, 1.19–5.88) for progression-free and overall survival, respectively ($P < 0.05$ for both). **Conclusion:** When ^{68}Ga-NOTA-AE105 PET was used to image uPAR in patients with NENs, uPAR-positive lesions were seen in most patients, notably in patients with both low-grade and high-grade NENs. Furthermore, uPAR expression was associated with a worse prognosis. We suggest that uPAR PET is relevant for risk stratification and that uPAR may be a promising target for therapy in patients with NENs.

Key Words: urokinase plasminogen activator receptor (uPAR); neuroendocrine neoplasms; PET; prognosis; molecular imaging

J Nucl Med 2022; 63:1371–1377
DOI: 10.2967/jnumed.121.263177

Neuroendocrine neoplasms (NENs) originate from the neuroendocrine cells and are found primarily in the gastrointestinal tract, pancreas, and lungs. The clinical course for patients diagnosed with NENs ranges from indolent to highly aggressive. The origin of the primary tumor, presence of metastases, tumor morphology, and proliferation activity (i.e., Ki-67) are known prognostic factors. Patients are stratified by the World Health Organization (WHO) classification into neuroendocrine tumor (NET) grade 1 (G1) (Ki-67, <3%), NET grade 2 (G2) (Ki-67, 3%–20%), NET grade 3 (G3) (Ki-67, >20% and well differentiated), and neuroendocrine carcinoma (NEC) (Ki-67, >20% and poorly differentiated) (*1*). To further improve prognostication and guide decisions on treatment, noninvasive monitoring of tumor markers may be useful. PET is ideally suited for this task, as different specific radiotracers may be applied to visualize whole-body expression of tumor markers noninvasively. In NENs particularly, radiotracers for somatostatin receptor expression (e.g., ^{64}Cu-DOTATATE or ^{68}Ga-DOTATATE) and glucose metabolism (^{18}F-FDG) are useful for diagnosis, prognostication, and therapy selection (*2,3*). In addition, peptide receptor radionuclide therapy (PRRT) with, for example, ^{177}Lu-DOTATATE targeting somatostatin receptors is approved for low-grade NENs, whereas lower somatostatin receptor expression in high-grade NENs can limit its application.

Urokinase plasminogen activator receptor (uPAR) is a promising diagnostic and prognostic biomarker, as well as a target for therapy, and has been extensively investigated in several cancer entities (*4*). uPAR is anchored to the cell membrane on the surface and localizes the proteolytic activity of its ligand, urokinase plasminogen activator (uPA). In normal tissues, uPAR expression is limited; however, in cancer, uPAR expression is upregulated. Apart from uPA, uPAR also interacts with other proteins, among them the integrin family of membrane proteins. Collectively, uPAR is involved in promoting cell proliferation, motility, invasion, proteolysis, and angiogenesis (*4–6*). Because of its integral role in cancer, our group has developed the PET radiotracer [^{68}Ga]Ga-NOTA-Asp-Cha-Phe-D-Ser-D-Arg-Tyr-Leu-Trp-Ser-OH (^{68}Ga-NOTA-AE105) using a high-affinity

---

Received Sep. 14, 2021; revision accepted Jan. 12, 2022.

For correspondence or reprints, contact Prof. Andreas Kjaer (akjaer@sund.ku.dk).

antagonist for uPAR (*7–9*). Safety and biodistribution were investigated in a phase I study, also showing accumulation of ^{68}Ga-NOTA-AE105 in primary tumors and metastases, as well as correlation with uPAR expression in excised tumor samples (*7*). Recently, we reported that ^{68}Ga-NOTA-AE105 uPAR PET is able to discriminate between low-risk and intermediate-risk profiles in prostate cancer (*10*). Furthermore, we have previously shown a high efficacy of uPAR-targeted PRRT in preclinical trials in prostate and colorectal cancers (*11,12*). Thus, uPAR, being a marker of aggressive disease, may show upregulation in high-grade NENs and provide a target for PRRT in these patients.

The aim of this phase II clinical trial of ^{68}Ga-NOTA-AE105 PET/CT in patients with NENs was to assess tumor uptake and clinical outcome. We hypothesized that uPAR PET/CT with ^{68}Ga-NOTA-AE105 would show accumulation in NENs and that the uptake of the uPAR tracer would be associated with progression-free survival (PFS) and overall survival (OS).

MATERIALS AND METHODS

Patients

Patients with histologically confirmed NENs were included from the Department of Endocrinology (managing low-grade NENs; Ki-67, ≤20%) and the Department of Oncology (managing high-grade NENs; Ki-67, >20%) at Copenhagen University Hospital–Rigshospitalet between November 1, 2017, and May 29, 2020. Rigshospitalet is a certified Neuroendocrine Tumor Center of Excellence by the European Neuroendocrine Tumor Society. The study was conducted in accordance with the Helsinki Declaration and good clinical practice. The study was approved by the Danish Medicines Agency (EudraCT 2017-002312-13), the Scientific Ethics Committee (H-17019400), and the Danish Data Protection Agency (2012-58-0004) and was registered on clinicaltrials.gov (NCT03278275).

Eligible patients were more than 18 y old, able to read and understand the patient information in Danish, and able to give informed consent. They had to have a diagnosis of a gastroenteropancreatic NEN of any grade or a bronchopulmonary NEN and have a WHO performance status of 0–2. Patients were excluded if they were pregnant or breast-feeding, had a body weight of more than 140 kg, had a history of allergic reaction to compounds of similar chemical or biologic composition to ^{68}Ga-NOTA-AE105, or—in cases of bronchopulmonary NENs—had small cell lung cancer as the subtype. After written informed consent had been obtained, the patients were referred to undergo ^{68}Ga-NOTA-AE105 PET/CT at the first given opportunity.

Image Acquisition

Data were acquired using a Biograph 128 mCT PET/CT device (Siemens Medical Solutions) with an axial field of view of 216 mm. On the basis of the previous phase I trial (*7*), the scan was acquired 20 min after intravenous administration of approximately 200 MBq of ^{68}Ga-NOTA-AE105. The tracer was produced as previously described (*7*). Whole-body PET scans (middle of orbita to middle of thigh) were acquired with a time of 4 min per bed position. Attenuation- and scatter-corrected PET data were reconstructed iteratively using a 3-dimensional ordinary Poisson ordered-subset expectation-maximization algorithm including point-spread function and time-of-flight information using the TrueX algorithm (Siemens Medical Solutions); the settings were 2 iterations, 21 subsets, and a 2-mm gaussian filter. A diagnostic CT scan was obtained before the PET scan, with a 2-mm slice thickness, 120 kV, and a quality reference of 225 mAs modulated by the Care Dose 4D automatic exposure control system (Siemens Medical Solutions). An automatic injection system was used to administer 75 mL of an iodine-containing contrast agent (Optiray 300; Covidien) for arterial- and venous-phase CT.

TABLE 1
Baseline Characteristics of Patients with NENs (n = 96)

Characteristic	Data
Median age (y)	66 (range, 34–82)
Sex	
Female	39 (41%)
Male	57 (59%)
Site of primary tumor	
Small intestine	61 (64%)
Pancreas	15 (16%)
Colon	10 (10%)
Lung	6 (6%)
Esophagus	1 (1%)
Stomach	2 (2%)
Rectum	1 (1%)
Metastatic disease	86 (90%)
Liver metastases	73 (76%)
Median Ki-67	7 (range, 1–100)
WHO grade	
NET G1	21 (22%)
NET G2	51 (53%)
NET G3	9 (9%)
NEC	15 (16%)
Median time from diagnosis to uPAR PET/CT (mo)	25 (range, 0.5–265)
Primary tumor resected	37 (39%)
Ongoing treatment at uPAR PET/CT scan time*	
Somatostatin analog	70 (73%)
Interferon	8 (8%)
Carboplatin or etoposide	19 (20%)
Capecitabine/5-fluorouracil	6 (6%)
Streptozotocin	5 (5%)
Temozolomide	2 (2%)
Everolimus	2 (2%)
Completed treatment before uPAR PET/CT*	
On first line of therapy	45 (47%)
PRRT	28 (29%)
Temozolomide	6 (6%)
Capecitabine/5-fluorouracil	6 (6%)
Streptozotocin	5 (5%)
Carboplatin or etoposide	10 (10%)
Everolimus or sunitinib	2 (2%)
Interferon	6 (6%)
Liver radiofrequency ablation or embolization	5 (5%)
Resection of liver metastases	4 (4%)

---

*Some patients had received more than one treatment; therefore, number of treatments exceed number of patients.

Data are number followed by percentage in parentheses, unless otherwise indicated. Percentages were rounded and may not add up to 100%.

TABLE 2
Proportion of Patients with uPAR PET–Positive Tumors by WHO Grade

Parameter	G1 ($n = 21$)	G2 ($n = 51$)	G3 ($n = 24$)	Overall ($n = 96$)
uPAR PET–positive	12 (57%)	35 (69%)	18 (75%)	65 (68%)

Data are number followed by percentage in parentheses. uPAR TLR was used to define lesions as uPAR-positive when lesion SUV_{max}–to–normal-liver SUV_{mean} was ≥2. Of patients with G3, 8 of 9 NET G3 and 10 of 15 NEC were uPAR PET–positive.

Image Analysis

An experienced board-certified nuclear medicine physician together with an experienced board-certified radiologist analyzed side by side the PET/CT scans. The readers were masked to patient data. Lesions were identified on CT and/or PET. SUV was calculated as decay-corrected measured radioactivity concentration/(injected activity/body weight). If more than one lesion was present in an organ, the lesion with the highest ^{68}Ga-NOTA-AE105 SUV_{max} was noted. If no uPAR-positive lesions were identified, but lesions were visible on CT, the largest lesion (based on viable tumor) on CT was used as a guide for delineation on the PET scan and SUV_{max} was determined. Physiologic liver uptake was assessed in all patients' normal liver tissue, preferable on the right side of the liver, avoiding major blood vessels. To standardize measurement of uPAR expression within and between patients, uPAR target-to-liver ratio (TLR) was used to define a lesion as uPAR-positive when lesion SUV_{max}–to–normal-liver SUV_{mean} ratio was at least 2.

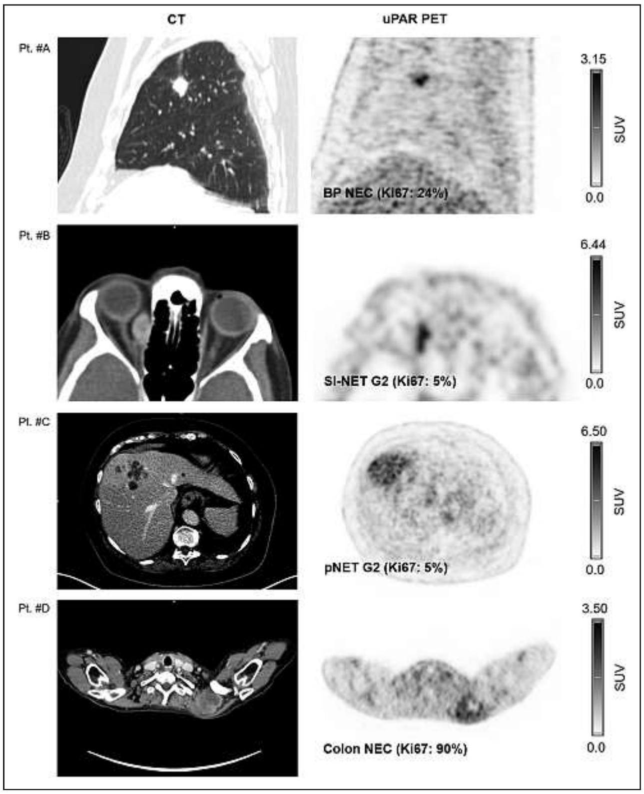

FIGURE 1. Representative examples of uPAR PET/CT imaging. CT (left column) and uPAR PET (right column) are shown for 4 patients (patients A–D) with high- and low-grade NENS. Top of individual scale bar corresponds to SUV_{max} of tumor. Pt. #A: Bronchopulmonary NEC (Ki67: 24%). Pt. #B: Orbital metastasis from small intestine NET G2 (Ki-67: 5%); Pt. #C: Large liver metastasis from pancreatic NET G2 (Ki-67: 5%). Pt. #D: Large intramuscular metastasis from primary colon NEC (Ki-67: 90%). BP = bronchopulmonary; SI = small intestine; pNET = pancreatic NET.

Follow-up

The patients were followed at the Rigshospitalet Neuroendocrine Tumor Center of Excellence with regular visits, including clinical examination, blood samples, and imaging (CT, MR, ultrasound, or PET/CT). The frequency was in accordance with European Neuroendocrine Tumor Society guidelines (*13*). Follow-up for endpoints was performed on July 8, 2021. Routine CT or MRI was used for evaluation of PFS in accordance with RECIST, version 1.1 (*14*). PFS was calculated as time from uPAR PET/CT to, if any, progression or death from any cause. If no progression or death from any cause occurred within the follow-up, the patient was censored at the time of the last available diagnostic imaging. OS was calculated as time from uPAR PET/CT to death by any cause. As all but 2 deaths were directly related to NENs, we refrained from analyzing disease-specific survival. Patients alive at follow-up were censored to the day of follow-up, that is, July 8, 2021.

Statistics

Sample size was based on previous studies of prognostic markers in patients with NENs (*15,16*), where a 1-y follow-up of 100 patients

TABLE 3
Treatment After uPAR PET/CT ($n = 96$)

Treatment	Data
Somatostatin analog	74 (77%)
Interferon	6 (6%)
PRRT	27 (28%)
Capecitabine/5-fluorourocil	10 (10%)
Everolimus or sunitinib	12 (13%)
Temozolomide	8 (8%)
Carboplatin or etoposide	11 (11%)
Streptozotocin	3 (3%)
Topotecan	2 (2%)
Docetaxel	2 (2%)
Irinotecan	1 (1%)
Surgery	9 (9%)
Liver embolization	7 (7%)
Liver radiofrequency ablation	2 (2%)
External radiation	11 (11%)

Some patients had received more than one treatment; therefore, number of treatments exceeds number of patients. Data are number followed by percentage in parentheses.

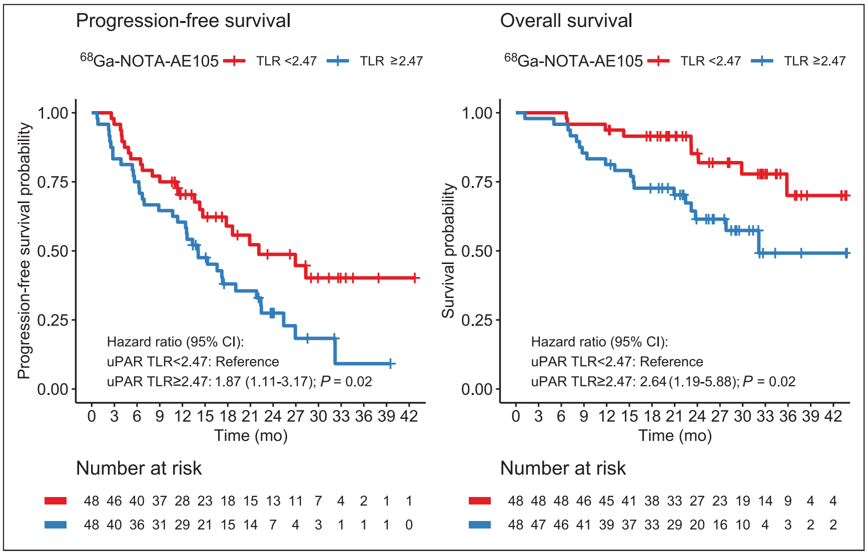

FIGURE 2. Kaplan–Meier plots of OS and PFS using ^{68}Ga-NOTA-AE105 uPAR PET. uPAR TLR was dichotomized at median (TLR, 2.47).

was sufficient to detect significant differences in PFS and OS among groups (with a risk of type I error of 0.05 and power of 0.8). To account for dropouts, 116 patients were included. Continuous variables are reported as mean ± SD or median with range. Kaplan–Meier analyses were used to estimate time to outcome (PFS and OS) and inverse Kaplan–Meier for median follow-up time. We used the Cutoff Finder application to determine the optimal cutoff for uPAR TLR (*17*). Univariate and multivariate Cox regression analyses for OS and PFS, with predictor variables of uPAR TLR and WHO grade, were performed. A P value of less than 0.05 was considered statistically significant. R, version 3.6.0 (R Foundation for Statistical Computing), was used for the analyses.

RESULTS

Patients and Image Acquisition

We prospectively included 116 patients, 17 of whom did not undergo uPAR PET/CT (worsening of disease, $n = 5$; withdrawal of consent, $n = 5$; death before uPAR PET/CT, $n = 4$; impossibility of performing uPAR PET/CT because of coronavirus disease 2019 restrictions, $n = 3$). Of 99 patients scanned with uPAR PET/CT, 96 had evaluable lesions (failure of uPAR PET/CT because of a technical issue, $n = 1$; lack of visible lesions on either CT or PET, $n = 2$). Patient demographic data for the study cohort ($n = 96$) are given in Table 1. Most patients had small intestinal NENs (64%, 61/96), and 90% (86/96) had metastatic disease. Also, patients with high-grade disease were well represented in the cohort, with 9% NET G3 (9/96) and 16% NEC (15/96).

Patients were injected with a median of 17.2 μg (range, 8.7–39.8 μg) of ^{68}Ga-NOTA-AE105, and the activity was 194 MBq (range, 104–236 MBq). The time from injection to the PET scan was a median of 22 min (range, 18–38 min). One patient experienced an adverse event (mild nausea), which was deemed unrelated to ^{68}Ga-NOTA-AE105 injection. No serious adverse events were recorded.

Image Analysis

Tracer uptake in normal liver tissue was used as a reference for tumor uptake. The mean (±SD) normal-liver SUV_{mean} was 1.50 ± 0.39. uPAR-positive lesions were seen in both patients with low-grade NEN (NET G1/G2) and patients with high-grade NEN (NET G3 and NEC) (Table 2). Representative examples of uPAR PET are shown in Figure 1 and Supplemental Fig. 1 (supplemental materials are available at http://jnm.snmjournals.org).

Follow-up

The median follow-up time after uPAR PET/CT was 28 mo. During follow-up, 59 (62%) patients experienced progressive disease (median, 17.3 mo) and 28 patients (30%) died. The patients' treatments after uPAR PET/CT are shown in Table 3. Treatment with a somatostatin analog was the most frequent (77%, 74/96), and 28% (27/96) of patients underwent PRRT during follow-up.

PFS and OS

uPAR TLR as a continuous variable was significantly associated with PFS, with an HR of 1.27 (95% CI, 1.02–1.60; $P = 0.04$). For OS, uPAR TLR as a continuous marker was borderline-significant, with an HR of 1.37 (95% CI, 0.98–1.92; $P = 0.06$). TLR was then dichotomized at the median value (2.47) for Kaplan–Meier analyses (Fig. 2). Median OS was not reached in the group with low uPAR expression (TLR < median) and was 32.1 mo (95% CI, 23.8–upper limit not reached) in the group with high uPAR expression (TLR ≥ median). Median PFS was 22.1 mo (95% CI, 14.7–upper limit not reached) in patients with low uPAR expression and 14.1 mo (95% CI, 11.4–22.4) in patients with high uPAR expression. uPAR TLR dichotomized at median was significantly associated with PFS and OS; patients with high uPAR expression had a significantly worse prognosis (Tables 4 and 5). Other cutoffs were evaluated using Cutoff Finder, shown in Supplemental Figure 2. When a lower cutoff for TLR (1.32) was used, a smaller group of patients ($n = 10$) with no or a very low risk of death or progression could be identified (Fig. 3). Patients with NET G3 and NEC had significantly worse PFS and OS than patients with NET G1, whereas no difference was seen between NET G2 and NET G1 (Tables 4 and 5). In multivariate analyses including uPAR expression and WHO classification, both remained significantly associated with PFS, whereas uPAR expression had a borderline-significant association with OS ($P = 0.06$) when we controlled for WHO grade.

DISCUSSION

Our major finding in this prospective phase II study of ^{68}Ga-NOTA-AE105 uPAR PET was that uPAR expression was seen in most patients with both low-grade and high-grade NENs. Furthermore, high uPAR expression was associated with a worse prognosis with regard to both PFS and OS. These findings imply that uPAR could be an attractive target for therapy both because of the availability of the target in patients with NENs and because of the possibility of specifically targeting the lesions associated with a poorer prognosis.

The role of uPA and uPAR in cancer has been extensively investigated in the last few decades, and it is well established that higher uPAR expression is associated with tumor growth, invasiveness, and metastatic spread, although this has not been

TABLE 4
Uni- and Multivariate Cox Regression Analyses for PFS

	Univariate Cox		Multivariate Cox	
PFS	HR	*P*	HR	*P*
uPAR TLR*				
Low	Reference	—	Reference	—
High	1.87 (1.11–3.17)	0.02	1.75 (1.02–2.99)	0.04
WHO grades				
NET G1	Reference		Reference	
NET G2	1.21 (0.57–2.55)	0.62	1.26 (0.59–2.66)	0.55
NET G3	4.16 (1.52–11.36)	<0.01	3.56 (1.29–9.82)	0.01
NEC	4.26 (1.82–9.95)	<0.001	4.43 (1.89–10.39)	<0.001

*Dichotomized at median (2.47).
HR = hazard ratio.
Data in parentheses are 95% CIs.

thoroughly investigated in patients with NENs (*18*). Accordingly, several therapies targeting uPA and uPAR are undergoing investigation, such as a uPAR antibody (huATN-658) (*19*) and a serine protease inhibitor targeting uPA (upamostat) (*20*). However, none of these therapies has yet been approved for clinical use.

Patients with NENs have highly varying aggressiveness of disease. The primary tumor site, presence of metastases, and WHO classification are important prognostic markers and used to guide selection of treatment (*21*). Our group and others have shown that, in addition, low somatostatin receptor density as determined by ^{64}Cu-DOTATATE PET and high glucose metabolism as determined by ^{18}F-FDG PET are prognostic factors (*2,3,16,22*). With the concept of tailored treatments, specific tumor markers are used to guide eligibility for targeted treatments. This concept has seen widespread implementation in the treatment of patients with NENs, with somatostatin receptor imaging being used as a companion to screen for eligibility for somatostatin receptor–targeted therapy with ^{177}Lu-DOTATATE. In a randomized trial of patients receiving ^{177}Lu-DOTATATE compared with a high dose of cold somatostatin analog treatment, the former group had significantly fewer deaths, a longer PFS, and an 18% response rate (*23*). One drawback of targeting somatostatin receptor–expressing tumors is the fact that lower expression of somatostatin receptors is seen with less differentiated and more aggressive tumors (*24*). In contrast, uPAR expression is particularly seen in lesions showing tumor growth, invasiveness, and metastatic capability. Previously, our group has investigated uPAR expression by immunohistochemical staining of primary tumor or metastasis from patients with NEN G3 (Ki-67, >20%), showing uPAR expression in stromal or tumor cells in 16 of 21 (76%) patients (*25*). However, to the best of our knowledge, expression of uPAR in patients with low-grade NENs has never been studied in situ but has been studied only indirectly by measurement of soluble uPAR (suPAR) in serum (*26*). suPAR is the cleaved version of the membrane-bound uPAR and may thus be measured as a circulating uPAR biomarker. The study reported higher levels of suPAR in NEN

TABLE 5
Uni- and Multivariate Cox Regression Analyses for OS

	Univariate Cox		Multivariate Cox	
OS	HR	*P*	HR	*P*
uPAR TLR*				
Low	Reference	—	Reference	—
High	2.64 (1.19–5.88)	0.02	2.23 (0.96–5.20)	0.06
WHO grades				
NET G1	Reference	—	Reference	—
NET G2	1.40 (0.29–6.76)	0.67	1.59 (0.33–7.70)	0.56
NET G3	9.94 (2.00–49.52)	0.01	7.82 (1.55–39.44)	0.01
NEC	15.55 (3.49–69.37)	<0.001	17.09 (3.80–76.81)	<0.001

*Dichotomized at median (2.47).
HR = hazard ratio.
Data in parentheses are 95% CIs.

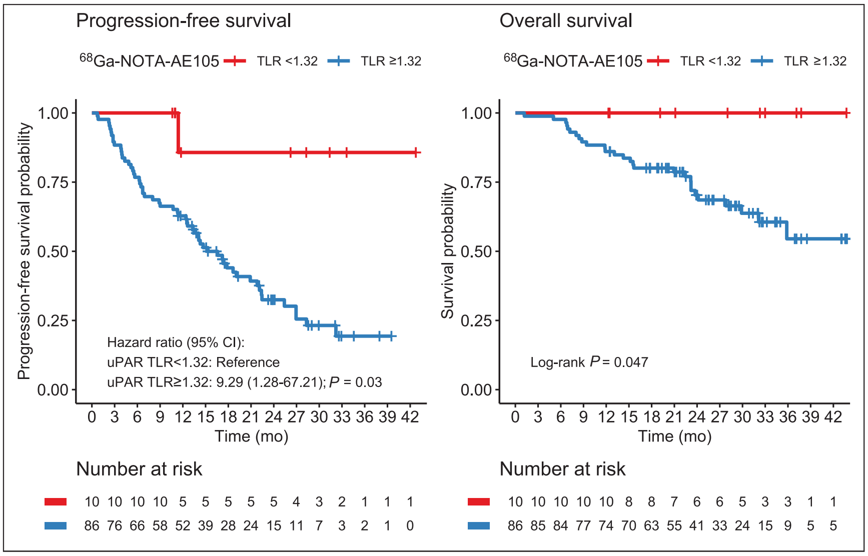

FIGURE 3. Kaplan–Meier plots of OS and PFS using ^{68}Ga-NOTA-AE105 uPAR PET. uPAR TLR was dichotomized at 1.32.

patients than in healthy controls, as well as elevated levels of suPAR in both patients with low-grade disease and patients with high-grade disease. However, no association between suPAR levels and OS was seen. Contrary to that study, using PET to visualize uPAR expression at the tumor level is a more direct approach, making it possible to identify the lesions with the greatest uPAR expression and their location. Also, the expression pattern of uPAR has previously been shown to be heterogeneous, with uPAR being highly expressed at the margin of the tumor and thus locally promoting tissue invasion and seeding of metastases, a hallmark of cancer (*27*). In support of this observation, we found that high uPAR expression on PET was associated with a worse prognosis, both with regard to PFS and with regard to OS. In line with our previous observations in patients with NEC and the data on suPAR in NENs, we found uPAR expression to be present in both low-grade and high-grade NENs. Hence, uPAR-targeted treatment may be relevant in patients with NENs of all grades. Our observations on uPAR expression should be viewed in light of the fact that the patients included in this study had mainly small intestinal or pancreatic primary tumors with metastatic disease and were previously treated.

A potential innovative perspective is to combine uPAR PET imaging and uPAR PRRT as a theranostic pair, hence using uPAR PET to assess eligibility for uPAR-targeted therapy. We have previously shown a high efficacy of uPAR PRRT in preclinical models of human prostate and colorectal cancer (*11,12*); however, further studies are warranted to assess the use of uPAR PRRT within NENs. The first step toward uPAR PRRT for NENs was to provide evidence for a high and specific uptake of our uPAR-targeting radioligand and the prognostic implications in NENs, as done in the present study.

CONCLUSION

uPAR expression assessed by ^{68}Ga-NOTA-AE105 PET is seen in most patients with both low-grade and high-grade NENs, and high uPAR expression is associated with a worse prognosis with regard to both PFS and OS. Collectively, this finding points to uPAR as a relevant target to pursue for risk stratification and possibly also for targeted therapy in patients with NENs.

DISCLOSURE

This project received funding from the European Union's Horizon 2020 Research and Innovation Program under grants 670261 (ERC Advanced Grant) and 668532 (Click-It), the Lundbeck Foundation, the Novo Nordisk Foundation, the Innovation Fund Denmark, the Danish Cancer Society, the Arvid Nilsson Foundation, the Neye Foundation, Novartis Health Care, the Research Foundation of Rigshospitalet, the Danish National Research Foundation (grant 126), the Research Council of the Capital Region of Denmark, the Danish Health Authority, the John and Birthe Meyer Foundation, the Research Council for Independent Research, and the Neuroendocrine Tumor Research Foundation. Andreas Kjaer is a Lundbeck Foundation Professor, inventor on a patent of the composition of matter of uPAR PET (WO 2014086364), and cofounder of Curasight, which has licensed the uPAR PET technology. No other potential conflict of interest relevant to this article was reported.

ACKNOWLEDGMENT

We are grateful to our dedicated colleagues at the Departments of Clinical Physiology, Nuclear Medicine, and PET; Endocrinology; and Oncology, Rigshospitalet, for assistance with patient recruitment, radiotracer production, and PET/CT acquisition. We express our sincere gratitude to all the patients who participated in the study.

KEY POINTS

QUESTION: Is uPAR expression seen in patients with NENs and associated with prognosis?

PERTINENT FINDINGS: Using ^{68}Ga-NOTA-AE105 for uPAR PET/CT imaging, we saw uPAR expression in most NEN patients, including both high-grade and low-grade NENs. Furthermore, increased uPAR expression, both as a continuous variable and dichotomized at median, was associated with increased hazard for progression of disease and death.

IMPLICATIONS FOR PATIENT CARE: uPAR PET imaging may be useful for risk stratification in patients with NENs. Furthermore, uPAR may be a possible treatment target given the expression of uPAR across patients with both high-grade and low-grade NENs and given that uPAR expression is associated with a poor outcome.

REFERENCES

1. Klimstra DS, Kloppel G, La Rosa S, Rindi G. *Digestive System Tumours.* 5th ed. International Agency for Research on Cancer; 2019:16–19.
2. Carlsen EA, Johnbeck CB, Loft M, et al. Semiautomatic tumor delineation for evaluation of 64Cu-DOTATATE PET/CT in patients with neuroendocrine neoplasms: prognostication based on lowest lesion uptake and total tumor volume. *J Nucl Med.* 2021;62:1564–1570.
3. Binderup T, Knigge U, Johnbeck CB, et al. ^{18}F-FDG PET is superior to WHO grading as a prognostic tool in neuroendocrine neoplasms and useful in guiding PRRT: a prospective 10-year follow-up study. *J Nucl Med.* 2021;62:808–815.

4. Mahmood N, Rabbani SA. Fibrinolytic system and cancer: diagnostic and therapeutic applications. *Int J Mol Sci.* 2021;22:4358.
5. Ahn SB, Mohamedali A, Pascovici D, et al. Proteomics reveals cell-surface urokinase plasminogen activator receptor expression impacts most hallmarks of cancer. *Proteomics.* 2019;19:e1900026.
6. Mahmood N, Mihalcioiu C, Rabbani SA. Multifaceted role of the urokinase-type plasminogen activator (uPA) and its receptor (uPAR): diagnostic, prognostic, and therapeutic applications. *Front Oncol.* 2018;8:24.
7. Skovgaard D, Persson M, Brandt-Larsen M, et al. Safety, dosimetry, and tumor detection ability of ^{68}Ga-NOTA-AE105: first-in-human study of a novel radioligand for uPAR PET imaging. *J Nucl Med.* 2017;58:379–386.
8. Persson M, Madsen J, Ostergaard S, Ploug M, Kjaer A. ^{68}Ga-labeling and in vivo evaluation of a uPAR binding DOTA- and NODAGA-conjugated peptide for PET imaging of invasive cancers. *Nucl Med Biol.* 2012;39:560–569.
9. Kriegbaum MC, Persson M, Haldager L, et al. Rational targeting of the urokinase receptor (uPAR): development of antagonists and non-invasive imaging probes. *Curr Drug Targets.* 2011;12:1711–1728.
10. Fosbøl MØ, Kurbegovic S, Johannesen HH, et al. Urokinase-type plasminogen activator receptor (uPAR) PET/MRI of prostate cancer for noninvasive evaluation of aggressiveness: comparison with Gleason score in a prospective phase 2 clinical trial. *J Nucl Med.* 2021;62:354–359.
11. Persson M, Rasmussen P, Madsen J, Ploug M, Kjaer A. New peptide receptor radionuclide therapy of invasive cancer cells: in vivo studies using ^{177}Lu-DOTA-AE105 targeting uPAR in human colorectal cancer xenografts. *Nucl Med Biol.* 2012;39:962–969.
12. Persson M, Juhl K, Rasmussen P, et al. uPAR targeted radionuclide therapy with ^{177}Lu-DOTA-AE105 inhibits dissemination of metastatic prostate cancer. *Mol Pharm.* 2014;11:2796–2806.
13. Knigge U, Capdevila J, Bartsch DK, et al. ENETS consensus recommendations for the standards of care in neuroendocrine neoplasms: follow-up and documentation. *Neuroendocrinology.* 2017;105:310–319.
14. Eisenhauer EA, Therasse P, Bogaerts J, et al. New response evaluation criteria in solid tumours: revised RECIST guideline (version 1.1). *Eur J Cancer.* 2009;45:228–247.
15. Johnbeck CB, Knigge U, Langer SW, et al. Prognostic value of ^{18}F-FLT PET in patients with neuroendocrine neoplasms: a prospective head-to-head comparison with ^{18}F-FDG PET and Ki-67 in 100 patients. *J Nucl Med.* 2016;57:1851–1857.
16. Binderup T, Knigge U, Loft A, Federspiel B, Kjaer A. ^{18}F-fluorodeoxyglucose positron emission tomography predicts survival of patients with neuroendocrine tumors. *Clin Cancer Res.* 2010;16:978–985.
17. Budczies J, Klauschen F, Sinn BV, et al. Cutoff Finder: a comprehensive and straightforward web application enabling rapid biomarker cutoff optimization. *PLoS One.* 2012;7:e51862.
18. Li Santi A, Napolitano F, Montuori N, Ragno P. The urokinase receptor: a multifunctional receptor in cancer cell biology: therapeutic implications. *Int J Mol Sci.* 2021;22:4111.
19. Mahmood N, Arakelian A, Khan HA, Tanvir I, Mazar AP, Rabbani SA. uPAR antibody (huATN-658) and Zometa reduce breast cancer growth and skeletal lesions. *Bone Res.* 2020;8:18.
20. Heinemann V, Ebert MP, Laubender RP, Bevan P, Mala C, Boeck S. Phase II randomised proof-of-concept study of the urokinase inhibitor upamostat (WX-671) in combination with gemcitabine compared with gemcitabine alone in patients with non-resectable, locally advanced pancreatic cancer. *Br J Cancer.* 2013;108:766–770.
21. Janson ET, Knigge U, Dam G, et al. Nordic guidelines 2021 for diagnosis and treatment of gastroenteropancreatic neuroendocrine neoplasms. *Acta Oncol.* 2021;60:931–941.
22. Carlsen EA, Johnbeck CB, Binderup T, et al. ^{64}Cu-DOTATATE PET/CT and prediction of overall and progression-free survival in patients with neuroendocrine neoplasms. *J Nucl Med.* 2020;61:1491–1497.
23. Strosberg J, El-Haddad G, Wolin E, et al. Phase 3 trial of ^{177}Lu-Dotatate for midgut neuroendocrine tumors. *N Engl J Med.* 2017;376:125–135.
24. Sorbye H, Kong G, Grozinsky-Glasberg S. PRRT in high-grade gastroenteropancreatic neuroendocrine neoplasms (WHO G3). *Endocr Relat Cancer.* 2020;27:R67–R77.
25. Olsen IH, Langer SW, Federspiel BH, et al. ^{68}Ga-DOTATOC PET and gene expression profile in patients with neuroendocrine carcinomas: strong correlation between PET tracer uptake and gene expression of somatostatin receptor subtype 2. *Am J Nucl Med Mol Imaging.* 2016;6:59–72.
26. Özdirik B, Stueven A, Knorr J, et al. Soluble urokinase plasminogen activator receptor (suPAR) concentrations are elevated in patients with neuroendocrine malignancies. *J Clin Med.* 2020;9:1647.
27. Hanahan D, Weinberg RA. Hallmarks of cancer: the next generation. *Cell.* 2011;144:646–674.

^{18}F-FDG PET/CT–Based Prognostic Survival Model After Surgery for Head and Neck Cancer

Gwenaelle Creff[1], Franck Jegoux[1], Xavier Palard[2], Adrien Depeursinge[3], Ronan Abgral[4], Remi Marianowski[5], Jean-Christophe Leclere[5], Thomas Eugene[6], Olivier Malard[7], Renaud De Crevoisier[8,9], Anne Devillers[2], and Joel Castelli[8,9]

[1]Department of Otolaryngology–Head and Neck Surgery (HNS), University Hospital, Rennes, France; [2]Department of Nuclear Medicine, Cancer Institute, Rennes, France; [3]Institute of Information Systems, HES-SO, Sierre, Switzerland; [4]Department of Nuclear Medicine, University Hospital, Brest, France; [5]Department of Otolaryngology–HNS, University Hospital, Brest, France; [6]Department of Nuclear Medicine, University Hospital, Nantes, France; [7]Department of Otolaryngology–HNS, University Hospital, Nantes, France; [8]Department of Radiation Oncology, Cancer Institute, Rennes, France; and [9]LTSI (Image and Signal Processing Laboratory), INSERM, U1099, Rennes, France

The aims of this multicenter study were to identify clinical and preoperative PET/CT parameters predicting overall survival (OS) and distant metastasis–free survival (DMFS) in a cohort of head and neck squamous cell carcinoma patients treated with surgery, to generate a prognostic model of OS and DMFS, and to validate this prognostic model with an independent cohort. **Methods:** A total of 382 consecutive patients with head and neck squamous cell carcinoma, divided into training ($n = 318$) and validation ($n = 64$) cohorts, were retrospectively included. The following PET/CT parameters were analyzed: clinical parameters, SUV$_{\text{max}}$, SUV$_{\text{mean}}$, metabolic tumor volume (MTV), total lesion glycolysis, and distance parameters for the primary tumor and lymph nodes defined by 2 segmentation methods (relative SUV$_{\text{max}}$ threshold and absolute SUV threshold). Cox analyses were performed for OS and DMFS in the training cohort. The concordance index (c-index) was used to identify highly prognostic parameters. These prognostic parameters were externally tested in the validation cohort. **Results:** In multivariable analysis, the significant parameters for OS were T stage and nodal MTV, with a c-index of 0.64 ($P < 0.001$). For DMFS, the significant parameters were T stage, nodal MTV, and maximal tumor–node distance, with a c-index of 0.76 ($P < 0.001$). These combinations of parameters were externally validated, with c-indices of 0.63 ($P < 0.001$) and 0.71 ($P < 0.001$) for OS and DMFS, respectively. **Conclusion:** The nodal MTV associated with the maximal tumor–node distance was significantly correlated with the risk of DMFS. Moreover, this parameter, in addition to clinical parameters, was associated with a higher risk of death. These prognostic factors may be used to tailor individualized treatment.

Key Words: head and neck cancer; PET/CT; prognosis; overall survival; distant metastasis

J Nucl Med 2022; 63:1378–1385
DOI: 10.2967/jnumed.121.262891

The therapeutic management of head and neck squamous cell carcinoma (HNSCC) is based on surgery, radiotherapy, and medical treatments, alone or in combination, according to the prognosis estimated by the American Joint Committee on Cancer (AJCC) staging system (*1*).

Despite therapeutic progress and the updating of the AJCC staging system, the prognosis of HNSCC patients remains poor because of a high recurrence rate (30%–40%) (*2*).

^{18}F-FDG PET/CT reveals the metabolic activity of a tumor (glycolysis) in addition to strict anatomic extent. This examination is now commonly used to assess the extent of HNSCC (*3*) and for posttreatment follow-up (*4*). The effectiveness of ^{18}F-FDG PET/CT parameters as prognostic biomarkers appears to be a promising research path for multiple tumor locations (*5–7*), without additional cost, time, or radiation dose (*8*). However, fewer data are available for HNSCC patients treated with surgery, although more than half of patients are treated with primary resection. These patients are mostly included in small numbers in the same group of analyses as patients treated with radiochemotherapy, who have different clinical and histologic profiles.

Moreover, whereas visual analysis is sufficient for diagnosis, staging, and the detection of recurrence, quantification appears necessary for the prediction of patient outcome (*5*). The SUV$_{\text{max}}$ is the most widely used parameter in clinical practice, but it corresponds only to the maximal pixel value in the tumor. More recently, volumetric ^{18}F-FDG PET/CT parameters—that is, metabolic tumor volume (MTV) and total lesion glycolysis (TLG), which consider overall tumor uptake—were developed. Moreover, studies on lung cancers introduced the concept of disease solidity (*9,10*), which consists of measuring disease spread by computing the relationship between the volume of the main tumor and all secondary nodes with respect to the volume of their convex hull (*11,12*). This concept has never been analyzed for HNSCC, and volumetric metabolic parameters have never been incorporated into this concept. Nonetheless, computing these parameters requires delineating the tumor. One of the most commonly chosen segmentation methods consists of using a threshold set at 41% of the SUV$_{\text{max}}$ (*13*). Although there are no consistent data for using this specific threshold to compute MTV (*14*), few studies have compared different thresholds for MTV or TLG.

Eventually, the lack of ^{18}F-FDG PET/CT acquisition parameter standardization between institutions (*15*) could affect the generalization of the existing data, as most of the studies published so far have been monocentric.

Received Jul. 11, 2021; revision accepted Nov. 16, 2021.

For correspondence or reprints, contact Gwenaelle Creff (gwenaelle.Creff@chu-rennes.fr).

In this context, the aims of the present study were to identify clinical and preoperative PET/CT parameters predicting overall survival (OS) and distant metastasis–free survival (DMFS) in an initial cohort of HNSCC patients treated with surgery, to generate a prognostic model of OS and DMFS, and to validate this prognostic scoring system with a second independent cohort of patients.

MATERIALS AND METHODS

Inclusion Criteria

All consecutive patients treated with primary surgery for HNSCC between January 1, 2010, and March 31, 2018, at 3 French hospital centers were retrospectively reviewed.

The inclusion criteria were as follows: 18 y of age or older, no history of cancer, histologically proven HNSCC, preoperative PET/CT, and a minimal follow-up of 3 mo.

Patients with carcinoma of unknown primary syndrome, nasopharyngeal, cutaneous, and salivary gland squamous cell carcinoma, discovery of distant metastases at the initial extension assessment, SUV_{max} for the primary tumor of less than 3, and tumor volume of less than 4 mL were systematically excluded from the study.

Access to the oncologic network databases was approved by the institutional ethics committees and by the French National Commission for Data Protection and Liberties (CNIL no. 2211146) and was in accordance with the 1964 Helsinki Declaration and its later amendments or comparable ethics standards. Confidentiality was assured for all participants regarding any personal responses and information provided, as all data collected were anonymized.

Patient Characteristics and Treatment Results

Of the 3,877 patients reviewed, 557 were eligible for the study and 382 were finally included (Fig. 1).

All patients underwent tumor resection that could be associated with neck dissection according to the clinical and radiologic preoperative stages. Postoperative radiotherapy was performed with or without chemotherapy in patients with a high risk of locoregional recurrence.

Physical examination and laryngoscopy were performed every 3 mo for the first 2 y, every 6 mo for the next 3 y, and then annually. The database was locked on August 31, 2019.

The entire cohort was divided into a training cohort from Rennes and Brest, including 318 patients, and a validation cohort from Nantes, including 64 patients.

PET/CT Acquisition

All patients underwent ^{18}F-FDG PET/CT for staging before surgical treatment. The PET/CT acquisition parameter data are summarized in Supplemental Table 1 (supplemental materials are available at http://jnm.snmjournals.org).

PET/CT Analysis

For each patient, the gross tumor volume (GTV) of the primary tumor (GTV) and the GTV of the lymph nodes (GTV) were manually segmented on each PET/CT scan by the same experienced investigator (radiation oncologist), who referred to the nuclear radiologist report. This delineation step was performed on axial, coronal, and sagittal sections using MIM Software SVVRTMIMS1 (version 6.7; MIM Software Inc.), with a CT window set from −160 to 240 Hounsfield units and a PET window set from 0 to 5 SUV. A region of interest (ROI) was then computed by adding a 3-dimensional margin of 5 mm to the GTV of the primary tumor (ROI-T) and the GTV of the lymph nodes (ROI-N). All lymph nodes were included in the same unique ROI.

A set of quantitative parameters based on SUV histograms were extracted from ROI-T and ROI-N on PET images using the Quant-Image web service (*16*). SUV_{max} was first computed from ROI-T as the SUV_{max} in the delineated volume. Various metabolic volumes were subsequently defined on the basis of 2 segmentation methods: an absolute threshold of the SUV (ranging from 0 to 20, with steps of 0.5) or a relative threshold of the SUV_{max} (ranging from 0% to 100%, with steps of 1%). Metabolic intensity parameters were computed using the 2 segmentation methods at each threshold for both ROI-T and ROI-N. Relative thresholds for ROI-N were computed on the basis of the SUV_{max} of the primary tumor. The MTV was computed as the metabolic volume of the segmented region in milliliters. If there were several nodes, then the MTV for nodes corresponded to the sum of the MTVs of each node. The TLG was computed as $\text{SUV}_{\text{mean}} \times$ MTV of the corresponding delineated region.

Tumor spread, also called disease solidity (*9*), was analyzed by computing various distance measures between the barycenter of the

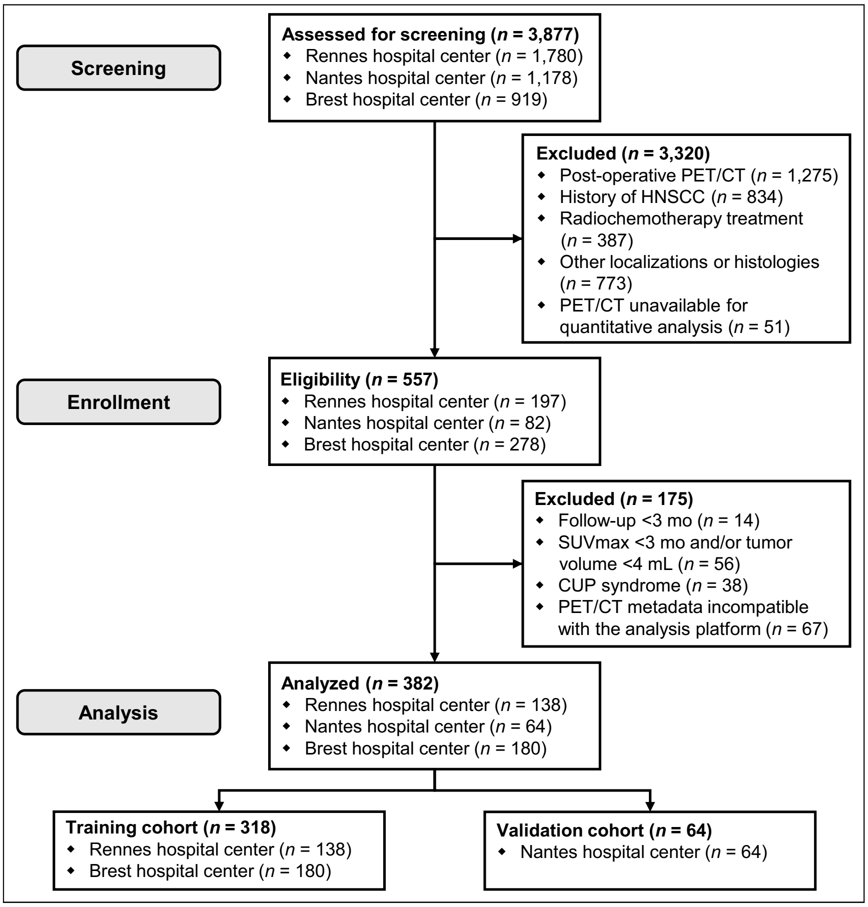

FIGURE 1. Flowchart. CUP = carcinoma of unknown primary.

TABLE 1

Univariable Cox Analyses for OS in Training Cohort*

Parameter	HR†	c-index	*P*
Clinical			
Age, in y	1.011 (0.99–1.03)	0.509	0.28
Sex			
Female	Reference		
Male	1.51 (0.89–2.6)	0.53	0.12
Tobacco use			
No	Reference		
Yes	2.13 (1.11–4.1)	0.52	0.02
Alcohol use			
No	Reference		
Yes	1.34 (0.99–4.1)	0.55	0.1
PS			
0–1	Reference		
2	2.65 (1.07–6.5)	0.52	0.03
T classification			
cT1–cT2	Reference		
cT3–cT4	2.01 (1.4–2.9)	0.61	0.003
N classification			
cN0	Reference		
cN1	1.19 (0.69–2.05)	0.53	0.5
cN2	1.13 (0.75–1.7)	0.53	0.5
cN3	2.32 (0.83–6.45)	0.53	0.1
AJCC staging			
I	Reference		
II	2.17 (0.89–5.3)	0.575	0.09
III	3.11 (1.36–7.1)	0.575	0.007
IV	2.59 (1.24–5.4)	0.575	0.01
Tumor site			
Oral cavity	Reference		
Hypopharynx	1.81 (1.08–3.03)	0.55	0.02
Larynx	1.29 (0.78–2.15)	0.55	0.3
Oropharynx	1.26 (0.75–2.12)	0.55	0.4
Metabolic data‡			
Tumor metabolic data			
SUV_{max}	1.004 (0.988–1.021)	0.54	0.58
MTV at 23% of SUV_{max}	1.02 (1.01–1.03)	0.64	<0.001
MTV at SUV of 2.5	1.01 (1.001–1.014)	0.61	0.038
TLG at 21% of SUV_{max}	1.001 (1.00–1.01)	0.61	0.04
TLG at SUV of 1.5	1.001 (1.000–1.002)	0.61	0.038
Node metabolic data			
MTV at 21% of SUV_{max}	1.007 (1.001–1.013)	0.566	0.014
MTV at SUV of 3.0	1.010 (1.000–1.019)	0.563	0.014
TLG at 21% of SUV_{max}	1.001 (1.000–1.002)	0.564	0.02
TLG at SUV of 3.0	1.001 (1.000–1.002)	0.551	0.036
Maximal tumor–node distance	1.04 (0.99–1.1)	0.57	0.08
dst_TBarycenterN	1.08 (1.01–1.16)	0.58	0.02

---

*There were 116 deaths.

†Values in parentheses are 95% CIs.

‡For PET parameters, data are given only for absolute and relative thresholds with highest c-index values.

PS = performance status; dst_TBarycenterN = distance between tumor and barycenter of all node metastases.

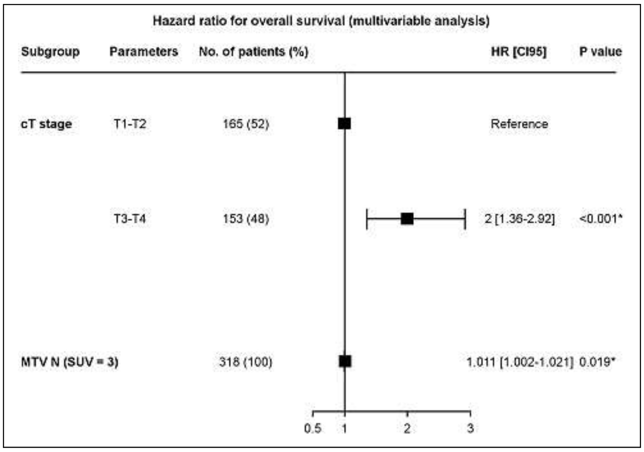

FIGURE 2. Parameters significantly affecting OS in training cohort in multivariable analysis (number of deaths = 116; c-index = 0.64).

main tumor (ROI-T) and the barycenter of each nodal metastasis (ROI-N) or of all nodal metastases (*16*).

Statistical Analysis

OS was calculated from the day of surgery to the date of death from any cause. Patients alive at the time of analysis were censored at the date of last follow-up.

DMFS was calculated from the day of surgery to the date of first distant progression or to the date of death.

Follow-up was calculated using reverse Kaplan–Meier estimation. Both DMFS and OS estimations were computed using the Kaplan–Meier method, and a 2-sided log-rank test was used to compare the groups.

The analyses were performed as suggested in the TRIPOD statement (*17*).

In the first step, the analysis was performed only on the training cohort. The association of the pretreatment parameters with OS and DMFS was first assessed using univariable Cox analyses. We used the inverse probability of censoring weighting version of the concordance index (c-index). Significant parameters were identified ($P < 0.05$), and Harrel's c-index was calculated (*18*). The c-index was used to determine the optimal SUV threshold giving the most predictive value for each PET parameter with a P value of <0.1.

Factors with a P value of <0.1 and with the highest c-index after univariable analyses were assessed with the multivariable Cox regression model using backward elimination. Variables were removed from the model if the P value was >0.1. Multivariable Cox analyses were performed to identify the significant parameters and the standardized coefficients of the prognostic model.

In the second step, the Cox prognostic models were used to compute the prognostic index for the patients in the validation cohort, and the corresponding c-index of each model was computed.

On the basis of this model, a nomogram was built to estimate the individual OS and DMFS probabilities at 24 mo.

Two types of validation of the prognostic model were performed. In the first step, an internal validation for the patients in the training cohort was performed by the bootstrap method (1,000 datasets constructed by random resampling with replacement from the original). This method was used to estimate the adjusted c-index and the 95% CI of each parameter. In the second step, the β-coefficients from the training model were applied to the external validation cohort, and the corresponding c-index was computed.

All analyses were performed using R software 3.4.0 (R Foundation for Statistical Computing).

RESULTS

Patient Outcomes

The median OSs for the training and validation cohorts were 63 mo (95% CI, 51 to not reached) and 91 mo (95% CI, 34 to not reached), respectively ($P = 0.79$). For the entire cohort, the 2-y OS rate was 75% (95% CI, 70%–80%). For the entire cohort, 35.34% died and 12.83% developed metastases. Among the patients who died, 36.30% had metastases. The patient, tumor, treatment, and follow-up characteristics of the training and validation cohorts are shown in Supplemental Table 2.

Identification of Cox Model for Predicting OS in Training Cohort

The results of the univariable analysis are shown in Table 1.

The retained significant parameters from the multivariable analysis were T stage and MTV for nodes with a threshold of 3 (Fig. 2). The c-index of the model was 0.64 ($P < 0.001$). The hazard ratios (HRs) of the corresponding Cox model are presented in Figure 2, allowing the calculation of a prognostic index (OS probability) for each patient. On the basis of the Cox model, a nomogram was computed (Fig. 3).

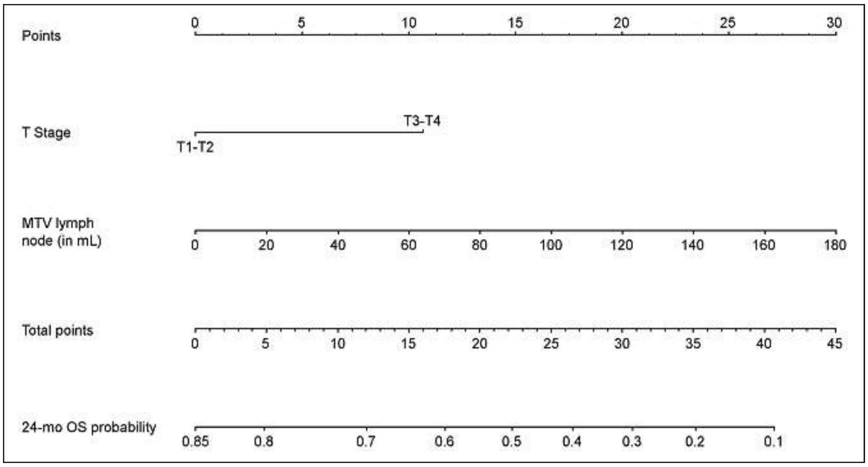

FIGURE 3. Nomogram for predicting OS at 24 mo. For each PET parameter, corresponding points were obtained by drawing line upward from corresponding values to "Points" line. Total points for each patient were obtained by summing points for each individual factor in nomogram and were plotted on "Total points" line. Line was drawn downward to read corresponding predictions of 24-mo OS.

Identification of Cox Model for Predicting DMFS in Training Cohort

The results of the univariable analysis are shown in Table 2.

The retained significant parameters from the multivariable analysis were T stage, MTV for nodes with a threshold of 3, and maximal tumor–node distance (Fig. 4). The c-index of the model was 0.76 ($P < 0.001$). The HRs of the corresponding Cox model are presented in Figure 4, allowing the calculation of a prognostic index (DMFS probability) for each patient. On the basis of the Cox model, a nomogram was computed (Fig. 5).

TABLE 2
Univariable Cox Analyses for DMFS in Training Cohort*

Parameter	HR†	c-index	P
Clinical			
Age, in y	1.020 (0.990–1.051)	0.540	0.197
Sex			
Female	Reference		
Male	1.861 (0.738–4.694)	0.532	0.188
Tobacco			
No	Reference		
Yes	2.112 (0.760–5.874)	0.533	0.152
Alcohol			
No	Reference		
Yes	1.111 (0.634–1.945)	0.517	0.714
PS			
0–1	Reference		
2	0.963 (0.133–6.988)	0.502	0.970
T classification			
cT1–cT2	Reference		
cT3–cT4	6.795 (1.981–23.334)	0.660	0.002
N classification			
cN0	Reference		
cN1	1.432 (0.530–3.874)	0.638	0.479
cN2	3.034 (1.518–6.088)	0.638	0.002
cN3	3.851 (1.072–13.827)	0.638	0.039
AJCC staging			
I	Reference		
II	1.389 (0.196–9.865)	0.595	0.742
III	3.116 (0.647–15.006)	0.595	0.156
IV	4.513 (1.089–18.708)	0.595	0.038
Tumor site			
Oral cavity	Reference		
Hypopharynx	1.946 (0.914–4.140)	0.578	0.084
Larynx	0.875 (0.374–2.049)	0.578	0.759
Oropharynx	1.094 (0.507–2.361)	0.578	0.818
Metabolic data			
Tumor metabolic data			
SUV_{max}	1.040 (1.010–1.072)	0.617	0.009
MTV at 15% of SUV_{max}	1.026 (1.016–1.036)	0.709	< 0.0001
MTV at SUV of 4.0	1.033 (1.020–1.046)	0.720	0.0000005
TLG at 21% of SUV_{max}	1.003 (1.002–1.005)	0.720	<0.0001
TLG at SUV of 4.0	1.003 (1.002–1.004)	0.714	0.0000008
Node metabolic data			
MTV at 21% of SUV_{max}	1.011 (1.000–1.021)	0.694	0.04
MTV at SUV of 3.0	1.016 (1.007–1.026)	0.693	0.0002
TLG at 21% of SUV_{max}	1.002 (1.001–1.003)	0.698	0.004
TLG at SUV of 3.0	1.002 (1.001–1.026)	0.694	0.0006
Distance parameters			
Maximal tumor–node distance	1.177 (1.092–1.269)	0.679	0.00002
dst_MTVweightedSumDistTN	1.002 (1.001–1.004)	0.696	0.00003
dst_MTVweightedMaxDistTN	1.003 (1.001–1.006)	0.68	0.01

---

*There were 51 patients with distant metastases.

†Values in parentheses are 95% CIs.

dst_MTVweightedSumDistTN = sum of distances weighted by respective MTVs of metastases; dst_MTVweightedMaxDistTN = metastasis remoteness weighted by MTV of corresponding metastasis.

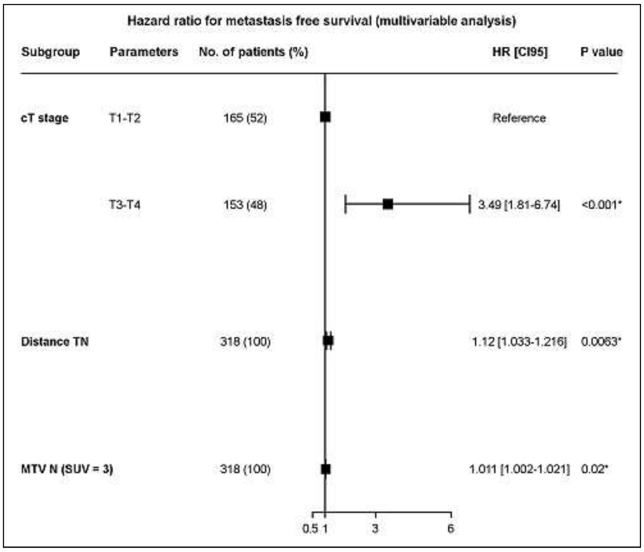

FIGURE 4. Parameters significantly affecting DMFS in training cohort in multivariable analysis (number of patients with distant metastasis = 51; c-index = 0.76).

Internal and External Validations of Prognostic Model

After internal bootstrap validation, the adjusted c-indices were estimated to be 0.63 ($P = 0.0002$) and 0.74 ($P < 0.001$) for OS and DMFS, respectively. The 95% CIs for the coefficients of the parameters of the model are shown in Supplemental Table 3 (OS) and Supplemental Table 4 (DMFS). Internal calibration showed a good adjustment between the predicted and observed OS and DMFS at 24 mo (Supplemental Fig. 1). The β-coefficients from the training model were applied to the external validation cohort, achieving c-indices of 0.63 ($P < 0.001$) and 0.71 ($P < 0.001$) for OS and DMFS, respectively.

DISCUSSION

To our knowledge, this is the first study presenting an ^{18}F-FDG PET/CT–based prognostic model including the concept of tumor dispersion to stratify the risks of distant metastases and death in patients with HNSCC treated with surgery. In this multicentric study of 382 patients, we demonstrated that the integration of pretreatment PET quantitative imaging features and conventional clinical prognostic factors enables the identification of patients with a high risk of distant relapse or death.

Patients with the same stage and type of tumor could respond differently to the same treatment and eventually have different outcomes (*19*). As we observed in the present study, stage cN was not correlated with OS, and the AJCC stage had a lower c-index than PET/CT volumetric and distance parameters (Tables 1 and 2). This result is consistent with reports in the literature for patients with HNSCC treated with radiochemotherapy (*20*). Indeed, among 470 patients with p16-negative oropharyngeal cancer treated with radiochemotherapy, the c-index of the PET prognostic model based on SUV entropy and asphericity was significantly higher than that of clinical parameters (Eastern Cooperative Oncology Group score, O'Sullivan stage, and AJCC stage), achieving c-indices of 0.75 versus 0.57 ($P < 0.001$) for the Eastern Cooperative Oncology Group score, 0.58 ($P < 0.001$) for the O'Sullivan classification, and 0.57 ($P < 0.001$) for the AJCC stage (*21*).

These new prognostic factors should allow better identification of patients with HNSCC at high risk of recurrence after surgery, with the aim of improving the therapeutic strategy through "personalized medicine" (*22*), based on characteristics inherent to each patient and not on population-based risk assessments such as staging (*23*).

The first PET parameter to be analyzed was the SUV_{max} (*24*). Although easy to use in routine clinical practice, this ^{18}F-FDG PET/CT parameter is now increasingly being seen as unreliable as a prognostic factor (*5,14*). Indeed, in the present study, the SUV_{max} was not correlated with OS or DMFS in the multivariable analysis. In a cohort of 162 patients with oral cavity carcinoma treated with surgery, pretreatment MTV and TLG were both independent predictive factors for OS (HR, 2.64 [95% CI, 1.35–5.21] [$P = 0.005$]; and HR, 3.30 [95% CI, 1.50–7.24] [$P = 0.003$]), whereas SUV_{max} was not (HR, 1.92 [95% CI, 0.92–3.96] [$P = 0.080$]) (*25*). In a systematic review of the prognostic value of PET parameters for patients with surgically treated HNSCC, MTV or TLG was found to have a higher prognostic value than SUV_{max} (*14*).

Nevertheless, to be used, these volumetric parameters need a specific delineation (*5*). Four techniques can be used: a threshold of the SUV (absolute [all voxels with an SUV greater than *x*], relative [greater than *x*% of SUV_{max}], or adaptive) or gradient-based, clustering, or statistical methods. No consensus has currently been found (*26*). However, it has been demonstrated that the results vary greatly depending on the segmentation technique used, much greater than the interoperator variability during contouring (*27*). We chose to use the intensity threshold thanks to its availability in nuclear medicine services and because our objective was to edit a prognostic model for patients with surgically treated HNSCC usable in routine clinical practice. However, we decided to explore a wide range of continuous thresholds from 0% to 100% of the SUV_{max} and from 0 to 20 of the SUV and not be restricted to the usual threshold of 41% of the SUV_{max}. Indeed, the limits of this

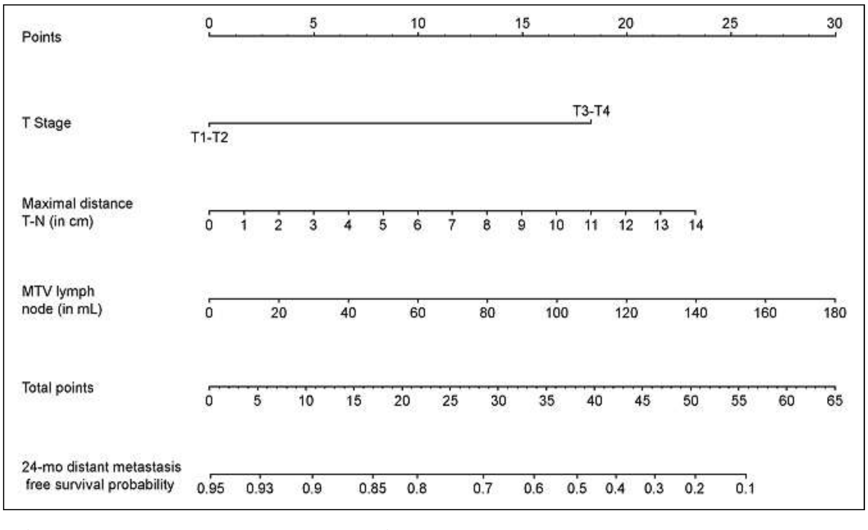

FIGURE 5. Nomogram for predicting DMFS at 24 mo.

threshold have already been displayed in patients with HNSCC treated with radiochemotherapy (*20,28*). To our knowledge, no study has analyzed different threshold values with such precise segmentation in patients treated with surgery. We demonstrated that the MTV of the primary tumor computed with a relative threshold of 23% was significantly associated with OS, with a c-index of 0.64 ($P < 0.001$). This relative threshold is lower than the threshold of 41% currently used. These data are consistent with the threshold that has been demonstrated in patients with locally advanced HNSCC treated with radiotherapy (35% of the SUV_{max}) (*29,30*). Conversely, in cancers of the cervix, among 89 patients treated with radiochemotherapy, a threshold of 50% of the SUV_{max} was most significantly correlated with recurrence-free survival (c-index, 0.752; HR, 1.065; $P < 0.001$) (*31*). Therefore, it appears that the threshold value used for the delineation of the tumor must be adapted to the tumor location and to the prognostic data sought. Indeed, in the present study, to predict DMFS and OS, lower thresholds (15%–25% of the SUV_{max}) seem to be more relevant. Despite the fact that we performed an external validation, because of the difference from the threshold of 41% used routinely, an additional validation of these thresholds by other groups would be interesting.

In addition to the volume parameters, the tumor dispersion parameters also seemed to be promising, especially for the DMFS (Fig. 4). This notion suggests that the quantitative imaging feature that examines spatial dispersion of the disease may also be relevant for prognosis (*9,32*). Indeed, the parameter of maximum distance between the tumor and the lymph node remained correlated with DMFS in multivariable analysis (HR, 1.12 [95% CI, 1.03–1.21]). For non–small cell lung cancers, the addition of distance parameters to the conventional model with prognostic factors alone yielded a significant improvement in the likelihood ratio test ($P = 0.007$) (*9*).

The present study had some limitations. First, the fact that the analysis was retrospective may have had an impact regarding the diagnosis of distant metastases. We only included patients with a minimal follow-up of 3 mo, to exclude deaths due to surgical complications (not related to oncologic evolution). Second, the impact of the heterogeneity of the work flows of acquiring ^{18}F-FDG PET/CT images on the data resulting from the quantification is the subject of debate (*15,26,33*). However, we developed a multicenter study with different acquisition parameters and performed an external validation of the prognostic model in an independent population of HNSCC patients. Although the prognostic value of p16 status in oropharyngeal cancer has already been demonstrated (*34*), it was excluded due to a lack of data. Besides, quantitative analyses from ^{18}F-FDG PET/CT revealed carbohydrate metabolic hyperactivity in tumor cells, named the Warburg effect (*35*). However, some of the cN3 stages and voluminous tumors have a necrotic central part, which is therefore not considered during the extraction of ^{18}F-FDG PET/CT parameters, which underestimates the tumor volume. Other radiotracers, such as ^{18}F-fluoromisonidazole and ^{18}F-fluoroazomycinarabinoside, could then be used; these have already demonstrated their potential prognostic interest in terms of OS (*36*) but are not yet used in clinical practice. Conversely, in case of contact between the primary tumor and an involved lymph node, an overestimation of the tumor volume may be calculated because of the inclusion of the lymph node tumor volume in the metabolic volume of the primary tumor. An SUV_{max} of less than 3 and a tumor volume of less than 4 mL were excluded to avoid high variability in a very small volume. Finally, we exclusively investigated PET/CT imaging; however, PET/MRI analyses also seem to be interesting in prognostic terms, although they are very rarely performed in HNSCC oncology (*37*).

CONCLUSION

The volumetric and distance parameters appeared to be independent prognostic factors in terms of OS and DMFS, with higher c-indices than the clinical parameters currently used.

By integrating them into a prognostic model, we could be able to identify HNSCC patients at higher risk of distance relapse (metastasis/DMFS) and death. These patients could then receive early therapeutic intensification to improve their prognosis.

DISCLOSURE

The LTSI, INSERM, U1099 (Rennes, France) and the Cancer Institute (Rennes, France) supported the study. No other potential conflict of interest relevant to this article was reported.

KEY POINTS

QUESTION: The aim of this study was to identify clinical and preoperative PET/CT parameters predicting OS and DMFS in a cohort of HNSCC patients treated with surgery.

PERTINENT FINDINGS: In this retrospective multicentric study of 382 patients, the nodal MTV associated with the maximal distance between the primary tumor and the lymph node or with clinical parameters was significantly correlated with a higher risk of distant metastasis or death, respectively.

IMPLICATIONS FOR PATIENT CARE: These parameters may be used to tailor individualized treatment.

REFERENCES

1. Huang SH, O'Sullivan B. Overview of the 8th edition TNM classification for head and neck cancer. *Curr Treat Options Oncol.* 2017;18:40.
2. Bray F, Ferlay J, Soerjomataram I, et al. Global cancer statistics 2018: GLOBOCAN estimates of incidence and mortality worldwide for 36 cancers in 185 countries. *CA Cancer J Clin.* 2018;68:394–424.
3. Salaün P-Y, Abgral R, Malard O, et al. Good clinical practice recommendations for the use of PET/CT in oncology. *Eur J Nucl Med Mol Imaging.* 2020;47:28–50.
4. Robin P, Abgral R, Valette G, et al. Diagnostic performance of FDG PET/CT to detect subclinical HNSCC recurrence 6 months after the end of treatment. *Eur J Nucl Med Mol Imaging.* 2015;42:72–78.
5. Castelli J, Bari BD, Depeursinge A, et al. Overview of the predictive value of quantitative 18 FDG PET in head and neck cancer treated with chemoradiotherapy. *Crit Rev Oncol Hematol.* 2016;108:40–51.
6. Bonomo P, Merlotti A, Olmetto E, et al. What is the prognostic impact of FDG PET in locally advanced head and neck squamous cell carcinoma treated with concomitant chemo-radiotherapy? A systematic review and meta-analysis. *Eur J Nucl Med Mol Imaging.* 2018;45:2122–2138.
7. Pellegrino S, Fonti R, Mazziotti E, et al. Total metabolic tumor volume by ^{18}F-FDG PET/CT for the prediction of outcome in patients with non-small cell lung cancer. *Ann Nucl Med.* 2019;33:937–944.
8. O'Connor JPB, Aboagye EO, Adams JE, et al. Imaging biomarker roadmap for cancer studies. *Nat Rev Clin Oncol.* 2017;14:169–186.
9. Fried DV, Mawlawi O, Zhang L, et al. Stage III non-small cell lung cancer: prognostic value of FDG PET quantitative imaging features combined with clinical prognostic factors. *Radiology.* 2016;278:214–222.
10. Fried DV, Mawlawi O, Zhang L, et al. Potential use of ^{18}F-fluorodeoxyglucose positron emission tomography-based quantitative imaging features for guiding dose escalation in stage III non-small cell lung cancer. *Int J Radiat Oncol Biol Phys.* 2016;94:368–376.

11. Apostolova I, Rogasch J, Buchert R, et al. Quantitative assessment of the asphericity of pretherapeutic FDG uptake as an independent predictor of outcome in NSCLC. *BMC Cancer.* 2014;14:896.
12. El Naqa I, Grigsby P, Apte A, et al. Exploring feature-based approaches in PET images for predicting cancer treatment outcomes. *Pattern Recognit.* 2009;42: 1162–1171.
13. Boellaard R, Delgado-Bolton R, Oyen WJG, et al. FDG PET/CT: EANM procedure guidelines for tumour imaging—version 2.0. *Eur J Nucl Med Mol Imaging.* 2015;42:328–354.
14. Creff G, Devillers A, Depeursinge A, et al. Evaluation of the prognostic value of FDG PET/CT parameters for patients with surgically treated head and neck cancer: a systematic review. *JAMA Otolaryngol Head Neck Surg.* 2020;146:471–479.
15. Boellaard R. Standards for PET image acquisition and quantitative data analysis. *J Nucl Med.* 2009;50(suppl):11S–20S.
16. Dicente Cid Y, Castelli J, Schaer R, et al. QuantImage: an online tool for high-throughput 3D radiomics feature extraction in PET-CT. In: Depeursinge A, Al-Kadi OS, Mitchell JR, eds. *Biomedical Texture Analysis.* New York, NY: Academic Press; 2017:349–377.
17. Moons KGM, Altman DG, Reitsma JB, et al. Transparent Reporting of a multivariable prediction model for Individual Prognosis Or Diagnosis (TRIPOD): explanation and elaboration. *Ann Intern Med.* 2015;162:W1–W73.
18. Harrell FE, Lee KL, Mark DB. Multivariable prognostic models: issues in developing models, evaluating assumptions and adequacy, and measuring and reducing errors. *Stat Med.* 1996;15:361–387.
19. Dehing-Oberije C, Yu S, De Ruysscher D, et al. Development and external validation of prognostic model for 2-year survival of non-small-cell lung cancer patients treated with chemoradiotherapy. *Int J Radiat Oncol Biol Phys.* 2009;74:355–362.
20. Abgral R, Keromnes N, Robin P, et al. Prognostic value of volumetric parameters measured by ^{18}F-FDG PET/CT in patients with head and neck squamous cell carcinoma. *Eur J Nucl Med Mol Imaging.* 2014;41:659–667.
21. Cheng N-M, Fang Y-HD, Tsan D-L, et al. Heterogeneity and irregularity of pretreatment ^{18}F-fluorodeoxyglucose positron emission tomography improved prognostic stratification of p16-negative high-risk squamous cell carcinoma of the oropharynx. *Oral Oncol.* 2018;78:156–162.
22. Schleidgen S, Klingler C, Bertram T, et al. What is personalized medicine: sharpening a vague term based on a systematic literature review. *BMC Med Ethics.* 2013;14:55.
23. Liao W-L, Tsai F-J. Personalized medicine: a paradigm shift in healthcare. *Biomedicine (Taipei).* 2013;3:66–72.
24. Chung MJ, Kim YS, Kim JY, et al. Predictors of distant metastasis after radical surgery followed by postoperative radiotherapy with or without chemotherapy for oropharyngeal cancer. *Cancer Res Treat.* 2016;48:1167–1176.
25. Ryu IS, Kim JS, Roh J-L, et al. Prognostic significance of preoperative metabolic tumour volume and total lesion glycolysis measured by ^{18}F-FDG PET/CT in squamous cell carcinoma of the oral cavity. *Eur J Nucl Med Mol Imaging.* 2014;41: 452–461.
26. Hatt M, Lee JA, Schmidtlein CR, et al. Classification and evaluation strategies of auto-segmentation approaches for PET: report of AAPM Task Group No. 211. *Med Phys.* 2017;44:e1–e42.
27. Guezennec C, Bourhis D, Orlhac F, et al. Inter-observer and segmentation method variability of textural analysis in pre-therapeutic FDG PET/CT in head and neck cancer. *PLoS One.* 2019;14:e0214299.
28. Kikuchi M, Koyasu S, Shinohara S, et al. Prognostic value of pretreatment ^{18}F-fluorodeoxyglucose positron emission tomography/CT volume-based parameters in patients with oropharyngeal squamous cell carcinoma with known p16 and p53 status. *Head Neck.* 2015;37:1524–1531.
29. Castelli J, Depeursinge A, Ndoh V, et al. A PET-based nomogram for oropharyngeal cancers. *Eur J Cancer.* 2017;75:222–230.
30. Castelli J, Depeursinge A, Devillers A, et al. PET-based prognostic survival model after radiotherapy for head and neck cancer. *Eur J Nucl Med Mol Imaging.* 2019; 46:638–649.
31. Du S, Sun H, Gao S, Xin J, Lu Z. Metabolic parameters with different thresholds for evaluating tumor recurrence and their correlations with hematological parameters in locally advanced squamous cell cervical carcinoma: an observational ^{18}F-FDG PET/CT study. *Quant Imaging Med Surg.* 2019;9:440–452.
32. Zhang N, Liang R, Gensheimer MF, et al. Early response evaluation using primary tumor and nodal imaging features to predict progression-free survival of locally advanced non-small cell lung cancer. *Theranostics.* 2020;10:11707–11718.
33. Nahmias C, Wahl LM. Reproducibility of standardized uptake value measurements determined by ^{18}F-FDG PET in malignant tumors. *J Nucl Med.* 2008;49:1804–1808.
34. Langendijk JA, Psyrri A. The prognostic significance of p16 overexpression in oropharyngeal squamous cell carcinoma: implications for treatment strategies and future clinical studies. *Ann Oncol.* 2010;21:1931–1934.
35. Chen XS, Li LJ, Guan Y, et al. Anticancer strategies based on the metabolic profile of tumor cells: therapeutic targeting of the Warburg effect. *Acta Pharmacol Sin.* 2016;37:1013–1019.
36. Graves EE, Hicks RJ, Binns D, et al. Quantitative and qualitative analysis of [^{18}F]FDG and [^{18}F]FAZA positron emission tomography of head and neck cancers and associations with HPV status and treatment outcome. *Eur J Nucl Med Mol Imaging.* 2016;43:617–625.
37. Kim YI, Cheon GJ, Kang SY, et al. Prognostic value of simultaneous ^{18}F-FDG PET/MRI using a combination of metabolo-volumetric parameters and apparent diffusion coefficient in treated head and neck cancer. *EJNMMI Res.* 2018;8:2.

Interrogating Glioma-Associated Microglia and Macrophage Dynamics Under CSF-1R Therapy with Multitracer In Vivo PET/MRI

Claudia Foray*[1,2], Cristina Barca*[1,2], Alexandra Winkeler[3], Stefan Wagner[4], Sven Hermann[1], Michael Schäfers[1,4], Oliver M. Grauer†[5], Bastian Zinnhardt†[1,2,4,6], and Andreas H. Jacobs†[1,2,7]

[1]European Institute for Molecular Imaging, University of Münster, Münster, Germany; [2]PET Imaging in Drug Design and Development, Münster, Germany; [3]Université Paris-Saclay, BioMaps, CEA, CNRS, INSERM, Orsay, France; [4]Department of Nuclear Medicine, University Hospital Münster, Münster, Germany; [5]Department of Neurology, University Hospital Münster, Münster, Germany; [6]Biomarkers and Translational Technologies, Neurosciences and Rare Diseases, Pharma Research and Early Development, F. Hoffmann-La Roche Ltd., Basel, Switzerland; and [7]Department of Geriatrics with Neurology, Johanniter Hospital, and Centre for Integrated Oncology of the University Hospital Bonn, Bonn, Germany

Glioma-associated microglia and macrophages (GAMMs) are key players in creating an immunosuppressive microenvironment. They can be efficiently targeted by inhibiting the colony-stimulating factor 1 receptor (CSF-1R). We applied noninvasive PET/CT and PET/MRI using ^{18}F-fluoroethyltyrosine (^{18}F-FET) (amino acid metabolism) and *N,N*-diethyl-2-[4-(2-^{18}F-fluoroethoxy)phenyl]-5,7-dimethylpyrazolo [1,5-*a*]pyrimidine-3-acetamide (^{18}F-DPA-714) (translocator protein) to understand the role of GAMMs in glioma initiation, monitor in vivo therapy-induced GAMM depletion, and observe GAMM repopulation after drug withdrawal. **Methods:** C57BL/6 mice (*n* = 44) orthotopically implanted with syngeneic mouse GL261 glioma cells were treated with different regimens using the CSF-1R inhibitor PLX5622 (6-fluoro-*N*-((5-fluoro-2-methoxypyridin-3-yl)methyl)-5-((5-methyl-1H-pyrrolo [2,3-b]pyridin-3-yl)methyl)pyridin-2-amine) or vehicle, establishing a preconditioning model and a repopulation model, respectively. The mice underwent longitudinal PET/CT and PET/MRI. **Results:** The preconditioning model indicated similar tumor growth based on MRI (44.5% ± 24.8%), ^{18}F-FET PET (18.3% ± 11.3%), and ^{18}F-DPA-714 PET (16% ± 19.04%) volume dynamics in all groups, suggesting that GAMMs are not involved in glioma initiation. The repopulation model showed significantly reduced ^{18}F-DPA-714 uptake (−45.6% ± 18.4%), significantly reduced GAMM infiltration even after repopulation, and a significantly decreased tumor volume (−54.29% ± 8.6%) with repopulation as measured by MRI, supported by a significant reduction in ^{18}F-FET uptake (−50.2% ± 5.3%). **Conclusion:** ^{18}F-FET and ^{18}F-DPA-714 PET/MRI allow noninvasive assessment of glioma growth under various regimens of CSF-1R therapy. CSF-1R–mediated modulation of GAMMs may be of high interest as therapy or cotherapy against glioma.

Key Words: glioma; GAMM; ^{18}F-DPA-714; TSPO; CSF-1R; C57BL/6

J Nucl Med 2022; 63:1386–1393
DOI: 10.2967/jnumed.121.263318

The aggressiveness and molecular complexity of glioblastoma multiforme challenges the current standard-care therapy, limiting the median overall survival to 14–16 mo (*1*). In the last few decades, new immunotherapeutic strategies have been developed for gliomas. Despite some promising results, there are currently no approved immunotherapies that proved to be efficient against glioblastoma multiforme (*2*). The high heterogeneity of the tumor microenvironment plays an important role in therapy resistance, and glioma-associated myeloid cells, such as glioma-associated microglia and macrophages (GAMMs), monocytes, and myeloid-derived suppressor cells (MDSCs) (including polymorphonuclear and monocytic MDSCs), are key players in the establishment of an immunosuppressive environment that favors glioma immune evasion and progression (*3*). Moreover, chronically activated resident immune cells exacerbate the inflammatory response, leading to a high state of neuroinflammation while participating in the development of an immunosuppressive tumor microenvironment (*4*). Therefore, targeting glioma-associated myeloid cells represents an important strategy to develop new glioma microenvironment-targeted therapies. These cell populations are dependent on colony-stimulating factor 1 receptor (CSF-1R) signaling for their survival (*5*). Small-molecule CSF-1R inhibitors are used to study the dynamics of these cells in glioma progression and glioma-associated inflammation, profiting from their ability to modulate GAMMs through a mechanism of depletion and repopulation.

MRI and amino acid PET imaging with methyl-^{11}C-methionine or ^{18}F-fluoroethyltyrosine (^{18}F-FET, amino acid transport) are part of the clinical imaging routine to diagnose and follow up patients with gliomas (*6–9*). The use of ^{18}F-FET has been reported to have a major clinical value in providing important information for tumor delineation and differentiation and for assessment of posttherapeutic modifications and relapses (*10*). ^{18}F-FET PET is highly specific for glioma tissue but falls short in visualizing the reactive and infiltrating myeloid component of the glioma microenvironment (*11*). Other radiotracers, including the 18-kDa translocator protein

---

Received Oct. 6, 2021; revision accepted Jan. 4, 2022.

For correspondence or reprints, contact Andreas H. Jacobs (ahjacobs@uni-muenster.de) or Claudia Foray (claudia.foray@uni-muenster.de).

*Contributed equally to this work.

†Contributed equally to this work.

(TSPO)–targeting PET tracer *N,N*-diethyl-2-[4-(2-^{18}F-fluoroethoxy)-phenyl]-5,7-dimethylpyrazolo[1,5-*a*]pyrimidine-3-acetamide (^{18}F-DPA-714), have been used to visualize the myeloid cell compartment in gliomas (*12*). ^{18}F-DPA-714 PET has been reported to give information complementary to that from ^{18}F-FET, especially with regard to resident and infiltrating immune cells in preclinical glioma models and in patients (*13,14*). Because the timing of immunomodulation may be critical for therapy outcome, noninvasive imaging tools are highly useful in the assessment of the glioma microenvironment before, during, and after therapeutic intervention with novel immunomodulatory compounds (*15*).

Here, we performed a multimodal, dual-tracer imaging study in a syngeneic mouse model of glioma applying ^{18}F-FET and ^{18}F-DPA-714 PET using a CSF-1R inhibitor to investigate the interplay between glioma progression and related immune cell dynamics. Performing a preconditioning study, we aimed to investigate the possible role of GAMMs in glioma initiation. In the repopulation model, we aimed to assess the therapeutic effect of CSF-1R inhibition–induced depletion and subsequent repopulation on GAMM dynamics in an established tumor.

We hypothesized that a GAMM depletion–repopulation approach would be beneficial, resulting in reduced tumor size and decreased neuroinflammation, and that ^{18}F-DPA-714 is a suitable imaging readout for in vivo investigation of GAMM dynamics during the course of CSF-1R inhibitor therapy. Taking advantage of the reversible inhibitory effect of the drug, we were able to noninvasively monitor the dynamics during CSF-1R inhibitor–mediated GAMM depletion and repopulation.

MATERIALS AND METHODS

Cell Culture

Mouse GL261 glioma cells were cultured in T-75 cell culture flasks as an adherent monolayer in Dulbecco modified Eagle medium supplemented with GlutaMAX (Thermo Fisher Scientific), 10% heat-inactivated fetal calf serum, and 1% penicillin/streptomycin at 37°C in a humidified incubator maintained at 5% CO_2 before intracranial implantation.

Study Approval

All experiments were conducted in accordance with the German law on the care and use of laboratory animals and approved by the Landesamt für Natur, Umwelt, und Verbraucherschutz of North Rhine–Westphalia and the ARRIVE guidelines (Animal Research: Reporting of In Vivo Experiments) (*16*).

Study Design

In total, 51 C57BL/6 female mice 8–10 wk old were orthotopically implanted (intrastriatal injection, coordinates in relation to bregma: lateral, −2.0 mm; anterior–posterior, +0.5 mm; dorsal–ventral, −3.0 mm) with 2×10^5 mouse GL261 cells in 2 μL of NaCl, 0.9%. During all experimental procedures, the mice were anesthetized with 1.5%–2% isoflurane (Abbott Animal Health) in 100% O_2. After surgery, the animals were weighed daily for at least 3 d and before each imaging session to monitor their health condition (Supplemental Fig. 1; supplemental materials are available at http://jnm.snmjournals.org). Applying different regimens of PLX5622 (6-fluoro-*N*-((5-fluoro-2-methoxy-pyridin-3-yl)methyl)-5-((5-methyl-1H-pyrrolo[2,3-b]pyridin-3-yl)methyl)pyridin-2-amine), we divided the study into 2 parts, a preconditioning model in which mice were treated with PLX5622 14 d before tumor implantation,

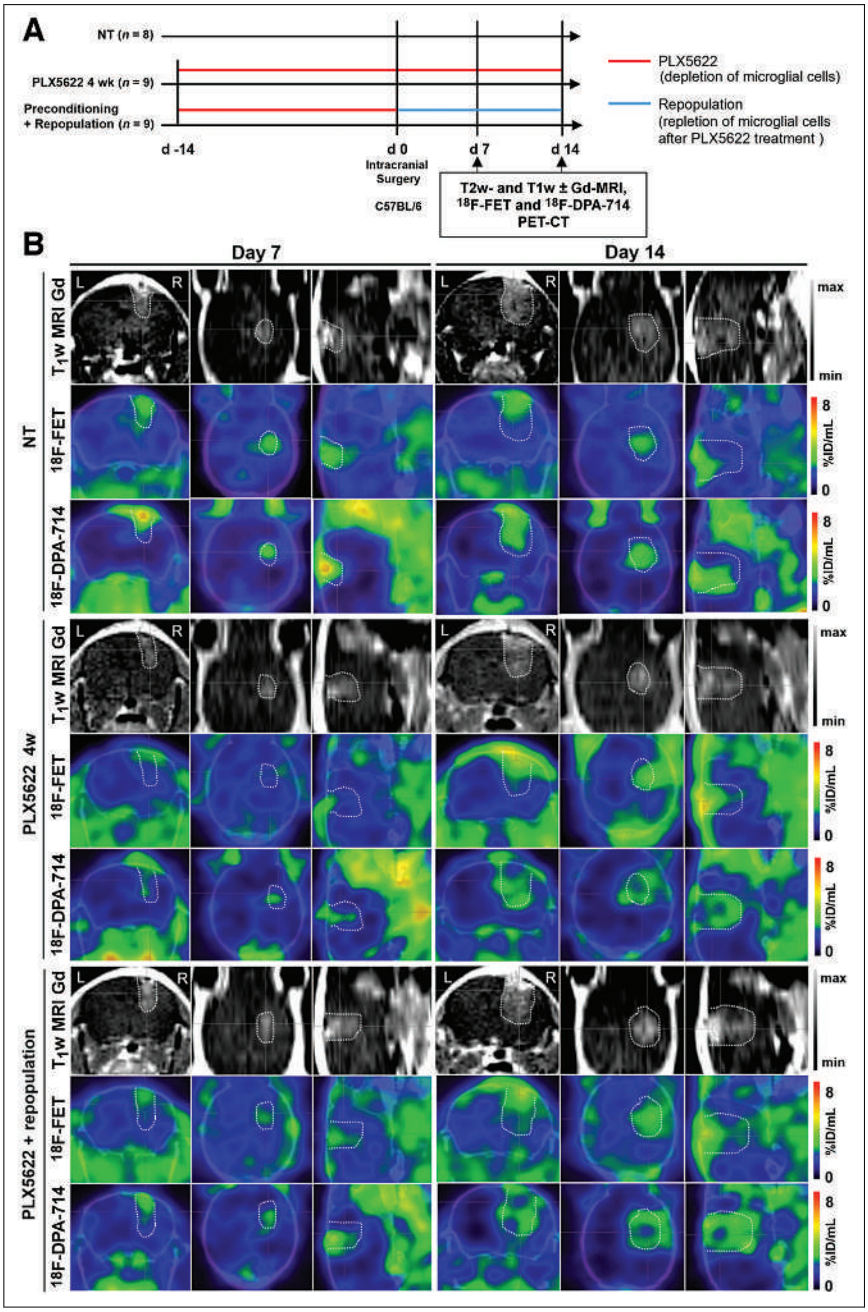

FIGURE 1. Suitability of longitudinal gadolinium-enhanced T1-weighted MRI, ^{18}F-FET, and ^{18}F-DPA-714 PET for monitoring immunotherapy-induced changes in preconditioning model. (A) Workflow of preconditioning model. (B) Images during different PLX5622 regimens. Dotted lines indicate tumor area depicted by MRI and transferred to PET images. %ID = percentage injected dose; NT = nontreated.

and a repopulation model in which microglial cells were acutely depleted and repopulated. The mice underwent sequential gadolinium-enhanced T1-weighted MRI, as well as ^{18}F-FET and ^{18}F-DPA-714 PET/CT, as described previously (*17*). Full details are available in the supplemental methods and in Figures 1A and 4A.

MRI Studies

MRI was conducted for 3-dimensional localization of the glioma and for coregistration with PET/CT images. The mice were anesthetized and the lateral tail vein was cannulated using a 26-gauge catheter. A T1-weighted spin-echo 2-dimensional sequence was acquired in a 1-T nanoScan PET/MRI scanner equipped with an MH20 coil (Mediso Medical Imaging Systems; resolution, 0.27 × 0.27 × 0.9 mm). Gadolinium contrast agent (Gadavist; Bayer Pharmaceutical) was injected via the catheter (50 μmol/kg), and a postgadolinium T1-weighted sequence was acquired.

PET Studies

PET images were acquired on a high-resolution small-animal PET scanner (32-module quadHIDAC; Oxford Positron Systems Ltd.) with uniform spatial resolution (<1 mm in full width at half maximum). ^{18}F-DPA-714 PET images were acquired 60–80 min after intravenous injection of 14.3 ± 2.6 MBq of ^{18}F-DPA-714. ^{18}F-FET PET images were acquired 20–30 min after intravenous injection of 10.6 ± 0.6 MBq of ^{18}F-FET. The supplemental methods provide further details.

Volumetric Analysis

Imaging data were analyzed using the in-house–developed software MEDgical as described previously (*17*). Briefly, an atlas-based right

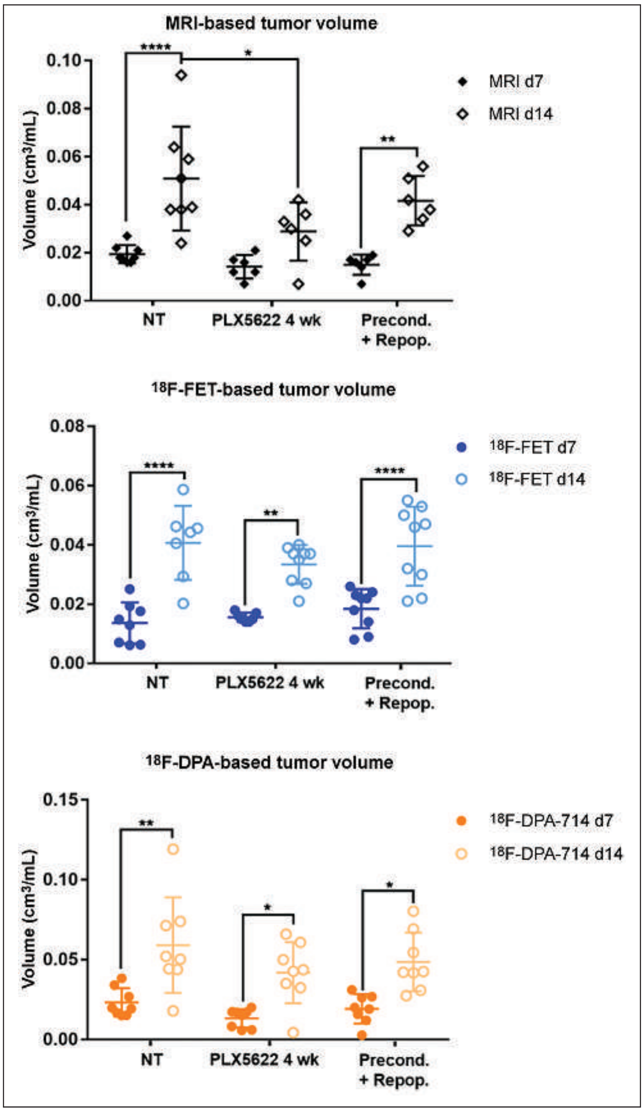

FIGURE 2. Analysis of tumor and tracer volumes in preconditioning model. Experimental groups include 8 nontreated patients; 9 PLX5622, 4 wk, patients; and 9 preconditioning-plus-repopulation patients. *$P \leq 0.05$. **$P \leq 0.01$. ****$P \leq 0.0001$. NT = nontreated.

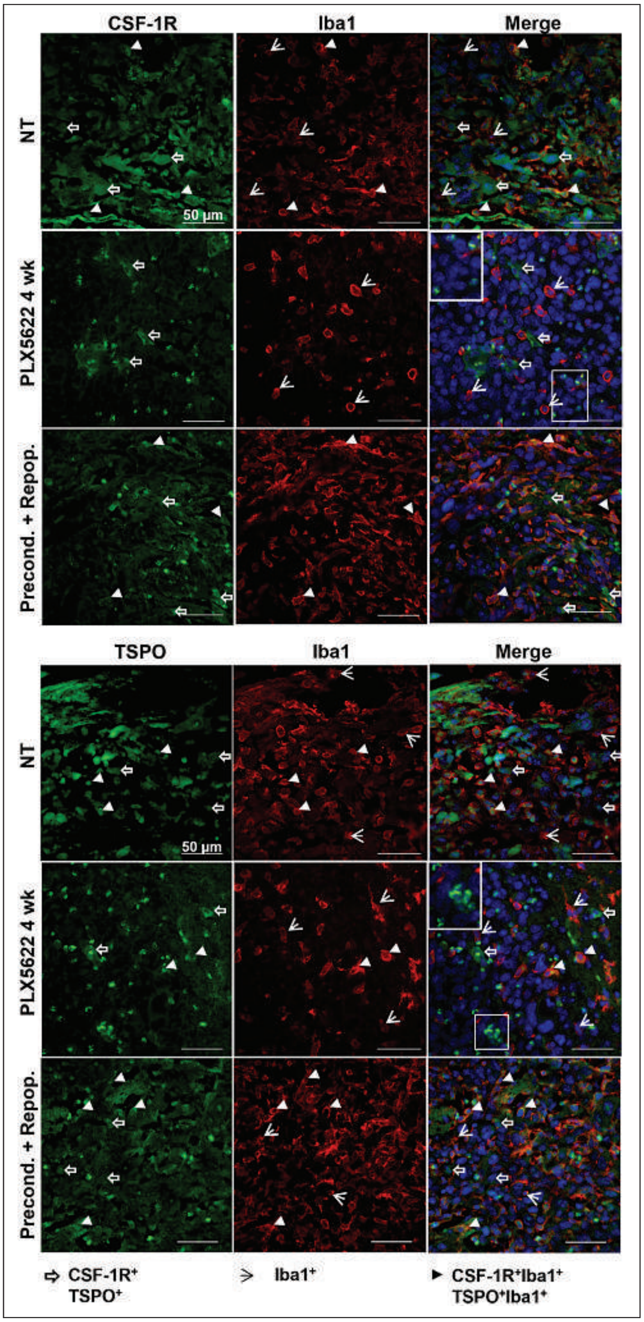

FIGURE 3. Dual labeling for CSF-1R/Iba1 and TSPO/Iba1 confirms presence of therapy-resistant cell populations. Paraffin-embedded tissues are labeled for CSF-1R/TSPO/Iba1. White boxes show unclassified infiltrating cells. Blue represents nuclear staining with DAPI (n = 3 mice/group). NT = nontreated. White open arrows = CSF-1R+ and TSPO+ cells; white arrowheads = Iba1+ cells; white filled arrowheads = CSF-1R+Iba1+ and TSPO+Iba1+ cells.

hemisphere volume of interest was thresholded to delineate tumor and tracer uptake volumes after coregistration of PET/CT scans with MR images. Tumor-to-background ratios were calculated.

Immunoreactivity

After the last imaging examination, the mice were killed and perfused with 0.9% NaCl and 4% perfluoroalkoxy alkane. The brains were fixed overnight in 4% perfluoroalkoxy alkane, embedded in paraffin, cut into coronal sections, and processed as previously described (*17*). To characterize the tumor microenvironment and therapy-induced modifications, CSF-1R/ionized calcium binding adaptor molecule 1 (Iba1) and TSPO/Iba1 dual labeling with fluorescent antibodies was performed on a preconditioning model and a repopulation model. Positive cells were quantified in biologic triplicates, counting manually or using the bioimage analysis software QuPath (*18*). The antibodies are listed in Supplemental Table 1.

Multiparametric Flow Cytometry

Myeloid tissue–derived cells were isolated after processing of the tissues as described previously (*17*). The cells were stained with a panel of directly labeled monoclonal antibodies (Supplemental Table 2). All samples were analyzed using the Navios flow cytometer and Kaluza software (version 2.1; Beckman Coulter). The supplemental methods provide additional data.

Statistical Analysis

Statistical analysis was performed using Prism (version 6; GraphPad Software, Inc.). Differences in radiotracer uptake ratios and tracer uptake volumes between and within groups over time were tested using either 1-way ANOVA with multiple comparisons corrected with a Holm–Šídák test or a *t* test followed by a Mann–Whitney *U* test on ranks and a Wilcoxon test with Bonferroni adjustment for multiple measurements. Correlations between tumor and tracer volumes were tested using Pearson correlation and linear regression. Significance levels were set at a *P* value of less than 0.05. All results are shown as mean ± SE or ± SD. Only animals with full a dataset were considered. Outliers were automatically excluded.

RESULTS

^{18}F-DPA-714 PET Imaging Reveals Therapy-Resistant Cells in Chronically Treated Mice

All the experimental groups in the preconditioning study showed similar gadolinium-enhanced T1-weighted MRI and ^{18}F-FET–based volume dynamics, together with ^{18}F-DPA-714–based volume, indicating increased tumor volume and inflammation over time (Figs. 1B and 2). Tumor volume was significantly reduced in the chronically treated group compared with the nontreated group on day 14. Interestingly, ^{18}F-DPA-714 signal was distributed at the borders and in the caudal parts of the tumors, especially in the chronically treated animals, highlighting spatial complementarities to ^{18}F-FET uptake (Fig. 1B).

The analyses of the tumor-to-background ratio displayed a significant reduction in ^{18}F-DPA-714 uptake already on day 7 in the chronically treated group compared with the nontreated group (Supplemental Fig. 2; Supplemental Tables 3 and 4).

A high density of Iba1-positive (+) cells was detected in preconditioned-and-repopulated mice, as well as in the nontreated group. Chronic treatment reduced the number of Iba-1+ cells, although not as expected, revealing a resistant Iba1+ cell population in both hemispheres. Repopulation significantly increased the number of Iba1+ cells after preconditioning (Supplemental Fig. 3). Those persistent cells were present within and at the periphery of the glioma and showed reduced CSF-1R and TSPO expression compared with the preconditioned-and-repopulated group; few of the cells expressed both markers. Interestingly, we observed an influx of apparently round CSF-1R+, TSPO+ cells within the tumor area (Fig. 3).

Volumetric Analyses Show Significant Reduction in Tumor and Tracer Uptake Volumes After Acute Treatment with Subsequent Repopulation

We then assessed the possible effects of acute treatment and subsequent microglial repopulation. In nontreated animals, gadolinium-enhanced T1-weighted MRI, ^{18}F-FET PET, and ^{18}F-DPA-714 PET showed a significant increase in tumor volume and both tracer volumes over time. In the group treated with PLX5622 (6-fluoro-*N*-((5-fluoro-2-methoxypyridin-3-yl)methyl)-5 -((5-methyl-1H-pyrrolo[2,3-b]pyridin-3-yl)methyl)pyridin-2-amine), gadolinium-enhanced T1-weighted MRI and ^{18}F-FET PET–derived volumes significantly increased between days 7 and 21 whereas ^{18}F-DPA-714 PET–derived volume significantly increased between days 7 and 14 (Figs. 4B and 5). A therapy effect was observed on day 21,

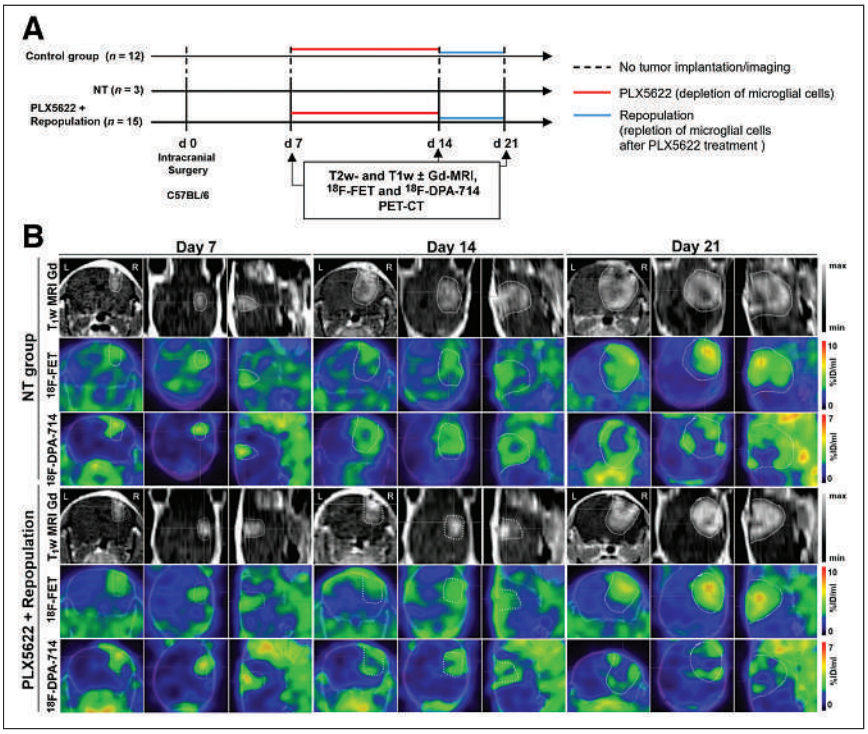

FIGURE 4. Monitoring glioma immunotherapy-induced changes after GAMM depletion and repopulation using multimodal PET/MRI. (A) Workflow of repopulation model. (B) Gadolinium-enhanced T1-weighted MR and PET images for ^{18}F-FET and ^{18}F-DPA-714 of nontreated and PLX5622-treated animals, before treatment, after treatment, and after GAMM repopulation (left to right). Dotted line is tumor area depicted by MRI and transferred to PET images. %ID = percentage injected dose; NT = nontreated.

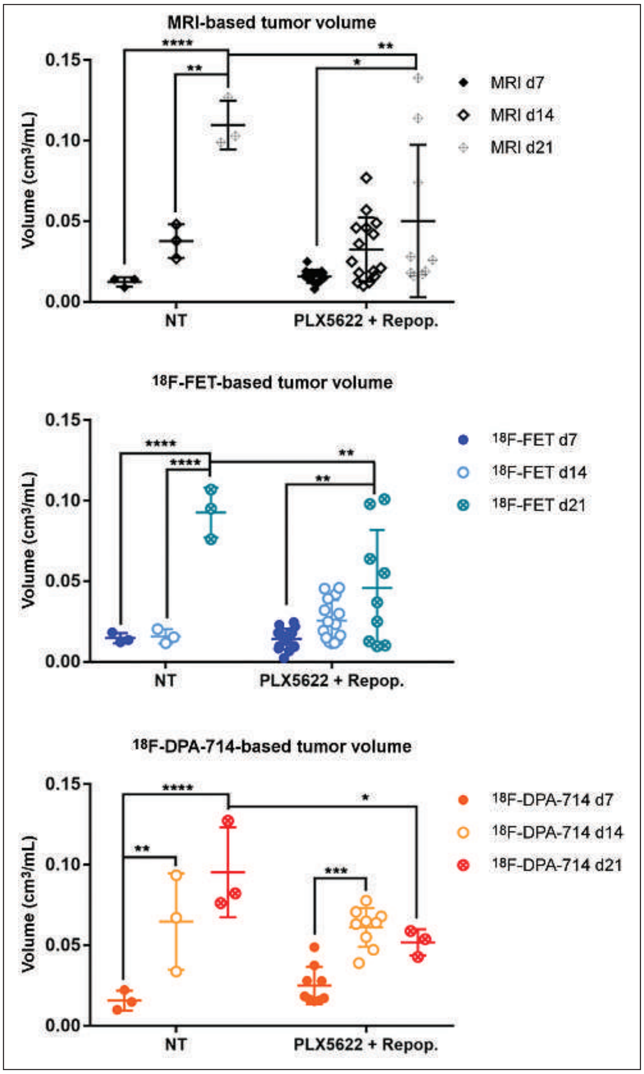

FIGURE 5. Analysis of tumor and tracer volumes in repopulation model. Experimental groups include 3 nontreated patients and 15 PLX5622-plus-repopulation patients. $^{*}P \leq 0.05$. $^{**}P \leq 0.01$. $^{***}P \leq 0.001$. $^{****}P \leq 0.0001$. NT = nontreated.

when repopulated animals showed significantly reduced tumor volumes, ^{18}F-FET PET–derived volumes, and ^{18}F-DPA-714 PET–derived volumes compared with nontreated animals (Supplemental Table 5).

In the nontreated group, ^{18}F-FET tumor mean/background mean significantly increased between days 7 and 21, whereas in the PLX5622-plus-repopulation group it increased between days 14 and 21. Similarly, ^{18}F-FET tumor maximum/background mean was increased in the nontreated group but was significantly reduced in repopulated animals on day 21 (Supplemental Fig. 4; Supplemental Table 6).

In-depth analyses already showed a statistically significant positive correlation between MRI-based tumor volume and ^{18}F-FET uptake on days 14 and 21 (Supplemental Fig. 7).

GAMMs Are Significantly Affected by CSF-1R Inhibition, with Persistent Reduction in CSF-1R and TSPO Expression After Drug Withdrawal

PLX5622 treatment successfully depleted most Iba1+ cells in glioma-bearing mice compared with the nontreated group ($P \leq 0.05$), in both the ipsilateral and the contralateral hemispheres, in line with TSPO PET. The remaining Iba1+ cells were at the periphery of the glioma or within the tumor borders, displaying an ameboidlike morphology indicative of an active state. After 1 wk of repopulation, the number of Iba-1+ cells on the contralateral side was significantly increased in the repopulation group compared with the PLX5622 group ($P \leq 0.05$) (Supplemental Fig. 5).

Similarly, CD68 expression was analyzed as a marker for GAMMs and specifically for macrophage-mediated immune suppression. A large number of CD68+ cells was detected infiltrating the glioma tissue in nontreated animals. The number of CD68+ cells was significantly reduced with PLX5622 treatment and remained significantly reduced after repopulation as shown by quantification (Supplemental Fig. 6).

CSF-1R+ tumor cells, Iba1+ microglial cells at the periphery and infiltrating the glioma, and CSF-1R+, Iba1+ cells within the tumor mass were detected in nontreated animals. PLX5622 treatment reduced CSF-1R expression, with few CSF-1R+, Iba1+ cells present at the border of the glioma. After repopulation, CSF-1R signal remained reduced and CSF-1R+ cells were visible at the periphery of the glioma (Fig. 6).

Similarly, TSPO+ cells and Iba1+ cells, as well as TSPO+, Iba1+ cells, surrounded and infiltrated the glioma tissue in the nontreated group. After CSF-1R inhibition, TSPO signal was detectable mostly at the border of the tumor mass, in line with the imaging results, together with a few Iba1+ and TSPO+Iba1+ cells. After repopulation and in accordance with the imaging results, the reduction in TSPO signal remained stable, and TSPO+ cells were visible at the periphery of the glioma whereas cells that were Iba1+, TSPO-negative and Iba1+, TSPO+ were detectable within the glioma tissue (Fig. 7). Interestingly, the depletion of Iba1+ cells seemed to promote the infiltration of as-yet-uncharacterized CSF-1R+, TSPO+ cells (Figs. 6 and 7).

CSF-1R Inhibition Shows Immune-Modulatory Effects on Glioma-Associated Myeloid Tissue–Derived Cells

To further evaluate therapy-induced changes in the tumor microenvironment and to characterize the phenotype of infiltrating cells, multiparametric flow cytometry was performed (Supplemental Fig. 8). PLX5622 treatment reduced the frequency of CD45+ tumor-infiltrating leukocytes compared with the nontreated group (15.2% vs. 22.3%, respectively), in which the frequency was slightly increased after repopulation (19.1%). The same results were found for GAMMs, confirming the histologic results. Comparable amounts of total MDSCs were detected in the PLX5622-treated and the nontreated groups (CD11b+, Gr1+: 5.1% vs. 3.6%), which significantly decreased after repopulation (CD11b+, Gr1+: 0.78%). Moreover, PLX5622 treatment produced a difference in the MDSC phenotype and affected the expression of different M2 activation markers, such as TSPO and major histocompatibility complex class II. The supplemental appendix provides additional information.

DISCUSSION

This study aimed to assess the suitability of a multitracer PET/MRI combination to investigate the effects of microglia-depleting immunotherapy in the tumor microenvironment in a syngeneic mouse glioma model. Using different treatment regimens, we demonstrated that the dual-tracer combination of ^{18}F-FET and ^{18}F-DPA-714 PET in conjunction with MRI allows monitoring of therapy-induced changes in glioma progression and GAMM dynamics in the tumor microenvironment. In contrast to ^{18}F-FET

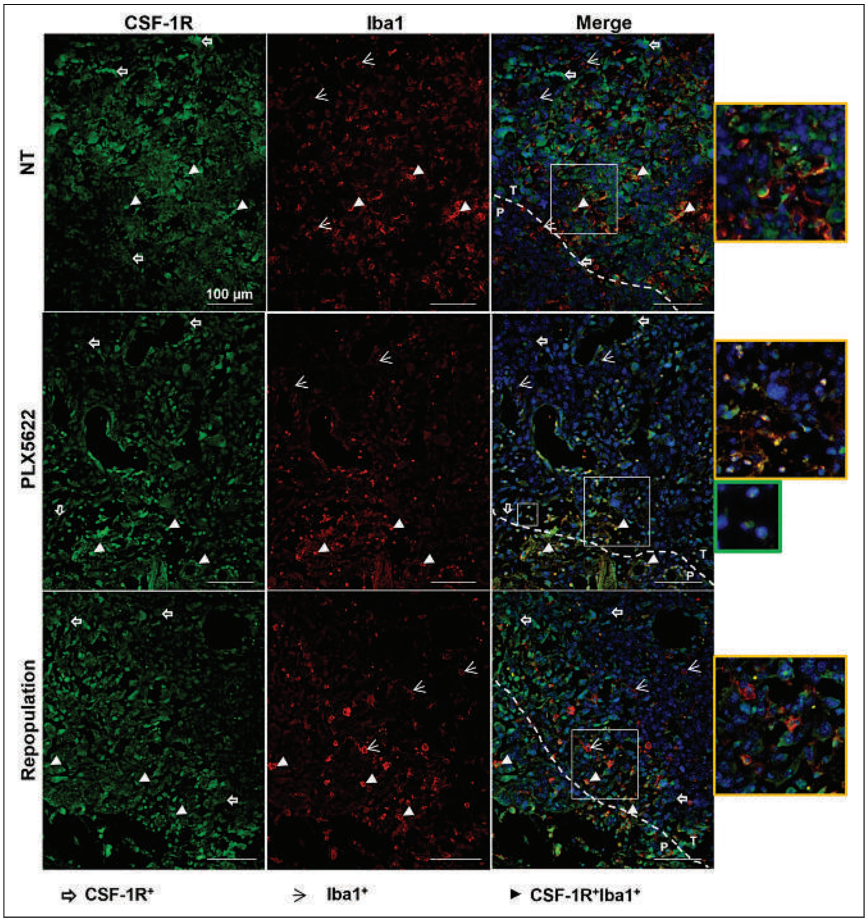

FIGURE 6. Immunofluorescence labeling for CSF-1R and Iba1 shows persistent reduction in CSF-1R signal after repopulation. Paraffin-embedded tissues are labeled for CSF-1R (green) and Iba1 (red) in nontreated, PLX5622-treated, and repopulated groups. Blue represents nuclear staining with DAPI. Yellow-framed images show magnification of area in larger white boxes. Green-framed image shows magnification of unclassified infiltrating cells (in smaller white box). Dotted line indicates separation between periphery and inner mass (n = 3 mice/group). NT = nontreated; P = periphery; T = tumor. White open arrows = CSF-1R+ cells; white arrowheads = Iba1+ cells; white filled arrowheads = CSF-1R+Iba1+ cells.

PET, ^{18}F-DPA-714 PET may be suitable to detect immunotherapy-induced changes within the glioma microenvironment when it is used in conjunction with detailed immunohistochemical analysis. We demonstrated that CSF-1R inhibition affects both glioma cells and specific glioma-associated myeloid-derived cell populations. GAMM inhibition was sustained even after drug withdrawal. Histologic analyses confirmed the efficacy of PLX5622 to deplete most Iba1+ cells over a short period, whereas longer treatment produced a therapy-resistant cell population. Interestingly, the results indicated that microglia cells and GAMMs do not seem essential for glioma initiation. However, a short-term brain repopulation period after CSF-1R therapy is highly effective in slowing glioma progression and maintaining a reduced inflammatory response. Finally, TSPO PET using ^{18}F-DPA-714 gives information complementary to that from the imaging marker ^{18}F-FET. Altogether, these findings provide new insight into CSF-1R therapy resistance in glioma and identify novel therapeutic glioma targets.

The role of the CSF-1R/CSF-1 axis has been studied in many cancer types, because tumor cells secrete CSF-1 to attract CSF-1R+ myeloid-derived cells to the tumor microenvironment to sustain tumor progression. Therefore, the expression levels of CSF-1R and circulating ligand are regarded as biomarkers for tumor progression, treatment failure, and poor prognosis (*19*). Different CSF-1R inhibitors have been tested in preclinical studies and clinical trials but failed to show substantial efficacy because of acquired resistance to CSF-1R therapy by the glioma microenvironment (*20*).

TSPO is reported to be upregulated by resident (microglia, astrocytes) and peripheral (monocytes, lymphocytes, neutrophils) immune cells during inflammatory conditions (*21*). In glioma tissue, TSPO is expressed by glioma cells, GAMMs, and endothelial cells (*22*). Our group recently described the suitability of TSPO PET using ^{18}F-DPA-714 to monitor treatment outcomes in a preclinical glioma model, by identifying areas of myeloid cell infiltration within the glioma microenvironment (*17*).

Our results show the efficacy of CSF-1R inhibition for the blockade of GAMM proliferation and that the combination of ^{18}F-FET and ^{18}F-DPA-714 PET can be used to monitor CSF-1R therapy–induced changes in the glioma microenvironment. The CSF-1R inhibitor PLX5622 proves to have a disease-changing effect, reducing glioma progression and neuroinflammation, particularly when administered for a short period during established glioma growth.

We report data on ablation of microglia cells and GAMMs before and during glioma development showing that the inhibition of these cell populations before glioma initiation does not influence glioma formation or the inflammatory response. Ex vivo characterization revealed the presence of a potentially resistant Iba1+ cell population as a possible major cellular source of TSPO expression, particularly in chronically treated animals. These findings were supported by in-depth histologic analyses that showed a persistent reduction in TSPO and CSF-1R signals coming from the glioma tissue, whereas a high number of TSPO+ and CSF-1R+ cells were infiltrating the glioma microenvironment. The same holds true for the preconditioned-and-repopulated group characterized by the presence of a high number of GAMMs and microglia cells positive for all the markers infiltrating the glioma tissue. These results might explain the increased ^{18}F-DPA-714 uptake over time, highlighting the importance of TSPO PET in detecting glioma-associated cell infiltration.

Whether the observed resistant cell population is pro- or antitumorigenic has yet to be clarified. However, it partially expressed TSPO, supporting the efficacy of TSPO PET in monitoring specific glioma-associated inflammation. Furthermore, TSPO PET has great potential for the characterization and imaging of the glioma-associated immunosuppressive tumor microenvironment, as shown in the first-in-patients study by Zinnhardt et al. (*14*).

The importance of choosing the proper therapeutic window for GAMM modulation is crucial, and TSPO PET may serve this purpose (*23*). In this regard, a short-term (1 wk) CSF-1R inhibition with subsequent brain repopulation during glioma progression led

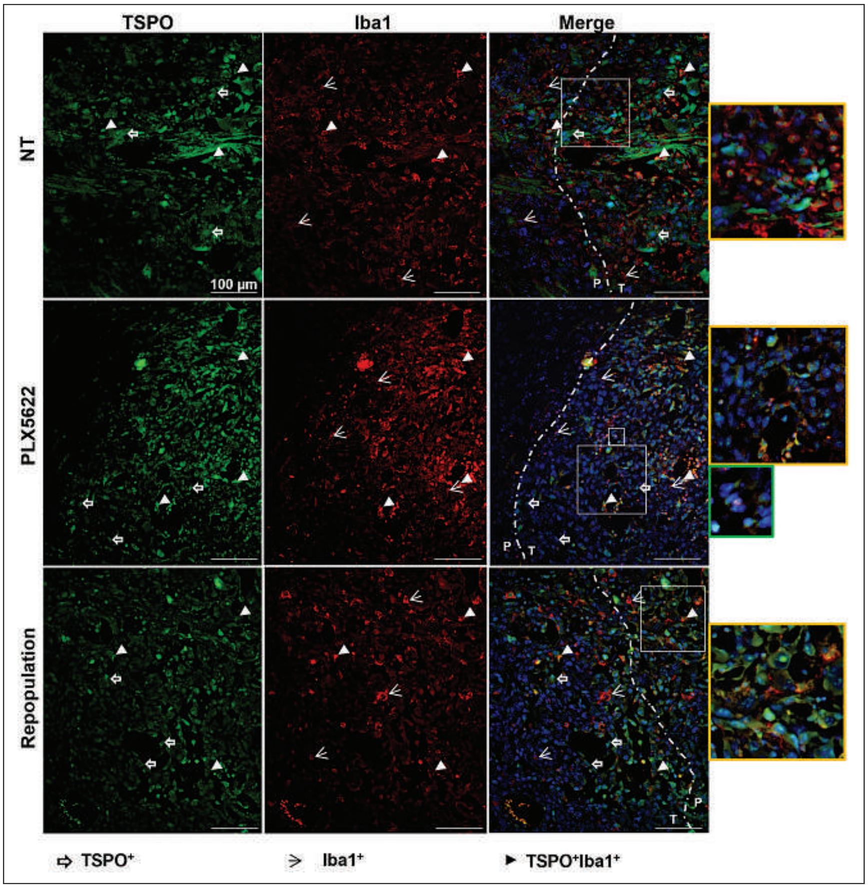

FIGURE 7. Immunofluorescence labeling for TSPO and Iba1 shows persistent reduction in TSPO signal after repopulation. Paraffin-embedded tissue are labeled for TSPO (green) and Iba1 (red) in nontreated, PLX5622-treated, and repopulated groups. Blue represents nuclear staining with DAPI. Yellow-framed images show magnification of area in larger white boxes. Green-framed image shows magnification of unclassified infiltrating cells (in smaller white box). Dotted line indicates separation between periphery and inner mass (n = 3 mice/group). NT = nontreated; P = periphery; T = tumor. White open arrows = TSPO+ cells; white arrowheads = Iba1+ cells; white filled arrowheads = TSPO+Iba1+ cells.

to a significant reduction in tumor volume as quantified by both gadolinium-enhanced MRI and ^{18}F-FET PET. In accordance with the literature, CSF-1R inhibition significantly reduced the number of Iba1+ cells in the brain (*24*). However, tumor cells also express TSPO, and the volumetric analysis showed increased ^{18}F-DPA-714 PET volumes on day 14 at the same level as in the nontreated group because of glioma progression, which may hide possible immunologically induced changes. Interestingly, after 7 d of brain repopulation, the ^{18}F-DPA-714 PET signal remained stable and a significant reduction in tracer volume was detected compared with the control group, suggesting long-lasting treatment effects. These findings were further confirmed by histology. Furthermore, we showed that CSF-1R inhibition significantly reduced the number of GAMMs infiltrating the glioma tissue, identified as CD68+ cells, and the inhibitory effect was detected also after brain repopulation. These results demonstrate that GAMMs are susceptible to acute CSF-1R–mediated intervention even after treatment withdrawal. In line with the results obtained after the chronic treatment, fluorescent labeling revealed the presence of TSPO+ and CSF-1R+ immune cells infiltrating the tumor after depletion of microglia cells. The presence of these potentially therapy-resistant cells supports the importance of microglia in preventing the influx of tumor-associated cells within the tumor microenvironment. Accordingly, previous studies reported increased peripheral immune cell infiltration after microglia depletion (*25,26*).

The CSF-1R therapy–induced effects on the immune component were further investigated by multiparametric flow cytometry analyses. Overall, the analyses indicated a strong effect of CSF-1R immune modulation on the MDSC population. The results suggest that the infiltrating component in the absence of Iba1+ cells might be represented by polymorphonuclear MDSCs. Moreover, PLX5622 effects resulted in the modulation of major histocompatibility complex class II and TSPO expression on GAMMs and MDSCs, in line with the reduction in ^{18}F-DPA-714 PET volumes. This finding may indicate that repopulation could modulate the immunosuppressive function toward an antitumor phenotype, highlighting the importance of targeting GAMMs.

As reported, single-agent therapy with CSF-1R inhibitors has demonstrated only modest results in glioblastoma clinical trials, showing no significant improvement in the progression-free survival of patients (*27*). Currently, other ongoing studies are combining CSF-1R therapy and immune-checkpoint inhibitors in different types of tumors (*28*). One pilot study evaluating the TSPO PET tracer ^{11}C-PBR28 in patients with primary glioblastoma multiforme or melanoma brain metastasis, treated with chemoradiation or immunotherapy, was completed recently; the results are to be determined (NCT02431572) (*29*).

Validation of TSPO PET tracers in clinical settings is necessary to improve the understanding of glioma-associated inflammation and therapy resistance mechanisms.

CONCLUSION

^{18}F-DPA-714 may be a useful imaging biomarker for longitudinal therapy monitoring and assessment of the glioma-associated inflammatory microenvironment, as well as for patient stratification. CSF-1R–targeting intervention and determination of the ideal treatment window for CSF-1R inhibitors may define a promising complementary therapy strategy in glioma.

DISCLOSURE

This work was supported by the EU Seventh Framework Programme (FP7/2007–2013) under grant 278850 (INMiND); the Horizon2020 Program under grant 675417 (PET3D); the EU/EFPIA/ Innovative Medicines Initiative 2 Joint Undertaking (Immune-Image GA831514) under grant 831514; the “Cells-in-Motion” Cluster of Excellence (CiM) Graduate School by the Interdisciplinary Center for Clinical Research (IZKF core unit PIX), Münster, Germany; and the Herbert-Worch-Foundation, Bonn, Germany. No other potential conflict of interest relevant to this article was reported.

ACKNOWLEDGMENTS

We thank Sarah Köster, Christine Bätza, Roman Priebe, Stefanie Bouma, Irmgard Hoppe, Christa Möllmann, Nina Kreienkamp, and Dirk Reinhardt for their excellent technical support, as well as Christian Döring for support with the volumetric analyses.

KEY POINTS

QUESTION: Is ^{18}F-DPA-714 PET suitable to decipher glioma-associated immune cell dynamics and CSF-1R therapy outcomes?

PERTINENT FINDINGS: ^{18}F-DPA-714 PET provided complementary information to ^{18}F-FET PET on glioma heterogeneity, allowed the imaging of immune cell dynamics, supported the assessment of brain target engagement, and elucidated CSF-1R inhibition–induced effects in vivo.

IMPLICATIONS FOR PATIENT CARE: ^{18}F-DPA-714 PET represents a promising tool for noninvasive imaging of therapeutic modulations of the immunosuppressive glioma microenvironment.

REFERENCES

1. Stupp R, Mason WP, van den Bent MJ, et al. Radiotherapy plus concomitant and adjuvant temozolomide for glioblastoma. *N Engl J Med.* 2005;352:987–996.
2. Xu S, Tang L, Li X, Fan F, Liu Z. Immunotherapy for glioma: current management and future application. *Cancer Lett.* 2020;476:1–12.
3. DeCordova S, Shastri A, Tsolaki AG, et al. Molecular heterogeneity and immunosuppressive microenvironment in glioblastoma. *Front Immunol.* 2020;11:1402.
4. Shabab T, Khanabdali R, Moghadamtousi SZ, Kadir HA, Mohan G. Neuroinflammation pathways: a general review. *Int J Neurosci.* 2017;127:624–633.
5. Rojo R, Raper A, Ozdemir DD, et al. Deletion of a Csf1r enhancer selectively impacts CSF1R expression and development of tissue macrophage populations. *Nat Commun.* 2019;10:3215.
6. Albert NL, Weller M, Suchorska B, et al. Response assessment in neuro-oncology working group and European Association for Neuro-Oncology recommendations for the clinical use of PET imaging in gliomas. *Neuro Oncol.* 2016;18:1199–1208.
7. Lundemann M, Munck Af Rosenschöld P, Muhic A, et al. Feasibility of multiparametric PET and MRI for prediction of tumour recurrence in patients with glioblastoma. *Eur J Nucl Med Mol Imaging.* 2019;46:603–613.
8. Stegmayr C, Willuweit A, Lohmann P, Langen K-J. O-(2-[^{18}F]-fluoroethyl)-L-tyrosine (FET) in neurooncology: a review of experimental results. *Curr Radiopharm.* 2019;12:201–210.
9. Dhermain FG, Hau P, Lanfermann H, Jacobs AH, van den Bent MJ. Advanced MRI and PET imaging for assessment of treatment response in patients with gliomas. *Lancet Neurol.* 2010;9:906–920.
10. Moreau A, Febvey O, Mognetti T, Frappaz D, Kryza D. Contribution of different positron emission tomography tracers in glioma management: focus on glioblastoma. *Front Oncol.* 2019;9:1134.
11. Cai L, Kirchleitner SV, Zhao D, et al. Glioblastoma exhibits inter-individual heterogeneity of TSPO and LAT1 expression in neoplastic and parenchymal cells. *Int J Mol Sci.* 2020;21:612.
12. Dupont A-C, Largeau B, Santiago Ribeiro M, Guilloteau D, Tronel C, Arlicot N. Translocator protein-18 kDa (TSPO) positron emission tomography (PET) imaging and its clinical impact in neurodegenerative diseases. *Int J Mol Sci.* 2017;18:785.
13. Zinnhardt B, Pigeon H, Thézé B, et al. Combined PET imaging of the inflammatory tumor microenvironment identifies margins of unique radiotracer uptake. *Cancer Res.* 2017;77:1831–1841.
14. Zinnhardt B, Müther M, Roll W, et al. TSPO imaging-guided characterization of the immunosuppressive myeloid tumor microenvironment in patients with malignant glioma. *Neuro Oncol.* 2020;22:1030–1043.
15. Foray C, Barca C, Backhaus P, et al. Multimodal molecular imaging of the tumour microenvironment. In: Birbrair A, ed. *Tumor Microenvironment: Recent Advances.* Springer; 2020:71–87.
16. Percie du Sert N, Ahluwalia A, Alam S, et al. Reporting animal research: explanation and elaboration for the ARRIVE guidelines 2.0. Boutron I, ed. *PLOS Biol.* 2020;18:e3000411.
17. Foray C, Valtorta S, Barca C, et al. Imaging temozolomide-induced changes in the myeloid glioma microenvironment. *Theranostics.* 2021;11:2020–2033.
18. Bankhead P, Loughrey MB, Fernández JA, et al. QuPath: open source software for digital pathology image analysis. *Sci Rep.* 2017;7:16878.
19. Achkova D, Maher J. Role of the colony-stimulating factor (CSF)/CSF-1 receptor axis in cancer. *Biochem Soc Trans.* 2016;44:333–341.
20. Quail DF, Joyce JA. Molecular pathways: deciphering mechanisms of resistance to macrophage-targeted therapies. *Clin Cancer Res.* 2017;23:876–884.
21. Fujinaga M, Luo R, Kumata K, et al. Development of a ^{18}F-labeled radiotracer with improved brain kinetics for positron emission tomography imaging of translocator protein (18 kDa) in ischemic brain and glioma. *J Med Chem.* 2017; 60:4047–4061.
22. Winkeler A, Boisgard R, Awde AR, et al. The translocator protein ligand [^{18}F]DPA-714 images glioma and activated microglia in vivo. *Eur J Nucl Med Mol Imaging.* 2012;39:811–823.
23. Press RH, Zhong J, Gurbani SS, et al. The role of standard and advanced imaging for the management of brain malignancies from a radiation oncology standpoint. *Neurosurgery.* 2019;85:165–179.
24. Elmore MRP, Najafi AR, Koike MA, et al. Colony-stimulating factor 1 receptor signaling is necessary for microglia viability, unmasking a microglia progenitor cell in the adult brain. *Neuron.* 2014;82:380–397.
25. Otxoa-de-Amezaga A, Miró-Mur F, Pedragosa J, et al. Microglial cell loss after ischemic stroke favors brain neutrophil accumulation. *Acta Neuropathol (Berl).* 2019;137:321–341.
26. Unger MS, Schernthaner P, Marschallinger J, Mrowetz H, Aigner L. Microglia prevent peripheral immune cell invasion and promote an anti-inflammatory environment in the brain of APP-PS1 transgenic mice. *J Neuroinflammation.* 2018; 15:274.
27. Lamb YN. Pexidartinib: first approval. *Drugs.* 2019;79:1805–1812.
28. Benner B, Good L, Quiroga D, et al. Pexidartinib, a novel small molecule CSF-1R inhibitor in use for tenosynovial giant cell tumor: a systematic review of pre-clinical and clinical development. *Drug Des Devel Ther.* 2020;14:1693–1704.
29. A pilot study to evaluate PBR PET in brain tumor patients treated with chemoradiation or immunotherapy. ClinicalTrials.gov website. https://clinicaltrials.gov/ct2/show/NCT02431572?term=tspo&cond=Glioma&draw=2&rank=1. Published May 1, 2015. Updated April 28, 2020. Accessed June 22, 2022.

^{68}Ga-DOTA-NT-20.3 Neurotensin Receptor 1 PET Imaging as a Surrogate for Neuroendocrine Differentiation of Prostate Cancer

Wenyu Wu[1], Fei Yu[1], Pengjun Zhang[1], Ting Bu[1], Jingjing Fu[1], Shuyue Ai[1], Qinqin You[1], Liang Shi[1], Guoqiang Shao[1], Feng Wang[1], Marina Hodolic[2,3], and Hongqian Guo[4]

[1]Department of Nuclear Medicine, Nanjing First Hospital, Nanjing Medical University, Nanjing, China; [2]Nuclear Medicine Research Department, IASON, Graz, Austria; [3]Department of Nuclear Medicine, Faculty of Medicine and Dentistry, Palacký University Olomouc, Olomouc, Czech Republic; and [4]Department of Urology, Drum Tower Hospital, Medical School of Nanjing University, Nanjing University, Nanjing, China

Prostate-specific membrane antigen (PSMA)–negative neuroendocrine prostate cancer (PCa) is a subtype of PCa likely to be lethal, with limited clinical diagnostic and therapeutic options. High expression of neurotensin receptor subtype 1 (NTR1) is associated with neuroendocrine differentiation of PCa, which makes NTR1 a potential target for neuroendocrine PCa. In this study, the NTR1-targeted tracer ^{68}Ga-DOTA-NT-20.3 was synthesized, and its affinity to androgen-dependent (LNCap) and androgen-independent (PC3) xenografts was determined. **Methods:** ^{68}Ga-DOTA-NT-20.3 was labeled using an automated synthesizer module, and its stability, labeling yield, and radiochemical purity were analyzed by radio–high-performance liquid chromatography. Receptor binding affinity was evaluated in NTR1-positive PC3 cells by a competitive binding assay. The biodistribution of ^{68}Ga-DOTA-NT-20.3 in vivo was evaluated in PC3 and LNCap xenografts by small-animal PET imaging. NTR1 expression was identified by immunohistochemistry and immunofluorescence evaluation. **Results:** ^{68}Ga-DOTA-NT-20.3 was synthesized successfully, with a yield of 88.07% ± 1.26%, radiochemical purity of at least 99%, and favorable stability. The NTR1 affinity (half-maximal inhibitory concentration) for ^{68}Ga-DOTA-NT-20.3 was 7.59 ± 0.41 nM. Small-animal PET/CT of PC3 xenograft animals showed high-contrast images with intense tumor uptake, which revealed specific NTR1 expression. The tumors showed significant radioactivity (4.95 ± 0.67 percentage injected dose per gram of tissue [%ID/g]) at 1 h, which fell to 1.95 ± 0.17 %ID/g ($P < 0.01$, $t = 8.72$) after specific blockage by neurotensin. LNCap xenografts had no significant accumulation (0.81 ± 0.06 %ID/g) of ^{68}Ga-DOTA-NT-20.3 at 1 h. In contrast, ^{68}Ga-PSMA-11 was concentrated mainly in LNCap xenografts (8.60 ± 2.11 %ID/g), with no significant uptake in PC3 tumors (0.53 ± 0.05 %ID/g), consistent with the in vitro immunohistochemistry findings. Biodistribution evaluation showed rapid clearance from the blood and main organs (brain, heart, lung, liver, muscle, and bone), with significantly high tumor-to-liver (4.41 ± 0.73) and tumor-to-muscle (12.34 ± 1.32) ratios at 60 min after injection. **Conclusion:** ^{68}Ga-DOTA-NT-20.3 can be efficiently prepared with a high yield and high radiochemical purity. Its favorable biodistribution and prominent NTR1 affinity make ^{68}Ga-DOTA-NT-20.3 a potential radiopharmaceutical for the detection of PSMA-negative PCa and identification of neuroendocrine differentiation.

Key Words: ^{68}Ga-DOTA-NT-20.3; neurotensin receptor subtype 1; prostate cancer; neuroendocrine differentiation; PET

J Nucl Med 2022; 63:1394–1400
DOI: 10.2967/jnumed.121.263132

The incidence of prostate cancer (PCa) has increased in line with the aging population and progress in diagnostic modalities (*1*). Patients usually have advanced or metastatic lesions at diagnosis, leading to high mortality. Prostate-specific antigen (PSA) level has been well documented for the diagnosis of PCa and evaluation of tumor response (*2*). However, a PSA increase is largely dependent on the tumor origin; PSA can be increased in benign prostatic hyperplasia and is likely not to increase in poorly differentiated PCa (*3,4*). Prostate-specific membrane antigen (PSMA) PET has been widely used clinically and has had merit in the detection of biomedical recurrence, allowing detection of micrometastasis at low PSA values (*5*). PSMA is commonly overexpressed in metastatic castration-resistant PCa (CRPC) and serves as an ideal target for the treatment of PCa (*6*). However, after long-term androgen deprivation therapy, poorly differentiated PCa originating from luminal and basal cells frequently acquires a neuroendocrine phenotype (neuroendocrine PCa [NEPC]), which lacks PSMA expression (*7*). Although the incidence of de novo NEPC is rare (<2%), treatment-driven neuroendocrine differentiation exists in up to 20% of patients with CRPC (*8*). As an aggressive subtype of CRPC, NEPC has a median survival time of less than 1 y because identification is difficult and because the androgen deficiency results in fewer treatment options (*9*). The lethal nature of NEPC is driven by a lack of therapeutic regimens capable of generating durable responses in the setting of extreme tumor heterogeneity at the genetic and cell biologic levels. It is therefore necessary to explore specific molecular targets and efficient therapeutic interventions for the clinical management of NEPC.

The neurotensin/neurotensin receptor (NT/NTR) axis has been identified as an alternative growth pathway in androgen-independent PCa and as a factor in the development of NEPC (*10*). NT, a tridecapeptide released from endocrine cells in the small bowel, stimulates pancreatic and biliary secretion, fatty acid absorption, intestinal motility, and growth of digestive organs (*11*). Additionally, NT secreted

---

Received Aug. 29, 2021; revision accepted Dec. 28, 2021.

For correspondence or reprints, contact Feng Wang (fengwangcn@hotmail.com) or Marina Hodolic (marina.hodolic@gmail.com).

from carcinoma cells acts as an autocrine growth factor in response to tumor cell proliferation and migration (*12*). The functions of NT are mediated primarily via 2 G-protein–coupled receptors: NTR subtype 1 (NTR1) (high-affinity receptor) and NTR subtype 2 (low-affinity receptor), whereas NTR subtype 3 serves as a single transmembrane domain localized in the trans-Golgi network (*13*). NTR1 is overexpressed in neuroendocrine differentiation of PCa and may promote neoplastic growth and metastasis after binding with NT produced by neuroendocrine cells in NEPC (*14,15*). The latest study showed that NTR1 was expressed in 91.8% of PCa tissues, and all PSMA-negative tissues showed positive NTR1 expression, suggesting the potential complementary role of NTR1-targeted imaging or therapy (*16*). LNCap (androgen-dependent PCa cells) showed negative NTR1 expression, whereas PC3 (androgen-independent PCa cells) had positive expression. Although native NT is sensitive to peptidases, various NT analogs with higher stability have been radiolabeled and used as valuable imaging and internal radioligand therapeutic tools for NTR1-positive tumors (*17–20*). Among them, ^{68}Ga-DOTA-NT-20.3 is confirmed to be a promising PET imaging probe for NTR1-positive tumors such as pancreatic adenocarcinoma and colon cancer (*21,22*). However, ^{68}Ga-DOTA-NT-20.3 PET for the quantitation of NTR1 expression in PCa that underwent neuroendocrine differentiation has not been reported. In this study, ^{68}Ga-DOTA-NT-20.3 was used to evaluate the neuroendocrine differentiation status in PCa xenografts.

MATERIALS AND METHODS

General

Vender-provided information on the chemicals, cells, reagents, and animals, as well as the cell culture and tumor model, is provided in the supplemental materials (available at http://jnm.snmjournals.org). All animal studies were approved by Nanjing First Hospital animal ethical committee and performed according to national regulations.

Radiolabeling of DOTA-NT-20.3/PSMA-11 with ^{68}Ga and Quality Control

An iQS-TS automated module was used for all radiolabeling steps, which were performed as previously described (*21–23*) with minor modifications. Briefly, DOTA-NT-20.3 (4.32 nmol, 20 μg) or PSMA-11 (19.72 nmol, 20 μg) dissolved in 1.0 mL of sodium acetate buffer (0.25 M, pH 8.0) and ^{68}Ga (370–450 MBq) eluted from the ^{68}Ge/^{68}Ga generator with 4.0 mL of 0.05 M HCl was introduced into the preheated reactor. The pH of the final labeling solution was 3.5–4.0. After reaction at 95°C for 14 min, the labeled product was concentrated using a disposable Sep-Pak C18 cartridge (Waters), eluted with 0.5 mL of 70% ethanol, and equilibrated with 0.9% sodium chloride injection or fresh medium before use. Quality control of radiopharmaceuticals was performed using radio–high-performance liquid chromatography and radio–thin-layer chromatography (details are in the supplemental materials).

Determination of Lipophilicity

The shake-flask method was used to determine the partition coefficient of ^{68}Ga-DOTA-NT-20.3 in *n*-octanol and phosphate-buffered saline (PBS) (pH 7.4) mixture. The organic and aqueous phases were presaturated 24 h before the experiment, and 500 μL of each layer were added to ^{68}Ga-DOTA-NT-20.3 (3.7 MBq) and mixed vigorously for 3 min. The layers were separated by centrifugation at 2,000 rpm (416*g*) for 5 min. Aliquots of 100 μL were removed from each phase and measured in a Wizard γ-counter (PerkinElmer). Calculated $\log D_{7.4}$ values were expressed as the mean ± SD from 3 experiments.

Stability In Vitro

For the stability assay, ^{68}Ga-DOTA-NT-20.3 was incubated in PBS (pH 7.4) or fresh human serum at 37°C for 15, 30, 60, 120, and 240 min. Plasma protein was precipitated with isovolumic acetonitrile and removed by centrifugation (12,000 rpm, 13,400*g*, 5 min) after incubation. The supernatants were analyzed by radio–high-performance liquid chromatography after filtering through a Cathivex-GV filter (22 μm; Merck).

Cell Binding Affinity and Uptake Assay

Human prostate adenocarcinoma PC3 cells were seeded into 24-well plates at a density of 1×10^5 cells per well overnight for the receptor-binding affinity and uptake study of ^{68}Ga-DOTA-NT-20.3. ^{68}Ga-DOTA-NT-20.3 and NT were diluted to 37 kBq/mL and 10^{-8}–10^2 μM, respectively, with fresh medium. For the receptor-binding affinity assay, ^{68}Ga-DOTA-NT-20.3 (37 kBq, 500 μL) was added to each well in the presence of varying concentrations (10^{-8}–10^2 μM, 500 μL) of NT. After incubation for 60 min at 37°C, the medium of each well was removed and the cells were washed twice with PBS. The removed medium and washing PBS were collected to represent the amount of free radioligand. The adherent cells were lysed with NaOH (0.1 M, 200 μL) and harvested after being washed twice by PBS. Finally, the cell-bound radioactivity (3×10^5 cells/mL) and the amount of free radioligand were measured in a γ-counter. The half-maximal inhibitory concentration was calculated using GraphPad Prism software. For the cell uptake study, the trial group PC3 cells were incubated with ^{68}Ga-DOTA-NT-20.3 (37 kBq, 500 μL) at 37°C for 15, 30, 60, and 120 min. The blocking group cells were saturated with an excess of NT (1 μM, 500 μL) before addition of ^{68}Ga-DOTA-NT-20.3 (37 kBq, 500 μL). The radioactivity of adherent cells (3×10^5 cells/mL) was then measured after they were extracted with NaOH (0.1 M, 200 μL) and washed twice with PBS.

Small-Animal PET/CT Imaging

The whole-body distribution of the tracer in tumor-bearing mice was examined with an Inveon small-animal PET/CT scanner. ^{68}Ga-DOTA-NT-20.3, ^{68}Ga-PSMA-11, and NT were diluted to 37 MBq/mL, 37 MBq/mL, and 2 mg/mL, respectively, with 0.9% sodium chloride injection. PC3-xenografted mice (18–25 g) were injected with ^{68}Ga-DOTA-NT-20.3 (7.4 MBq, 200 μL) via the tail vein under isoflurane anesthesia, and 10-min static PET images were acquired at 0.5, 1, 1.5, 2, and 4 h after injection. For the blocking group, the mice were pretreated with an excess of NT (20 mg/kg of body weight, 200 μL) via the tail vein 15 min before injection of ^{68}Ga-DOTA-NT-20.3 (7.4 MBq, 200 μL), and static PET images were acquired at 1 h after injection. PC3- and LNCap-xenografted mice were imaged at 1 h after receiving ^{68}Ga-DOTA-NT-20.3 (7.4 MBq, 200 μL) or ^{68}Ga-PSMA-11 (7.4 MBq, 200 μL). Images were reconstructed using 3-dimensional ordered-subset expectation maximization with attenuation correction. Regions of interest were drawn over the tumors and main organs, and average signal levels in the regions were measured using an Inveon Research Workplace workstation.

Ex Vivo Biodistribution

PC3 xenograft mouse models (18–25 g) were used to evaluate the distribution of tracer in blood and major organs. ^{68}Ga-DOTA-NT-20.3 was diluted to 37 MBq/mL with 0.9% sodium chloride injection for use. The mice were killed at 5, 15, 30, 60, and 120 min after intravenous injection of ^{68}Ga-DOTA-NT-20.3 (3.4 MBq, 100 μL) ($n = 3$ per group). Blood and major organs were harvested immediately, weighed, and counted using a γ-counter. The radioactivity of each sample was calculated as the percentage of injected dose per gram of tissue (%ID/g) and corrected for radioactive decay.

Immunohistochemical Staining

NTR1 and PSMA expression was evaluated by immunohistochemistry in LNCap- and PC3-derived prostate tumors. PCa tissues were fixed in 4% paraformaldehyde, paraffin-embedded, and sectioned. The sections were then dewaxed and hydrated with xylene and graded alcohol at room temperature before heat-induced antigen retrieval. Endoperoxidase activity was inactivated by 3% H_2O_2, and nonspecific sites were blocked with 3% bovine serum albumin. The sections were incubated overnight with NTR1 antibody (catalog number YT3203, 1:200 dilution; ImmunoWay) at 4°C followed by horseradish peroxidase–labeled goat antirabbit second antibody (catalog number GB23303, 1:200 dilution; Servicebio) and then staining with 3,3-diaminobenzidine and counterstaining with hematoxylin solution for 2 min. The samples were finally dehydrated and mounted with neutral resin, and images were acquired using an optical microscope (with camera attached; Nikon Eclipse E100).

Histologic Analysis

The tissues were fixed in 4% paraformaldehyde and embedded in paraffin for sectioning. Tumor sections were dewaxed, stained with hematoxylin and eosin, fixed with neutral resin after dehydration, and observed using an optical microscope.

Immunofluorescent Staining

Cells in 12-well culture plates were fixed with 4% paraformaldehyde and permeabilized with 0.5% Triton X-100 (Union Carbide Chemicals and Plastics) in PBS for 20 min at room temperature. Nonspecific antibodies were blocked with 5% bovine serum albumin in PBS for 30 min at room temperature. NTR1 antibody (1:100 dilution) was added to each well and incubated at 4°C overnight to detect NTR1. The sections were then incubated with CY3-labeled goat antirabbit IgG secondary antibody (catalog number GB21303, 1:300 dilution; Servicebio) followed by antifade medium containing 4,6-diamidino-2-phenylindole and were observed under a fluorescence microscope.

Statistical Analysis

Quantitative data were described as mean ± SD, and differences between groups were analyzed by Student *t* testing or ANOVA using GraphPad Prism software, version 6.0. A *P* value of less than 0.05 was considered statistically significant.

RESULTS

Radiosynthesis of ^{68}Ga-DOTA-NT-20.3 and ^{68}Ga-PSMA-11

^{68}Ga-DOTA-NT-20.3 (Fig. 1) and ^{68}Ga-PSMA-11 were labeled successfully within 14 min, with yield rates of 88.07% ± 1.26% and 86.82% ± 2.57%, respectively. The final molar activity (radioactivity of product divided by amount of peptide used) of ^{68}Ga-DOTA-NT-20.3 was at least 54.4 GBq/μmol. Radio–high-performance liquid chromatography showed more than 99% radiochemical purity for ^{68}Ga-DOTA-NT-20.3 and ^{68}Ga-PSMA-11, and the elution times were 13.49 and 8.19 min, respectively (Supplemental Figs. 1 and 2). Radio–thin-layer chromatography of ^{68}Ga-DOTA-NT-20.3 showed only 1 spot, with a retention factor of 0.60 (Supplemental Fig. 3).

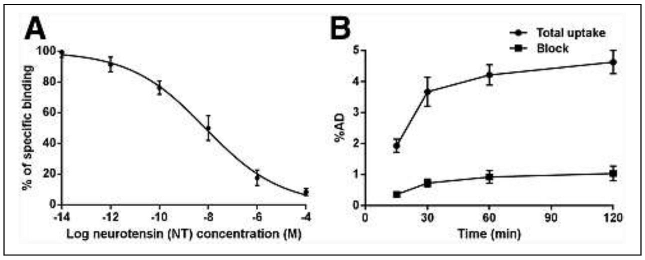

FIGURE 2. (A) Competitive binding curves for half-maximal inhibitory concentration determination of ^{68}Ga-DOTA-NT-20.3 in PC3 cells, using NT as competitive inhibitor. (B) Uptake of ^{68}Ga-DOTA-NT-20.3 in PC3 cells. %AD = percentage administered dose.

Lipophilicity and In Vitro Stability

The lipophilicity of the peptide radiotracer was represented by the partition coefficient of ^{68}Ga-DOTA-NT-20.3, determined as a $\log D_{7.4}$ value of -3.68 ± 0.14 in *n*-octanol and PBS. The radiochemical purity of ^{68}Ga-DOTA-NT-20.3 was still at least 99% after incubation in PBS and human serum at 37°C for 4 h, indicating that the tracer was sufficiently stable for further in vitro and in vivo studies (Supplemental Fig. 4).

In Vitro Cell Binding Affinity and Uptake

Competitive cell binding assays revealed that NT inhibited the binding of ^{68}Ga-DOTA-NT-20.3 to NTR1-positive PC3 cells in a concentration-dependent manner (Fig. 2A). The half-maximal inhibitory concentration for ^{68}Ga-DOTA-NT-20.3 was 7.59 ± 0.41 nM. Cell blocking studies were conducted to evaluate the specificity of ^{68}Ga-DOTA-NT-20.3 in vitro (Fig. 2B). The uptake rate of ^{68}Ga-DOTA-NT-20.3 by PC3 cells plateaued (4.21% ± 0.33% administered dose) at 1 h of incubation and decreased significantly when blocked with an excess of NT (0.92% ± 0.20% administered dose, $P < 0.01$, $t = 14.71$).

Small-Animal PET/CT Imaging

PC3-xenograft tumors were clearly visible as early as 0.5 h after injection, and region-of-interest analysis showed tumor uptake of

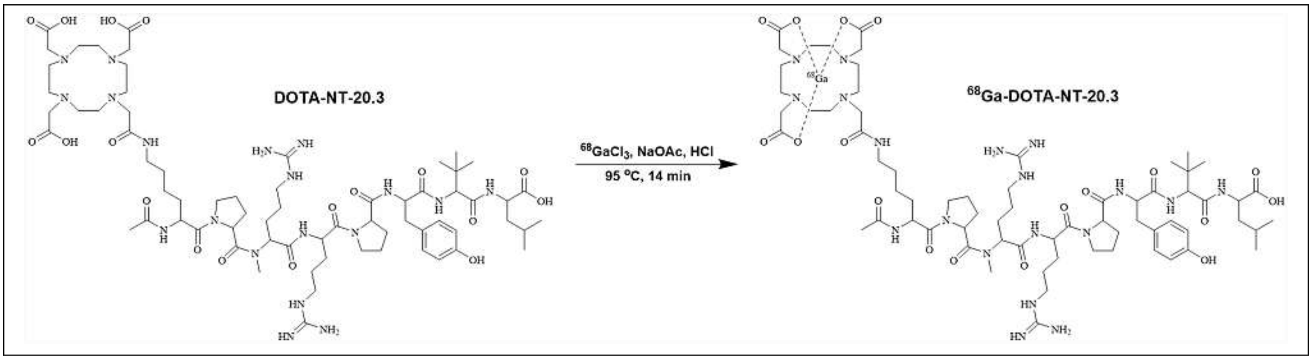

FIGURE 1. Radiosynthesis and structure of ^{68}Ga-DOTA-NT-20.3.

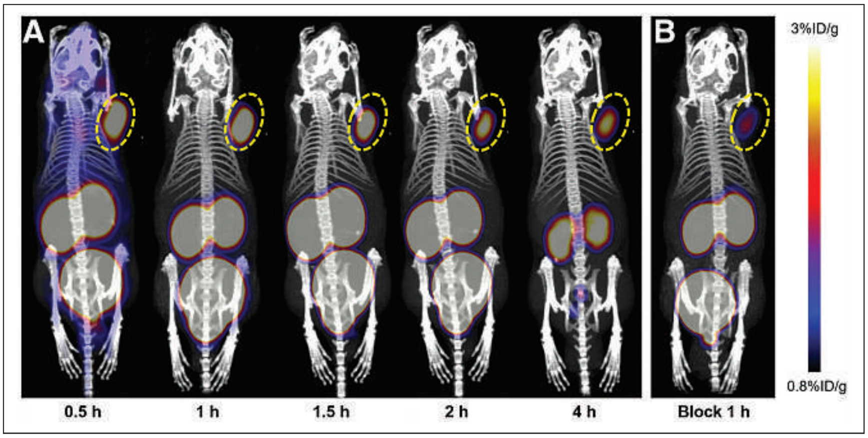

FIGURE 3. (A) Small-animal PET/CT images of PC3 tumor–bearing mice at different times after injection of ^{68}Ga-DOTA-NT-20.3. (B) Blocked by excess NT at 1 h after injection of ^{68}Ga-DOTA-NT-20.3, blocking ratio [(total radioactivity uptake − blocked radioactivity uptake)/total radioactivity uptake] was 60.03% ± 6.48%. Tumor site is encircled.

4.53 ± 1.26 %ID/g (Fig. 3). The tumor-to-background ratio (5.61 ± 0.69) and tumor uptake (4.95 ± 0.67 %ID/g) at 1 h after injection were significantly higher than for the blocking group (1.95 ± 0.17 %ID/g, $P < 0.01$, $t = 8.72$), demonstrating the specificity of ^{68}Ga-DOTA-NT-20.3 for NTR1-positive tumors. Quantitative analysis showed that radioactivity peaked in main organs such as heart, lung, brain, bone, and muscle early and then cleared over 1 h. Liver showed no striking radioactivity compared with kidney and bladder, confirming that the tracer was rapidly excreted via the urinary system. LNCap tumor–bearing mice were used as a negative control, and PET imaging demonstrated minimal tumor accumulation of ^{68}Ga-DOTA-NT-20.3 (0.81 ± 0.06 %ID/g) (Fig. 4). ^{68}Ga-PSMA-11 was subsequently injected into PC3- and LNCap-xenograft mice, and high radioactivity uptake (8.60 ± 2.11 %ID/g) was detected in LNCap but not in PC3 tumors (0.53 ± 0.05 %ID/g). The results indicated that ^{68}Ga-DOTA-NT-20.3 specifically targeted NTR1 and could be a promising new tool to complement PSMA PET for the diagnosis of PCa.

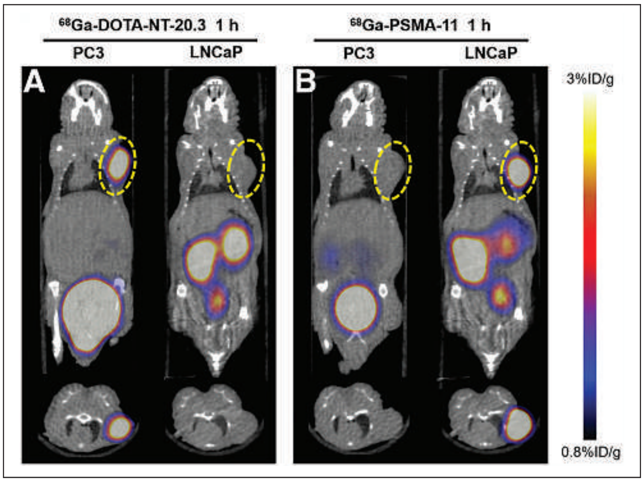

FIGURE 4. Small-animal PET/CT images of PC3 and LNCap tumor–bearing mice at 1 h after injection of ^{68}Ga-DOTA-NT-20.3 (A) or ^{68}Ga-PSMA-11 (B). Tumor site is encircled.

Biodistribution

The metabolic characteristics and targeting specificity of ^{68}Ga-DOTA-NT-20.3 in vivo were further evaluated by biodistribution experiments in PC3 tumor models (Table 1). The highest tumor uptake (6.26 ± 0.41 %ID/g) was measured at 60 min after injection and decreased slightly to 3.74 ± 0.56 %ID/g by 120 min. The radiotracer cleared quickly from blood and major organs (brain, heart, lung, liver, muscle, and bone), with significantly high tumor-to-liver (4.41 ± 0.73) and tumor-to-muscle (12.34 ± 1.32) ratios at 60 min. As a consequence of renal excretion, kidney uptake at 30, 60, and 120 min after injection was 23.06 ± 1.94, 24.55 ± 0.98, and 26.08 ± 0.79 %ID/g, respectively, further supporting renal clearance as the primary metabolic pathway of ^{68}Ga-DOTA-NT-20.3.

Immunohistochemical, Immunofluorescent, and Histologic Analyses

To further validate the NTR1 and PSMA expression in different types of PCa, immunohistochemistry was performed for tumor tissues. PC3 xenografts showed high NTR1 expression levels but no obvious PSMA expression (Figs. 5A and 5B), whereas LNCap tumors showed overexpression of PSMA rather than NTR1 (Figs. 5D and 5E). Tumor immunohistochemistry findings corresponded to the small-animal PET/CT imaging results. Hematoxylin and eosin staining (Figs. 5C and 5F) revealed the different morphologic features of PCa, having irregularly arranged tumor cells that varied in size, with deep staining, obvious atypia, and high mitotic rates. Strong red fluorescence was seen in PC3 cells, confirming the abundant NTR1 expression (Fig. 6).

DISCUSSION

Despite great progress in the clinical management of localized PCa, metastatic PCa treated with androgen deprivation therapy inevitably develops resistance, leading to CRPC (*24*). Novel antiandrogens (enzalutamide or abiraterone) further prevent tumor progression by inhibiting the reactivated androgen and androgen receptor signaling in CRPC (*25,26*). However, prolonged inhibition of the androgen and androgen receptor pathway converts 15%–20% of CRPC into androgen-independent NEPC, with loss of canonic androgen receptor and PSMA expression, clinically resulting in a rapidly progressive disease course and no significant increase in PSA, thus hindering clinical diagnosis and therapy (*7*). PSMA PET/CT and radioligand therapy had limited value for more aggressive PSMA-negative PCa phenotypes in clinical practice. NT/NTR signaling, recruited as an alternative growth pathway in the absence of androgen receptor, plays a crucial role in the proliferation, migration, and invasion of NEPC cells (*10*). Acute NTR1 expression is associated with neuroendocrine differentiation of PCa, making it a promising biomarker that may compensate for the PSMA negativity of NEPC (*16*). Various radiopharmaceuticals developed to trace NTR1 in vivo may aid the early diagnosis, distant metastasis detection, endoradiotherapy, and mechanistic investigation of NEPC (*17*). For this purpose, we radiolabeled ^{68}Ga-DOTA-NT-20.3 as an NTR1-targeted radiotracer and

TABLE 1

Biodistribution of ^{68}Ga-DOTA-NT-20.3 in PC3 Tumor–Bearing Mice at Various Times After Injection

Site	5 min	15 min	30 min	60 min	120 min
Blood	8.11 ± 1.54	4.15 ± 0.59	2.56 ± 0.23	1.12 ± 0.22	0.43 ± 0.08
Heart	7.70 ± 0.90	3.88 ± 0.18	2.78 ± 0.36	1.57 ± 0.18	0.58 ± 0.11
Liver	5.46 ± 1.01	3.17 ± 0.45	2.02 ± 0.48	1.44 ± 0.20	0.86 ± 0.49
Spleen	3.97 ± 0.39	2.81 ± 0.47	1.85 ± 0.43	1.06 ± 0.27	0.41 ± 0.04
Lung	5.18 ± 0.16	3.28 ± 0.62	1.91 ± 0.15	1.20 ± 0.23	0.75 ± 0.15
Kidney	18.36 ± 1.27	21.22 ± 1.95	23.06 ± 1.94	24.55 ± 0.98	26.08 ± 0.79
Stomach	3.56 ± 0.31	2.49 ± 0.35	1.75 ± 0.38	0.91 ± 0.18	0.37 ± 0.05
Intestine	3.28 ± 0.30	2.31 ± 0.92	1.47 ± 0.26	0.77 ± 0.24	0.38 ± 0.04
Pancreas	2.88 ± 0.61	2.03 ± 0.26	1.59 ± 0.60	1.05 ± 0.07	0.36 ± 0.04
Muscle	1.93 ± 0.65	1.44 ± 0.17	0.96 ± 0.08	0.51 ± 0.02	0.32 ± 0.04
Bone	2.27 ± 0.29	2.35 ± 0.52	1.27 ± 0.08	0.86 ± 0.17	0.53 ± 0.17
Brain	1.91 ± 0.39	1.35 ± 0.15	0.88 ± 0.10	0.60 ± 0.05	0.33 ± 0.10
Fat	1.42 ± 0.23	1.11 ± 0.23	0.62 ± 0.11	0.32 ± 0.03	0.32 ± 0.07
Testis	1.62 ± 0.11	1.31 ± 0.05	0.80 ± 0.06	0.42 ± 0.04	0.31 ± 0.10
Tumor	2.81 ± 0.39	3.93 ± 0.43	5.70 ± 0.80	6.26 ± 0.41	3.74 ± 0.56

Data are mean %ID/g ± SD ($n = 3$).

evaluated its imaging ability in 2 PCa xenograft models (PC3 and LNCap).

^{68}Ga-DOTA-NT-20.3 was efficiently prepared using an iQS-TS automated module, with high yield and high radiochemical purity. The tracer showed good stability in vitro, with a radiochemical purity of at least 99% at 4 h after incubation in PBS or plasma, providing the basis for further biologic evaluations. The lipophilicity of ^{68}Ga-DOTA-NT-20.3 was −3.68 ± 0.14, indicating favorable in vivo radiopharmacokinetics, demonstrated by its predominantly renal elimination with little radioactivity in the liver. We also verified the binding affinity and specificity of ^{68}Ga-DOTA-NT-20.3 to NTR1 in PC3 cells, which show high levels of NTR1 expression, and further verified the binding by immunofluorescence. ^{68}Ga-DOTA-NT-20.3 showed significant time-dependent radioactivity accumulation in PC3 cells. Its binding ability was effectively blocked by an excess of NT within a low-nanomolar range, verifying the specificity of ^{68}Ga-DOTA-NT-20.3 for NTR1 in PC3 cells in vitro. A high target (NTR1)-binding affinity is required for high tumor uptake and retention of the radiopeptide, as the basic premise of molecular imaging in vivo.

The specificity of ^{68}Ga-DOTA-NT-20.3 was further confirmed by PET imaging in both NTR1-positive/PSMA-negative PC3 and NTR1-negative/PSMA-positive LNCap tumor xenografts. The results showed high and specific accumulation of ^{68}Ga-DOTA-NT-20.3 in PC3 tumor lesions at all time points but very low uptake in LNCap-derived tumors. The small molecular size of ^{68}Ga-DOTA-NT-20.3 and its hydrophilic nature enable fast clearance of radioactivity from the blood and nontarget tissues, resulting in a high tumor-to-muscle ratio of 5.61 ± 0.69 at 1 h after intravenous injection. Blocking successfully reduced the localization of ^{68}Ga-DOTA-NT-20.3 within the tumor because of the presence of an excess of cold NT analogs, clearly demonstrating the receptor specificity of this imaging agent. However, the radioactivity uptake could not be completely blocked by NT, with a blocking ratio of 60.03% ± 6.48% (Fig. 3B), possibly because of an insufficient amount of cold NT; further verifications may be needed. In contrast, ^{68}Ga-PSMA-11 PET showed no uptake in PC3-derived tumors but high uptake in LNCap-derived tumors. The different levels of radioactivity uptake in 2 different tumor models can be attributed to the different numbers of NTR1 and PSMA binding sites in PC3 and LNCap cells, respectively. Immunohistochemistry further confirmed high NTR1 expression in

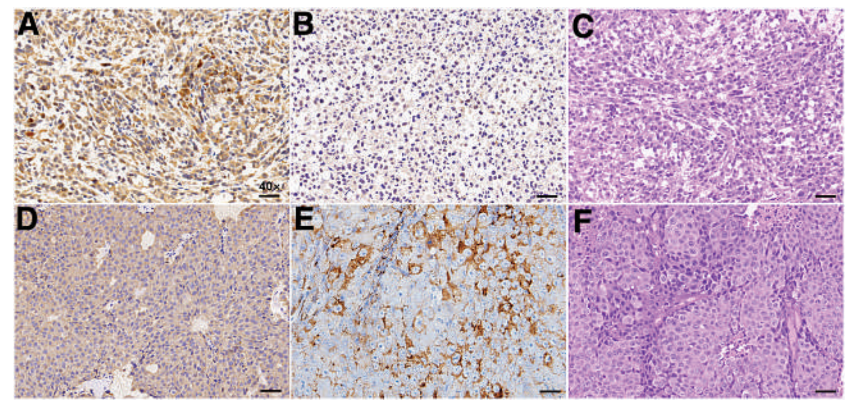

FIGURE 5. Representative immunohistochemical and histologic images. (A) NTR1 immunohistochemical staining of PC3 tumors. (B) PSMA immunohistochemical staining of PC3 tumors. (C) Hematoxylin and eosin staining of PC3 tumors. (D) NTR1 immunohistochemical staining of LNCap tumors. (E) PSMA immunohistochemical staining of LNCap tumors. (F) Hematoxylin and eosin staining of LNCap tumors. (Scale bar, 10 μm; ×40.)

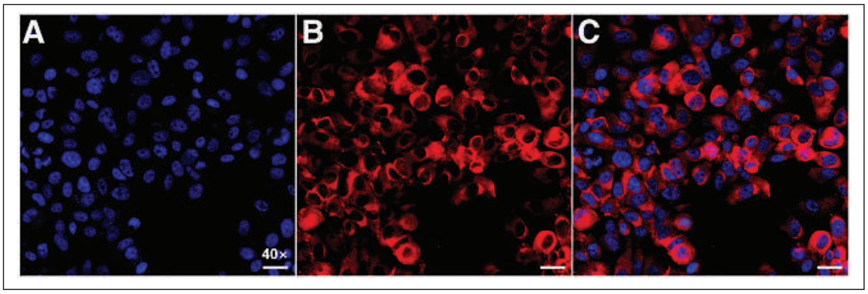

FIGURE 6. Representative immunofluorescence images. PC3 cells stained with 4-6-diamidino-2-phenylindole showed DNA content (blue) (A) and incubated with fluorescent NTR1 antibody showed NTR1 expression (red) (B). (C) Digital combination (merge) of the 2 previous images is shown to visualize the localization of NTR1 in PC3 cell. (Scale bar, 10 μm; ×40.)

PC3-derived tumors and, conversely, high PSMA expression in LNCap-derived tumors.

^{68}Ga-DOTA-NT-20.3 showed a prolonged tumor retention time of up to 4 h and quicker clearance from blood, heart, lung, liver, muscle, and other organs or tissues, except kidney—as correlated well with the PET imaging findings. ^{68}Ga-DOTA-NT-20.3 cleared predominantly via the renal pathway, leading to accumulation in kidney and bladder. The radioactivity in bladder can be excreted through urine, which is conducive to the detection of paravesical and prostatic bed lesions. Regretfully, kidney may become a dose-limiting organ because of the slower clearance of ^{68}Ga-DOTA-NT-20.3. The exact mechanism is not clear, but efforts should be taken to reduce the renal retention and potential nephrotoxicity for future internal radioligand therapy. Biodistribution analysis indicated a high tumor-to-muscle ratio (12.34 ± 1.32) at 1 h after injection, identifying ^{68}Ga-DOTA-NT-20.3 as a promising PET tracer for imaging NTR1-expressing tumors. However, compared with the high binding affinity in vitro (half-maximal inhibitory concentration, 7.59 ± 0.41 nmol/L), the radiotracer demonstrated moderate PC3 tumor uptake in vivo (6.26 ± 0.41 %ID/g at 1 h), suggesting that many other factors in addition to binding affinity may affect the tumor uptake. Further systematic investigations are therefore needed to improve the absolute tumor uptake.

CONCLUSION

This study showed that ^{68}Ga-DOTA-NT-20.3 has a high affinity to NTR1 and a favorable distribution and kinetics. The high-contrast images of ^{68}Ga-DOTA-NT-20.3 in PC3 xenografts with NTR1-avid expression indicated its potential for detecting poorly differentiated or neuroendocrine differentiation of PCa. The high stability and long intratumor retention of ^{68}Ga-DOTA-NT-20.3 hold promise for use in peptide-receptor radionuclide therapy of PCa by exchanging ^{68}Ga with the therapeutic radionuclide ^{177}Lu/^{225}Ac. In addition, ^{68}Ga-DOTA-NT-20.3 might be an alternative targeted radiopharmaceutical for identifying neuroendocrine differentiation of PCa. Further preclinical studies are warranted to explore the molecular mechanisms of NTR1 in this context.

DISCLOSURE

This work was supported by the Jiangsu Provincial Key Research and Development Special Fund (BE2017612), the Nanjing Medical and Health International Joint Research and Development Project (201911042), the General Project of Science and Technology Development Fund of Nanjing Medical University (NMUB2019154), the National Natural Science Foundation of China (82003532), and the second-round fund of Nanjing Clinical Medical Center "Nanjing Nuclear Medicine Center." No other potential conflict of interest relevant to this article was reported.

ACKNOWLEDGMENT

We thank Susan Furness, PhD, from Liwen Bianji (Edanz) (www.liwenbianji.cn) for editing the English text of a draft of the manuscript.

KEY POINTS

QUESTION: Can ^{68}Ga-DOTA-NT-20.3 serve as an NTR1-targeted radiotracer for the detection of neuroendocrine differentiation in PSMA-negative PCa?

PERTINENT FINDINGS: ^{68}Ga-DOTA-NT-20.3 can be an ideal PET tracer, with favorable characteristics. ^{68}Ga-DOTA-NT-20.3 is stable in vitro and has high affinity to NTR1. Cellular uptake studies on the PC3 PCa cell line (NTR1-positive) demonstrated that the uptake is specific. High-contrast images were achieved in PC3 tumor xenografts but not in NTR1-negative/PSMA-positive LNCap tumors.

IMPLICATIONS FOR PATIENT CARE: In the detection of neuroendocrine differentiation in PCa, ^{68}Ga-DOTA-NT-20.3 has merits that may contribute to NTR1-based theranostics and provide a novel strategy for the management of NEPC, especially for neuroendocrine differentiation in metastatic CRPC.

REFERENCES

1. Li X, Zeng XY. Advances in epidemiology of prostate cancer in China. *Cancer Res Prev Treatment.* 2021;48:98–101.
2. Loeb S. Guideline of guidelines: prostate cancer screening. *BJU Int.* 2014;114:323–325.
3. Sardana G, Dowell B, Diamandis EP. Emerging biomarkers for the diagnosis and prognosis of prostate cancer. *Clin Chem.* 2008;54:1951–1960.
4. Thompson IM, Pauler DK, Goodman PJ, et al. Prevalence of prostate cancer among men with a prostate-specific antigen level < or =4.0 ng per milliliter. *N Engl J Med.* 2004;350:2239–2246.
5. Rowe SP, Johnson GB, Pomper MG, et al. Recent updates and developments in PET imaging of prostate cancer. *Abdom Radiol (NY).* 2020;45:4063–4072.
6. Will L, Sonni I, Kopka K, Kratochwil C, Giesel FL, Haberkorn U. Radiolabeled prostate-specific membrane antigen small-molecule inhibitors. *Q J Nucl Med Mol Imaging.* 2017;61:168–180.
7. Yamada Y, Beltran H. Clinical and biological features of neuroendocrine prostate cancer. *Curr Oncol Rep.* 2021;23:15.
8. Hsu EC, Rice MA, Bermudez A, et al. Trop2 is a driver of metastatic prostate cancer with neuroendocrine phenotype via PARP1. *Proc Natl Acad Sci USA.* 2020;117:2032–2042.
9. Wang HT, Yao YH, Li BG, Tang Y, Chang JW, Zhang J. Neuroendocrine prostate cancer (NEPC) progressing from conventional prostatic adenocarcinoma: factors associated with time to development of NEPC and survival from NEPC diagnosis—a systematic review and pooled analysis. *J Clin Oncol.* 2014;32:3383–3390.
10. Zhu S, Tian H, Niu X, et al. Neurotensin and its receptors mediate neuroendocrine transdifferentiation in prostate cancer. *Oncogene.* 2019;38:4875–4884.
11. Nikolaou S, Qiu S, Fiorentino F, et al. The role of neurotensin and its receptors in non-gastrointestinal cancers: a review. *Cell Commun Signal.* 2020;18:68.
12. Christou N, Blondy S, David V, et al. Neurotensin pathway in digestive cancers and clinical applications: an overview. *Cell Death Dis.* 2020;11:1027.

13. Tyler-McMahon BM, Boules M, Richelson E. Neurotensin: peptide for the next millennium. *Regul Pept.* 2000;93:125–136.
14. Huang J, Wu CY, diSant'Agnese PA, Yao JL, Cheng L, Na YQ. Function and molecular mechanisms of neuroendocrine cells in prostate cancer. *Anal Quant Cytol Histol.* 2007;29:128–138.
15. Hashimoto K, Kyoda Y, Tanaka T, et al. The potential of neurotensin secreted from neuroendocrine tumor cells to promote gelsolin-mediated invasiveness of prostate adenocarcinoma cells. *Lab Invest.* 2015;95:283–295.
16. He T, Wang M, Wang H, et al. Evaluation of neurotensin receptor 1 as potential biomarker for prostate cancer theranostic use. *Eur J Nucl Med Mol Imaging.* 2019; 46:2199–2207.
17. Maschauer S, Prante O. Radiopharmaceuticals for imaging and endoradiotherapy of neurotensin receptor-positive tumors. *J Labelled Comp Radiopharm.* 2018;61:309–325.
18. Teodoro R, Faintuch BL, Fernández Núñez EG, Guimarães Queiróz R. Neurotensin (8-13) analogue: radiolabeling and biological evaluation using different chelators. *Nucl Med Biol.* 2011;38:113–120.
19. Wu Z, Li L, Liu S, et al. Facile preparation of a thiol-reactive ^{18}F-labeling agent and synthesis of ^{18}F-DEG-VS-NT for PET imaging of a neurotensin receptor–positive tumor. *J Nucl Med.* 2014;55:1178–1184.
20. Deng H, Wang H, Wang MZ, Li ZB, Wu ZH. Synthesis and evaluation of ^{64}Cu-DOTA-NT-Cy5.5 as a dual-modality PET/fluorescence probe to image neurotensin receptor-positive tumor. *Mol Pharm.* 2015;12:3054–3061.
21. Alshoukr F, Prignon A, Brans L, et al. Novel DOTA-neurotensin analogues for ^{111}In scintigraphy and ^{68}Ga PET imaging of neurotensin receptor-positive tumors. *Bioconjug Chem.* 2011;22:1374–1385.
22. Prignon A, Provost C, Alshoukr F, et al. Preclinical evaluation of ^{68}Ga-DOTA-NT-20.3: a promising PET imaging probe to discriminate human pancreatic ductal adenocarcinoma from pancreatitis. *Mol Pharm.* 2019;16:2776–2784.
23. Zhang LL, Li WC, Xu Z, et al. ^{68}Ga-PSMA PET/CT targeted biopsy for the diagnosis of clinically significant prostate cancer compared with transrectal ultrasound guided biopsy: a prospective randomized single-centre study. *Eur J Nucl Med Mol Imaging.* 2021;48:483–492.
24. Friedlander TW, Ryan CJ. Targeting the androgen receptor. *Urol Clin North Am.* 2012;39:453–464.
25. de Bono JS, Logothetis CJ, Molina A, et al. Abiraterone and increased survival in metastatic prostate cancer. *N Engl J Med.* 2011;364:1995–2005.
26. Beer TM, Armstrong AJ, Rathkopf DE, et al. Enzalutamide in metastatic prostate cancer before chemotherapy. *N Engl J Med.* 2014;371:424–433.

Molecular Imaging of Neuroendocrine Prostate Cancer by Targeting Delta-Like Ligand 3

Joshua A. Korsen[1,2], Teja M. Kalidindi[1], Samantha Khitrov[1], Zachary V. Samuels[1], Goutam Chakraborty[3,4], Julia A. Gutierrez[1], John T. Poirier[5], Charles M. Rudin[2,3], Yu Chen[3,6], Michael J. Morris[3], Nagavarakishore Pillarsetty[1], and Jason S. Lewis[1,2]

[1]Department of Radiology, Memorial Sloan Kettering Cancer Center, New York, New York; [2]Department of Pharmacology, Weill Cornell Medicine, New York, New York; [3]Department of Medicine, Memorial Sloan Kettering Cancer Center, New York, New York; [4]Department of Urology, Icahn School of Medicine at Mount Sinai, New York, New York; [5]Perlmutter Cancer Center, New York University Langone Health, New York, New York; and [6]Human Oncology and Pathogenesis Program, Memorial Sloan Kettering Cancer Center, New York, New York

Treatment-induced neuroendocrine prostate cancer (NEPC) is a lethal subtype of castration-resistant prostate cancer. Using the ^{89}Zr-labeled delta-like ligand 3 (DLL3) targeting antibody SC16 (^{89}Zr-desferrioxamine [DFO]-SC16), we have developed a PET agent to noninvasively identify the presence of DLL3-positive NEPC lesions. **Methods:** Quantitative polymerase chain reaction and immunohistochemistry were used to compare relative levels of androgen receptor (AR)–regulated markers and the NEPC marker DLL3 in a panel of prostate cancer cell lines. PET imaging with ^{89}Zr-DFO-SC16, ^{68}Ga-PSMA-11, and ^{68}Ga-DOTATATE was performed on H660 NEPC–xenografted male nude mice. ^{89}Zr-DFO-SC16 uptake was corroborated by biodistribution studies. **Results:** In vitro studies demonstrated that H660 NEPC cells are positive for DLL3 and negative for AR, prostate-specific antigen, and prostate-specific membrane antigen (PSMA) at both the transcriptional and the translational levels. PET imaging and biodistribution studies confirmed that ^{89}Zr-DFO-SC16 uptake is restricted to H660 xenografts, with background uptake in non-NEPC lesions (both AR-dependent and AR-independent). Conversely, H660 xenografts cannot be detected with imaging agents targeting PSMA (^{68}Ga-PSMA-11) or somatostatin receptor subtype 2 (^{68}Ga-DOTATATE). **Conclusion:** These studies demonstrated that H660 NEPC cells selectively express DLL3 on their cell surface and can be noninvasively identified with ^{89}Zr-DFO-SC16.

Key Words: neuroendocrine prostate cancer; immuno-PET; molecular imaging; DLL3

J Nucl Med 2022; 63:1401–1407
DOI: 10.2967/jnumed.121.263221

Androgen receptor (AR) signaling is a critical driver of prostate cancer (PC). Androgen deprivation therapy (ADT) is used in the setting of high-risk, recurrent, or metastatic PC. Although ADT can initially be highly effective, resistance develops in most patients, leading to metastatic castration-resistant PC (mCRPC) and ultimately death. Treatment resistance to ADT in mCRPC arises from multiple mechanisms including AR amplification, AR bypass, and complete AR independence (*1*). The introduction of more potent AR signaling inhibitors (e.g., abiraterone and enzalutamide) in mCRPC patients has led to an increasing incidence of lesions that may display AR loss or adapt to low androgen levels through activation of alternative pathways (*2*). AR-independent tumors can be aggressive and can demonstrate markedly elevated proliferation, an enhanced capacity for organ metastasis, and phenotypic heterogeneity with a variable admixture of adenocarcinoma and small cell neuroendocrine phenotypes (*2*). Treatment-induced neuroendocrine PC (NEPC) has been shown to arise from treatment-induced lineage plasticity and to lead to a highly aggressive and lethal subtype of PC (*3*). This reprogramming is linked to the reactivation of developmental transcriptional programs and the transcription factor SOX2, which promotes phenotypic plasticity and acquisition of a stemlike phenotype (*4*). NEPC displays genetic similarities to small cell lung cancer (SCLC), including frequent loss of the tumor suppressor genes *TP53* and *RB1* (*5*).

The lineage transcription factor achaete-scute complex homolog 1 (ASCL1) is overexpressed and promotes tumorigenesis in mouse models of SCLC (*6*). ASCL1 plays a key role in suppressing notch signaling activity through markedly upregulated expression of the inhibitory notch ligand delta-like ligand 3 (DLL3) (*7*). DLL3 expression in adult tissues is substantially lower and restricted to intracellular compartments such as the Golgi; in contrast, in SCLC tumor cells DLL3 is aberrantly expressed on the cell surface (*7*). In PC, DLL3 has been shown to be similarly dysregulated in most NEPC samples (76.6%), with minimal to no expression in mCRPC (12.5%), localized PC (0.5%), and normal, unaffected prostate tissue (0%) (*8*). With no detectable expression of cell surface DLL3 in nonmalignant cells and preferential expression in NEPC lesions, DLL3 may be a target for a biomarker-based method of tumor detection.

SC16 is a humanized monoclonal antibody that selectively binds to both human and murine DLL3 (*9*). Our previous work with SC16 demonstrated the successful synthesis of ^{89}Zr-radiolabeled SC16 and its use as a PET radiopharmaceutical for noninvasive detection of DLL3 expression in SCLC models (*10*). PET is a powerful diagnostic tool that can noninvasively visualize and molecularly characterize lesions and aid in optimizing therapy. It has proven to be a successful platform in PC detection and management of AR-dependent lesions. However, the 2018 National Cancer Institute Workshop on Lineage Plasticity and Androgen Receptor-Independent Prostate Cancer identified a "lack of imaging capabilities" as 1 of 2 major knowledge gaps in NEPC management (*11*). The PET probes thus far developed directly target AR (*12*) or prostate-specific membrane antigen (PSMA)

Received Oct. 3, 2021; revision accepted Jan. 12, 2022.

For correspondence or reprints, contact Nagavarakishore Pillarsetty (pillarsn@mskcc.org) or Jason S. Lewis (lewisj2@mskcc.org).

(*13*) and may not detect NEPC lesions if they display AR loss or PSMA suppression (*14*). Therefore, it is imperative to have a non–PSMA-based imaging agent for NEPC detection. To our knowledge, ^{89}Zr-radiolabeled SC16 is the only imaging agent currently in development that has potential to differentiate NEPC from prostate adenocarcinoma by an increase in signal above background. This is advantageous over current PET imaging agents that target AR-dependent PC, as reduced expression of these surface antigens is possible and can increase susceptibility to high false-positives or inconclusive findings when signal approaches the noise floor. Because of the molecular similarities to SCLC and encouraging results from preclinical studies in SCLC models, we evaluated the performance of our ^{89}Zr-radiolabeled SC16 PET imaging agent in the detection of DLL3-expressing NEPC tumors in preclinical mouse models.

MATERIALS AND METHODS

The supplemental materials (available at http://jnm.snmjournals.org) provide information on cell lines, quantitative real-time polymerase chain reaction, antibody functionalization and radiolabeling (*15*), in vitro binding assays (*16*), immunohistochemistry, and generation of subcutaneous xenograft models.

Animals and Tumor Models

All animal experiments were approved by the Institutional Animal Care and Use Committee and Research Animal Resource Center at Memorial Sloan Kettering Cancer Center.

Biodistribution Studies

Biodistribution studies were performed by killing mice bearing subcutaneous H660 or DU145 tumors at chosen time points to evaluate uptake of the radiotracers. To evaluate nonspecific uptake in the DLL3-positive tumor, mice bearing subcutaneous H660 xenografts were injected with isotype-matched IgG ^{89}Zr-desferrioxamine (DFO)-IgG. The supplemental materials provide further details.

PET Imaging

PET imaging of subcutaneous PC cell line xenograft mouse models was performed on an Inveon small-animal PET/CT instrument (Siemens). The supplemental materials provide further details.

Statistical Analysis

Data are expressed as mean ± SEM. Data for the in vitro cell binding assay were analyzed by unpaired, 2-tailed *t* testing using Prism software (version 8; GraphPad), with the threshold for statistical significance set at a *P* value of less than 0.05. To evaluate the blocking study in the subcutaneous xenografts, a 2-way ANOVA test using Prism software was performed, with the threshold for statistical significance set at a *P* value of less than 0.05. A correction for multiple comparisons was performed using the Holm–Sidak method to determine statistical significance ($\alpha = 0.05$).

RESULTS

Evaluation of DLL3 Expression in NEPC

We evaluated messenger RNA and protein expression of AR and SOX2 transcription factors and their downstream targets that have been shown to differentiate adenocarcinoma or neuroendocrine phenotype, respectively, in established PC cell lines using quantitative real-time polymerase chain reaction and immunohistochemistry. For prostate adenocarcinoma genes, we evaluated *FOLH1* (gene encoding for PSMA) and *KLK3* (gene encoding for prostate-specific antigen); for neuroendocrine-regulated genes, we examined *ASCL1* and *DLL3*. The panel of PC cell lines included LNCaP (hormone-sensitive prostate adenocarcinoma, AR-positive/neuroendocrine-negative), DU145 (androgen-independent PC, AR-negative/neuroendocrine-negative), PC3 (androgen-independent PC, AR-negative/neuroendocrine-negative), and H660 (NEPC, AR-negative/neuroendocrine-positive). H660 expressed the highest of *SOX2,* which encodes a transcription factor that promotes lineage plasticity, facilitates histologic transformation, and has been associated with resistance to AR-targeted therapies (*5,17*). PC3, LNCaP, and DU145 all demonstrated significantly lower levels of *DLL3*. H660 cells showed *ASCL1* expression, encoding a key transcription regulator of notch signaling proteins, including DLL3 (Fig. 1A). At the protein level, using immunohistochemistry, we could detect DLL3 expression only in the H660 line, not in the other PC lines (Fig. 1B). Verification of the NEPC lineage of H660 was confirmed by the presence of the clinically validated neuroendocrine marker synaptophysin (SYP), which was absent in all LNCaP, PC3, and DU145 cell lines (Fig. 1B). When transcript levels of *AR, KLK3,* and *FOLH1* were evaluated, only LNCaP cells showed

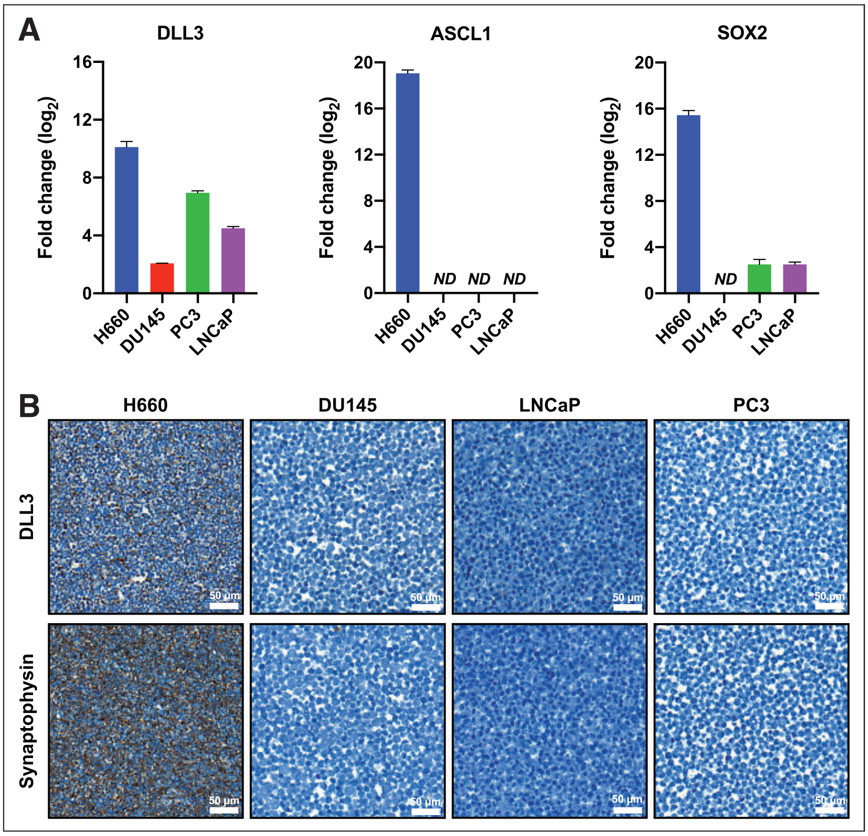

FIGURE 1. DLL3 is uniquely expressed in H660 cells at transcriptional and translational level. (A) Real-time polymerase chain reaction shows expression patterns of *DLL3, ASCL1,* and *SOX2* genes in H660, DU145, PC3, and LNCaP cells compared with A549-negative control (not shown). (B) Representative immunohistochemistry images of H660 (DLL3-positive/SYP-positive) DU145 (DLL3-negative/SYP-negative), LNCaP (DLL3-negative/SYP-negative), and PC3 (DLL3-negative/SYP-negative) tumor cell sections for DLL3 and SYP. ND = not detected.

expression, whereas H660, PC3, and DU145 had minimal detectable transcripts (Supplemental Fig. 1A). Immunohistochemistry provided similar results at the translational level, demonstrating intense staining of AR and PSMA in LNCaP cells, with no detectable expression seen in H660, PC3, or DU145 (Supplemental Fig. 1B).

We then analyzed the PC transcriptomic atlas dataset (*18*), an extensive transcriptome databank comprising 1,321 clinical specimens from 38 PC cohorts. We observed higher expression of *DLL3* in mCRPC than in primary PC ($P < 0.001$ mCRPC vs. primary; Supplemental Fig. 2A). Moreover, in the cohort of Ross-Adams et al. (*19*) (259 men with PC in Cambridge discovery cohort and Stockholm validation cohort), we found that high *DLL3* expression was associated with shorter biochemical recurrence-free survival (Supplemental Fig. 2B). Together, these data indicate that *DLL3* messenger RNA expression may be associated with a poor prognosis for PC patients. This hypothesis will require further testing in a larger cohort to confirm the prognostic significance of *DLL3* messenger RNA expression in PC.

We next compared the expression levels of DLL3 in H660 and H82 tumor cells. H82 was derived from the pleural fluid of a patient with SCLC and H660 derived from the lymph node of an NEPC patient. Both cell lines displayed a neuroendocrine phenotype and aberrant DLL3 trafficking to the cell surface. Despite low expression of DLL3 on H82 cells, PET imaging successfully delineated H82 tumor in mouse models (*10*). Immunohistochemistry demonstrated an even lower abundance of DLL3 expression in the H660 tumor cells than in the H82 tumor cells (Supplemental Fig. 3). However, we still envision that DLL3 PET imaging would be feasible because of the absence of DLL3 expression on the cell surface of nonmalignant cells.

^{89}Zr-DFO-SC16 Characterization and Its Detection of Cell Surface DLL3 Expression

The DLL3-targeting SC16 antibody was functionalized through non–site-specific conjugation to the free lysine moieties available on the monoclonal antibody with the siderophore-derived DFO chelator (Supplemental Fig. 4). Matrix-assisted laser desorption/ionization time-of-flight mass spectrometry revealed that the ratio of chelator to monoclonal antibody was 0.44, which implies that, on average, half of the antibody molecules were functionalized with DFO covalently (Supplemental Fig. 5).

Radiolabeling of the DFO-SC16 conjugate provided ^{89}Zr-DFO-SC16 in high radiochemical yield (>99%) (Supplemental Fig. 6A) and high specific activity (370 MBq/mg). The radioimmunoconjugate demonstrated at least 92% stability when incubated in human serum at 37°C for 5 d (Supplemental Fig. 6B). The target-binding fraction of the radioimmunoconjugate—the fraction of the antibody that retains its binding to its target after modification—was more than 90% for ^{89}Zr-DFO-SC16 toward DLL3 (Fig. 2A). ^{89}Zr-DFO-SC16 binding to DLL3 could be blocked in the presence of a 5,000-fold excess of unlabeled SC16. In vitro cell binding assays revealed ^{89}Zr-DFO-SC16 to be bound to DLL3 expressed on the cell surface of H660 cells, with no binding observed in the DLL3-negative cell lines LNCaP, DU145, or PC3 (Fig. 2B). Binding of ^{89}Zr-DFO-SC16 to H660 cells could be blocked in the presence of a 1,000-fold excess of unlabeled SC16. A saturation binding assay with H660 cells revealed a dissociation constant of less than 1 nM and a maximum specific binding of 86.3 fM/10^6 cells for ^{89}Zr-DFO-SC16 (Supplemental Fig. 6C). These studies demonstrated that the immunoreactivity of SC16 is retained after DFO conjugation and radiolabeling with ^{89}Zr.

PET Imaging and Biodistribution of DLL3 Expression with ^{89}Zr-DFO-SC16 in Subcutaneous Xenograft Models

PET imaging with ^{89}Zr-DFO-SC16 was performed on male nude mice bearing H660 (DLL3-positive, AR-negative/neuroendocrine-positive) or DU145 (DLL3-negative, AR-negative/neuroendocrine-negative) subcutaneous xenografts. PET imaging with ^{89}Zr-DFO-SC16 showed clear delineation of H660 tumor xenografts 120 h after administration of the radioimmunoconjugate (Fig. 3A). Increasing uptake in the H660-bearing mice could be observed in the tumors from the time of injection to 120 h after injection. As expected, because of lack of DLL3 expression, minimal uptake of ^{89}Zr-DFO-SC16 was observed in DU145-bearing mice, with tumor uptake remaining constant over the 120-h imaging time course (Fig. 3B). Low and nonspecific uptake was observed in H660 tumor xenografts 120 h after injection of isotype-matched IgG (^{89}Zr-DFO-IgG) (Supplemental Figs. 7A–7C).

Biodistribution data at 24, 72, and 120 h after intravenous administration confirmed a progressive increase in H660 tumor uptake over time, reaching 17.50 ± 3.19 percentage injected dose per gram (%ID/g) at 120 h (Fig. 4A; Supplemental Fig. 8). As expected, a concurrent decrease in blood-pool activity was observed (24 h, 6.60 ± 0.90 %ID/g; 72 h, 3.16 ± 1.37 %ID/g; 120 h, 3.07 ± 0.45 %ID/g) as the tumor activity increased over time. Because of heterogeneous uptake of the radioimmunoconjugate between the H660 tumors, 2 independent cohorts of 3 mice each were evaluated at 120 h. Linear regression analysis displayed a positive correlation between time after intravenous administration and %ID/g in H660 tumors across both independent cohorts, with tumor uptake increasing over time ($P = 0.00971$; Supplemental Fig. 9). Uptake of the radioimmunoconjugate could be blocked by coinjection of a 50-fold excess of unlabeled SC16 antibody, confirming the specificity of the radioimmunoconjugate for the H660 tumor (Fig. 4A; Supplemental Fig. 10). At 120 h after injection,

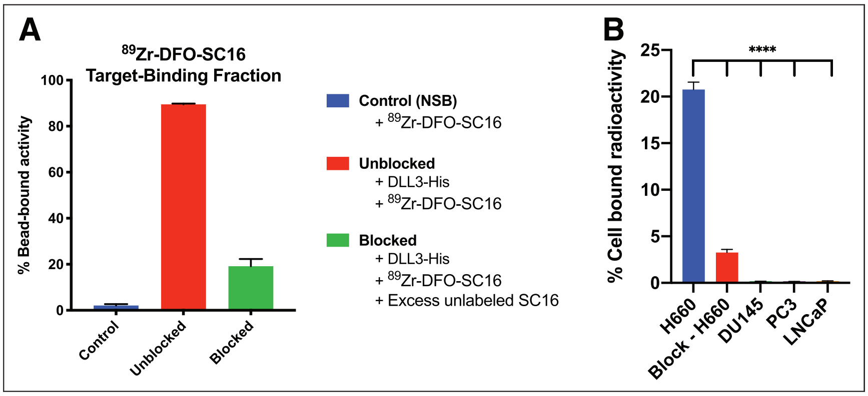

FIGURE 2. DLL3 is expressed on cell surface of H660 tumor cells that can be targeted by ^{89}Zr-DFO-SC16. (A) ^{89}Zr-DFO-SC16 shows high and specific binding to Ni-NTA beads coated with His-tagged DLL3. Minimum nonspecific binding is observed (control). Specificity of binding to His-tagged DLL3 was shown in presence of 5,000-fold excess of unlabeled SC16. (B) In vitro cell binding data on ^{89}Zr-DFO-SC16 binding to H660 cells confirms DLL3 expression on cell surface that can be targeted using our anti-DLL3 monoclonal antibody SC16. Minimal binding of ^{89}Zr-DFO-SC16 is observed to DLL3-negative DU145, PC3, and LNCaP cells. Specificity of binding to H660 cells was shown in presence of 1,000-fold excess of unlabeled SC16. ****$P < 0.0001$. NSB = nonspecific binding.

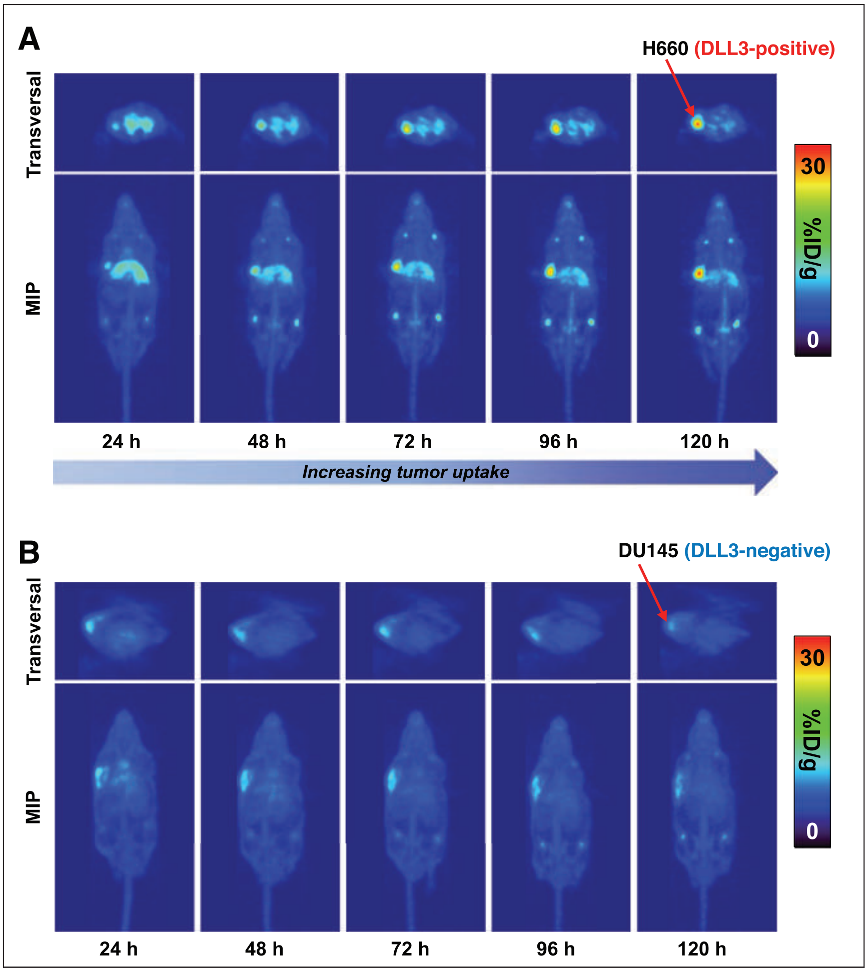

FIGURE 3. DLL3-expressing subcutaneous H660 tumors could be imaged with ^{89}Zr-DFO-SC16 in vivo. (A) PET images of ^{89}Zr-DFO-SC16 in athymic nude male mouse bearing subcutaneous H660 tumor xenografted on left shoulder. PET imaging was performed at 24-h intervals up to 120 h after injection of ^{89}Zr-DFO-SC16. (B) PET images of ^{89}Zr-DFO-SC16 in athymic nude male mouse bearing subcutaneous DU145 tumor xenografted on left shoulder. PET imaging was performed at 24-h intervals up to 120 h after injection of ^{89}Zr-DFO-SC16. Images represent maximum-intensity projection and transverse planar images at designated time points after injection of radiotracer. MIP = maximum-intensity projection.

high tumor-to-background contrast ratios were observed (Fig. 4B), with a tumor-to-muscle ratio of 33.91 ± 5.73. In contrast, ^{89}Zr-DFO-SC16 uptake in the DU145 (DLL3-negative) tumors was low and nonspecific, at 5.47 ± 0.25 %ID/g 120 h after intravenous administration, consistent with an in vivo enhanced permeability and retention effect (Fig. 4C; Supplemental Fig. 11). Comparing tumor uptake at each time point in the H660 and DU145 tumors demonstrated the specificity and selectivity of ^{89}Zr-DFO-SC16 for DLL3 (Supplemental Fig. 12A). Mean uptake in H660 tumors increased over time and was statistically significant when compared with mean uptake in DU145 tumors at 72 and 120 h after injection. Tumor-to-muscle ratios also increased over time in the H660 tumors and were statistically significant at 72 and 120 h after injection when compared with DU145 tumors, in which this ratio remained relatively constant at all time points (Supplemental Fig. 12B). Considering potential clinical implications, taken together these data suggest that patients could be effectively imaged in a wide time window (72–120 h). Immunohistochemistry on resected H660 subcutaneous xenografts confirmed retained expression of DLL3 and SYP, which were absent in resected DU145 subcutaneous xenografts (Fig. 4D; Supplemental Fig. 13 shows SYP immunohistochemistry and corresponding hematoxylin- and eosin-stained slides).

NEPC Is Detectable Only by DLL3 Imaging, Not by PSMA or Somatostatin Imaging

To demonstrate the dichotomy between AR-positive prostate adenocarcinoma and AR-negative NEPC, male nude mice were subcutaneously xenografted with PSMA-positive/DLL3-negative LNCaP tumors and PSMA-negative/DLL3-positive H660 tumors on opposite flanks and imaged by DLL3- and PSMA-based PET. The dually tumor-bearing mice were imaged 1 h after administration of ^{68}Ga-PSMA-11, a PSMA-targeted PET agent. The radiotracer accumulated exclusively in the LNCaP tumor and could be successfully imaged with high contrast (Fig. 5). The NEPC model H660 does not express AR or PSMA, and H660 tumors could not be detected through PSMA-based imaging. Two days later, the same cohort of mice was administered ^{89}Zr-DFO-SC16 and imaged 5 d after administration. The radiotracer selectively bound to the H660 tumor but not to LNCaP and finally allowed for site-specific identification of the NEPC lesion.

Somatostatin receptor (SSTR) imaging has been widely used as a method to detect the presence of gastroenteropancreatic neuroendocrine neoplasms, including the Food and Drug Administration–approved agent ^{68}Ga-DOTATATE. ^{68}Ga-DOTATATE is a peptide-based PET imaging agent that demonstrates high affinity for the SSTR subtype 2 (SSTR2) and has been tested in NEPC patients with inconclusive results (*20*). As a comparator, we sought to image tumor-bearing mice by ^{68}Ga-DOTATATE. We first analyzed *SSTR2* messenger RNA expression in H660 and LNCaP cells. We could not detect significantly upregulated *SSTR2* expression in H660 cells relative to LNCaP cells (Supplemental Fig. 14A). Shifting to in vivo analysis, we conducted an imaging study with ^{68}Ga-DOTATATE on H660-bearing male nude mice. No accumulation of the radiotracer was observed in the tumor 1 h after administration, demonstrating an inability to detect this NEPC tumor through SSTR imaging (Supplemental Fig. 14B).

DISCUSSION

NEPC is a lethal disease, and detecting the presence of NEPC lesions noninvasively remains challenging. One of the barriers to understanding the biology of mCRPC is the inaccessibility of the tissue and consequent undersampling of disease heterogeneity. Biopsies (the gold standard in terms of phenotypic characterization with immunostaining) and genotypic characterization with next-generation sequencing techniques describe only a single lesion

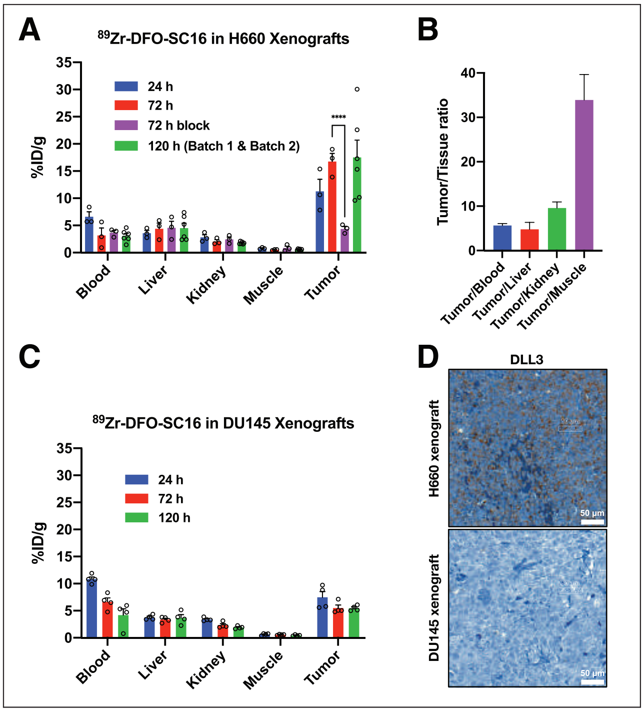

FIGURE 4. Biodistribution of ^{89}Zr-DFO-SC16 in subcutaneous xenograft model of NEPC. (A) Select organ biodistribution data at 24, 72, and 120 h after intravenous injection of ^{89}Zr-DFO-SC16 in athymic nude mice bearing subcutaneous H660 tumors. Bars at 24 and 72 h represent data obtained from batch 1 ($n = 3$). Bars at 120 h represent data obtained from batches 1 and 2 ($n = 6$). Supplemental materials provide details on the 2 different cohorts used in biodistribution study. H660 tumor uptake could be blocked at 72 h after injection of ^{89}Zr-DFO-SC16 with 50-fold excess of unlabeled SC16 antibody. (B) Tumor-to-background contrast ratios from uptake of ^{89}Zr-DFO-SC16 in H660 xenograft–bearing mice. (C) Select organ biodistribution at 24, 72, and 120 h after injection of ^{89}Zr-DFO-SC16 in athymic nude mice bearing subcutaneous DU145 tumors. (D) Representative immunohistochemistry images of H660 and DU145 subcutaneous tumor xenografts for DLL3. ****$P < 0.0001$.

rather than the full diversity of the disease. Furthermore, bone biopsies are difficult because tumors are frequently embedded deep within the densely sclerotic bone, a result of exuberant hydroxyapatite deposition from tumoral stimulation of osteoblasts. Circulating tumor cells and cell-free DNA can be used to characterize the biology of mCRPC and can reflect posttreatment changes in tumor burden but cannot localize the emergence of resistant disease on a lesional level. A noninvasive, whole-body method for detecting the emergence of NEPC will overcome these limitations of standard methods of tumor analysis, allow for identification and characterization of lesions in real time, and facilitate earlier intervention to improve patient survival. Here, we confirmed that the NEPC cell line H660 is devoid of the commonly targeted prostate biomarkers AR, PSMA, and prostate-specific antigen but selectively expresses DLL3 on the cell surface. However, this is an idealized preclinical model, and a varied range of prostate biomarker expression may still be observed in patients with NEPC lesions. In our previous work using the SCLC tumor model H82, we successfully showed that, though expression of DLL3 is less abundant than other commonly imaged tumor-associated antigens (e.g., human epidermal growth factor receptor 2, human epidermal growth factor receptor, and PSMA), the highly tumor-restricted cell surface expression of DLL3 on SCLC allows for successful PET imaging (*10*). Although the expression levels of DLL3 observed in the H660 NEPC tumor cells were lower than in the H82 SCLC tumor cells, PET imaging was still feasible because of the absence of detectable cell surface DLL3 in nonmalignant cells. We demonstrated that ^{89}Zr-DFO-SC16 shows high specific uptake in H660 (DLL3-positive) tumors through biodistribution studies and PET imaging. PET imaging in a dual tumor model with H660 (DLL3-positive/PSMA-negative) and LNCaP (DLL3-negative/PSMA-positive) tumor cells demonstrated an inability to detect PSMA-negative NEPC lesions with other commonly used imaging approaches. Neuroendocrine differentiation in prostate adenocarcinoma lesions due to selective treatment pressure can lead to the activation of different pathways, including the possibility of low AR and low AR-pathway signaling, which may result in the inability to detect such lesions with ^{68}Ga-PSMA-11 (*14*) or other AR-targeted tracers such as ^{18}F-16β-fluoro-5α-dihydrotestosterone (*12,21*). Therefore, using ^{68}Ga-PSMA-11 only, NEPC lesions may not be detected.

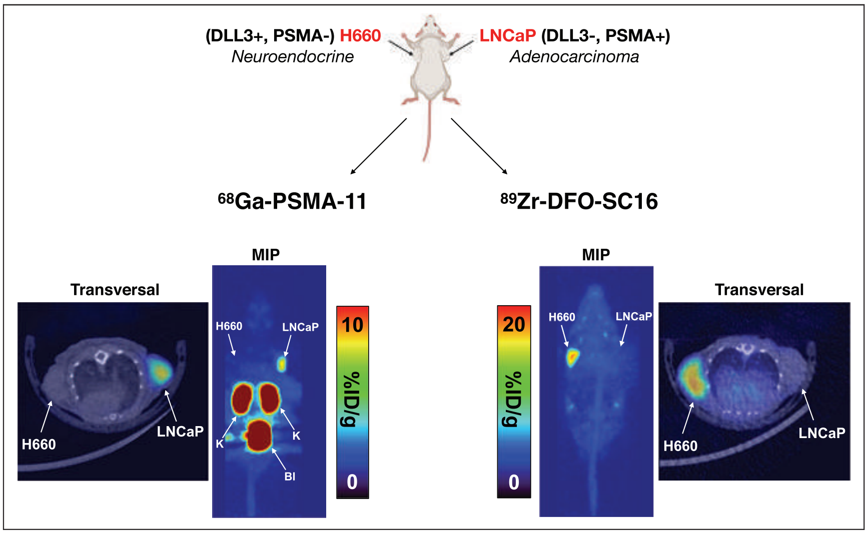

FIGURE 5. ^{68}Ga-PSMA-11 cannot image NEPC lesions in vivo. Shown are PET images of ^{68}Ga-PSMA-11 (1 h after injection) or ^{89}Zr-DFO-SC16 (120 h after injection) in male athymic nude mouse bearing H660 and LNCaP tumors xenografted on left and right shoulders, respectively. MIP = maximum-intensity projection.

DLL3 imaging can provide patient stratification and suggests a rationale for DLL3-targeted therapeutic approaches. Four DLL3-specific therapies have been tested clinically: the antibody–drug conjugate rovalpituzumab tesirine, the bispecific T cell engager AMG757, the chimeric antigen receptor T cell AMG119, and the trispecific T-cell engager HPN328. Rovalpituzumab tesirine therapy demonstrated minimal responses in SCLC and other neuroendocrine carcinomas (9/69; 13%) (*22*), whereas AMG757 (NCT03319940), AMG119 (NCT03392064), and HPN328 (NCT04471727) are currently being tested in SCLC patients in first-in-humans studies. One avenue yet to be explored could use a targeted radionuclide therapy with ^{177}Lu in patients with detected DLL3-positive PC lesions via ^{89}Zr-DFO-SC16 PET. Recent work by our lab has demonstrated the exceptional efficacy of ^{177}Lu-labeled-SC16 for the treatment of SCLC in preclinical models (*23*).

Lastly, we demonstrated an inability to target SSTRs in a subcutaneous NEPC model. Reports on the presence of SSTRs in NEPC have been contradictory and inconclusive, with some studies suggesting that SSTR2 expression is upregulated (*24,25*) whereas others have shown low or absent expression (*26,27*). Here, we showed that H660 tumor cells do not express SSTRs and therefore cannot be imaged in vivo through somatostatin-based receptor PET imaging.

Although DLL3 appears to be a potential target for PET imaging in NEPC lesions, the biologic consequences of PC treatments on preexisting NEPC lesions are not understood. PC lesions in patients may have distinct adenocarcinoma, neuroendocrine, or mixed phenotypes. Therefore, even with detection of NEPC, patients may continue ADT. ADT influences the expression of prostate-specific antigen and PSMA and blocks AR-targeting agents and therefore influences the outcomes of PET imaging studies that are specific for these targets (*28–30*). There is no clear understanding of the biologic consequence of ADT on neuroendocrine cells or on the expression of DLL3. Likewise, it has been shown that the phosphatidylinositol 3-kinase pathway is activated in ADT-resistant mCRPC and influences the expression of neuroendocrine markers (*31,32*). Two phosphatidylinositol 3-kinase inhibitors, everolimus (NCT00976755) and BKM-120 (NCT01385293), are in clinical trials for mCRPC. Further studies to evaluate the potential influence of PC treatments on NEPC lesions and DLL3 expression are warranted.

Overall, the selective expression of DLL3 in the tumor, with no detectable expression in nonmalignant cells, and the high specificity of tumor uptake of ^{89}Zr-DFO-SC16 suggest the possibility of translating this imaging method into the clinic. With a clinical trial (NCT04199741) currently under way at Memorial Sloan Kettering Cancer Center—the first-in-humans clinical trial of DLL3 PET imaging in patients with SCLC—our data encourage the use of DLL3 PET imaging in patients with NEPC lesions. Ultimately, DLL3-targeted PET imaging might confirm the presence of NEPC lesions through a noninvasive whole-body PET scan, aid patient selection, and improve therapeutic outcomes in NEPC-directed clinical trials.

CONCLUSION

These findings suggest that ^{89}Zr-DFO-SC16 is a noninvasive diagnostic PET agent that can be used as a tool to detect the presence of DLL3-positive NEPC lesions at single-lesion resolution. We hope these findings will improve on the current approach of biopsy-based and genotypic characterization in identifying these patients.

DISCLOSURE

The study was supported in part by NIH T32 GM073546 (Joshua Korsen), NIH R35 CA232130-01A1 (Jason Lewis), R35 CA263816 (Charles Rudin), the Geoffrey Beene Cancer Research Center (Jason Lewis, Nagavarakishore Pillarsetty, Charles Rudin, and Yu Chen), and the Department of Defense Idea Award grant W81XWH-19-1-0536 (Nagavarakishore Pillarsetty). The Radiochemistry and Molecular Imaging Probes Core Facility, the Small Animal Imaging Facility, and the Molecular Cytology Core Facility were supported in part by NIH P30 CA08748. Goutam Chakraborty is supported by a Prostate Cancer Foundation Young Investigator Award. Jason Lewis is an associate editor of *The Journal of Nuclear Medicine* but had no involvement or access to information regarding the peer review of this article. No other potential conflict of interest relevant to this article was reported.

ACKNOWLEDGMENTS

We acknowledge the Radiochemistry and Molecular Imaging Probes Core Facility, the Small Animal Imaging Facility, and the Molecular Cytology Core Facility. The graphical abstract and part of Figure 5 were made in Biorender.com.

KEY POINTS

QUESTION: Can DLL3-targeted PET be used as a tool for the noninvasive diagnosis of NEPC?

PERTINENT FINDINGS: DLL3 is expressed exclusively on the cell surface of the H660 NEPC cell line and can be detected with the DLL3-targeting tracer ^{89}Zr-DFO-SC16. In vivo PET imaging studies showed that ^{89}Zr-DFO-SC16 is selective for DLL3-expressing NEPC lesions and cannot be imaged with ^{68}Ga-PSMA-11 or ^{68}Ga-DOTATATE. The selective expression of DLL3 in the tumor and specific tumor uptake of ^{89}Zr-DFO-SC16 suggest potential translation of this imaging method to the clinic.

IMPLICATIONS FOR PATIENT CARE: PET imaging of DLL3 may allow for the identification of NEPC in patients in a benign, noninvasive way early enough to better inform clinical decision making.

REFERENCES

1. Watson PA, Arora VK, Sawyers CL. Emerging mechanisms of resistance to androgen receptor inhibitors in prostate cancer. *Nat Rev Cancer.* 2015;15:701–711.
2. Bluemn EG, Coleman IM, Lucas JM, et al. Androgen receptor pathway-independent prostate cancer is sustained through FGF signaling. *Cancer Cell.* 2017;32:474–489.e6.
3. Quintanal-Villalonga Á, Chan JM, Yu HA, et al. Lineage plasticity in cancer: a shared pathway of therapeutic resistance. *Nat Rev Clin Oncol.* 2020;17:360–371.
4. Davies AH, Beltran H, Zoubeidi A. Cellular plasticity and the neuroendocrine phenotype in prostate cancer. *Nat Rev Urol.* 2018;15:271–286.
5. Ku SY, Rosario S, Wang Y, et al. Rb1 and Trp53 cooperate to suppress prostate cancer lineage plasticity, metastasis, and antiandrogen resistance. *Science.* 2017;355:78–83.
6. Borromeo MD, Savage TK, Kollipara RK, et al. ASCL1 and NEUROD1 reveal heterogeneity in pulmonary neuroendocrine tumors and regulate distinct genetic programs. *Cell Rep.* 2016;16:1259–1272.
7. Owen DH, Giffin MJ, Bailis JM, Smit MD, Carbone DP, He K. DLL3: an emerging target in small cell lung cancer. *J Hematol Oncol.* 2019;12:61.
8. Puca L, Gavyert K, Sailer V, et al. Delta-like protein 3 expression and therapeutic targeting in neuroendocrine prostate cancer. *Sci Transl Med.* 2019;11:eaav0891.
9. Saunders LR, Bankovich AJ, Anderson WC, et al. A DLL3-targeted antibody-drug conjugate eradicates high-grade pulmonary neuroendocrine tumor-initiating cells in vivo. *Sci Transl Med.* 2015;7:302ra136.
10. Sharma SK, Pourat J, Abdel-Atti D, et al. Noninvasive interrogation of DLL3 expression in metastatic small cell lung cancer. *Cancer Res.* 2017;77:3931–3941.
11. Beltran H, Hruszkewycz A, Scher HI, et al. The role of lineage plasticity in prostate cancer therapy resistance. *Clin Cancer Res.* 2019;25:6916–6924.
12. Fox JJ, Gavane SC, Blanc-Autran E, et al. Positron emission tomography/computed tomography-based assessments of androgen receptor expression and glycolytic activity as a prognostic biomarker for metastatic castration-resistant prostate cancer. *JAMA Oncol.* 2018;4:217–224.
13. Schwarzenboeck SM, Rauscher I, Bluemel C, et al. PSMA ligands for PET imaging of prostate cancer. *J Nucl Med.* 2017;58:1545–1552.
14. Bakht MK, Derecichei I, Li Y, et al. Neuroendocrine differentiation of prostate cancer leads to PSMA suppression. *Endocr Relat Cancer.* 2018;26:131–146.
15. Holland JP, Sheh Y, Lewis JS. Standardized methods for the production of high specific-activity zirconium-89. *Nucl Med Biol.* 2009;36:729–739.

16. Sharma SK, Lyashchenko SK, Park HA, et al. A rapid bead-based radioligand binding assay for the determination of target-binding fraction and quality control of radiopharmaceuticals. *Nucl Med Biol.* 2019;71:32–38.
17. Mu P, Zhang Z, Benelli M, et al. SOX2 promotes lineage plasticity and antiandrogen resistance in TP53- and RB1-deficient prostate cancer. *Science.* 2017; 355:84–88.
18. You S, Knudsen BS, Erho N, et al. Integrated classification of prostate cancer reveals a novel luminal subtype with poor outcome. *Cancer Res.* 2016;76:4948–4958.
19. Ross-Adams H, Lamb AD, Dunning MJ, et al. Integration of copy number and transcriptomics provides risk stratification in prostate cancer: a discovery and validation cohort study. *EBioMedicine.* 2015;2:1133–1144.
20. Luboldt W, Zophel K, Wunderlich G, Abramyuk A, Luboldt HJ, Kotzerke J. Visualization of somatostatin receptors in prostate cancer and its bone metastases with Ga-68-DOTATOC PET/CT. *Mol Imaging Biol.* 2010;12:78–84.
21. Vargas HA, Kramer GM, Scott AM, et al. Reproducibility and repeatability of semiquantitative ^{18}F-fluorodihydrotestosterone uptake metrics in castration-resistant prostate cancer metastases: a prospective multicenter study. *J Nucl Med.* 2018;59:1516–1523.
22. Mansfield AS, Hong DS, Hann CL, et al. A phase I/II study of rovalpituzumab tesirine in delta-like 3-expressing advanced solid tumors. *NPJ Precis Oncol.* 2021;5:74.
23. Tully KM, Tendler S, Carter LM, et al. Radioimmunotherapy targeting delta-like ligand 3 in small cell lung cancer. *Clin Cancer Res.* 2022;28:1391–1401.
24. Hansson J, Bjartell A, Gadaleanu V, Dizeyi N, Abrahamsson PA. Expression of somatostatin receptor subtypes 2 and 4 in human benign prostatic hyperplasia and prostatic cancer. *Prostate.* 2002;53:50–59.
25. Morichetti D, Mazzucchelli R, Stramazzotti D, et al. Immunohistochemical expression of somatostatin receptor subtypes in prostate tissue from cystoprostatectomies with incidental prostate cancer. *BJU Int.* 2010;106:1072–1080.
26. Cariaga-Martinez AE, Lorenzati MA, Riera MA, et al. Tumoral prostate shows different expression pattern of somatostatin receptor 2 (SSTR2) and phosphotyrosine phosphatase SHP-1 (PTPN6) according to tumor progression. *Adv Urol.* 2009; 2009:723831.
27. Hennigs JK, Muller J, Adam M, et al. Loss of somatostatin receptor subtype 2 in prostate cancer is linked to an aggressive cancer phenotype, high tumor cell proliferation and predicts early metastatic and biochemical relapse. *PLoS One.* 2014;9: e100469.
28. Blee AM, Huang H. Lineage plasticity-mediated therapy resistance in prostate cancer. *Asian J Androl.* 2019;21:241–248.
29. Sasaki T, Sugimura Y. The importance of time to prostate-specific antigen (PSA) nadir after primary androgen deprivation therapy in hormone-naive prostate cancer patients. *J Clin Med.* 2018;7:565.
30. Afshar-Oromieh A, Debus N, Uhrig M, et al. Impact of long-term androgen deprivation therapy on PSMA ligand PET/CT in patients with castration-sensitive prostate cancer. *Eur J Nucl Med Mol Imaging.* 2018;45:2045–2054.
31. Crumbaker M, Khoja L, Joshua AM. AR signaling and the PI3K pathway in prostate cancer. *Cancers (Basel).* 2017;9:34.
32. Chen R, Li Y, Buttyan R, Dong X. Implications of PI3K/AKT inhibition on REST protein stability and neuroendocrine phenotype acquisition in prostate cancer cells. *Oncotarget.* 2017;8:84863–84876.

Short-Term Colony-Stimulating Factor 1 Receptor Inhibition–Induced Repopulation After Stroke Assessed by Longitudinal ^{18}F-DPA-714 PET Imaging

Cristina Barca[1], Amanda J. Kiliaan[2], Lydia Wachsmuth[3], Claudia Foray[1], Sven Hermann[1], Cornelius Faber[3], Michael Schäfers[1,4], Maximilian Wiesmann[2], Bastian Zinnhardt*[1,4,5], and Andreas H. Jacobs*[1,6]

[1]European Institute for Molecular Imaging, University of Münster, Münster, Germany; [2]Department of Medical Imaging/Anatomy, Radboud University Medical Center, Radboud, The Netherlands; [3]Translational Research Imaging Center, University Hospital Münster, Münster, Germany; [4]Department of Nuclear Medicine, University Hospital Münster, Münster, Germany; [5]Biomarkers and Translational Technologies, Pharma Research and Early Development, F. Hoffmann-La Roche Ltd., Basel, Switzerland; and [6]Department of Geriatrics and Neurology, Johanniter Hospital, Bonn, Germany

Studies on colony-stimulating factor 1 receptor (CSF-1R) inhibition–induced microglia depletion indicated that inhibitor withdrawal allowed the renewal of the microglia compartment via repopulation and resolved the inflammatory imbalance. Therefore, we investigated for the first time (to our knowledge) the effects of microglia repopulation on inflammation and functional outcomes in an ischemic mouse model using translocator protein (TSPO)-PET/CT and MR imaging, ex vivo characterization, and behavioral tests. **Methods:** Eight C57BL/6 mice per group underwent a 30-min transient occlusion of the middle cerebral artery. The treatment group received CSF-1R inhibitor in 1,200 ppm PLX5622 chow (Plexxikon Inc.) from days 3 to 7 to induce microglia/macrophage depletion and then went back to a control diet to allow repopulation. The mice underwent T2-weighted MRI on day 1 after ischemia and ^{18}F-labeled *N,N*-diethyl-2-(2-[4-(2-fluoroethoxy)phenyl]-5,7-dimethylpyrazolo[1,5-α]pyrimidine-3-yl)acetamide (^{18}F-DPA-714) (TSPO) PET/CT on days 7, 14, 21, and 30. The percentage injected tracer dose per milliliter within the infarct, contralateral striatum, and spleen was assessed. Behavioral tests were performed to assess motor function recovery. Brains were harvested on days 14 and 35 after ischemia for ex vivo analyses (immunoreactivity and real-time quantitative polymerase chain reaction) of microglia- and macrophage-related markers. **Results:** Repopulation significantly increased ^{18}F-DPA-714 uptake within the infarct on days 14 ($P < 0.001$) and 21 ($P = 0.002$) after ischemia. On day 14, the ionized calcium binding adaptor molecule 1 (Iba-1)–positive cell population showed significantly higher expression of TSPO, CSF-1R, and CD68, in line with microglia repopulation. Gene expression analyses on day 14 indicated a significant increase in microglia-related markers (*csf-1r, aif1,* and *p2ry12*) with repopulation, whereas peripheral cell recruitment–related gene expression decreased (*cx3cr1* and *ccr2*), indicative of peripheral recruitment during CSF-1R inhibition. Similarly, uncorrected spleen uptake was significantly higher on day 7 after ischemia with treatment ($P = 0.001$) and decreased after drug withdrawal. PLX5622-treated mice walked a longer distance ($P < 0.001$) and more quickly ($P = 0.009$), and showed greater forelimb strength ($P < 0.001$), than control mice on day 14. **Conclusion:** This study highlighted the potential of ^{18}F-DPA-714 PET/CT imaging to track microglia and macrophage repopulation after short-term CSF-1R inhibition in stroke.

Key Words: colony-stimulating factor 1 receptor; microglia; stroke; ^{18}F-DPA-714; repopulation

J Nucl Med 2022; 63:1408–1414
DOI: 10.2967/jnumed.121.263004

Microglia play a major role in the stroke-induced neuroinflammatory response, as part of the early proinflammatory and later restorative processes (*1*). Microglia survival and proliferation are dependent on signaling through the colony-stimulating factor 1 receptor (CSF-1R) (*2*). Administration of the CSF-1R inhibitor PLX5622 progressively leads to almost complete microglia depletion after 1 wk of treatment in wild-type mice (*3*). Microglia depletion in acute or subacute ischemia (1–3 d) was associated with increased immune cell infiltration and aggravated brain inflammation (*4,5*). Inhibitor withdrawal triggers microglia repopulation, indicated by microglia proliferation and increased activity. Besides, long-lasting treatment effects were observed on other cell populations (*6*). Recently, we demonstrated that CSF-1R inhibition–induced microglia/macrophage depletion could be tracked using an ^{18}F-labeled radiotracer—*N,N*-diethyl-2-(2-[4-(2-fluoroethoxy) phenyl]-5,7-dimethylpyrazolo[1,5-α]pyrimidine-3-yl)acetamide (^{18}F-DPA-714)—targeting the translocator protein (TSPO) (*7*): TSPO-dependent neuroinflammation was significantly decreased within the first weeks after stroke, although long-term CSF-1R inhibition was associated with a poor disease outcome. Therefore, PLX5622 represents an attractive microglia- and macrophage-targeting pharmacologic tool allowing modulation of the inflammatory environment after stroke. However, microglia repopulation has yet to be investigated.

The therapeutic effect of short-term CSF-1R inhibition has scarcely been investigated but has shown promising applications. In a neuronal injury mouse model, renewal of the microglia compartment after short-term CSF-1R inhibition reduced lesion-induced inflammatory markers, resolved the active phenotype of microglia, and reversed behavioral impairment (*3*). Therefore, short-term

---

Received Aug. 5, 2021; revision accepted Jan. 12, 2022.

For correspondence or reprints, contact Andreas H. Jacobs (ahjacobs@uni-muenster.de) or Cristina Barca (cristina.barca@uni-muenster.de).

*Contributed equally to this work.

PLX5622 treatment represents an opportunity to renew the cellular compartment and reprogram microglia activity to reduce ischemia-associated inflammation.

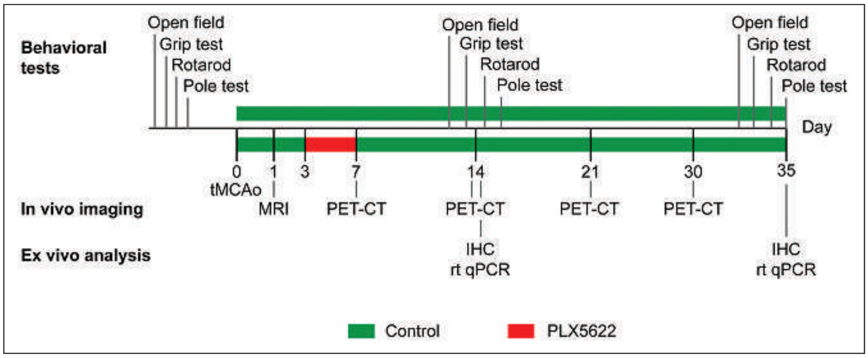

FIGURE 1. Study design. IHC = immunohistochemistry; rt qPCR = real-time quantitative polymerase chain reaction; tMCAo = transient middle cerebral artery occlusion.

In this study, we aimed to longitudinally investigate the effects of microglia repopulation in a stroke mouse model. We investigated the therapeutic effect of microglia repopulation on stroke outcomes by inhibiting CSF-1R between days 3 and 7 after ischemia. Few studies in stroke models have investigated how microglia affect outcomes after CSF-1R inhibition (*4,5,8*). Results indicated that absence of microglia within the first days after stroke worsened disease outcomes, including increased brain injury, enhanced excitotoxicity, and brain inflammation. Therefore, we aimed to leverage the phagocytic activity on infiltrating immune cells and cell debris within the first days after ischemia (*4*), to reduce microglia-related excitotoxicity, to renew the microglia compartment, and to take advantage of the repopulation process on lesion-associated inflammation at the peak of TSPO-dependent inflammation reported between days 10 and 14 after ischemia (*9–11*).

To investigate the kinetics of immune cell activation, we performed longitudinal PET using the TSPO radiotracer ^{18}F-DPA-714 as a marker for neuroinflammation, together with CT and MRI. Imaging data were cross-correlated with protein and gene expression profiles of microglia, macrophages and inflammation-related markers using immunohistochemistry and real-time quantitative polymerase chain reaction. In addition, we studied the therapeutic effect on motor functions using a set of behavioral tests.

We hypothesized that subacute PLX5622 treatment may induce immunomodulatory effects by triggering microglia repopulation, ultimately showing a positive effect on stroke outcomes. The repopulation process, indicated by an increased TSPO PET signal, may be detected noninvasively by ^{18}F-DPA-714 PET/MRI.

MATERIALS AND METHODS

Study Approval

All experiments were conducted in accordance with the German Law on the Care and Use of Laboratory Animals and approved by the Landesamt für Natur, Umwelt, und Verbraucherschutz of North Rhine–Westphalia and according to the ARRIVE 2.0 guidelines (Animal Research: Reporting of In Vivo Experiments; https://www.nc3rs.org.uk/arrive-guidelines).

Study

Male C57BL6/J mice 3–4 mo old ($n = 32$) were provided by the local animal facility. They were housed under a standard 12 h:12 h light:dark cycle with free access to food and water. All mice underwent a 30-min transient occlusion of the middle cerebral artery (day 0) and were randomized into either a control group or a PLX5622-treated group by an external person. All mice underwent T2-weighted MRI on day 1. The treatment group received 1,200 ppm PLX5622 chow from days 3 to 7 after ischemia (Fig. 1). The experimenters did not know the group assignment.

Exclusion criteria were lack of reperfusion (<50% baseline cerebral blood flow recovery) as assessed by laser Doppler, an infarct exceeding the striatal and cortical regions, and extreme weight loss (>20% of the initial body weight). The dropout rate was 8%.

Eight animals per group were used for in vivo PET imaging on days 7, 14, 21, and 30 after ischemia. The same animals were used for behavioral assessment before and after surgery. They were killed on day 35 after ischemia to obtain late invasive data. An extra group of 8 animals was added to characterize the 14-d time point as indicated in Supplemental Table 1 (supplemental materials are available at http://jnm.snmjournals.org).

On the last day of the experiment, the mice were killed by transcardial perfusion with phosphate-buffered saline. The brains that were reserved for immunoreactivity were fixed with 4% paraformaldehyde in phosphate-buffered saline, whereas the others, which were kept for real-time quantitative polymerase chain reaction, were flash-frozen in nitrogen and stored at −80°C.

Surgery

Stroke was induced by the intraluminal suture method as previously described (*12*). Briefly, the mice were anesthetized with 5% isoflurane/O_2 (Forene; Abbott) after intraperitoneal injection of buprenorphine (0.03 mg/kg of body weight) and maintained at 2.5% v/v isoflurane/O_2 on a heating pad during the entire procedure.

A 7–0 silicon rubber-coated monofilament (diameter with coating, 0.19 ± 0.01 mm) (Doccol Corp.) was inserted into the right internal carotid artery to block the middle cerebral artery origin. After 30 min, the monofilament was removed to allow reperfusion. The mice received buprenorphine (0.1 mg/kg body of weight) and were placed under the infrared heating lamp until full recovery. Successful occlusion and reperfusion of the middle cerebral artery were assessed by measuring the cerebral blood flow by laser Doppler flowmetry (Periflux 5000; Perimed).

Treatment

PLX5622 was provided by Plexxikon Inc., formulated in AIN-76A standard chow by Research Diets Inc. at 1,200 ppm and stored at 4°C until use. Both control and PLX5622-enriched diets were provided ad libitum as described in Figure 1. Body weight was reported as an index of food intake (Supplemental Fig. 1).

^{18}F-DPA-714 PET/CT Imaging

^{18}F-DPA-714 (TSPO) PET imaging was performed on days 7, 14, 21, and 30 after ischemia using a high-resolution small-animal PET scanner (32-module quadHIDAC; Oxford Positron Systems Ltd.) with a uniform spatial resolution of less than 1 mm (in full width at half maximum) over a cylindric field of view (165-mm diameter, 280-mm axial length) (*13*).

Radiotracer was prepared as previously described with more than a 99% radiochemical purity (*14*). Once anesthetized, the mice received 12.9 ± 2.2 MBq via the tail vein (specific activity, 40–80 GBq/µmol).

The animals were kept anesthetized in a warmed environment for 45 min. The scan was acquired from 45 to 65 min after injection. PET data were reconstructed using a 1-pass list-mode expectation-maximization algorithm with resolution recovery (*13*). The images were corrected only for activity decay. After the PET scan, the animal bed was transferred into a CT scanner (Inveon; Siemens Medical Solutions) with a spatial resolution of 86 μm. The PET/CT images were coregistered using a landmark approach.

MRI

T2-weighted MRI was performed on day 1 to delineate the infarct. After anesthesia (5% isoflurane/air, Forene; Abbott), the mice were positioned on a heated MRI cradle and fixed by bite and ear bars. The animals were continuously supplied with 2% isoflurane/air until the end of the experiment. Respiration and body temperature (37.0°C ± 0.5°C) were constantly monitored. A small sheet prepared from 1% v/v agar/water solution was placed directly on the animal's head to reduce susceptibility artifacts and covered with parafilm (Merck KGaA). Two different systems were used.

With the first system, the cradle was manually positioned in the center of the 9.4-T small-animal MRI scanner (Biospec 94/20; Bruker Biospin GmbH). All images were processed and generated using Paravision 5.1 (Bruker Biospin MRI). T2-weighted images were acquired with a fast spin-echo sequence (rapid acquisition with relaxation enhancement) (repetition time, 7,700 ms; effective echo time, 100 ms; rapid-acquisition-with-relaxation-enhancement factor, 30; field of view, 2 × 2 cm; slice thickness, 0.5 mm; interslice distance, 0 cm; number of slices, 20; matrix, 192 × 192; number of averages, 8).

With the second system, a T2-weighted fast spin-echo 2-dimensional sequence was acquired in a 1-T nanoScan PET/MRI scanner equipped with an MH20 coil (resolution, 0.27 × 0.27 × 0.9 mm; Mediso Medical Imaging Systems).

Behavioral Tests

Open-field (OF), grip, rotarod, and pole testing was performed to assess the treatment effect on motor function recovery as previously described (*7,15*). The 4 behavioral tests were performed the week before surgery and on days 14 and 35, as indicated in Figure 1. The protocols are described in the supplemental materials and methods.

Image Analysis

PET/CT images from the same mouse were manually coregistered with T2-weighted MR images acquired on day 1. An atlas was adjusted to anatomic landmarks, following bone structures and ventricles, and manually corrected. The infarct was delineated using a thresholding approach previously described (*11*). Uptake was assessed within the T2-weighted MRI-defined infarct, the atlas-based contralateral striatum, and manually delineated spleen. Uptake was reported as percentage injected dose per milliliter in both regions, and the infarct-to-contralateral striatum ratio was calculated.

Immunoreactivity

Brains were fixed in 4% paraformaldehyde, embedded in paraffin, and cut into 5-μm coronal sections. Immunohistochemistry and immunofluorescence were performed as previously described (*7*). Ionized calcium binding adaptor molecule 1 (Iba-1), glial fibrillary acidic protein (GFAP), and TSPO expression level were visualized and quantified by immunoreactivity. Moreover, the TSPO cellular source was assessed with Iba-1/TSPO, CSF-1R/TSPO, CD68/TSPO, and GFAP/TSPO costaining. Primary and secondary antibodies are reported in Supplemental Table 2.

Images were obtained using a confocal microscope (Eclipse NI-E; Nikon) and displayed with ImageJ software.

Real-Time Quantitative Polymerase Chain Reaction

Real-time quantitative polymerase chain reaction was performed from snap-frozen half-brain tissues as previously described (*7*). The forward- and reverse-primer sequences are reported in Supplemental Table 3. Relative gene expression was assessed using the ΔΔCt method, with Gapdh (Biomol Gmbh) as a housekeeping gene.

Statistical Analysis

All statistical analyses were performed using SigmaPlot, version 13.0 (Systat Software). The datasets were tested for normal distribution and equal variance.

The sample size was based on effect size ($P = 0.05$; power, 1-β = 0.80), mortality rates, and previous stroke studies (*7,15*), in which we investigated the therapeutic effect of dietary approaches on brain inflammation as assessed by ^{18}F-DPA-714 PET imaging. Intraindividual ^{18}F-DPA-714 PET imaging data, behavioral testing, gene expression, and immunoreactivity datasets were analyzed by repeated-measures ANOVA followed by the Sidak post hoc test for multiple comparisons, unless stated otherwise. All data are expressed as mean ± SEM.

RESULTS

Both experimental groups showed a similar infarct size on day 1 ($P = 0.59$) (Supplemental Fig. 2).

We performed longitudinal ^{18}F-DPA-714 PET/CT imaging to assess the repopulation process (Fig. 2A). ANOVA indicated significantly increased uptake within the infarct compared with the

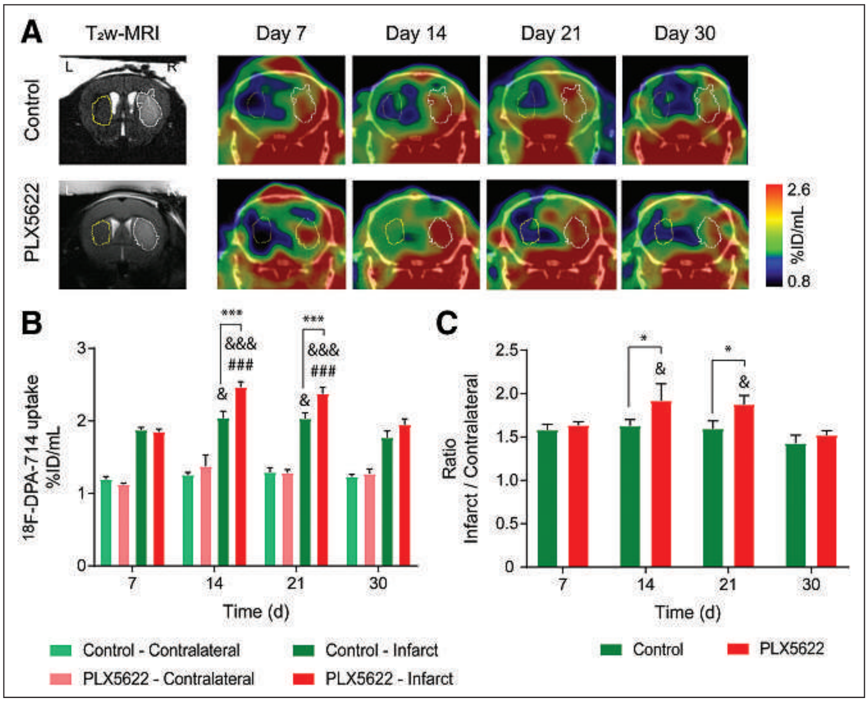

FIGURE 2. (A) Representative ^{18}F-DPA-714 PET/CT images and corresponding T2-weighted MR images. (B) Quantification of mean ^{18}F-DPA-714 uptake (percentage injected dose/mL) within infarct and contralateral striatum. (C) Infarct-to-contralateral striatum ratio. Treatment: $^{***}P < 0.005$. Day 7: $^{###}P < 0.005$. Day 30: $^{\&}P < 0.05$, $^{\&\&\&}P < 0.005$. %ID = percentage injected dose; T_2w = T2-weighted.

contralateral striatum over time (Supplemental Fig. 3). Two-way repeated-measures ANOVA indicated a significant effect of time ($P < 0.001$), treatment ($P = 0.007$), and time × treatment ($P = 0.009$) on uptake within the infarct (Fig. 2B). In the control group, intraindividual comparison indicated that the mean uptake decreased on day 30 compared with days 14 ($P = 0.024$) and 21 ($P = 0.022$). In PLX5622-treated mice, uptake increased from day 7 to day 14 ($P < 0.001$) and remained elevated on day 21 ($P < 0.001$). Later, uptake significantly decreased on day 30 compared with days 14 ($P < 0.001$) and 21 ($P < 0.001$) after ischemia. A treatment effect was observed on days 14 and 21 after ischemia: PLX5622-treated mice showed increased ^{18}F-DPA-714 uptake within the infarct on both day 14 ($P < 0.001$) and day 21 ($P = 0.002$) compared with control mice. Similarly, the infarct-to-contralateral striatum ratio indicated a significant effect of both time ($P = 0.008$) and treatment ($P = 0.043$) (Fig. 2C). Treatment effects were observed on days 14 and 21: PLX5622-treated mice showed higher mean ratios than did control mice on both day 14 ($P = 0.043$) and day 21 ($P = 0.041$). ^{18}F-DPA-714 PET imaging data on days 14 and 30 were further cross-validated by immunohistochemistry (Supplemental Fig. 4).

The temporal dynamic of ^{18}F-DPA-714 uptake within the spleen indicated a treatment effect ($P = 0.027$) on days 7 and 30 after ischemia, with PLX5622-treated mice showing higher uptake than control mice (Supplemental Fig. 5).

We determined the number of Iba-1–positive cells (microglia and macrophages) within the infarct, at the periphery of the infarct, and in the contralateral striatum for both experimental groups on both day 14 and day 35 (Supplemental Fig. 6). On day 14, qualitative assessment of Iba-1–positive cell morphology indicated a greater ramification in control than in PLX5622-treated mice at both the periphery and the contralateral side. On day 35, PLX5622-treated mice showed a significantly decreased percentage of Iba-1–positive area within the infarct compared with control mice ($P < 0.001$).

We further characterized the Iba-1–positive cell population within the infarct by immunofluorescence (Fig. 3). Both control and PLX5622-treated mice showed a mixed population of Iba-1–positive, TSPO–positive, and Iba-1–positive TSPO-negative cells within the infarct, whereas TSPO expression was higher in PLX5622-treated mice, in line with the ^{18}F-DPA-714 PET data acquired on day 14. However, PLX5622-treated mice showed a higher number of Iba-1–positive CSF-1R–positive, and Iba-1–positive CD68–positive (activated myeloid cells) cells within the infarct than did control mice, in line with the repopulation process.

We investigated the potential treatment effect of short-term CSF-1R inhibition on (GFAP-positive) astrocytes on days 14 and 35 after ischemia (Supplemental Fig.7). On day 14, PLX5622-treated mice showed a significantly higher percentage of GFAP-positive area than did control mice within the infarct ($P = 0.014$) or the contralateral striatum ($P < 0.001$). A sustained effect was observed in the contralateral striatum on day 35. However, no colocalization between GFAP and TSPO was observed, indicating that astrocytes did not contribute to ^{18}F-DPA-714 PET signal.

Gene expression of microglia- or macrophage-related markers was assessed on day 14 (Fig. 4). PLX5622-treated mice showed significantly higher *csf-1r* ($P = 0.001$) and *aif1* (also known as Iba-1) ($P = 0.008$) expression than did control mice in the contralateral hemisphere. A good correlation between *csf-1r* and *aif1* was observed ($R^2 = 0.86$, $P = 0.34$, Supplemental Fig. 8). Moreover, PLX5622-treated mice showed a significant increase in *p2ry12* expression, a marker for antiinflammatory activated microglia, compared with control mice in both infarct ($P = 0.043$) and contralateral ($P = 0.01$) hemispheres. On the other hand, PLX5622 treatment significantly decreased *cx3cr1* (fractalkine receptor constitutively present on microglia and macrophages, $P = 0.009$) in the contralateral hemisphere and *mrc1* (mannose receptor expressed by central nervous system macrophages, $P = 0.009$) expression in the infarct hemisphere. Expression of *ccr2,* found mostly on monocytes, was significantly increased in the contralateral hemisphere ($P = 0.002$) but decreased in the ipsilateral hemisphere ($P = 0.048$) (Fig. 4). No treatment effect was observed on *trem2* expression, a marker of phagocytic activity ($P > 0.05$). Gene expression analysis on day 35 after ischemia indicated long-lasting treatment effects on *aif1, cx3cr1,* and *trem2* gene expression (Supplemental Fig. 9).

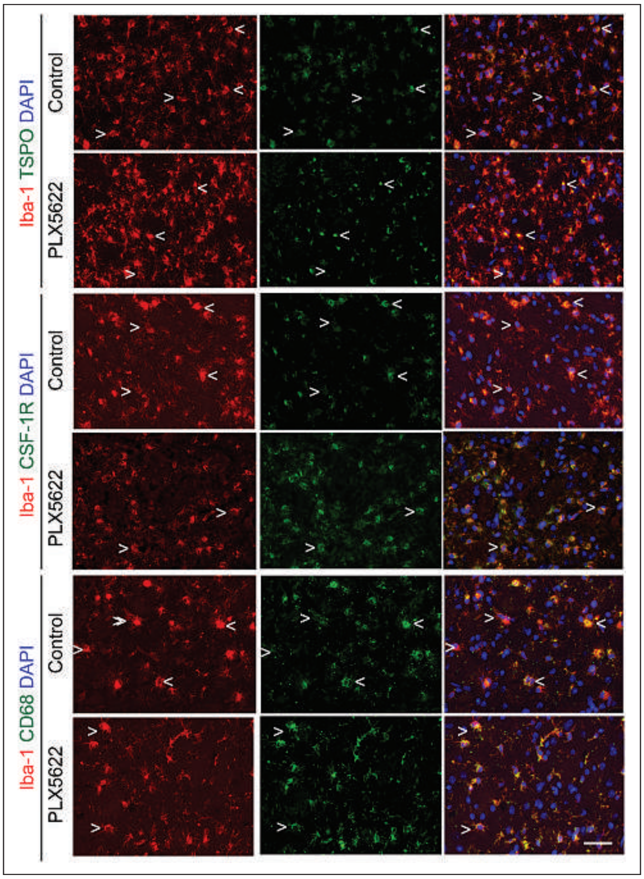

FIGURE 3. Immunofluorescent staining for TSPO, CSF-1R, and CD68 in Iba-1–positive cell population in both control and PLX5622-treated mice on day 14 after ischemia. < = Iba-1–positive cell positive for marker; > = Iba-1–positive cell negative for marker; scale bar = 20 μm. DAPI = 4′,6-diamidino-2-phenylindole.

Behavioral tests indicated that PLX5622-treated mice traveled a longer distance ($P < 0.001$) and more quickly on day 14 ($P = 0.009$) than did control mice in the OF (Figs. 5A and 5B). A treatment effect was also observed on the latency to fall in the rotarod test, with PLX5622-treated mice having an increased latency to fall compared with control mice ($P < 0.005$) on both day 14 and day 35 after ischemia (Fig. 5C). No treatment effect was observed on motor functions or coordination assessed with the pole test ($P = 0.47$) (Fig. 5D). Additionally, forelimb strength was significantly better

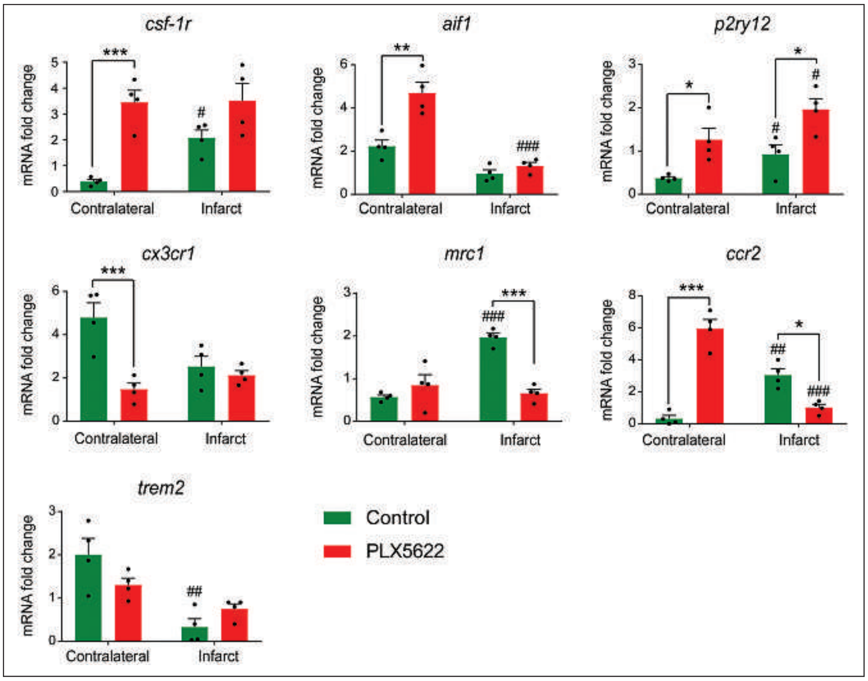

FIGURE 4. Gene expression of microglia- or macrophage-related markers on day 14 after ischemia. Treatment: $^{*}P < 0.05$, $^{**}P < 0.01$, $^{***}P < 0.005$. Contralateral hemisphere: $^{\#}P < 0.05$, $^{\#\#}P < 0.01$, $^{\#\#\#}P < 0.005$. mRNA = messenger RNA.

in PLX5622-treated mice on day 14 ($P = 0.038$) (Fig. 5E). No correlation between behavioral parameters and tracer uptake on day 14 was observed (OF $R^2 = 0.01$ [$P = 0.34$], rotarod $R^2 = 0.1$ [$P = 0.44$], grip $R^2 = 0.55$ [$P = 0.11$]).

DISCUSSION

In this study, we investigated for the first time (to our knowledge) the immunomodulatory effect of CSF-1R inhibition–induced microglia repopulation in the subacute ischemic period using in vivo multimodal imaging. We demonstrated that ^{18}F-DPA-714 PET imaging serves as a sensitive biomarker of glial repopulation. In both experimental groups, the Iba-1–positive cell population was one of the major sources of TSPO expression whereas astrocytes did not express TSPO. After 1 wk of repopulation, the Iba-1–positive cells displayed significantly higher expression of TSPO, CSF-1R, and CD68, with altered morphology at the periphery of the infarct and in the contralateral striatum, indicative of an activated state. Gene expression analysis indicated a treatment effect on microglia- and macrophage-related gene expression in line with the repopulation process. *Csf-1r* and *p2ry12* expression increased during repopulation, and increased *csf-1r* expression positively correlated with *aif1* levels, indicative of microglia and macrophage repopulation with a potential switch toward an antiinflammatory state. Gene expression of peripheral cell recruitment markers was altered during repopulation, indicating increased recruitment of peripheral immune cells during microglia depletion whereas repopulation may reverse the effect. This hypothesis was supported by the significantly increased spleen uptake after depletion, as a sign of increased systemic inflammation, and by the subsequent decrease during the repopulation process in PLX5622-treated mice. Additionally, functional outcomes were improved with repopulation: PLX5622-treated mice showed faster motor recovery on day 14 after ischemia, including a longer distance traveled and a higher velocity in 3 of the 4 selected tests, suggesting that repopulation could rescue motor functions. Altogether, this study highlighted the renewal of the microglia and macrophage compartment with CSF-1R inhibitor as a possible new immunomodulatory treatment paradigm after stroke that might be tracked by ^{18}F-DPA-714 PET imaging.

TSPO is a transmembrane protein found at the outer mitochondrial membrane involved in metabolic functions (*16*). TSPO expression is markedly increased in glial cells (microglia and astrocytes) and peripheral immune cells (monocytes and lymphocytes) under inflammatory conditions, making it a suitable biomarker of inflammation or activated immune cells (*17*).

^{18}F-DPA-714 PET has been used in many translational studies to track TSPO-dependent inflammatory reactions after stroke (*7,9,10,15*). Many studies have confirmed that the dynamics of ^{18}F-DPA-714 tracer correlate with CD11b-positive TSPO-positive or Iba-1–positive TSPO-positive cell number, supporting its use for in vivo tracking of microglia- and macrophage-targeting immunomodulatory therapies. However, TSPO PET imaging alone may not be suitable to determine a treatment time window or assess the therapeutic outcome. The main reason is that TSPO has multiple cellular sources, which show a continuum of differentiated states going from pro- to antiinflammatory phenotypes. Therefore, interpretation of the TSPO PET signal benefits from dedicated ex vivo analyses for characterization of the inflammatory response. Nevertheless, in vivo PET imaging may support the determination of therapeutic windows of immunomodulatory compounds by allowing intraindividual follow-up and visualization of disease-relevant molecular processes.

This study supports the use of ^{18}F-DPA-714 to track microglia/macrophage repopulation after CSF-1R inhibitor withdrawal. We observed an increased TSPO PET signal within the infarct on days 14 and 21, cross-validated by immunohistochemistry or fluorescence. Dual labeling indicated Iba-1–positive cells as one of the major cellular sources of TSPO expression, whereas astrocytes did not show any TSPO expression, indicating that uptake was modulated mostly by the microglia/macrophage activity.

On the basis of previously published data (*7*), a partial depletion can be expected. According to previous studies, CSF-1R inhibition triggers increased peripheral immune cell infiltration (*4,5*). Altogether, it could explain the similar uptake at the end of the treatment period (day 7). Additionally, a recent report indicated that the repopulation kinetic depends on the extent of microglia depletion (*18*). Partial depletion resulted in a slower repopulation rate than did full depletion. Microglia numbers did not recover within the first week after partial depletion, whereas the numbers exceeded control level by +160% after complete depletion (*19*). This effect may partly explain the significantly increased TSPO expression on days 14 and 21 after ischemia. Expression of many microglia-related markers was increased on day 14 after ischemia in the infarct or contralateral hemisphere, in line with the repopulation process.

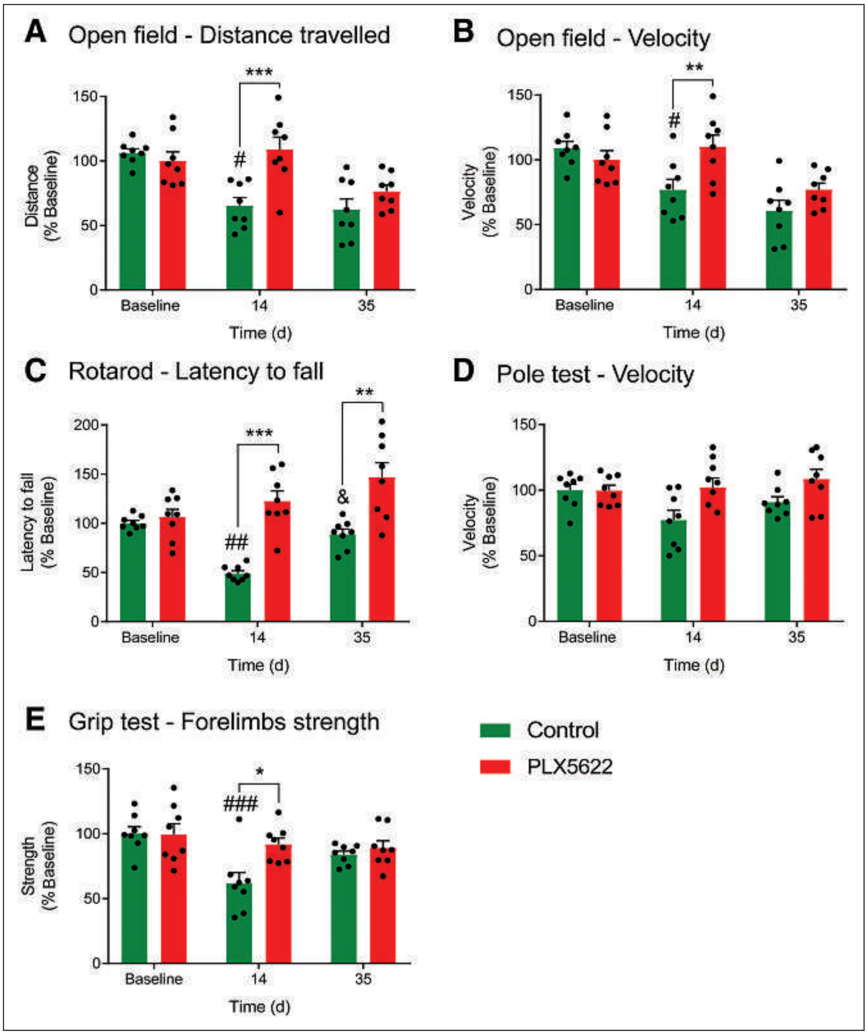

FIGURE 5. Behavioral tests: distance traveled (A), speed in open field (B), latency to fall during rotarod test (C), velocity during pole test (D), and forelimb strength as assessed with grip test (E). Treatment: $^{*}P < 0.05$, $^{**}P < 0.01$, $^{***}P < 0.005$. Baseline: $^{\#}P < 0.05$, $^{\#\#}P < 0.01$, $^{\#\#\#}P < 0.005$. Day 14: $^{\&}P < 0.05$.

The CSF-1R/CSF-1 axis regulates developmental functions such as proliferation and survival of microglia (*20*). Here, our data indicated a global significant increase in *csf-1r* and CSF-1R expression in PLX5622-treated mice on day 14 after ischemia, compared with control animals, as a sign of microglia repopulation after inhibitor withdrawal. Additionally, P2ry12 is a specific marker for microglia that is downregulated in a proinflammatory environment and upregulated with exposure to antiinflammatory stimuli, turning into an interesting biomarker for antiinflammatory microglia (*21*). Our data indicated a flare effect on *p2ry12* expression on day 14 after ischemia, suggesting that repopulation may trigger a beneficial antiinflammatory state favoring tissue recovery. Further characterization indicated the presence of a highly activated Iba-1–positive CD68–positive cell population in PLX5622-treated mice triggered by the repopulation process, as previously reported (*18*).

Although gene expression analysis indicated increased microglia-related genes such as *csf-1r, p2ry12,* and *aif1*, peripheral immune cell–related genes such as *ccr2* and *cx3cr1* were significantly downregulated during repopulation within the infarct. Therefore, we hypothesized that subacute CSF-1R inhibition triggered peripheral recruitment and that repopulation reversed the process. Supporting this hypothesis, we observed significantly increased ^{18}F-DPA-714 uptake in the spleen during depletion, suggesting an increased adaptive or peripheral inflammatory response with treatment. However, uptake in peripheral organs must be corrected for metabolites for exact interpretation. Still, we supported previous studies showing that CSF-1R inhibition could trigger the engraftment of peripherally derived macrophages into parenchyma and that repopulation reduced gene expression involved in monocyte chemoattraction and leukocyte transmigration (*3,4,22*).

In our model of mild cerebral ischemia, repopulation accelerated motor function recovery as shown in 3 of the 4 behavioral tests. Behavioral parameters did not correlate with the TSPO PET signal assessed on day 14. We hypothesized that changes in the immune cell population could partly explain the faster recovery in PLX5622-treated mice, including renewal of the microglia compartment or an increased antiinflammatory central or peripheral cell population within the infarct. A few studies reported that short-term depletion after a brain lesion promoted functional recovery (*3,23*), correlating with changes in neuroprotective factor expression.

Late invasive data indicated that repopulation reduced the number of Iba-1–positive cells within the infarct, decreased *cx3cr1* expression and *trem2*-dependent phagocytic activity on day 35 after ischemia, but increased astrogliosis. This result suggests that repopulation may resolve the stroke-induced microglia and macrophage phenotype.

CONCLUSION

We demonstrated that microglia/macrophage repopulation after short-term CSF-1R inhibition could be assessed by in vivo ^{18}F-DPA-714 PET/CT and MR imaging. Repopulation induced changes in glial morphology, phenotype, gene expression, and cell recruitment, with signs of improved functional recovery. Further evaluations should identify which cell subpopulations are responsive to CSF-1R inhibition and repopulation. Overall, we propose a promising immunotherapy paradigm targeting microglia activity potentiating stroke recovery.

DISCLOSURE

This work was partly funded by the Horizon 2020 Programme under grant agreement 675417 (PET3D); the "Cells-in-Motion" Cluster of Excellence (DFG EXC1003–CiM), Münster, Germany; the Interdisciplinary Center for Clinical Research (IZKF core unit PIX), Münster, Germany; and the Herbert Worch Foundation, Bonn, Germany. No other potential conflict of interest relevant to this article was reported.

ACKNOWLEDGMENTS

We thank Dirk Reinhardt, Sarah Köster, Christine Bätza, Roman Priebe, Stefanie Bouma, Irmgard Hoppe, Christa Möllmann, Nina Knubel, and Florian Breuer for their excellent technical support.

KEY POINTS

QUESTION: Is PET imaging a valuable tool to assess the immunomodulatory effect of microglia-targeting therapy?

PERTINENT FINDINGS: Brain repopulation in the inflammatory environment showed therapeutic effects on stroke outcomes.

IMPLICATIONS FOR PATIENT CARE: ^{18}F-DPA-714 PET imaging allows tracking of the repopulation process after short-term CSF-1R inhibition.

REFERENCES

1. Jiang CT, Wu W, Deng Y, Ge J. Modulators of microglia activation and polarization in ischemic stroke. *Mol Med Rep.* 2020;21:2006–2018.
2. Elmore MRP, Najafi AR, Koike MA, et al. Colony-stimulating factor 1 receptor signaling is necessary for microglia viability, unmasking a microglia progenitor cell in the adult brain. *Neuron.* 2014;82:380–397.
3. Rice RA, Pham J, Lee RJ, Najafi AR, West BL, Green KN. Microglial repopulation resolves inflammation and promotes brain recovery after injury. *Glia.* 2017; 65:931–944.
4. Otxoa-de-Amezaga A, Miró-Mur F, Pedragosa J, et al. Microglial cell loss after ischemic stroke favors brain neutrophil accumulation. *Acta Neuropathol (Berl).* 2019;137:321–341.
5. Jin W-N, Shi SX-Y, Li Z, et al. Depletion of microglia exacerbates postischemic inflammation and brain injury. *J Cereb Blood Flow Metab.* 2017;37: 2224–2236.
6. Lei F, Cui N, Zhou C, Chodosh J, Vavvas DG, Paschalis EI. CSF1R inhibition by a small-molecule inhibitor is not microglia specific; affecting hematopoiesis and the function of macrophages. *Proc Natl Acad Sci U S A.* 2020;117:23336–23338.
7. Barca C, Kiliaan AJ, Foray C, et al. A longitudinal PET/MRI study of colony-stimulating factor 1 receptor-mediated microglia depletion in experimental stroke. *J Nucl Med.* 2022;63:446–452.
8. Szalay G, Martinecz B, Lénárt N, et al. Microglia protect against brain injury and their selective elimination dysregulates neuronal network activity after stroke. *Nat Commun.* 2016;7:11499.
9. Martín A, Boisgard R, Thézé B, et al. Evaluation of the PBR/TSPO radioligand ^{18}F-DPA-714 in a rat model of focal cerebral ischemia. *J Cereb Blood Flow Metab.* 2010;30:230–241.
10. Zinnhardt B, Viel T, Wachsmuth L, et al. Multimodal imaging reveals temporal and spatial microglia and matrix metalloproteinase activity after experimental stroke. *J Cereb Blood Flow Metab.* 2015;35:1711–1721.
11. Barca C, Foray C, Hermann S, et al. Characterization of the inflammatory postischemic tissue by full volumetric analysis of a multimodal imaging dataset. *Neuroimage.* 2020;222:117217.
12. Engel O, Kolodziej S, Dirnagl U, Prinz V. Modeling stroke in mice: middle cerebral artery occlusion with the filament model. *J Vis Exp.* 2011;47:2423.
13. Schäfers KP, Reader AJ, Kriens M, Knoess C, Schober O, Schäfers M. Performance evaluation of the 32-module quadHIDAC small-animal PET scanner. *J Nucl Med.* 2005;46:996–1004.
14. James ML, Fulton RR, Vercoullie J, et al. DPA-714, a new translocator protein-specific ligand: synthesis, radiofluorination, and pharmacologic characterization. *J Nucl Med.* 2008;49:814–822.
15. Barca C, Wiesmann M, Calahorra J, et al. Impact of hydroxytyrosol on stroke: tracking therapy response on neuroinflammation and cerebrovascular parameters using PET-MR imaging and on functional outcomes. *Theranostics.* 2021;11:4030–4049.
16. Veenman L, Gavish M. The role of 18 kDa mitochondrial translocator protein (TSPO) in programmed cell death, and effects of steroids on TSPO expression. *Curr Mol Med.* 2012;12:398–412.
17. Varrone A, Lammertsma AA. Imaging of neuroinflammation: TSPO and beyond. *Clin Transl Imaging.* 2015;3:389–390.
18. Najafi AR, Crapser J, Jiang S, et al. A limited capacity for microglial repopulation in the adult brain. *Glia.* 2018;66:2385–2396.
19. Elmore MRP, Lee RJ, West BL, Green KN. Characterizing newly repopulated microglia in the adult mouse: impacts on animal behavior, cell morphology, and neuroinflammation. *PLoS One.* 2015;10:e0122912.
20. Stanley ER, Chitu V. CSF-1 receptor signaling in myeloid cells. *Cold Spring Harb Perspect Biol.* 2014;6:a021857.
21. Villa A, Klein B, Janssen B, et al. Identification of new molecular targets for PET imaging of the microglial anti-inflammatory activation state. *Theranostics.* 2018;8: 5400–5418.
22. Cronk JC, Filiano AJ, Louveau A, et al. Peripherally derived macrophages can engraft the brain independent of irradiation and maintain an identity distinct from microglia. *J Exp Med.* 2018;215:1627–1647.
23. Henry RJ, Ritzel RM, Barrett JP, et al. Microglial depletion with CSF1R inhibitor during chronic phase of experimental traumatic brain injury reduces neurodegeneration and neurological deficits. *J Neurosci.* 2020;40:2960–2974.

Cardiac Fibroblast Activation in Patients Early After Acute Myocardial Infarction: Integration with MR Tissue Characterization and Subsequent Functional Outcome

Johanna Diekmann*[1], Tobias Koenig*[2], James T. Thackeray[1], Thorsten Derlin[1], Christoph Czerner[1,2], Jonas Neuser[2], Tobias L. Ross[1], Andreas Schäfer[2], Jochen Tillmanns[2], Johann Bauersachs*[2], and Frank M. Bengel*[1]

[1]Department of Nuclear Medicine, Hannover Medical School, Hannover, Germany; and [2]Department of Cardiology and Angiology, Hannover Medical School, Hannover, Germany

After acute myocardial infarction (AMI), fibroblast activation protein (FAP) upregulation exceeds the infarct region. We sought further insights into the physiologic relevance by correlating FAP-targeted PET with tissue characteristics from cardiac MRI (CMR) and functional outcome. **Methods:** Thirty-five patients underwent CMR, perfusion SPECT, and ^{68}Ga-FAP inhibitor (FAPI)-46 PET/CT within 11 d after AMI. Infarct size was determined from SPECT by comparison to a reference database. For PET, regional SUVs and isocontour volumes of interest determined the extent of cardiac FAP upregulation (FAP volume). CMR yielded functional parameters, area of injury (late gadolinium enhancement [LGE]) and T1/T2 mapping. Follow-up was available from echocardiography or CMR after 139.5 d (interquartile range, 80.5–188.25 d) (n = 14). **Results:** The area of FAP upregulation was significantly larger than the SPECT perfusion defect size (58% ± 15% vs. 23% ± 17%, $P < 0.001$) and infarct area by LGE (28% ± 11%, $P < 0.001$). FAP volume significantly correlated with CMR parameters at baseline (all $P < 0.001$): infarct area ($r = 0.58$), left ventricle (LV) mass ($r = 0.69$), end-systolic volume ($r = 0.62$), and end-diastolic volume ($r = 0.57$). Segmental analysis revealed FAP upregulation in 308 of 496 myocardial segments (62%). Significant LGE was found in only 56% of FAP-positive segments, elevated T1 in 74%, and elevated T2 in 68%. Fourteen percent (44/308) of FAP-positive segments exhibited neither prolonged T1 or T2 nor significant LGE. Of note, FAP volume correlated only weakly with simultaneously measured LV ejection fraction at baseline ($r = -0.32$, $P = 0.07$), whereas there was a significant inverse correlation with LV ejection fraction obtained at later follow-up ($r = -0.58$, $P = 0.007$). **Conclusion:** Early after AMI and reperfusion therapy, activation of fibroblasts markedly exceeds the hypoperfused infarct region and involves noninfarcted myocardium. The ^{68}Ga-FAPI PET signal does not match regional myocardial tissue characteristics as defined by CMR but is predictive of the evolution of ventricular dysfunction. FAP-targeted imaging may provide a novel biomarker of LV remodeling that is complementary to existing techniques.

Key Words: myocardial infarction; fibroblast activation protein; PET; left ventricular remodeling

J Nucl Med 2022; 63:1415–1423
DOI: 10.2967/jnumed.121.263555

Fibrotic tissue remodeling after injury leads to functional impairment and an adverse outcome in the affected structure or organ. In cardiac disease, myocardial fibrosis contributes to the development and progression of heart failure. Recent evidence has highlighted molecular pathways that activate quiescent cardiac fibroblasts, which have emerged as attractive therapeutic targets to support cardiac repair and mitigate loss of function (*1–4*).

Acute myocardial infarction (AMI) is an important contributor to the development of heart failure (*5*). An immediate and organized inflammatory immune reaction triggers the activation of quiescent fibroblasts (*6,7*). Activated myofibroblasts migrate to injured tissue and contribute to fibrotic scar formation. A sufficient scar is required for adequate repair, but an excessive profibrotic response and involvement of remote myocardium support adverse ventricular remodeling, culminating in progressive contractile dysfunction (*6,8*). Accordingly, whereas fibrosis has emerged as a potential therapeutic target, its double-edged nature after AMI likely requires a personalized approach for medical decision making. Noninvasive, quantitative, fibrosis-targeted imaging may be instrumental for this purpose.

Fibroblast activation protein (FAP) is a membrane-bound serine protease (*2,9*) highly expressed by activated myofibroblasts. Recently, several FAP inhibitors (FAPIs) have been introduced for targeted PET. Initially, ^{68}Ga-FAPI PET was used for imaging of various tumors (*10*), but retrospective analysis of oncologic cohorts established an association between FAP signal and cardiac risk factors, including arterial hypertension and diabetes mellitus (*11*). Increased cardiac signal has also been reported after chemotherapy or chest radiotherapy (*12*). Recently, experimental studies supported the feasibility of ^{68}Ga-FAPI PET to identify fibroblast activation in animal models of AMI (*13,14*). Additionally, clinical reports confirmed a strong ^{68}Ga-FAPI PET signal in patients with AMI—signal that frequently exceeded the nonviable infarct area (*15–17*). Whether this phenomenon is predictive of adverse functional outcome, however, remains unknown. Likewise, the relationship between ^{68}Ga-FAPI PET signal and cardiac MRI (CMR) tissue characteristics is not well defined. CMR identifies late gadolinium enhancement (LGE) in injured regions, and it provides extracellular volume and native T1 and T2 relaxation times as measures of tissue fibrosis (T1) and edema (T2) throughout the entire myocardium (*18*). In contrast to ^{68}Ga-FAPI PET, which identifies a cellular signal from activated myofibroblasts, these CMR-derived parameters reflect mostly extracellular tissue composition.

We hypothesized that ^{68}Ga-FAPI PET reflects a myocardial signal early after AMI that is not identical to CMR-derived tissue

---

Received Nov. 23, 2021; revision accepted Feb. 17, 2022.

For correspondence or reprints, contact Frank M. Bengel (bengel.frank@mh-hannover.de) or Johanna Diekmann (diekmann.johanna@mh-hannover.de).

*Contributed equally to this work.

characteristics and that predicts later development of ventricular dysfunction. Our hypothesis was tested on a cohort of AMI patients who underwent multiparametric, multimodality noninvasive cardiac imaging early after standard-of-care reperfusion therapy.

MATERIALS AND METHODS

Study Design and Participants

This retrospective single-center study included 35 consecutive patients (30 men, 5 women; mean age ± SD, 57 ± 11 y) who had undergone clinical resting myocardial perfusion SPECT, FAP-targeted PET with ^{68}Ga-FAPI-46, and CMR within 11 d after reperfusion therapy for AMI at Hannover Medical School. All subjects had been treated by percutaneous coronary intervention and stenting within 4 ± 3 h of symptom onset and received dual-antiplatelet therapy. All had ST-segment elevation, absence of a prior history of AMI or coronary intervention or other cardiac procedures, success of reperfusion immediately after angioplasty, absence of systemic immunologic or infectious or profibrotic disease, and availability of complete imaging datasets, clinical records, and laboratory parameters. Clinical characteristics and medication at the time of imaging are summarized in Table 1. Routinely recorded laboratory values, as determined by standard Hannover Medical School clinical procedures, included peak creatine kinase as a

TABLE 1
Characteristics of the 35 Patients

Variable	Characteristic	Data
Age (y)		57 ± 11
Sex	Female	5/35 (14.3)
	Male	30/35 (85.7)
Height (cm)		178 ± 7
Weight (kg)		86.8 ± 15.8
Cardiovascular risk factors	Diabetes	11/35 (31.4)
	Arterial hypertension	19/35 (54.3)
	Dyslipidemia	25/35 (71.4)
	Obesity (BMI > 30 kg/m^2)	9/35 (25.7)
	Smoking	21/35 (60.0)
Culprit vessel	LAD	24/35 (68.6)
	LCX	3/35 (8.6)
	RCA	8/35 (22.9)
Symptom to wire time (min)		234 ± 190
Peak creatine kinase (U/L)		3416 ± 3104
Peak C-reactive protein (mg/L)		42.6 ± 53.2
Peak leukocyte count (1,000/mm^3)		14.4 ± 4.4
Peak creatinine (mg/dL)		97.1 ± 20.7
Medication at PET	ASS	32/35 (91.4)
	P2Y12 antagonists	35/35 (100)
	OAK	3/35 (8.5)
	Statins	35/35 (100)
	β-blockers	33/35 (94.3)
	Noninsulin glucose-lowering drugs	11/35 (31.4)
	Insulin	2/35 (5.7)
	ACE inhibitors	22/35 (62.9)
	ATII blockers	13/35 (37.1)

BMI = body mass index; LAD = left anterior descending coronary artery; LCX = left circumflex coronary artery; RCA = right coronary artery; ASS = aspirin; P2Y12 = the adenosine diphosphate receptor on platelets; OAK = oral anticoagulation; ACE = angiotensin-converting enzyme; ATII = angiotensin 2.

Qualitative data are number and percentage; continuous data are mean ± SD.

TABLE 2
CMR Data for the 35 Patients

Global function parameters	Mean ± SD	Range
LVM (g)	132.6 ± 27.4	87–183
EDV (mL)	144.5 ± 35.5	79–206
ESV (mL)	79.9 ± 25.0	40–139
SV (mL)	64.7 ± 20.1	25–105
LVEF (%)	45.1 ± 9.6	23–64
LGE (mL)	39.9 ± 19.0	0.8–87
LGE (% of ventricle)	28.3 ± 11.2	0.7–49
MO (%)	1.0 ± 1.2	0–5.2

LVM = LV mass; EDV = end-diastolic volume; ESV = end-systolic volume; SV = stroke volume; MO = microvascular obstruction.

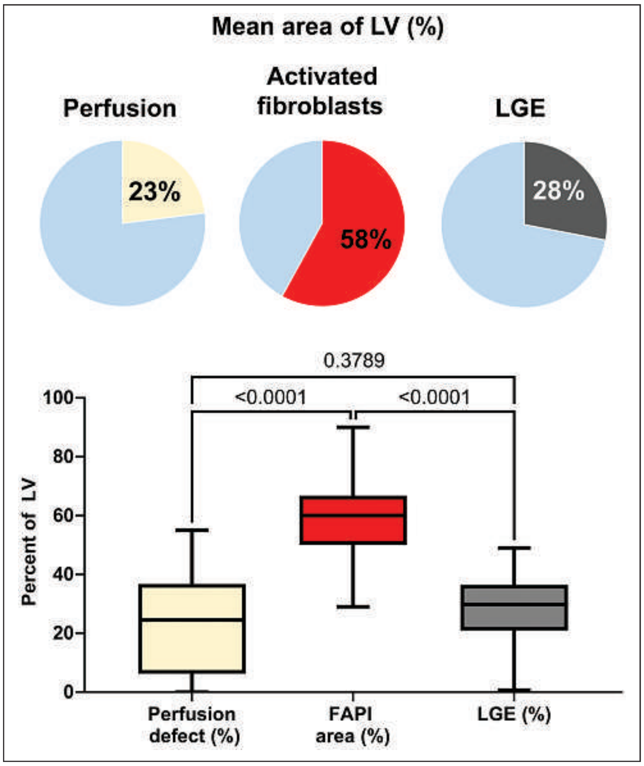

FIGURE 1. Box plot of perfusion defect size (yellow), activated fibroblasts (red), and LGE (gray) in entire patient group, expressed as percentage of LV. Bars are mean with range.

marker of myocardial injury, and C-reactive protein and leukocyte count as markers of systemic inflammatory response. The institutional review board approved the project (approval 9553_BO_K_2021), and all subjects signed a consent form.

Radionuclide Imaging

At 5.0 ± 1.5 d after AMI (median, 5.0; range, 3–8 d), resting myocardial perfusion SPECT was performed to determine the success of reperfusion, using 388 ± 32 MBq of ^{99m}Tc-tetrofosmin and a dedicated cardiac camera (Discovery 530c; GE Healthcare). Infarct size was determined using commercially available software for polar map generation (4DM; Invia) and a local reference database for comparison.

FAP-targeted PET was conducted at 7.5 ± 1.3 d (range, 5–11 d) using the specific ligand ^{68}Ga-FAPI-46, which was synthesized in-house by good manufacturing practices as previously described (*19*) and used clinically according to §13.2b of the German Pharmaceuticals Act, for determination of myocardial injury. Static PET images were acquired for 20 min using a Biograph mCT 128 PET/CT system (Siemens), beginning 60 min after intravenous injection of 114 ± 22 MBq of ^{68}Ga-FAPI-46. Low-dose CT was used for attenuation correction. Images were iteratively reconstructed, using time-of-flight and point-spread-function information (True X; Siemens). SUV_{peak} and SUV_{mean} were obtained for infarct, remote myocardium, blood pool (left atrium), and other organs using volumes of interest of 1 cm^3 and commercial software (syngo.via, V50B; Siemens Healthcare). Cardiac FAP volume was determined by an isocontour volume of interest including all voxels above an individual threshold (blood pool SUV_{mean} +2 SDs). We set this threshold because of lack of an established alternative standard. Additionally, the area of FAP upregulation was calculated by polar map analysis, using the same threshold, as previously described (*15*). Mean segmental SUV was calculated using the AHA 17-segment model and polar maps.

CMR

CMR was performed using a 1.5-T scanner (Magnetom Avanto; Siemens) in 33 of 35 patients (94%) at 4 ± 2 d after AMI (median, 4; range, 2–10 d). Cine images were obtained using a balanced steady-state free-precession sequence (True FISP; Siemens). Parametric T1 and T2 maps were acquired in 3 short-axis slices (basal, midventricular, and apical left ventricle [LV] covering 16 segments [available for 31 patients]). T1 mapping was performed using the modified look-locker inversion recovery sequence before (native) and after administration of contrast agent. Quantitative balanced steady-state free-procession–based T2 maps (True FISP) were acquired in corresponding short-axis slices. The upper threshold of normal T1 was defined as 1,023 ms and T2 as 60 ms according to our clinical standard (*20,21*). LGE was imaged by phase-sensitive inversion recovery sequences, 10–15 min after injection of a 0.15 mmol/kg bolus of gadolinium-diethylenetriaminepentaacetic acid (gadobutrol; Bayer Healthcare). Extracellular volume fraction was calculated by measurement of myocardial and blood T1 relaxation times before and after administration of contrast agent and using hematocrit value. Global analysis included determination of LV ejection fraction (LVEF), volumes, mass, extent of LGE, and microvascular obstruction. Segmental analysis included wall thickening, native T1 and T2 relaxation times, and extracellular volume fraction, using the 16-segment model. cvi42 software (Circle Cardiovascular Imaging) was used.

Follow-up LV Function

In 14 of 35 patients (40%), follow-up LVEF was available from standardized in-house echocardiography (biplane Simpson method, $n = 12$) or repeat cine CMR ($n = 2$), at a mean of 133 ± 63 d (median, 140 d; range, 42–214 d) after AMI.

Statistical Analysis

Statistical analyses were performed using SPSS, version 27, and GraphPad Prism, version 9. Categoric variables are presented with absolute and relative frequencies. For quantitative continuous variables, testing of gaussian distribution was performed using Shapiro– Wilk tests. For data with a gaussian distribution, paired Student t tests or 1-way ANOVA with Tukey multiple-comparison tests were used. Nonparametric unpaired data were analyzed with Mann–Whitney U tests. Pearson correlation coefficients were calculated for bivariate correlation analyses. All statistical analyses were performed 2-sided, and a P value of less than 0.05 indicated statistical significance.

RESULTS

FAP Signal Exceeds the Infarct Region and Correlates with Blood Markers of Tissue Damage and Inflammation

The perfusion defect size in SPECT was 23% ± 17% of the LV, ranging from 0% to 55%. In 7 of 35 (20.0%) patients, complete

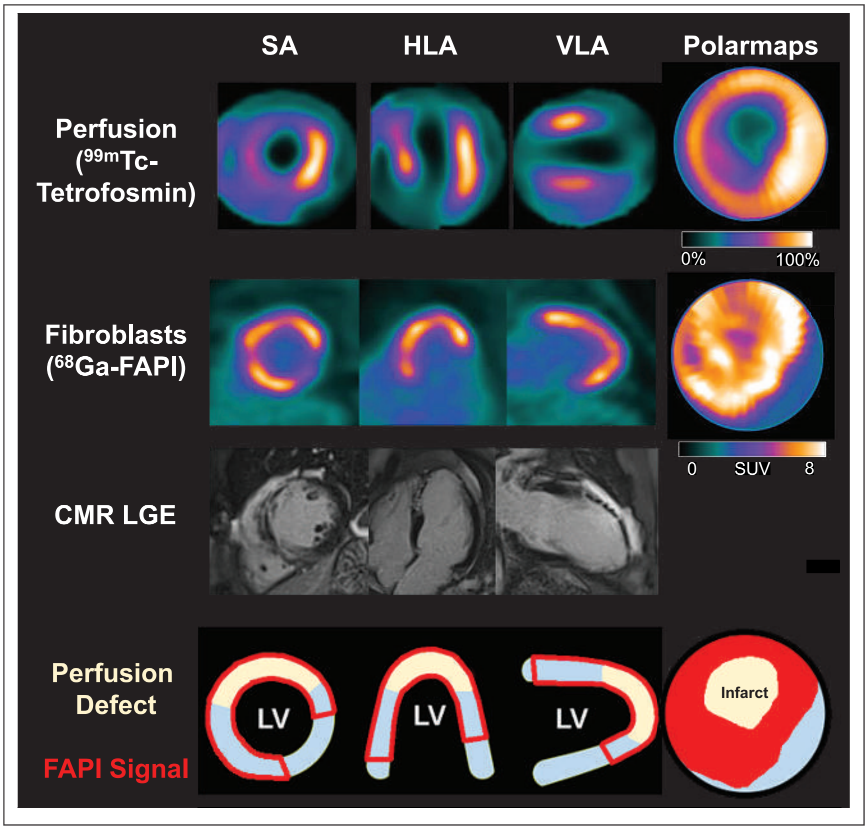

FIGURE 2. Myocardial perfusion images using ^{99m}Tc-tetrofosmin at rest, ^{68}Ga-FAPI PET, LGE from CMR, and schematic drawings of LV. Area of fibroblast activation as indicated by ^{68}Ga-FAPI-46 PET signal exceeds infarct area and LGE signal, the most common type of myocardial FAP distribution. HLA = horizontal long axis; SA = short axis; VLA = vertical long axis.

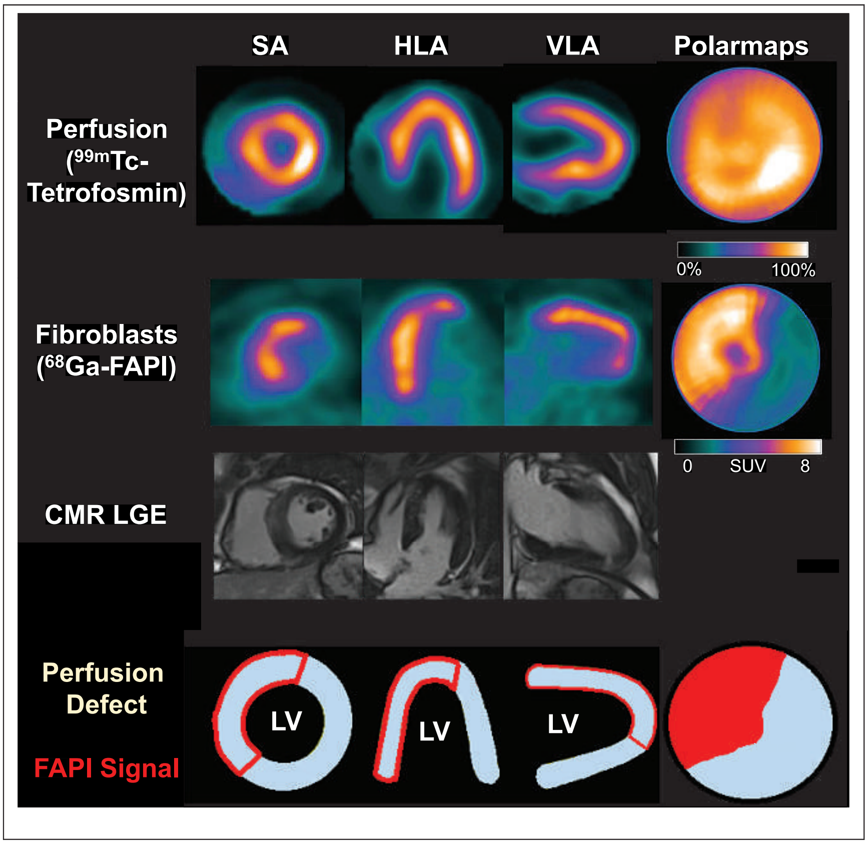

FIGURE 3. Myocardial perfusion images using ^{99m}Tc-tetrofosmin at rest, ^{68}Ga-FAPI PET, LGE from CMR, and schematic drawings of LV. No relevant perfusion defect is seen after AMI, because of complete reperfusion, and there is no significant LGE, but large area of fibroblast activation is seen. HLA = horizontal long axis; SA = short axis; VLA = vertical long axis.

reperfusion was documented by absence of a significant perfusion defect. Myocardial injury as measured by LGE volume comprised 40 ± 19 mL, or 28% ± 11% of the LV (range, 1%–49%), and correlated with perfusion defect size ($r = 0.646$, $P < 0.001$). Other CMR-derived global parameters are summarized in Table 2.

^{68}Ga-FAPI PET showed a significantly elevated signal in the territory of the culprit infarct vessel (SUV_{peak}, 6.4 ± 1.5) in all patients. PET imaging ranged from 5 to 11 d after AMI, and no significant relationship between myocardial FAP volume and time after AMI was detected within this interval (Spearman ρ: $r = 0.056$, $P = 0.750$). Consistent with prior reports, most patients showed markedly increased areas of elevated FAP signal when compared with either the SPECT perfusion defect (58% ± 15% vs. 23% ± 17%, $P < 0.001$) or the extent of myocardial injury measured by LGE (28% ± 11%, $P < 0.001$; Figs. 1 and 2). Even among the 7 patients with complete reperfusion and absence of a SPECT perfusion defect, an elevated FAP signal was consistently detected in the affected coronary territory (Fig. 3). Low amounts of LGE were detected in patients without a residual SPECT perfusion defect; however, LGE was less prominent than in other patients (13.7% ± 9.8% vs. 31.5% ± 8.8%, $P < 0.001$), and FAP signal was significantly greater (54.7% ± 19.4%, $P < 0.001$). Only 3 of 35 patients had a difference between FAP area and an infarct size of less than 15%, all of whom exhibited large perfusion defects (Fig. 4). The area of FAP upregulation correlated with perfusion defect size ($r = 0.407$, $P = 0.015$) and LGE ($r = 0.344$, $P = 0.050$), suggesting that larger infarcts also lead to larger amounts of replacement fibrosis. However, the mismatch area between FAP area and perfusion defect size as a marker of viable myocardium with activated fibroblasts inversely correlated with perfusion defect size ($r = -0.622$, $P < 0.001$). The specific number of days after AMI at which imaging was performed in this study did not have a significant effect on differences between CMR, perfusion, and ^{68}Ga-FAPI PET patterns. Further results of ^{68}Ga-FAPI PET are summarized in Table 3. Only 2 patients presented with small amounts of microvascular obstruction (<5%). At 69% (24/35), the left anterior descending coronary artery was the most frequent culprit vessel (Table 1). FAP area was larger than in the other coronary territories (left anterior descending coronary artery, 64.8 ± 12.6, vs. left circumflex coronary artery, 41.0 ± 13.8, vs. right coronary artery, 44.1 ± 8.7; P (ANOVA) < 0.001), but mismatch between FAP area and perfusion defect size did not show significant differences among coronary territories.

Signal in remote myocardium and other regions (liver, spleen, bone marrow, and lung) was low and did not correlate with infarct signal. Significant correlations were detected between FAP volume and maximum creatine kinase ($r = 0.42$, $P = 0.012$) as well as inflammatory markers (maximum C-reactive protein: $r = 0.43$, $P = 0.010$; maximum white blood cell count: $r = 0.31$, $P = 0.07$). Diabetes mellitus was associated with a larger FAP volume (134 ± 53 cm^3 vs. 93 ± 36 cm^3 for patients without diabetes, $P = 0.012$), whereas other cardiovascular risk factors were not associated with FAP signal.

FAP Signal Does Not Match Regional CMR Tissue Characteristic Segmental Analysis

For segmental correlation with CMR, apex was excluded from studies, leaving 16 segments per patient and a total of 496 segments (CMR T1 and T2 mapping available in 31 patients). Overall, the segmental mean FAP signal correlated with LGE extent ($r = 0.660$, $P < 0.001$), T1 and T2 relaxation times ($r = 0.485$, $P < 0.001$, and $r = 0.475$, $P < 0.001$, respectively), and extracellular volume ($r = 0.557$, $P < 0.001$). But there were marked differences when classifying segments as positive or negative for the respective tissue parameter (Fig. 5): 308 of 496 (64%) segments were classified as FAP-positive, using blood pool $\text{SUV}_{\text{mean}} + 2$ SDs as a threshold (*15*). A transmural LGE signal of more than 25% was present in 172 of 308 segments (56%). A prolonged T1 relaxation time above 1,023 ms (*22*), a threshold indicative of tissue fibrosis, was present in 227 of 308 segments (74%). A prolonged T2 relaxation time longer than 60 ms (*21*), consistent with edema, was present in 210 of 308 segments (68%). Of note, 44 of 308 (14%) FAP-positive segments had normal T1 and T2 relaxation and no relevant LGE. This confirms that FAP signal frequently

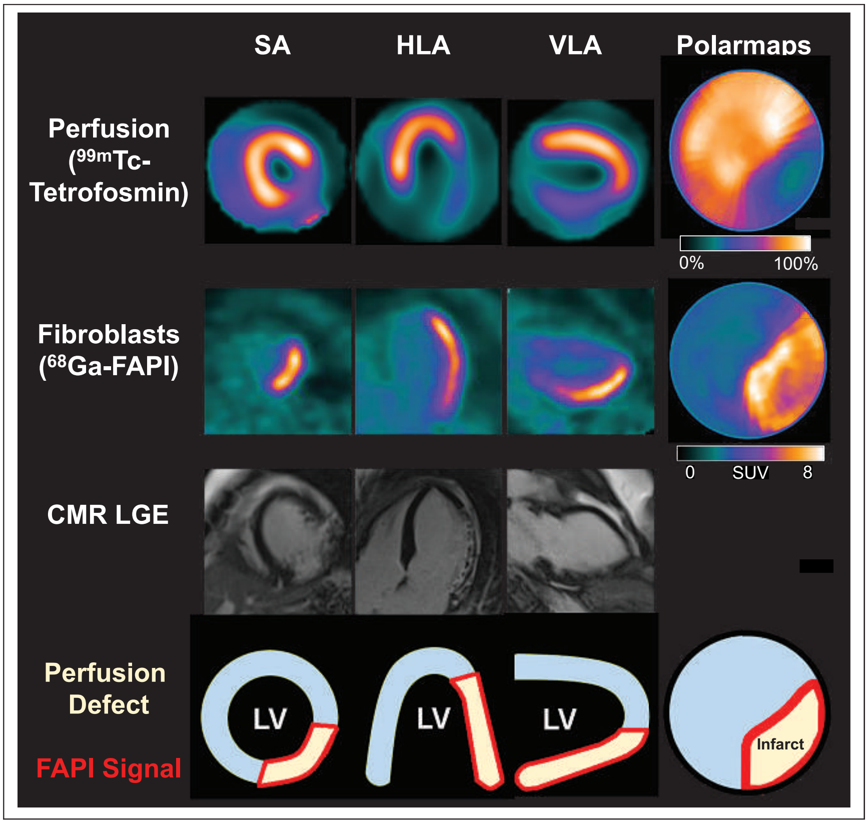

FIGURE 4. Myocardial perfusion images using ^{99m}Tc-tetrofosmin at rest, ^{68}Ga-FAPI PET, LGE from CMR, and schematic drawings of LV. Fibroblast activation only marginally exceeds infarct region. HLA = horizontal long axis; SA = short axis; VLA = vertical long axis.

extends beyond areas that are abnormal at CMR tissue characterization. Only few FAP segments showed LGE or altered T1 and T2 relaxation times. In these segments, LGE most likely reflects chronic stages of preexisting scar, potentially due to cardiovascular comorbidities. Furthermore, elevated signal in T1 and T2 mapping in the absence of FAP signal may identify segments with edema but no fibroblast activity.

FAP-Positive Segments Present with Impaired Contractility

Segmental $\mathrm{SUV}_{\mathrm{mean}}$ (496 segments) showed a mild but significant inverse correlation with segmental wall thickening ($r = -0.224$, $P < 0.001$). When 3 subgroups of segments were compared, normally perfused segments without FAP signal had significantly greater wall thickening than normally perfused segments with elevated FAP signal, whereas wall thickening was least in hypoperfused segments, all of which had an elevated FAP signal (Fig. 6).

FAP Signal Correlates with Ventricular Geometry and Functional Outcome

At baseline, FAP volume significantly correlated with LV mass ($r = 0.69$, $P > 0.001$), end-diastolic volume ($r = 0.57$, $P > 0.001$), end-systolic volume ($r = 0.62$, $P > 0.001$), and LGE volume ($r = 0.58$, $P > 0.001$). A trend to correlation was detected between FAP volume and initial LVEF ($r = -0.32$, $P = 0.07$). Interestingly, FAP volume showed a stronger, significant correlation with LVEF at follow-up ($r = -0.583$, $P = 0.007$; Fig. 7). Among patients with complete follow-up, those with at least 1 FAP-positive but T1-, T2-, and LGE-negative segment ($n = 6$) had a lower follow-up LVEF than those without such segments ($n = 6$; 47% ± 8% vs. 57% ± 3%, $P = 0.02$). Overall, this finding suggests that a higher number of activated fibroblasts early after AMI is associated with more severe LV dysfunction in the subsequent chronic stage after AMI.

DISCUSSION

Our results confirm that regional upregulation of FAP by activated fibroblasts yields a very high contrast between the injured

TABLE 3
Radionuclide Imaging Data

Variable	All patients (n = 35)		CMR available (n = 33)	
	Mean ± SD	Range	Mean ± SD	Range
Perfusion defect (SPECT % of polar map)	23.2 ± 17.4	0–55	23.6 ± 17.4	0–55
PET signal (^{68}Ga-FAPI-46 $\mathrm{SUV}_{\mathrm{peak}}$)				
Spleen	1.43 ± 0.40	0.96–2.61	1.43 ± 0.41	0.96–2.61
Liver	1.50 ± 0.47	0.82–2.93	1.48 ± 0.47	0.82–2.93
Bone marrow	1.05 ± 0.29	0.61–2.04	1.05 ± 0.29	0.61–2.04
Lungs	0.82 ± 0.32	0.34–2.17	0.81 ± 0.33	0.34–2.17
Blood pool (left atrium)	1.97 ± 0.40	1.32–3.21	1.97 ± 0.40	1.32–3.21
Remote myocardium	1.41 ± 0.38	0.91–2.84	1.41 ± 0.39	0.91–2.84
Infarct	6.41 ± 1.53	3.52–10.60	6.54 ± 1.46	4.24–10.60
Area of FAP upregulation (% of polar map)	58.0 ± 15.4	29–90	57.7 ± 15.8	29–90
Volume of FAP signal (cm^3)	105.8 ± 45.6	33.6–215.4	105.9 ± 46.6	33.6–215.4

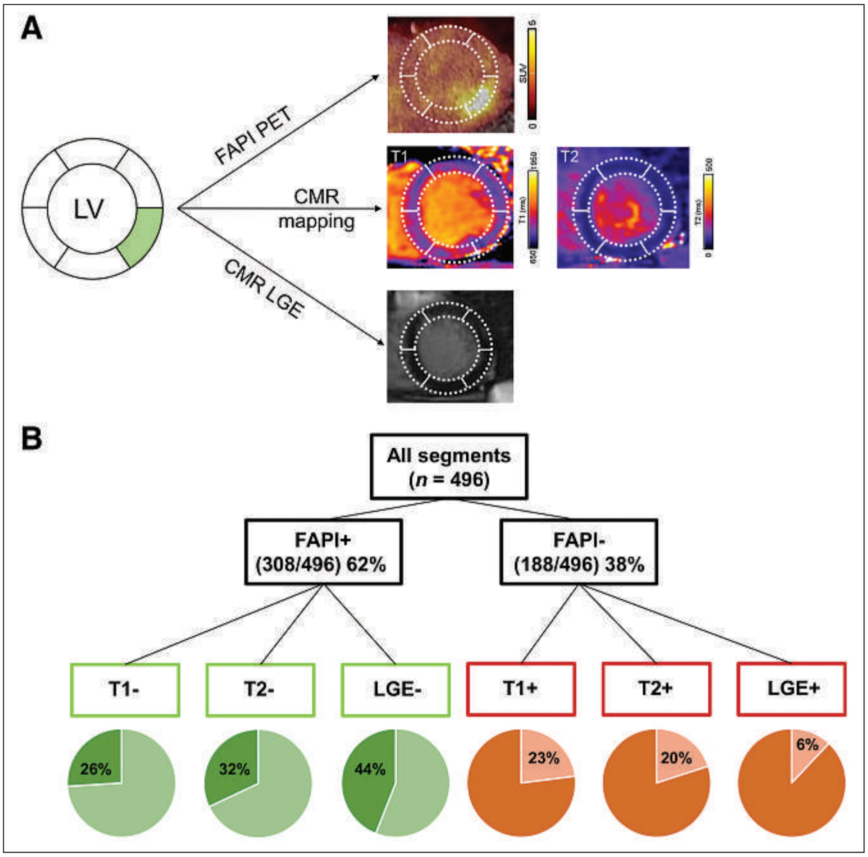

FIGURE 5. (A) Patient example with FAP-positive, T1-negative, T2-negative, and LGE-negative segment. (B) Segmental comparison of myocardial ^{68}Ga-FAPI-46 distribution, native T1 and T2 mapping, and LGE from CMR, using 16-segment model (apex excluded) in 31 AMI patients with complete datasets, resulting in total of 496 segments.

infarct and periinfarct region and unaffected remote myocardium, blood pool, and surrounding structures. FAP upregulation markedly exceeds the infarct region in patients early after AMI and standard-of-care reperfusion therapy. This result is consistent with the notion that FAP upregulation plays a role not only in replacement fibrosis in the primary injured region but also in reactive fibrosis that may compromise noninfarcted myocardium (*15,23*). Our observation of a link between extent of early FAP signal and LV dysfunction at later follow-up lends further support to this concept. Our results suggest that the FAPI signal is a multifactorial parameter that integrates a variety of influencing factors in the commonly heterogeneous clinical setting of patients early after AMI. Yet, the association with functional outcome makes the parameter intriguing for further exploration.

Integrative multimodal segmental analysis provides further insights into the relationship between fibroblast activation and extracellular tissue composition. Interestingly, the mismatch between FAP area and perfusion defect size was larger when infarct size was smaller. Speculatively, larger amounts of myocardial salvage and reperfusion injury may contribute to this elevated FAP signal as a potential precursor of interstitial fibrosis. Future studies may provide further insights into these interrelations. Although we found that FAP upregulation grossly correlated with CMR tissue parameters, there were relevant regional discordances. A significant fraction of FAP-positive segments not only exhibited absent LGE but also lacked prolongation of T1 and T2 relaxation times on CMR. This finding is of particular interest because it suggests that the results of ^{68}Ga-FAPI PET are not interchangeable with CMR tissue characteristics. Rather, ^{68}Ga-FAPI PET may add further, biologically distinct, information. Currently, LGE imaging is well established for detection of focal, mostly replacement fibrosis after myocardial injury in ischemia, inflammation, or cardiomyopathy. But cardiac pathologies, including diffuse, mostly interstitial alterations such as fibrosis or edema, cannot be quantified adequately by LGE (*24*). For this purpose, CMR mapping techniques that quantitatively determine tissue relaxation times for T1 (prolonged, for example, in interstitial fibrosis and infiltration) and T2 (primarily reflecting water content and prolonged in edema and inflammation) have been successfully designed. These parameters are increasingly applied in clinics (*25*) and provide information about the extent and composition of extracellular space. Myocardial fibrosis is commonly defined as an expansion of the cardiac interstitium by deposition of extracellular matrix proteins such as collagen. But modern concepts of the pathogenesis of fibrosis increasingly emphasize the role of cellular components, for which there is a tight interplay between functionally diverse subsets of fibroblasts, extracellular matrix composition, and regulation by the immune system (*26*). ^{68}Ga-FAPI PET identifies the cellular component of this process by specifically visualizing expression of FAP on activated myofibroblasts (*9,13,14*). Our results suggest that this profibrotic cellular signal is abundant in the territory of the infarct vessel early after AMI, that it may be present in myocardial segments that do not yet show elevated T1 relaxation as a measure of interstitial protein deposition, and that it may be present in segments that still do not show elevated T2 as a measure of edema. Speculatively, elevated FAP signal is an early and abundant fibroblast response after reperfusion and its immediate inflammatory reaction. The cellular FAP signal may then precede the subsequent deposition of extracellular matrix that establishes overt fibrosis. Clearly, further work is needed to elucidate the relative time course of the cellular, PET-derived signal and the interstitial, CMR-derived signal, along with their importance for functional outcome and for guidance of therapeutic interventions. In this regard, it should be noted that PET with other, immune cell–targeted, tracers may also identify the cellular component of inflammation, for integration with fibrosis-targeted imaging (*27,28*).

Regional patterns in our AMI patients suggest that the area of FAP upregulation may be interlinked with the ischemic area at risk. Prior SPECT studies have shown the feasibility of area-at-risk assessment using perfusion imaging after radiotracer injection before and after reperfusion of AMI (*29*). Yet, this logistically demanding approach is not broadly feasible and has not been available in our setting. In CMR, area at risk has been proposed to be estimated via quantity of edema in T2-weighted images, but preclinical histologic validation delivered partly inconclusive

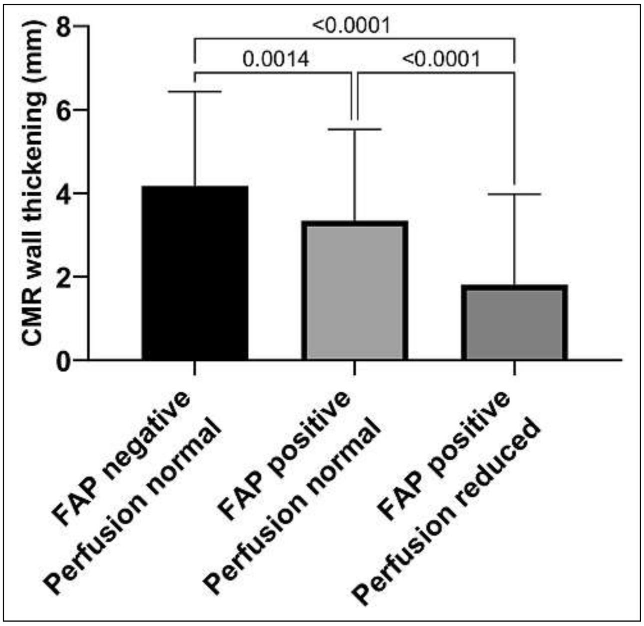

FIGURE 6. Three groups for analysis of wall thickening and contractility: FAP-negative and normally perfused segments representing remote myocardium, FAP-positive but normally perfused segments representing border zone, and FAP-positive segments with reduced perfusion representing core infarct zone. Wall thickening was significantly impaired in all FAP-positive segments with or without reduced perfusion (infarct and border zones).

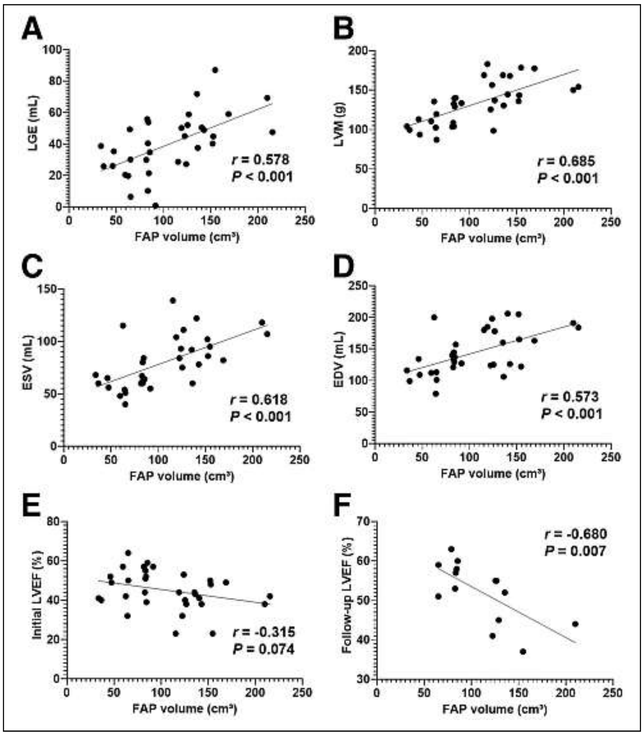

FIGURE 7. Correlation between global myocardial FAP volume early after AMI and synchronously measured markers of cardiac geometry and function from CMR. (A–D) Volume of LGE (mL) (A), LV mass (LVM; g) (B), end-systolic volume (ESV; mL) (C), and end-diastolic volume (EDV; mL) (D). (E and F) Nonsignificant trend to correlation with LVEF at baseline (E), and significant correlation with follow-up LVEF (F).

results on colocalization of edema and area at risk (*30*). In our study, FAP signal partly colocalized with detected edema in T2-weighted images. Interestingly, the mismatch of FAP area and perfusion defect size was larger when infarct size was smaller, suggesting a relationship with successful reperfusion. FAP-positive segments also showed impaired wall thickening both in the infarct and in the border zone, where it may reflect regional postischemic stunning. And last, the detected correlation of FAP uptake with levels of creatine kinase suggest an association between number of activated fibroblasts and ischemia/reperfusion ischemic injury. Ultimately, the relationship between area of fibroblast activation and area at risk warrants further investigation. Inclusion of myocardial perfusion imaging after tracer injection before revascularization, or the addition of stress perfusion imaging for flow reserve measurements, may be helpful in this regard in the future.

The long-term importance of imaging the myofibroblast component of profibrotic activity will depend on its predictive value for subsequent LV remodeling and heart failure progression. Our results show that the area of fibroblast activation at the time of PET imaging was associated with the extent of injury and geometric features such as the mass and volume of the LV, whereas the relation with contractile function was less pronounced initially. This relationship, however, changed at follow-up in the chronic post-AMI stage, when a larger extent of FAP signal early after AMI was associated with more severe contractile dysfunction. Notably, we even observed a lower mean follow-up LVEF in patients with a FAP-positive but CMR-negative tissue signal early after AMI. This might be a first indicator supporting an independent relevance of myocardial FAP signal for functional outcome; however, follow-up of LV function was available in only 14 patients. A larger prospective work will be needed to confirm these results.

We also observed a larger extent of myocardial fibroblast activation in a subgroup of patients with diabetes mellitus, whereas no differences were found analyzing other cardiovascular risk factors (age, sex, arterial hypertension, hyperlipidemia, smoking, and obesity). This finding was independent of infarct size. In AMI, diabetes mellitus is associated with elevated long-term mortality (*31,32*). Also, it has been shown that patients with adult-onset diabetes may exhibit extensive perivascular, interstitial, and even replacement fibrosis, in the absence of hypertension or coronary artery disease (*33*). The molecular mechanisms responsible for the contribution of diabetes mellitus to cardiac fibrosis remain poorly understood (*34*). Whether a more pronounced fibroblast activation in response to ischemic hypoperfusion plays a role in the adverse outcome of diabetic patients is another hypothesis generated by our preliminary observation that should be tested in subsequent studies.

A strong FAP signal was measured in the affected region, whereas signal from remote myocardium and other regions (liver, spleen, bone marrow, and lungs) was much lower. This supports the feasibility of FAP-targeted imaging to guide antifibrotic therapeutic strategies. Importantly, it also supports the feasibility of FAP-targeted therapies themselves, which may modulate and attenuate profibrotic activity if administered precisely in suitable individuals and at the right time (*3*). In the future, molecular imaging using FAPI ligands might help us to understand mechanisms and select patients for individual treatment using advanced antifibrotic measures.

Some limitations of our work should be considered. The sample size was small, and the analysis was retrospective, leading to even smaller samples for follow-up. No serial imaging was performed, and the time course of the FAP signal after AMI remains incompletely defined. We chose to use a threshold for detection of FAP-positive myocardial areas because of absence of an established standard. This approach was pursued as a best possible approach in the absence of validated alternatives. Other measures such as the SUV or segmental analyses were threshold-independent and confirm the major conclusions of our work. Our work should be seen as hypothesis-generating for further studies, which may aim at identifying the optimal time point for imaging FAP expression to predict the progression of postinfarct remodeling most effectively. Further work may also focus on defining the incremental value of FAP-targeted imaging over standard clinical risk markers, CMR, and other molecular targeted approaches such as imaging of the inflammatory response to injury (*35*). The outcome sample of this study was too small for meaningful multivariate analyses. Finally, matching of PET and CMR results may not have been perfect because studies were obtained on separate camera systems on different days. We also cannot completely discount possible variation of imaging parameters over time in this study, although we sought to minimize effects by performing imaging on 3 consecutive days, when possible. PET signal was significantly elevated in the infarct region and in the periinfarct region, where wall thickening was impaired as a consequence of ischemic injury. Partial-volume effects were considered minor therefore, and in the absence of established methods, no correction for partial-volume effects was applied. In the future, hybrid PET/MRI systems may offer simultaneous acquisition of CMR and PET parameters of myocardial repair after AMI (*36*).

CONCLUSION

Taken together, this work provides new insights into the regional pattern of fibroblast activation early after AMI. The area of elevated FAP signal reaches beyond the injured infarct region and may even involve regions without prolonged T1 or T2 relaxation as CMR markers of interstitial fibrosis, infiltration, or edema. This suggests that the cell-based signal of fibroblast activation is distinct from CMR-derived interstitial characteristics and may be complementary. Importantly, the early FAP signal was associated with a subsequent impairment of LV function, suggesting that it may be a predictor of adverse LV remodeling.

DISCLOSURE

This work was supported by the Deutsche Forschungsgemeinschaft (DFG, Clinical Research Unit KFO 311: Johann Bauersachs and Frank Bengel; Clinician Scientist Program PRACTIS: Johanna Diekmann), the Leducq Foundation (Transatlantic Network "Immunofib HF": Frank Bengel, James Thackeray, and Johanna Diekmann), and "REBIRTH—Research Center for Translational Regenerative Medicine" (State of Lower Saxony: James Thackeray, Johann Bauersachs, and Frank Bengel). No other potential conflict of interest relevant to this article was reported.

ACKNOWLEDGMENT

Precursor for ^{68}Ga-FAPI-46 was kindly provided by Uwe Haberkorn, MD, University of Heidelberg.

KEY POINTS

QUESTION: Does myocardial fibroblast activation early after AMI correlate with CMR tissue characteristics, and is it predictive of subsequent development of ventricular dysfunction?

PERTINENT FINDINGS: Thirty-five patients underwent ^{68}Ga-FAPI-46 PET and CMR within 11 d after reperfusion therapy for AMI. The region of fibroblast activation on ^{68}Ga-FAPI PET extended beyond the fibrotic scar. Also, there were segmental discrepancies between FAPI signal and T1 and T2 relaxation times from CMR. FAPI signal early after AMI correlated with reduced LVEF in the subsequent chronic stage.

IMPLICATIONS FOR PATIENT CARE: ^{68}Ga-FAPI PET may be complementary to CMR and serve as an independent marker of the risk of adverse cardiac remodeling after AMI.

REFERENCES

1. Travers JG, Kamal FA, Robbins J, Yutzey KE, Blaxall BC. Cardiac fibrosis: the fibroblast awakens. *Circ Res.* 2016;118:1021–1040.
2. Furtado MB, Nim HT, Boyd SE, Rosenthal NA. View from the heart: cardiac fibroblasts in development, scarring and regeneration. *Development.* 2016;143: 387–397.
3. Aghajanian H, Kimura T, Rurik JG, et al. Targeting cardiac fibrosis with engineered T cells. *Nature.* 2019;573:430–433.
4. Gourdie RG, Dimmeler S, Kohl P. Novel therapeutic strategies targeting fibroblasts and fibrosis in heart disease. *Nat Rev Drug Discov.* 2016;15:620–638.
5. Conrad N, Judge A, Tran J, et al. Temporal trends and patterns in heart failure incidence: a population-based study of 4 million individuals. *Lancet.* 2018;391: 572–580.
6. Prabhu SD, Frangogiannis NG. The biological basis for cardiac repair after myocardial infarction: from inflammation to fibrosis. *Circ Res.* 2016;119:91–112.
7. Lafuse WP, Wozniak DJ, Rajaram MVS. Role of cardiac macrophages on cardiac inflammation, fibrosis and tissue repair. *Cells.* 2020;10:51.
8. Sutton MG, Sharpe N. Left ventricular remodeling after myocardial infarction: pathophysiology and therapy. *Circulation.* 2000;101:2981–2988.
9. Tillmanns J, Hoffmann D, Habbaba Y, et al. Fibroblast activation protein alpha expression identifies activated fibroblasts after myocardial infarction. *J Mol Cell Cardiol.* 2015;87:194–203.
10. Kratochwil C, Flechsig P, Lindner T, et al. ^{68}Ga-FAPI PET/CT: tracer uptake in 28 different kinds of cancer. *J Nucl Med.* 2019;60:801–805.
11. Siebermair J, Kohler MI, Kupusovic J, et al. Cardiac fibroblast activation detected by Ga-68 FAPI PET imaging as a potential novel biomarker of cardiac injury/remodeling. *J Nucl Cardiol.* 2021;28:812–821.
12. Heckmann MB, Reinhardt F, Finke D, et al. Relationship between cardiac fibroblast activation protein activity by positron emission tomography and cardiovascular disease. *Circ Cardiovasc Imaging.* 2020;13:e010628.
13. Varasteh Z, Mohanta S, Robu S, et al. Molecular imaging of fibroblast activity after myocardial infarction using a ^{68}Ga-labeled fibroblast activation protein inhibitor, FAPI-04. *J Nucl Med.* 2019;60:1743–1749.
14. Langer LBN, Hess A, Korkmaz Z, et al. Molecular imaging of fibroblast activation protein after myocardial infarction using the novel radiotracer [^{68}Ga]MHLL1. *Theranostics.* 2021;11:7755–7766.
15. Diekmann J, Koenig T, Zwadlo C, et al. Molecular imaging identifies fibroblast activation beyond the infarct region after acute myocardial infarction. *J Am Coll Cardiol.* 2021;77:1835–1837.
16. Kessler L, Kupusovic J, Ferdinandus J, et al. Visualization of fibroblast activation after myocardial infarction using ^{68}Ga-FAPI PET. *Clin Nucl Med.* 2021;46:807–813.
17. Notohamiprodjo S, Nekolla SG, Robu S, et al. Imaging of cardiac fibroblast activation in a patient after acute myocardial infarction using ^{68}Ga-FAPI-04. *J Nucl Cardiol.* April 15, 2021 [Epub ahead of print].
18. González A, Schelbert EB, Diez J, Butler J. Myocardial interstitial fibrosis in heart failure: biological and translational perspectives. *J Am Coll Cardiol.* 2018;71: 1696–1706.
19. Loktev A, Lindner T, Burger EM, et al. Development of fibroblast activation protein-targeted radiotracers with improved tumor retention. *J Nucl Med.* 2019;60: 1421–1429.

20. Goebel J, Seifert I, Nensa F, et al. Can native T1 mapping differentiate between healthy and diffuse diseased myocardium in clinical routine cardiac MR imaging? *PLoS One.* 2016;11:e0155591.
21. Verhaert D, Thavendiranathan P, Giri S, et al. Direct T2 quantification of myocardial edema in acute ischemic injury. *JACC Cardiovasc Imaging.* 2011;4:269–278.
22. Rosmini S, Bulluck H, Captur G, et al. Myocardial native T1 and extracellular volume with healthy ageing and gender. *Eur Heart J Cardiovasc Imaging.* 2018;19: 615–621.
23. Nagaraju CK, Dries E, Popovic N, et al. Global fibroblast activation throughout the left ventricle but localized fibrosis after myocardial infarction. *Sci Rep.* 2017;7:10801.
24. Salerno M, Kramer CM. Advances in parametric mapping with CMR imaging. *JACC Cardiovasc Imaging.* 2013;6:806–822.
25. Messroghli DR, Moon JC, Ferreira VM, et al. Clinical recommendations for cardiovascular magnetic resonance mapping of T1, T2, T2* and extracellular volume: a consensus statement by the Society for Cardiovascular Magnetic Resonance (SCMR) endorsed by the European Association for Cardiovascular Imaging (EACVI). *J Cardiovasc Magn Reson.* 2017;19:75.
26. Humeres C, Frangogiannis NG. Fibroblasts in the infarcted, remodeling, and failing heart. *JACC Basic Transl Sci.* 2019;4:449–467.
27. Hess A, Thackeray JT, Wollert KC, Bengel FM. Radionuclide image-guided repair of the heart. *JACC Cardiovasc Imaging.* 2020;13:2415–2429.
28. Glasenapp A, Derlin K, Gutberlet M, et al. Molecular imaging of inflammation and fibrosis in pressure overload heart failure. *Circ Res.* 2021;129:369–382.
29. Matsunari I, Schricke U, Bengel FM, et al. Extent of cardiac sympathetic neuronal damage is determined by the area of ischemia in patients with acute coronary syndromes. *Circulation.* 2000;101:2579–2585.
30. Beijnink CWH, van der Hoeven NW, Konijnenberg LSF, et al. Cardiac MRI to visualize myocardial damage after ST-segment elevation myocardial infarction: a review of its histologic validation. *Radiology.* 2021;301:4–18.
31. Gholap NN, Achana FA, Davies MJ, Ray KK, Gray L, Khunti K. Long-term mortality after acute myocardial infarction among individuals with and without diabetes: a systematic review and meta-analysis of studies in the post-reperfusion era. *Diabetes Obes Metab.* 2017;19:364–374.
32. Johansson S, Rosengren A, Young K, Jennings E. Mortality and morbidity trends after the first year in survivors of acute myocardial infarction: a systematic review. *BMC Cardiovasc Disord.* 2017;17:53.
33. Regan TJ, Lyons MM, Ahmed SS, et al. Evidence for cardiomyopathy in familial diabetes mellitus. *J Clin Invest.* 1977;60:884–899.
34. Russo I, Frangogiannis NG. Diabetes-associated cardiac fibrosis: cellular effectors, molecular mechanisms and therapeutic opportunities. *J Mol Cell Cardiol.* 2016;90: 84–93.
35. Werner RA, Koenig T, Diekmann J, et al. CXCR4-targeted imaging of post-infarct myocardial tissue inflammation: prognostic value after reperfused myocardial infarction. *JACC Cardiovasc Imaging.* 2022;15:372–374.
36. Abgral R, Dweck MR, Trivieri MG, et al. Clinical utility of combined FDG-PET/MR to assess myocardial disease. *JACC Cardiovasc Imaging.* 2017;10:594–597.

The Impact of Semiautomatic Segmentation Methods on Metabolic Tumor Volume, Intensity, and Dissemination Radiomics in ^{18}F-FDG PET Scans of Patients with Classical Hodgkin Lymphoma

Julia Driessen*[1], Gerben J.C. Zwezerijnen*[2], Heiko Schöder[3], Esther E.E. Drees[4], Marie José Kersten[1], Alison J. Moskowitz[5], Craig H. Moskowitz[6], Jakoba J. Eertink[7], Henrica C.W. de Vet[8], Otto S. Hoekstra[2], Josée M. Zijlstra[7], and Ronald Boellaard[2]

[1]Department of Hematology, Amsterdam UMC, University of Amsterdam, LYMMCARE (Lymphoma and Myeloma Center, Amsterdam), Cancer Center Amsterdam, Amsterdam, The Netherlands; [2]Department of Radiology and Nuclear Medicine, Amsterdam UMC, Vrije Universiteit Amsterdam, Cancer Center Amsterdam, Amsterdam, The Netherlands; [3]Department of Molecular Imaging and Therapy Service, Memorial Sloan Kettering Cancer Center, New York, New York; [4]Department of Pathology, Amsterdam UMC, Vrije Universiteit Amsterdam, Cancer Center Amsterdam, Amsterdam, The Netherlands; [5]Department of Medicine, Memorial Sloan Kettering Cancer Center, New York, New York; [6]Department of Medicine, Sylvester Comprehensive Cancer Center, Miami, Florida; [7]Department of Hematology, Amsterdam UMC, Vrije Universiteit Amsterdam, Cancer Center Amsterdam, Amsterdam, The Netherlands; and [8]Department of Epidemiology and Data Science, Amsterdam Public Health research institute, Amsterdam, Netherlands

---

Consensus about a standard segmentation method to derive metabolic tumor volume (MTV) in classical Hodgkin lymphoma (cHL) is lacking, and it is unknown how different segmentation methods influence quantitative PET features. Therefore, we aimed to evaluate the delineation and completeness of lesion selection and the need for manual adaptation with different segmentation methods, and to assess the influence of segmentation methods on the prognostic value of MTV, intensity, and dissemination radiomics features in cHL patients. **Methods:** We analyzed a total of 105 ^{18}F-FDG PET/CT scans from patients with newly diagnosed (n = 35) and relapsed/refractory (n = 70) cHL with 6 segmentation methods: 2 fixed thresholds on SUV4.0 and SUV2.5, 2 relative methods of 41% of $\mathrm{SUV_{max}}$ (41max) and a contrast-corrected 50% of $\mathrm{SUV_{peak}}$ (A50P), and 2 combination majority vote (MV) methods (MV2, MV3). Segmentation quality was assessed by 2 reviewers on the basis of predefined quality criteria: completeness of selection, the need for manual adaptation, and delineation of lesion borders. Correlations and prognostic performance of resulting radiomics features were compared among the methods. **Results:** SUV4.0 required the least manual adaptation but tended to underestimate MTV and often missed small lesions with low ^{18}F-FDG uptake. SUV2.5 most frequently included all lesions but required minor manual adaptations and generally overestimated MTV. In contrast, few lesions were missed when using 41max, A50P, MV2, and MV3, but these segmentation methods required extensive manual adaptation and overestimated MTV in most cases. MTV and dissemination features significantly differed among the methods. However, correlations among methods were high for MTV and most intensity and dissemination features. There were no significant differences in prognostic performance for all features among the methods. **Conclusion:** A high correlation existed between MTV, intensity, and most dissemination features derived with the different segmentation methods, and the prognostic performance is similar. Despite frequently missing small lesions with low ^{18}F-FDG avidity, segmentation with a fixed threshold of SUV4.0 required the least manual adaptation, which is critical for future research and implementation in clinical practice. However, the importance of small, low ^{18}F-FDG–avidity lesions should be addressed in a larger cohort of cHL patients.

Key Words: Hodgkin lymphoma; segmentation methods; ^{18}F-FDG PET/CT; outcome prediction; radiomics

J Nucl Med 2022; 63:1424–1430
DOI: 10.2967/jnumed.121.263067

The ^{18}F-FDG PET/CT scan is standard of care for staging and response evaluation in the treatment of classical Hodgkin lymphoma (cHL) (*1*). Optimizing baseline risk stratification contributes to the implementation of individualized treatment strategies aiming to lower toxicity in patients with favorable prognostic characteristics and identification of patients with unfavorable prognostic characteristics early for treatment with other therapies (*2–4*). The use of quantitative PET features to improve risk stratification could be implemented in clinical practice if workflows are optimized.

Several studies have shown that metabolic tumor volume (MTV) is a potential prognostic marker in newly diagnosed (ND) and relapsed/refractory (R/R)-cHL (*4–11*). However, there are different methods for assessing MTV, and there is no consensus which method performs best in cHL patients in terms of prognostic performance, ease of use, and interobserver variability (*12*). MTV assessment is especially challenging in disseminated diseases such as lymphoma. cHL is a heterogeneous disease that is typically localized in the mediastinal and paraaortic regions, mainly affecting young patients who frequently show high physiologic ^{18}F-FDG uptake in brown fat and muscles (*1*). These regions with high physiologic ^{18}F-FDG uptake impede accurate delineation of tumor lesions nearby. Therefore, it is important to evaluate different segmentation methods specifically for cHL.

Received Aug. 17, 2021; revision accepted Dec. 28, 2021.

For correspondence or reprints, contact Ronald Boellaard (r.boellaard@amsterdamumc.nl).

*Contributed equally to this work.

Although manual segmentation is the current standard for determining MTV, it is time-consuming and prone to interobserver variability (*12*). Semiautomatic segmentation includes algorithms that select regions with high ^{18}F-FDG uptake above the threshold of a certain SUV. Segmentation of the MTV can be performed by either predefining regions of interest in which lesions will be automatically selected or by starting with automatic segmentation and deleting regions with high physiologic ^{18}F-FDG uptake (e.g., brain, liver, kidneys) thereafter. Although the segmentation method applied can significantly impact the MTV, it is unknown how each method affects other quantitative PET radiomics features, such as patient-level dissemination parameters (*13–17*). Besides, no comparative studies have been performed that address representativeness of the segmented MTV with the visual interpretation of the MTV in cHL patients.

The aim of our research was to evaluate the delineation and completeness of lesion selection, and the need for manual adaptation with 6 different semiautomatic segmentation methods, and to assess the influence of the segmentation method on the prognostic value of MTV, intensity, and dissemination radiomics features in scans of cHL patients.

MATERIALS AND METHODS

Study Population

PET/CT scans from ND-cHL patients were collected from study cohorts of the Amsterdam UMC ($n = 35$) (*2,18*). PET/CT scans of patients with RR-cHL were collected from 3 clinical trials conducted in Amsterdam UMC, The Netherlands ($n = 47$) and Memorial Sloan Kettering Cancer Center, New York ($n = 23$) (*2–4*). All patients had biopsy-proven cHL, and the PET/CT scan was obtained before the start of therapy. All patients provided written informed consent for participation in the clinical trials (NCT02280993, NCT00255723, NCT01508312) or biobank cohort (*18*) of which the study protocols were approved by Institutional Review Boards and Ethics Committees of the centers that conducted the trials. For secondary use of data for this analysis, a waiver was obtained from the Ethics Committee.

^{18}F-FDG PET/CT Scans and Quality Control

The PET/CT systems used to acquire the scans were EANM Research GmbH (EARL, Europe)– or American College of Radiology (ACR, United States)–accredited (*19*). PET/CT scans were deidentified at the participating centers and centrally collected. PET scans that did not meet the following 4 criteria, described by European Association of Nuclear Medicine guidelines (*19*), were excluded from analysis: plasma glucose < 11 mmol/L; reconstruction of attenuation-corrected PET according to guidelines described by EARL or ACR; total image activity (MBq) between 50% and 80% of the total injected ^{18}F-FDG activity or liver SUV_{mean} between 1.3 and 3.0; and essential PET acquisition data and clinical data available (*19*).

Segmentation of the Volume of Interest (VOI)

Attenuation-corrected PET scans were analyzed using the ACCURATE tool (*20*). Six different semiautomatic methods were used for each scan to select the VOI: 2 fixed thresholds of SUV4.0 and SUV2.5, 2 relative thresholds of 41% of SUV_{max} (41max) and a contrast-corrected 50% of SUV_{peak} (A50P), and 2 majority vote (MV) methods selecting voxels that are chosen with ≥ 2 (MV2) and ≥ 3 (MV3) of the previously mentioned fixed or relative methods, respectively. The VOI was delineated by automatic preselection of ^{18}F-FDG–avid structures using the 6 different segmentation methods and a volume threshold of ≥ 3 mL. Nontumor regions were deleted and lymphoma lesions < 3 mL were added with single mouse clicks. If tumor regions were adjacent to nontumor ^{18}F-FDG–avid regions (e.g., heart, liver, bladder), nontumor regions were either removed manually or tumor segmentation was restricted by placing a border or mask, which prevented selection of lesions outside the border (Fig. 1A). Only focal extranodal and splenic lesions were included in the VOI. A global increase in ^{18}F-FDG uptake of the spleen or bone marrow was not included in the VOI. Delineations were performed under supervision of a nuclear medicine physician.

Quality Scores of Representativeness of Segmentations Compared with Visual Judgment

The quality of the segmentation by the 6 different methods was assessed using 3 quality score (QS) criteria (Table 1): completeness of selection of the VOI (i.e., were all tumor-lesions selected); requirement of manual adaptation after semiautomatic segmentation (i.e., manual removal of nontumor regions); and delineation quality of the VOI (i.e., does the VOI border reflect the visual interpretation of the ^{18}F-FDG–avid tumor area on the PET scan?).

Two reviewers performed the QS assessment for each of the 6 segmentations for all scans, masked to patient outcome. Completeness of

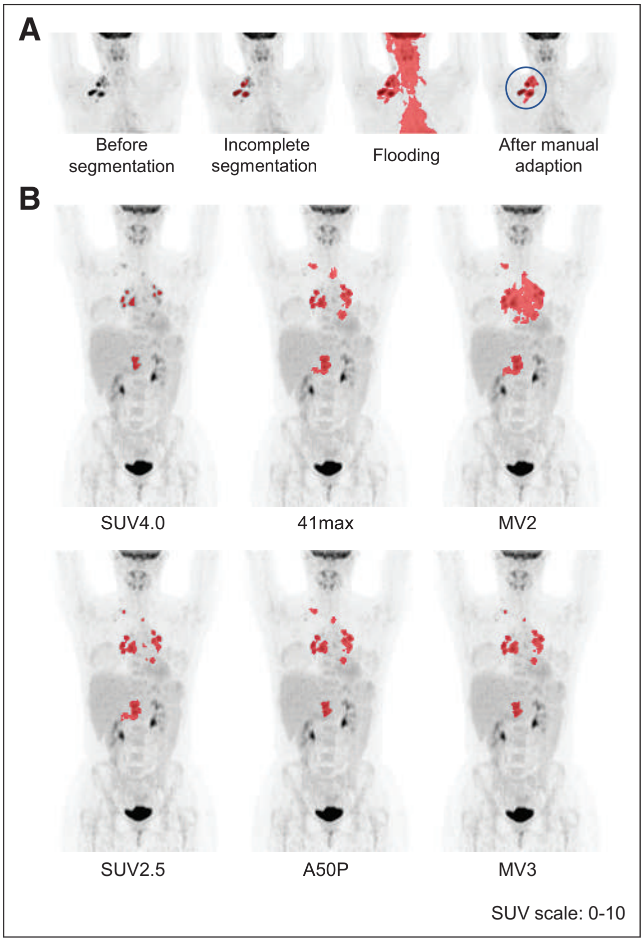

FIGURE 1. Examples of semiautomatic segmentation. (A) Minimal-intensity projection (MIP) of the PET scan before segmentation; automatic selection with the 41max method missed multiple lesions; adding missing lesions resulted in flooding into the heart, tonsils, and brain; manual adaptation by placing a border around the volume of interest before segmentation resulted in complete selection. (B) Segmentation with SUV4.0 was scored as "missing minor lesions" and "representative delineation." Segmentation with SUV2.5, 41max, A50P, MV2, and MV3 were scored as "complete segmentation" with "overestimation of delineation." Segmentation with 41max flooded into the heart and required minor manual adaptation. Segmentation with MV2 flooded into the heart and liver and required major manual adaptations.

TABLE 1
Definitions of Quality Scores for Visual Assessment of Segmentation Quality

Quality score	Level	Definition
Completeness of selection	Complete	All visible tumor lesions are selected.
	Missing minor lesions	Missing lesions are < 3 mL and within the selected VOI region (e.g., considered not to influence the Dmax).
	Missing major lesions	Lesions are missing that are either ≥ 3 mL or outside the selected VOI region (e.g., considered to influence the Dmax).
Manual adaptation	No adaptation	No manual adaptation is required. Adding lesions with single mouse clicks is not considered manual adaptation.
	Minor adaptation	Manual adaptation is required to obtain a representative selection of the VOI by removing a maximum of 1 nontumor region.
	Major adaptation	Extensive manual adaptation is required by removing > 1 nontumor region.
Delineation	Representative	Delineation of VOI borders is representative of the visual interpretation of the tumor.
	Underestimation	Delineation of VOI borders is underestimated.
	Overestimation	Delineation of VOI borders is overestimated.

selection and delineation QS were assessed independently, followed by a consensus meeting in which the reviewers reached a consensus on all discrepancy scores and assigned a final QS to each segmentation. The manual adaptation QS was assessed in consensus between the reviewers during review of the segmentation of scans. An example of the QS assessment by the 6 segmentation methods is included in Figure 1B.

Radiomics Feature Extraction

RaCat software (developed by Professor Ronald Boellaard; Amsterdam UMC) was used to extract 18 patient-level dissemination features from the complete MTV at patient level (*21*). Dissemination features included several novel features addressing interlesional heterogeneity based on distance, volume, SUV_{max}, and SUV_{peak} (the 1 mL with the highest SUV within the VOI). In addition, MTV, SUV_{max}, SUV_{peak}, SUV_{mean}, and total lesion glycolysis were extracted from the VOI. An overview of all features and its definitions are provided in Supplemental Table 1 (supplemental materials are available at http://jnm.snmjournals.org).

Statistical Analysis

QS of segmentations were analyzed descriptively and compared using χ^2 tests for the whole cohort and separately for ND-cHL and RR-cHL patients. MTV, intensity, and dissemination radiomics features were compared between the ND-cHL and RR-cHL cohorts using the Wilcoxon rank sum test for nonparametric data. Further analyses were performed on the whole cohort. Correlations of MTV, intensity, and dissemination radiomics features among the 6 different segmentation methods were assessed using Spearman rank coefficients correlation. Receiver-operating-characteristics analysis was used to calculate the area under the curve (AUC) for each feature per segmentation method on the whole cohort. An event was defined as the occurrence of progressive disease within 3 y, and patients who died without progression were excluded. AUC curves were compared using a paired *t* test as described by DeLong et al. (*22*).

Statistical analysis was performed using R software (version 4.0.3; R Core Team). A P value of < 0.05 was considered statistically significant.

RESULTS

Patient Characteristics

A total of 105 PET/CT scans of patients with ND-cHL ($n = 35$) and RR-cHL ($n = 70$) were included in the analysis (Supplemental Table 2). A comparison of radiomics features between ND-cHL and RR-cHL showed no significant differences for most features, except for MTV, SUV_{peak}, and Dvol (the maximum difference in volume between lesions), which were all higher in ND patients than in RR patients (Supplemental Table 3).

Quality Scores of Segmentations

Agreement of QS assessment between the 2 reviewers was high (91% for segmentation quality and 82% for delineation quality).

Segmentation resulted in complete selection of all lesions in most cases (Fig. 2A; Supplemental Table 4). SUV2.5 showed the highest rate of complete selection, followed by 41max, MV2, A50P, and MV3, while SUV4.0 frequently missed minor (59%) and major (10%) lesions. When the SUV4.0 method was used, 91% of scans could be segmented without any manual adaptation (Fig. 2B). The SUV2.5 method required minor adaptations in 37% of scans and 7% major adaptations. When the 41max and MV2 methods were used, only 30% and 34% of scans could be segmented without manual adaptation, and in 47% and 33% of cases, major manual adaptations were required, respectively. When A50P and MV3 were used, about 50% of scans did not require manual adaptation. None of the methods resulted in a high percentage of representative delineation of tumor borders (Fig. 2C). SUV4.0, SUV2.5, and MV3 resulted in representative delineation in about 50% of cases, whereas SUV4.0 tended to underestimate the MTV and SUV2.5 and MV3 tended to overestimate the MTV in the remaining cases. The 41max, A50P, and MV2 methods resulted in representative delineation in less than 30% and usually overestimated the MTV.

No significant differences were observed for QS between ND and RR patients, except for completeness of selection in which complete selection rates were higher in RR patients than in ND patients with 41max, A50P, or MV3 (Supplemental Fig. 1).

Comparison of Features

MTV differed significantly among the segmentation methods. The median MTV per method ranged between 44 and 143 mL (Fig. 3; Supplemental Table 5). SUV4.0 resulted in a significantly lower MTV than all other segmentation methods ($P < 0.001$). The number

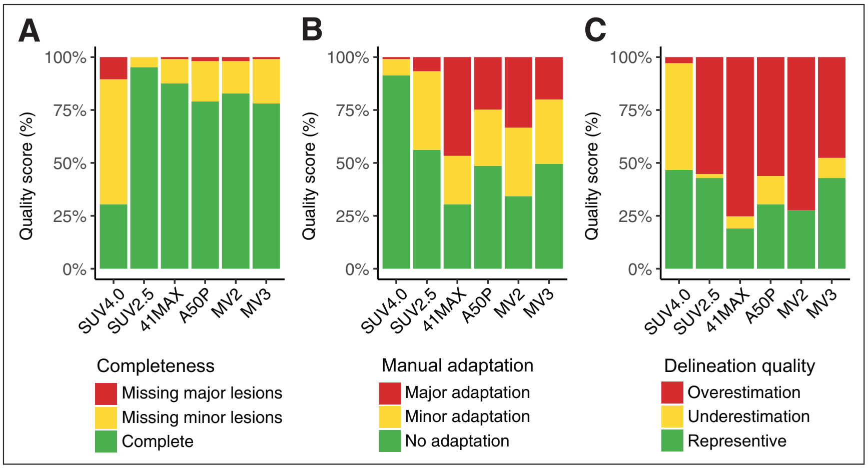

FIGURE 2. Quality scores (QS) of segmentation methods. (A) Completeness of selection. (B) Manual adaptations required for representative segmentation. (C) Delineation of tumor borders.

of lesions was significantly lower with 41max and MV2 than with SUV4.0 and SUV2.5 segmentation methods ($P < 0.05$). Dmax (the maximum distance between 2 lesions) was not significantly different among the segmentation methods.

MTV, the number of lesions, and Dmax showed high correlations among most methods (Fig. 4; Supplemental Table 6). For MTV and the number of lesions, the highest correlations were observed between the 2 fixed methods (SUV4.0 and SUV2.5), and between the relative and MV methods, with lower correlations between the fixed and relative or MV methods. SUV_{max} and SUV_{peak} had identical median values and were strongly correlated ($R = 1$) across all methods. Dissemination features addressing differences in volume or SUV_{peak} among lesions showed lower correlations between SUV4.0 and the other 5 segmentation methods (Supplemental Table 6).

To assess the effect of incomplete selection of lesions, several features derived with SUV4.0 were plotted against SUV2.5 (Supplemental Fig. 2). Scans that missed major lesions with SUV4.0 did not show large deviations in the correlation between SUV4.0 and SUV2.5 when compared with scans that had complete selection or missed only minor lesions.

Prognostic Performance per Method

Except for MV2, the AUC of the receiver-operating characteristics did not differ significantly among the segmentation methods for all features assessed (Fig. 5; Supplemental Table 7). The highest AUCs were observed for MTV (range, 0.62–0.65), total lesion glycolysis (range, 0.63–0.65), number of lesions (range, 0.55–0.63), spread in volume (VolSpread) (range, 0.58–0.65), and the difference in SUV_{peak} between the hottest lesion and all other lesions (DSUVpeakSumHot) (range, 0.56–0.63). Of all methods MV2 showed the lowest AUC for the various features (median AUC of all variables, 0.55). The other 5 methods showed comparable median AUCs, with the highest median AUC of all variables of 0.62 for SUV4.0.

DISCUSSION

MTV has shown prognostic value in cHL, but the use of different segmentation methods hampers direct comparisons between studies (*4–10*). This is especially true if a cutoff for MTV is used to divide patients in low- and high-risk groups, since absolute MTV values significantly differ between methods. Harmonization of MTV assessment enables the evaluation of MTV as a prognostic marker in cHL in a multicohort setting. The same holds for other quantitative PET features including dissemination features.

We evaluated the completeness of lesion selection, need for manual adaptations, and delineation quality of 6 semiautomatic segmentation methods to assess MTV and dissemination features in 105 cHL patients. Segmentation with SUV4.0 required the least manual adaptations because this method, in contrast to other methods, rarely floods into regions with high physiologic ^{18}F-FDG uptake. SUV2.5 often required minor adaptations, but seldomly major adaptations. Although segmentation using SUV4.0 frequently did not include all lesions (missing those with a SUV < 4.0), these lesions were often small and scans with major lesions missing did not cause significant deviations in the correlation between SUV4.0 and SUV2.5, which

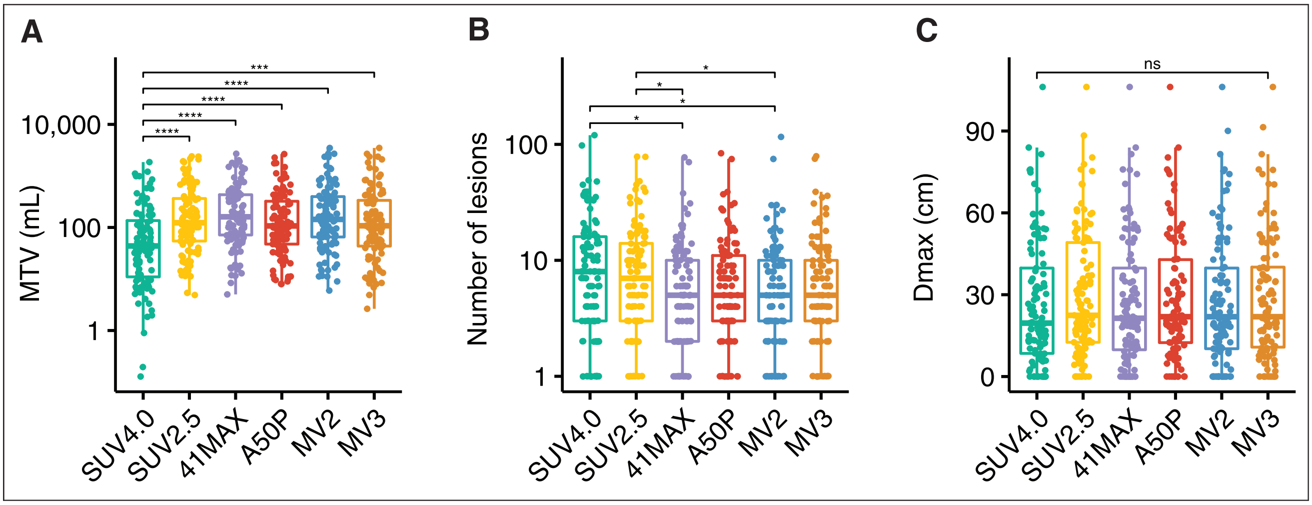

FIGURE 3. Radiomics features derived with 6 different semiautomatic segmentation methods. (A) MTV in mL. (B) Number of lesions. (C) Dmax in cm. *$P < 0.05$. ***$P < 0.001$. ****$P < 0.0001$. ns = not significant.

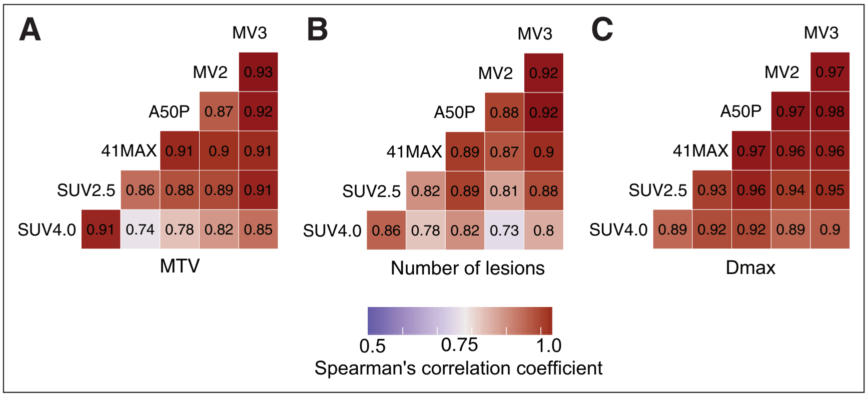

FIGURE 4. Spearman rank correlation coefficients for radiomics features among different segmentation methods. (A) MTV. (B) Number of lesions. (C) Dmax. All correlations assessed had a *P* value of <0.01.

was the most complete method. Additionally, the prognostic performance between all methods was similar, and SUV4.0 and SUV2.5 showed the highest AUCs for most variables.

The results of our evaluation suggest that small lesions with low SUV uptake, that are frequently not included with SUV4.0, probably do not contain critical prognostic information, which could be partly explained by the low contribution to total MTV of small lesions. However, small lesions could still influence dissemination features, of which the prognostic value needs to be established in a larger set of patients with more progression events. Additionally, small low-uptake lesions are potentially of higher importance in response assessment, thus, SUV4.0 may be less suitable for quantitative interim PET analyses in cHL (*1*).

All segmentation methods, except SUV4.0, frequently overestimated the MTV assessed by visual interpretation. This overestimation may be less relevant when using only patient-level features, as correlations among methods are high; however, lesion-based radiomics analysis involving texture features may be adversely affected by oversegmentation, that is, by selection of voxels that are not part of the tumor (*23*). Methods that tended to overestimate the MTV also showed a lower number of lesions, because lesions close to each other were frequently clustered into 1 lesion, as illustrated in Figure 1. This explains the discrepancy that SUV4.0 often misses small or low-uptake lesions but still shows the highest number of lesions (Fig. 3).

In a recent comparison of 6 segmentation methods in diffuse large B-cell lymphoma (DLBCL), a fixed threshold of SUV4.0 was considered the best method to derive MTV (*24*). Similar to our findings, MTV significantly differed among the methods, but the prognostic performance was comparable. Interestingly, method performance in DLBCL at interim PET has been shown to depend on the lesional SUV_{max}, in which lesions with $SUV_{max} < 10$ were delineated most successfully using MV3, whereas SUV4.0 was most successful in lesions with $SUV_{max} > 10$ (*25*). Correlations for MTV were significantly higher in our cohort than previously described for DLBCL, possible because our correlations were assessed after manual adaptation (*24,25*). Additionally, and contrary to our findings, the 41max, A50P, and MV3 methods yielded lower exact MTV values than SUV4.0 in baseline DLBCL, showing that performance of different methods can be disease-dependent. In our cohort, 41max resulted in the highest MTV, which can be explained by the lower SUV in our cHL cohort (median SUV_{max}, 11.3), compared with DLBCL patients (median SUV_{max} 22.6) (*26*). Because SUV_{max} is a patient-level feature, and cHL shows heterogeneous ^{18}F-FDG uptake, other lesions within a patient may have a much lower SUV_{max}, resulting in overestimation of the MTV and flooding with relative methods such as 41max.

Methods based on relative thresholds (e.g., 41max and A50P) are less suitable for assessing MTV in diseases with heterogeneous ^{18}F-FDG uptake, such as cHL, because a high lesional SUV_{max}

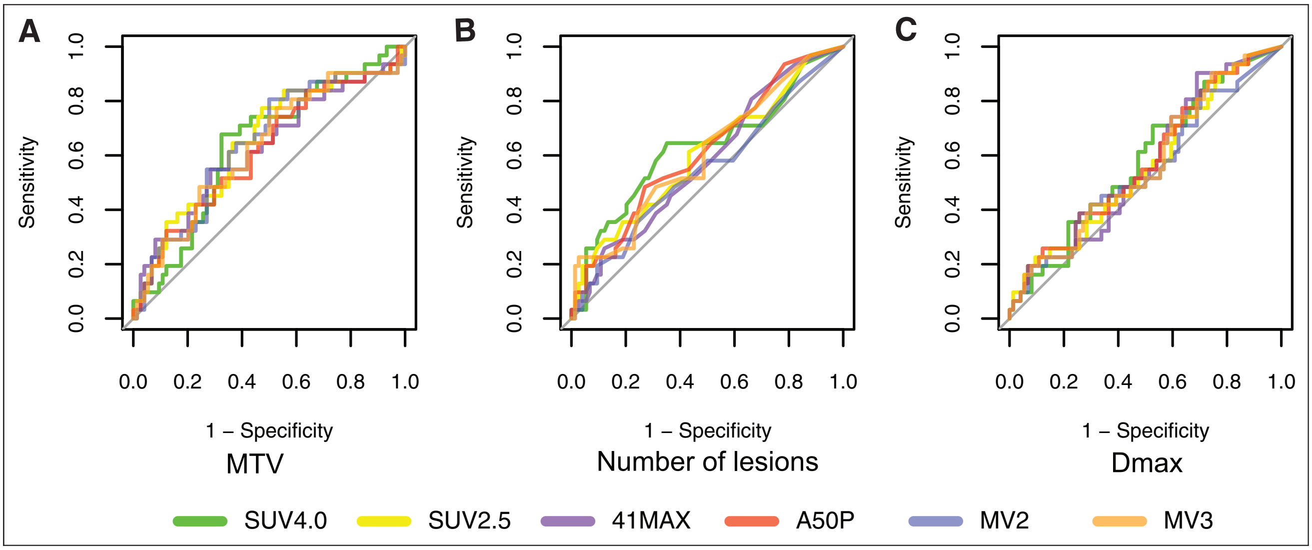

FIGURE 5. Prognostic performance of radiomics features per method assessed by area under the curve of receiver operating characteristics analysis. (A) MTV. (B) Number of lesions. (C) Dmax.

may exclude the lower avid voxels of the lesion, causing undersegmentation. A low lesional SUV$_{\text{max}}$, however, results in a low threshold, leading to flooding into regions with physiologic ^{18}F-FDG uptake. The MV methods could not overcome this disadvantage of the relative methods. MV2 frequently uses voxels that are being selected with 41max and A50P, and although MV3 needs a third method this did not result in better segmentation than methods with a fixed threshold.

Although the 41max method is recommended for MTV segmentation and has been used in several lymphoma studies, this method requires extensive manual adaptation, which is time-consuming and more susceptible to interobserver variation (*13,15,19*). Additionally, the recommendation for 41max is based on solid malignancies rather than disseminated diseases such as cHL, and 41max has not been compared directly to a fixed threshold of SUV4.0 (*27–29*). Therefore, this recommendation should be reconsidered for cHL.

CONCLUSION

For PET/CT segmentation in cHL, we showed a high correlation among MTV and most intensity and dissemination features derived with different segmentation methods, except for dissemination features addressing differences in volume and SUV$_{\text{max}}$/$_{\text{peak}}$. The prognostic performance of all features is comparable among the methods. The SUV4.0 method required the least manual adaptation, which is critical for future research and implementation in clinical practice. Although segmentation with SUV4.0 often missed small lesions with low^{18}F-FDG avidity, which may in particular affect dissemination features such as the Dmax, this seemed not to influence the prognostic performance of most features, including Dmax. However, to be conclusive about recommending SUV4.0 for cHL segmentation, the prognostic importance of small lesions with low uptake should be evaluated in a larger cohort of cHL patients with more progression events.

DISCLOSURE

This work was financially supported by SHOW (Dutch Foundation of hematooncologic research, a nonprofit donation fund of Amsterdam UMC). There is no financial support for this work that could have influenced the outcomes described in the article. Ronald Boellaard is a scientific advisor and chair of the EARL accreditation program. Marie José Kersten is a consultant for BMS/Celgene, Kite/Gilead, Miltenyi Biotech, Novartis, and Takeda and has received honoraria from Kite/Gilead, Novartis, and Roche as well as research funding from Kite/Gilead, Takeda. Craig H. Moskowitz is an advisor for and received research funding from Celgene, Genentech, Merck, and Seattle Genetics. Alison J. Moskowitz is a consultant for Takeda, Imbrium Therapeutics, Janpix, Merck, and Seattle Genetics and has received research funding from Incyte, Merck, Seattle Genetics, ADC Therapeutics, Beigene, Miragen, and Bristol-Myers Squibb. Josée M. Zijlstra has received research funding from Takeda.

ACKNOWLEDGMENTS

We thank the patients and collaborating investigators who kindly supplied their data.

KEY POINTS

QUESTION: Which segmentation method provides the best delineation and completeness of lesion selection with the least manual adaptation in scans of cHL patients, and what is the influence of the segmentation method on the prognostic value of MTV, intensity, and dissemination radiomics features?

PERTINENT FINDINGS: Segmentation with a fixed threshold of SUV4.0 required the least manual adaptation, with SUV2.5 resulting in the most complete selection of all lesions. The prognostic performance of features was comparable per segmentation method, and there was a high correlation for MTV and intensity features, but not for all dissemination features, assessed with the different methods.

IMPLICATIONS FOR PATIENT CARE: Semiautomated estimation of MTV, intensity, and dissemination radiomics features in cHL patients is feasible using a method with a fixed threshold.

REFERENCES

1. Cheson BD, Fisher RI, Barrington SF, et al. Recommendations for initial evaluation, staging, and response assessment of Hodgkin and non-Hodgkin lymphoma: the Lugano classification. *J Clin Oncol.* 2014;32:3059–3068.
2. Kersten MJ, Driessen J, Zijlstra JM, et al. Combining brentuximab vedotin with dexamethasone, high-dose cytarabine and cisplatin as salvage treatment in relapsed or refractory Hodgkin lymphoma: the phase II HOVON/LLPC Transplant BRaVE study. *Haematologica.* 2021;106:1129–1137.
3. Moskowitz CH, Matasar MJ, Zelenetz AD, et al. Normalization of pre-ASCT, FDG-PET imaging with second-line, non-cross-resistant, chemotherapy programs improves event-free survival in patients with Hodgkin lymphoma. *Blood.* 2012;119:1665–1670.
4. Moskowitz AJ, Schoder H, Gavane S, et al. Prognostic significance of baseline metabolic tumor volume in relapsed and refractory Hodgkin lymphoma. *Blood.* 2017;130:2196–2203.
5. Albano D, Mazzoletti A, Spallino M, et al. Prognostic role of baseline ^{18}F-FDG PET/CT metabolic parameters in elderly HL: a two-center experience in 123 patients. *Ann Hematol.* 2020;99:1321–1330.
6. Milgrom SA, Elhalawani H, Lee J, et al. A PET radiomics model to predict refractory mediastinal Hodgkin lymphoma. *Sci Rep.* 2019;9:1322.
7. Rogasch JMM, Hundsdoerfer P, Hofheinz F, et al. Pretherapeutic FDG-PET total metabolic tumor volume predicts response to induction therapy in pediatric Hodgkin's lymphoma. *BMC Cancer.* 2018;18:521.
8. Cottereau AS, Versari A, Loft A, et al. Prognostic value of baseline metabolic tumor volume in early-stage Hodgkin lymphoma in the standard arm of the H10 trial. *Blood.* 2018;131:1456–1463.
9. Procházka V, Gawande RS, Cayci Z, et al. Positron emission tomography-based assessment of metabolic tumor volume predicts survival after autologous hematopoietic cell transplantation for Hodgkin lymphoma. *Biol Blood Marrow Transplant.* 2018;24:64–70.
10. Song MK, Chung JS, Lee JJ, et al. Metabolic tumor volume by positron emission tomography/computed tomography as a clinical parameter to determine therapeutic modality for early stage Hodgkin's lymphoma. *Cancer Sci.* 2013;104:1656–1661.
11. Mettler J, Muller H, Voltin CA, et al. Metabolic tumour volume for response prediction in advanced-stage Hodgkin lymphoma. *J Nucl Med.* 2018;60:207–211.
12. Barrington SF, Meignan M. Time to prepare for risk adaptation in lymphoma by standardizing measurement of metabolic tumor burden. *J Nucl Med.* 2019;60:1096–1102.
13. Tutino F, Puccini G, Linguanti F, et al. Baseline metabolic tumor volume calculation using different SUV thresholding methods in Hodgkin lymphoma patients: interobserver agreement and reproducibility across software platforms. *Nucl Med Commun.* 2021;42:284–291.
14. Martín-Saladich Q, Reynés-Llompart G, Sabaté-Llobera A, Palomar-Muñoz A, Domingo-Domènech E, Cortés-Romera M. Comparison of different automatic methods for the delineation of the total metabolic tumor volume in I-II stage Hodgkin Lymphoma. *Sci Rep.* 2020;10:12590.
15. Camacho MR, Etchebehere E, Tardelli N, et al. Validation of a multifocal segmentation method for measuring metabolic tumor volume in Hodgkin lymphoma. *J Nucl Med Technol.* 2020;48:30–35.
16. Kanoun S, Tal I, Berriolo-Riedinger A, et al. Influence of software tool and methodological aspects of total metabolic tumor volume calculation on baseline [^{18}F]FDG PET to predict survival in Hodgkin lymphoma. *PLoS One.* 2015;10:e0140830.

17. Weisman AJ, Kim J, Lee I, et al. Automated quantification of baseline imaging PET metrics on FDG PET/CT images of pediatric Hodgkin lymphoma patients. *EJNMMI Phys.* 2020;7:76.
18. Drees EEE, Roemer MGM, Groenewegen NJ, et al. Extracellular vesicle miRNA predict FDG-PET status in patients with classical Hodgkin Lymphoma. *J Extracell Vesicles.* 2021;10:e12121.
19. Boellaard R, Delgado-Bolton R, Oyen WJ, et al. FDG PET/CT: EANM procedure guidelines for tumour imaging: version 2.0. *Eur J Nucl Med Mol Imaging.* 2015; 42:328–354.
20. Boellaard R. Quantitative oncology molecular analysis suite: ACCURATE. *J Nucl Med.* 2018;59(suppl 1):1753.
21. Pfaehler E, Zwanenburg A, de Jong JR, Boellaard R. RaCaT: an open source and easy to use radiomics calculator tool. *PLoS One.* 2019;14:e0212223.
22. DeLong ER, DeLong DM, Clarke-Pearson DL. Comparing the areas under two or more correlated receiver operating characteristic curves: a nonparametric approach. *Biometrics.* 1988;44:837–845.
23. Pfaehler E, Beukinga RJ, de Jong JR, et al. Repeatability of ^{18}F-FDG PET radiomic features: a phantom study to explore sensitivity to image reconstruction settings, noise, and delineation method. *Med Phys.* 2019;46:665–678.
24. Barrington SF, Zwezerijnen B, de Vet HCW, et al. Automated segmentation of baseline metabolic total tumor burden in diffuse large B-cell lymphoma: which method is most successful? a study on behalf of the PETRA consortium. *J Nucl Med.* 2021;62:332–337.
25. Zwezerijnen GJ, Eertink JJ, Burggraaff CN, et al. Interobserver agreement in automated metabolic tumor volume measurements of Deauville score 4 and 5 lesions at interim ^{18}F-FDG PET in DLBCL. *J Nucl Med.* 2021;62:1531–1536.
26. Eertink JJ, van de Brug T, Wiegers SE, et al. ^{18}F-FDG PET baseline radiomics features improve the prediction of treatment outcome in diffuse large B-cell lymphoma. *Eur J Nucl Med Mol Imaging.* 2022;49:932–942.
27. Frings V, de Langen AJ, Smit EF, et al. Repeatability of metabolically active volume measurements with ^{18}F-FDG and ^{18}F-FLT PET in non-small cell lung cancer. *J Nucl Med.* 2010;51:1870–1877.
28. Krak NC, Boellaard R, Hoekstra OS, Twisk JW, Hoekstra CJ, Lammertsma AA. Effects of ROI definition and reconstruction method on quantitative outcome and applicability in a response monitoring trial. *Eur J Nucl Med Mol Imaging.* 2005;32:294–301.
29. Boellaard R, Krak NC, Hoekstra OS, Lammertsma AA. Effects of noise, image resolution, and ROI definition on the accuracy of standard uptake values: a simulation study. *J Nucl Med.* 2004;45:1519–1527.

^{18}F-FDG Uptake in Brown Adipose Tissue After Exposure to the Cold: From Possible Pitfall in Early PET Scans to Metabolic Biomarker

Paola A. Erba[1], Andrea Natali[2], H. William Strauss[3], and Giuliano Mariani[1]

[1]Regional Center of Nuclear Medicine, Department of Translational Research and Advanced Technologies in Medicine and Surgery, University of Pisa, Pisa, Italy; [2]Laboratory of Metabolism, Nutrition, and Atherosclerosis, Department of Clinical and Experimental Medicine, University of Pisa, Pisa, Italy; and [3]Weill Cornell Medical College and Molecular Imaging and Targeted Therapy Service of the Department of Radiology, Memorial Sloan Kettering Cancer Center, New York, New York

See the associated article on page 1433.

There are 3 types of fat in the human body: white, brown, and beige (*1*). White adipocytes deposit extra energy into triglycerides, whereas beige and brown adipocytes have the unique ability to convert mitochondrial energy into heat (rather than adenosine triphosphate) via uncoupling protein 1. Obesity, especially excess fat in tissue that is normally lean, increases the risk of cardiovascular disease (*2*). In addition to the amount of fat, the distribution of fat, especially increased abdominal fat, evaluated by the ratio of waist to hip circumferences, predicts glucose intolerance, insulin resistance, hypertension, and hypertriglyceridemia (*3,4*). PET/CT with ^{18}F-FDG provides a unique opportunity to view the metabolic activity of brown adipose tissue (BAT). However, even though visceral and subcutaneous fat are substantially less metabolically active than BAT, both are metabolically active tissues (*5*). Visceral adipose tissue is more metabolically active than subcutaneous fat.

BAT is a thermoregulatory organ that consumes stored energy to produce heat through the expression of uncoupling protein 1. This phenomenon is called nonshivering thermogenesis and plays an important role in glucose and lipid metabolism (*6*). It is particularly intense in newborns, in whom it helps to maintain a normal body temperature; although declining with age, islets of brown adipocytes remain in the white adipose tissue of adult humans (*7*). Such islets are activated by exposure to cold, with a higher prevalence in children, women, and lean subjects (*8*). Experimental evidence suggests that BAT may also play an important role in the development and progression of cancer—through secretion of adipokines, inflammatory cytokines, growth factors, and free fatty acids (*9*). In this regard, the biologic mechanism of BAT hypermetabolism as quantified by ^{18}F-FDG PET/CT is similar to hypermetabolism of cancer cells.

In this issue of *The Journal of Nuclear Medicine,* Crandall et al. report the metabolic changes associated with the cold-activation of BAT in a group of young adult volunteers. The investigators injected ^{18}F-FDG for PET/CT imaging immediately after 2 h of exposure to cold. In addition to the imaging study, the investigators compared baseline blood metabolites in participants with varying amounts of active BAT (*10*). From the perspective of a clinician with expertise in glucose and lipid metabolism, there are at least 4 puzzling points in the results: the surprising variability in BAT volume (0–430 cm^3) and ^{18}F-FDG uptake in BAT (SUV$_{\max}$ normalized to lean body weight, 0–38) in a rather homogeneous cohort of young, healthy individuals; the impressive correlation of fasting insulin with both BAT volume (r = 0.90) and BAT ^{18}F-FDG uptake (r = 0.74); the substantial differences in lifestyle between the low-BAT and high-BAT groups, who were neither on a calorie-restricted diet nor engaging in regular physical exercise and had only a marginally higher body mass index (1.4 kg/m^2); and the decline in glucose and insulin levels induced by acute exposure to cold observed only in the high-BAT subjects.

Such extreme physiologic heterogeneity in BAT volume and activated metabolism raises questions. Is there any relationship between volume and function (i.e., activated glucose uptake)? Does BAT volume or activation correlate with the individual tolerance to cold (shivering threshold)? Elucidation of these issues would help us learn whether BAT can be "trained," or expanded by exposure to cold.

The amazing association between insulin and BAT volume suggests that BAT is expanded in subjects with relative insulin resistance, which is confirmed by the concomitantly higher glucose values. If this is this case, then these individuals are probably at a higher risk of developing diabetes.

On the other hand, the extreme difference in lifestyle, despite a minor difference in body mass index, suggests that these subjects with expanded BAT are less prone to becoming obese. The decline in glucose observed after exposure to cold only in the high-BAT subjects suggests that these individuals are more resistant to the stress induced by cold. Indeed, BAT-negative lean subjects display reduced epinephrine levels after exposure to cold when compared with BAT-positive subjects, despite a similar increase in energy expenditure (*11*). This finding could be interpreted as a higher sensitivity of thermogenesis to catecholamines and could be another mechanism that protects the high-BAT subjects from developing obesity. The possibility that BAT expansion would protect from development of diabetes might be related to this protection.

Received May 1, 2022; revision accepted May 10, 2022.

For correspondence or reprints, contact Giuliano Mariani (giuliano.mariani@med.unipi.it).

DOI: 10.2967/jnumed.122.264188

BROWN ADIPOSE TISSUE ACTIVITY • Erba et al. 1431

Somewhat less impressive, from a clinical perspective, are the differences in basal glucose, insulin, and triglycerides between low and high BAT, as might be driven by the difference in body mass index. Also, the different changes in lipid profiles induced by such a short-term exposure to cold are difficult to interpret, considering the extremely slow kinetics of these substrates.

Overall, Crandall et al. are to be congratulated on their novel use of PET/CT to investigate thermogenesis in a study that casts novel perspectives on the application of a mature imaging method such as PET with ^{18}F-FDG. In this regard, accurate imaging quantification made possible by recent scientific and technologic advances can address the combined challenges of deriving robust imaging biomarkers for artificial intelligence applications and of capitalizing the full potential of PET systems with a long axial field of view. An exciting application for such new systems is the possibility of determining the kinetics of tracer biodistribution through different compartments of the body—given the possibility of recording quasidynamic acquisitions of virtually the whole body (*12*). These developments cast our interest back to the origin by reminding us that the essence of ^{18}F-FDG PET/CT is not just reporting the presence of uptake in a target lesion: every single PET/CT scan has much more than this to offer, and "signals" are there just to be detected and correctly interpreted. ^{18}F-FDG uptake in BAT is the perfect example of this scenario (*13*).

DISCLOSURE

No potential conflict of interest relevant to this article was reported.

REFERENCES

1. Okla M, Kim J, Koehler K, Chung S. Dietary factors promoting brown and beige fat development and thermogenesis. *Adv Nutr.* 2017;8:473–483.
2. Piché ME, Tchernof A, Despres J-P. Obesity phenotypes, diabetes, and cardiovascular diseases. *Circ Res.* 2020;126:1477–1500.
3. Kalkhoff RK, Hartz AH, Rupley D, Kissebah AH, Kelber S. Relationship of body fat distribution to blood pressure, carbohydrate tolerance, and plasma lipids in healthy obese women. *J Lab Clin Med.* 1983;102:621–627.
4. Krotkiewski M, Björntorp P, Sjöström L, Smith U. Impact of obesity on metabolism in men and women: importance of regional adipose tissue distribution. *J Clin Invest.* 1983;72:1150–1162.
5. Christen T, Sheikine Y, Rocha VZ, et al. Increased glucose uptake in visceral versus subcutaneous adipose tissue revealed by PET imaging. *JACC Cardiovasc Imaging.* 2010;3:843–851.
6. Bos SA, Gill CM, Martinez-Salazar EL, Torriani M, Bredella MA. Preliminary investigation of brown adipose tissue assessed by PET/CT and cancer activity. *Skeletal Radiol.* 2019;48:413–419.
7. Huang Y-C, Chen T-B, Hsu C-C, et al. The relationship between brown adipose tissue activity and neoplastic status: an ^{18}F-FDG PET/CT study in the tropics. *Lipids Health Dis.* 2011;10:238.
8. Cypess AM, Lehman S, Williams G, et al. Identification and importance of brown adipose tissue in adult humans. *N Engl J Med.* 2009;360:1509–1517.
9. Himbert C, Delphan M, Scherer D, Bowers LW, Hursting S, Ulrich CM. Signals from the adipose microenvironment and the obesity-cancer link: a systematic review. *Cancer Prev Res (Phila).* 2017;10:494–506.
10. Crandall JP, Fraum TJ, Wahl RL. Brown adipose tissue: a protective mechanism in "prepediabetes"? *J Nucl Med.* 2022;63:1433–1440.
11. Kulterer OC, Herz CT, Prager M, et al. Brown adipose tissue prevalence is lower in obesity but its metabolic activity is intact. *Front Endocrinol (Lausanne).* 2022; 13:858417.
12. Pantel AR, Mankoff DA, Karp JS. Total-body PET: will it change science and practice? *J Nucl Med.* 2022;63:646–648.
13. Crandall JP, Wahl RL. Perspectives on brown adipose tissue imaging: insights from preclinical and clinical observations from the last and current century. *J Nucl Med.* 2021;62(suppl 2):34S–43S.

Brown Adipose Tissue: A Protective Mechanism Against "Preprediabetes"?

John P. Crandall, Tyler J. Fraum, and Richard L. Wahl

Mallinckrodt Institute of Radiology, Washington University School of Medicine, St. Louis, Missouri

See an invited perspective on this article on page 1431.

Brown adipose tissue (BAT) is present in a significant number of adult humans and has been postulated to exert beneficial metabolic effects. Lean, nondiabetic patients undergoing clinical PET/CT imaging are more likely to exhibit incidental BAT activation. The aim of this study was to assess metabolic changes associated with the cold activation of BAT and to compare baseline blood metabolites in participants with varying amounts of active BAT. **Methods:** Serum blood samples were collected from healthy adult volunteers (body mass index, 18.0–25.0, and age $\leq$ 35 y) before and after 2 h of exposure to cold. ^{18}F-FDG PET/CT imaging was performed immediately after cold exposure. Activated BAT was segmented, and fasting glucose, insulin, lipid, and other blood metabolite levels were correlated with volume and intensity of active BAT. Using a median cutoff, subjects were classified as high-BAT ($\mathrm{BAT_{high}}$) or low-BAT ($\mathrm{BAT_{low}}$). **Results:** A higher volume of activated BAT was associated with significantly higher precooling glucose and insulin levels ($P < 0.001$ for each). Precooling thyroid-stimulating hormone and triglyceride levels were significantly higher in the $\mathrm{BAT_{high}}$ than the $\mathrm{BAT_{low}}$ group ($P = 0.002$ and $P < 0.001$, respectively). Triglyceride levels tended to increase over the cooling period in both BAT groups but increased significantly more in the $\mathrm{BAT_{high}}$ group (15.7 ± 13.2 mg/dL; $P < 0.001$) than in the $\mathrm{BAT_{low}}$ group (4.5 ± 12.2 mg/dL; $P = 0.061$). **Conclusion:** These findings may indicate that BAT is recruited to counteract incipient "preprediabetic" states, potentially serving as a first-line protective mechanism against very early metabolic or hormonal variations.

Key Words: endocrine; molecular imaging; PET/CT; brown fat; FDG; metabolism

J Nucl Med 2022; 63:1433–1440
DOI: 10.2967/jnumed.121.263357

Brown adipose tissue (BAT) uses a variety of metabolic substrates to produce heat in mammals and so constitutes a potential target for the treatment of obesity and other metabolic disorders (*1*). White adipose tissue (WAT) stores energy as triacylglycerols, which can be released as nonesterified fatty acids (NEFAs) for energy consumption by metabolically active organs. BAT uses fatty acids released from intracellular triglyceride stores for β-oxidation to generate heat by a process known as adaptive thermogenesis (*2*).

The presence of BAT in adult humans was initially recognized mainly on ^{18}F-FDG PET/CT examinations performed for oncologic indications (*3,4*). ^{18}F-FDG PET has since become the most commonly used technique for the in vivo detection of cold-activated BAT in humans (*5,6*). Studies using PET with ^{18}F-FDG or fatty-acid tracers have demonstrated that BAT consumes glucose and fatty acids (*7–9*).

Two primary pathways are known to regulate BAT glucose metabolism: adrenergic and insulin signaling (*1*). On sympathetic nervous system activation, norepinephrine is released, which binds to adrenergic receptors (β_1-, β_2-, and β_3- adrenoceptors) expressed on BAT cell surfaces, causing an increase in cytosolic cyclic adenosine monophosphate levels (*10*). The result is an increase in glucose transporter 1 transcription and, via activation of the mammalian target of rapamycin complex 2, the translocation of this newly synthesized glucose transporter 1 to the cell membrane (*11*). Alternatively, insulin binds to BAT insulin receptors, and phosphoinositide 3-kinases phosphorylate protein kinase B, inducing the translocation of glucose transporter 4 to the cell membrane. Glucose, having been taken up by BAT cells using either pathway, is used for glycolysis, maintaining fatty acid oxidation, or activation of uncoupling protein 1 via de novo lipogenesis and fatty-acid synthesis (*2*).

The regulation of glucose by activated BAT may have important therapeutic implications, as exposure to cold has been shown to reverse glucose intolerance and insulin resistance in animal models (*12–14*). Cold acclimation may also result in increased fractional uptake in BAT (*15*). Observational human studies have indicated that the presence of active BAT is associated with lower glucose levels and a decreased risk of diabetes (*16–18*). However, the role of BAT in whole-body glucose consumption remains unclear since several prospective studies have indicated a minimal contribution by BAT to systemic glucose utilization (*8,19*). Still, others have shown a protective effect of BAT against diabetes (*20*).

Current evidence indicates that lipid metabolism in humans is modulated, at least to some degree, by BAT. BAT activation has been correlated with cold-induced increases in WAT lipolysis and NEFA oxidation, indicating that NEFAs are mobilized from WAT to fuel activated BAT. It has been hypothesized that increased BAT activity or volume increases uptake of NEFAs in BAT, improving overall lipid metabolism (*12,21*). A recent retrospective study found that nonstimulated BAT was associated with lower concentrations of circulating triglycerides (*22*). Rodent studies have demonstrated the clearance of triglyceride-rich lipoproteins and cholesterol from circulation by BAT (*12,23*) and have even seemed to demonstrate that active BAT modulates fuel selection in non-BAT organs (*24*). Even during fasting and postprandial conditions, BAT has been shown to take up significant amounts of circulating free fatty acids in mice (*25*). However, the practical implications of active BAT on lipid metabolism in humans remain unclear (*26,27*).

Received Dec. 4, 2021; revision accepted Mar. 21, 2022.

For correspondence or reprints, contact Richard L. Wahl (rwahl@wustl.edu).

The primary aim of this study was to assess whether there are differences in baseline glucose, insulin, lipid, and other metabolite levels between subjects with varying amounts of cold-activated BAT. A secondary aim was to evaluate changes in these blood markers between precooling and postcooling serum blood samples. An additional aim was to assess how different lifestyle parameters are associated with BAT volume. These data were collected as part of a prospective study assessing the repeatability of BAT activity levels on ^{18}F-FDG PET/CT (*28*).

MATERIALS AND METHODS

This prospective study was approved by the Washington University Institutional Review Board. All subjects provided written informed consent before participation. Between March 2016 and January 2020, 34 healthy volunteers were enrolled and underwent ^{18}F-FDG PET/CT imaging after a cooling procedure intended to activate BAT (subject characteristics provided in Table 1). The median ^{18}F-FDG uptake time was 61.0 min, with a range of 59.0–76.6 min. Median blood glucose, measured immediately before ^{18}F-FDG administration, was 78 mg/dL, and the range was 58–103 mg/dL. Since younger age and lower body mass index have been shown to correlate with higher amounts of metabolically active BAT (*7,29,30*), healthy adult volunteers aged 18–35 with a body mass index between 18 and 25 were eligible for this study. Furthermore, as drugs targeting the sympathetic nervous system (e.g., nicotine, β-blockers, and amphetamines) can interfere with BAT activation (*31*), individuals with a history of consuming these agents were excluded. A complete list of inclusion and exclusion criteria can be found in Supplemental Table 1 (supplemental materials are available at http://jnm.snmjournals.org). Subjects were recruited using flyers posted at various locations on the Washington University in St. Louis medical campus.

Subject Preparation

A schematic representation of the imaging visit is shown in Figure 1. All subjects were instructed to fast for at least 6 h before imaging and to avoid high-carbohydrate and high-fat foods. Subjects were also asked to avoid cold exposure and to refrain from exercise during the 24 h before the imaging sessions. To prevent premature BAT activation, subjects were kept warm for 60 min, using warmed blankets, before the start of the cold-exposure procedure. During this period, the precooling blood sample was drawn for metabolite analysis. After the preparatory phase, participants were outfitted in a cooling suit (CureWrap; MRTE Advanced Technologies) that circulates chilled water at a set temperature.

TABLE 1
Subject Characteristics

Characteristic	Total	BAT$_{high}$	BAT$_{low}$
Sex			
Male	7	4	3
Female	34	17	17
Age (y)	23.8 ± 3.5	23.2 ± 2.7	24.7 ± 4.3
Height (m)	1.66 ± 0.09	1.67 ± 0.09	1.65 ± 0.09
Weight (kg)	62.3 ± 8.8	64.6 ± 9.1	59.6 ± 7.9
Body mass index (kg/m^2)	22.3 ± 1.8	23.0 ± 1.7	21.6 ± 1.5
Race			
White	20	12	8
Black	2	0	2
Asian	12	5	7
Ethnicity			
Hispanic		1	1
Non-Hispanic	32	16	16

Qualitative data are number; continuous data are mean ± SD

Lifestyle Interview

During the preparatory phase, subjects were asked a series of questions to assess the impact of lifestyle on BAT activity. Volunteers were asked to describe any specific diet they followed within the year before the study, to report any dietary supplements they consume regularly, and to estimate their weekly caffeine and alcohol intake. Subjects were asked to describe their normal exercise habits, if any, during the previous year. Exercise descriptions were recorded and coded as mostly aerobic, mostly anaerobic, or combination aerobic/anaerobic.

Cooling Protocol

An individualized cooling protocol was used with a goal of cooling the subject to just above the shivering point (*5*). Initially, the water temperature of the cooling suit was set at 10°C for all subjects. Subjects were monitored for shivering, both visibly and via electromyogram (electrodes placed over the vastus lateralis, pectoralis major, and latissimus dorsi muscles). If shivering was observed or reported, the water temperature was increased at 0.5°C increments every 60 s until shivering stopped. Oral temperature and blood pressure were measured every 5 min during the cooling procedure. A 185-MBq dose of ^{18}F-FDG was administered intravenously after 60 min of cooling. Cooling continued during the 60-min ^{18}F-FDG uptake phase. Immediately before ^{18}F-FDG PET/CT imaging, subjects were removed from the cooling suit.

Imaging Protocol

Imaging and reconstruction parameters are detailed in Supplemental Table 2. All subjects were imaged on a Biograph 40 PET/CT TruePoint/TrueView scanner (Siemens AG). In humans, most active BAT depots are located in the supraclavicular and paravertebral regions, with additional foci commonly seen in the axillary, intercostal, mediastinal, and perirenal areas. Therefore, PET imaging (three 8-min list-mode acquisitions) was performed from the skull base to the umbilicus. A low-dose CT scan (using CARE Dose [Siemens] tube current modulation) was obtained immediately before the PET scan. The imaging protocol followed the standards set forth by the Uniform Protocols for Imaging in Clinical Trials for ^{18}F-FDG PET/CT and the Radiologic Society of North America–Quantitative Imaging Biomarker Alliance's profile for quantitative ^{18}F-FDG PET/CT (*32,33*).

Image Analysis

Images were analyzed using MIM, version 6.9.3 (MIM Software). Activated BAT was segmented (Fig. 2) and quantified according to the recommendations of version 1.0 of the Brown Adipose Reporting Criteria in Imaging Studies (*5*). Areas known to contain BAT were qualitatively assessed, and likely BAT depots were identified. Volumes of interest were drawn on coronal ^{18}F-FDG PET/CT images slice-by-slice, taking care not to include any adjacent normal ^{18}F-FDG–avid tissues. Thresholds were then applied to this manual volume of interest to first remove voxels with lean body mass–adjusted SUVs (SULs) below 1.2 and then to remove voxels with Hounsfield units outside the −190 to −10 range. Thus, the final activated BAT volumes consisted of voxels with SULs above normal background levels and within the fat density range.

The total activated BAT metabolic volume (BMV) was the sum of all segmented BAT volumes. For participants included in the test–retest study, BMV and the maximum SUL (SUL$_{max}$) for each imaging session were analyzed separately. The SUL$_{max}$ was defined as the

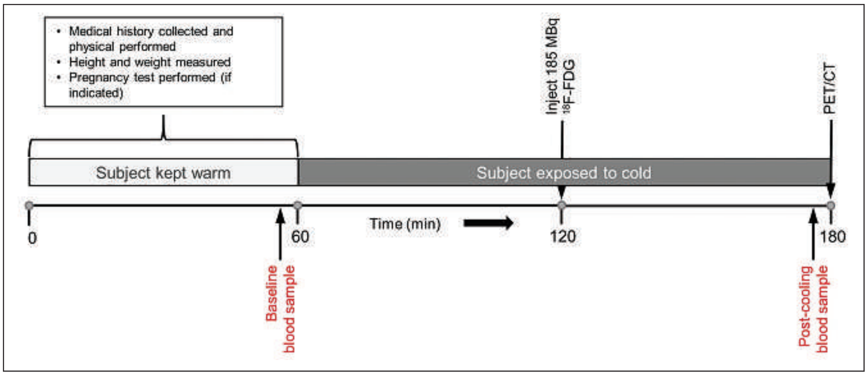

FIGURE 1. BAT activation and imaging process. After 1-h warming period, volunteers were exposed to cold for ~2 h to activate BAT. After first hour of cooling, 185 MBq of ^{18}F-FDG were administered intravenously. Cooling continued for a second hour, and PET/CT imaging was performed immediately afterward.

single voxel within all the segmented BAT depots with the greatest ^{18}F-FDG uptake. The version of MIM used for our analyses uses the James equation for lean body mass computation (*34*). For subjects without visually detectable BAT, the SUL$_{\text{max}}$ was instead based on the background activity of the fat in the right supraclavicular fossa, using a spheric region of interest (3.0-cm radius). This region was chosen because the supraclavicular fossa most commonly contains the BAT depot with the most ^{18}F-FDG uptake.

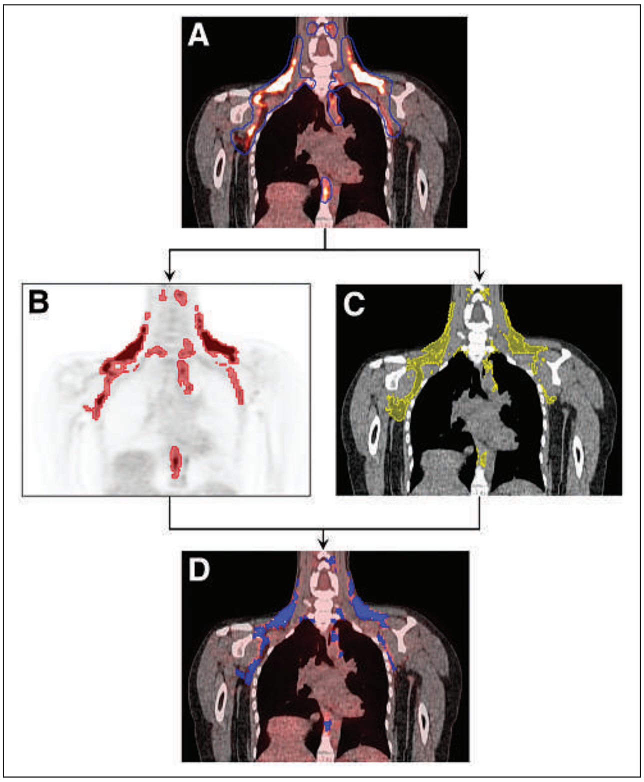

FIGURE 2. BAT segmentation was performed per Brown Adipose Reporting Criteria in Imaging Studies, version 1.0, guidelines. (A) Areas known to contain BAT depots were manually delineated. (B and C) On PET images, voxels with SUL$_{\text{max}}$ less than 1.2 were removed (B) and on CT images, voxels with Hounsfield units outside range of −190 to −10 were removed (C). (D) Boolean intersection of PET and CT images was used to obtain final volumes of interest.

Biologic Assays

Methods used for blood sample analyses are provided in Supplemental Table 3. All tests were performed using either Cobas 6000 or Cobas 8000 (Roche Diagnostics). Blood samples were analyzed in the Barnes Jewish Clinical Chemistry Laboratory, which holds College of American Pathologists and Clinical Laboratory Improvement Amendments certifications. Lipid data were available for all subjects, whereas insulin, glucose, and other metabolite data were available for only a subset of participants.

Statistics

Numeric results are reported as mean and SD or as median and interquartile range. Subject characteristics were summarized descriptively via means, medians, SD, and ranges. A subset of participants was included in a test–retest repeatability study ($n = 29$) and underwent the cooling and imaging protocol twice on separate days. Blood samples collected during these visits were pooled with the remaining data and considered independent samples. Baseline and postcooling metabolite measurements were compared using paired *t* tests. Serum metabolite differences between high-BAT (BAT$_{\text{high}}$) and low-BAT (BAT$_{\text{low}}$) groups were assessed using unpaired *t* tests or Mann–Whitney *U* tests, depending on group normality. Group normality was assessed using D'Agostino–Pearson tests. The Fisher exact test was used to assess differences in demographics and lifestyle assessments between subjects without versus with detectable BAT. Data were analyzed using R, version 4.0.3 (http://cran.r-project.org/), and Excel, version 2016 (Microsoft Corp.). A *P* value of less than 0.05 was considered significant, unless otherwise indicated. A Bonferroni adjustment for multiple comparisons was applied when necessary to control for type I errors.

RESULTS

Subject Characteristics

During cold exposure, oral temperatures varied by a mean of ±0.4°C. Systolic pressure increased during cooling by a minimum of 8 mm Hg and a maximum of 42 mm Hg. Diastolic pressure increased during cooling by a minimum of 11 mm Hg and a maximum of 39 mm Hg. Heart rate increased by 11–30 beats per minute throughout cooling.

Activated BAT was detected in 28 of 34 (82.4%) subjects. Using a median volume cutoff, PET/CT studies showing an activated BMV greater than or less than 120 cm^3 were classified as BAT$_{\text{high}}$ or BAT$_{\text{low}}$, respectively. The mean BMV of the BAT$_{\text{low}}$ group ($n = 17$) was 36.9 ± 29.1 cm^3, and the mean BMV of the BAT$_{\text{high}}$ group ($n = 17$) was 224.3 ± 78.4 cm^3. There were no substantial differences in age, height, or weight between groups. A significant difference in body mass index was found, with BAT$_{\text{high}}$ subjects having a higher body mass index than BAT$_{\text{low}}$ subjects ($P = 0.026$).

Insulin and Glucose

Mean baseline insulin and glucose levels were significantly lower in the BAT$_{\text{low}}$ than the BAT$_{\text{high}}$ group (Table 2). Between baseline and postcooling samples, mean insulin levels increased by 1.6 ± 1.2 μIU/mL in the BAT$_{\text{low}}$ group and decreased by 2.7 ± 1.4 μIU/mL in the BAT$_{\text{high}}$ group. Baseline glucose and insulin showed significant positive correlations with both BMV and SUL$_{\text{max}}$ (Figs. 3 and 4). The change in glucose and insulin levels from baseline to postcooling samples showed significant negative correlations with both

TABLE 2
Glucose and Insulin *t* Test and Regression Analysis Results

Metabolite	Time point	μ (BAT_{low})	σ	μ (BAT_{high})	σ	*r* (BMV)	*r* (SUL_{max})	*P*
Insulin (μIU/mL)	Baseline	3.3	0.8	8.7	3.0	0.90	0.74	<0.001
	Postcooling	4.9	1.9	6.1	2.6	0.71	0.43	0.327
	Change	1.6	1.2	−2.7	1.4	−0.79	−0.64	<0.001
Glucose (mg/dL)	Baseline	70.8	10.2	88.3	11.4	0.59	0.54	<0.001
	Postcooling	84.3	12.3	85.2	7.3	0.12	0.06	0.815
	Change	3.0	5.6	−3.1	5.5	−0.58	−0.54	0.013

P values were generated using unpaired *t* tests comparing BAT_{high} and BAT_{low} groups. Using Bonferroni adjustment, $P < 0.025$ was considered significant.

BMV and SUL_{max}. Baseline insulin and glucose also significantly correlated with one another ($r = 0.67$; $P < 0.001$), as were the changes in insulin and glucose ($r = 0.51$; $P = 0.019$).

Lipids

Groupwise serum lipid results are shown in Table 3. Baseline total cholesterol, triglycerides, and high-density lipoprotein were significantly higher ($P = 0.002$, $P < 0.001$, and $P = 0.004$, respectively) in BAT_{low} versus BAT_{high} subjects. The BAT_{low} group also showed higher baseline low-density lipoprotein and non–high-density lipoprotein levels than the BAT_{high} group, though not statistically different. Between baseline and postcooling blood samples, serum total cholesterol, high-density lipoprotein, non–high-density lipoprotein, and low-density lipoprotein increased significantly for both groups (all *P* values below 0.01). Serum triglycerides increased significantly between baseline and postcooling samples for BAT_{high} subjects (15.7 ± 13.2 mg/dL; $P < 0.001$) but did not increase significantly in the BAT_{low} group (4.5 ± 12.2 mg/dL; $P = 0.061$).

Baseline triglycerides, cholesterol, and high-density lipoprotein also significantly correlated with BMV and SUL_{max} (Supplemental Figs. 1 and 2). The change in triglycerides from baseline to postcooling samples also significantly correlated with BMV and SUL_{max}.

Other Metabolites

Several additional metabolites showed groupwise differences and varied significantly between baseline and postcooling blood samples (Table 4). Mean baseline thyroid-stimulating hormone (TSH) was significantly lower in the BAT_{low} than the BAT_{high} group ($P = 0.002$). Mean baseline sodium, anion gap, urea nitrogen, albumin, and alkaline phosphatase were significantly higher in the BAT_{low} than the BAT_{high} group.

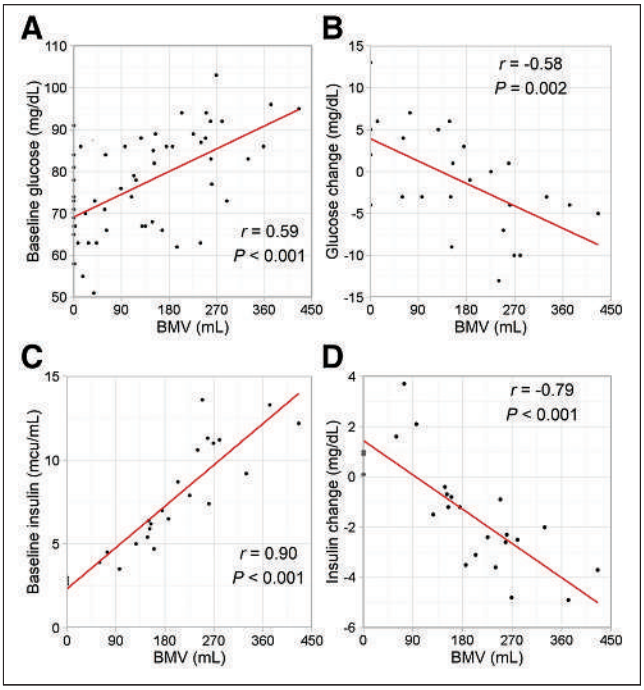

FIGURE 3. Regression analysis shows correlation between BMV and baseline serum glucose (A), change in glucose from baseline to postcooling (B), baseline serum insulin (C), and change in insulin (D). Baseline values were subtracted from postcooling values.

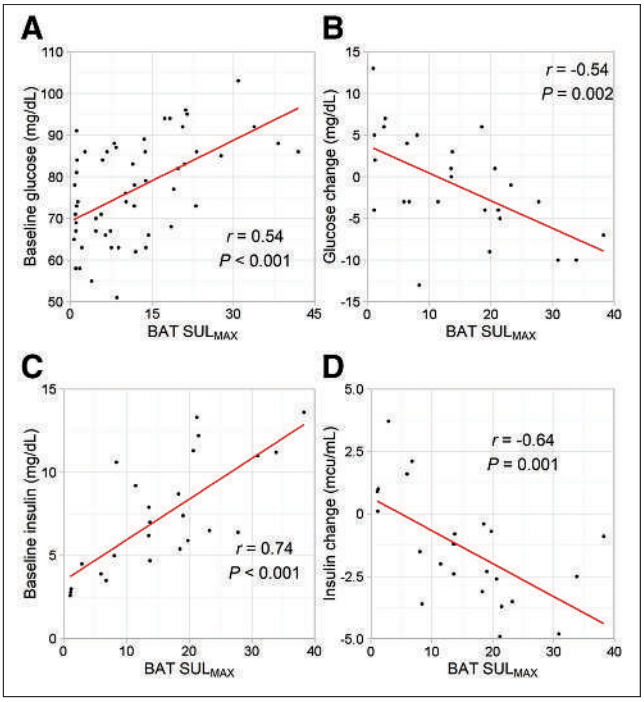

FIGURE 4. Regression analysis shows correlation between BAT SUL_{max} and baseline serum glucose (A), change in glucose from baseline to postcooling (B), baseline serum insulin (C), and change in insulin (D). Baseline values were subtracted from postcooling values.

TABLE 3
Serum Lipid *t* Test and Regression Analysis Results

		BAT_{low}		BAT_{high}		*r*		
Lipid	Time point	μ	σ	μ	σ	BMV	SUL_{max}	*P*
Cholesterol (mg/dL)	Baseline	164.0	34.0	141.9	19.8	−0.43	−0.42	0.002
	Postcooling	174.0	32.4	156.0	21.2	−0.34	−0.34	0.010
	Change	9.0	11.0	14.9	7.9	0.33	0.26	0.023
Triglycerides (mg/dL)	Baseline	63.6	24.1	89.6	26.7	0.56	0.45	<0.001
	Postcooling	66.5	24.5	105.7	31.2	0.60	0.48	<0.001
	Change	4.5	12.2	15.7	13.2	0.45	0.34	<0.001
High-density lipoprotein (mg/dL)	Baseline	66.5	14.4	56.0	16.4	−0.41	−0.35	0.004
	Postcooling	70.6	13.6	62.4	20.9	−0.28	−0.22	0.181
	Change	3.4	4.9	6.4	12.0	0.21	0.23	0.231
Low-density lipoprotein (mg/dL)	Baseline	83.7	28.9	73.8	21.3	−0.16	−0.23	0.058
	Postcooling	86.4	26.8	80.7	22.3	−0.11	−0.15	0.173
	Change	−0.9	29.2	7.5	9.1	0.15	0.16	0.153
Non–high-density lipoprotein (mg/dL)	Baseline	97.2	29.5	89.2	19.5	−0.14	−0.19	0.093
	Postcooling	103.6	29.8	97.8	20.3	−0.13	−0.17	0.182
	Change	6.1	7.7	9.2	8.3	0.02	0.06	0.185

P values were generated using unpaired *t* tests comparing BAT_{high} and BAT_{low} groups. Using Bonferroni adjustment, $P < 0.010$ was considered significant.

Lifestyle

Participants reported engaging in either no strict dietary regimen or adhering to a vegetarian, vegan, gluten-free, low-carbohydrate, or pescatarian diet. BAT_{low} subjects were significantly more likely to report observing a controlled diet than BAT_{high} subjects ($P = 0.007$). Only 1 of 17 BAT_{high} participants reported following a specific diet (pescatarian), whereas 8 of 17 BAT_{low} subjects reported adhering to a strict diet. The use of dietary supplements also varied between groups, with BAT_{high} subjects reporting either no use of dietary supplements or use of protein, melatonin, biotin, omega-6 fatty acids, or magnesium (8/17 subjects), whereas BAT_{low} subjects reported either no diet supplementation or using only a daily multivitamin (7/17 subjects). There were no significant differences between groups with respect to self-reported weekly intake of caffeine or alcohol.

Exercise habits also differed between groups. Those who reported not regularly exercising were significantly more likely to have higher BAT volumes (7/17 BAT_{high} vs. 0/16 BAT_{low}; $P = 0.018$). Among those who exercised regularly, the self-reported mean number of hours spent exercising per week was 3.4 in the BAT_{low} group and 1.9 in the BAT_{high} group ($P = 0.011$). Within the BAT_{low} group, 1 participant reported engaging in mostly anaerobic exercise, 10 in mostly aerobic exercise, and 6 in exercise that incorporated aerobic and anaerobic elements. Three BAT_{high} subjects reported engaging in mostly anaerobic exercise, 2 in mostly aerobic exercise, and 5 in exercise that was both aerobic and anaerobic.

DISCUSSION

BAT has emerged as a potential therapeutic target for obesity and related metabolic diseases. Using a previously described method, BAT was activated in this study using cold exposure and then imaged using ^{18}F-FDG PET/CT. Higher baseline insulin and glucose levels correlated with higher BMV (Supplemental Fig. 3). Greater declines in insulin and glucose levels after BAT activation also correlated with higher BMV.

Glucose and Insulin Activity

Activated BAT has been shown to act as a glucose sink in both warm and cold conditions (*35,36*), which is consistent with the significant positive correlation seen here between BMV and decreases in glucose and insulin levels during cooling. BAT thermogenesis likely resulted in significant uptake of glucose in BAT, especially in subjects with higher amounts of BAT, consistent with previous studies. However, our results are inconsistent with studies showing increased BAT uptake of glucose during warm conditions, as baseline glucose and insulin both positively correlated with BMV in our subjects. Retrospective analyses have generally concluded that patients with active BAT are more likely to have lower fasting glucose levels and less likely to be diabetic (*7,16,17,37,38*). Though, as these observational studies consisted mostly of patients undergoing clinical ^{18}F-FDG PET/CT, the populations evaluated were mostly much older than the volunteers enrolled in the current study.

Lipid Metabolism

The role of BAT in systemic lipid metabolism is supported by previous studies showing that the amount of detectable BAT correlates with cold-induced increases in WAT lipolysis and NEFA oxidation, suggesting that BAT activation plays a role in mobilization of NEFAs from WAT and their oxidative disposal in BAT (*19,21*). Din et al. found that in BAT regions, subjects with higher volumes of activated BAT took up more NEFAs from circulation than subjects with lower volumes of BAT (*39*). It has also been shown that administration of nicotinic acid, an inhibitor of triglyceride lipolysis, suppresses the cold-induced BAT metabolic rate, implying that lipolysis is central to BAT thermogenesis (*40*). Although it seems clear that BAT relies on lipids to fuel thermogenesis during cold

TABLE 4
Additional Baseline Serum Metabolite *t* Test and Regression Analysis Results

	BAT_{low}		BAT_{high}		*r*		
Metabolite	μ	σ	μ	σ	BMV	SUL_{max}	*P*
TSH (μIU/mL)	1.6	0.7	2.8	2.1	0.52	0.64	0.002
Sodium (mmol/L)	141.0	1.8	139.0	1.3	−0.40	−0.39	<0.001
Potassium (mmol/L)	3.8	0.3	4.0	0.3	0.31	0.26	0.002
Chloride (mmol/L)	102.5	2.1	103.3	3.0	0.14	0.31	0.329
CO_2 (mmol/L)	26.0	1.7	25.9	2.1	0.07	−0.14	0.964
Anion gap (mmol/L)	12.4	2.4	9.7	1.8	−0.51	−0.53	<0.001
Blood urea nitrogen (mg/dL)	13.2	2.8	10.7	2.2	−0.43	−0.50	<0.001
Creatinine (mg/dL)	0.8	0.1	0.8	0.1	0.14	−0.08	0.654
Calcium (mg/dL)	9.4	0.5	9.3	1.0	−0.05	−0.13	0.454
Bilirubin (mg/dL)	0.6	0.3	0.4	0.3	−0.30	−0.37	0.447
Protein (g/dL)	7.5	0.5	7.1	0.4	−0.41	−0.46	0.002
Albumin (g/dL)	4.6	0.3	4.3	0.3	−0.49	−0.54	<0.001
Alkaline phosphatase (U/L)	57.3	17.3	45.2	13.7	−0.35	−0.44	<0.001
Alanine aminotransferase (U/L)	18.3	4.4	34.0	26.4	0.53	0.24	0.006
Aspartate transaminase (U/L)	21.9	4.2	29.7	12.8	0.58	0.32	0.006

P values were generated using unpaired *t* tests comparing BAT_{high} and BAT_{low} groups. Using Bonferroni adjustment, $P < 0.003$ was considered significant.

exposure, most studies have not found a corresponding increase in serum or plasma lipid levels (*8,14,19*). One possible explanation for the significant increases we found in circulating lipid levels is that activated BMVs elicited in this study were considerably higher than in most other published work. A higher degree of activation would likely deplete intracellular fuel and require additional substrates from other sources. This type of control mechanism over triglyceride metabolism via clearance by BAT has been demonstrated in cold-exposed mice (*12*).

Early Metabolic Dysfunction

Orava et al. found BAT to be highly sensitive to stimulation by insulin (*35*). In young, healthy adults, it may be the case that higher insulin levels result in routine activation of BAT, which has been shown to increase overall BMV (*15,41*). Free fatty acids, derived from triglyceride lipolysis, are thought to be activators of uncoupling protein 1. We found higher thermoneutral circulating triglyceride levels in subjects with greater volumes of BAT. This may be another mechanism of routine BAT activation. Additionally, baseline plasma TSH was found to be significantly elevated in subjects with higher amounts of cold-activated BAT. TSH receptors are present in adipose tissue and have been linked to an increase in uncoupling protein 1 expression in preadipocytes (*42*). This may indicate that increased TSH levels stimulate BAT production. These findings, along with the strong positive correlations between BMV and thermoneutral insulin, glucose, and triglyceride levels, may suggest BAT plays a role in protecting against early stages of insulin resistance (preprediabetes) and hyperlipidemias.

Metabolic Profile

Previous studies have tended to show that activated BAT is associated with a healthier metabolic profile (i.e., lower fasting glucose, greater insulin sensitivity, and less likelihood of diabetes, obesity, and cardiometabolic diseases) (*16–18,22,37*). The results of our study show that within a group of young, lean, healthy adults, those with a higher BMV had a potentially poorer overall metabolic profile. Higher baseline insulin, glucose, TSH, and serum triglycerides were associated with a higher BMV. Those with less activated BAT also exercised more (about twice as much per week) and were more likely to report adhering to diets that could be considered healthier. The effect of exercise on BAT is unclear in humans, as relevant studies have produced conflicting results. However, exercise is known to cause secretion of endocrine factors that modulate BAT activity, including cardiac natriuretic peptides (induction of uncoupling protein 1 expression and mitochondrial biogenesis) (*43*), fibroblast growth factor 21 (increased BAT activity) (*44*), and interleukin 6 (improved BAT-mediated metabolic homeostasis) (*13*).

Dietary differences are particularly interesting, as certain diet regimens likely include foods known to contain BAT-promoting compounds (*45*). At least part of a vegetarian or vegan diet may contain foods rich in phytochemicals such as capsaicin (*46*) or curcumin (*47*), which have been linked to increased BAT activation. There is also accumulating evidence that eicosapentaenoic acid and docosahexaenoic acid, found abundantly in fish oils (a likely component of a pescatarian diet), may stimulate BAT thermogenesis (*48*) and WAT browning (*49*). It may be somewhat surprising, then, that all but one subject who reported adhering to a strict dietary regimen were part of the BAT_{low} group. It may be the case that the high BMV exhibited by subjects in the BAT_{high} group who exercised less and consumed less healthy diets played a protective role against the early symptoms of metabolic disorders, which are driven at least in part by lifestyle choices.

Adipokines Released from BAT (BATokines)

Although BAT is hypothesized to shift caloric balance in a net-negative direction, its endocrine effects may be more potent. In animal models, BAT transplants can improve glucose tolerance, increase whole-body insulin sensitivity, and reverse type 1 diabetes (*13,25,50*). These improvements are unlikely the result of caloric expenditure or glucose consumption alone but appear to be caused by BAT endocrine signaling (*51*). BATokines are substances preferentially released by BAT versus WAT, which may have endocrine effects (*52*). BAT is known to release significant amounts of fibroblast growth factor 21 (*53,54*), which has a role in improving glucose intolerance and increasing fatty acid oxidation in the liver (*55*). An increase in insulin-like growth factor 1 is thought to be mostly responsible for the reversal of diabetes seen in mouse models (*56*). Neuregulin 4 is highly expressed in BAT and its overexpression correlates with improved glucose tolerance and decreased insulin insensitivity (*57*). BATokines such as these, which are potentially released routinely in people such as those in the $\mathrm{BAT_{high}}$ group, may help to mitigate the impacts of early metabolic or hormonal disturbances.

It is important to note that although significant differences in metabolite levels were found between groups with higher and lower activated BAT volumes, almost all metabolite levels detected during this study were within reference ranges. In otherwise healthy individuals, such as those studied here, who present with borderline metabolic results (e.g., upper end of the normal range of insulin or glucose) it would be useful to correlate their levels of BAT activity with clinical outcomes over time. It may also be beneficial to collect additional samples at subsequent time points to assess the short-term impact of cooling and BAT activation on lipid and other metabolite levels.

CONCLUSION

Our data, obtained under conditions that strongly activate BAT, show significant systemic differences between individuals with higher and lower volumes of active BAT. From these data, we believe that BAT may be recruited to counteract incipient prediabetic states, potentially serving as a first-line protective mechanism against very early metabolic and hormonal variations.

DISCLOSURE

No potential conflict of interest relevant to this article was reported.

ACKNOWLEDGMENTS

The work presented here was conducted using the scanning and special services in the MIR Center for Clinical Imaging Research, located at the Washington University Medical Center. We thank Lauren Ash, Jessica Cartier, and Lisa Schmidt for assistance with data collection.

KEY POINTS

QUESTION: Is active BAT associated with a particular metabolic profile in healthy, young adults?

PERTINENT FINDINGS: In a young, otherwise healthy sample of adults, a higher volume of active BAT was found to be associated with significantly higher preactivation levels of serum glucose, insulin, TSH, and triglycerides.

IMPLICATIONS FOR PATIENT CARE: Imaging BAT using ^{18}F-FDG PET/CT may help identify patients with very early metabolic abnormalities.

REFERENCES

1. Klepac K, Georgiadi A, Tschop M, Herzig S. The role of brown and beige adipose tissue in glycaemic control. *Mol Aspects Med.* 2019;68:90–100.
2. Cannon B, Nedergaard J. Brown adipose tissue: function and physiological significance. *Physiol Rev.* 2004;84:277–359.
3. Hany TF, Gharehpapagh E, Kamel EM, Buck A, Himms-Hagen J, von Schulthess GK. Brown adipose tissue: a factor to consider in symmetrical tracer uptake in the neck and upper chest region. *Eur J Nucl Med Mol Imaging.* 2002;29:1393–1398.
4. Cohade C, Osman M, Pannu HK, Wahl RL. Uptake in supraclavicular area fat ("USA-Fat"): description on ^{18}F-FDG PET/CT. *J Nucl Med.* 2003;44:170–176.
5. Chen KY, Cypess AM, Laughlin MR, et al. Brown Adipose Reporting Criteria in Imaging Studies (BARCIST 1.0): recommendations for standardized FDG-PET/CT experiments in humans. *Cell Metab.* 2016;24:210–222.
6. Chondronikola M, Beeman SC, Wahl RL. Non-invasive methods for the assessment of brown adipose tissue in humans. *J Physiol (Lond).* 2018;596:363–378.
7. Cypess AM, Lehman S, Williams G, et al. Identification and importance of brown adipose tissue in adult humans. *N Engl J Med.* 2009;360:1509–1517.
8. Ouellet V, Labbe SM, Blondin DP, et al. Brown adipose tissue oxidative metabolism contributes to energy expenditure during acute cold exposure in humans. *J Clin Invest.* 2012;122:545–552.
9. Coolbaugh CL, Damon BM, Bush EC, Welch EB, Towse TF. Cold exposure induces dynamic, heterogeneous alterations in human brown adipose tissue lipid content. *Sci Rep.* 2019;9:13600.
10. Blondin DP, Nielsen S, Kuipers EN, et al. Human brown adipocyte thermogenesis is driven by β2-AR stimulation. *Cell Metab.* 2020;32:287–300.e7.
11. Albert V, Svensson K, Shimobayashi M, et al. mTORC2 sustains thermogenesis via Akt-induced glucose uptake and glycolysis in brown adipose tissue. *EMBO Mol Med.* 2016;8:232–246.
12. Bartelt A, Bruns OT, Reimer R, et al. Brown adipose tissue activity controls triglyceride clearance. *Nat Med.* 2011;17:200–205.
13. Stanford KI, Middelbeek RJ, Townsend KL, et al. Brown adipose tissue regulates glucose homeostasis and insulin sensitivity. *J Clin Invest.* 2013;123:215–223.
14. Iwen KA, Backhaus J, Cassens M, et al. Cold-induced brown adipose tissue activity alters plasma fatty acids and improves glucose metabolism in men. *J Clin Endocrinol Metab.* 2017;102:4226–4234.
15. Blondin DP, Labbe SM, Tingelstad HC, et al. Increased brown adipose tissue oxidative capacity in cold-acclimated humans. *J Clin Endocrinol Metab.* 2014;99: E438–E446.
16. Ouellet V, Routhier-Labadie A, Bellemare W, et al. Outdoor temperature, age, sex, body mass index, and diabetic status determine the prevalence, mass, and glucose-uptake activity of ^{18}F-FDG-detected BAT in humans. *J Clin Endocrinol Metab.* 2011;96:192–199.
17. Jacene HA, Cohade CC, Zhang Z, Wahl RL. The relationship between patients' serum glucose levels and metabolically active brown adipose tissue detected by PET/CT. *Mol Imaging Biol.* 2011;13:1278–1283.
18. Becher T, Palanisamy S, Kramer DJ, et al. Brown adipose tissue is associated with cardiometabolic health. *Nat Med.* 2021;27:58–65.
19. Blondin DP, Labbe SM, Phoenix S, et al. Contributions of white and brown adipose tissues and skeletal muscles to acute cold-induced metabolic responses in healthy men. *J Physiol (Lond).* 2015;593:701–714.
20. Chondronikola M, Volpi E, Borsheim E, et al. Brown adipose tissue improves whole-body glucose homeostasis and insulin sensitivity in humans. *Diabetes.* 2014;63:4089–4099.
21. Chondronikola M, Volpi E, Børsheim E, et al. Brown adipose tissue activation is linked to distinct systemic effects on lipid metabolism in humans. *Cell Metab.* 2016;23:1200–1206.
22. Wang Q, Zhang M, Xu M, et al. Brown adipose tissue activation is inversely related to central obesity and metabolic parameters in adult human. *PLoS One.* 2015;10:e0123795.
23. Berbée JF, Boon MR, Khedoe PP, et al. Brown fat activation reduces hypercholesterolaemia and protects from atherosclerosis development. *Nat Commun.* 2015;6:6356.
24. Schlein C, Talukdar S, Heine M, et al. FGF21 lowers plasma triglycerides by accelerating lipoprotein catabolism in white and brown adipose tissues. *Cell Metab.* 2016;23:441–453.
25. Gunawardana SC, Piston DW. Reversal of type 1 diabetes in mice by brown adipose tissue transplant. *Diabetes.* 2012;61:674–682.
26. Blondin DP, Tingelstad HC, Noll C, et al. Dietary fatty acid metabolism of brown adipose tissue in cold-acclimated men. *Nat Commun.* 2017;8:14146.
27. U Din M, Saari T, Raiko J, et al. Postprandial oxidative metabolism of human brown fat indicates thermogenesis. *Cell Metab.* 2018;28:207–216.e3.
28. Fraum TJ, Crandall JP, Ludwig DR, et al. Repeatability of quantitative brown adipose tissue imaging metrics on positron emission tomography with ^{18}F-fluorodeoxyglucose in humans. *Cell Metab.* 2019;30:212–224.e4.

29. Cohade C, Mourtzikos KA, Wahl RL. “USA-Fat”: prevalence is related to ambient outdoor temperature-evaluation with ^{18}F-FDG PET/CT. *J Nucl Med.* 2003;44:1267–1270.
30. Saito M, Okamatsu-Ogura Y, Matsushita M, et al. High incidence of metabolically active brown adipose tissue in healthy adult humans: effects of cold exposure and adiposity. *Diabetes.* 2009;58:1526–1531.
31. Baba S, Tatsumi M, Ishimori T, Lilien DL, Engles JM, Wahl RL. Effect of nicotine and ephedrine on the accumulation of ^{18}F-FDG in brown adipose tissue. *J Nucl Med.* 2007;48:981–986.
32. Graham MM, Wahl RL, Hoffman JM, et al. Summary of the UPICT protocol for ^{18}F-FDG PET/CT imaging in oncology clinical trials. *J Nucl Med.* 2015;56:955–961.
33. Kinahan PE, Perlman ES, Sunderland JJ, et al. The QIBA profile for FDG PET/CT as an imaging biomarker measuring response to cancer therapy. *Radiology.* 2020;294:647–657.
34. Tahari AK, Chien D, Azadi JR, Wahl RL. Optimum lean body formulation for correction of standardized uptake value in PET imaging. *J Nucl Med.* 2014;55:1481–1484.
35. Orava J, Nuutila P, Lidell ME, et al. Different metabolic responses of human brown adipose tissue to activation by cold and insulin. *Cell Metab.* 2011;14:272–279.
36. Weir G, Ramage LE, Akyol M, et al. Substantial metabolic activity of human brown adipose tissue during warm conditions and cold-induced lipolysis of local triglycerides. *Cell Metab.* 2018;27:1348–1355.e4.
37. Lee P, Greenfield JR, Ho KK, Fulham MJ. A critical appraisal of the prevalence and metabolic significance of brown adipose tissue in adult humans. *Am J Physiol Endocrinol Metab.* 2010;299:E601–E606.
38. Persichetti A, Sciuto R, Rea S, et al. Prevalence, mass, and glucose-uptake activity of ^{18}F-FDG-detected brown adipose tissue in humans living in a temperate zone of Italy. *PLoS One.* 2013;8:e63391.
39. Din MU, Raiko J, Saari T, et al. Human brown fat radiodensity indicates underlying tissue composition and systemic metabolic health. *J Clin Endocrinol Metab.* 2017;102:2258–2267.
40. Blondin DP, Frisch F, Phoenix S, et al. Inhibition of intracellular triglyceride lipolysis suppresses cold-induced brown adipose tissue metabolism and increases shivering in humans. *Cell Metab.* 2017;25:438–447.
41. van der Lans AA, Hoeks J, Brans B, et al. Cold acclimation recruits human brown fat and increases nonshivering thermogenesis. *J Clin Invest.* 2013;123:3395–3403.
42. Zhang L, Baker G, Janus D, Paddon CA, Fuhrer D, Ludgate M. Biological effects of thyrotropin receptor activation on human orbital preadipocytes. *Invest Ophthalmol Vis Sci.* 2006;47:5197–5203.
43. Hansen D, Meeusen R, Mullens A, Dendale P. Effect of acute endurance and resistance exercise on endocrine hormones directly related to lipolysis and skeletal muscle protein synthesis in adult individuals with obesity. *Sports Med.* 2012;42:415–431.
44. Hanssen MJ, Broeders E, Samms RJ, et al. Serum FGF21 levels are associated with brown adipose tissue activity in humans. *Sci Rep.* 2015;5:10275.
45. Okla M, Kim J, Koehler K, Chung S. Dietary factors promoting brown and beige fat development and thermogenesis. *Adv Nutr.* 2017;8:473–483.
46. Yoneshiro T, Aita S, Kawai Y, Iwanaga T, Saito M. Nonpungent capsaicin analogs (capsinoids) increase energy expenditure through the activation of brown adipose tissue in humans. *Am J Clin Nutr.* 2012;95:845–850.
47. Wang S, Wang X, Ye Z, et al. Curcumin promotes browning of white adipose tissue in a norepinephrine-dependent way. *Biochem Biophys Res Commun.* 2015;466:247–253.
48. Oudart H, Groscolas R, Calgari C, et al. Brown fat thermogenesis in rats fed high-fat diets enriched with n-3 polyunsaturated fatty acids. *Int J Obes Relat Metab Disord.* 1997;21:955–962.
49. Zhao M, Chen X. Eicosapentaenoic acid promotes thermogenic and fatty acid storage capacity in mouse subcutaneous adipocytes. *Biochem Biophys Res Commun.* 2014;450:1446–1451.
50. Liu X, Zheng Z, Zhu X, et al. Brown adipose tissue transplantation improves whole-body energy metabolism. *Cell Res.* 2013;23:851–854.
51. White JD, Dewal RS, Stanford KI. The beneficial effects of brown adipose tissue transplantation. *Mol Aspects Med.* 2019;68:74–81.
52. Lee MW, Lee M, Oh KJ. Adipose tissue-derived signatures for obesity and type 2 diabetes: adipokines, batokines and microRNAs. *J Clin Med.* 2019;8:854.
53. Chartoumpekis DV, Habeos IG, Ziros PG, Psyrogiannis AI, Kyriazopoulou VE, Papavassiliou AG. Brown adipose tissue responds to cold and adrenergic stimulation by induction of FGF21. *Mol Med.* 2011;17:736–740.
54. Di Franco A, Guasti D, Squecco R, et al. Searching for classical brown fat in humans: Development of a novel human fetal brown stem cell model. *Stem Cells.* 2016;34:1679–1691.
55. Fisher FM, Maratos-Flier E. Understanding the physiology of FGF21. *Annu Rev Physiol.* 2016;78:223–241.
56. Gunawardana SC, Piston DW. Insulin-independent reversal of type 1 diabetes in nonobese diabetic mice with brown adipose tissue transplant. *Am J Physiol Endocrinol Metab.* 2015;308:E1043–E1055.
57. Wang G-X, Zhao X-Y, Meng Z-X, et al. The brown fat–enriched secreted factor Nrg4 preserves metabolic homeostasis through attenuation of hepatic lipogenesis. *Nat Med.* 2014;20:1436–1443.

MIRD Pamphlet No. 27: MIRDcell V3, a Revised Software Tool for Multicellular Dosimetry and Bioeffect Modeling

Sumudu Katugampola*, Jianchao Wang*, Alex Rosen, and Roger W. Howell

Division of Radiation Research, Department of Radiology, New Jersey Medical School, Rutgers University, Newark, New Jersey

Radiopharmaceutical therapy is growing rapidly. However, yet to be addressed is the implementation of methods to plan treatments for circulating tumor cells, disseminated tumor cells, and micrometastases. Given the capacity of radiopharmaceuticals to specifically target and kill single cells and multicellular clusters, a quality not available in chemotherapy and external-beam radiation therapy, it is important to develop dosimetry and bioeffect modeling tools that can inform radiopharmaceutical design and predict their effect on microscopic disease. This pamphlet describes a new version of MIRDcell, a software tool that was initially released by the MIRD committee several years ago. **Methods:** Version 3 (V3) of MIRDcell uses a combination of analytic and Monte Carlo methods to conduct dosimetry and bioeffect modeling for radiolabeled cells within planar colonies and multicellular clusters. A worked example is provided to assist users to learn old and new features of MIRDcell and test its capacity to recapitulate published responses of tumor cell spheroids to radiopharmaceutical treatments. Prominent capabilities of the new version include radially dependent activity distributions, user-imported activity distributions, cold regions within the cluster, complex bioeffect modeling that accounts for radiation type and subcellular distribution, and a rich table of output data for subsequent analysis. **Results:** MIRDcell V3 effectively reproduces experimental responses of multicellular spheroids to uniform and nonuniform distributions of therapeutic radiopharmaceuticals. **Conclusion:** MIRDcell is a versatile software tool that can be used for educational purposes and design of radiopharmaceutical therapies.

Key Words: dosimetry; radionuclide; multicellular cluster; cell survival; nonuniform activity distribution

J Nucl Med 2022; 63:1441–1449
DOI: 10.2967/jnumed.121.263253

The widespread use of ^{223}Ra-dichloride (Xofigo; Bayer) and ^{177}Lu-DOTATATE (Lutathera; Advanced Accelerator Applications) has rejuvenated radiopharmaceutical therapy (RPT) of cancer. RPT delivers radioactive drugs to the primary tumor, metastases, disseminated tumor cells, and circulating tumor cells. Different classes of radionuclides are used for therapy, including α-, β-, and Auger electron emitters (*1*). The different ranges of these radiations in tissue, and their differences in relative biological effectiveness, contribute to the complexity of predicting therapeutic efficacy and normal-tissue toxicity (*1*). However, like external-beam radiation therapy, the future of RPT will depend in part on our capacity to plan treatments that maximize therapeutic effect while minimizing adverse effects on normal tissues. Key to the long-term success of RPT is to implement strategies that overcome limitations of the intrinsic nonuniform uptake of radiopharmaceuticals by cancer cells, which can impact our capacity to sterilize tumors, metastases, disseminated tumor cells, and circulating tumor cells.

Although treatment of primary tumors, distant metastases visible by external imaging, and microscopic metastases in locoregional lymph nodes can be addressed with external beams of radiation, most micrometastases, disseminated tumor cells, and circulating tumor cells cannot. There are commercial tools, based on external imaging, to assist with calculating absorbed dose to macroscopic disease in the context of both external-beam radiation therapy and RPT. The resulting absorbed doses have been used to predict response of tumor and normal tissues. However, there is a dearth of readily available tools that can be used to optimize and plan RPT of microscopic disease.

In 2014, the MIRD committee released version 2.0.15 of MIRDcell, a Java applet, to address the need for software tools for dosimetry and bioeffect modeling of microscopic disease treated with RPT. The software interface and its capabilities were described in MIRD pamphlet no. 25 (*2*). That version, and a later version, 2.0.16, ran on a web browser until 2017, when web browser support for Java applets was discontinued because of security concerns. Version 2.1 (V2.1), a Java application, was released in 2017 to eliminate the web browser requirement and permit the program to run as an application on the user computer.

This new version of our MIRDcell software application, version 3.10 (V3), was created in collaboration with the MIRD committee. MIRDcell V3 can run on all operating systems supporting Java. The software can model radiation absorbed dose and cell survival responses in single cells, cell pairs, and 2-dimensional (2-D) and 3-dimensional (3-D) cell populations. 2-D cell populations are constrained to lie on a plane (e.g., monolayer cell cultures), whereas 3-D populations can be organized within a variety of geometries. The organization of the tabs and the options within each tab, as well as other important details regarding the version history, are provided in detail in the downloadable user manual. The nomenclature used is consistent with dosimetric terminology published in MIRD pamphlet no. 21 (*3*). The app and user manual can be downloaded via https://mirdsoft.org or directly at https://mirdcell.njms.rutgers.edu/. The primary purpose of this present MIRD pamphlet is to describe some of the changes in interactive features, new activity distributions, and new bioeffect models that have been

---

Received Sep. 29, 2021; revision accepted Jan. 26, 2022.

For correspondence or reprints, contact Roger W. Howell (rhowell@rutgers.edu).

*Contributed equally to this work.

added to the software. More importantly, this pamphlet provides several examples of how to use these new features.

MATERIALS AND METHODS

Preamble

The distribution of radioactivity within small tissue elements can have a profound effect on the absorbed dose distribution and, correspondingly, the response of the tissue. Aside from other factors, the absorbed dose distribution and biologic response are strongly dependent on the type, yield, and energy of the radiations emitted by the radionuclide and its subcellular distribution. Most notable are radionuclides that decay by electron capture or internal conversion (e.g., ^{111}In, ^{123}I, ^{125}I), which are followed by the emission of a shower of low-energy Auger electrons. Auger electrons deposit their energy over subcellular dimensions; therefore, these radionuclides invariably produce nonuniform absorbed-dose distributions at all spatial levels (*4,5*). Similarly, the short range of α-particles in biologic tissues (40–100 μm) also leads to nonuniform dose distributions from radionuclides such as ^{223}Ra, ^{225}Ac, and other α-particle emitters of potential use for RPT (*5–10*). Medium- and high-energy β-particle emitters such as ^{177}Lu and ^{90}Y have a greater degree of cross-irradiation because their mean range in tissue is at least several hundred microns. However, the nonuniform distribution of these radionuclides invariably leads to nonuniform dose distributions as well (*11–15*).

Although the distributions of absorbed dose that arise from nonuniform distributions of radioactivity are important, an additional factor that determines biologic response is whether a given absorbed dose arises from radioactive decays within a cell itself (self-dose) or from decays in surrounding cells or other parts of the body (cross-dose). The response of a cell to self-dose from a radiopharmaceutical can be different from its response to cross-dose from the same radiopharmaceutical. This difference is most notable for Auger electron emitters, for which the relative biological effectiveness for the self-dose can be an order of magnitude greater than the relative biological effectiveness for cross-dose (*16*). This observation has also been seen for DNA-incorporated β-particle emitters, for which the self-dose from ^{131}I was 3 times more lethal than the cross-dose (*17*).

There is a growing body of experimental data on the biologic effects of nonuniform distributions of radioactivity at the multicellular level (*17–23*). These findings can have significant consequences for therapeutic uses of these and other radionuclides. MIRDcell V3 provides new tools that can be used to assist in understanding the dependence of radiopharmaceutical efficacy on numerous factors, such as radiation type and energy; distribution at the subcellular, cellular, and multicellular levels; and spatial arrangement of the cells within the multicellular structure (2-D plane [e.g., colony], 3-D cluster, and packing density). These capabilities and new bioeffect modeling features, which are expanded on through examples below, can be helpful in designing RPT strategies.

"Source Radiation" Tab

The "Source Radiation" tab allows the user to select the radioactivity in the source cells (i.e., cells labeled with radioactivity). Three choices are available: predefined MIRD radionuclide, monoenergetic particle emitter, and user-defined radionuclide. User-defined radionuclides include decay chains for ^{211}At, ^{213}Bi, ^{223}Ra, and ^{225}Ac. Details on the differences between these options can be found in the user manual.

"Cell Source/Target" Tab

As described in detail by Goddu et al. (*24,25*), cells are modeled as 2 concentric spheres with radii corresponding to those for the nucleus and cell, respectively. The cells are modeled as liquid water of unit density. The eligible source regions are cell, cell nucleus, cytoplasm, and cell surface. MIRDcell V3 newly permits the user to distribute the activity among cell nucleus, cytoplasm, and cell surface. The eligible target regions for which the radiation absorbed dose is calculated and used for bioeffect modeling are cell, cell nucleus, and cytoplasm. The addition of cytoplasm as a target is new to MIRDcell V3. No limit has been set on the maximum cell radius; however, extensive testing has been conducted only up to 10 μm. Although the algorithms should be adequate for calculating absorbed doses to larger spheres, caution should be exercised when interpreting results for cell radii larger than 10 μm. To facilitate this option, MIRDcell V3 now allows entering the radii in the text box. Users should be mindful that photons are ignored in this and earlier versions of MIRDcell; photon contributions to the absorbed dose can become significant for large sphere sizes.

"Radiobiologic Parameters" Tab

MIRDcell enables the user to model the surviving fraction (SF) of cells in a specified cell population based on the calculated absorbed doses to the individual cells. Two options are available in V3 for calculating the probability that a given cell survives: simple radiobiologic parameters and complex radiobiologic parameters.

Simple Radiobiologic Parameters. As in MIRDcell V2.1 (*2*), a modified linear-quadratic (LQ) model is used to calculate the probability $P(r_k)$ that the k_{th} cell survives a radiation absorbed dose to a region within, r_k (*26,27*):

$$P(r_k)=e^{-\alpha_{\mathrm{self}}D_{\mathrm{self}}-\beta_{\mathrm{self}}D^2_{\mathrm{self}}}\times e^{-\alpha_{\mathrm{cross}}D_{\mathrm{cross}}-\beta_{\mathrm{cross}}D^2_{\mathrm{cross}}}, \qquad \text{Eq. 1}$$

where α_{self} and β_{self} characterize the response of the cell to self-dose (D_{self}), α_{cross} and β_{cross} characterize the cellular response to cross-dose (D_{cross}), and the effect of self- and cross-dose are independent (*5,17,28*). The distinction between self- and cross-dose is often required for Auger electron emitters (*18,29*) and is sometimes required for β-particle emitters when they are DNA-incorporated (*17*). The determination of whether a given cell survives (alive) or not (dead) is determined by a Monte Carlo method by which the surviving probability, calculated using Equation 1, is compared with a randomly generated number.

Complex Radiobiologic Parameters (New). A new feature of V3 is the capacity to specify LQ parameters not only for self-dose and cross-dose but also independently for each type of radiation (e.g., α, β, and Auger) and for each target region (cell [*C*], cell nucleus [*N*], and cytoplasm [*Cy*]). A modified LQ model is again implemented in V3.10. For example, when the cell nucleus is the target region and the source radiation type is designated by ICODE, the probability that the k^{th} cell survives the insult is given by Equation 2:

$$\begin{aligned}
&P_{\mathrm{ICODE}}(N_k)\\
&= e^{-\alpha^{\mathrm{self}}_{\mathrm{ICODE}}(N_k\leftarrow N_k)D^{\mathrm{self}}_{\mathrm{ICODE}}(N_k\leftarrow N_k)-\beta^{\mathrm{self}}_{\mathrm{ICODE}}(N_k\leftarrow N_k)[D^{\mathrm{self}}_{\mathrm{ICODE}}(N_k\leftarrow N_k)]^2}\\
&\quad\times e^{-\alpha^{\mathrm{self}}_{\mathrm{ICODE}}(N_k\leftarrow Cy_k)D^{\mathrm{self}}_{\mathrm{ICODE}}(N_k\leftarrow Cy_k)-\beta^{\mathrm{self}}_{\mathrm{ICODE}}(N_k\leftarrow Cy_k)[D^{\mathrm{self}}_{\mathrm{ICODE}}(N_k\leftarrow Cy_k)]^2}\\
&\quad\times e^{-\alpha^{\mathrm{self}}_{\mathrm{ICODE}}(N_k\leftarrow CS_k)D^{\mathrm{self}}_{\mathrm{ICODE}}(N_k\leftarrow CS_k)-\beta^{\mathrm{self}}_{\mathrm{ICODE}}(N_k\leftarrow CS_k)[D^{\mathrm{self}}_{\mathrm{ICODE}}(N_k\leftarrow CS_k)]^2}\\
&\quad\times e^{-\alpha^{\mathrm{cross}}_{\mathrm{ICODE}}(\mathrm{N}_k\leftarrow N_j)D^{\mathrm{cross}}_{\mathrm{ICODE}}(N_k\leftarrow N_{\mathrm{numcell}})-\beta^{\mathrm{cross}}_{\mathrm{ICODE}}(N_k\leftarrow N_j)[D^{\mathrm{cross}}_{\mathrm{ICODE}}(N_k\leftarrow N_{\mathrm{numcell}})]^2}\\
&\quad\times e^{-\alpha^{\mathrm{cross}}_{\mathrm{ICODE}}(N_k\leftarrow Cy_j)D^{\mathrm{cross}}_{\mathrm{ICODE}}(N_k\leftarrow Cy_{\mathrm{numcell}})-\beta^{\mathrm{cross}}_{\mathrm{ICODE}}(N_k\leftarrow Cy_j)[D^{\mathrm{cross}}_{\mathrm{ICODE}}(N_k\leftarrow Cy_{\mathrm{numcell}})]^2}\\
&\quad\times e^{-\alpha^{\mathrm{cross}}_{\mathrm{ICODE}}(N_k\leftarrow CS_j)D^{\mathrm{cross}}_{\mathrm{ICODE}}(N_k\leftarrow CS_{\mathrm{numcell}})-\beta^{\mathrm{cross}}_{\mathrm{ICODE}}(N_k\leftarrow CS_j)[D^{\mathrm{cross}}_{\mathrm{ICODE}}(N_k\leftarrow CS_{\mathrm{numcell}})]^2},
\end{aligned} \qquad \text{Eq. 2}$$

where j denotes another cell, numcell implies that the cross-dose can arise from all cells within the cluster, and

$$D^{\mathrm{self}}_{\mathrm{ICODE}}(N_k\leftarrow N_k)=f_N\tilde{A}(C_k)\;S^{\mathrm{self}}_{\mathrm{ICODE}}(N_k\leftarrow N_k). \qquad \text{Eq. 3}$$

The ICODEs for the different radiation types are as defined in the *MIRD: Radionuclide Data and Decay Schemes* monograph (*30*). Here, f_N is the fraction of cell activity in the nucleus, $\tilde{A}(C_k)$ is the time-integrated activity in the source region N_k, and $S^{\mathrm{self}}_{\mathrm{ICODE}}(N_k\leftarrow N_k)$ is the self–S coefficient corresponding to the absorbed dose per decay from $N_k\leftarrow N_k$ and is given by Equation 4:

$$S^{\mathrm{self}}_{\mathrm{ICODE}}(N_k\leftarrow N_k)=\sum_{\mathrm{irad}=1}^{\mathrm{irad}N}\frac{\Delta_{\mathrm{ICODE,irad}}\phi_{\mathrm{ICODE,irad}}(N_k\leftarrow N_k)}{m(N_k)}, \qquad \text{Eq. 4}$$

where the sum runs through all irad$N$ radiations of type ICODE, $\Delta_{\mathrm{ICODE,irad}}$ is the mean energy emitted per nuclear transition of the irad$^{\mathrm{th}}$ radiation of type ICODE, and $\phi_{\mathrm{ICODE,irad}}(N_k \leftarrow N_k)$ is the fraction of energy emitted from the source region N_k that is absorbed in the target region N_k of the irad$^{\mathrm{th}}$ radiation of type ICODE. The terms corresponding to the self-dose from other cell compartments of the same cell (cytoplasm, cell surface) can be written similarly, as can the terms corresponding to the cross-doses from other cells. Finally, the overall probability of the k^{th} cell surviving, after the effects of all radiation types on the k^{th} cell nucleus N_k, is written as follows:

$$P(N_k) = \prod_{\mathrm{ICODE}=1}^{\text{number of ICODEs}} P_{\mathrm{ICODE}}(N_k). \qquad \text{Eq. 5}$$

Here, MIRDcell adopts an independent interaction model in which the effect of each radiation type is considered independently of the other. As in prior versions of MIRDcell, the determination of whether a given cell survives is determined by a Monte Carlo method in which the probability of survival, calculated using Equation 5, is compared with a random number ($0 \leq x \leq 1$). The user manual provides details.

A complete set of equations for all possible scenarios of source and target regions is provided in the user manual. Default values are arbitrary, and the user is cautioned to enter values that are relevant to the application. The user is provided with the option of importing a desired set of LQ parameters and saving a set of custom parameters used in the model.

"Multicellular Geometry" Tab

Cluster Geometry. As in MIRDcell V2.1, MIRDcell V3 has 3 basic geometric configurations of spherical cells: 1-dimensional (1-D), 2-D, and 3-D. These are summarized here, and details are provided in the user manual.

The 1-D option is presented in the "1-D Cell Pair" tab and is used to calculate the self- and cross-doses for a pair of cells. The user can set the distance between the centers of 2 cells. The self-dose and cross-dose S coefficients (formerly S values) are calculated using analytic methods based on range–energy relationships for electrons (*31,32*) and α-particles (*33*) as described in the supplemental materials (available at http://jnm.snmjournals.org).

The 2-D option is used to create a cell population that resides on a plane (i.e., colony). The cell-packing density can be specified by changing the distance between the cells, and the shape (circle, rectangle, ellipse) and dimensions of the colony can be set.

The 3-D option is attained by extending the planar cell configuration to a 3-D cluster. The shape of the cluster is selectable as a sphere, ellipsoid, rod, or cone cell-packing density, and the dimensions of the cluster are specified by the user. The cluster is assembled in a 3-D Cartesian coordinate system in a close-packed cubic lattice.

Cell Labeling. The distribution of activity among the labeled cell population is set by the user in the "2-D Cluster" and "3-D Cluster" tabs. As in MIRDcell V2.1, both the 2-D and the 3-D configurations offer several random distributions by which the activity is distributed among the labeled cells according to a uniform, normal, or lognormal distribution. Labeled cells are selected randomly, and each cell is randomly assigned an initial activity according to the user-selected distribution. A uniform activity distribution among the labeled cells implies that each labeled cell has the same initial activity A in its source region. In the normal distribution, the initial activity per cell is distributed according to the probability density function:

$$f(A) = \frac{1}{A\sigma\sqrt{2\pi}} e^{\frac{-(A-\langle A\rangle)^2}{2\sigma^2}}, \qquad \text{Eq. 6}$$

where $\langle A\rangle$ is the mean initial activity per cell and σ is the SD of the mean. In the case of the lognormal distribution, the activity per cell is distributed according to the probability density function:

$$f(A) = \frac{1}{A\sigma\sqrt{2\pi}} e^{-\frac{\left(lnA-(ln\langle A\rangle-\sigma^2/2)\right)^2}{2\sigma^2}}, \quad A>0, \qquad \text{Eq. 7}$$

where σ is the lognormal shape-parameter. The functional forms of the 3 distributions are best viewed in the "Activity Histogram" tab.

New functionality in MIRDcell V3 includes both built-in and user-provided radial activity distributions. The built-in radial distributions are linear, exponential, polynomial, and 4-parameter lognormal distributions. Polynomial distributions up to the 10th degree are possible by setting the parameters accordingly. In all the radial activity distributions, a radius of 0 μm corresponds to the center of the cell cluster. The user-defined activity distribution feature is available only for the spherical cluster geometry. Furthermore, for the ellipsoid cluster geometry, only the standard normal, lognormal, and uniform activity distributions are available as cell-labeling methods. Details on each distribution are provided in the user manual.

MIRDcell V2.1 assumed that the radiopharmaceutical penetrates all the way into the cell cluster. MIRDcell V3 now provides the option of creating a cold region at the center of the cluster and specifying the depth (in μm) to which the drug penetrates the cluster from its outer surface. This situation is common for clusters with radii of more than 50 μm. The cold region at the center of the cluster will contain unlabeled cells. The various activity distributions described in the previous paragraph can be assigned to the cluster's outer region, which has the labeled cells. The complex algebraic algorithms that are used to label cells according to the drug penetration depth are provided for different geometries in the user manual.

Visualization of Radial Distributions (New). MIRDcell V3 now has tools to visualize the radial distributions of mean activity per labeled cell, mean self-dose to labeled cells, mean cross-dose to labeled cells, mean cross-dose to unlabeled cells, mean decays per labeled cell, and mean dose to all cells. This feature can be accessed from the "Radial Histogram" tab, which is available only for 3-D cluster geometries. It is an important tool for checking that the specified activity distribution meets the user's expectations.

Visualization of Tomographic Sections (New). Visual representations of the 3-D cell cluster with color-coded labeled/unlabeled and alive/dead cells is accessible from the "3-D Cluster" tab. New to MIRDcell V3 are views of tomographic sections (illustrated in the worked example below) of the 3-D geometry in the "3D Slice" tab. The tomographic sections of each layer of cells (specified in cell diameters) can be viewed by scrolling the mouse (Fig. 1).

SF and Tumor Control Probability (TCP) (New). In MIRDcell V2.1, the SF of a cell cluster can be plotted as a function of mean activity per cell (Bq), mean absorbed dose to cells (Gy), mean activity per labeled cell (Bq), mean absorbed dose to labeled cells (Gy), and mean absorbed dose to unlabeled cells (Gy). New to MIRDcell V3 are mean decays per cell and mean decays per labeled cell. Also new is presentation of the TCP on the vertical axis, which can be visualized as a function of any of the domains specified above. The TCP is calculated using 2 different approaches. In the first approach, the TCP is calculated using the Poisson model expression (*34*):

$$\mathrm{TCP}(D) = \left(1-\mathrm{SF}(D)\right)^n, \qquad \text{Eq. 8}$$

where SF(D) is the SF at a mean absorbed dose D, and n is the number of cells in the cluster. The Poisson model of TCP works under the assumption that the number of surviving cells is Poisson-distributed with an average nSF(D). The second approach takes the survival probability of each cell into account when

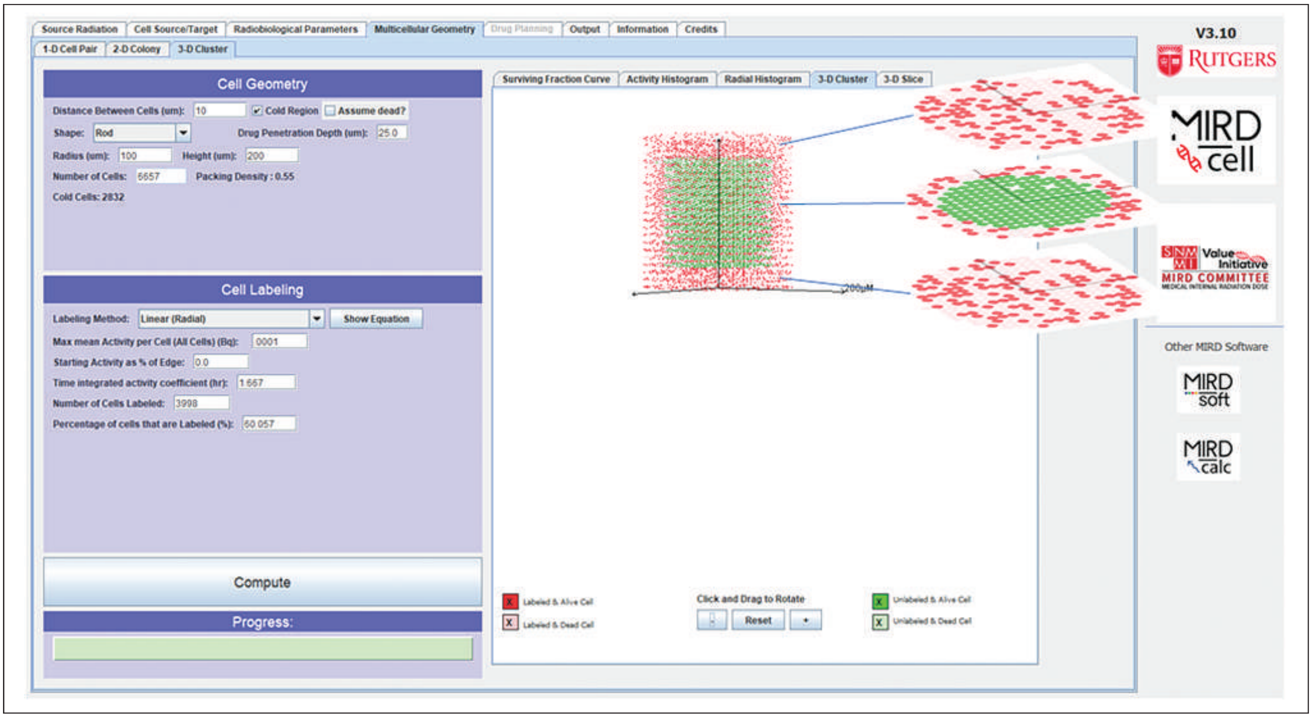

Distance Between Cells (um): 10 ☑ Cold Region ☐ Assume dead?

Shape: Rod

Drug Penetration Depth (um): 25.0

Radius (um): 100

Height (um): 200

Number of Cells: 6657

Packing Density : 0.55

Cold Cells: 2832

Labeling Method: Linear (Radial)

Max mean Activity per Cell (All Cells) (Bq): 0001

Starting Activity as % of Edge: 0.0

Time integrated activity coefficient (hr): 1.667

Number of Cells Labeled: 3998

Percentage of cells that are Labeled (%): 60.057

FIGURE 1. View of 3 tomographic sections of rod-shaped cluster of cells with cold region in interior. Red cells are labeled with radionuclide. Green cells are unlabeled. Opaque cells are alive, and translucent cells are dead. Blue lines point to tomographic section of corresponding cell layer.

calculating the TCP (*22,35*). The TCP is calculated using the following expression:

$$\text{TCP} = \prod_{i=1}^{n} (1-P_i). \qquad \text{Eq. 9}$$

Here, P_i is the survival probability of the i^{th} cell.

Output (New). Similarly to MIRDcell V2.1, in MIRDcell V3 the output data are written to 2 boxes in the "Output" tab. The right-hand box of the "Output" tab contains the cellular self- and cross-dose S coefficients for all target←source combinations. The left-hand box of the "Output" tab contains most of the information and data used to calculate the absorbed doses and bioeffect. These data are used to create the various plots that are available in the "Multicellular Geometry" tab. New information in the left-hand box of MIRDcell V3 includes additional input information and the option of saving the output data as a .txt file. More granular data are provided, as well absorbed doses from each radiation type, radial dose distributions, and other important data used to make the plots.

WORKED EXAMPLE

In this section, the overall functionality and accuracy of MIRDcell V3 in predicting biologic response to radiopharmaceuticals is illustrated by a worked example based on data in the literature.

^{213}Bi Bound to Cells on the Surface of Spherical Cell Clusters

Data published by Kennel et al. (*21*) are used in this example to model the radiotoxicity of ^{213}Bi bound to the surface of EMT-6 or LINE-1 tumor cells grown as spheroids. Briefly, monoclonal antibody 13A to murine CD44 was labeled with ^{213}Bi (^{213}Bi-MAb13A). Only the outer cell layer of the spheroid was labeled, such that the activity was localized to a layer 10 μm from the spheroid surface. The dosimetry was performed using Monte Carlo methods with an assumed nuclear radius of 5.35 μm. The average spheroid diameter in their Figure 6 was 250 μm. On the basis of their Table 4, we estimated that a cluster of this diameter had 3,743 cells. These and other parameters set below were used for both EMT-6 and LINE-1 tumor cells as per Kennel et al. (*21*).

Methods

From the "Source Radiation" tab in MIRDcell, the β average-energy spectrum of ^{213}Bi plus daughters is selected (Fig. 2). By selecting ^{213}Bi plus daughters, all radiation types emitted by the daughters of the ^{213}Bi decay chain are considered in the model and the daughters are assumed to be in equilibrium with the parent. The radiation data are displayed in the "Input Data for Calculation" box.

In the "Cell Source/Target" tab, the nucleus is selected as the target region and the single source region is the cell surface. The radius of the nucleus is set to 5 μm. The radius of the cell and the distance between cells (μm) in the "Multicellular Geometry" tab are adjusted until the number of cells in the spherical cluster matches the experimental observations (3,473). This requires a cell radius of 6 μm and a distance between cells of 13 μm (Fig. 3).

Since the ^{213}Bi decay chain involves many different radiation types, and the LQ parameters vary depending on the type of radiation and the target←source regions, the "Complex Radiobiologic Parameters" tab is used rather than the "Simple Radiobiologic Parameters" tab (Fig. 4). Kennel et al. (*21*) reported a D_0 of ~1.8 Gy using a planar α-particle source for both cell lines applied in their experiment. Therefore, the α parameter for α-particles in the LQ model is changed to 1/1.8 Gy^{-1}~ 0.56 Gy^{-1}. Default values are kept for the other radiation types. The model was also run with zeros for all the parameters of Auger electrons and β-particles, and the results were the same as when run with default values (i.e., Auger electrons and β-particles play no significant role in the response).

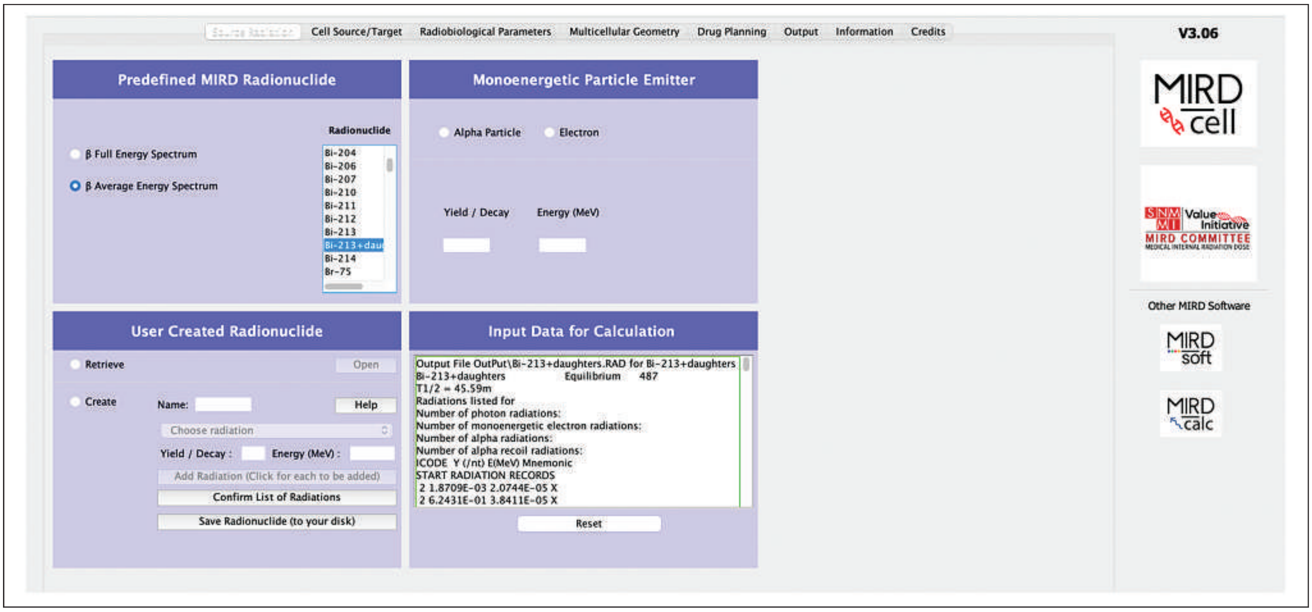

○ β Full Energy Spectrum
● β Average Energy Spectrum

Radionuclide: Bi-213+dau

Yield / Decay
Energy (MeV)

Name:
Yield / Decay :
Energy (MeV) :

```
Output File OutPut\Bi-213+daughters.RAD for Bi-213+daughters
Bi-213+daughters              Equilibrium    487
T1/2 = 45.59m
Radiations listed for
Number of photon radiations:
Number of monoenergetic electron radiations:
Number of alpha radiations:
Number of alpha recoil radiations:
ICODE  Y (/nt) E(MeV) Mnemonic
START RADIATION RECORDS
 2 1.8709E-03 2.0744E-05 X
 2 6.2431E-01 3.8411E-05 X
```

FIGURE 2. “Source Radiation” tab.

From the “Multicellular Geometry” tab, the “3-D Cluster” tab is selected and the radius of the cluster is set to 125 μm. The distance between cells is adjusted until the number of cells matches the experimental observations (described in the “Complex Radiobiological Parameters” section). A drug penetration depth of 12 μm is set, and a radial exponential activity distribution is selected from the drop-down labeling-method menu; the exponential factor is set to 0.4. Since the drug penetrates to only a single cell layer (~12 μm), the selection of the activity distribution has minimal effect on the rest of the cluster. The time-integrated activity coefficient is set to $T_p/\ln(2) = 1.11$ h (where T_p is the physical half-life of the radionuclide). Even though what ultimately matters is the product of the time-integrated activity coefficient and the maximum mean activity per cell, which provides the mean number of decays per cell (after correcting h to s), it is helpful to know the time-integrated activity coefficient for reasonability checks. The percentage of cells that are labeled in MIRDcell is set to 100%. The maximum mean activity per cell (all cells) (Bq) is adjusted until the maximum mean absorbed dose to cells in the MIRDcell SF curve matches the maximum average dose (Gy) given in Figure 6 of Kennel et al. (*21*). When the “Compute” button is clicked the first time, an error message will pop up indicating that 100% of the cells cannot be labeled because this number exceeds the number of cells within the drug penetration depth; the percentage of labeled cells will be automatically set to the maximum number allowed when the error message is accepted. Therefore, a good rule is to let the program decide the percentage of labeled cells when a drug penetration depth is specified. Alternatively, if there is a specific desired percentage, the value can be set before the “Compute” button is clicked. Once the model is run, the SF as a function of different domains can be visualized under the “SF Curve” tab. The maximum mean activity per cell that matched the desired absorbed dose was 0.02 Bq (Fig. 5). The radial activity histograms and tomographic sections (Fig. 6) of the selected cell cluster geometry are displayed in the “Radial Histogram” and “3-D Slice” tabs, respectively. Tomographic sections of each cell

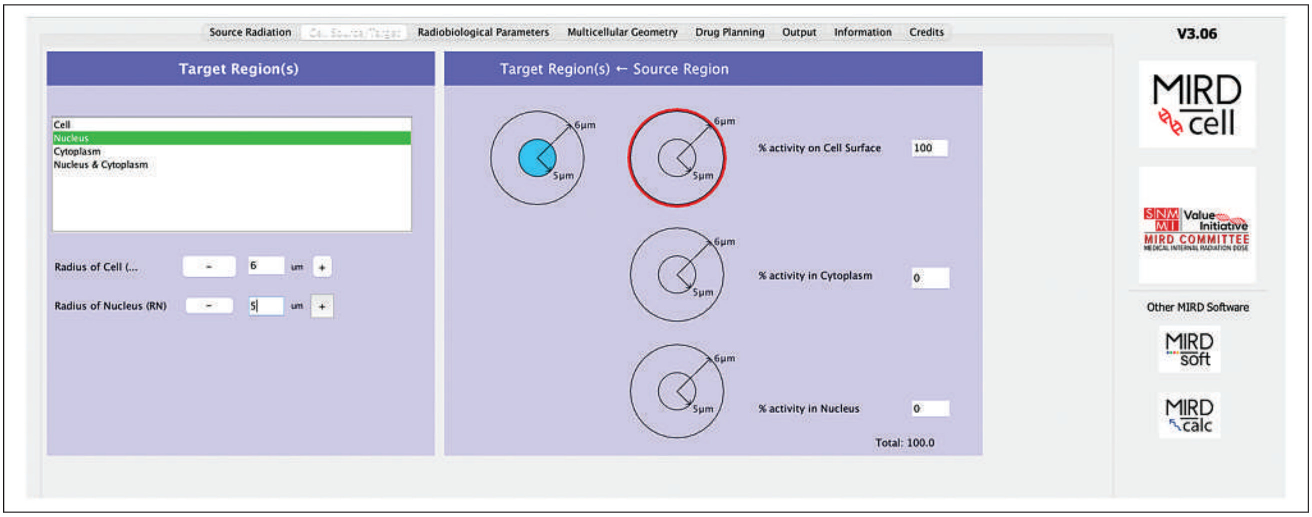

Radius of Cell (... 6 um

Radius of Nucleus (RN) 5 um

% activity on Cell Surface 100

% activity in Cytoplasm 0

% activity in Nucleus 0

Total: 100.0

FIGURE 3. “Cell Source/Target” tab.

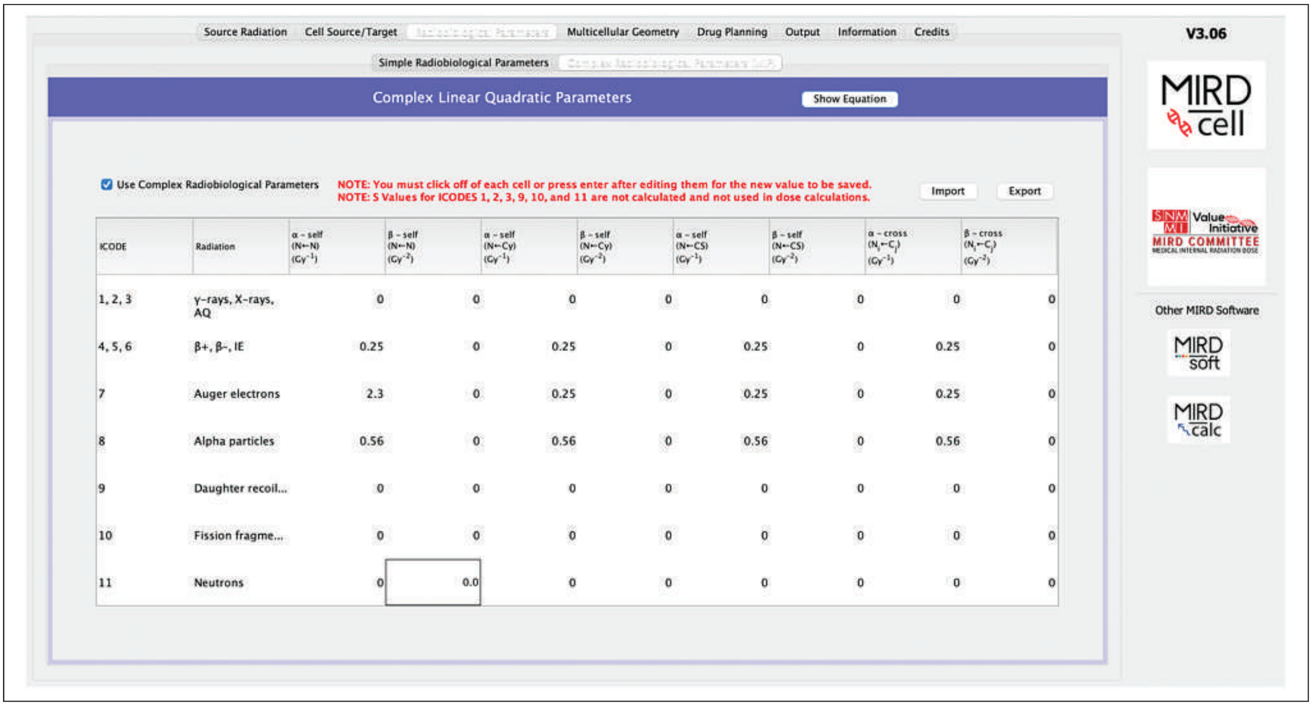

Complex Linear Quadratic Parameters

☑ Use Complex Radiobiological Parameters

NOTE: You must click off of each cell or press enter after editing them for the new value to be saved.
NOTE: S Values for ICODES 1, 2, 3, 9, 10, and 11 are not calculated and not used in dose calculations.

ICODE	Radiation	α – self (N←N) (Gy^{-1})	β – self (N←N) (Gy^{-2})	α – self (N←Cy) (Gy^{-1})	β – self (N←Cy) (Gy^{-2})	α – self (N←CS) (Gy^{-1})	β – self (N←CS) (Gy^{-2})	α – cross (N$_i$←C$_j$) (Gy^{-1})	β – cross (N$_i$←C$_j$) (Gy^{-2})
1, 2, 3	γ-rays, X-rays, AQ	0	0	0	0	0	0	0	0
4, 5, 6	β+, β–, IE	0.25	0	0.25	0	0.25	0	0.25	0
7	Auger electrons	2.3	0	0.25	0	0.25	0	0.25	0
8	Alpha particles	0.56	0	0.56	0	0.56	0	0.56	0
9	Daughter recoil...	0	0	0	0	0	0	0	0
10	Fission fragme...	0	0	0	0	0	0	0	0
11	Neutrons	0	0.0	0	0	0	0	0	0

FIGURE 4. Complex radiobiologic parameters.

layer can be displayed by specifying the value, in terms of cell diameters, in the box labeled "Axial Height." Alternatively, the sections can be scrolled through using the wheel of the mouse.

The "Output" tab lists the values of all the parameters used in the model, along with the results. The left panel lists all the output data used for the plots; these data can be viewed under the "Multicellular Geometry" tab. The right panel lists all the self-dose S coefficients and the cross-dose S coefficients as a function of the distance between the center of the source cell and the center of the target cell.

Results and Comparison with Experimental Observations

Figure 7 compares the experimental observations for the SF as a function of mean absorbed dose for the 2 cell lines as taken from Figure 6 of Kennel et al. (*21*). The triangles represent the

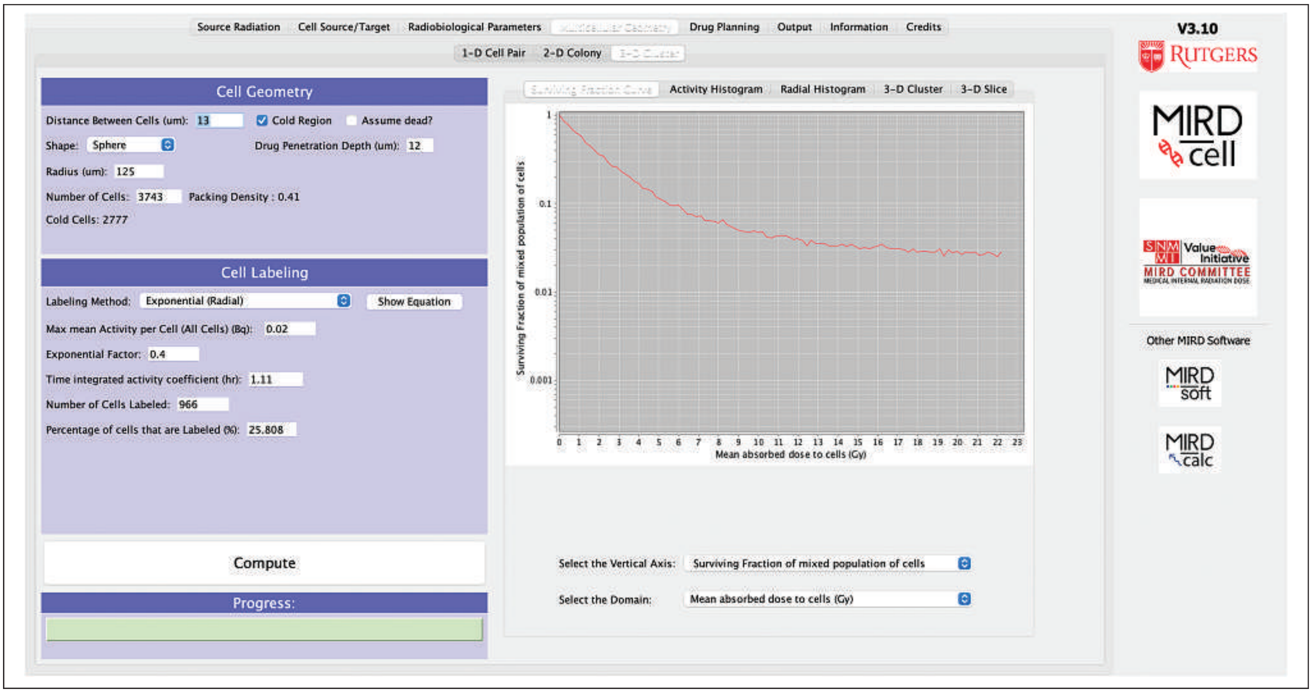

Cell Geometry

Distance Between Cells (um): 13 ☑ Cold Region ☐ Assume dead?
Shape: Sphere
Drug Penetration Depth (um): 12
Radius (um): 125
Number of Cells: 3743 Packing Density : 0.41
Cold Cells: 2777

Cell Labeling

Labeling Method: Exponential (Radial)
Max mean Activity per Cell (All Cells) (Bq): 0.02
Exponential Factor: 0.4
Time integrated activity coefficient (hr): 1.11
Number of Cells Labeled: 966
Percentage of cells that are Labeled (%): 25.808

Select the Vertical Axis: Surviving Fraction of mixed population of cells
Select the Domain: Mean absorbed dose to cells (Gy)

FIGURE 5. "Multicellular Geometry" tab. SF variation as function of mean activity per cell is shown on right.

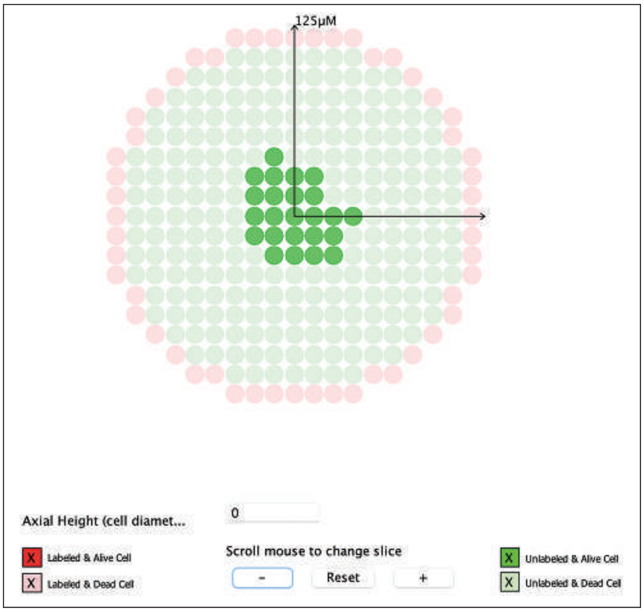

Axial Height (cell diamet... 0

FIGURE 6. Tomographic section through center of spherical cell cluster illustrating drug penetration depth, labeled cells (red), unlabeled cells (green), alive cells (opaque), and dead cells (translucent). Only unlabeled cells at center of cluster are alive.

radiolabeled antibody data, and the predictions from MIRDcell are given by the red lines. It can be seen from both plots that the data are better represented by the MIRDcell prediction than by the single-component exponential fit used by Kennel et al. Notably, the MIRDcell prediction for the LINE-1 cells is superior to that for the EMT-6 cells. Of greatest importance to radiopharmaceutical bioeffect modeling is that MIRDcell predicts the appearance of a tail in the curve as the absorbed dose is increased.

Two additional examples are in the supplemental materials. Example 2 predicts the radiotoxicity of ^{111}In-epidermal growth factor distributed in spherical cell clusters (Supplemental Figs. 1–7). Example 3 describes the use of several new features in MIRDcell V3 (Supplemental Figs. 8–10). Additional examples, published previously (*2*), are in the user manual.

Also included in the supplemental materials are comparisons between S coefficients calculated for 50-keV electrons with MIRDcell and the Monte Carlo code, TOPAS-nBio (Supplemental Figs. 11–12) (*36*). These S coefficients were used in MIRDcell to generate and compare SF and TCP curves for a 100-μm-radius multicellular cluster with uniform or exponential activity distributions (Supplemental Figs. 13–20). S coefficients were calculated similarly for ^{177}Lu and compared (Supplemental Fig. 21). A final comparison for electrons was made with S coefficients that were calculated on the basis of the Emfietzoglou range–energy relationship (Supplemental Fig. 22) (*37*). Lastly, comparisons between S coefficients calculated for 5-MeV α-particles and ^{210}Po are made between MIRDcell and TOPAS-nBio (Supplemental Figs. 23–24).

DISCUSSION

Several other codes for multicellular dosimetry and bioeffect modeling have been published over the years (*5,38–40*). Charlton published a program for multicellular dosimetry that used analytic approaches to predict cell survival in micrometastases consisting of 2 cell types (*41*). Hobbs et al. created a GEANT4-based program for multicellular dosimetry with features to calculate TCP (*35*). Howell et al. expanded on his earlier work by studying the impact of lognormal distributions of activity among the cell population in multicellular clusters (*42*). Marcatili et al. developed general-purpose software tools to generate randomized 3-D cell culture geometries based on experimentally determined parameters (cell size, cell density, cluster density, average cluster size, cell cumulated activity). Their models were used in conjunction with analytic and Monte Carlo dosimetry calculations to predict the fraction of surviving cells after uptake of ^{177}Lu radiopharmaceuticals (*43*). Cai et al. developed a multicellular model that used MCNP radiation transport (*44*). Sizeable differences of up to about 30% in the cross-dose S coefficients produced by their code versus MIRDcell V2.1 were noted. These differences, and their modest impact on SF and TCP, are discussed in the supplemental materials. The most detailed model was published by Raghavan et al. (*45*). The Raghavan model accounts for time-dependent advection and diffusion of radiopharmaceuticals into cells surrounding the cavity that remains after resecting brain tumors. Although MIRDcell does not have a similar capability, we are developing a Python code that processes 3-D activity distribution snapshots over time and calculates the radially dependent time-integrated activity on a cell-by-cell basis.

Although many multicellular dosimetry programs have been developed, they are largely in the hands of their creators and not available widely for general use. Supplemental Table 1 compares the features of MIRDcell with 2 codes that are available for users, namely COOLER (*46*) and PARaDIM (*47*). Although these can accommodate more diverse geometric shapes for the cells, they have a limited scope of other options compared with MIRDcell and they lack user-friendly graphic user interfaces.

Except for the added new features in MIRDcell V3.10, the underlying modeling concepts and assumptions are the same as those of MIRDcell V2.1. The cell and the cell nucleus are still modeled as concentric spheres. The effect of the shape of the cell on the calculated absorbed dose is usually small (*25*), except for certain electron energies that have ranges similar to cellular dimensions (*46*). Furthermore,

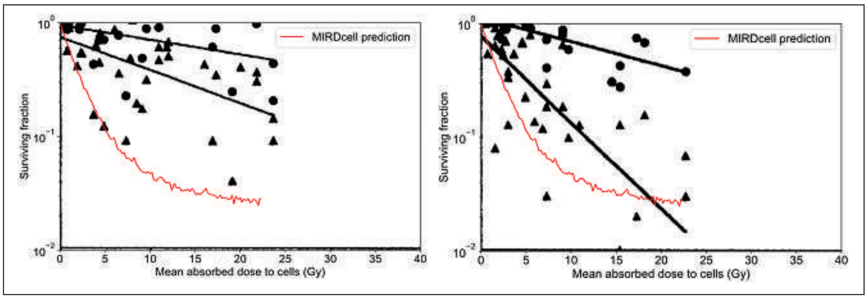

FIGURE 7. Comparison of MIRDcell prediction with experimental observations. Original plots extracted from Kennel et al. (*21*) have been overlayed with MIRDcell predictions (red). (A) EMT-6 cells. (B) LINE-1 cells. Triangles are data obtained for MAb13A, and circles are those obtained for MAb14, which is nonbinding with tissue. Solid lines are least-squares fits to exponential function provided by Kennel et al. MIRDcell simulation was run for MAb13A cells.

unlike PARaDIM (*47*), V3 also assumes a constant size for all the cells in the population. Like MIRDcell V2.1, the dosimetry and bioeffect modeling in MIRDcell V3 does not account for the stochastic variations in the number of α-particle decays, hits, and energy deposited. Furthermore, users should be mindful that photons are ignored in V3.10 and earlier versions of MIRDcell; photon contributions to the absorbed dose can become significant for large cluster sizes. MIRDcell V3.10 does not take bystander and abscopal effects into account in the model either (*48–50*). Also, any dose rate effects and temporal effects such as proliferation are not explicitly accounted for in modeling the biologic response. However, as mentioned in MIRD pamphlet no. 25 (*2*), this limitation can be compensated for by using suitable values for the LQ parameters in the “Radiobiologic Parameters” tab.

Similarly to MIRDcell V2.1, V3.10 also uses a variation of the LQ model that accounts for self- and cross-doses when modeling the biologic response of cell clusters to different radiation types. The effect of lesion interactions produced by mixtures of self- and cross-dose on biologic response are ignored; rather, their effects are considered independently. New in V3, accommodated by the “Complex Radiobiologic Parameters” tab, is a new target region (cytoplasm) and the capacity to adjust the LQ parameters for each individual radiation type. Again, the effects of each radiation type are treated independently, as are the effects from absorbed doses arising from decays in different source regions. This approach can underestimate the effect, particularly at high doses. However, the exact mechanisms behind interactions with mixed–linear-energy-transfer radiations are not well understood. Various theoretic formulations for bioeffect modeling of mixed radiations have been proposed by both experimental and theoretic groups over the years (*51–53*). They include the addition of interaction terms between the various radiation insults that can arise. Although our worked examples here and in the supplemental materials show that the present MIRDcell bioeffect models behave satisfactorily, the introduction of interaction terms is under investigation for possible inclusion in MIRDcell algorithms.

CONCLUSION

Given the highly nonuniform cellular exposures received in nuclear medicine, designing treatment plans for therapeutic radiopharmaceuticals is challenging. Therefore, the revisions to this software application were developed to improve visualization and understanding of the impact of radionuclide choice, distribution of activity in and among cells, cell dimensions, intercell distances, cluster size, and radiobiologic response parameters on the capacity to kill populations of cells. These parameters can play a substantial role in determining the SF of cells and TCP. Accordingly, MIRDcell is a versatile software tool that can be used for educational purposes and design of RPTs.

DISCLOSURE

This work was supported in part by NIH R01CA198073 and 1R01CA245139. MIRDcell V2 is patented under USPTO 9,623,262. No other potential conflict of interest relevant to this article was reported.

ACKNOWLEDGMENTS

This work was done in collaboration with the SNMMI MIRD committee: Vikram Adhikarla, Rachel Marie Bartlett, Wesley E. Bolch, Yuni K. Dewaraja, William D. Erwin, Darrell R. Fisher, Robert Francois Hobbs, Roger W. Howell, Adam L. Kesner, Richard Laforest, Joseph G. Rajendran, George Sgouros, and Pat B. Zanzonico (chair). Special thanks are given to the NJMS Rutgers IT team, who created and support the MIRDcell website and maintain the server. Thanks to Adam Kesner for supporting the distribution of MIRDcell via the MIRDsoft platform. Finally, thanks to Caroline Bolch for designing the MIRDcell icon and logo.

REFERENCES

1. Sgouros G, Bodei L, McDevitt MR, Nedrow JR. Radiopharmaceutical therapy in cancer: clinical advances and challenges. *Nat Rev Drug Discov.* 2020;19:589–608.
2. Vaziri B, Wu H, Dhawan AP, Du P, Howell RW. MIRD pamphlet no. 25: MIRDcell V2.0 software tool for dosimetric analysis of biologic response of multicellular populations. *J Nucl Med.* 2014;55:1557–1564.
3. Bolch WE, Eckerman KF, Sgouros G, Thomas SR. MIRD pamphlet no. 21: a generalized schema for radiopharmaceutical dosimetry—standardization of nomenclature. *J Nucl Med.* 2009;50:477–484.
4. Makrigiorgos GM, Adelstein SJ, Kassis AI. Limitations of conventional internal dosimetry at the cellular level. *J Nucl Med.* 1989;30:1856–1864.
5. Goddu SM, Rao DV, Howell RW. Multicellular dosimetry for micrometastases: dependence of self-dose versus cross-dose to cell nuclei on type and energy of radiation and subcellular distribution of radionuclides. *J Nucl Med.* 1994;35:521–530.
6. Humm JL, Chin LM. A model of cell inactivation by alpha-particle internal emitters. *Radiat Res.* 1993;134:143–150.
7. Roeske JC, Stinchcomb TG. Dosimetric framework for therapeutic alpha-particle emitters. *J Nucl Med.* 1997;38:1923–1929.
8. Akabani G, Zalutsky MR. Microdosimetry of astatine-211 using histological images: application to bone marrow. *Radiat Res.* 1997;148:599–607.
9. Fisher DR. Alpha-particle emitters in medicine. In: Adelstein SJ, Kassis AI, Burt RW, eds. *Dosimetry of Administered Radionuclides.* American College of Nuclear Physicians; 1990:194–214.
10. Hobbs RF, Song H, Watchman CJ, et al. A bone marrow toxicity model for ^{223}Ra alpha-emitter radiopharmaceutical therapy. *Phys Med Biol.* 2012;57:3207–3222.
11. Kwok CS, Prestwich WV, Wilson BC. Calculation of radiation doses for nonuniformly distributed beta and gamma radionuclides in soft tissue. *Med Phys.* 1985; 12:405–412.
12. Wessels BW, Griffith MH. Miniature thermoluminescent dosimeter absorbed dose measurements in tumor phantom models. *J Nucl Med.* 1986;27:1308–1314.
13. Humm JL, Cobb LM. Nonuniformity of tumor dose in radioimmunotherapy. *J Nucl Med.* 1990;31:75–83.
14. Sgouros G, Chiu S, Pentlow KS, et al. Three-dimensional dosimetry for radiotherapy treatment planning. *J Nucl Med.* 1993;34:1595–1601.
15. Erdi AK, Wessels BW, DeJager R. Tumor activity confirmation and isodose curve display for patients receiving iodine-131-labelled 16.88 human monoclonal antibody. *Cancer.* 1994;73:932–944.
16. Humm JL, Howell RW, Rao DV. Dosimetry of Auger electron emitting radionuclides: report no. 3 of the AAPM Nuclear Medicine Task Group No. 6. *Med Phys.* 1994;21:1901–1915.
17. Neti PV, Howell RW. Isolating effects of microscopic nonuniform distributions of ^{131}I on labeled and unlabeled cells. *J Nucl Med.* 2004;45:1050–1058.
18. Howell RW, Bishayee A. Bystander effects caused by nonuniform distributions of DNA-incorporated ^{125}I. *Micron.* 2002;33:127–132.
19. Neti PV, Howell RW. When may a nonuniform distribution of ^{131}I be considered uniform? An experimental basis for multicellular dosimetry. *J Nucl Med.* 2003;44: 2019–2026.
20. Neti PVSV, Howell RW. Biological response to nonuniform distributions of ^{210}Po in multicellular clusters. *Radiat Res.* 2007;168:332–340.
21. Kennel SJ, Stabin M, Roeske JC, et al. Radiotoxicity of bismuth-213 bound to membranes of monolayer and spheroid cultures of tumor cells. *Radiat Res.* 1999; 151:244–256.
22. Falzone N, Lee BQ, Able S, et al. Targeting micrometastases: the effect of heterogeneous radionuclide distribution on tumor control probability. *J Nucl Med.* 2018;60:250–258.
23. Zhu C, Sempkowski M, Holleran T, et al. Alpha-particle radiotherapy: for large solid tumors diffusion trumps targeting. *Biomaterials.* 2017;130:67–75.
24. Goddu SM, Howell RW, Rao DV. Cellular dosimetry: absorbed fractions for monoenergetic electron and alpha particle sources and S-values for radionuclides uniformly distributed in different cell compartments. *J Nucl Med.* 1994;35:303–316.
25. Goddu SM, Howell RW, Bouchet LG, Bolch WE, Rao DV. *MIRD Cellular S values: Self-Absorbed Dose per Unit Cumulated Activity for Selected Radionuclides*

and Monoenergetic Electron and Alpha Particle Emitters Incorporated into Different Cell Compartments. Society of Nuclear Medicine and Molecular Imaging; 1997:183.

26. Rajon D, Bolch WE, Howell RW. Lognormal distribution of cellular uptake of radioactivity: Monte Carlo simulation of irradiation and cell killing in 3-dimensional populations in carbon scaffolds. *J Nucl Med.* 2011;52:926–933.
27. Akudugu JM, Howell RW. Flow cytometry-assisted Monte Carlo simulation predicts clonogenic survival of cell populations with lognormal distributions of radiopharmaceuticals and anticancer drugs. *Int J Radiat Biol.* 2012;88:286–293.
28. Howell RW, Neti PV. Modeling multicellular response to nonuniform distributions of radioactivity: differences in cellular response to self-dose and cross-dose. *Radiat Res.* 2005;163:216–221.
29. Howell RW. Advancements in the use of Auger electrons in science and medicine during the period 2015-2019. *Int J Radiat Biol.* October 23, 2020 [Epub ahead of print].
30. Eckerman KF, Endo A. *MIRD: Radionuclide Data and Decay Schemes.* 2nd ed. Society of Nuclear Medicine and Molecular Imaging; 2008:671.
31. Cole A. Absorption of 20 eV to 50,000 eV electron beams in air and plastic. *Radiat Res.* 1969;38:7–33.
32. Howell RW, Rao DV, Sastry KSR. Macroscopic dosimetry for radioimmunotherapy: nonuniform activity distributions in solid tumors. *Med Phys.* 1989;16:66–74.
33. *Report 49: Stopping Powers and Ranges for Protons and Alpha Particles.* International Commission on Radiation Units and Measurements; 1993.
34. Zaider M, Minerbo GN. Tumour control probability: a formulation applicable to any temporal protocol of dose delivery. *Phys Med Biol.* 2000;45:279–293.
35. Hobbs RF, Baechler S, Fu DX, et al. A model of cellular dosimetry for macroscopic tumors in radiopharmaceutical therapy. *Med Phys.* 2011;38:2892–2903.
36. Schuemann J, McNamara AL, Ramos-Mendez J, et al. TOPAS-nBio: an extension to the TOPAS simulation toolkit for cellular and sub-cellular radiobiology. *Radiat Res.* 2019;191:125–138.
37. Emfietzoglou D, Kostarelos K, Hadjidoukas P, et al. Subcellular S-factors for low-energy electrons: a comparison of Monte Carlo simulations and continuous-slowing-down calculations. *Int J Radiat Biol.* 2008;84:1034–1044.
38. Kassis AI, Adelstein SJ, Haydock C, Sastry KS. Thallium-201: an experimental and a theoretical radiobiological approach to dosimetry. *J Nucl Med.* 1983;24:1164–1175.
39. Howell RW, Rao DV, Haydock C. Dosimetry techniques for therapeutic applications of incorporated radionuclides. In: Adelstein SJ, Kassis AI, Burt RW, eds. *Dosimetry of Administered Radionuclides.* American College of Nuclear Physicians; 1990:215–256.
40. O'Donoghue JA, Bardies M, Wheldon TE. Relationships between tumor size and curability for uniformly targeted therapy with beta-emitting radionuclides. *J Nucl Med.* 1995;36:1902–1909.
41. Charlton DE. Radiation effects in spheroids of cells exposed to alpha emitters. *Int J Radiat Biol.* 2000;76:1555–1564.
42. Howell RW, Rajon D, Bolch WE. Monte Carlo simulation of irradiation and killing in three-dimensional cell populations with lognormal cellular uptake of radioactivity. *Int J Radiat Biol.* 2012;88:115–122.
43. Marcatili S, Pichard A, Courteau A, et al. Realistic multi-cellular dosimetry for ^{177}Lu-labelled antibodies: model and application. *Phys Med Biol.* 2016;61:6935–6952.
44. Cai Z, Kwon YL, Reilly RM. Monte Carlo N-particle (MCNP) modeling of the cellular dosimetry of ^{64}Cu: comparison with MIRDcell S values and implications for studies of its cytotoxic effects. *J Nucl Med.* 2017;58:339–345.
45. Raghavan R, Howell RW, Zalutsky MR. A model for optimizing delivery of targeted radionuclide therapies into resection cavity margins for the treatment of primary brain cancers. *Biomed Phys Eng Express.* 2017;3:035005.
46. Siragusa M, Baiocco G, Fredericia PM, et al. The COOLER code: a novel analytical approach to calculate subcellular energy deposition by internal electron emitters. *Radiat Res.* 2017;188:204–220.
47. Carter LM, Crawford TM, Sato T, et al. PARaDIM: a PHITS-based Monte Carlo tool for internal dosimetry with tetrahedral mesh computational phantoms. *J Nucl Med.* 2019;60:1802–1811.
48. Blyth BJ, Sykes PJ. Radiation-induced bystander effects: what are they, and how relevant are they to human radiation exposures? *Radiat Res.* 2011;176:139–157.
49. Canter BS, Leung CN, Fritton JC, et al. Radium-223-induced bystander effects cause DNA damage and apoptosis in disseminated tumor cells in bone marrow. *Mol Cancer Res.* 2021;19:1739–1750.
50. Leung CN, Canter BS, Rajon D, et al. Dose-dependent growth delay of breast cancer xenografts in the bone marrow of mice treated with radium-223: the role of bystander effects and their potential for therapy. *J Nucl Med.* 2020;61:89–95.
51. Zaider M, Rossi HH. The synergistic effects of different radiations. *Radiat Res.* 1980;83:732–739.
52. Lam GKY. An isoeffect approach to the study of combined effects of mixed radiations: the nonparametric analysis of *in vivo* data. *Radiat Res.* 1989;119:424–431.
53. Pfuhl T, Friedrich T, Scholz M. Prediction of cell survival after exposure to mixed radiation fields with the local effect model. *Radiat Res.* 2020;193:130–142.

Antibody-Guided Molecular Imaging of *Aspergillus* Lung Infections in Leukemia Patients

Johannes Schwenck*[1], Andreas Maurer*[1], Nicolas Beziere[1], Francesco Fiz[1], Frederic Boschetti[2], Susanne Geistlich[3], Dominik Seyfried[1], Matthias Gunzer[4], Gerald Reischl[1], Jöri Wehrmüller[3], Walter Ehrlichmann[1], Marius Horger[1], Sergios Gatidis[1], Genna Davies[5], Wichard Vogel[1], Christian la Fougère*[1], Bernd Pichler*[1], and Christopher Thornton*[5]

[1]University Hospital of Tübingen, Tübingen, Germany; [2]Chematech, Dijon, France; [3]Paul Scherrer Institute, Villigen, Switzerland; [4]University of Duisburg–Essen, Essen, Germany; and [5]University of Exeter, Exeter, United Kingdom

Invasive pulmonary aspergillosis (IPA) caused by the fungus *Aspergillus fumigatus* (Fig. 1A) is a life-threatening lung disease of acute myeloid leukemia patients, with the diagnosis currently being reliant on invasive, slow, or nonspecific procedures, including chest CT (*1*). Here, we showcase the (to our knowledge) first-time use in humans of an *Aspergillus*-specific radiotracer (*2,3*) administered to acute myeloid leukemia patients diagnosed with no IPA or with IPA according to consensus definitions of the disease. The subjects underwent ^{64}Cu-NODAGA-hJF5-PET/MRI on a compassionate-use basis according to the German Medicinal Products Act (Arzneimittelgesetz §13.2b). Scientific analysis was approved by the institutional review board (approval 206/2020BO2). Written informed consent was obtained from all patients.

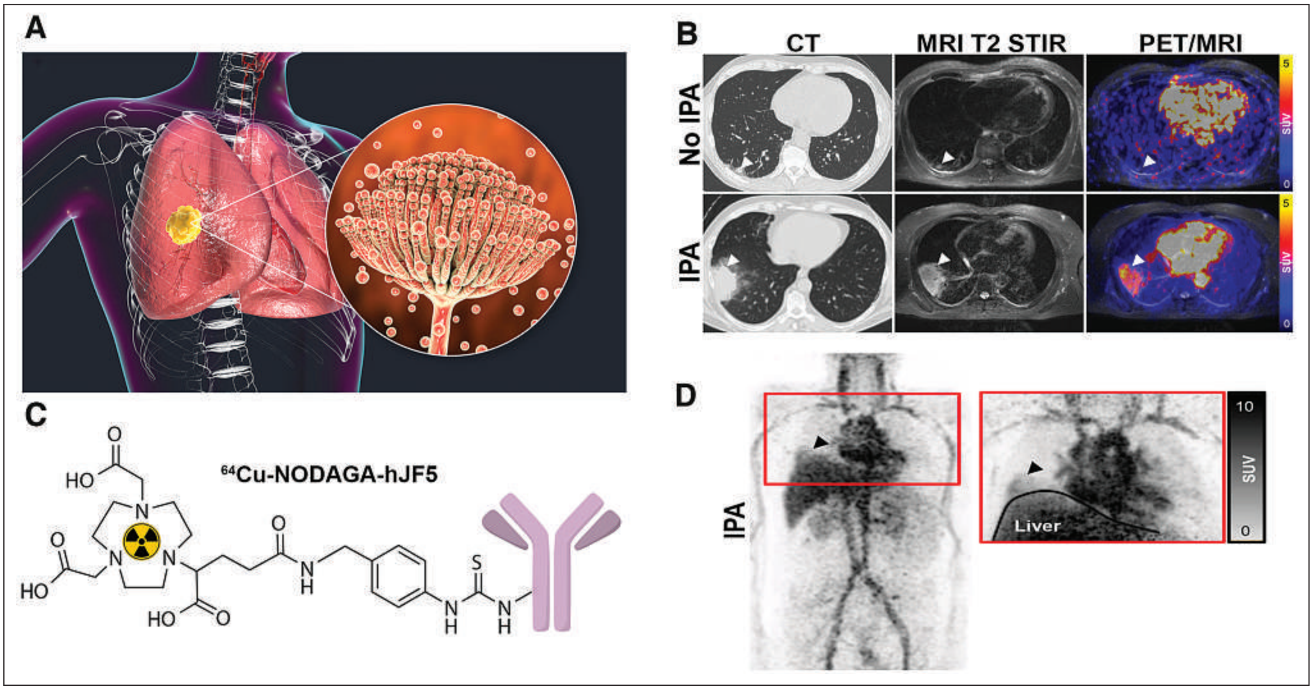

FIGURE 1. (A) Inhaled spores of opportunistic fungal pathogen *Aspergillus fumigatus* (inset) can lead to IPA in AML patients. (B) Immuno-PET/MRI of patient 1 (no IPA) shows no tracer uptake in lung lesion (arrowheads); patient 2, diagnosed with IPA, shows enhanced tracer uptake in pulmonary lesion of right lower lobe (arrowheads). CT scans were acquired 1 wk before PET/MRI. (C) Chemical structure is shown for *Aspergillus*-specific radiotracer ^{64}Cu-NODAGA-hJF5. (D) Maximum-intensity projection of ^{64}Cu-NODAGA-hJF5 in patient 2 shows pulmonary lesion (arrowheads).

Uptake of the tracer in pulmonary lesions was determined using PET/MRI 15–18 h after intravenous injection with 196–287 MBq (Figs. 1B and 1C). In patient 1, no tracer uptake (SUV_{max}, 2.5; SUV_{mean}, 1.1;

Received Oct. 18, 2021; revision accepted Jan. 12, 2022.

For correspondence or reprints, contact Christopher Thornton (c.r.thornton@exeter.ac.uk).

*Contributed equally to this work.

DOI: 10.2967/jnumed.121.263251

size [CT], 1.3 × 1.2 × 1.6 cm) above background levels (SUV_{mean} liver, 5.9; SUV_{mean} blood pool, 6.5; SUV_{mean} lung, 0.9) was observed in the lung lesion, concordant with no IPA. Patient 2, diagnosed with IPA, showed pronounced uptake of the tracer in the pulmonary lesion of the right lower lobe (SUV_{max}, 5.94; size [CT], 6.2 × 4.0 × 4.1 cm; SUV_{mean} liver, 6.1; SUV_{mean} blood pool, 7.0; SUV_{mean} lung, 0.8; maximum-intensity projection, Fig. 1D). This first-in-humans study shows the potential of antibody-guided PET for noninvasive IPA detection.

DISCLOSURE

Christopher Thornton is the director of ISCA Diagnostics Limited. No other potential conflict of interest relevant to this article was reported.

ACKNOWLEDGMENT

We thank the Werner Siemens Foundation and EU 7th Framework Programme (grant 602820) for funding.

REFERENCES

1. Rolle A-M, Hasenberg M, Thornton CR, et al. ImmunoPET/MR imaging allows specific detection of *Aspergillus* lung infection *in vivo*. *Proc Natl Acad Sci USA.* 2016;113:E1026–E1033.
2. Davies G, Rolle A-M, Maurer A, et al. Towards translational immunoPET/MR imaging of invasive pulmonary aspergillosis: the humanised monoclonal antibody JF5 detects *Aspergillus* lung infections *in vivo*. *Theranostics.* 2017;7:3398–3414.
3. Henneberg S, Hasenberg A, Maurer A, et al. Antibody-guided *in vivo* imaging of *Aspergillus fumigatus* lung infections during anti-fungal azole treatment. *Nat Commun.* 2021;12:1707.

IMMUNO-PET/MRI OF ASPERGILLOSIS • Schwenck et al. 1451

Brain Metabolic PET Findings on the Long-Term Effects of COVID-19

TO THE EDITOR: We would like to thank Meyer et al. for their impressive systematic review on brain PET and SPECT findings on the acute and long-term effects of coronavirus disease 2019 (COVID-19) (*1*). We anticipate that this article will constitute an important reference for this topic, especially for long COVID, also by identifying roadmap points for further studies. Moreover, we believe that the authors' recommendations are reasonable and correspond to our own practice, namely, possible use of PET/SPECT: (a) for differential diagnosis in selected cases after clinical evaluation within the framework of existing authorizations and recommendations (*2*), particularly for encephalitis and neurodegenerative diseases; and (b) when neurologic disorders have persisted several months, or—in the event of worsening—for cerebral assessment of such patients after a clinical evaluation to confirm such impairments, which we believe cannot be limited to the cognitive domain and consequently only to neuropsychiatric testing (e.g., dysautonomia).

We would like to clarify several points concerning our previous publications, on which recommendations for long COVID are partly based.

As accurately highlighted by our colleagues (*1*), the inclusion criteria of time spans from initial infection have fluctuated in our studies (*3,4*), albeit in accordance with the fluctuations of the French and international definitions of the condition (3 wk, 1 mo, and now 3 mo). The definition used at the time of publication was justified in our articles (*3,4*). We fully recognize the possible impact of this delay on PET findings and the need for further standardized studies based on the current clinical definition of long COVID. In this line, we recently showed, in a multicentric study including 143 patients, a consensual profile of brain hypometabolism on visual interpretation for approximately one half of patients with suspected neurologic long COVID approximately 11 mo after symptom onset, whereas the second half of patients had normal brain PET metabolism (*5*). We also agree that recommendations for the clinical use of PET imaging must take into account a delay of confirmed persistent symptoms (>3–6 mo for Meyer et al. (*1*)).

Meyer et al. suggested that our PET results were unjustifiably obtained with 2 distinct statistical thresholds in the 2 studies ("$P < 0.05$, FWE-corrected [familywise-error–corrected] in adults; $P < 0.001$, uncorrected in children") (*1*). The same statistical thresholds were in fact used for the 2 studies (*3,4*). The reader can refer to the methods and Table 2 of the 2 studies (P [voxel] < 0.001; P [cluster] < 0.05, familywise-error–corrected) (*3,4*).

Meyer et al. mentioned that we reported a "weak" negative association between the number of complaints and the PET metabolism of the brain stem and cerebellum ("$r^2 = 0.1$ and 0.34, respectively") (*1*). Similarly, the reader can refer to the results of our study: the r^2 was in fact 0.19 and 0.34 ($r = -0.440$ and -0.581, $P = 0.004$ and $P < 0.001$, respectively) (*3*).

Meyer et al. mentioned that our hypotheses concerning metabolic modifications in long COVID changed between the 2 studies, from "neurotropism" to "inflammatory," "dysimmune," or "vascular" damage (*1*). The term *neurotropism* refers both to the direct hypothetic effects of brain viral propagation and to the possible indirect effects of the virus on inflammatory, dysimmune, or vascular damage (*6*). We believe that these hypotheses are well explained in our previous papers (*3,4,7,8*), including the one (*3*) quoted specifically by Meyer et al. supposedly to exclude alternative explanations (*1*) (immune-inflammation disorder; lesions possibly involving direct infection injury, hypoxia, and immune injuries; hypothesis of brain hypometabolic dysfunction secondary to earlier hypermetabolic inflammation; treatment of the possible inflammatory olfactive gateway and stimulation of this hypofunctional brain network). Meyer et al. also pointed out that the hypothesis of neurotropism from olfactory bulbs is independent of anosmia, since not all patients with long COVID and brain hypometabolism have functional complaints of olfactory functions. Brain impairment is not systematically associated with functional complaints, and anosognosia of olfactory deficits has been reported in patients with long COVID (*9*). Importantly, a recent controlled longitudinal study with MRI performed on 785 subjects before and during the outbreak demonstrated an increased reduction in gray matter thickness and tissue contrast within limbic regions connected to the olfactory regions in infected patients (*6*).

Meyer et al. mentioned that we considered psychologic explanation as an equal hypothesis in our last article (*4*) (Table 2 (*1*): "[s]everal possible explanations [inflammatory, immune, neurotropism, vascular, gut–brain disturbance, psychologic], but none clearly favored"). Psychologic factors were considered in our 2 previous publications as possible contributors to organic explanations and not as exclusive alternatives (possible entanglement with other factors and particularly psychologic factors (*3*) and possible interactions with psychologic factors (*4*)). Importantly, our PET results were also obtained by comparing long-COVID patients with age-matched control patients with functional symptoms, in whom somatic cerebral diseases were thereafter excluded at follow-up (*4*), bringing additional arguments against exclusive psychologic explanations. We also noticed that this profile is distinct from those associated with the lockdown impact (*10*).

Finally, Meyer et al. proposed an interesting methodologic discussion on various postprocessing choices, including the tricky issue of activity normalization, with the proposal to further develop principal-component analyses. Such considerations have been extensively discussed regarding possible advantages and limits, as have discrepancies among studies in addition to the heterogeneity of patients (*7*).

REFERENCES

1. Meyer PT, Hellwig S, Blazhenets G, Hosp JA. Molecular imaging findings on acute and long-term effects of COVID-19 on the brain: a systematic review. *J Nucl Med.* February 17, 2022 [Epub ahead of print].
2. Guedj E, Varrone A, Boellaard R, et al. EANM procedure guidelines for brain PET imaging using. *Eur J Nucl Med Mol Imaging.* 2022;49:632–651.
3. Guedj E, Campion JY, Dudouet P, et al. ^{18}F-FDG brain PET hypometabolism in patients with long COVID. *Eur J Nucl Med Mol Imaging.* 2021;48:2823–2833.
4. Morand A, Campion JY, Lepine A, et al. Similar patterns of [^{18}F]-FDG brain PET hypometabolism in paediatric and adult patients with long COVID: a paediatric case series. *Eur J Nucl Med Mol Imaging.* 2022;49:913–920.

---

5. Verger A, Kas A, Dudouet P, Goehringer F, Salmon-Ceron D, Guedj E. Visual interpretation of brain hypometabolism related to neurological long COVID: a French multicentric experience. *Eur J Nucl Med Mol Imaging.* March 23, 2022 [Epub ahead of print].
6. Douaud G, Lee S, Alfaro-Almagro F, et al. SARS-CoV-2 is associated with changes in brain structure in UK Biobank. *Nature.* 2022;604:697–707.
7. Guedj E, Morbelli S, Kaphan E, et al. From early limbic inflammation to long COVID sequelae. *Brain.* 2021;144:e65.
8. Guedj E, Lazarini F, Morbelli S, et al. Long COVID and the brain network of Proust's madeleine: targeting the olfactory pathway. *Clin Microbiol Infect.* 2021;27:1196–1198.
9. Voruz P, Cionca A, Jacot de Alcântara I, et al. Functional connectivity underlying cognitive and psychiatric symptoms in post-COVID-19 syndrome: is anosognosia a key determinant? *Brain Commun.* 2022;4:fcac057.
10. Guedj E, Campion JY, Horowitz T, Barthelemy F, Cammilleri S, Ceccaldi M. The impact of COVID-19 lockdown on brain metabolism. *Hum Brain Mapp.* 2021;43: 593–597.

Eric Guedj*
Tatiana Horowitz
**Timone Hospital, Marseille, France*
E-mail: eric.guedj@ap-hm.fr

DOI: 10.2967/jnumed.122.264179


IMPACT FACTOR
11.082
#1 NUCLEAR MEDICINE, MOLECULAR IMAGING AND MOLECULAR RADIOTHERAPY JOURNAL
FEATURED ARTICLE
Immune response
1
2
COVID-19 vaccination

CALL FOR ABSTRACTS

If you are a young professional in the field, we invite you to a submit clinical or scientific abstract for the **2023 SNMMI Mid-Winter and ACNM Annual Meeting** on one of the following topics:

- Aspects of Clinical and Basic Science in Nuclear Medicine
- Correlative Imaging in Nuclear Medicine and Radiology
- Nuclear Pharmacy and Physics
- Nuclear Cardiology
- Theranostics
- Quality and Safety in Nuclear Medicine

2023 ACNM Annual Meeting Abstract AWARDS

Learn more about award opportunities available when you submit your abstract for the 2023 ACNM Annual Meeting.

ABSTRACT SUBMISSION DEADLINE:

OCTOBER 12, 2022

www.snmmi.org/MWM2023

JANUARY 26-28
2023

SNMMI
2023 Mid-Winter Meeting

ACNM
ANNUAL MEETING

SNMMI MID-WINTER AND ACNM ANNUAL MEETING

San Francisco

SNMMI Designated Radiopharmaceutical Therapy Centers of Excellence

SNMMI designated centers meet strict regulatory, training, qualification, experience, and performance criteria to help assure patients, their families, referring physicians, and payors that rigorous procedures are in place and followed, leading to appropriate patient selection and outcomes from radiopharmaceutical therapy.

THE FOLLOWING SITES HAVE BEEN DESIGNATED AS SNMMI RADIOPHARMACEUTICAL THERAPY CENTERS OF EXCELLENCE:

CLINICAL CENTERS OF EXCELLENCE

- ARA Theranostics Center
- ChristianaCare
- Excel Diagnostics and Nuclear Oncology Center
- Hoag Memorial Hospital Presbyterian
- Kettering Health Main Campus
- Northwestern Memorial Hospital

COMPREHENSIVE CENTERS OF EXCELLENCE

- Ahmanson Translational Theranostics Division, David Geffen School of Medicine at UCLA, UCLA Heath Medical Center
- Dana-Farber /Brigham and Women’s Cancer Center
- Duke University Health
- Emory University Hospital
- M Health Fairview University of Minnesota Medical Center - East Bank Hospital
- Mayo Clinic
- MD Anderson Cancer Center
- Memorial Sloan Kettering Cancer Center
- Mount Sinai Health System
- SSM Saint Louis University Hospital
- Stanford University - Stanford HealthCare
- The Ohio State University Wexner Medical Center - The James Hospital and Solove Research Institute
- University of California, San Francisco
- University of Colorado Anschutz Medical Center
- University of Iowa
- University of Pittsburgh Medical Center (UPMC)

SNMMI is currently accepting applications from centers based in the United States (its territories) and Canada.

Visit **www.snmmi.org/RPTCoE** to get started.

SNMMI Value Initiative
SOCIETY OF NUCLEAR MEDICINE & MOLECULAR IMAGING

9/22

The Journal of Nuclear Medicine

September 2022 ■ Vol. 63 ■ Pages 1285–1453